Arab J Sci Eng
DOI 10.1007/s13369-016-2236-x

RESEARCH ARTICLE - CIVIL ENGINEERING

Water Surface Profile Computation for Compound Channels with Narrow Flood Plains

B. Naik[1] · **K. K. Khatua**[1]

Received: 7 October 2015 / Accepted: 8 June 2016

Abstract A multivariable regression model has been developed to predict the water surface profile for different compound channels with the non-prismatic flood plain. The nonlinear regression models are developed using relevant experimental data obtained from laboratory experiments. Three sets of laboratory experiments were carried out to exhibit the overbank flow in converging flood plains. The water surface profiles flow measurement was then related to various dimensionless parameters such as converging angle, width ratio and relative distance to develop the model. The results of calculations of water surface profile from the present model show good agreement with the observed data and data of other researchers. Several statistically based analyses were performed to verify the reliability of the developed multivariable regression model.

Keywords Water surface profile · Non-prismatic compound channel · Converging angle · Relative depth

List of symbols

B	Width of compound channel
b	Width of the main channel
h	Height of the main channel
H	Bank full depth
L	Converging length
S	Bottom slope
α	Width ratio (B/b)
δ	Aspect ratio (b/h)
β	Relative depth ($(H-h)/H$))
X_{r}	Relative distance (x/L)
x	Distance between two consecutive sections
θ	Converging angle
Ψ	Non-dimensional water surface profile (H/h)
P_i	Predicted value
O_i	Observed value
MAE	Mean absolute error
MAPE	Mean absolute percentage error
MSE	Mean-squared error
RMSE	Root-mean-squared error

1 Introduction

Rivers play an important role for human civilizations, as we depend upon the river for day-to-day functioning of our life. Due to the continuous use of rivers, larger settlements have grown on the waterway floodplains and made the floodplain convergent. So during the flood, it has resulted in increased loss of life and economic costs due to improper estimation of water surface profile. Generally, natural compound rivers have varying floodplains, so they are called as non-prismatic compound rivers. As natural rivers are non-prismatic in nature, the flow always changes from uniform to non-uniform. Flow modelling in the non-prismatic compound channel is a complex task. Several investigators such as (Sellin [1], Myers and Elsawy [2], Knight et al [3], Khatua et al [4]) have performed extensive research on flow modelling on straight and meandering prismatic compound channels but very less report are found on non-prismatic compound channels. James and Brown [5] investigated that the flow on the expanding floodplain accelerated, whilst the

✉ B. Naik
banditanaik1982@gmail.com

K. K. Khatua
kkkhatua@yahoo.com

[1] Department of Civil Engineering, N.I.T. Rourkela, Rourkela 769008, India

Published online: 25 June 2016

flow on the converging floodplain decelerated. First experiments on converging compound channels with symmetrically narrowing floodplains were performed by Bousmar [6], Bousmar et al. [7] and Rezaei [8] and Rezaei and Knight [9]. These experiments highlighted the geometrical momentum transfer and the associated additional head loss. Proust et al. [10] investigated an asymmetric geometry with a more abrupt convergence. He concluded that larger mass transfer and total head loss resulted from the higher convergence angle (22°). Chlebek et al [11] analysed and compared the flow behaviour of different geometries compound channels namely, skewed channel, symmetrically converging and diverging channels. Recently, Rezaei and Knight [12], Hojjat et al. [13], Naik and Khatua [14] carried out a new experiment on the converging compound channel and produced much more detailed data sets than the previously existing ones. But all the above-mentioned studies have focused on the effect of changes in floodplain sections to evaluate the discharge. The effect of geometry and flow conditions on water surface profile in non-prismatic compound channels has not yet been considered properly. Therefore, a reliable water surface profile modelling is required to identify flooded areas which will be helpful for flood mitigation and risk management study. The effect of contraction of floodplain width on the water depth prediction in a compound channel is now investigated to analyse the dependency of different geometrical and a hydraulic parameter for prediction of water surface profile of a converging compound channel. In the present work, based on the experimental data of National Institute of Technology, Rourkela and Rezaei [8] data, an attempt has been made to develop a reliable mathematical model to predict the water surface profile of compound channel with converging floodplains for different converging angles. The results have been compared well with the observed data sets.

2 Experimental Set-up

Present work on surface water profile of compound channel with converging floodplains has been performed at the Hydraulics and Fluid mechanics Laboratory of Civil Engineering Department of National Institute of Technology, Rourkela, India. All the experiments were carried out in a concrete flume of 15 m long, 0.90 m wide, 0.10 m deep and average bottom slope(s) of 0.0011. Three sets of converging compound channels with varying cross sections were built inside the concrete flume with Perspex sheet. The width ratio of the prismatic part of the channel was $\alpha = 1.8$, and the aspect ratio of the main channel was $\delta = 5$. Keeping the geometry constant, the converging angles of the channels were varied as 12.38°, 9° and 5°, respectively. These have been done to study the effect of converging floodplain angles and water surface profile prediction of converging compound channels. The converging length of the channels was found to be 0.84, 1.26 and 2.28 m, respectively. The roughness of the floodplain and main channel was maintained identical, and the Manning's n was determined as 0.011 from the experimental runs in the channel. Water was supplied to the flume from an underground sump via an overhead tank by series of centrifugal pumps (15 hp capacity each) and recirculated to the sump after flowing through the converging compound channels. A downstream volumetric tank fitted with closure valves for measuring the actual discharge flowing through the channel. An adjustable vertical gate along with flow straighteners was provided in upstream section sufficiently ahead of the head gate to reduce turbulence and velocity of approach. A movable bridge was provided across the flume for both spanwise and streamwise movements of the instrument over the channel area so that each location on the plain of the converging compound channel could be accessed for taking measurements. Series of micro-pitot tubes of 4.77 mm external diameter in conjunction with a suitable vertical manometer and a 16-Mhz Micro-ADV (Acoustic Doppler Velocity-meter) were used to measure longitudinal velocities at a number of locations across the predefined channel section. Water surface depths were measured directly with a point gauge located on an instrument carriage. The flow depth measurements were taken along the centre of the flume at an interval of 0.5 m in both upstream and downstream prismatic parts of the flume and at every 0.1 m in converging part of the flume. Figure 1a shows the plan view of the compound channel with converging floodplains. Figure 1b shows the longitudinal and cross-sectional dimension of the non-prismatic compound channels. Figure 1c shows the non-prismatic compound channel with travelling bridges and flow instruments. Similarly, experiments were conducted by using an 18-m flume at the University of Birmingham, Department of Civil Engineering. A compound channel of simple rectangular cross section was selected, and all experiments were performed in a straight flume, 18 m long, almost 1200 mm wide, 400 mm deep, and with the average bottom slope of 2.003×10^3. Using PVC material, rigid and smooth boundaries were constructed, both for the main channel of 0.398 m width and 0.05 m depth, as also for the floodplains 0.4 m wide. Three sets of experiments were performed in non-prismatic compound channels of convergence angles $\theta = 1.91°$, $\theta = 3.81°$ and $\theta = 11.31°$ [8].

3 Experimental Results

Stage discharge relationship of the starting test reaches prismatic and midsections of non-prismatic part for the different converging compound channel of angle 12.38°, 9°, 5° from in-bank to overbank flow conditions which are shown in Fig. 2a, b, respectively. A total 13-stage discharge runs

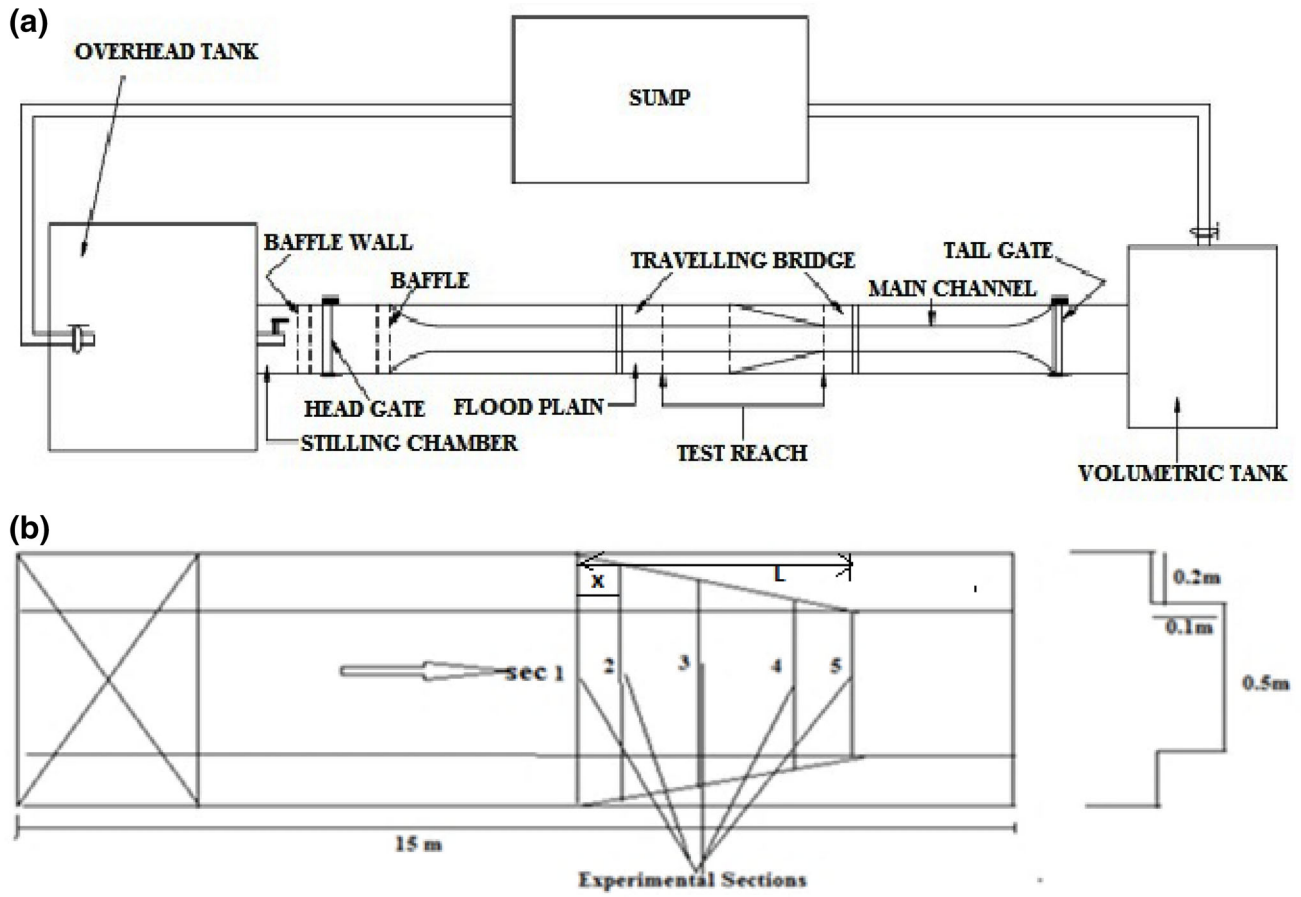

(c)

Fig. 1 **a** Plan view of compound channel with non-prismatic floodplains. **b** Longitudinal and cross-sectional dimension of the non-prismatic compound channels. **c** Non-prismatic compound channel with travelling bridges and flow instruments

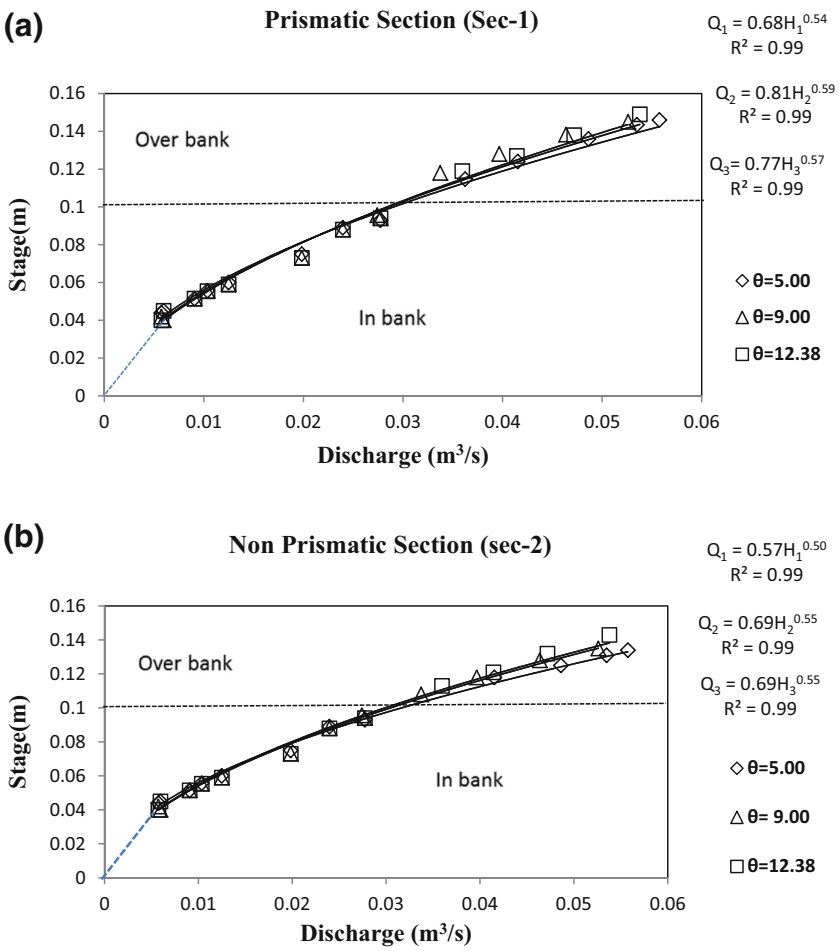

Fig. 2 **a** Stage discharge relationship at the entry of compound channels with converging floodplain of angles 12.38°, 9°, 5° (*prismatic part*) **b** Stage discharge at the middle section of compound channels with converging floodplain of angles 12.38° 9°, 5° (*non-prismatic part*)

of the compound channel with converging flood plains are observed. From Fig 2a, b, we observed that when the converging angle increases for the same stage, discharge also increases. The trends of stage discharge relationships are found to be power functions with high values of R^2 as shown in Fig 2a, b, respectively. Again, all the stage discharge relationships are following the trend $Q = a(H)^n$,where a and n are coefficients as shown in Fig 2a, b. Figure 3a–c shows the water surface profile for different relative depths of different converging floodplains, i.e., 12.38°, 9° and 5°, respectively. It can be noticed from Fig. 3a–c that when the relative distance increases the depth of flow decreases and the decrease is sharp for lower converging angle as compared to higher converging angle. For reference, the typical velocity contour of both prismatic and midsections of non-prismatic part for converging compound channel of angle 12.38° for different flow depths is shown in Fig. 4a, b, respectively. From Fig. 4a, we observed that minimum velocity occurs at the bottom corner of the main channel and floodplain. Maximum velocity occurs at both sides of centreline of the main channel. From Fig. 4b, it can be noticed that maximum velocity occurs at the central region of the main channel.

4 Water Surface Profile Computation and Model Development

An attempt has been made here to model water surface profile for the compound channel with different converging floodplains. The flow can be assumed to be uniform till prismatic part, whereas for the non-prismatic part the flow is found to be non-uniform. Non-dimensional water surface profile has been derived from three different types of converging compound channels fabricated at Hydraulics Laboratory of NIT, Rourkela, India, along with three sets data of Rezaei [8] (details of the data sets are given in Table 1). All these channels have been made homogeneous roughness in both the main channel and floodplain surfaces. Manning's n values for all these smooth surfaces are found to be 0.01. A distinct multiple variable linear regression model has been developed to predict taking five most influencing dimensionless independent parameters. The relationships are expressed as

$$\Psi = F(\alpha, \beta, \delta, \theta, X_r) \text{ for a compound channel with non-prismatic flood plain} \quad (1)$$

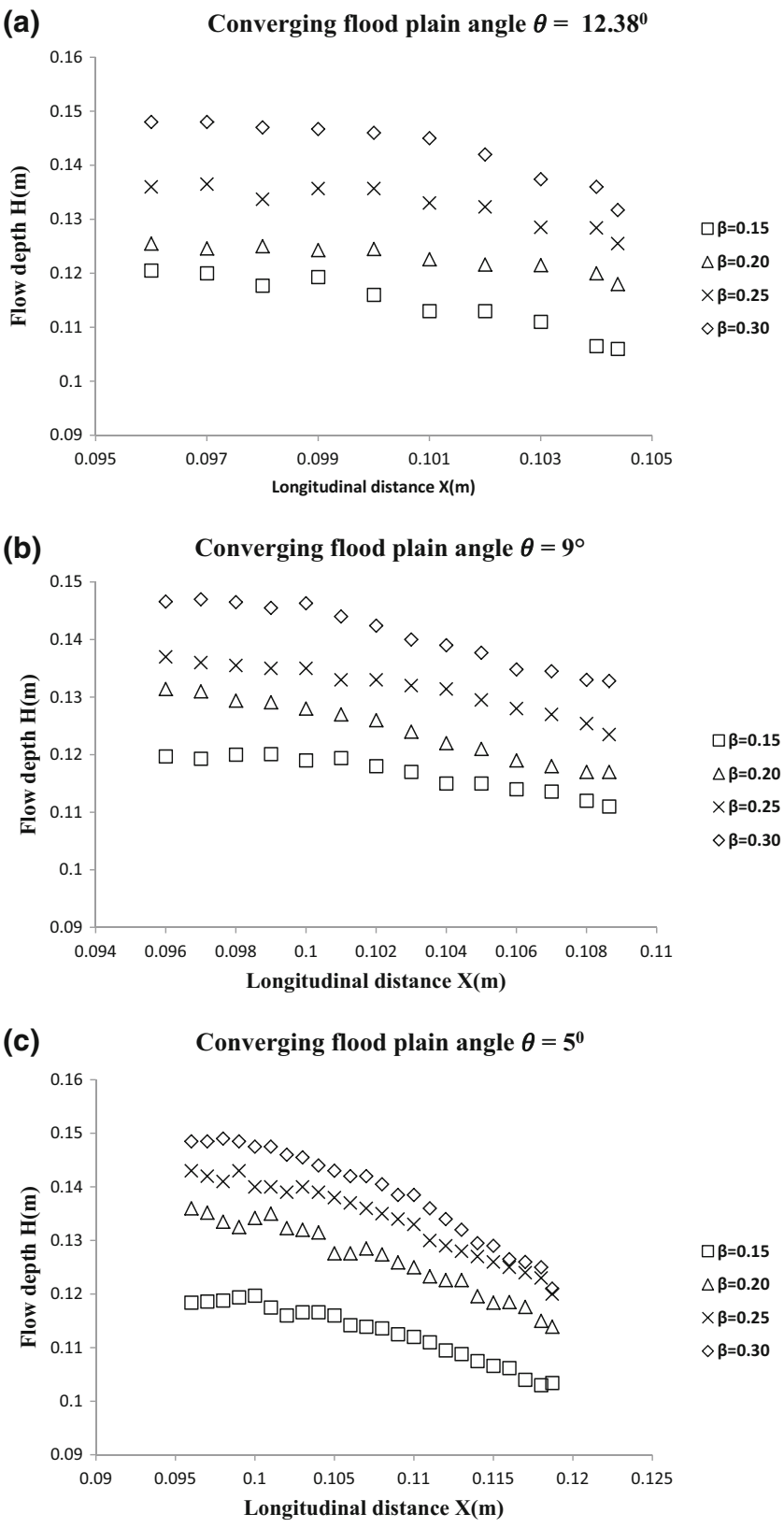

Fig. 3 Water surface profile for compound channel with different converging floodplains for different flow depths (β). **a** 12.38°, **b** $\theta = 9°$, **c** $\theta = 5°$

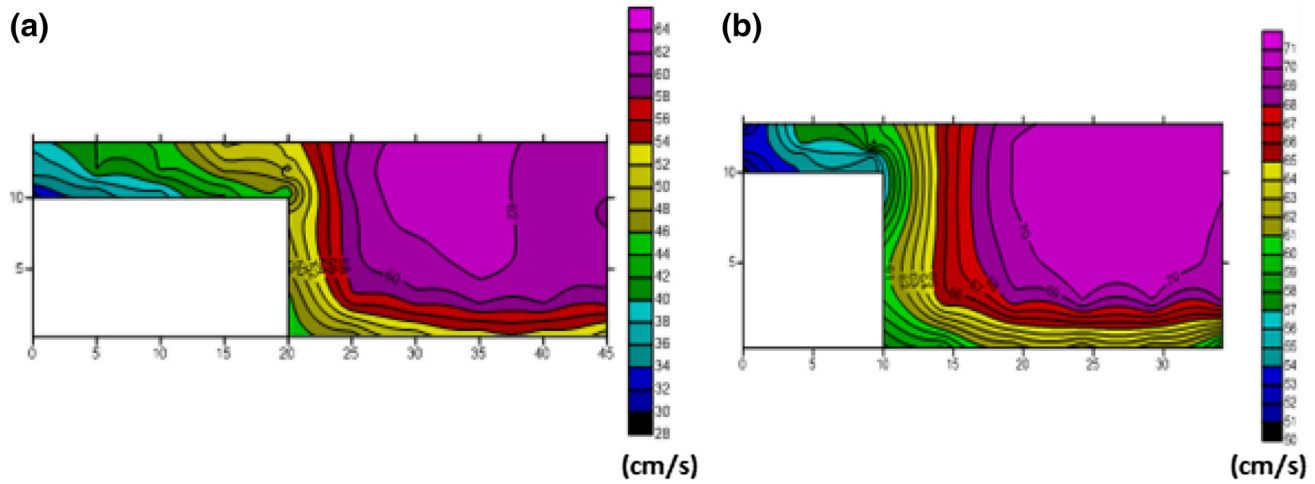

Fig. 4 Velocity contour for compound channel with converging floodplain 12.38°. **a** Prismatic section (sec-1), **b** non-prismatic sections (sec-2) (typical case)

where F represents the functional symbol, α is the width ratio (B/b), β is the relative depth $(H - h/H)$, δ is the channel aspect ratio (b/h), θ is converging angle and X_r is relative distance (x/total non-prismatic length). The independent parameter of β and δ has been chosen from the prismatic part, whereas α, θ and X_r have been chosen from non-prismatic part of the channels. Here, our intension is to predict the non-dimensional water surface profile along the non-prismatic part of the channel. The dependency of non-dimensional water surface profile and the best functional relationships of it have been found out from different plots described below.

4.1 Variation of Non-dimensional Water Surface Profile with Width Ratio α

The variation of non-dimensional water surface profile Ψ in terms of width ratio θ for different converging angles θ is presented in Figs. 5, 6, 7, 8, 9 and 10. Figures 5, 6 and 7 show the variation of water surface profile of converging compound channels of different converging angles of 12.38°, 9°, 5°, respectively. Here, the Ψ has been plotted for four flow discharge cases which bear the relative flow depth β of 0.15, 0.2, 0.25 and 0.3 at the entry of converging part, i.e., prismatic floodplain section (sec-1), respectively. Here, the relative flow depth β at sec-1, i.e., end of the prismatic part of the flood plain, is considered here as reference. The main observation obtained from Figs. 5, 6 and 7 is that for all the discharges, the non-dimensional water surface profile Ψ is found to increase while we travel along the cross-sectional length and along the flow direction. Again, the water surface profile Ψ is found to increase as the relative depth increase. The best fit curves for their relationship are found to be power functions. Figures 8, 9 and 10 show the plot of non-dimensional water surface profile Ψ of non-prismatic part for converging compound channels of the data of Rezaei [8]. Figure 8 is meant for converging angle 11.31°, and Figs. 9 and 10 are for converging angle 3.81° and 1.91°, respectively. The trend of non-dimensional water surface profile Ψ for Rezaei [8] channels is same as NIT Rourkela data. But the best fit curves for Rezaei [8] channels are found to be linear functions because of different aspect ratio and slope of channel.

The fundamental relationships of Ψ with α for different channels of different aspect ratios are presented below. All the equations bear the R^2 value varying between 0.95 and 0.99.

$$\Psi = F_1(\alpha) = 1.06(\alpha)^{0.22} \quad \text{for lower-aspect-ratio channel 1} \tag{2}$$

$$\Psi = F_2(\alpha) = 1.16(\alpha)^{0.22} \quad \text{for lower-aspect-ratio channel 2} \tag{3}$$

$$\Psi = F_3(\alpha) = 1.21(\alpha)^{0.29} \quad \text{for lower-aspect-ratio channel 3} \tag{4}$$

$$\Psi = F_4(\alpha) = 0.07(\alpha) + 1.78 \quad \text{for higher-aspect-ratio channel 1} \tag{5}$$

$$\Psi = F_5(\alpha) = 0.05(\alpha) + 1.28 \quad \text{for higher-aspect-ratio channel 2} \tag{6}$$

$$\Psi = F_6(\alpha) = 0.13(\alpha) + 1.25 \quad \text{for higher-aspect-ratio channel 3} \tag{7}$$

4.2 Variation of Non-dimensional Water Surface Profile with Relative Distance X_r

The effect of relative distance X_r on the non-dimensional water surface profiles has been investigated in this section.

Table 1 Hydraulic parameters for the experimental channel data sets

Verified test channel	Type of channels	Converging angle (Θ)	Longitudinal slope (S)	Cross-sectional geometry	Total channel width (B, m)	Main channel width (b, m)	Main channel depth (h, m)	Width ratio at begining B/b (α)	Converging length ratio (X_r, m)	Aspect ratio b/h (δ)
Rezaei (2006)	Convergent (CV2)	11.31°	0.002	Rectangular	1.2	0.398	0.05	3	2	7.96
Rezaei (2006)	Convergent (CV6)	3.81°	0.002	Rectangular	1.2	0.398	0.05	3	6	7.96
Rezaei (2006)	Convergent (CV6)	1.91°	0.002	Rectangular	1.2	0.398	0.05	3	6	7.96
N.I.T. Rkl	Convergent	5°	0.0011	Rectangular	0.9	0.5	0.1	1.8	2.28	5
N.I.T. Rkl	Convergent	9°	0.0011	Rectangular	0.9	0.5	0.1	1.8	1.26	5
N.I.T. Rkl	Convergent	12.38°	0.0011	Rectangular	0.9	0.5	0.1	1.8	0.84	5

The variation of Ψ in terms of relative distance X_r for different converging angles θ is presented in Figs. 11, 12, 13, 14, 15 and 16. It can be noticed from Figs. 11, 12, 13, 14, 15 and 16 that the water surface profile is found to fall when the relative distance X_r increases. It shows that converging transition increases the velocity head rapidly, hence lowering the potential head. This can also be clarified from velocity contours of Fig. 4a, b. The fall is very high for higher converging floodplain angles. The trends of fall are found to be linear for all the converging compound channels. Rezaei [8] channels provide flatter water surface profile variations as compared to present experimental channels because present experimental channels have low width ratio, i.e., narrow floodplain as compared to Rezaei [8] channels.

Again the relationships of Ψ with X_r for different channels of different aspect ratios are presented below. All equations bear R^2 value varying between 0.93 and 0.99.

$$\Psi = F_7(X_r) = -0.14(X_r) + 1.22 \quad \text{for lower-aspect-ratio channel 1} \tag{8}$$

$$\Psi = F_8(X_r) = -0.15(X_r) + 1.32 \quad \text{for lower-aspect-ratio channel 2} \tag{9}$$

$$\Psi = F_9(X_r) = -0.22(X_r) + 1.37 \quad \text{for lower-aspect-ratio channel 3} \tag{10}$$

$$\Psi = F_{10}(X_r) = -0.15(X_r) + 2.01 \quad \text{for higher-aspect-ratio channel 1} \tag{11}$$

$$\Psi = F_{11}(X_r) = -0.16(X_r) + 1.45 \quad \text{for higher-aspect-ratio channel 2} \tag{12}$$

$$\Psi = F_{12}(X_r) = -0.21(X_r) + 1.67 \quad \text{for higher-aspect-ratio channel-3} \tag{13}$$

Relationships of these non-dimensional parameters with Ψ presented from Eqs. (1) to (12) are attempted to compile to get a generalize expression for Ψ. To achieve this, we have applied all these equations to multilinear regression software and finally six equations are obtained for different converging angles, i.e., (lower-aspect-ratio and higher-aspect-ratio channel 1, 2, 3). The equations are obtained

$$\Psi = F_{13}(\alpha, X_r) = -1.22 + 2.27(\alpha)^{0.22} + 0.18(X_r) \quad \text{for lower-aspect-ratio channel 1} \tag{14}$$

$$\Psi = F_{14}(\alpha, X_r) = -1.21 + 2.28(\alpha)^{0.22} + 0.19(X_r) \quad \text{for lower-aspect-ratio channel 2} \tag{15}$$

$$\Psi = F_{15}(\alpha, X_r) = -0.58 + 1.63(\alpha)^{0.29} + 0.18(X_r) \quad \text{for lower-aspect-ratio channel 3} \tag{16}$$

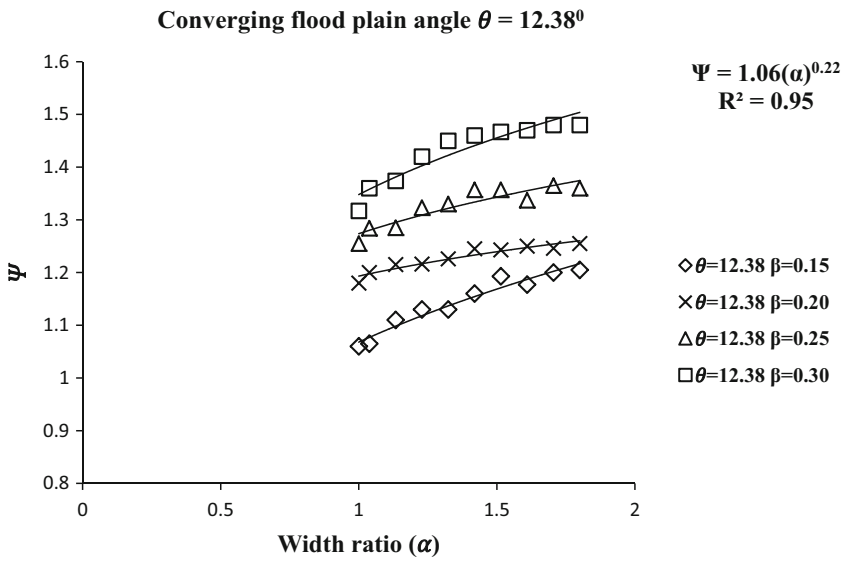

Fig. 5 Variation of water surface profile versus width ratio of different relative depth for converging angle 12.38°

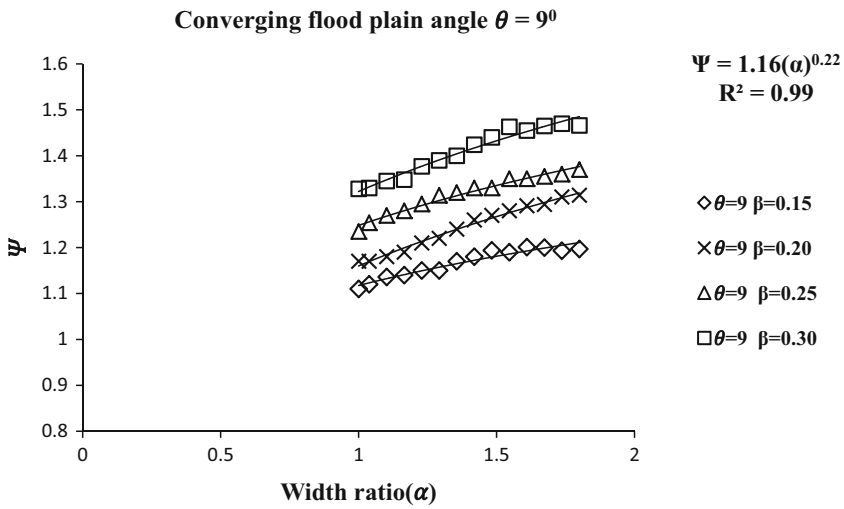

Fig. 6 Variation of water surface profile versus width ratio of different relative depth for converging angle 9°

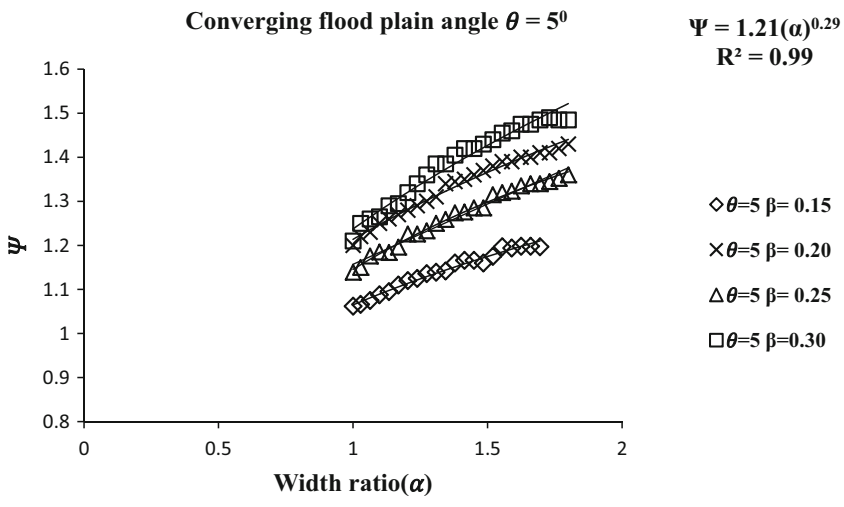

Fig. 7 Variation of water surface profile versus width ratio of different relative depth for converging angle 5°

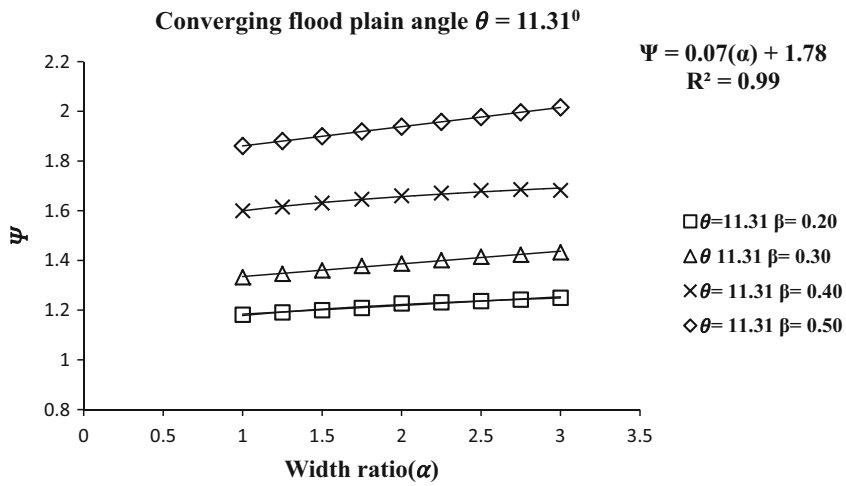

Fig. 8 Variation of water surface profile versus width ratio of different relative depth for converging angle 11.31°

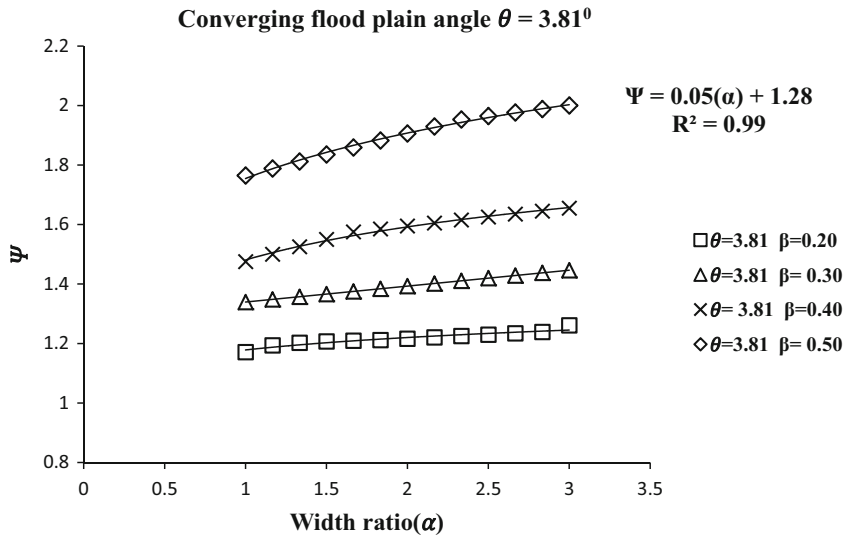

Fig. 9 Variation of water surface profile versus width ratio of different relative depth for converging angle 3.81°

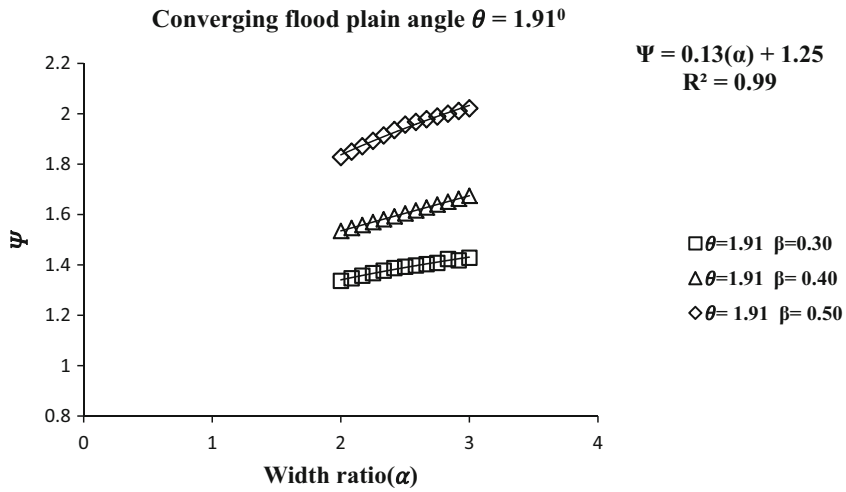

Fig. 10 Variation of water surface profile versus width ratio of different relative depth for converging angle 1.91°

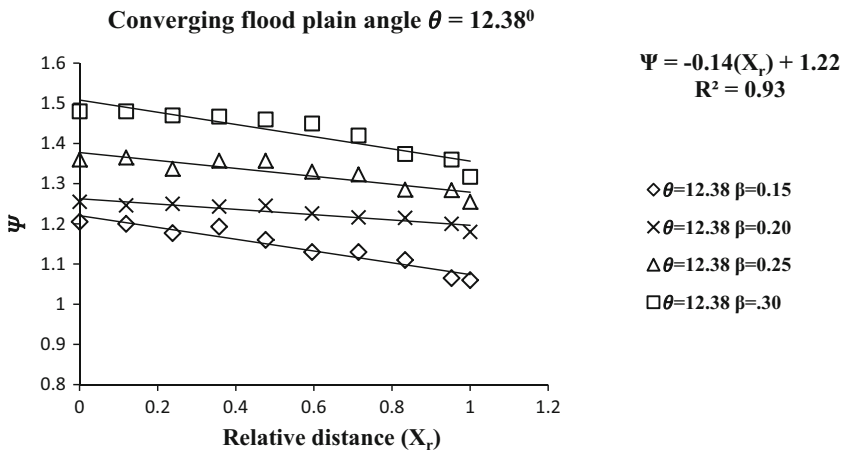

Fig. 11 Variation of water surface profile versus relative distance of different relative depth for converging angle 12.38°

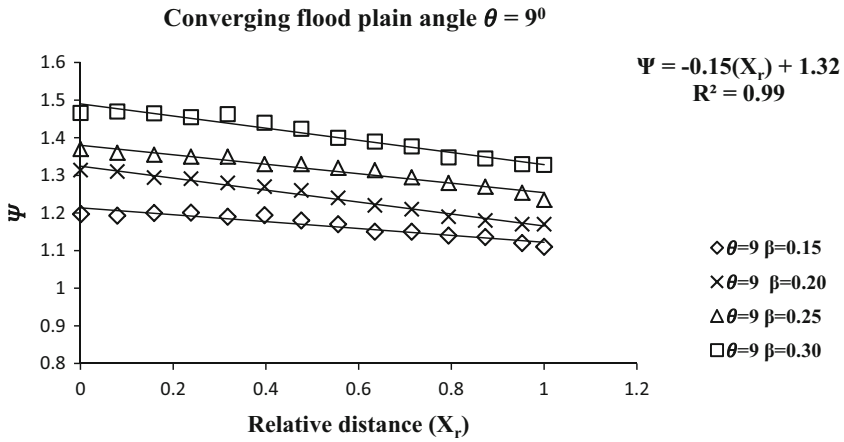

Fig. 12 Variation of water surface profile versus relative distance of different relative depth for converging angle 9°

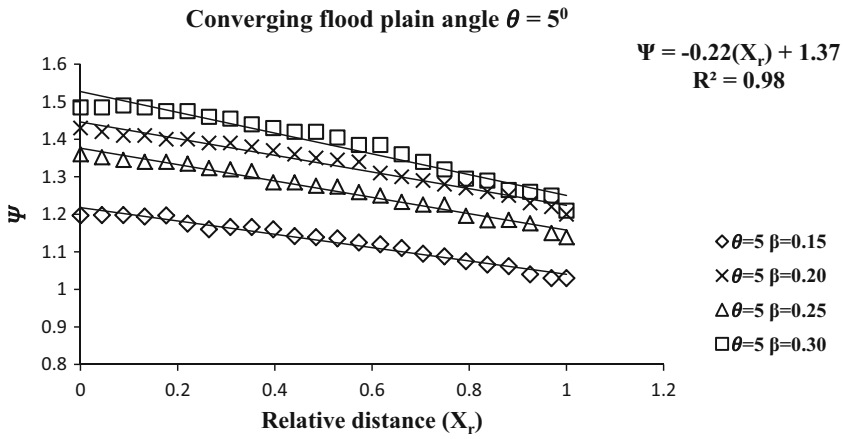

Fig. 13 Variation of water surface profile versus relative distance of different relative depth for converging angle 5°

$$\Psi = F_{16}(\alpha, X_r) = -0.66 + 0.29(\alpha) + 0.12(X_r) \quad \text{for higher-aspect-ratio channel 1} \tag{17}$$

$$\Psi = F_{17}(\alpha, X_r) = 0.86 + 0.29(\alpha) + 0.11(X_r) \quad \text{for higher-aspect-ratio channel 2} \tag{18}$$

$$\Psi = F_{18}(\alpha, X_r) = 0.86 + 0.29(\alpha) + 0.12(X_r) \quad \text{for higher-aspect-ratio channel 3} \tag{19}$$

For lower-aspect-ratio channels, the non-dimensional water surface profile Ψ bears a nonlinear relationship with width ratio α and longitudinal distance X_r, whereas for higher-aspect-ratio cases it provides linear relationship with inde-

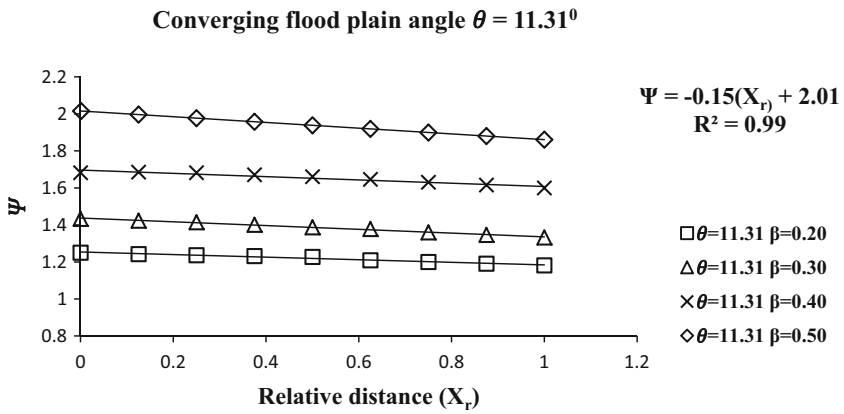

Fig. 14 Variation of water surface profile versus relative distance of different relative depth for converging angle 11.31°

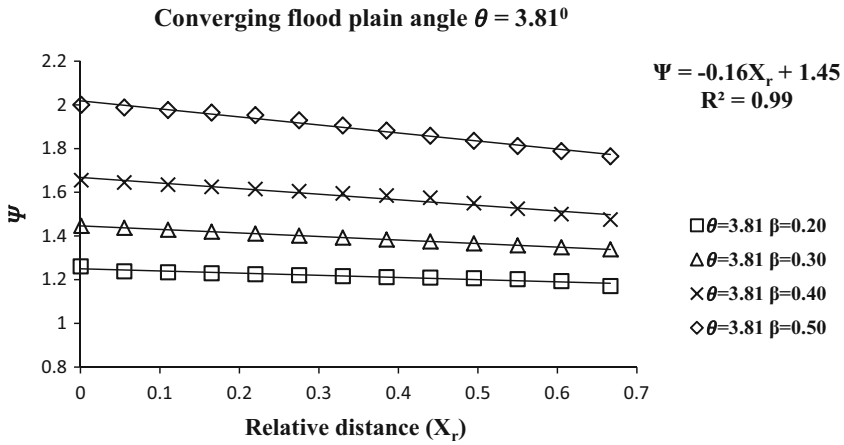

Fig. 15 Variation of water surface profile versus relative distance of different relative depth for converging angle 3.81°

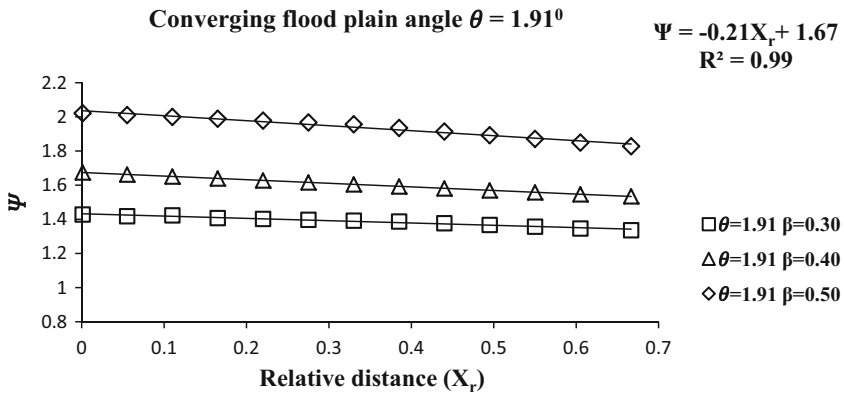

Fig. 16 Variation of water surface profile versus relative distance of different relative depth for converging angle 1.91°

pendent variables. Table 2 provides the total error analysis from Eqs. (13)–(18) obtained from multilinear regression model. The equations bearing least error have been chosen for further improvement of the model.

Table 3 represent the unstandardized coefficient and regression statistics of the regression analysis. The multivariable linear regression techniques have been used to estimate the regression coefficients associated with the derived multivariable regression models after performing the necessary linear transformations of the dimensionless groups. When deriving the generalized empirical models for Ψ as presented in Eq. (13), optimization of 4 main regression statistics was done to arrive at the best possible prediction regression equation. The estimated values of the 4 deployed statistics are provided in Table 3. The corresponding variable coefficient t statistic values are generally high ranging from 3.28 to 25.96 which results in a confidence level of 99.99 %. The empirical prediction models for Ψ presented in Eq. (13) are significant at a confidence level of 99.99 % as the model F-statistic is equal to the value of 541.23 as provided in Table 3. The predictive models have a determination coefficient (R^2) of 0.895. The last statistic used is the model standard error of

Table 2 Detail error analysis of six equations

Sl. no.	Equations	MAPE
Equation 13	$\Psi = -1.22 + 2.27(\alpha)^{0.22} + 0.18X_r$	2.49
Equation 14	$\Psi = -1.21 + 2.28(\alpha)^{0.22} + 0.19X_r$	4.51
Equation 15	$\Psi = -0.58 + 1.63(\alpha)^{0.29} + 0.18X_r$	5.56
Equation 16	$\Psi = -0.66 + 0.29\,(\alpha) + 0.12X_r$	8.61
Equation 17	$\Psi = 0.86 + 0.29\,(\alpha) + 0.114X_r$	7.65
Equation 18	$\Psi = 0.86 + 0.29\,(\alpha) + 0.12X_r$	9.73

estimate which is generally small compared to Ψ the predicted values with its value being equal to 0.043.

An attempt is further made to compile the dependency of Ψ with the effect of converging angle θ which is now discussed in the next section.

4.3 Variation of Non-dimensional Water Surface Profile with Converging Angle θ

Non-dimensional water surface profile (Ψ) is dependent upon the geometry and flow variables. Thus, (Ψ) is found to be varying along the length of the channel and is greatly affected by the variations of converging floodplain angle θ. Our intension is to develop a generalized model taking care of these parameters. Equations (13)–(18) have been found to provide good results for particular converging angles, e.g., Eq. (13) found to provide good results for converging angles θ of 12.38°. Same equation cannot be applied for other converging angle cases; if we applied for other converging angle cases, it provides poor results. This may be due to non-inclusion of converging angle θ. So there is a need for further improvement for the model for incorporating the effect of converging angle θ.

After obtaining six multilinear equations based on geometry, i.e., width ratio α and relative distance X_r, Eq. (13) is found to provide least error. It can be noticed from Fig. 17 that Ψ^* is found to increase when the relative depth increases. The best fit curves for their relationship are found to be an exponential function, and the value of R^2 is found to be 0.94.

$$\Psi^*(\theta) = \frac{\text{Actual } \Psi}{Eq.\ (13)} \tag{20}$$

$$\frac{\text{Actual } \Psi}{Eq.\ (13)} = e^{0.0017\theta} \tag{21}$$

$$\Psi = e^{0.0017\theta}[-1.21 + 2.25(\alpha)^{0.22} + 0.18\,(X_r)] \tag{22}$$

Equation 22 represents the final form of mathematical expression for the water surface profile of a compound channel with the converging flood plain. Similar mathematical model using this multivariable regression model has been done by other researchers, e.g., Bjerkile et al. [15], Dash and Khatua [16]

Table 3 Summary of statistics associated with multivariable regression predictive models

Predicted variable	Model coefficients	Coefficient t statistic	Confidence level (%)	Model F statistic	Model R^2	Model standard error
Intercept	0.33	3.28	99.99	541.23	0.75	0.043
β	1.95	25.96	99.99			
X_r	−1.18	−8.97	99.99			

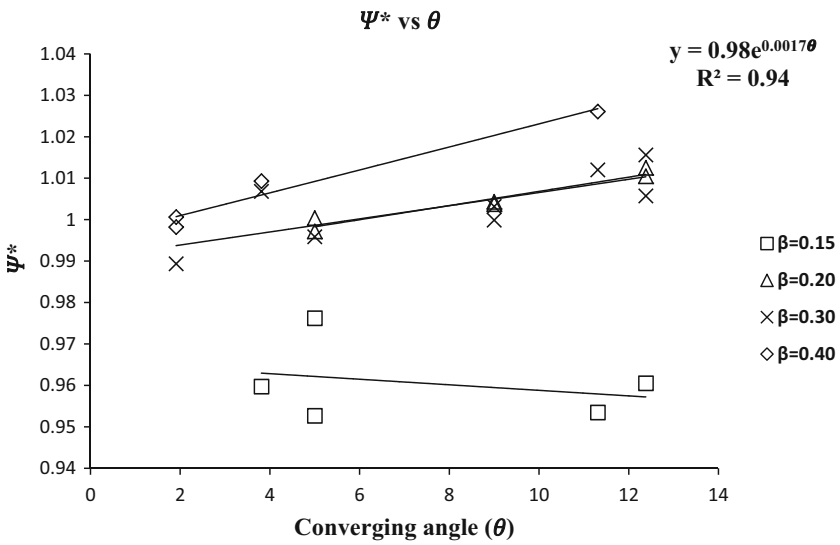

Fig. 17 Variation of Ψ^* versus converging angles (θ) for different relative flow depths (β)

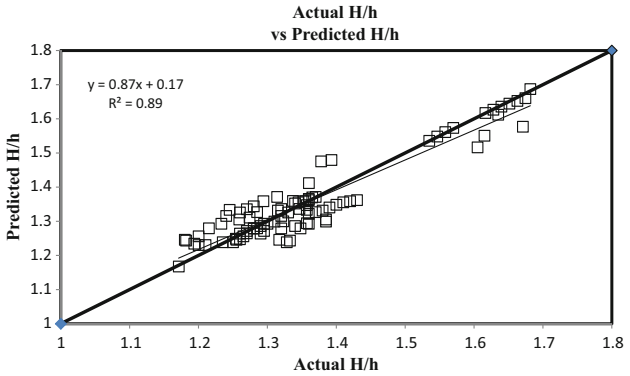

Fig. 18 Scatter plot for observed and modelled value of water surface profile

5 Results and Discussion

5.1 Error Analysis

The variation between the calculated values of water surface profile using Eq. (21) and the corresponding observed values for all the six types of channels is shown in Fig. 18. A regression curve is plotted between observed and calculated values of water surface profile. The present work is a development of a model based on regression analysis, in which around 70 % of data have been used for modelling and 30 % for validation. It can be observed from the data that a high degree of the coefficient of correlation R^2 of 0.89 is obtained, which indicates that the predicted water surface profile is well matching with that of observed values for present experimental channels, as well as Rezaei [8] channels.

To check the strength of the model, error analyses have been done. Mean absolute error (MAE), the mean absolute percentage error (MAPE), mean-squared error (MSE) and the root-mean-squared error (RMSE) for all the converging compound channel for different flow conditions have been estimated. Efficiency criterion like R^2, Nash–Sutcliffe efficiency (E) and index of agreement (I_d) has also been estimated to provide more information on the systematic and dynamic errors present in the model simulation. The definitions of error terms are described below, which have also been used by many researchers such as Dash and Khatua [16]. The detailed results of the error analysis are presented in Table 4.

The expressions used to estimate the various errors include:

1. Mean absolute error (MAE)

The mean absolute error has been evaluated as,

$$\mathrm{MAE} = \frac{1}{n}\sum_{i}^{n}\left|\frac{P_i - O_i}{O_i}\right| \tag{23}$$

Table 4 Different error analysis for Eq. 21

MAE	0.0015
MAPE	2.4296
MSE	0.0019
RMSE	0.0431
E	0.8945
R^2	0.8960
I_d	0.7260

where P_i = predicted values, O_i = observed values

Mean absolute error (MAE) measures how far predicted values are away from observed values. Thus, minimum the deviation of the predicted value from the observed value, better the result will be.

2. Mean absolute percentage error (MAPE)

Mean absolute percentage error is also known as mean absolute percentage deviation. It was usually expressed as a percentage and was defined by the formula

$$\mathrm{MAPE} = \frac{1}{n}\sum_{i}^{n}\left|\frac{O_i - P_i}{O_i}\right| \tag{24}$$

Mean percentage deviation of the predicted value from the observed value is within 10 %; then, the model can be regulated as a good prediction model.

3. Mean-squared error (MSE)

Mean-squared error measures the average of the squares of the errors. It is computed as

$$\mathrm{MSE} = \frac{1}{n}\sum_{i}^{n}(P_i - O_i)^2 \tag{25}$$

The MSE value zero signifies that the estimated data of the observed parameter are likely to be most accurate or ideally best. Since it is difficult to achieve zero value, it is seen that the closest value to zero is reasonably acceptable.

4. Root-mean-squared error (RMSE)

Root-mean-squared error or root-mean-squared deviation is also a measure of the differences between values predicted by a model or an estimator and the actually observed values. These individual differences are called as residuals when the calculations are performed over the data sample that is used for estimation and are known as estimation errors when computed out of the sample. The RMSE is defined as,

$$\mathrm{RMSE} = \sqrt{\mathrm{MSE}} \tag{26}$$

When two data sets, i.e., one set from theoretical prediction and the other from actual measurement of some physical variable (which is in our case is observed versus predicted), are compared, the RMSE of the pairwise deviation among the

two data sets can function as a measure how far on average the error is from 0.

5. Coefficient of correlations R^2

The coefficient of correlation R^2 can be expressed as the squared ratio between the covariance and the multiplied standard deviations of the observed and predicted values. The range of R^2 lies between 0 and 1.0 which describes how much of the observed dispersion is explained by the prediction. A value of zero means no correlation at all, whereas a value of 1 means that the dispersion of the prediction is equal to that of the observation.

6. Nash–Sutcliffe efficiency E

The efficiency E proposed by Nash and Sutcliffe [17] is defined as:

$$E = 1 - \frac{\sum_i^n (O_i - P_i)^2}{\sum_i^n (O_i - \bar{O})^2} \tag{27}$$

where $\bar{O}$ represents the mean of calculated values. The range of E lies between 1.0 (perfect fit) and $-\infty$.

7. Index of agreement I_d

The index of agreement I_d was proposed by Willmot [18]. The index of agreement represents the ratio of the mean square error and the potential error [18] and is defined as:

$$I_d = 1 - \frac{\sum_i^n (O_i - P_i)^2}{\sum_i^n (|P_i - \bar{O} + |O_i - \bar{O}||)^2} \tag{28}$$

The range of I_d is similar to that of R^2 and lies between 0 (no correlation) and 1.0 (perfect fit).

6 Conclusions

From the experimental results on compound channels with converging flood plains, the variation of non-dimensional water surface profile Ψ with relative depth β, converging angle θ, relative distance X_r and width ratio α has been analysed.

The non-dimensional water surface profile Ψ is found to increase with increase in width ratio and relative distance of converging compound channels. Further, the non-dimensional water surface profile Ψ is found to increase exponentially with overbank flow depth for lower-aspect-ratio channels and increase linearly for higher-aspect-ratio channels. Again, the non-dimensional water surface profile Ψ is found to increase when the relative depth increases for different converging angles θ. The dependency of non-dimensional water surface profile Ψ with five most influencing non-dimensional geometric and hydraulic parameters of a converging compound channels is analysed. For all the parameters, it is found to bear the nonlinear relationship.

A multivariable regression model has been presented to model a generalized expression to predict the water surface profile of compound channels with converging flood plains. Different error analyses are performed to test the strength of the present model. It is found that MAE is 0.0015, MAPE is 2.4296 which is less than 10 %, MSE is 0.0019, RMSE is 0.0431, E is 0.8945, R^2 is 0.896, and I_d is 0.726. From these error analyses, it is seen that the present model is capable of predicting confidently the water surface profile with narrowing flood plain.

The limitation of the model is that it can be utilized to predict the water surface profile of compound channel with converging flood plain for homogeneous roughness only. The model can be improved with more data sets from wider flood plains and for differential roughness in the main channel and flood plains.

Acknowledgments The author wishes to acknowledge thankfully the support from the Institute and the UGC UKIERI Research project (ref no UGC-2013 14/017) by the second authors for carrying out the research work in the Hydraulics laboratory at National Institute of Technology, Rourkela.

References

1. Sellin, R.H.J: A laboratory investigation into the interaction between flow in the channel of a river and that of its flood plain. La Houille Blanche **7**, 793–801 (1964)
2. Myers, W.R.C.; Elsawy, E.M.: Boundary shears in channel with flood plain. J. Hydraul. Div. ASCE **101**(7), 933–946 (1975)
3. Knight, D.W.; Tang, X.; Sterling, M.; Shiono, K.; McGahey, C.: Solving open channel flow problems with a simple lateral distribution model. River Flow. **1**, 41–48 (2010)
4. Khatua, K.K.; Patra, K.C.; Mohanty, P.K.: Stage-discharge prediction for straight and smooth compound channels with wide floodplains. J. Hydraul. Eng. ASCE **138**(1), 93–99 (2012)
5. James, M.; Brown; R.J.: Geometric parameters that influence flood plain flow. In: U.S. Army Engineer Waterways Experimental Station. Vicksburg Miss, June, Research report H-77 (1977)
6. Bousmar, D.; Zech, Y.: Periodical turbulent structures in compound channels. In: River Flow International Conference on Fluvial Hydraulics. Louvain-la-Neuve, Belgium, pp. 177–185 (2002)
7. Bousmar, D.; Wilkin, N.; Jacquemart, J.H.; Zech, Y.: Overbank flow in symmetrically narrowing floodplains. J. Hydraul. Eng. ASCE **130**(4), 305–312 (2004)
8. Rezaei, B.: Overbank flow in compound channels with prismatic and non-prismatic floodplains. Ph.D. Thesis. University of Birmingham, UK (2006)
9. Rezaei, B.; Knight, D.W.: Application of the Shiono and Knight Method in the compound channel with non-prismatic floodplains. J. Hydraul. Res. **47**(6), 716–726 (2009)
10. Proust, S.; Rivière, N.; Bousmar, D.; Paquier, A.; Zech, Y.: Flow in the compound channel with abrupt floodplain contraction. J. Hydraul. Eng. **132**(9), 958–970 (2006)
11. Chlebek, J.; Bousmar, D.; Knight, D.W.; Sterling, M.A.: comparison of overbank flow conditions in skewed and converging/diverging channels. In: River Flows International Conference, pp. 503–511 (2010)
12. Rezaei, B.; Knight, D.W.: Overbank flow in compound channels with non prismatic floodplains. J. Hydraul. **137**, 815–824 (2011)

13. Hojjat, A.Y.; Mohammad, H.O.; Seyed, A.A.: The hydraulics of flow in non-prismatic compound channels. J. Civ. Eng. Urban. **3**(6), 342–356 (2013)
14. Naik, B.; Khatua, K.K.; Miri Kamel: Energy loss along the non-prismatic reach of a compound channel using ANN river flow. In: International Conference on Fluvial Hydraulics (September 3–5), Lausanne, Switzerland (2014)
15. Bjerklie, D.M.; Dingman, S.L.; Bolster, C.H.: Comparison of constitutive flow resistance equations based on the Manning and Chezy equations applied to natural rivers. Water Resour. Res. **41**(11), 14 W11502 (2005)
16. Dash, S.S.; Khatua, K.K.: Sinuosity dependency on stage discharge in meandering channels. Am. Soc. Civ. Eng. doi:10.1061/(ASCE)IR.1943-4774.0001037 (2016)
17. Nash, J.E.; Sutcliffe, J.V.: River flow forecasting through conceptual models, part I. A discussion of principles. J. Hydrol. **10**, 282–290 (1970)
18. Willmot, C.J.: On the validation of models. Phys. Geogr. **2**, 184–194 (1981)
19. Khiabani, M.H.; Kandasamy, J.: Friction factor for spatially varied flow with increasing discharge. J. Hydraul. Eng. **131**(9), 792–799 (2005)

International Journal of Advance Research in Science and Engineering
Vol. No.6, Issue No. 04, April 2017
www.ijarse.com
IJARSE
ISSN (O) 2319 - 8354
ISSN (P) 2319 - 8346

IMPLEMENTATION OF THE CONTRAST ENHANCEMENT AND WEIGHTED GUIDED IMAGE FILTERING ALGORITHM FOR EDGE PRESERVATION FOR BETTER PERCEPTION

Chiruvella Suresh

Assistant professor, Department of Electronics & Communication Engineering,
SRTIST, Nalgonda, Telanga, (India)

ABSTRACT

Digital image processing has revolutionized the content perception from physical photo appearance to digital image appearance by implementing the digitalization. Digital image processing helps to achieve good process in various research fields but still enhancing the degraded content to normal content is concerned area. Image enhancement attains attention due to its high application applicability. A novel framework is proposed in this paper by combine the edge based weighting scheme with guided image filtering to get proposed weighted guide image filtering (WGIF). WGIF scheme yields low complexity as GIF and preserve the sharp gradient information. WGIF has ability to provide the local and global smoothing filters advantages and successful to avoid the halo artifacts. In practical WGIF is for single image feature enhancement. Experimental results provide low complexity and high performance over traditional state of art methods.

Keywords: Guided Image Filter, Halo Artifacts, Low Complexity, Image Enhancement

I INTRODUCTION

Digital image is defined as “An image is not an image without any object in it”. Human visual system has ability to perceive the objects in digital image using edges in efficient manner. Halo artifacts introduces blur in digital image which makes perception of content difficult. Various filtering techniques have designed in literature to preserve the global and local statistics but none can meet the desired requirements and various algorithms yields high complexity which fails them to achieve practical reliability.

Digital image processing domain has different research fields and all these research fields have applications ranging from low level to high level. Edge preservation in all these research fields attains attention and implementation of smoothing filters has ability to filter noise content by preserving the edge information. Smoothing algorithms can be classified into two types namely global filters such as bilateral filter , tri-lateral filters , and finally guided image filter . Global filters attain images with good quality but these filters are highly expensive. Local filters are

IJARSE
ISSN (O) 2319 - 8354
ISSN (P) 2319 - 8346

considered as alternative to global filters which are simple and cost effective but fail to conserve the sharp edges information like global filters.

When local filters are forcefully adopts to smooth edges it results halo artifacts. Halo artifacts produced by bi-lateral filter and guided image filter are fixed in equipped way using similarity parameter in terms of range and spatial. Bi-lateral filtering mechanism is considered as adaptive filter and this adaptive mechanism helps to handle the halo artifacts and on negative side it destroys the 3D convolutional form . An interesting algorithm named weighted guided image filtering scheme is proposed in this paper by combining the edge-based weighting scheme along with guided image filtering. Calculation of edge based weighting scheme is calculated by using 3×3 local variance in a guidance image. This local variance scheme of one individual pixel is normalized by all pixels local variance in guidance image. The acquired normalized weights of all pixels are then adaptively adapted to WGIF. WGIF helps to avoid halo artifacts in accurate manner for excellent visual quality. The intricacy of WGIF is same as GIF. The proposed weighted guide image filtering (WGIF) is applied for multiple purposes as single image mist removal, single image detail enhancement and different exposed images fusion.

II RELATED WORK

Pierre Charbonnier, Laure Blanc-Feraud, Gilles Aubert, and Michel Barlaud [1] proposed an algorithm, called ARTUR, to avoid problems that are ill posed and must be regularized. Usually, a roughness penalty is imposed on the solution. The difficulty is to avoid the smoothing of edges, which are very important attributes of the image. In this paper, they first give conditions for the design of such an edge-preserving regularization in which under the few conditions it is possible to introduce an auxiliary variable whose role is twofold. First, it marks the discontinuities and ensures their preservation from smoothing. Second, it makes the criterion half-quadratic. The optimization is then easier, as well as a deterministic strategy, based on alternate minimizations on the image and the auxiliary variable, and can be applied in a large number of applications in image processing.

Z. Farbman, R. Fattal, D. Lischinski, and R. Szeliski [2] paved the new way to construct edge-preserving multi-scale image decomposition in order to control the spatial scale of the extracted details, and it is often desirable to manipulate details at multiple scales, while avoiding visual artifacts. It current base detail decomposition techniques, based on the bilateral filter, are limited in their ability to extract detail at arbitrary scales. Thus they advocate the use of an alternative edge-preserving smoothing operator, based on the weighted least squares optimization framework, which is particularly well suited for progressive coarsening of images and for multi-scale detail extraction and effectiveness of edge-preserving decompositions in the context of LDR and HDR tone mapping, detail enhancement, and other applications.

J. Chen, S. Paris, and F. Durand [3] presented a new data structure—the bilateral grid, that enables fast edge-aware image processing. By working in the bilateral grid, algorithms such as bilateral filtering, edge-aware painting, and local histogram equalization become simple manipulations that are both local and independent.It parallelize algorithms on modern GPUs to achieve real-time frame rates on high-definition video Also demonstrated the

IJARSE
ISSN (O) 2319 - 8354
ISSN (P) 2319 - 8346

method on a variety of applications such as image editing, transfer of photographic look, and contrast enhancement of medical images.

K. He, J. Sun, and X. Tang [4] represented a novel explicit image filter called guided filter which is derived from a local linear model, the guided filter computes the filtering output by considering the content of a guidance image, which can be the input image itself or another different image. The guided filter can be used as an edge-preserving smoothing operator like the popular bilateral filter, but it has better behaviors near edges. The guided filter is also a more generic concept beyond smoothing: It can transfer the structures of the guidance image to the filtering output, enabling new filtering applications like dehazing and guided feathering. Moreover, the guided filter naturally has a fast and no approximate linear time algorithm, regardless of the kernel size and the intensity range. Currently, it is one of the fastest edge-preserving filters. Experimental result shows that the guided filter is both effective and efficient in a great variety of computer vision and computer graphics applications, including edge-aware smoothing, detail enhancement, HDR compression, image matting/feathering, dehazing, joint upsampling, etc.

III METHODLOGY

Digital image composed of three contents namely color, shape and texture. Assessing the image information based on edges (gradient) has ability to perform the enhancement tasks and fusion in reliable way in the field of digital image processing. Acquiring the digital content of images with good visual quality in computational photography and other applications with complexity is still concerned area because many global filters yields high complexity which show adverse impact on enhancement process.. In this paper, a strategy is implemented to enhance the image contents based on edge information by incorporating the guided image filter (GIF) with novel edge based weighting scheme to form weighted guided image filter with minimal complexity and better visual quality.

The edge information plays an important role in implementing weighted guide image filtering algorithm for various applications. The key element of proposed algorithm is to ensure a confined linear model between a guidance image (G) and filtering output ($\hat{J}$). The confined linear model ensures filtering output ($\hat{J}$) has an edge only if the respective guidance image (G) has an edge. Consider G as guidance image and the respective variance is denoted by $\sigma^{2(P')}$. The edge based weighting scheme $\gamma G(P')$ is well defined by local variance of 3×3 local variance windows of all pixels as follows

$$\gamma G(P') = \left(\frac{1}{N}\right) \sum_{p=1}^{N} \frac{[\sigma]^2 G(P') + \varepsilon}{\sigma^2 G(P) + \varepsilon} \quad (1)$$

Where

ε denotes a small constant selected for input image dynamic range “L” and its value is $(0.001 \times L)\hat{}2$. All guidance image pixels are used in the computation of $\gamma G(P')$. The pixel P' importance is measured by weighting mechanism with respect to whole guidance image. The value of weighting mechanism is larger than 1 if P' is at an edge and value is small if P' is in a flat area. The feasible blocking artifacts appearance can be efficiently prevented in the final image and the smoothing operation is carried out at weighting mechanism. The proposed weighted

International Journal of Advance Research in Science and Engineering
Vol. No.6, Issue No. 04, April 2017
www.ijarse.com
IJARSE
ISSN (O) 2319 - 8354
ISSN (P) 2319 - 8346

filtering scheme is incorporated with cost function and finally the minimization of differences between image to be filtered and filtered output as follows

$$E = \sum_{P\varepsilon\Omega_\varsigma}\left[\left[(ap'G(p) + bp' - \rrbracket X(p))^2 + \frac{\lambda}{\gamma G(p')} ap'^2\right]\right] \quad (2)$$

The computation of ap' and bp' are as follows

$$ap' = \frac{\mu G \odot X, \varsigma 1(P') - \mu G, \varsigma 1(P')\mu X, \varsigma 1(P')}{\sigma^2 G, \varsigma 1(P') + \left(\frac{\lambda}{\gamma G(P')}\right)} \quad (3)$$

$$bp' = \mu X, \varsigma 1(P') - ap'\mu G, \varsigma 1(P') \quad (4)$$

Where $\odot$ is represented as two matrices element by element product and along with matrices mean values are also taken into consideration in order to yield final value as

$$\ddot{J}(p) = apG(P) + bp \quad (5)$$

To make the analysis easy both X and G are assumed to be same for perfection and when we consider a pixel with a edge has value larger than 1 and in WGIF it is close to 1 is better than GIF value. The above analysis show better edge information is obtained by WGIF than GIF

IV RESULTS

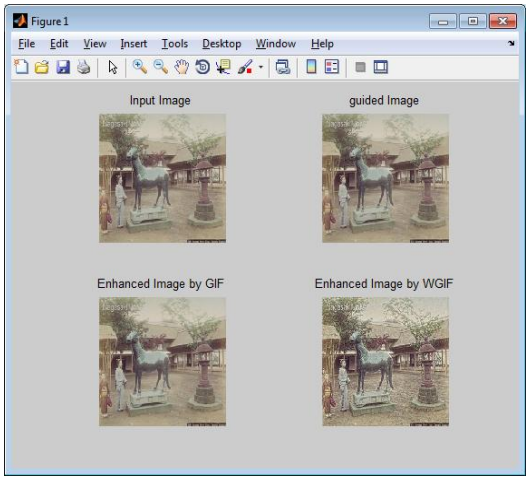

Figure 1: (a) Input image (b) Guided image (c) Enhanced image by GIF (d) Enhanced image by WGIF

International Journal of Advance Research in Science and Engineering
Vol. No.6, Issue No. 04, April 2017
www.ijarse.com
IJARSE
ISSN (O) 2319 - 8354
ISSN (P) 2319 - 8346

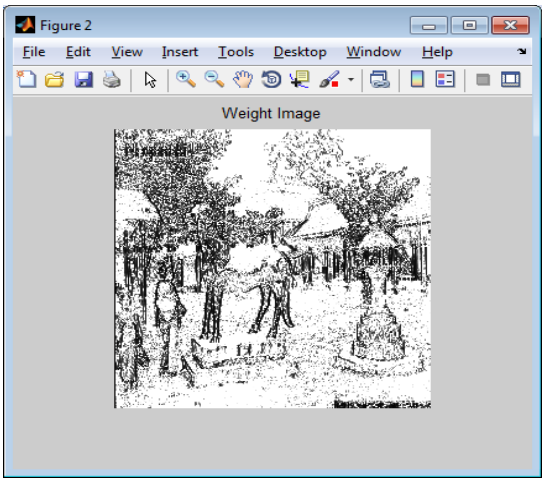

Figure 2: Weighted image

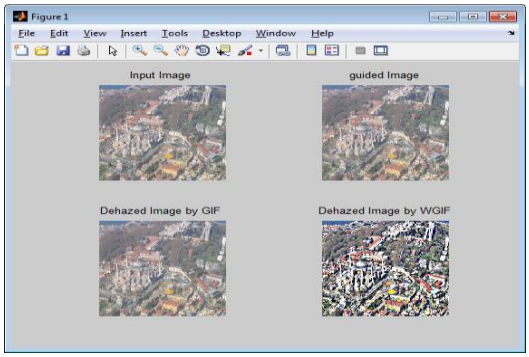

Figure 3: (a) Input image (b) Guided image (c) Dehazed image by GIF (d) Dehazed image by WGIF

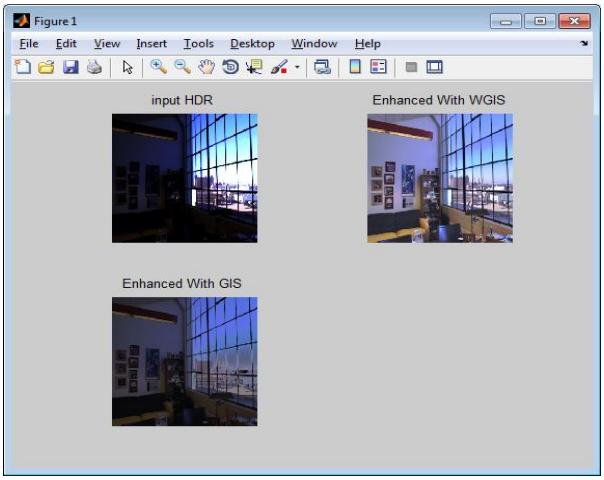

Figure 4: (a) Input HDR (b) Enhanced with WGIS (c) Enhanced with GIS

V CONCLUSION

An optimized framework is proposed in this work by incorporating the edge based weighting scheme with guided image filtering to get proposed weighted guide image filtering (WGIF). WGIF scheme yields low complexity as

IJARSE
ISSN (O) 2319 - 8354
ISSN (P) 2319 - 8346

GIF and preserve the sharp gradient information. WGIF has ability to provide the local and global smoothing filters advantages and successful to avoid the halo artifacts. In practical WGIF is for single image feature enhancement.

REFERENCES

[1] P. Charbonnier, L. Blanc-Feraud, G. Aubert, and M. Barlaud, "Deterministic edge-preserving regularization in computed imaging," IEEE Trans. Image Process., vol. 6, no. 2, pp. 298–311, Feb. 1997.

[2] Z. Farbman, R. Fattal, D. Lischinski, and R. Szeliski, "Edge-preserving decompositions for multi-scale tone and detail manipulation," ACM Trans. Graph., vol. 27, no. 3, pp. 249–256, Aug. 2008.

[3] J. Chen, S. Paris, and F. Durand, "Real-time edge-aware image processing with the bilateral grid," ACM Trans. Graph., vol. 26, no. 3, pp. 103–111, Aug. 2007.

[4] K. He, J. Sun, and X. Tang, "Guided image filtering," IEEE Trans. Pattern Anal. Mach. Intell., vol. 35, no. 6, pp. 1397–1409, Jun. 2013.

[5] L. I. Rudin, S. Osher, and E. Fatemi, "Nonlinear total variation based noise removal algorithms," Phys. D, Nonlinear Phenomena, vol. 60, nos. 1–4, pp. 259–268, Nov. 1992.

[6] Z. G. Li, J. H. Zheng, and S. Rahardja, "Detail-enhanced exposure fusion," IEEE Trans. Image Process., vol. 21, no. 11, pp. 4672–4676, Nov. 2012.

[7] Z. Farbman, R. Fattal, D. Lischinski, and R. Szeliski, "Edge-preserving decompositions for multi-scale tone and detail manipulation," ACM Trans. Graph., vol. 27, no. 3, pp. 249–256, Aug. 2008.

[8] R. Fattal, M. Agrawala, and S. Rusinkiewicz, "Multiscale shape and detail enhancement from multi-light image collections," ACM Trans. Graph., vol. 26, no. 3, pp. 51:1–51:10, Aug. 2007.

[9] P. Pérez, M. Gangnet, and A. Blake, "Poisson image editing," ACM Trans. Graph., vol. 22, no. 3, pp. 313–318, Aug. 2003.

[10] K. He, J. Sun, and X. Tang, "Single image haze removal using dark channel prior," IEEE Trans. Pattern Anal. Mach. Intell., vol. 33, no. 12, pp. 2341–2353, Dec. 2011.

[11] L. Xu, C. W. Lu, Y. Xu, and J. Jia, "Image smoothing via L0 gradient minimization," ACM Trans. Graph., vol. 30, no. 6, Dec. 2011, Art. ID 174.

[12] C. Tomasi and R. Manduchi, "Bilateral filtering for gray and color images," in Proc. IEEE Int. Conf. Comput. Vis., Jan. 1998, pp. 836–846.

[13] Z. Li, J. Zheng, Z. Zhu, S. Wu, and S. Rahardja, "A bilateral filter in gradient domain," in Proc. Int. Conf. Acoust., Speech Signal Process., Mar. 2012, pp. 1113–1116.

[14] P. Choudhury and J. Tumblin, "The trilateral filter for high contrast images and meshes," in Proc. Eurograph. Symp. Rendering, pp. 186–196, 2003.

[15] F. Durand and J. Dorsey, "Fast bilateral filtering for the display of highdynamic-range images," ACM Trans. Graph., vol. 21, no. 3, pp. 257–266, Aug. 2002

Arab J Sci Eng
DOI 10.1007/s13369-017-2963-7

RESEARCH ARTICLE - CIVIL ENGINEERING

Loss of Energy in the Converging Compound Open Channels

B. Naik[1] · K. K. Khatua[1] · E. Padhi[2] · P. Singh[1]

Received: 21 June 2017 / Accepted: 5 November 2017

Abstract In overbank flow due to the interaction mechanism between the main channel and floodplain, the flow property of the compound sections gets affected. The complexity is more when the compound channels have non-prismatic floodplains. Additional complexity occurs during the interaction between the subsections as well as due to non-uniformity of flow through converging parts of the compound channel. For prediction of flow, calculation of energy loss parameters from section to section is an important task for river engineers. In this paper, an experimental investigation for the energy losses of converging compound channels for different flow depths along the converging path is performed. The loss of energy due to contraction and compound geometry for a compound channel is evaluated, and the dependency of energy loss for such channels is analyzed. A generalized multivariable regression model has been developed to predict the energy slope with high accuracy. Using the expression of the energy loss concept, the discharge capacity in the converging compound is found to provide good results as compared to other standard model exists in the literature.

✉ P. Singh
Prateek.k.singh1992@gmail.com

B. Naik
banditanaik1982@gmail.com

K. K. Khatua
kkkhatua@yahoo.co.in

E. Padhi
ellora.padhi@yahoo.co.in

[1] Department of Civil Engineering, National Institute of Technology Rourkela, Rourkela, India

[2] Department of Civil Engineering, Indian Institute of Technology Kharagpur, Kharagpur, India

Keywords Converging angle · Non-prismatic compound channel · Non-uniform flow · Velocity distribution · Energy loss

List of symbols

B	Width of compound channel
b	Width of the main channel
E_1	Total energy heads of section 1
E_2	Total energy heads of section 2
h_l	Energy loss
h	Height of the main channel
H	Bank full depth
L	Converging length
R	Hydraulic Radius
S_0	Bed slope
S_e	Energy slope
S_f	Friction slope
V_1	Mean flow velocities at section1
V_2	Mean flow velocities at section2
Y_1	Mean flow depths at section 1
Y_2	Mean flow depths at section 2
Z_1	Bed elevations above a given datum for section 1
Z_2	Bed elevations above a given datum for section 2
α	Width ratio (B/b)
α_1	correction factors for velocity head for section 1
α_2	correction factors for velocity head for section 2
δ	Aspect ratio (b/h)
n	Composite Roughness
β	Relative depth $((H-h)/H)$
θ	Angle of convergence
X_r	Relative distance (x/L)

Published online: 16 November 2017

1 Introduction

In natural rivers, due to changes in the cross-sectional area, the state of the flow may be changed from uniform to non-uniform. Under such conditions, the hydraulic analysis will be more complicated compared to simple uniform flow. Calculation of energy loss in a compound channel is one of the key issues in river engineering studies, and it needs to be handled properly. In general, a compound channel consists of the main channel and two flood plains. Because of the exchange of momentum between the main channel and the floodplain, consumption of energy is more in a compound section as compared to a simple channel section. There is a continuous settlement of people near the bank of the river, causing a reduction in width of the compound channel, and as a result the converging of floodplains occurs. Wrong estimation of discharges in these regions will lead to much loss of life and properties. In converging compound channels, because of constant variation in the geometry of the floodplain along the direction of flow, the resultant interactions and exchange of momentum are increased further (Bousmar et al. [1]; Proust et al. [2]; Rezaei [3]). This increased momentum exchange is really an essential parameter and should be taken into consideration while doing flow modeling of such channel sections. The interaction of the flow between the main channel and a prismatic floodplain has been examined by many researchers such as Knight and Demetriou [4], Shiono and Knight [5], Khatua and Patra [6], and Khatua et al. [7]. Even in uniform flow conditions, there is a loss of energy occurs and the main sources of energy losses are bed friction, momentum flux due to both turbulent exchange and secondary current across the channel cross section. But in a non-prismatic compound channel (i.e., converging floodplain), the flow is non-uniform. Due to this non-uniformity, an additional contraction loss of energy is generated. Several two- and three-dimensional approaches have been applied to the discharge prediction in compound channels (Knight and Shiono [8]; Cater and Williams [9]; Jazizadeh and Zarrati [10]; Marjang and Merkley [11]), but these models are complex and take too much time to reach satisfactory solutions. Therefore, one-dimensional analytical methods are still widely used in engineering applications. Researchers have proposed a number of 1D methods to estimate the discharge capacity, which can be classified into six types: single channel method (SCM), divided channel method (DCM), area method(AM), Shiono and Knight method (SKM), coherence method (COHM), and apparent shear force method (ASFM). Although most of the modified discharge-estimating methods include the effect of momentum transfer mechanism and account for the interaction effect due to geometry and roughness conditions of a prismatic compound channel only, but there are no models exist in the literature which will account for the non-prismatic action of a compound channel. Several studies on contractions of the channels have been studied by many researchers. Head losses in different sections of the converging channel were being studied by Hager [12], and also he showed the effects of head losses on the computation of discharge. Molinas and Marcus [13] and Naik et al. [14] gave a model for discharge evaluation short, in abrupt channel contractions incorporating the energy losses due to contractions.

The present work investigates experimental findings on the effect of different converging angle and geometry on predicting the energy loss in such cases. Finally, an efficient approach is developed to compute the loss of energy in a compound channel with converging floodplains. Experimental work on non-prismatic compound channels has been done in the Hydraulics Laboratory of Civil Engineering Department at NIT, Rourkela, mainly to examine the water surface profile and the loss of energy caused by the convergence of the floodplains. Computation of the energy losses in different converging sections of a non-prismatic compound channel is carried out by considering different hydraulic and geometric conditions, and the functional relationships of energy loss with most influencing parameter are studied. An attempt is finally made to derive a generalized mathematical expression to predict the energy losses in a converging compound channel for different geometry and flow conditions. The results were finally tested with the observed experimental data and the data of other investigators. The work will be helpful for accurate flow estimation in different sections of a non-prismatic compound channel reaches.

2 Analyses of Energy Losses and Influencing Parameters

Under a uniform flow condition, the total energy loss gradient (S_e), bed slope (S_0), and friction slope (S_f) are equal. But in a symmetrically converging floodplain, the width of the compound channel reduces gradually in the flow direction due to which the flow depth varies significantly and the flow becomes non-uniform. Flow resistance increases with the presence of floodplain contractions. There are some methods exist for accounting the additional resistance occurred due to contraction, but they are valid for simple channels and meandering channels. So when those methods are applied to a converging compound straight channel, they failed to give a satisfactory result for calculation of discharge. In non-uniform flow conditions, the head loss gradient or energy slope (S_e) consists of a friction slope (S_f), head loss due to shear stress related to interfacial turbulent exchanges (S_t) and head loss due to the mass exchange (S_m) (2009). So for computation of discharge, it is required to consider these losses so that we can get a better a model which can predict the discharge more accurately than any other existing method. An energy profile for a prismatic compound channel is shown in

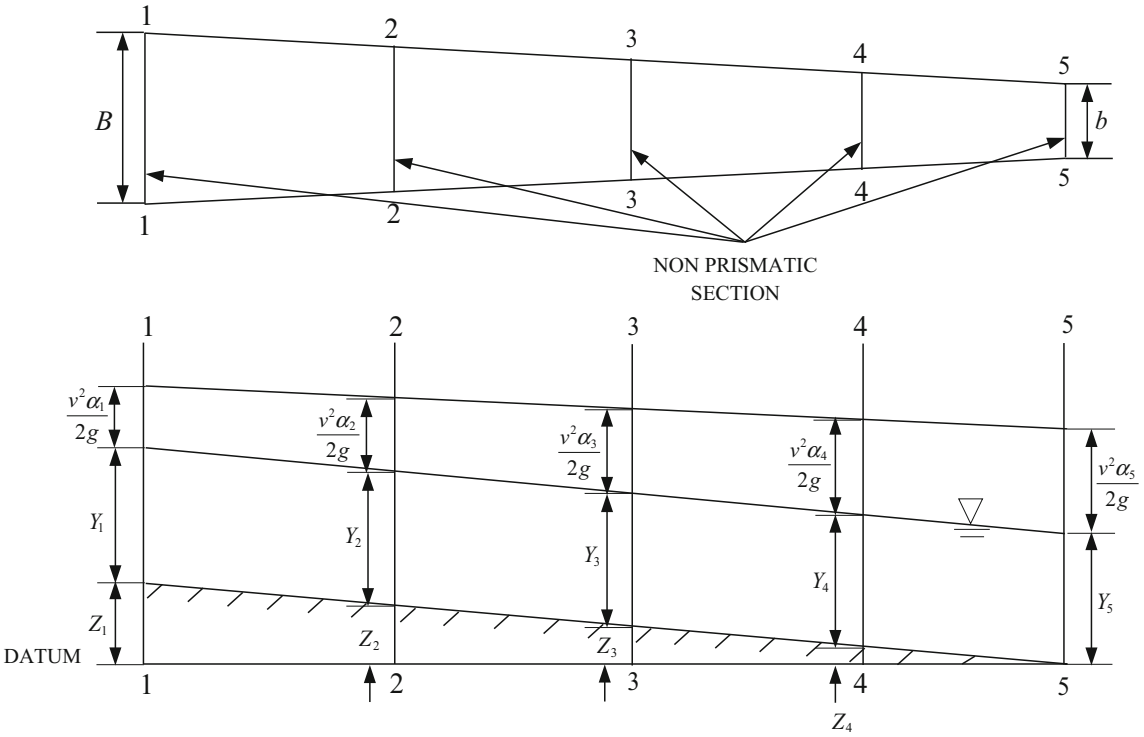

Fig. 1 Sketch of energy profile for converging channels at NIT RKL

Fig. 1. The width of the compound and the main channel are considered as B and b, respectively. The width of the compound channel is being reduced gradually and becomes equal to the width of the main channel in the longitudinal direction (Fig. 1) (same as that of Naik and Khatua [15]). This non-prismatic section is being divided into five parts in the direction of the fluid flow. The mean flow depths at section 1 to section 5 are adopted as Y_1, Y_2, Y_3, Y_4, and Y_5, respectively. In a non-prismatic compound channel, along with frictional and viscosity loss, another two more energy loss factors exist such as the interaction loss and contraction loss. The interaction loss occurs due to the interaction between the main channel and floodplain, while the contraction loss takes place due to floodplain contraction. Head loss between two consecutive sections can be obtained by using the conservation of energy principle. For the energy calculation, the channel bottom at section 5 (i.e., extreme downstream end of the converging part of the channel) is considered as the datum of the channel. Applying the conservation of energy principle for the sections 1 and 2

$$E_1 = Z_1 + Y_1 + \frac{V_1^2\alpha_1}{2g} \tag{1}$$

$$E_2 = Z_2 + Y_2 + \frac{V_2^2\alpha_2}{2g}, \tag{2}$$

where E_1 and E_2 are the total energy heads of section 1 and 2, respectively, Z_1 and Z_2 are the bed elevations above a given datum for sections 1 and 2, respectively, V_1 and V_2 are the mean flow velocities at sections 1 and 2, respectively, and α_1 and α_2 are the correction factors for velocity head (Naik and Khatua [16]). Let h_1 be the total head loss between sections 1 and 2. The conservation of energy principle can be written as:

$$Z_1 + Y_1 + \frac{V_1^2\alpha_1}{2g} = Z_2 + Y_2 + \frac{V_2^2\alpha_2}{2g} + h_1. \tag{3}$$

The energy loss (h_1) in a converging compound channel does not linearly vary between sections to sections rather it changes with channel geometry, converging angle, and surface and flow conditions. So h_1 can be written as:

$$h_1 = E_1 - E_2. \tag{4}$$

After estimating the energy loss, the energy slope S_e for the given channel can be obtained by using the Eq. 5a,

$$S_e = h_1/l = (E_1 - E_2)/l \quad \text{(Neglecting the } S_t \text{ and } S_m\text{)}. \tag{5a}$$

Alternately the energy slope can also be computed from Manning's equations

$$Q = \frac{1}{n} R_e^{\frac{2}{3}} S_e^{\frac{1}{2}} \tag{5b}$$

$$R = \frac{A}{P}, \tag{5c}$$

where Q = total discharge, n = composite roughness (Lotters Method), R = hydraulic radius i.e., (A/P).

So by putting the computed value of the energy slope in Manning's, Chezys or Darcy–Weisbach equations, the flow or average velocity calculation can be done in any part of the non-prismatic channel. In this paper, using Eq. 5, the energy slope between sections is calculated and applied in the present experimental channels and channels of Rezaei [3] for different cross sections of the channel and flow conditions. Here, section 1 is adopted as a reference for computation of the length of the reach. The energy slope calculation is based on a prediction of the total energy at any section. The computation of energy slope is an important issue as it has a significant effect on predicting the important variables like stage–discharge relationship, distribution of shear stress, flow distribution, etc., so by looking at these aspects, an attempt is made here to develop a model to predict the energy slope of a converging compound channel using the multi-linear regression approach.

2.1 Selection of Hydraulic Parameters

Flow fields in a non-prismatic compound channel are significantly influenced by both geometrical and hydraulic parameters. The computation of the energy slope becomes complicated when the width of the floodplain is contracted and becomes zero. The factors which are considered to be responsible for the estimation of the energy slope are given below:

(i) Angle of convergence (θ)
(ii) Relative flow depth [β= bank full depth (H)− depth of main channel (h/H)]
(iii) Width ratio (α) [i.e., ratio of the width of the floodplain (B) to the width of the main channel (b)]
(iv) Aspect ratio (δ) (i.e., ratio of the width of the main channel to depth of the main channel)
(v) Longitudinal relative distance (X_r) (i.e., of point velocity in the lengthwise direction of the channel /total length of the non-prismatic channel).

3 Experimental Setup and Procedure

Experimentation had been carried out in three different sets of non-prismatic compound channels by varying the cross section built over a cement concrete flume. The dimension of the flume was 15 m long × 0.90 m width × 0.55 m depth. Perspex sheets of same dimensions are used inside the concrete flume. The width ratio (α) and the aspect ratio (δ) of the channel were 1.8 and 5, respectively. Three different angles of convergence for the channels were adopted such as 5°, 9°, and 12.38°, respectively. The converging lengths of the channels for three different angles were found to be 2.28, 1.26, and 0.84 m, respectively. Centrifugal pumps of 11.2 kW capacities were used for water supply into a large overhead tank. There is a measuring tank built at the downstream end of the channel. A sump is also built nearer to the measuring tank. The water was supplied to the overhead tank from this sump through pumping. Due to this arrangement, there is a complete recirculation of water is possible within experimental channels. Figure 2a shows the plan view of experimental sections while Fig. 2b shows the experimental setup of the channel. At the downstream, a regulating tailgate was provided to maintain the flow depth and to keep the flow uniform in the channel. A movable bridge was provided across the flume for taking measurements of each location on the plan of the compound converging channel. Velocity readings were taken by the Pitot tube having an outer diameter of 4.77 mm

The Pitot tube was rotated manually with respect to the flow direction till it records the maximum manometer reading. The steady uniform discharge was preserved in every run of the experiments, and several runs were performed for overbank flow with different relative depths varying from 0.15 to 0.51. Table 1 shows the hydraulic parameters of the experimental channels of NITRKL as well as Rezaei [3] channel. The energy losses in the flow due to the convergence of floodplain at different sections of the converging lengths were being evaluated.

4 Experimental Results

The stage–discharge relationship of prismatic and non-prismatic sections for the converging compound channels of angles 5°·9° and 12.38° from in bank to overbank flow conditions are shown in Fig. 3a–c. A total 13 stage–discharge runs are observed at each test reach. The stage–discharge relationship for all cases is found to be power function given by $H = AQ^n$ where A, n are coefficents with R^2 value more than 0.97.

5 Development of the Energy Slope Model

Generally, for the prismatic compound channel, the energy slope S_e depends importantly upon the geometrical parameter like width ratio, depth ratio, aspect ratio i.e $S_e = F(\alpha, \beta, \delta)$ where F is the functional symbol. But for converging compound channel which has a non-prismatic cross section the energy slope depends on two more influencing geometrical parameters such as converging angle θ and relative distance X_r so $S_e = F(\alpha, \beta, \delta, \theta, X_r)$ for a converging compound channel cases. From the experimental results, different plots are drawn between the energy slope S_e and these

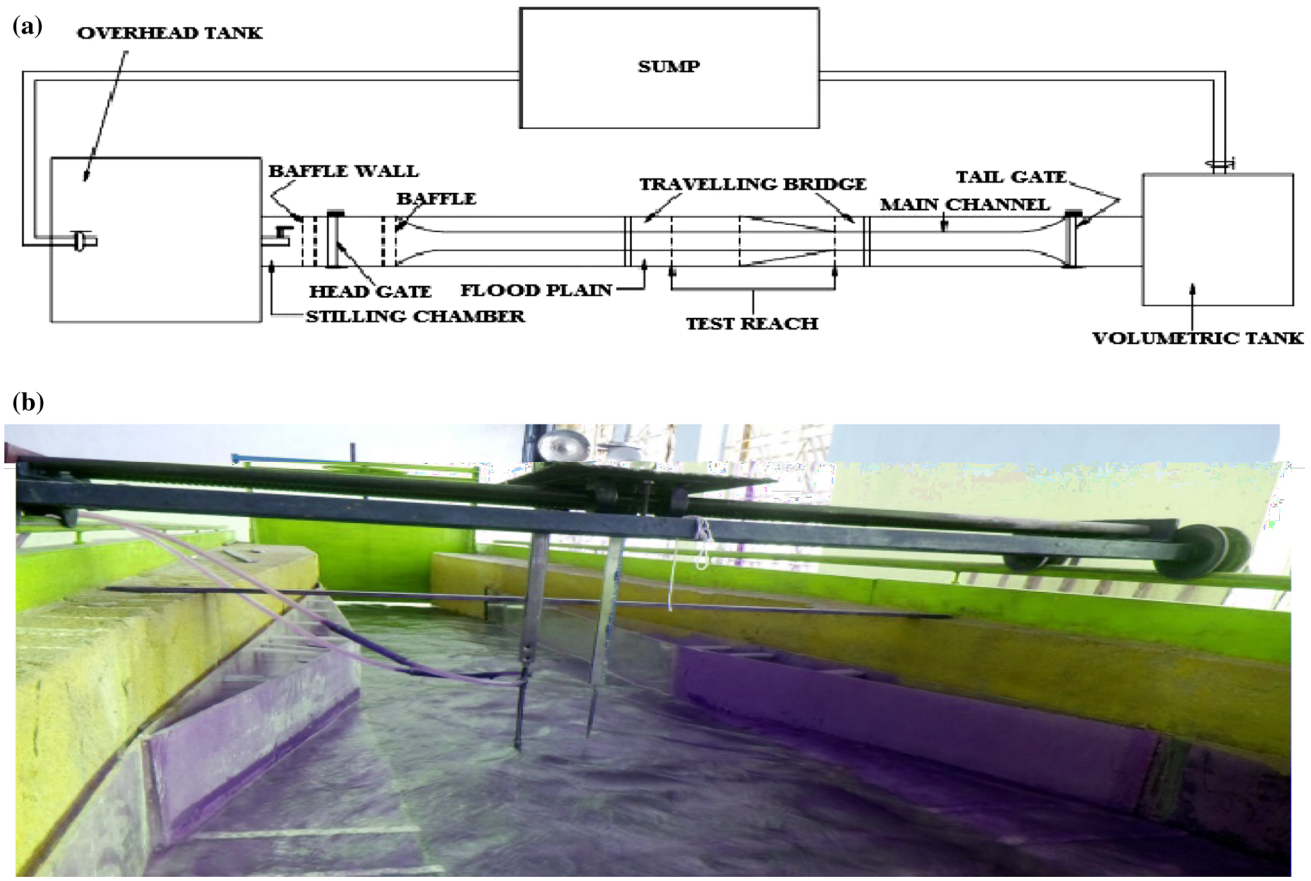

Fig. 2 **a** Plan view of experimental setup. **b** Experimental setup of the channel with velocity readings using Pitot tube and pointer gauge

five non-dimensional independent parameters. The S_e has been calculated from a wide range of experimental datasets of NIT, Rourkela, India, and three more series of converging compound channels data of Rezaei [3] (details of experimentation are provided in Table 1). All these converging compound channels have homogeneous roughness both in the main channel and floodplain subsections with Manning's n values 0.01 bearing smooth surface. This will help us to investigate the effect of all these influencing parameters of prediction of flow variables without considering the roughness effects. The variation of S_e has been found out for all the six converging compound channels. The variation of S_e with relative depth β, converging angle θ, relative distance X_r and width ratio α are plotted for different converging angles θ, respectively, and shown in Figs. 4, 5, 6 and 7. Figure 4 shows that the S_e increase with increase in relative depth and this happen for lower aspect ratio of NIT Rourkela channel, but for higher aspect ratio channel of Rezaei [3] the S_e found to decrease exponentially this may be because of more energy consumed in higher aspect ratio channels as compared to that in low aspect ratio channels. However, the best fit for both the cases (higher and lower aspect ratio channel) are found to exponential nature shown in Fig. 4. Again, by fitting the curve between S_e and the converging angle θ, a relationship can be established (Fig. 5).

It increases with converging angle θ, and the best trend follows a power function with R^2 value 0.97. Similarly, S_e has been plotted with X_r for all the relative flow depths for all the channels shown in Fig. 6, and the best fits are found to be exponential functions with a very high R^2 value of 0.98. Finally, the variations of S_e have been plotted with a different width ratios keeping the same angle and same relative flow depths, i.e., plotted to keep relative flow depth constant, i.e., 0.2, 0.25, 0.3, and 0.4 shown in Fig.7. Figure shows that the S_e decreases with width ratio α for different relative depths and the best trend found for S_e with width ratio α found to be logarithmic in nature for all the cases. Finally, the best functional relationships between S_e with five non-dimensional parameters are listed below. All the equations bear the R^2 value varying between 0.91 and 0.99.

$$S_e = F_1(\beta) = A(e)^{-3.38\beta} \quad \text{For higher aspect ratio, i.e., } \delta \text{ up to 5} \tag{6}$$

$$S_e = F_2(\beta) = B(e)^{1.98\beta} \quad \text{For lower aspect ratio, i.e., } \delta > 5 \tag{7}$$

$$S_e = F_3(\theta) = C(\theta)^{0.57} \tag{8}$$

Table 1 Hydraulic parameters for the experimental channel dataset collected from literature experiments

Verified test channel	Types of channel	Angle of convergence (θ)	Longitudinal slope (S)	Cross-sectional geometry	Total channel width (B) in m	Main channel width (b) in m	Main channel depth (h) in m	Width ratio (s^{-1}) B/b (α)	Longitudinal relative distance (X_r) in m	Aspect Ratio b/h (δ)
Rezaei [3]	Convergent (CV2)	11.31°	0.002	Rectangular	1.2	0.398	0.05	3	2	7.96
Rezaei [3]	Convergent (CV6)	3.81°	0.002	Rectangular	1.2	0.398	0.05	3	6	7.96
Rezaei [3]	Convergent (CV6)	1.91°	0.002	Rectangular	1.2	0.398	0.05	3	6	7.96
N.I.T. Rkl	Convergent	5°	0.0011	Rectangular	0.9	0.5	0.1	1.8	2.28	5
N.I.T. Rkl	Convergent	9°	0.0011	Rectangular	0.9	0.5	0.1	1.8	1.26	5
N.I.T. Rkl	Convergent	12.38°	0.0011	Rectangular	0.9	0.5	0.1	1.8	0.84	5

$$S_e = F_4(x_r) = D(e)^{0.56x_r} \tag{9}$$

$$S_e = F_5(\alpha) = E\log(\alpha) + 0.0023 \tag{10}$$

All these relationships of the non-dimensional parameters with S_e are attempted to compiled to get a generalize expression for S_e. To achieve this, we have applied all these Eqs. (6–10) to get multi-linear regression model and finally Eq. 11 is obtained. Table 2 represents the Unstandardized Coefficient and Regression Statistics of the regression analysis. Equations 11 and 12 represent the final form of the multiple linear regression results after compiling Eq. 6 to 10.

$$S_e = 0.0073 + 0.00024(F_1) - 0.00013(F_2) - 0.0022(F_3) - 0.0036(F_4) \tag{11}$$

After simplifying the above equation for higher aspect ratio, i.e., δ up to 5

$$S_e = -0.0016 + 0.00024e^{-3.38} - 0.0009\theta^{0.57} + 0.0092e^{0.56X_r} \tag{12a}$$

For channels with Lower aspect ratio, i.e., $\delta > 5$

$$S_e = -0.0016 + 0.00013e^{1.98} - 0.0009\theta^{0.57} + 0.0092e^{0.56X_r} \tag{12b}$$

The modified energy slope of a converging compound channel can now be calculated using the results of S_e from Eq. 12. Here, the effect of momentum transfer, as well as the effect of converging angle and other geometrical effects of such channels, has been incorporated in terms of the improved energy slope expressions. Knowing the energy slope, the stage–discharge relationships of a converging compound channel from section to sections can now be calculated using Manning's equation (Eq. 5).

6 Results and Discussion

6.1 Error Analysis

The variation between the calculated values of (S_e) using Eq. (12) and the corresponding observed values for all the six types of channels is shown in Fig. 8. The percentage error in estimated (S_e) is less when compared to observed values for both present experimental channel and Rezaei [3] channel.

6.2 Stage–Discharge Models

The discharge results obtaining from the Eq. (12) are compared with six standard 1D approaches. The datasets used for validation purpose are different from the calibrated datasets.

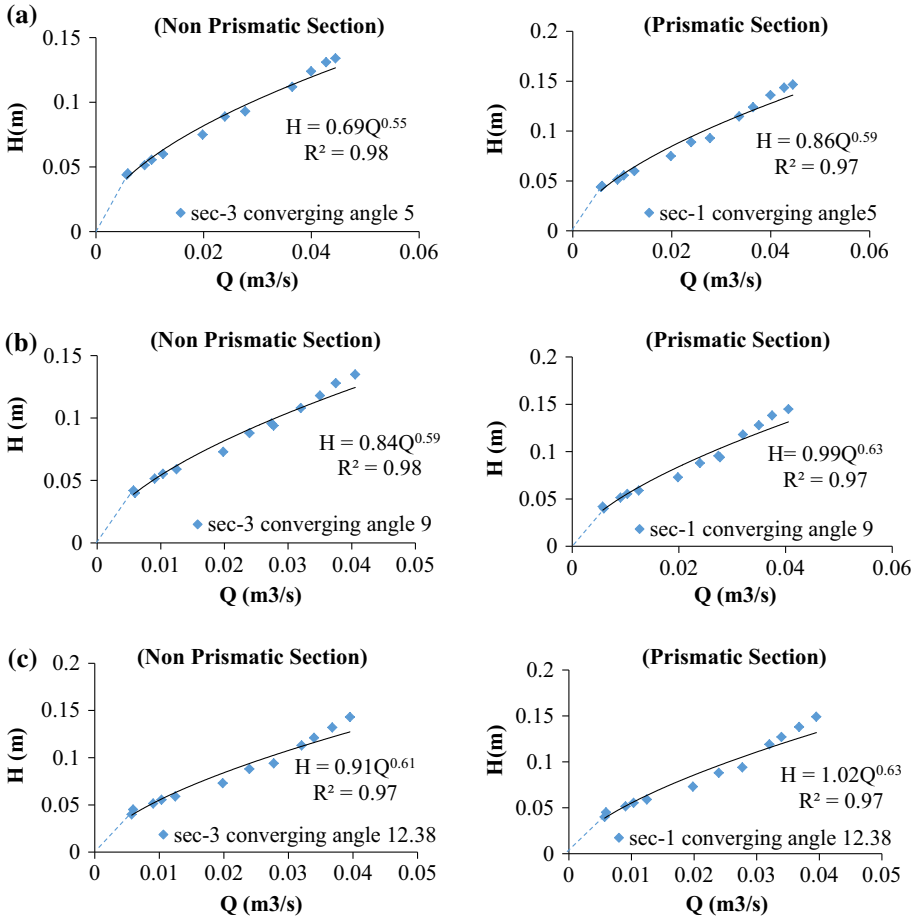

Fig. 3 Stage–discharge curve of the Converging compound channel at the prismatic and non-prismatic reaches. **a** $\theta = 5^{\circ}$, **b** $\theta = 9^{\circ}$, **c** $\theta = 12.38^{\circ}$

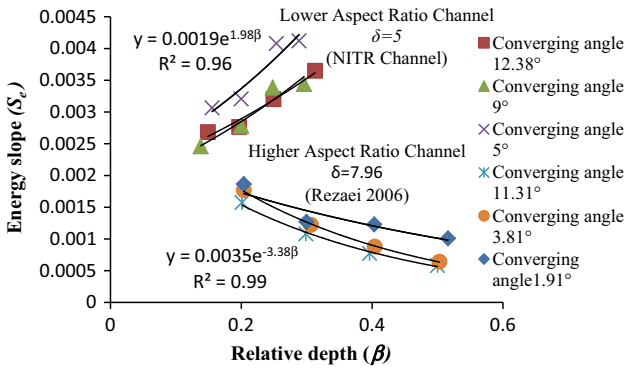

Fig. 4 Variation of S_e of non-prismatic compound channel at typical sections

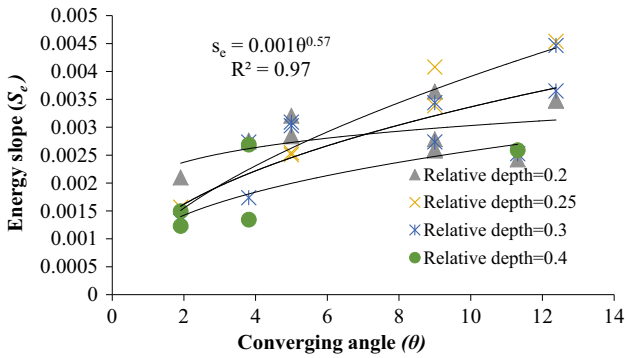

Fig. 5 Variation of S_e with converging angles for different relative depths

This means dataset considered for contrasting the new model with other models are not from the dataset, which are used for the regression and calibration of the model. Total dataset was divided in the ratio of 7:3 where approximately 70% data were used in the regression meanwhile remaining datasets were used for the validation purpose. Among the other approaches, the following methods are considered, i.e., single channel methods (SCM), vertical division methods (VDM), horizontal division methods (HDM), diagonal division method (DDM), area method (AM), apparent shear force method (ASFM). The standard errors for calculating discharge by different methods are shown in Fig. 9. It indicates that the proposed approach appears to be better method among all the discussed methods. The method is finally tested with the results obtained from the software package developed in the Conveyance Estimation System (CES). The free software has been developed by joint

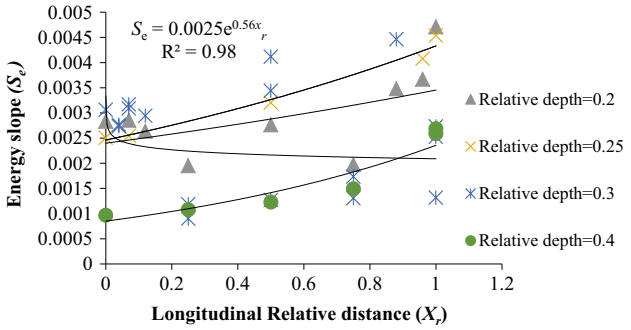

Fig. 6 Variation of Se with section to section along the converging angle for different relative depths

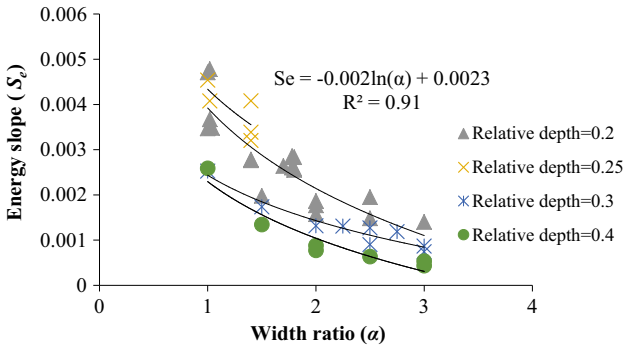

Fig. 7 Variation of S_e with width ratio for different relative depths

Table 2 Unstandardized coefficient and regression statistics

	Coefficients	Regression statistics	
Intercept	0.0073	Multiple *R*	0.911
β	0.00024	*R* square	0.861
θ	− 0.00013	Adjusted *R* square	0.846
X_r	− 0.0022	–	–
α	− 0.0036	–	–

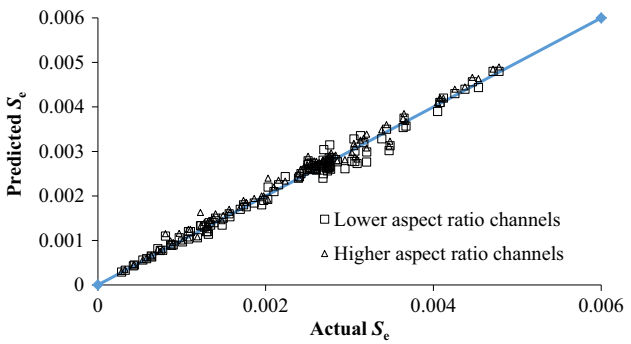

Fig. 8 Scatter plot for observed and modeled value of Energy slope

Agency/DEFRA research program on flood defense, with contributions from the Scottish Executive and the Northern Ireland Rivers Agency, HR Wallingford, This proves the adequacy of the proposed energy slope models for a converging compound channel.

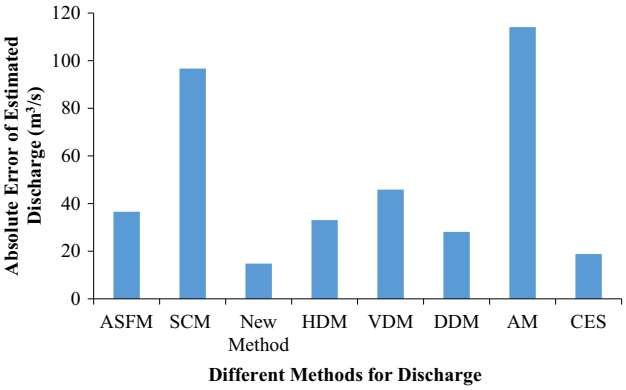

Fig. 9 Absolute error of discharge calculation for present experimental channel and channel of Rezaei [3]

7 Conclusions

The following conclusions can be derived from the above research work on converging compound channels presented in this work.

1. The energy slope is found to decrease with increase in width ratio of compound channels and increase with increase in converging angle θ of the floodplains. Further the energy slope is S_e found to increase exponentially with overbank flow depth for higher aspect ratio channels and decrease exponentially for lower aspect ratio channels; this is due to consumption of more energy in higher aspect ratio channels as compared to that in low aspect ratio channels.
2. The dependency of energy slope with five most influencing non-dimensional geometric and hydraulic parameters of a converging compound channel is analyzed. For all the parameters, it is found to bear the nonlinear functions. A multiple linear regression analysis has been done to model a generalized expression to predict the energy slope of a converging compound channel.
3. Different standard models to predict the energy slope are applied to the present channel and the converging compound channels of other investigators. CES is found to provide good discharge prediction results as compared to other approaches; however, the present approach is providing the least discharge error as compared to all other approaches.

The overall model developed for the converging compound channel using non-prismatic characterized parameters is giving good result though converging angle ranges from only

1.91° to 12.38°. In case of higher angles or any case where angle falls out of this bracket are not investigated. Beside this, the overall roughness criteria for two-stage channel are normalized considering same roughness throughout the channel, which is not the case in real field scenario. However, roughness effect can also be considered in the further investigation and can give this model a comprehensive investigation in the near future.

Acknowledgements The authors wish to acknowledge thankfully the support from the National Institute of Technology, Rourkela, and the UGC UKIERI Research project (ref no UGC-2013 14/017) by the second author for carrying out the research work in the Hydraulics Laboratory at National Institute of Technology, Rourkela is thankfully acknowledged.

References

1. Bousmar, D.; Wilkin, N.; Jacquemart, J.H.; Zech, Y.: Overbank flow in symmetrically narrowing floodplains. J. Hydraul. Eng. ASCE **130**(4), 305–312 (2004)
2. Proust, S.; Rivière, N.; Bousmar, D.; Paquier, A.; Zech, Y.; Morel, R.: Flow in compound channel with abrupt floodplain contraction. J. Hydraul. Eng. ASCE **132**(9), 958–70 (2006)
3. Rezaei, B.: Overbank flow in compound channels with prismatic and non-prismatic floodplains. Ph.D. thesis, University of Birmingham, U.K (2006)
4. Knight, D.W.; Dometriou, J.D.: Floodplain and main channel flow interaction. J. Hydraul. Eng. **109**(HY), 1073–1092 (1983)
5. Shiono, K.; Knight, D.W.: Turbulent open channel flows with variable depth across the channel. J. Fluid Mech. **222**, 617–646 (1991)
6. Khatua, K.K.; Patra, K.C.: Boundary shear stress distribution in compound open channel flow. J. Hydraul. Eng. ISH **12**(3), 39–55 (2008)
7. Khatua, K.K.; Patra, K.C.; Mohanty, P.K.: Stage discharge prediction for straight and smooth compound channels with wide floodplains. J. Hydraul. Eng. ASCE **138**, 93–99 (2012)
8. Knight, D.W.; Shiono, K.: River channel and floodplain hydraulics. Floodplain Process. **5**, 139–181 (1996)
9. Cater, J.E.; Williams, J.J.R.: Large eddy simulation of a long asymmetric compound open channel. J. Hydraul. Res. IAHR **46**(4), 445–453 (2008)
10. Jazizadeh, F.; Zarrati, A.R.: Development of a three-dimensional numerical model to solve shallow-water equations compound channels. Can. J. Civ. Eng. **35**(9), 963–974 (2008)
11. Marjang, N.; Merkley, G.P.: Velocity profile modeling in rectangular and compound open-channel cross sections. Irrig. Sci. **27**(6), 471–484 (2009)
12. Hager, W.H.: Discharge characteristics of a local discontinuous contraction (part II). J. Hydraul. Res. IAHR **25**(2), 197–214 (1987)
13. Molinas, A.; Marcus, K.B.: Choking in water supply structures and open channels. J. Hydraul. Res. IAHR **36**(4), 675–694 (1998)
14. Naik, B.; Khatua, K.K.; Wright, N.G.; Sleigh, A.: Stage-discharge prediction for converging compound channels with narrow floodplains. J. Irrig. Drain. Eng. **143**(8), 04017017 (2017)
15. Naik, B.; Khatua, K.K.: Boundary shear stress distribution for a converging compound channel. ISH J. Hydraul. Eng. **22**(2), 212–219 (2016)
16. Naik, B.; Khatua, K.K.: Water surface profile computation for compound channels with narrow flood plains. Arab. J. Sci. Eng. **42**(3), 941–955 (2017)

Journal of Biomimetics, Biomaterials and Biomedical Engineering
ISSN: 2296-9845, Vol. 28, pp 36-43
doi:10.4028/www.scientific.net/JBBBE.28.36

Submitted: 2016-06-22
Revised: 2016-07-15
Accepted: 2016-07-18
Online: 2016-07-27

Study on the Impact of Light on Human Physiology and Electroencephalogram

John William Carey Medithe*, Usha Rani Nelakuditi

Department of Electronics and Communication Engineering
Vignan's University, Guntur, INDIA

careymedithe@gmail.com*, usharani.nsai@gmail.com

Keywords: Alertness, Electroencephalogram, Light, Neurophysiology, Ocular Artifacts

Abstract: The influence of light on Electroencephalogram seems to be more critical, when physician depends on its readings to diagnose subject brain disorder according to its level. Although, bright light brings various changes in human physiological variables. But, Neurophysiological changes for specific light level still remain unclear. Thereby, in the present study, the response of brain electrical activity towards various light levels has been classified and verified. The reasons for alteration in different physiological variables due to bright light which results change in the state of electroencephalographic recordings has been reviewed. Additionally, the effects of bright light towards Ocular artifacts are also put forward. A novel hypothesis has been made using subjective analysis and experimental analysis in low luminance or darkness. It is observed that a poor lighting condition affects both behavioral task and brain activity.

Introduction

The electroencephalogram is a significant neuromedical imaging tool for the analysis and interpretation of brain electrical activity. Human brain consists of millions of neurons. Due to firing of these neurons the electric potential induced over the scalp. This potential would be in an order of microvolt and millivolt when acquired using subdural electrodes [8, 13, 16, 18, 19, 20]. Light is a transverse and electromagnetic wave that be experienced by the humans by perception of vision. There are various physiological changes occurs in humans when exposed to bright illumination. Neurophysiology and Ocular Physiology factors are noticeably affected. The luminosity reflected into the human eyes elicits changes in the state of electroencephalographic recordings. Here, Type of the surface, the angle of the incidence and spectral composition are prime factors to study about the lighting parameters. If the EEG experimental rooms colored with reflective color like silver results in more effect of light on the subject. Though, Exposure to light brings alterations in human physiology like suppression of melatonin hormone and core body temperature [11]. Thus, affects the neurobehavioral measures like alertness, performance and reaction time which consequences to Change in EEG frequencies [10]. To contemplate changes in neural behaviour, Central study weighting upon the alpha activity in occipital region, which is correlated to the light exposed. Another important study that light alters the state of subject alertness which is entirely dependent on the release of melatonin hormone in the human brain during poor lighting conditions. However, exposure to bright illumination does not affect behavioral task perform by the subject, but it affects the brain electrical activity.

Physiological changes when exposed to bright light

When a subject exposed to a bright illumination condition without changing the behavioral task, it alters many physiological changes like subjective alertness, incidence of slow eye movements, plasma melatonin hormone, core body temperature and other ocular physiological changes.

The illumination caused by the luminous object in a distance d is given in Eq. (1).

$$E = I / d^2 \tag{1}$$

Where E is the illumination caused by the light source from a distance d, I is the luminous intensity of a respective light source. From Eq. 1 it is to be known that, the illuminating conditions done by the light source is entirely dependent on the distance between the light source and illuminating region. Various physiological effects of illumination are studied below.

The study on the Melatonin hormone extends the correlation between the lighting parameters and the physiological variables. Melatonin is the natural hormone which is found in the human brain, which is originated in the pineal grand of the human brain. It is entirely reliant on the circadian rhythm generated by the light and dark cycles [11]. Melatonin synthesis was inhabited when the retinas of eyes detected the amount of light. Iain M. McIntyre, et al. (1989) gives the relation and response between the percentage suppression of Melatonin to various levels of illumination conditions. The percentage of suppression increases with an increase in illumination levels which results increase of alertness in the subject. Thus, change in the EEG spectra with change in illumination [4, 6, 7, 9, 14]. The response curve of percentage suppression of melatonin hormone in increase in amount of lux is shown in below Fig. 1.

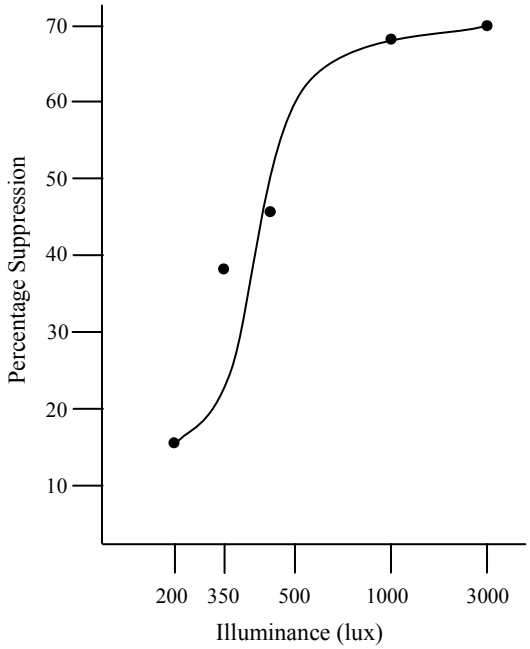

Fig. 1. The Response to a Percentage Suppression of a Melatonin Hormone with different illumination levels

As exposure to bright illumination suppress the release of melatonin hormone also affects the subjective alertness. The response of subjective alertness is proportional to the increment of illumination levels. The suppression of melatonin hormone is greater than 50% when subject is exposed to illumination of 100 lux and more. Incidence of Slow eye movements is another physiological change which is a quiet reversal to subjective alertness towards increment of illumination levels. Here, the incidence of slow eye movements is optimum till the subject is exposed to less than 100 lux. The incidence of slow eye movements has decreased when the melatonin hormone is suppressed to more than 50% with an increment of illumination levels. The subjective alertness, response is obtained to the different levels of illumination given by Christian cajochen (2007) shown in below Fig. 2. Where closed symbol identifies individuals whose suppression of melatonin hormone is less than 50%, while open symbol identifies individuals whose melatonin suppression is greater than 50%.

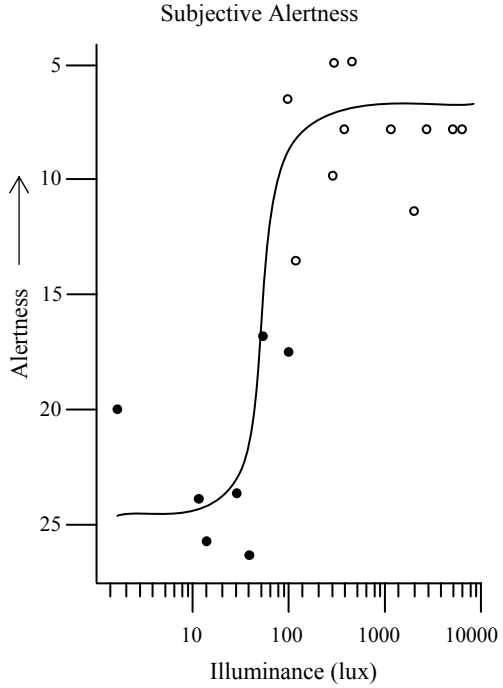

Fig. 2. The subjective alertness response to with increment of illumination level

It can be observed that the incidence of slow eye movements is high with low subjective alertness and vice-versa. This is shown in Fig. 3.

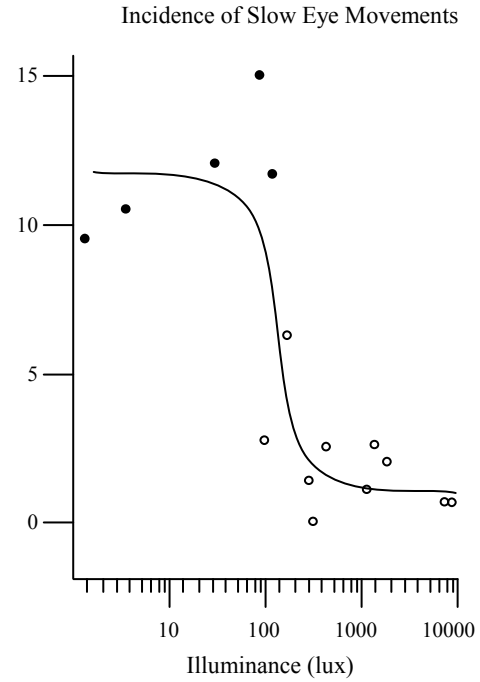

Fig. 3. The reduction of incidence of slow eye movements with increase of illumination levels

It is verified that the effects when the subject is exposed light are not limited to physiological variables, but also neurobehavioral performance which is replicated into electroencephalographic readings.

Electroencephalographic changes when to exposure to bright light

As light results in various physiological changes in the human circadian rhythm, incidentally effect on the electroencephalographic readings. Considering alpha rhythm which occurs usually in the occipital and temporal region alters when subject is in relaxed state.

The electroencephalographic alpha spectra range in frequency of 8-13 Hz, which is between theta and beta frequencies [2, 5, 13, 15]. It can also be rephrased as it is the range between more conscious to subconscious state. By analysis and interpretation of this frequency stretches the status of subject's state of alertness. This range of frequency usually strong when subject is very much relaxed like inability to focus or day dreaming. It is observed that when subject's eyes are closed and makes visual suppression for duration, which drops subject alertness into relaxation mode results in an increment of alpha activity in the occipital region.

Alpha blocking is the phenomena which reduces alpha activity when subject shows any anxiety and concentration to do any mental activity. This makes suppression in production of alpha activity and increase in higher frequency. On this aspect, it can be stated that vision alters the alpha activity, thus affects the state of the subjective alertness. A subject can have the clear perceptive vision over a specific region only when that region has good lightning conditions. Alpha spectral power increases with the visual suppression. Alpha rhythm replicate changes in physiological variables with increment in illumination levels. It can be illustrated that less illuminated environment or no light cause increase of alpha rhythm in the occipital region of the EEG. The Alpha frequency range is very much similar to the spindle which range from 7-14 Hz [2]. As alpha waves behave like a sleep spindles which usually occurs between two states of alertness.

An additional important electroencephalographic change due to light is EEG power density. It is observed that the percentage of total power in theta and lower alpha frequency is reduced. Here, presence of theta and lower alpha frequency were found in the normal adult during drowsiness and sleep. As an effect of bright light, this alters the state of the subject by suppressing the EEG power density of the frequency 5-9 Hz and increase in alertness. The response of the percentage of total power of frequency 5-9 Hz to different illumination levels are given by Christian cajochen, et al. (2000) shown in Fig. 4.

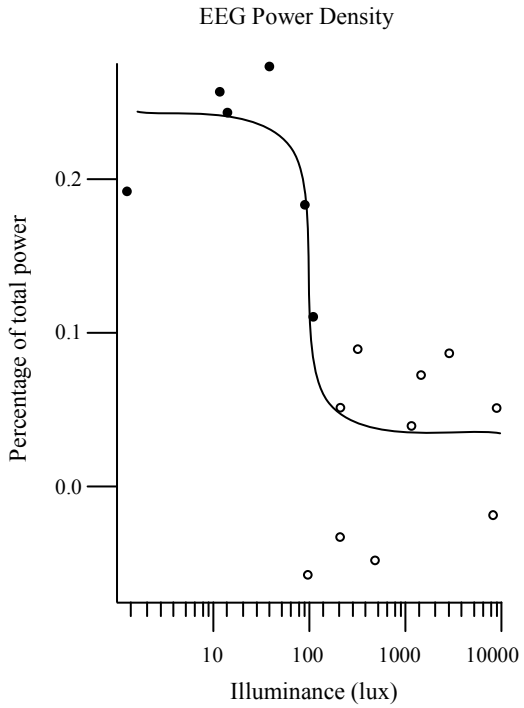

Fig. 4. Percentage Reduction of EEG Power Density of frequency 5-9 Hz with Increment of Illumination [3]

Effect of bright light on electroencephalographic Ocular Artifacts

Ocular artifacts are the undesired bio-potential induced by eye along with brain Neuro potential. The artifacts which are caused by the ocular blink or movements of an eye create a noticeable change in EEG recording. These artifacts are caused voluntary or involuntarily from the side of

patient. Here, ocular organ artifact is considered as a chief artifact among all the artifacts contaminated into EEG. Because Ocular organ region is very much near to the electrodes placed on the frontal region to acquire EEG [17]. Ocular potential is induced near and around the ocular region because the eye acts as a dipole where the cornea is more positive than the retina [13, 19]. The episode of the blink takes place, when the eye lid slides over the cornea. In this episode eye lid picks up the potential from the positively charged cornea and imposed on to the nearby frontal electrodes of EEG which are placed near around Ocular region [19, 21, 22], equivalent is obtained in Eq. (2).

$$\text{Contaminated EEG} = \text{True EEG} + \text{Ocular Artifact} \tag{2}$$

In this consequence, it is interesting to know that the ocular artifacts are also affected by the various illumination levels. When acquiring EEG, it is observed that the increase in amplitude of artifact when subject is exposed to illumination caused by the luminous objects in EEG recording room. Visually evoked potential attains by external illumination is added to the Cornea-Retina dipole potential results as developed superimposed artifact potential, specified in Eq. (3). Visually evoked potential depends on the lighting parameters around the acquisition system.

$$\text{Ocular Artifact Potential (OA)} = \text{Dipole Potential} + \text{Visually Evoked Potential (VEP)} \tag{3}$$

By correlating basic electrostatic physics to the ocular organ, the electric field due to Cornea-Retina dipole potential induced on to the electrode is given as

$$V_{Dipole} = \frac{1}{4\pi\varepsilon_0}\left[\frac{q_c}{r_c} - \frac{q_r}{r_r}\right] \tag{4}$$

Where q_c and q_r are the charges of cornea and retina of an Ocular dipole. Cornea is more positive than the Retina where r_c and r_r are the distance between the poles and the nearest electrode respectively. The total Ocular artifact potential along with visually evoked potential induced on to the nearest frontal can be specified as V_{OA}.

$$V_{OA} = \frac{1}{4\pi\varepsilon_0}\left[\frac{q_c}{r_c} - \frac{q_r}{r_r}\right] + V_{VEP} \tag{5}$$

The resultant voltage across the electrode when artifact potential in bright illumination is added with desired neuro potential, which is given in Eq. (6) and Eq. (7).

$$V_{Electrode} = V_{Neuro\ Potential} + V_{Dipole} + V_{VEP} \tag{6}$$

$$V_{Electrode} = V_{Neuro\ Potential} + V_{OA} \tag{7}$$

This visually evoked potential is varied in the various factors like subjects Age, gender, visual acuity, pupillary size etc. Visually evoked potential alters the amplitude and the latency of Peak of the wave. Latency increases with increase in subject's age. This happens because of reduction in visual acuity with increase in age [12].

Hypothetical observation

It is a hypothesis that behavioral task done in the no luminance or darkness condition which results to increase in the frontal frequency. This hypothesis has been analyzed and verified using subjective analysis and experimental analysis which is to be correlated with the frequency characteristics in the frontal region.

Experimental Procedure

This study was carried out in the laboratory on 25 healthy subjects containing 14 male and 11 female participants of age ranges from 18 to 60 years, who are studying and working in the university. All the participants are first allowed and arranged to be relaxed before the test in the recording room, where the room temperature is maintained at around 25°C. Examination room is

set to perform experimental analysis in no luminance or darkness. In order to eliminate contamination of muscular artifacts (EMG) into EEG, all the participants were made to sit on a proper base with headrest. AgCl electrodes are placed on the scalp in the frontal and front polar regions of international 10-20 standard. The reference electrode is clipped on lower end of left ear. Now each participant was asked to perform different behavioral task like locating objects which their place was interchanged from earlier. The acquired bio potential is amplified using bioamplifer and smoothed using filters. The resultant frequency characteristics of experimental analysis are compared with the ratings given by participant for subjective analysis.

Observation

As expected, It is observed that the increment in the frontal region frequency when the subject apply more mental activity. In this experimental task, subject applied more mental activity in order to approximate the location of the object in the poor light levels. The response frequency of the mental activity done by the subject is in the range of 12-25 Hz, which falls in to the range of Beta frequency. The state of occurrence of Beta activity in the frontal region shows up when subject applies more mental activity to perform the task. This observation brings out that subject goes into the problem solving mentality which result in increase in the frontal frequency. Here, on the observation of all the participants with good health and in normal mental condition. The low luminance condition alters the behavioral task and the frontal brain activity. This assessment can also use to test the subjects electroencephalographic Beta rhythm. Deficiency of Beta activity in the subject to perform any task results in lack of concentration and problem solving. Extreme Beta activity may results in sleep disorders.

Discussion

After completing the hypothetical examination in the laboratory, each participant is asked to give the rating for mental ability or stress applied to do any behavioral task in the darkness condition. It is a rating from point 1 to 5. Where rating 1 indicates the very less mental ability and rating 5 indicates subject applies high mental ability or stress to perform such behavioral task. Many of the subjects feel to apply more mental ability to do any behavioral task with 3-5 rating. If 4 and 5 rating shows requirement of high mental application, 76% of the participants feels to apply high mental activeness to do any behavioral task in darkness. From this outcome of subjective analysis, it can be stated that the subject feel to apply high mental activity to perform any behavioral task in darkness condition. When comparing the results of subjective analysis with the electroencephalographic rhythm in frontal region, we found similar characteristics between subjective and experimental analysis. The graphical representation of a subjective analysis is given in below Fig. 5.

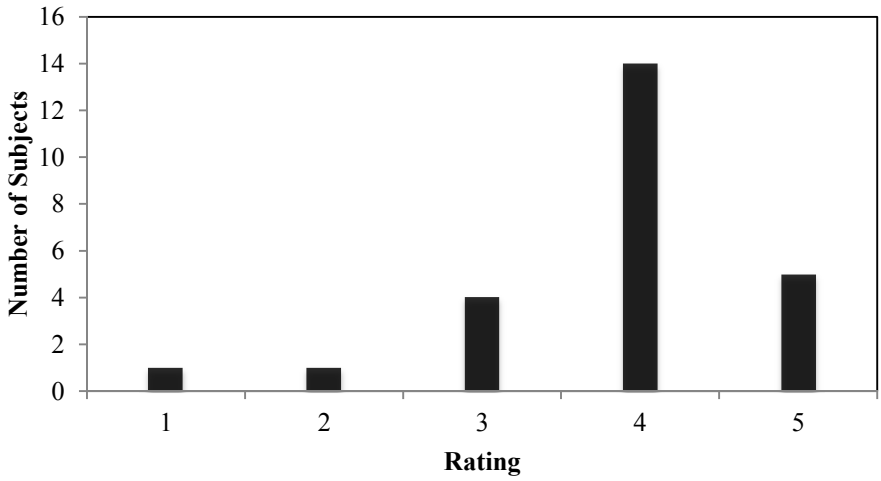

Fig. 5. Graphical representation of ratings given by the number of subjects to do any behavioral task in darkness

On correlating the experimental outcome with the subjective analysis, the frame of mentality of the subject on performing any task is replicated as characteristics of the frontal frequency. As subject feels more stress and complicated to perform any task in the darkness than in luminance condition. If the subject does not exhibit such frequency characteristics while performing any behavioral task in low luminance is considered as abnormal frequency rhythm. Abnormalities like sleep disorders and poor concentration can be evaluated. The subject who exhibits abnormal characteristics may call for the diagnosis by the physician. Different case studies are observed on performing different tasks to study the neural behaviour in darkness or low luminance condition.

Conclusion

As the light alters the various physiological variables, it also alters the spectral rhythm of various regions of the brain. The illumination conditions caused by the luminous objects in the EEG recording room bring enormous changes in human physiology and brain activity. An increment in the illumination level leads to inhibition of melatonin hormone, which increases the subjective alertness and reduction in incidence of slow eye movements. It also affects the brain activity by suppressing the EEG power density of 5-9Hz which increases in subjective alertness. Blocking Alpha frequency in the occipital region is another change due to increment in light levels. Improper lighting conditions also bring unusual results in neural behavior which can be misjudged by the physician and call subject for diagnosis. The study on Melatonin hormone analysis with effect of light brought various physiological changes are brought onto the screen. Characteristics of Blink artifact are also altered due to addition of visually evoked potential results in change of amplitude and latency. The novel hypothesis observation verified using experimental and subjective analysis. The behavioral task performed in darkness results in increase of frequency in the frontal region. From this it is to be known that no luminance or darkness condition affects both the behavioral task and brain electrical activity.

References

[1] Maher A, Kirkup L, Swift P, Martin D, Searle A, Tran Y, Craig, A Effect of luminance level on electro-encephalogram alpha-wave synchronisation. Medical & Biological Engineering & Computing (2001) 39:672-677

[2] Toscani M, Marzi T, Righi S, Viggiano M, Baldassi S, Alpha waves: a neural signature of visual suppression. Exp Brain Res (2010) 207:213-219

[3] Cajochen C, Zeitzer J, Czeisler C, Dijk D, Dose-response relationship for light intensity and ocular and electroencephalographic correlates of human alertness. Behavioural Brain Research(2000) 115:75-83

[4] Shieh K, Chen M, Wang Y, Effects of display medium and luminance contrast on memory performance and EEG response. International Journal of Industrial Ergonomics (2005) 35:797-805

[5] Brown B, Recognition of Aspects Of Consciousness Through Association With EEG Alpha Activity Represented By A Light Signal. Psychophysiology (1970) 6:442-452

[6] Cajochen C, Krauchi K, Danilenko K, Wirz-Justice A, Evening administration of melatonin and bright light: Interactions on the EEG during sleep and wakefulness. Journal of Sleep Research(1998) 7:145-157

[7] Park J, Min B, Jung Y, Pak H, Jeong Y, Kim E, Illumination influences working memory: An EEG study. Neuroscience (2013) 247:386-394

[8] Spehlmann R, EEG primer. Elsevier/North-Holland Biomedical, Amsterdam,1981

[9] Mclntyre I, Norman T, Burrows G, Armstrong S, Human Melatonin Suppression by Light is Intensity Dependent. J Pineal Res (1989) 6:149-156

[10] Cajochen C, Alerting effects of light. Sleep Medicine Reviews (2007) 11:453-464

[11] Myers Badia P, Immediate effects of different light intensities on body temperature and alertness. Physiology & Behavior (1993) 54:199-202

[12] Narayan S, Subramanian S, Gaur G, Low luminance/eyes closed and monochromatic stimulations reduce variability of flash visual evoked potential latency. Ann Indian AcadNeurol 16:614(2013

[13] A. Kandaswamy, V. Krishnaveni, S. Jayaraman, N. Malmurugan and K. Ramadoss, Removal of Ocular Artifacts from EEG—A Survey, IETE Journal of Research, (2005) vol. 51, no. 2, 121-130

[14] M. Murugappan, M. Juhari, R. Nagarajan and S. Yaacob, An investigation on visual and audiovisual stimulus based emotion recognition using EEG, IJMEI, (2009) vol. 1, no. 3, p. 342

[15] S. Bong, M. Murugappan and S. Yaacob, Methods and approaches on inferring human emotional stress changes through physiological signals: a review, (2013) IJMEI, vol. 5, no. 2, p. 152

[16] S. Singh and D. Bansal, Design and development of BCI for online acquisition, monitoring and digital processing of EEG waveforms, IJBET, (2014) vol. 16, no. 4, p. 359

[17] D. Bansal, R. Mahajan, S. Roy, D. Rathee and S. Singh, Real-time man-machine interface and control using deliberate eye blink, IJBET, (2015) vol. 18, no. 4, p. 370

[18] M. Sheoran, S. Kumar and S. Chawla, Methods of denoising of electroencephalogram signal: a review, IJBET, (2015) vol. 18, no. 4, p. 385

[19] J. Medithe and U. Nelakuditi, "Removal of Ocular Artifacts in EEG," in IEEE International Conference on Intelligent Systems and Control (ISCO-2016), Coimbatore, India, Jan. 2016

[20] J. Medithe and U. Nelakuditi, "Study of Normal and Abnormal EEG", in IEEE International Conference on Advanced Computing and Communication Systems (ICACCS-2016), Coimbatore, India, Jan. 2016

[21] C. Zhang and A. Kareem Abdullah, Discussion of Approach for Extracting Pure EOG Reference Signal from EEG Mixture Based on Wavelet Denoising Technique, Journal of Biomimetics, Biomaterials and Biomedical Engineering, (2015) vol. 23, pp. 9-17

[22] C. Zhang, A. Kareem Abdullah and A. Abdullabs Abdullah, Electroencephalogram-Artifact Extraction Enhancement Based on Artificial Intelligence Technique, Journal of Biomimetics, Biomaterials and Biomedical Engineering, (2016) vol. 27, pp. 77-91

Journal of Biomimetics, Biomaterials and Biomedical Engineering Vol. 28
10.4028/www.scientific.net/JBBBE.28

Study on the Impact of Light on Human Physiology and Electroencephalogram
10.4028/www.scientific.net/JBBBE.28.36

Article:
Naik, B, Khatua, KK, Wright, NG et al. (1 more author) (2017) Stage-Discharge Prediction for Converging Compound Channels with Narrow Floodplains. Journal of Irrigation and Drainage Engineering, 143 (8). 04017017. ISSN 0733-9437

https://doi.org/10.1061/(ASCE)IR.1943-4774.0001184

IR7753

Stage-Discharge Prediction for Converging Compound Channels with Narrow Floodplains

B. Naik[1], K. K. Khatua[2], N. G. Wright[3], and A. Sleigh[4]

1 Ph.D. Research Scholar, Department of Civil Engineering, National Institute of Technology Rourkela, India (corresponding author). Email: banditanaik1982@gmail.com

2 Associate Professor, Department of Civil Engineering, National Institute of Technology Rourkela, India. Email: kkkhatua@yahoo.com

3 Professor of Water and Environmental Engineering, University of Leeds, School of Civil Engineering, UK. Email: n.g.wright@leeds.ac.uk

4 Professor, Department of Water and Environmental Engineering, University of Leeds, School of Civil Engineering, UK. Email: p.a.sleigh@leeds.ac.uk

ABSTRACT: Momentum transfer between the main channel and the side flood plains tends to increase the floodplain shear whereas the main channel shear decreases. The increase and decrease in shear are greatly influenced when a compound channel is with non-prismatic flood plains. In converging compound channels water flow on the floodplain crosses over water flow in the main channel, resulting in increased interactions and momentum exchanges. An experimental analysis concerning the distribution of shear stress in the main channel and floodplain for both prismatic and non-prismatic compound channels under different over-bank flow conditions are performed. New equations are developed for predicting boundary shear

stress distribution for a compound channel with the non-prismatic flood plain. Using these expressions the stage-discharge relationships for both prismatic and non-prismatic compound channels of lower width ratio have been successfully estimated. The efficiency of the models has also been verified by applying natural river data sets.

Author Keywords: overbank flow, boundary shear, stage discharge, Prismatic, non-prismatic, low width ratio

INTRODUCTION

Compound channels are the usual pattern of rivers during floods. These are very vital for environmental, ecological and design issue. It has become essential to study the flow behavior of rivers both in inbank and overbank flow conditions. Sellin (1964) first demonstrated the momentum transfer phenomena in a compound channel on the basis of experimental investigation. After that many investigators proved that momentum transfer mechanism causes the non-uniformity of the boundary shear stress distribution along the subsection perimeters. Knight and Hamed (1984) proposed boundary shear distribution models for both homogeneous and non-homogeneous compound channels of width ratio α (α =width ratio = Flood plain width (B)/ main channel width (b)) value up to 4. Mohanty et al. (2014) found a new expression of boundary shear distribution for compound channel of width ratio α up to 11.96. When these expressions are used for lower width ratio prismatic and non-prismatic compound channels, significant errors were observed in estimation of shear distribution due to not accounting the mass and momentum transfer (Bousmar and Zech (1999), Bousmar et al. (2004), Rezaei (2006)

and Proust et al. (2006)). These important factors should be considered in the flow modeling for the non-prismatic compound channel. Experiments have been conducted on compound channels with various converging flood plains to obtain expressions for $\%S_{fp}$ ($\%S_{fp} = 100\times S_{fp} / SF$, S_{fp} = boundary shear force occurring in the floodplains and SF the total shear force of the compound cross section) and finally, procedure has been given for stage discharge prediction for the compound channel of low width ratio for both prismatic and non-prismatic flood plain.

EXPERIMENTAL WORKS

Experimental Procedure

Experiments on non-prismatic compound channel have been performed at the Hydraulics and Fluid mechanics Laboratory of National Institute of Technology, Rourkela, India. Three sets of compound channels with converging floodplains made up of Perspex sheet were fabricated inside a concrete flume of size 15m long × 0.9m width × 0.5m depth. The upstream part of the non-prismatic compound channel was considered for taking a measurement of the prismatic part. The width ratio of the prismatic part of the compound channel was found to be α = 1.8 and the aspect ratio of the main channel were found to be δ = 5 (δ =aspect ratio =main channel width (b) / main channel height (h)) which was maintained constant throughout the length. Keeping the geometry of main channel constant, the converging angles of the flood plains were changed to 12.38°, 9^o and 5^0 respectively. The converging length of the fabricated channels was estimated to be 0.84m, 1.26m and 2.28m respectively. Longitudinal bed slope of the channel was maintained at 0.0011, satisfying subcritical flow conditions. The roughness of the floodplain and main channel were alike and the Manning's n was find out as 0.011 from the inbank experimental runs

in the channel. A complete re-circulating system of water supply from the underground sump to the channels through overhead tank and volumetric tank was done with the series of centrifugal pumps. In the upstream section of the rectangular notch flow strengtheners were provided to reduce the turbulence and velocity approach. At the downstream end of the channel an adjustable tailgate was present to maintain the uniform flow throughout the test reach of the channel. Water flowing over the channel was collected by a volumetric tank that helps to record the discharge by time rise method. Figure 1(a) shows the plan view of the experimental setup. Figure1 (b) shows the Longitudinal & Cross-sectional dimension of the non-prismatic compound channels. Figure 1(c) Grid showing the velocity measurement at the test section. A series of micro-Pitot tubes of 4.77 mm external diameter in combination with suitably inclined manometers as well as 16-MHz Micro-ADV (Acoustic Doppler Velocity-meter) were used to measure velocity at the predefined flow-grid points. Boundary shear stresses were measured at the predefined boundary points along the wetted perimeter of the compound channels using Patel's (1965) relationship. Summary of geometrical parameters of present experimental channels (both prismatic and non-prismatic) with details of other investigators channels are given in Table 1 and Table 2 respectively.

EXPERIMENTAL RESULTS

Stage-discharge relationship for both prismatic and non-prismatic section are shown in Figure 2(a) and 2(b) respectively. A total 15 number of runs are observed at these test reaches. Using the stage-discharge data for the NITR series (both for prismatic and non-prismatic sections), a line of best-fit curves were obtained mathematically in the form of a simple power function. A

typical longitudinal velocity contour of the prismatic section with relative depth 0.15 is shown in Figure 2(c). The maximum point's velocities are found to occur near the middle free surface of the main channel and minimum velocities are found to be at the corners of flood plains. This is because of the converging flood plain from both sides which accelerates the flow diverting to the main channel sections. At the non-prismatic sections i.e.section-2, the boundary shears distribution for a typical case of relative flow depth 0.15 for converging floodplain angle 12. 38º and of relative depth 0.5 for the converging angle 11.31° of Rezaei (2006) are shown in Figure 3(a) and 3(b) respectively. These data are useful for examining the force balance along the channel, for calibration of the numerical model and for finding the location of secondary flow cells. Looking to the boundary shear distribution in Figure 3(a) it can be observed that there is a peak at the mid of the main channel and the value decreases towards the flood plain regions. There is a sudden drop of boundary shear value noticed at the interfaces. This happened to all the experimental section covering from prismatic to non-prismatic parts. Further from sec-1 to sec-3, the peak value of boundary shear stress is found to increases. The nature of boundary shear stress distribution is a little bit different in Figure 3(b). At sec-1of Rezaei (2006) channel, the pattern of boundary shear stress distribution is similar to that of NITR channel results however at the last section the peak value is not at the mid of the main channel but at the interfaces i.e. particularly at the turbulent region. This is due to that Rezaei (2006) channel bears higher aspect ratio where as NITR channel has a lower aspect ratio as well as due to the higher slope of NITR channel as compared to Rezaei (2006) channel. This also occurred due to higher order of secondary flow that occurs at the corner of the main channel and at the interfaces.

BOUNDARY SHEAR DISTRIBUTION

Compound channel with Prismatic Flood Plain

Different boundary sections of the compound channel for both prismatic and non-prismatic sections involving the wetted parameters are labelled as (1), (2), (3) and (4) are presented in Figure (4). Label (1) indicates the two vertical edges of the floodplain [2(H- h)], and (2) indicates floodplain beds (B - b). Label (3) indicates the two main channel height (2h) and the width of the main channel bed (b) is indicated by label (4) (where H = Total height of the compound channel, B = Total width of the compound channel). To find out the relevant boundary shear force per unit length for each element experimental shear stress distributions at each point of the wetted perimeter are numerically integrated over the respective sub-lengths of each boundary element (l), (2), (3) and (4). Total boundary shear forces have been computed by adding all the beds and walls of the compound channel. Then it has been used as a divisor to calculate the percentages of shear force carried by the boundary elements of the compound channel. Percentage of shear force by floodplains comprising elements (1) and (2) is represented as $\%S_{fp}$. An equation of $\%S_{fp}$ with α and β (β = relative depth = (H- h)/H) for lower width prismatic compound channels have now been obtained. Formerly different researchers have presented their model for $\%S_{fp}$. Knight and Demetriou (1983) proposed an equation for $\%S_{fp}$

$$\%S_{fp} = 48(\alpha - 0.8)^{0.289}(2\beta)^{m} \quad (1)$$

Where m is calculated from the relation

$$m = 1/[0.75e^{0.38\,\alpha}] \quad (2)$$

Equation (1) is relevant for homogeneous compound channels. Again Knight and Hamed (1984) developed a new equation for non-homogeneous compound channels

$$\%S_{fp} = 48(\alpha - 0.8)^{0.289}(2\beta)^{m}[1 + 1.02\sqrt{\beta}\log\gamma] \quad (3)$$

Where γ = Ratio of Manning's roughness of floodplain (n_{fp}) and the Manning's roughness of main channel (n_{mc})

Equation (1) is useful for $\alpha \leq 4$. Khatua and Patra (2007) developed equation (3) for α up to = 5.25

$$\%S_{fp} = 1.23(\beta)^{0.1833}(38Ln\alpha + 3.6262)[1 + 1.02\sqrt{\beta}\log\gamma] \quad (4)$$

Khatua et al (2012) developed a new equation for $\%S_{fp}$ for α = 6.67

$$\%S_{fp} = 4.1045(\%A_{fp})^{0.691} \quad (5)$$

Mohanty et al. (2014) again proposed a model for α up to 12

$$\%S_{fp} = 3.3254(\%A_{fp})^{0.746} \quad (6)$$

The equations of the above investigators are for width ratio α >3.0 so significant errors are obtained when all equations are analyzed against compound channels of lower width ratio i.e $\alpha \leq$ 2.2. Following the work of previous investigators, the expression for estimating shear in floodplain has been attempted. Observing the energy gradient equation, it can be stated that SF is a function of corresponding flow area A. Then $\%S_{fp}$ of a compound channel should be a function of $\%A_{fp}$ ($\%A_{fp} = 100 \times A_{fp}/A$ where A_{fp} is the area of flood plain). Therefore, a functional relationship between $\%S_{fp}$ and $\%A_{fp}$ can be derived from data sets of five different types of compound channels with α ranging from 1.5 to 3.0. The functional correlation between $\%S_{fp}$ and $\%A_{fp}$ for the compound channel has been found out. This has been obtained by best-fit curve between $\%A_{fp}$ and $\%S_{fp}$ which gave the highest regression coefficient i.e. R^2=0.95. The data used by this model are two series of compound channel data of Knight and Demetrious (1983) , the data of experimental compound channel of NIT, Rourkela, India as well as FCF-A-03 channel, along with four series of compound channel data of Rezaei (2006) (details of the data sets are

given in Table.1). Manning's n values for all these smooth surfaces are taken as 0.01. Figure (5) shows the best fit curve and its equation is found as

$$\%S_{fp} = 3.779(\%A_{fp})^{0.691} \quad (7)$$

In terms of α, β, equation (7) can be expressed as

$$\%S_{fp} = 3.779\left[\frac{100\beta(\alpha-1)}{1+\beta(\alpha-1)}\right]^{0.691} \quad (8)$$

Following the work of Knight and Hamed (1984) the equation (8) (says present model I) can be written for non-homogeneous channel as

$$\%S_{fp} = 3.779(\%A_{fp})^{0.691}[1 + 1.02\sqrt{\beta}\log\gamma] \quad (9)$$

The deviation among the calculated values of ($\%S_{fp}$) using equations (1), (5), (6) and (8) and the subsequent observed values are shown in Figure (6). Here the accuracy of the developed model i.e. Equation (8) is verified.

The error percentage in estimating $\%S_{fp}$ is always less when compared to the result of previous models for both present experimental channel as well as channel of Rezaei (2006), Knight & Demetriou (1983) and are shown in Figure 7 (a), (b), (c) and (d) respectively.

Compound channel with Converging Flood plains

Observing equations of various researchers i.e. equation (1), (2), (6) etc. it is noticed that $\%S_{fp}$ = F (α, β, δ) for the prismatic compound channel, Where F is the functional symbol. Considerable error are observed when all the equations are verified against compound channels with converging flood plains due to variation of geometry and converging effect in such channels. So an effort has been given here to analyse the variation of $\%S_{fp}$ with respect to different geometric and hydraulic parameters of compound channels with the converging flood plain. $\%S_{fp}$ has been

evaluated from experimental data sets of three different types of converging compound channels of NIT, Rourkela, India along with data of Rezaei (2006) (details are given in Table.2). For a compound channel with converging flood plain two more parameters can be added to describe boundary shear distribution as the boundary shear distribution changes from section to section. The dependency of $\%S_{fp}$ with most influencing parameters and the best functional relationships can be expressed in the following form

$$\%S_{fp} = F\ (\alpha, \beta, \delta, \theta, X_r) \quad (10)$$

Where θ=Converging angle, X_r=Relative distance(x/L), x=distance between two consecutive sections , L=Total Non-prismatic length.

The variation of $\%S_{fp}$ with β, X_r , θ, has been plotted in different plots. The best individual relationship has been obtained as shown in Fig.8, 9 and 10.

By considering the above plots a generalized mathematical empirical relation of $\%S_{fp}$ for compound channel with converging floodplain has been modeled as

$$\%S_{fp} = 18.505 + 62.140(\beta)^{0.631} - 24.42(X_r) + 1.38(\theta) \quad (11)$$

Equation (11) represents the final expression of the model (says Model II) . More details can be found out in Naik and Khatua (2016). After finding the $\%S_{fp}$ the stage discharge relationship at different sections of a compound channel with converging floodplain can be estimated as described below.

APPLICATION OF THE MODEL

After obtaining equations to estimate $\%S_{fp}$ for the compound channel with lower width ratio for both prismatic reach and non-prismatic reach, now these can be used to predict discharge at the

prismatic and non-prismatic reach compound channels especially for lower width ratio cases. Khatua et al (2012) developed MDCM where the proportionate length of interface from the main channel and from flood plain can be evaluated by balancing the apparent shear at the vertical interface. The new expressions can be adopted instead to evaluate the momentum transfer in terms of apparent shear force occurring at the interface in terms of an appropriate length of the interface between the main channel and floodplain of a compound channel. The proportionate length of interface X_{mc} to be included in the main channel perimeter and proportionate length of interface X_{fp} to be excluded from the flood plain perimeter has been expressed as

$$X_{mc} = \mathrm{P_{mc}}\left[\frac{100}{(100-\%S_{fp})}\left(\frac{A_{mc}}{A}-1\right)\right] \quad (12)$$

$$X_{fp} = \mathrm{P_{fp}}\left[\frac{100}{\%S_{fp}}\left(\frac{A_{mc}}{A}-1\right)+1\right] \quad (13)$$

Where P_{mc} and P_{fp} are the wetted perimeters of the main channel and floodplains respectively. Further details of the derivation of equation 12 and equation 13 are found in Khatua et al (2012). After evaluating X_{mc} and X_{fp} the discharge for main channel and floodplain are evaluated using Manning's equation and added together to give over all discharge of both prismatic and non-prismatic sections of a compound channel as

$$Q = \frac{\sqrt{S}}{n_{mc}} A_{mc}^{\frac{5}{3}} (P_{mc}+X_{mc})^{-2/3} + \frac{\sqrt{S}}{n_{fp}} A_{fp}^{5/3} \left((P_{fp}+X_{fp}\right)^{-2/3} \quad (14)$$

Where S_0 is the bed slope of both main channel and floodplain and X_{mc} and X_{fp} are depending on geometrical parameters and $\%S_{fp}$. Therefore $\%S_{fp}$ can be evaluated from equation (8) and (11) respectively for prismatic compound channels and non-prismatic compound channels of lower width ratio respectively. Now, equations (8), (12), (13), (14) are used to estimate the discharge of prismatic compound channel and now let denoted as EMDCM I. Similarly equations (11), (12), (13), (14) are used to estimate the discharge of compound channel with converging flood plain

and denoted as EMDCM II. The result from EMDCM I and EMDCM II with other traditional methods like VDM, HDM, DDM are compared well when applied to the experimental channel and other data sets.

Using the equation (14), along with standard traditional methods are applied to estimate discharge in the Present experimental converging compound channel of Rourkela and Rezaei (2006) Channel both for Prismatic and non-prismatic case. Methods used are horizontal division method (HDM), vertical division method (VDM), diagonal division method (DDM). The percentage of error in estimating the discharge is computed as

$$\text{Mean } Absolute\ Error(\%) = \frac{100\%}{N} \Sigma \left| \frac{Q_{cal} - Q_{act}}{Q_{act}} \right| \quad (15)$$

Where Q_{cal} is the estimated discharge, Q_{act} is actual discharge; N is the total number of data.

After estimating discharge by different approaches with the present approach, the results are compared in Figure 11. In Figure 11, the proposed modified approach provides the best discharge result whereas HDM method is providing the worst among all methods.

Figure (12) shows the results among various methods applied to the Present experimental Channel of NIT Rourkela and Rezaei (2006) Non-prismatic channel cases. In Figure 12, the proposed modified approach provides the best discharge result whereas SCM method is providing the worst among all methods.

PRACTICAL APPLICATION OF THE METHOD

Modified Equation I (prismatic section)

After applying the modified equation I and II to the new experimental lower width channel of NIT, Rourkela and the existing narrow channel data of Rezaei (2006), it was decided to test the

approaches for its suitability in a natural river data. Therefore, the published river data of river Main (Myers and Lynness 1990) is selected in this work. The river is straight, uniform in cross section. The width ratio is less as compared to other natural rivers and it varies from 1.2 to 2.5 against the corresponding relative depth value between 0.006 and 0.47. The observed discharge ranges between 18.34 and 57.7 m^3/s. The lateral cross section of River Main has been shown in Figures (13).

The previous four standard methods have been applied to estimate discharge and the computed discharge values are then compared with actual discharge. Figure 14 shows the results of the different approaches it is seen that the present approach (EMDCM I) provide good results. Figure 14 clearly establishes the fact that EMDCM I can also be used to estimate discharge even in natural rivers having narrow flood plains with width ratio in the range of 1.5–2.2

Modified Equation II (Nonprismatic section)

For verification of the model in non-prismatic section, the River Main (Martin & Myers 1991) is chosen here. The experimental reach consists of a 1 km section of the River Main in Northern Ireland which has been reconstructed to form a compound section consisting of a central main channel and two side flood plains. A plan view of the reach was shown in Fig. 15 , which illustrates that the river was almost straight in this section. Cross-sectional dimensions of sections 14 and 6, at the limits of the reach, were shown in Fig. 16. The topographical data of these and the intermediate sections are shown in Fig. 15, were supplied by the Department of Agriculture for Northern Ireland, Drainage Division. The bed material in the main channel was coarse gravel with a D_{50} size varying from 100 mm to 200 mm, while the banks of the main

channel consist of large boulders up to 1 m in diameter. The flood plains were sown in grass. The average longitudinal bed slope of the reach was 0.003.The definitions of 'main channel' and 'flood plain' are shown in Fig.16 , showing that a vertical division had been adopted.

Geometrical properties and surface conditions of these rivers are given in Table 3. Table 4 shows the results of actual discharge and the predicted discharge using the present approach (EMDCM II) provide good results. Table 4 clearly establishes the fact that EMDCM II can also be used to estimate discharge even in natural rivers having converging flood plains.

CONCLUSIONS

1. From the experimental results on compound channels with converging flood plains, the boundary shear at the wetted perimeter for different sections are measured and the distribution of shear force carried by flood plains and in main channel perimeters were analysed. It is observed that there is a peak value of shear at the mid of the main channel and the value decreases towards the flood plains. There is a sudden drop of boundary shear value noticed at the interface. This happens to all the experimental sections covering from prismatic to non-prismatic part. But at the last section of Rezaei (2006) channel, the peak value is not at the mid of the main channel but at the interfaces in particularly at the turbulent region.

2. The shear stress percentage carried by flood plains ($\%S_{fp}$) is found to decrease from section to section of all the compound channels with converging flood plains. For the channels of the same converging angle, the shear force percentage carried by flood plains is found to increase with the increase of overbank flow depths.

3. The percentage of shear stress carried by flood plain of a lower width compound channel for prismatic part (α = 1.8) are found to be a non-linear function of the percentage of area occupied by the flood plains ($\%A_{fp}$) and the former has been expressed mathematically as a power function of the latter. The present mathematical model derived for $\%S_{fp}$ provides the least error when compared with previous models applied to lower width compound channels with width ratio ($1.5 < \alpha < 3$).

4. For a compound channel with converging flood plains mathematical expression for $\%S_{fp}$ has been expressed in terms of non-dimensional geometric and hydraulic parameters α, β, γ, θ, X_r which is specifically applicable to lower width converging compound channels.

5. The New expression of boundary shear stress distribution for the present converging compound channel has been utilized to predict the stage-discharge relationship of the compound channel for both prismatic and converging flood plains. The proposed approaches have been applied to predict discharge values for present lower width compound channel of NIT, Rourkela and Rezaei (2006) data for Prismatic and non-prismatic case. The approach is very suitable for a channel of lower width ratio and believes to predict discharge with more accuracy. Both the approaches is also found satisfactory in predicting discharge accurately in a real river case having lower width flood plains.

6. The limitation of the present work is that the new models can be utilized for prediction of the conveyance of a converging compound channel with lower width of flood plain and for homogeneous roughness in the subsections. These models can further be improved for wider flood plains and for differential roughness by utilizing more data sets for such cases.

ACKNOWLEDGMENTS

We acknowledge thankfully the support from the Institute and the UGC UKIERI Research project (ref no UGC-2013 14/017) for carrying out the experimental research work in the Hydraulics laboratory at National Institute of Technology, Rourkela.

Notation

The following symbols are used in this paper:

A = total area of the compound channel

A_{fp} = corresponding area by floodplain

B = Total width of compound channel

b = Total width of the main channel

h = Total height of the main channel

H = bank full depth

L = converging length

MAE = Mean absolute error

MAPE = Mean absolute percentage error

MSE = Mean squared error

RMSE = Root Mean squared error

S_0 = bed slope

α = width ratio (B/b)

δ = aspect ratio (b/h)

β = relative depth ((H-h)/H))

Xr = relative distance(x/L)

x = distance between two consecutive sections

θ = converging angle

S_{fp} = boundary shear carried by the floodplains

SF = total shear force of the compound channel

REFERENCES

Bousmar, D. and Zech, Y. (1999). "Momentum transfer for practical flow computation in the compound channel." J. Hydraul. Eng., 125 (7), 696-706.

Bousmar, D., Wilkin, N., Jacquemart, J.H. and Zech, Y. (2004). "Overbank flow in symmetrically narrowing floodplains." J. Hydraul. Eng., ASCE, 130(4), 305-312.

Khatua, K.K. and Patra, K.C. (2007). "Boundary shear stress distribution in compound open channel flow". J. Hydraul. Eng., ISH, 13 (3), 39–54.

Khatua, K.K.., Patra, K.C. and Mohanty, P.K.. (2012). "Stage-Discharge prediction for straight and smooth compound channels with wide floodplains. "J. Hydraul. Eng., ASCE, 138(1), 93–99.

Knight, D.W. and Demetriou, J.D. (1983). "Flood plain and main channel flow interaction." J. Hydraul. Eng., ASCE, 109(8), 1073–1092.

Knight, D.W. and Hamed, M.E. (1984). "Boundary shear in symmetrical compound channels. "J Hydraul. Eng., ASCE, 110(10), 1412-1430.

Martin, L.A., MYERS, W. Rc. (1991). "Measurement of overbank flow in a compound river channel."Proc. Instn Cio. Engrs, Part 2, 91, 645-657.

Myers, W.R.C. and Lynness, J.F. (1990). "Flow resistance in rivers with floodplains." Final report on research grants GR/D/45437, University of Ulster.

Mohanty, K. P., Khatua, K. K.and Dash, S. S. (2014). "Flow prediction in two stage wide compound channels." Journal of Hydraulic Engineering, ISH, 20 (2), 151-160.

Naik, B. & Khatua, K. K. (2016). "Boundary shear stress distribution for a converging compound channel", ISH Journal of Hydraulic Engineering, Volume 22, Issue 2.

Patel, V.C. (1965). "Calibration of the Preston tube and limitations on its use in pressure gradients.*"* J. Fluid Mech., 23(1),185–208. Cam- bridge University Press.

Proust, S., Rivière, N., Bousmar, D., Paquier, A., Zech, Y. & Morel, R. (2006). "Flow in the compound channel with abrupt floodplain contraction." J. Hydr. Eng., ASCE, 132(9), 958-970.

Rezaei, B. (2006). "Overbank flow in compound channels with prismatic and non-prismatic floodplains." PhD Thesis, Univ. of Birmingham, U.K..

Sellin, R. H. J. (1964). "A laboratory investigation of the interaction between the flow in the channel of a river and that over its flood plain." La Houilte Blanche, 7,793–801.

Figure Captions

Figure 1. (a) Plan view of experimental setup (Naik and Khatua 2016); (b) longitudinal and cross-sectional dimension of the non-prismatic compound channels; (c) grid showing the arrangement of velocity measurement points at the test section (Naik and Khatua 2016)

Figure 2. (a) Stage-discharge relationship for the Present experimental Channel (Prismatic sections); (b) stage-discharge relationship for compound channels with converging flood plains (Non-Prismatic sections of angle 12.38^0,9^0, 5^0); (c) longitudinal velocity contour for lower aspect ratio experimental channel (NITR) of relative depth 0.15(for converging angle 12.38°)

Figure 3. (a) Boundary shear distribution for lower aspect ratio experimental channel (NITR) of relative depth 0.15 (for converging angle 12.38°); (b) boundary shear distribution for higher

aspect ratio experimental channel Rezaei (2006) of relative depth 0.5 (for converging angle 11.31º) [(a and b) Naik and Khatua 2016]

Figure 4. Interface planes dividing a compound section into sub areas (Naik and Khatua 2016)

Figure 5. Variation of % of floodplain shear with % of area of floodplain

Figure 6. Scatter plot for observed and modeled value of $\%S_{fp}$

Figure 7. (a) Comparison for $\%S_{fp}$ for various models in the present experimental channel; (b) **c**omparison for $\%S_{fp}$ for various models in lower width (α=1.5) Rezaei (2006) Channel; (c) comparison for $\%S_{fp}$ for various models in lower width (α=2) Rezaei (2006) Channel; (d) comparison for $\%S_{fp}$ for various models in lower width (α=2.5) Rezaei (2006) Channel

Figure 8. Variation of $\%S_{fp}$ of floodplain shear with relative depth at typical sections (Naik and Khatua 2016)

Figure 9. Variation of $\%S_{fp}$ of floodplain shear with relative distance for different relative depths (Naik and Khatua 2016)

Figure 10. Variation of $\%S_{fp}$ of floodplain shear with converging angles for different relative depths (Naik and Khatua 2016)

Figure 11. Absolute Error of Discharge for Present experimental and Rezaei (2006) channel data (Prismatic case)

Figure 12. Absolute Error of Discharge for Present experimental and Rezaei (2006) channel data (Non-Prismatic case)

Figure 13. Lateral cross section of River Main (From CES v2.0 help manual 2007)

Figure 14. Absolute Error of Discharge of River Main

Figure 15. Plan view of experimental reach of River Main

Figure 16. Cross-sectional geometries of River Main at (a) upstream end of experimental reach (section 14); (b) downstream end of experimental reach (section 6)

Table 1 Details of geometrical parameters of the experimental and other Prismatic channels

Experimental/ other test channels	Series No.	Longitudinal slope(S)	Main channel width (b)in (m)	Main channel depth (h)in (m)	Main channel side slope	Width ratio (α= B/b)	Relative depth(β= H-h/H)	Observed discharge for lower width ratio compound channel α<3 (Q)in m^3/s
Present Channel	1	0.0011	0.5	0.1	0	1.8	0.15-0.3	0.037-0.051
Knight and Demetriou (1983)	1	0.00096	0.304	0.076	0	2	0.11-0.41	0.005-0.017
	2	0.00096	0.304	0.076	0	3	0.21-0.49	0.006-0.023
FCF Series-A-03	1	0.001027	1.5	0.15	1	2.2	0.05-0.5	0.225-0.834
Rezaei (2006)	1	0.00203	0.398	0.05	0	1.5	0.05-0.54	0.010-0.045
	2	0.00203	0.398	0.05	0	2	0.05-0.52	0.010-0.050
	3	0.00203	0.398	0.05	0	2.5	0.06-0.47	0.012-0.050
	4	0.00203	0.398	0.05	0	3	0.07-0.47	0.012-0.050

Table 2 Hydraulic parameters for the compound channels with converging flood plain data

Verified test channel	Types of channel	Angle of convergent (Θ)	Longitudinal slope (S)	Cross-sectional geometry	Total channel width (B in m)	Main channel width (b in m)	Main channel depth (h in m)	Width ratio (sec-1) B/b (α)	Converging length (X_r in m)	Aspect Ratio b/h (δ)
Rezaei (2006)	Converging (CV2)	11.31°	0.002	Rectangular	1.2	0.398	0.05	3	2	7.96
Rezaei (2006)	Converging (CV6)	3.81°	0.002	Rectangular	1.2	0.398	0.05	3	6	7.96
Rezaei (2006)	Converging (CV6)	1.91°	0.002	Rectangular	1.2	0.398	0.05	3	6	7.96
Present study	Converging	5°	0.0011	Rectangular	0.9	0.5	0.1	1.8	2.28	5
Present study	Converging	9°	0.0011	Rectangular	0.9	0.5	0.1	1.8	1.26	5
Present study	Converging	12.38°	0.0011	Rectangular	0.9	0.5	0.1	1.8	0.84	5

Table 3 Details of geometrical parameters of the experimental reach of River Main

Sl. No	Item Description	Converging Compound Channel
1	Geometry of main channel	Trapezoidal
2	Geometry of flood plain	Converging
3	Top width of compound channel (B_1)	before convergence 30.4m
4	Top width of compound channel (B_2)	after convergence 27.3m
5	Converging length of the channels	800m
6	Slope of the channel	0.003
7	Angle of convergence of flood plain (^{0})	0.138
8	Position of experimental section 1	start of the converging part
9	Position of experimental section 2	800 m away from sec-1
10	Roughness of main channel	0.035 (v.T. Chow 1959)
11	Roughness of main channel banks	0.050 (v.T. Chow 1959)
12	Roughness of flood plains	0.041 (v.T. Chow 1959)

Table 4 Details of of the experimental runs of River Main

Sections	H=total water depth	β=relative depth	calculated discharge	observed discharge	% error
14.00	1.01	0.01	16.92	18.45	8.29
14.00	1.02	0.02	17.08	19.87	14.03
14.00	1.10	0.09	18.29	19.40	5.73
14.00	1.16	0.13	19.37	21.16	8.48
14.00	1.11	0.10	18.42	21.82	15.58
14.00	1.27	0.21	22.07	28.48	22.50
14.00	1.33	0.25	23.92	31.65	24.43
14.00	1.44	0.30	27.64	37.41	26.14
6.00	0.94	0.05	15.10	16.55	8.77
6.00	0.97	0.07	15.49	15.54	0.31
6.00	1.05	0.14	16.67	18.02	7.49
6.00	1.09	0.18	17.52	19.43	9.79
6.00	1.06	0.15	16.88	19.81	14.77
6.00	1.09	0.18	17.53	21.51	18.53
6.00	1.15	0.22	18.75	20.84	10.05
6.00	1.30	0.31	22.62	29.14	22.38

Figures

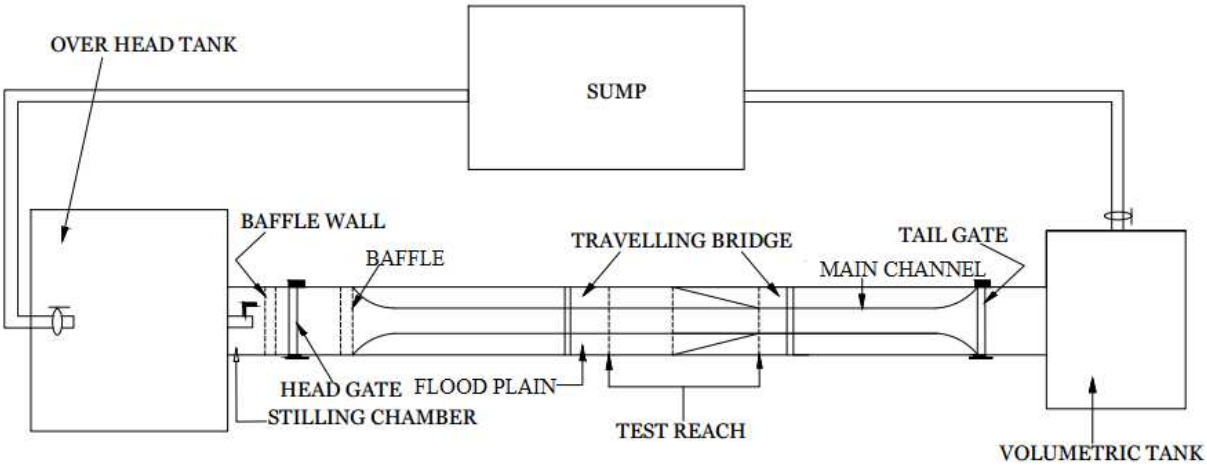

Figure 1 (a) Plan view of Experimental setup (Naik & Khatua 2016)

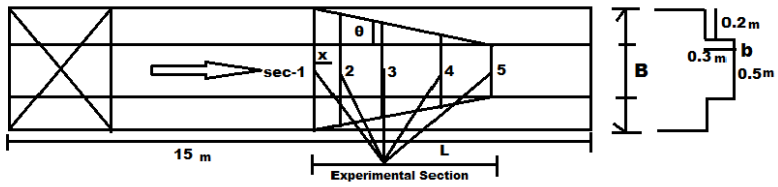

Figure1 (b) Longitudinal & Cross sectional dimension of the non-prismatic compound channels

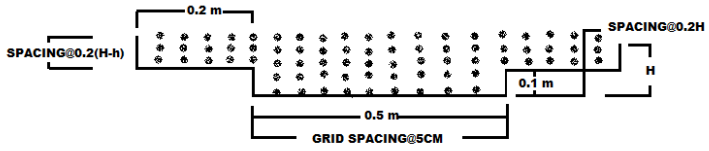

Figure 1(c) Grid showing the velocity measurement at the test section (Naik & Khatua 2016)

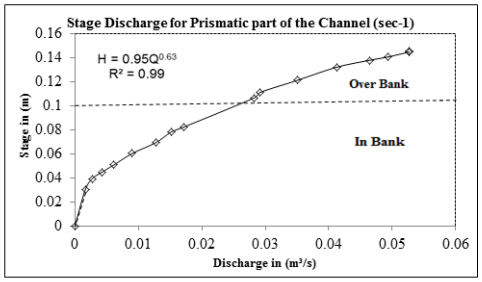

Figure 2(a) Stage discharge relationship for the Present experimental Channel (Prismatic sections)

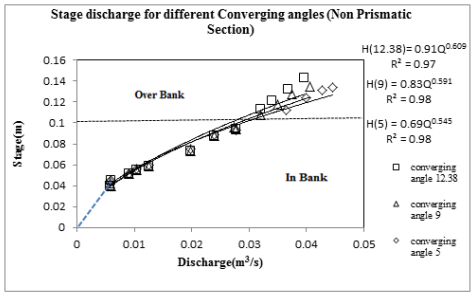

Figure 2(b) Stage discharge relationship for compound channels with converging flood plains

(Non Prismatic sections of angle 12.38⁰,9⁰, 5⁰)

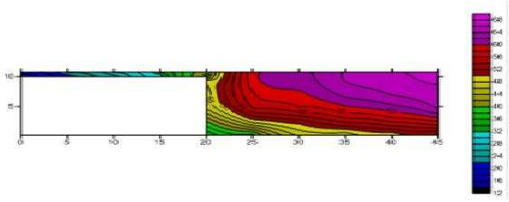

Figure 2(c) Longitudinal Velocity (cm/s) contour for lower aspect ratio experimental channel (NITR) of relative depth 0.15(for converging angle 12.38°)

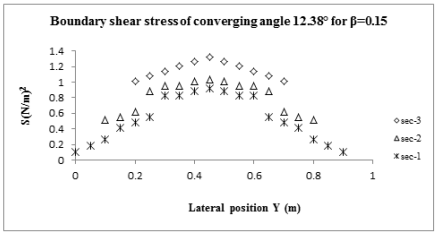

Figure 3(a) Boundary shear distribution for lower aspect ratio experimental channel (NITR) of relative depth 0.15(for converging angle 12.38°) (Naik & Khatua 2016)

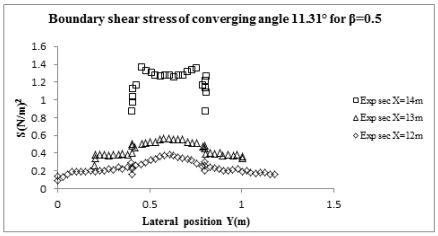

Figure 3(b). Boundary shear distribution for higher aspect ratio experimental channel Rezai(2006) of relative depth 0.5(for converging angle 11.31⁰) (Naik & Khatua 2016)

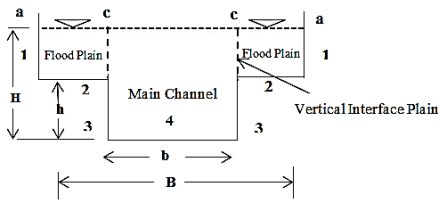

Figure 4 Interface planes dividing a compound section into sub areas (Naik & Khatua 2016)

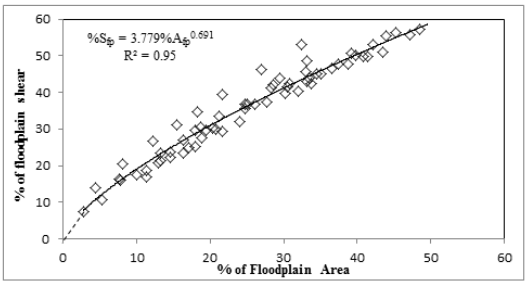

Figure 5 Variation of % of floodplain shear with % of area of floodplain

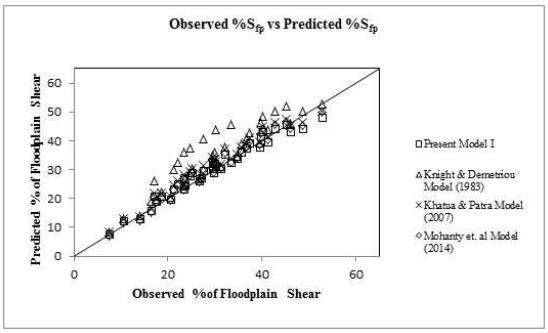

Figure 6 Scatter plot for observed and modeled value of $\%S_{fp}$

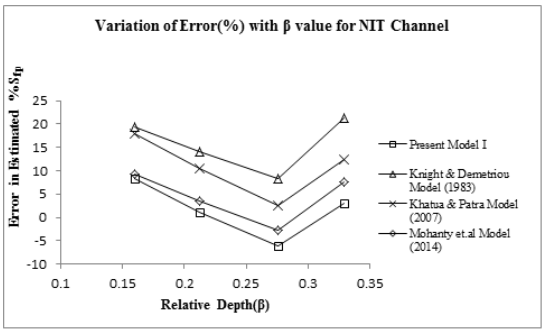

Figure 7 (a) Comparison for $\%S_{fp}$ for various models in the present experimental channel

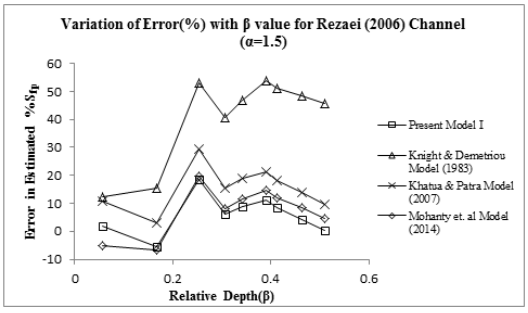

Figure 7 (b) Comparison for $\%S_{fp}$ for various models in lower width (α=1.5) Rezaei (2006) Channel

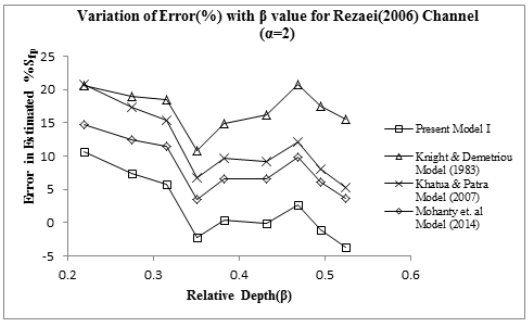

Figure 7 (c) Comparison for $\%S_{fp}$ for various models in lower width (α=2) Rezaei (2006) Channel

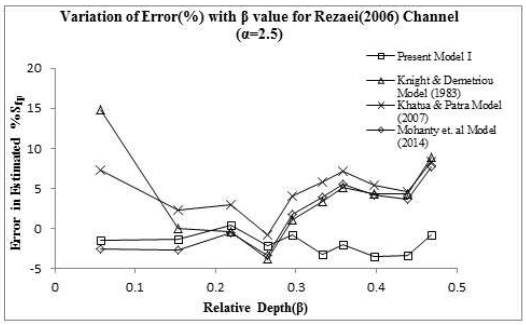

Figure 7(d) Comparison for $\%S_{fp}$ for various models in lower width (α=2.5) Rezaei (2006) Channel

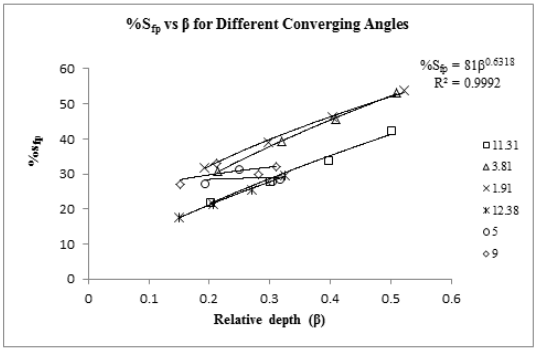

Figure 8 Variation of $\%S_{fp}$ of floodplain shear with relative depth at typical sections (Naik & Khatua 2016)

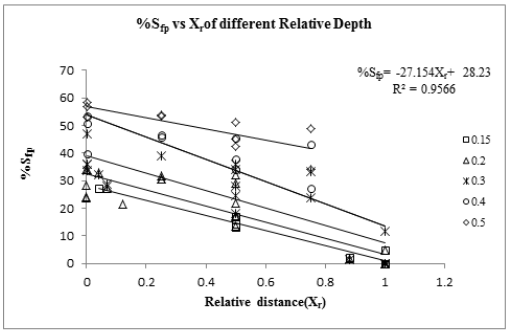

Figure 9 Variation of $\%S_{fp}$ of floodplain shear with relative distance for different relative depths (Naik & Khatua 2016)

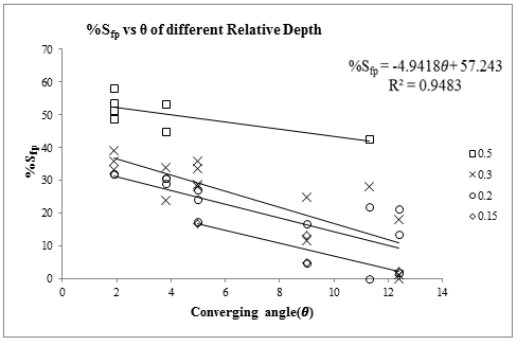

Figure 10 Variation of *%Sfp* of floodplain shear with converging angles for different relative depths Naik & Khatua (2016)

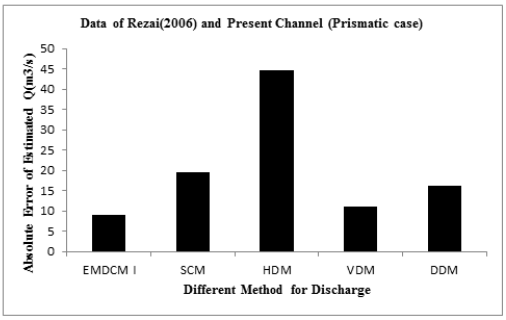

Figure 11 Absolute Error of Discharge for Present experimental and Rezaei (2006) channel data (Prismatic case)

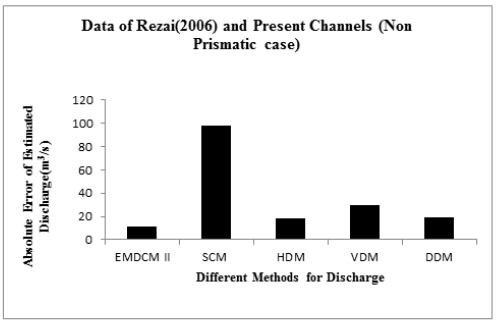

Figure 12 Absolute Error of Discharge for Present experimental and Rezaei (2006) channel data (Non Prismatic case)

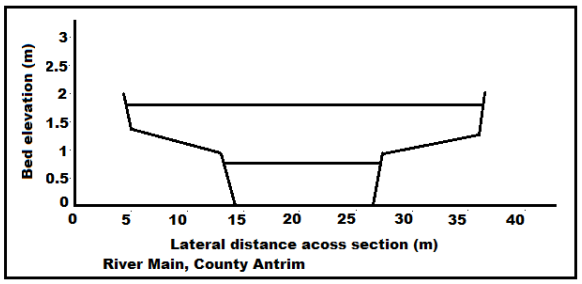

Figure 13 The lateral cross section of River Main

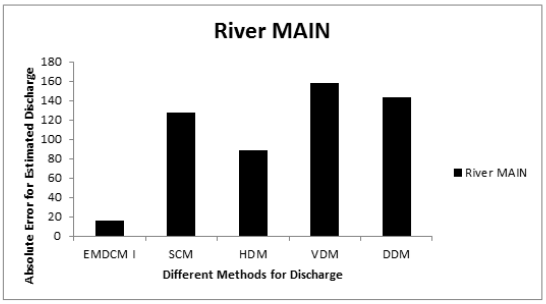

Figure 14 Absolute Error of Discharge of River Main

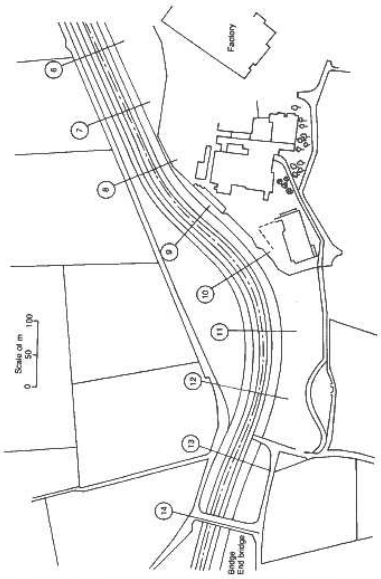

Figure 15 Plan view of experimental reach of River Main

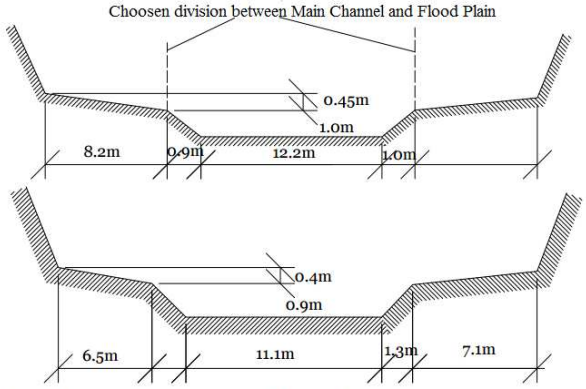

Figure 16 Cross-sectional geometries of River Main at (a) upstream end of experimental reach (section14), (b)downstream end of experimental reach (section 6)

IMPACT OF CUSTOMER RELATIONSHIP MANAGEMENT ON CUSTOMER LOYALTY

Sumalya Shoukath*

ABSTRACT

Customer relationship management is a branch of marketing which deals with one of the most important assets of the market, i.e. the customers. It is an art of effectively managing the customers, addressing their needs and handling their grievances to improve the efficiency of the business. Customer satisfaction plays a key role in the brand loyalty of the customers which in turn, has a huge impact on the success or failure of a business. Customers' needs and wants keep changing with the changes in technology and they quickly incline to the other brands when they feel that the existing brand is obsolete. Customer relationship management helps the business to retain their existing customers and assures them that their expectations would be met in the course of time. This paper focuses on the concept of customer relationship management, its need and benefits. It also studies the impact that customer relationship management has on the customers' loyalty and commitment. Customer relationship management helps the firms to make pace and sustain in this highly competitive market which constantly strives to improvise the existing products and attract the new customers.

****

Introduction

Customer relationship management is a term which explains therelationship between a business and its customers.Customer relationship management refers to all the business activities directed towards initiating, establishing, maintaining and developing successful long term relational exchanges(Heide,1994;Reinartz & Kumar,2003).It is very essential for every business to identify, understand and cater to the needs of its existing and prospective customers. Customer Relationship management is everything in business,because it is the catalyst for a responsible, profitable and customer focused organization.(Wali,Wright & Uduma,2015). Besides getting standardized products and quality service from a business,customers also seek to maintain strong relationship with the business. They also expect some benefits to be given to them for being loyal and old customers to the firm. The benefits of customer loyalty to a provider of either services or products are numerous and thus organizations are eager to secure as significant a loyal customer base as possible. Customer relationship is a tool which the business uses to maintain good customer relations. In this highly competitive market,it is very important for the firms to maintain good relations with the customers because if the customers are unsatisfied,they have plenty of substitute brands to get inclined to. A strong and positive customer relationship brings goodwill to the firm whereas a negative customer relationship highly affects the reputation of the firm. Assal (1998) have observed brand loyalty from the behavioral context, where he referred brand loyalty as the repeat purchase of a single brand out of varieties of offerings by product service provider.

Objectives of the Study

- To study the concept of customer relationship management

* Assistant Professor,Department of Business Management,Methodist College of Engineering and Technology.

- To analyse the effectivess of customer relationship management on customer satisfaction
- To study the impact of customer relationship management on customer loyalty

Research Methodology

This study is based on secondary data. The secondary data is collected from various published sources like journals, magazines, reports and newspapers.

Benefits of Customer Relationship Management

- Enhancing the association with existing clients
- finding new imminent customers
- winning back previous customers
- enhanced client relations
- better inward correspondence
- increased sales & profits
- customer satisfaction
- referrals

Impact of Customer Relationship Management on Customer Loyalty

The following are the impacts of CRM on various sectors:

Social networking and internet

CRM frameworks coordinate web-based social networking locales like Twitter, LinkedIn and Facebook to track and speak with clients. These clients likewise impart their own insights and encounters with an organization's items and administrations, giving these organizations more understanding. In this manner, these organizations can both impart their own particular insights and furthermore track the suppositions of their customers.

Telecom Industry

Airtel is regarded as one of the best service providers in India. Customers stay loyal because they feel they get all the necessities that they expect from a service provider best from airtel than compared to others. It provides good network, a wide range of benefits to old customers and excellent service in national and international roaming. Customer compaints are well adressed and they feel they are important to the business.

Banking Industry

HDFC,HSBC,AXIS and ICICI banks are regarded as few most reliable banks by the customers.These banks attend to their customers issues in a polite manner and they solve them very patiently whereas the customer relationship management in state bank is poor .Customers are not loyal to these banks because they feel it doesn't respond to customer grieviances in the specified time. And so customer loyalty in state bank groups is comparatively less when compared to other private sector banks.

Hotels

Customers are always ready to spend money in places they feel are worthy of .A customer relationship management in a hotel industry is also useful in maintaining customer loyalty.They want that hospitality from the management in order to revisit the hotel.Serving food is the not theh only thing that the customers expect from the hotels. Customers are more loyal to the hotels which treat customers as they are the people from the management. Customer reviews about the food quality, taste, service from the waiters etc are taken and customers feel they are important to the business. They become loyal to places where they are welcomed as guests and at the same time are treatedas decision makers in certain cases.

Hospitals

Hospital is a place where people stay in

unavoidable situations. And at this time everyone is into stress and customers expect the management to handle them with very delicacy and patiently. Customers get more loyal to the places where they are given benefits of providing excellent treatment, making payments as per the convenience at the time of discharge, getting good facilities for patients and attendants, good staff ,hygiene ,pharmacy, ambulance facility etc. Besides this ,customers also look forward to having benefits of the hospital health cards which would give them certain discounts in the bills or treatments etc.

Conclusion

Customer relationship management framework helps in changing client's dedication conduct . Hence it is basic for entrepreneurs to grasp the place of client relationship administration technique in winning clients' dedication, dependability and expanding client's penchant for backing. The review presumes that CRM hones affect on clients' capacity to get focused on the offerings by the business; customer loyalty was weighted higher than brand devotion in changing a client from only a purchaser to turning into a backer. The basis is that customers try to boost their utilization esteem (input) and limits installment (yield); accordingly that brand duty takes full of feeling measurement while mark faithfulness takes duration measurement. Nonetheless, the qualification between the two idea is that a submitted client is dedicated to expending the result of his provider even in the midst of less expensive choices. Though mark steadfast client is not completely dedicated in essence, he disparages his specialist organization when his coveted administration or item is accessible and is inclined to extending his support to rivals if his provider administration or item is not accessible. Peppard (2000) opined that technological tools have improved interactivity between the customer and firm, and are keys to explaining and predicting business success as well as CRM. The definitions on CRM as a mechanical is solid in that without innovation every one of the clients information assembled by firm would be repetitive; for instance a firm with say five thousand client quality can't keep close client relationship without utilizing a CRM instrument in today's business condition, thus associations not withstanding their budgetary quality endeavor to obtain a piece of CRM programming to empower firms be in tone with market patterns.The human variable or workers, assumes the most vital part in driving CRM programme.This is on the grounds that it facilitates and guides the CRM procedure and innovation to meet optimality.

References

1. Amine, A. (2011). Consumers' true brand loyalty: the central role of commitment. Journal of Strategic Marketing, 6(4), 305-319. Arnould, E.J. & Thompson, C.J. (2005).
2. www.canadabusiness.ca

Original Article

Influence of light through Optical Glasses on Electroencephalogram

John William Carey Medithe*, Usha Rani Nelakuditi

Department of Electronics and Communications Engineering, Vignan's University, Guntur, India, 522213

ABSTRACT

Background: In General, optical powered glasses are used to have good focus and clear vision. But, this practice may also bring noticeable variation in light intensity which in turn affects neural behavior. These changes can be interpreted from the EEG recordings. Thus, in this present study, the grounds for amendments in different physiological variables due to light intensity through optical glasses experienced by the subject have been reviewed and verified. **Experiment:** Changes in light intensity through optical powered glasses have been demonstrated using a Light Dependent Resistor (LDR) test for various cases. From this study, it was found that positive powered optical glass increases the light intensity falling on an eye, while negative powered optical glass reduces light intensity. **Case Study:** A case study was performed using experimental and subjective analysis were made to confirm that misfocused or unclear vision bring changes in frontal frequency and makes subject fatigue and eyes strain which is prone to severe headache and development of seizures. **Recommendations:** It is to be noted by the EEG practitioner to confirm that, whether optical powered glasses used by the subject is to be match with refractive error of an eye. If not, the frontal frequency gets increased and may suspect as seizures or other any abnormality.

Key words: Electroencephalogram, Light, Light Dependent Resistor, Optical glass, Neurophysiology

INTRODUCTION

Human brain is systematized in controlling and integrating various sensing organs in the human system. Brain consists of millions of neurons; these neurons are special group of cells that are capable of being excited and the action potential generated and induced over the scalp. Electroencephalogram is a significant medical imaging test for the study and interpretation of electrical activity of the brain with respect to time. These electric potentials would be an array of microvolt. Subdural electrodes are used for invasive studies during surgery. Visible light is a part of an electromagnetic spectrum sensed by the humans by their Ocular sensor. There are various changes which occur in human physiology when exposed to different intensities of light. There are noticeable and major alterations in subjects Ocular Physiology and Neurology due to light exposure. The changes in light intensity which illuminate on to the human eye also reflect on electroencephalographic readings.[1-3]

Optical powered glasses are used by people to correct refractive errors of an eye. These optical powered glasses help them to have clear vision and proper focus to perform any visual task. An anomalous refractive condition such as myopia, hypermetropia and astigmatism of an eye makes an image fail to focus properly upon the retina. Myopia or near-sightedness is a result of the eyeball being too long than usual leading to misfocus the target object; this misfocused condition can be corrected by wearing negative powered optical glass. On the contrary, Hypermetropia or farsightedness occurs when the eyeball becomes shorter, and can be corrected by wearing positive powered optical glasses. Presbyopia and Astigmatism are other kinds of refractive errors which occur in eye due to age and other factors. When light enters the eye through these corrective lenses it brings noticeable changes in the human physiology and neuronal behavior. In this study, when a subject is exposed to light, remarkable changes in the human physiological parameters like change in release of percentage of melatonin hormone, change in core body temperature and more were observed which in turn affects the neuronal

Submission Date: 30-08-2016;
Revision Date: 17-11-2016;
Accepted Date: 23-11-2016

DOI: 10.5530/ijper.51.1.18

Correspondence:
John William Carey Medithe,
Department of Electronics and Communications Engineering, Vignan's University, Guntur, India, 522213
Phone: +91 89771 83538
E-mail: careymedithe@gmail.com*

www.ijper.org

measures such as change in EEG frequencies and EEG spectral density when exposed to light. To explore consequences due to light through optical glasses in neural behavior; alpha activity in occipital region is centrally weighted. This alpha activity is synchronized with intensity of light.

Previous literature describes the altering effects of light in various physiological parameters and EEG spectra when exposed to light with naked eye.[4-6] But, in this study the variation of light through optical glasses are illustrated.

HYPOTHESIS OF VARIATION IN LIGHT INTENSITY THROUGH OPTICAL GLASSES

Powered optical glass or spectacle lens is an optical device that alters the focus of a light beam through refraction. Optical lenses are different from normal lenses. The optical prescription given by the ophthalmologist is to correct the refractive errors of the human visual system. But, these corrective lenses used to overcome ametropic conditions cause a variation in light intensity experienced by the subjects. There are various components in the prescription suggested by the ophthalmologists such as spherical component which is used for focal correction and cylindrical component for fine tuning. Eyeglasses are convex in front and concave at the back surface. Positive powered lens is also identified as convex lens which is thicker in the middle and thinner at the edges. While negative powered lenses are concave lenses which are thicker on the edges than in the middle.

Variations of light intensity through positive powered optical lenses

Positive powered lens or converging lenses are suggested by the ophthalmologist to correct the refractive errors in the eye when subject experiences difficulty in focusing nearby objects. This difficulty occurs, when the light rays entering the eye focus behind the retina, rather than directly focusing on it. When the positive powered correcting lens is used, the light intensity coming from the light source fall on lens and gets converged at a point. It is observed that there is a variance in light experienced by the normal subject compared to subjects with positive powered lens, with same illumination conditions. The subjects who are having hypermetropia and got their refractive error corrected with positive powered lenses experienced more light intensity than the normal.

Variations of light intensity through negative powered optical lenses

Ophthalmologist suggests, Negative powered or diverging lens when the subject experiences the refractive error in the eye and faces difficulty in focusing the far objects. Here in this case, the light rays coming from the light source and falling on the diverging lens deviate from the principal axis. By wearing these types of glasses, there will be variation in light experienced by the subject with negative powered lens when compared to the normal subject. It is to be observed that subjects with myopia corrected with negative powered optical glass experiences the less light intensity with that of normal subjects in same illumination conditions.

LIGHT DEPENDENT RESISTOR TEST TO OBSERVE THE CHANGES IN LIGHT INTENSITY DUE TO OPTICAL POWERED GLASSES

In order to check the above hypothesis, the variations in light intensity from a source like White LED or ambient light are processed through optical lenses of different powers. Here, to prove and verify that the wearable optical glasses alter the light intensity which enters into an eye. To examine the alterations in the intensity, Light dependent resistance test has been performed.

Experimental Procedure

A quality light dependent resistor was placed on the breadboard and it is connected to the multimeter. Initially, the illumination conditions of the LDR were calibrated to random value. The lenses of different prescriptions are obtained from an optical store are need to be placed at a uniform distance in front of the Light Dependent Resistor. Secondly, the lenses also kept at 3 cm, 5 cm, and 7 cm distances in front of the Light Dependent Resistor. The change in reading for different powers of lenses placed in front of LDR is obtained in multimeter connected. This arrangement is shown in below Figure 1.

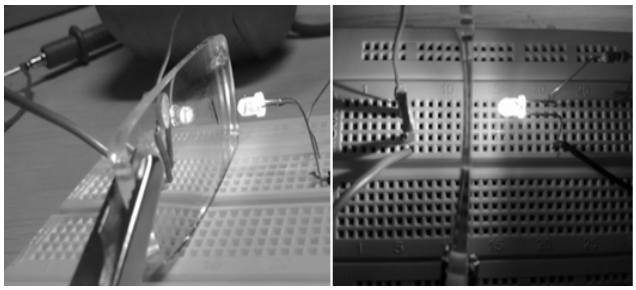

Figure 1: An LDR test to study the variation of light intensity through optical lenses

Results

A resistance of 5.2 K Ω is observed, when the LDR is placed in ambient light normal reading room illumination conditions when no lens or obstacle is kept before it, this observed resistance value is considered as a calibrated resistance. The alterations in readings when the powered lenses kept before the LDR are stated in Table 1.

Discussion

The general exploit of the light dependent resistor (LDR) is to vary the resistance with respect to the light intensity falling on the face of the LDR. The resistance of the LDR reaches to its optimum, when the light intensity is not falling or poor luminance condition. The increment in the intensity of the light falling on the LDR leads to the decrement in resistance developed by the LDR. When the eyeglasses are placed before the face of the LDR, there is a noticeable resistance change observed in the multimeter. When lenses are placed before LDR, It is observed that the positive (+) powered optical glass increases the light intensity falling on the LDR which results in reduction of resistance developed by the LDR. In the case of the lens having minus (-) power, it reduces the light intensity falling on the LDR, which makes LDR to increase its resistance.

From the above experimental study, it is observed that the high powered positive or negative optical lens will bring noticeable change in the light at focal point compared to the light falling on the lens. It is also to be noted and observed that the back vertex distance from the lens to LDR also plays a vital role. The light intensity experiencing by a subject varies as the change in the distance between the back vertexes of optical lens to an eye. This is proved in Table 2.

Table 1: LDR Reading for the different optical powered lens

Prescription of lens (DIOPTERS)	LDR reading (KΩ)
+15	2.80
+12	3.15
Reading glasses Add +2	5.10
-1.75 Cyl	5.64
-2.5-0.5-X90	5.87
-2.5-0.5-X180	5.80
-3 Sph	5.97
-3.5 Sph	6.12

Table 2: LDR Reading for the different optical powered lens when LDR calibrated to 11.10 KΩ and lens are kept at distances 3cm, 5cm, 7cm between LDR and LED

Prescription of lens (DIOPTERS)	LDR reading (KΩ)		
	3Cm	5Cm	7Cm
+15	7.21	6.74	6.42
+12	9.01	8.79	8.23
Reading glasses Add +2	10.3	10.4	10.1
-1.75 Cyl	12.3	12.8	12.6
-2.5-0.5-X90	13.09	13.8	13.5
-2.5-0.5-X180	13.11	13.6	13.5
-3 Sph	13.21	13.9	13.6
-3.5 Sph	13.48	14.09	13.9

CHANGES IN THE HUMAN PHYSIOLOGICAL VARIABLES WHEN SUBJECT EXPOSURE TO LIGHT THOUGH OPTICAL GLASSES

In view of the fact that, optical powered glasses influences and alters the light intensity experienced by the eye. Here, different illumination levels can cause a fusion of variations in many physiological parameters like alterations in subjective alertness, incidence of slow eye movements; plasma melatonin hormone, core body temperature and other ocular physiological changes.[4-11] The lighting or the illumination on specific area caused by the luminous object is entirely dependent on the distance between illuminating area and the luminous object. The equation for illumination caused by the luminous object in a distance d is given in (Equation 1).

Where E is the lighting caused by the luminous object at a distance d, I is the amount of luminous intensity of a respective light source.

$$E = I / d^2$$

Here, to comprehend the effect of light on human physiology, the release of amount of melatonin hormone in the subject is directly correlated with the amount of light intensity experiencing by the subject. It is a natural hormone which is initiated in pineal grand of the human brain. The synthesis of melatonin hormone is inhabited when the eye experiences the amount of light. As the intensity of the light increases, the release of melatonin hormone suppressed which results in increase of subjective alertness. Iain M. McIntyre, *et al.* (1989) enlightens the relation between the intensity of the light and the percentage suppression in melatonin hormone. This can be shown in Figure 2.

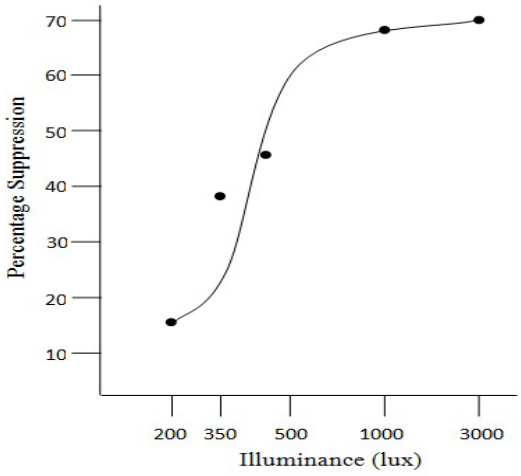

Figure 2: Response of a Melatonin Hormone to Different Illumination Levels.[12]

There are other physiological variables which are getting influenced by the bright illumination conditions with reference to variation in release of melatonin hormone. Subjective alertness is an additional physiological variable that is proportional to the light intensity experiencing by the subject and inversely proportional to release of melatonin hormone. Christian Cajochen (2007) correlated various physiological parameters with the light intensity experiencing by the subject with respect to melatonin hormone. More than 50% of release of melatonin hormone is suppressed when the subject is exposed to the illumination beyond 100 Lux. Then, the subjective alertness is increased when subject is exposed to illumination beyond 100 lux. Incidence of Slow eye movements is another human physiological change which is correlated with the release of melatonin hormone. The incidence of slow eye movements is getting increased with increase in the release of melatonin hormone. Release of melatonin hormone, subjective alertness and incidence of slow eye movements are inter-correlated physiological parameters with change in illumination conditions experiencing by the subject. The response of these physiological parameters towards different illumination rate with respect to melatonin hormone is shown below in Figure 3 and Figure 4. Here, closed symbols are

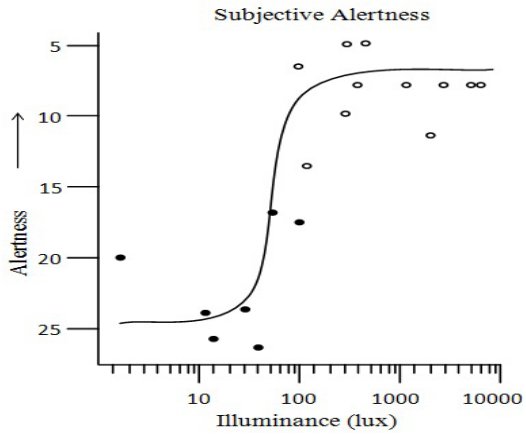

Figure 3: The subjective alertness response to with increment of illumination level.[5]

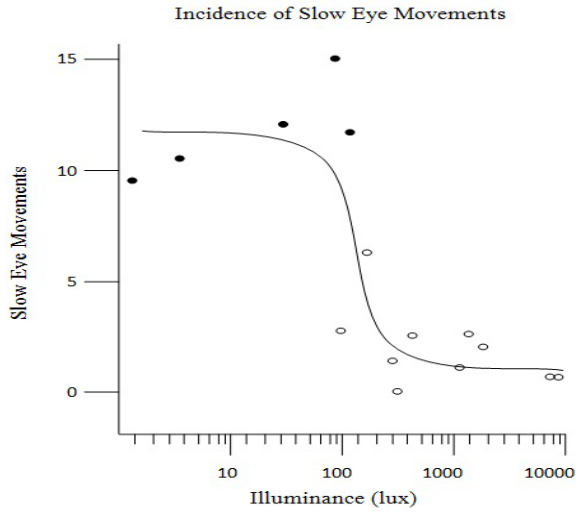

Figure 4: The reduction of incidence of slow eye movements with increase of illumination levels.[5]

to be identified as an individual, where suppression. The variation in these physiological changes due to different illumination conditions experiencing by the subject also brings numerous changes in the neurological behavior of the human system of melatonin hormone to less than 50%, open symbol shows as an individual where melatonin hormone is suppressed beyond 50% which can bring alterations various physiological and neurological parameters.

ELECTROENCEPHALOGRAPHIC CHANGES WHEN TO EXPOSURE TO DIFFERENT ILLUMINATIONS

Effects on EEG frequencies

Due to numerous changes in the human physiological variables when exposed to different illumination ranges, it also affects the rhythm of the neurological behavior. Here, Visual Cortex in occipital region is the responsible for the central vision of the human system. Central intent up on the alpha frequency in the occipital region shows vital association between neural changes and light intensity. When the subject eyes are closed or not experiencing light intensity visually, it is observed that the increment in alpha activity in the occipital region. Usually, alpha frequency is the state which occurs when the subject is in relaxing mode. Alpha blocking is another phenomenon which alters the alpha activity. This occurs when the subject is exposed to light and allowed to do any mental activity. This makes the reduction in alpha activity and increase the frequency. Alpha rhythm replicates changes in physiological variables with increment in illumination levels. It can be illustrated that less illuminated environment or no light cause increase of alpha rhythm in the occipital region of the EEG. The frequency range of Alpha exhibits the properties of sleep spindles which occur between two states of alertness which ranges from 7-14 Hz.[13]

Effect on EEG Power density

The effect on EEG power density is the premier electroencephalographic changes due to exposure of subject to more illuminating conditions. Christian Cajochen, *et al*. (2000) gives the relation between the percentages of total power to the different range of the Illuminance shown in Figure 5. EEG power density of frequency in range of 5-9Hz has been suppressed.

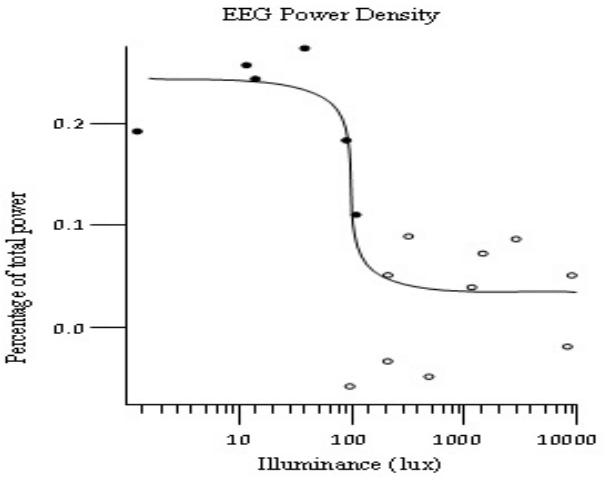

Figure 5: Percentage Reduction of EEG Power Density of frequency 5-9 Hz with Increment of Illumination.

NEURAL BEHAVIOR WHEN SUBJECT WITH IMPROPER FOCUSED LENSES

Changes in Neural behavior are replicated in the readings of EEG when a subject is using improper focused lenses or with incorrect prescription which doesn't match to the refractive error are analyzed and verified in the laboratory using subjective and experimental analysis.

Experimental Procedure

This experimental study was carried out on 80 subjects, 38 male and 42 female participants of age ranges from 20-55 available in the university. In these participants, 52 subjects are with myopia and 28 subjects are with hypermetropia. All the subjects are corrected with different optical positive and negative powered glasses with different prescription given by the licensed ophthalmologist. All the participants were called individually to the laboratory which is temperature is maintained at around 25°C. The prescription of every individual participant is noted. Now, AgCl electrodes are placed over the scalp in frontal and occipital regions of the international 10-20 standard. The reference electrode is placed with electrode gel on the left ear.[14-17]

Now each participant was asked to wear a different prescription powered optical glass than suggested by the ophthalmologist. Each participant was asked to read the chart with good font size at the distant or to read a book with an improper focused lens. The resultant changes in the EEG readings are analyzed.

Observation

As it is expected, when the subject tries to read the chart with improper focused lens, it is found that the subject is using more mental ability than usual. The characteristics of the frontal region frequency changes when the subject tries to focus and tries to read or approximate the chart placed in the laboratory. This makes increment in the frontal frequency. The frequency response for the mental activity done by the subject is showing up in frontal region as 12-25Hz. This can be considered as lower beta frequency. The state of occurrence of the beta frequency activity in frontal and front polar region is when subject applies more mental activity than usual.

DISCUSSION

After completion of experimental analysis, each individual subject was asked to give the rating for their mental stress used to read the chart with different prescription with improper focused optical powered glass suggested by the ophthalmologist. The ratings for this activity were asked to give by the subject from 1 to 5. Rating 1 show as no mental stress ability used to read the chat or to focus an object. Where rating 5 shows as high mental stress activity is performed by the subject. Maximum of the subjects participated in the subjective analysis have given a rating of 4 to 5. This shows improper focused optical powered glasses cause subject to use more mental activity than usual. It is found that similar characteristics between experimental and subjective analysis. The graphical representation of ratings given by subjects with myopia and hypermetropia to carry out the subjective analysis is given below.

Optical powered lens is used to correct the difficulty of refractive errors in the ocular sensing. If the prescription given by the licensed ophthalmologist is not matching to the refractive error of the subject brings various noticeable consequences in the human neurological and physiological parameters. Initially, improper vision causes the subject to feel fatigue and strain. Long time stains to the eye while acquiring vision through improper focused lens results in headache. Squinting is the noticeable consequence and symptom when the subject is using different powered optical lens. It is recommended to the physician or EEG practitioner that to confirm optical powered glasses used by the subject is able to correct the refractive error of eye properly. If not, the frontal frequency gets increased and may suspect as seizures or other any abnormality.

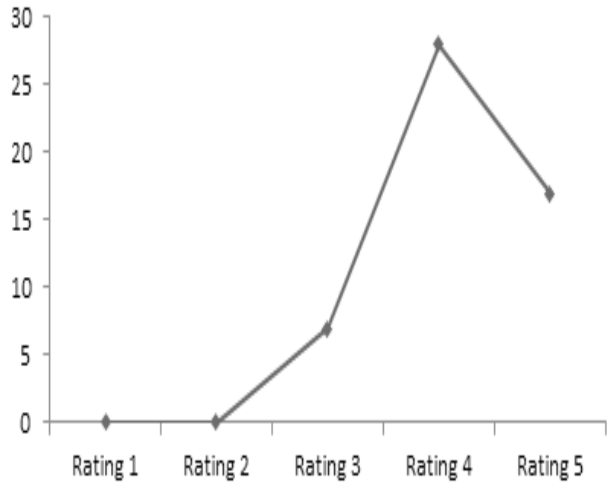

Figure 6: Subjective analysis performed on 52 subjects with Myopia.

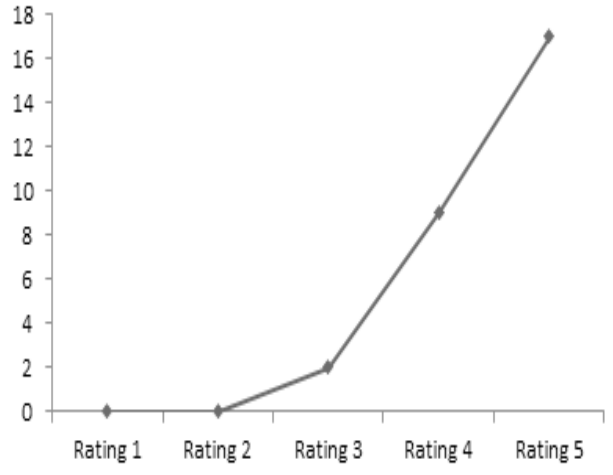

Figure 7: Subjective analysis performed on 28 subjects with Hypermetropia.

CONCLUSIONS

Light through optical powered glasses can bring a numerous amendments to the physiological parameters of the human system. These changes in the physiological parameters lead to noticeable alterations in the neurological parameters. Hence, in this study, the grounds for the alterations in light intensity through the optical powered lens have been verified. Light dependent resistor test has been performed to prove and analyze alterations of light intensity through optical powered glasses. It is found that the positive powered glasses increases the light intensity through optical powered glasses. Because, it converges all the light rays at a focal point. This make subject to experience more light intensity than usual. While, negative powered optical glasses diverges all the light rays falling on the lens make the subject to feel less light intensity than normal.

It is also observed that improper and unfocused vision through optical lens make subject feel fatigue and which is prone to the headache and development of seizures in human brain. Experimental and subjective analyses are performed on 80 subjects to confirm that misfocused or unclear vision increases the mental activity when each subject is trying to focus and to have a clear vision. It is proved that increment in frontal frequency to the lower beta frequency range shows that subject applied more mental stress than usual. Subjective analysis has been performed individually and separately for the subjects using positive and negative powered glasses. It shows similar characteristics to the experimental analysis that subjects feel to apply more mental activity like problem solving.

CONFLICT OF INTEREST

There is no conflict of interest

ABBREVIATIONS:

EEG: Electroencephalogram; EOG: Electroculogram; LDR: Light Dependent Resistor.

REFERENCES

1. Medithe J and Nelakuditi U. "Study of normal and abnormal EEG", 2016 3rd International Conference on Advanced Computing and Communication Systems (ICACCS), 2016. https://doi.org/10.1109/icaccs.2016.7586341.
2. Krishnan RS. "Scattering of light in optical glasses", Proceedings of the Indian Academy of Sciences-Section A, 1936;3(3)211-20.
3. Medithe J and Nelakuditi U. "Removal of ocular artifacts in EEG", 2016 10th International Conference on Intelligent Systems and Control (ISCO), 2016. https://doi.org/10.1109/isco.2016.7726941.
4. Myers BL, Badia P. Immediate effects of different light intensities on body temperature and alertness. Physiology & behavior. 1993;31;54(1):199-202.
5. Cajochen C. Alerting effects of light. Sleep medicine reviews. 2007;31;11(6):453-64.

6. J. Park, B. Min, Y. Jung, H. Pak, Y. Jeong and E. Kim, "Illumination influences working memory: An EEG study", Neuroscience. 2013;247;386-394. https://doi.org/10.1016/j.neuroscience.2013.05.016; PMid:23694704.
7. Cajochen C, Zeitzer JM, Czeisler CA, Dijk DJ. Dose-response relationship for light intensity and ocular and electroencephalographic correlates of human alertness. Behavioural brain research. 2000; 31;115(1):75-83.
8. Maher AM, Kirkup L, Swift P, Martin D, Searle A, Tran Y, Craig A. Effect of luminance level on electro-encephalogram alpha-wave synchronisation. Medical and Biological Engineering and Computing. 2001;1;39(6):672-7.
9. Toscani M, Marzi T, Righi S, Viggiano MP, Baldassi S. Alpha waves: a neural signature of visual suppression. Experimental brain research. 2010;1;207(3-4):213-9.
10. Cajochen C, KRÄUCHI K, Danilenko KV, WIRZ-JUSTICE AN. Evening administration of melatonin and bright light: interactions on the EEG during sleep and wakefulness. Journal of sleep research. 1998;1;7(3):145-57.
11. Brown BB. Recognition of aspects of consciousness through association with EEG alpha activity represented by a light signal. Psychophysiology. 1970;1;6(4):442-52..
12. Mclntyre IM, Norman TR, Burrows GD, Armstrong SM. Human melatonin suppression by light is intensity dependent. Journal of pineal research. 1989;1;6(2):149-56.
13. Narayan S, Subramanian S and Gaur G, "Low luminance/eyes closed and monochromatic stimulations reduce variability of flash visual evoked potential latency", Annals of Indian Academy of Neurology, 2013;16(4):614. https://doi.org/10.4103/0972-2327.120492; PMid:24339591 PMCid:PMC3841612.
14. R. Cooper, J. Osselton and J. Shaw, EEG technology, 1st ed. London: Butterworths, 1969.
15. E. Niedermeyer and F. Lopes da Silva, Electroencephalography, 1st ed. Philadelphia: Wolters Kluwer Health, 2011.
16. Medithe J and Nelakuditi U. "Study on the Impact of Light on Human Physiology and Electroencephalogram", Journal of Biomimetics, Biomaterials and Biomedical Engineering, 2016;28:36-43. https://doi.org/10.4028/www.scientific.net/JBBBE.28.36.
17. Bong SZ, Murugappan M, Yaacob S. Methods and approaches on inferring human emotional stress changes through physiological signals: A review. International Journal of Medical Engineering and Informatics. 2013;1;5(2):152-62

PICTORIAL ABSTRACT

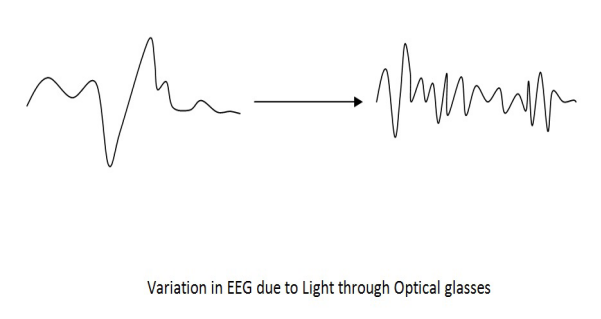

Variation in EEG due to Light through Optical glasses

SUMMARY

- The influence of light on EEG is given but it is correlated with Variation of light intensity through optical glasses
- Some changes in physiological parameters like release of melatonin hormone etc, which in turn bring changes brain electrical activity like suppression of alpha activity in occipital region
- Light through optical glass bring noticeable variation in the aptitude of the blink, contaminates in the frontal electrodes
- Light dependent resistor test has been performed to prove and analyze alterations of light intensity through optical powered glasses.
- Greater than equal to ±3D bring noticeable change
- It is also observed that improper and unfocused vision through optical lens make subject feel fatigue and which is prone to the headache and development of seizures in human brain.
- Experimental and subjective analyses are performed on 80 subjects to confirm that misfocused or unclear vision increases the mental activity when each subject is trying to focus and to have a clear vision
- Brightness coating has to be made to negative powered glasses and dullness coating is to be applied to positive powered glasses to neutral the light variation in optical glasses
- It is recommended to physician that, Optical Glass test whether suits the refractive error are to be checked before the test

About Authors

John William Carey Medithe received the B.Tech. degree in electronics and communication engineering from Jawaharlal Nehru Technological University, Kakinada, India, in 2012 and M.Tech. degree in communication systems from Andhra University, Visakhapatnam, India, in 2014. Since 2015, he has been with the Vignan's Foundation For Science, Technology & Research University, where he is currently working toward the Ph.D. degree at the Image processing and Machine Vision Research centre. He is awarded with the UGC Fellowship Award in 2016, in recognition of his academic background and the impact of his research plan. His research interests include signal processing, Biomedical circuits and systems.

Usha Rani Nelakuditi received the Doctoral degree (PhD) in a field of Medical Imaging from Jawaharlal Nehru Technological University, Anantapur, India, in 2013. She has published more than 30 research articles in various reputed journals and International Conferences. She was the principal investigator for three government funded research projects from various funding agencies like AICTE and DST, Government of India. She was being as a Head of the Electronics and Communications Engineering department since 2013 in Vignan's Foundation for Science, Technology and Research University. Her areas of research include Biomedical Signal and Image Processing, VLSI, Instrumentation and Automation.

Cite this article: To be available soon

ISH Journal of Hydraulic Engineering

ISSN: 0971-5010 (Print) 2164-3040 (Online) Journal homepage: http://www.tandfonline.com/loi/tish20

Numerical modeling of converging compound channel flow

B. Naik, K. K. Khatua, Nigel Wright, A. Sleigh & P. Singh

To cite this article: B. Naik, K. K. Khatua, Nigel Wright, A. Sleigh & P. Singh (2017): Numerical modeling of converging compound channel flow, ISH Journal of Hydraulic Engineering, DOI: 10.1080/09715010.2017.1369180

To link to this article: http://dx.doi.org/10.1080/09715010.2017.1369180

Published online: 20 Sep 2017.

ISH JOURNAL OF HYDRAULIC ENGINEERING, 2017
https://doi.org/10.1080/09715010.2017.1369180

Taylor & Francis
Taylor & Francis Group

Numerical modeling of converging compound channel flow

B. Naik[a], K. K. Khatua[a], Nigel Wright[b], A. Sleigh[b] and P. Singh[a]

[a]Department of Civil Engineering, National Institute of Technology, Rourkela, India; [b]Department of Water and Environmental Engineering, School of Civil Engineering, University of Leeds, Leeds, UK

ABSTRACT

This paper presents numerical analysis for prediction of depth-averaged velocity distribution of compound channels with converging flood plains. Firstly, a 3D Computational Fluid Dynamics model is used to establish the basic database under various working conditions. Numerical simulation in two phases is performed using the ANSYS-Fluent software. *k-ω* turbulence model is executed to solve the basic governing equations. The results have been compared with high-quality flume measurements obtained from different converging compound channels in order to investigate the numerical accuracy. Then Artificial Neural Network are trained based on the Back Propagation Neural Network technique for depth-averaged velocity prediction in different converging sections and these test results are compared with each other and with actual data. The study has focused on the ability of the software to correctly predict the complex flow phenomena that occur in channel flows.

ARTICLE HISTORY
Received 22 November 2016
Accepted 15 August 2017

KEYWORDS
Compound channel; stage discharge; prismatic; non-prismatic; ANN; ANSYS

1. Introduction

Distribution of depth-averaged velocity is an important aspect in river hydraulics and engineering problems in order to give a basic understanding of the resistance relationship, to understand the mechanisms of sediment transport and to design sustainable channels. Due to continuous settlement of people near the river bank and due to natural causes, the channel with floodplain cross-sections behaves as converging type non-prismatic compound channels. An improper estimation of floods in these regions, will lead to an increase in the loss of life and property. The depth-averaged velocity distribution and flow resistance in prismatic compound cross-sections have been investigated by a number of authors (Ervine et al. 2000; Ghosh and Jena 1971; Khatua and Patra 2008; Khatua et.al. 2012; Myers and Elsawy 1975; Rhodes and Knight 1994; Shiono and Knight 1988, 1991).These models are not appropriate to predictions in compound channels with converging flood plain because non-uniform flow occurs from section to section. Therefore, there is a need to evaluate the depth-averaged velocity in the main channel and floodplain at various locations of a converging compound channel. Converging channel flows, being highly complicated, are a matter of recent and continued research. For a better understanding of the structure of turbulent flow in converging compound channels, it is necessary to undertake detailed measurements. Because of the difficulty in obtaining sufficiently accurate and comprehensive field measurements of velocity and shear stress in converging compound channels under non-uniform flow conditions, considerable reliance must still be placed on well-focused laboratory investigations under steady flow conditions to provide the information concerning the details of the flow structures and lateral momentum transfer. Attention must be paid to the fact that physical models are very expensive, especially when a large number of influencing parameters have to be studied. Sometimes, it is impossible to construct a physical model for certain prototypes. Therefore, there is urgent need for economic mathematical prediction models. In past a lot of experimental research has been done on prismatic compound channel flows but relatively less usage has been made of numerical techniques on non-prismatic compound sections. After the development of powerful computers and sophisticated Computational Fluid Dynamics (CFD) techniques, much research is now being conducted using these techniques in different research areas. This is not only due to economy and less time required with CFD methodology but also due to the fact that through CFD one can cover those aspects of flow behavior which are very difficult to observe through experimentation. In recent years, numerical modeling of open channel flows has successfully reproduced experimental results. CFD has been used to model open channel flows ranging from main channels to flood plains. Simulations have been performed by Krishnappan and Lau (1986), Kawahara and Tamai (1988) and Cokljat (1993). CFD has also been used to model flow features in natural rivers by Sinha et al. (1998), Lane et al. (1999), and Morvan (2001). Hodskinson (1996, 1998) was one of the first to present results using a commercial CFD. In this case FLUENT was used to predict the 3D flow structure in a 90-degree bend on the River Dean in Cheshire. Pan and Banerjee (1995), Hodges and Street (1999), and Nakayama and Yokojima (2002) studied free surface fluctuations in open channel flow by employing the LES method. Hsu et al. (2000) have reported the existence of the inner secondary currents in the rectangular open channels, which occur at the junction of the free surface and side wall. Knight et al. (2005) applied state-of-the-art CFD software to explore the physics within openchannel flows. In their research work they applied three different turbulent models, namely the *k*-ϵ, Reynolds Stress model by Speziale, Sarkar, and Gatski (SSG) by Speziale et al. (1991) and Reynolds Stress ω or SMC-ω

CONTACT P. Singh prateek.k.singh1992@gmail.com

(implemented in ANSYS-CFX) models to trapezoidal channel. Thomas and Williams (1995a) and Cater and Williams (2008) simulated an asymmetric rectangular compound channel using LES for a relative depth of $\beta = 0.5$. They have predicted mean stream wise velocity distribution, secondary currents, bed shear stress distribution, turbulence intensities, TKE, and calculated lateral distribution of apparent shear stress. Gandhi et al. (2010) determined the velocity profiles in two directions under different real flow field conditions and also investigated the effects of bed slope, upstream bend and a convergence/divergence of channel width. Kara et al. (2012) compared the depth-averaged stream wise velocities obtained by LES with calculated by analytical solution of Shiono and Knight Method (SKM), and concluded that the analytical approach to their problem requires calibration of the lateral eddy viscosity coefficient, λ, and the secondary current parameter, Γ. Xie et al. (2013) used LES to simulate asymmetric rectangular compound channel. In this study the distributions of the mean velocity and secondary flows, boundary shear stress, turbulence intensities, TKE and Reynolds stresses were in a good agreement with the experimental data. Filonovich (2015) used ANSYS-CFX package to allow the simulation of uniform flows in straight asymmetric trapezoidal and rectangular compound channels with several different RANS turbulence closure models.

In the last decade machine-learning methods were the subject of many researches in engineering problems and also in water resources engineering (Cheng et al. 2002; Ghosh et al. 2010; Lin et al. 2006; Muzzammil 2008; Safikhani et al. 2011; Wang et al. 2009; Wu et al. 2009). Bilgil and Altun (2008) predicted friction factor in smooth open channel flow using ANN. Sahu et al. (2011) proposed an artificial neural network (ANN) model for accurate estimation of discharge in compound channel flume and Moharana and Khatua (2014) studied the flow resistance in meandering compound channels using ANFIS. Abdeen (2008) adopted an ANN technique to simulate the impacts of vegetation density, flow discharge, and the operation of distributaries on the water surface profile of open channels. Yuhong and Wenxin (2009) studied the application of ANN for prediction of friction factor of open channel flows. The ANN technique has also been successfully applied to compound open channel flow for the prediction of the hydraulics characteristics, such as integrated discharge and stage-discharge relations (Bhattacharya and Solomatine 2005; Jain 2008; Sahu et al. 2011; Unal et al. 2010)

In the first part of this paper, 3D numerical simulations of flow field with two phases (water + air) are carried out with the software ANSYS FLUENT to study the variation of velocity profiles in different converging sections of a compound channel. In multiphase fluid flow, a phase is described as a particular class of material that has a certain inertial response and interaction with the fluid flow and the potential field in which it is immersed. Currently, there are two approaches for the numerical calculation of multiphase flows: The Euler–Lagrange approach and the Euler–Euler approach. Even though air is considered as a secondary material, we have taken it in analysis to give it more real-time analogy, by compromising over the computational time.

In order to solve turbulence equations, the k-ω model is used since more accurate near wall treatment with automatic switch from wall function to a low Reynolds number formulation based on grid spacing. Numerical results are verified using experimental data obtained in an experimental analysis in the Hydraulics and Fluid Mechanics Laboratory of the Civil Engineering Department of NIT, Rourkela. This study shows that the numerical model results have good agreement with experimental ones. There are always some limitations in experimental studies and obtaining experimental data in every point of a channel is not easy. Also after doing an experimental test and obtaining the velocity in the desired point, measuring the velocity in other points needs to do the experimental test again. Artificial intelligence is evaluated here as a solution to this problem. By training an ANN based on experimental data of the points that are available, the ANN assists investigators in calculating the velocity at other points of the channel with good accuracy. This paper employs ANN for the prediction of depth average velocity of converging compound channel, after using the CFD technique to establish the basic database under various working conditions. Quite a few model available for prediction of depth average velocity usually under performs when the meager data-sets are used for estimation. Generally, this happens while predicting the depth average velocity for a wide range of hydraulic conditions and geometries of compound channel. To alleviate the above problem, a robust prediction strategy based on an ANN has been proposed. It is demonstrated that the ANN model is quite capable of predicting a depth average velocity with reasonable accuracy for a wide range of hydraulic conditions.

2. Experimental works

Experiments have been conducted at the Hydraulics and Fluid mechanics Laboratory of Civil Engineering Department of National Institute of Technology, Rourkela, India. Three sets of non-prismatic compound channels with varying cross-section were built inside a concrete flume with Perspex sheet measuring 15 m long × 0.90 m width × 0.5 m depth. The width ratio (α = flood plain width (B)/main channel width (b)) of the channel was 1.8 and the aspect ratio (δ = main channel width (b)/main channel depth (h)) was 5. Keeping the geometry constant, the converging angles of the channels were varied as 12.38°, 9°, and 5°, respectively. Converging length of the channels fabricated were found to be 0.84, 1.26, and 2.28 m, respectively. Longitudinal bed slope of the channel was measured to be 0.0011, satisfying subcritical flow conditions at all the sections of the non-prismatic compound channels. Roughness of both floodplain and main channel were kept smooth with the Manning's n 0.011 determined from the inbank experimental runs in the channel. The flow conditions in all sections were turbulent. A re-circulating system of water supply was established with pumping of water from the large underground sump located in the laboratory to an overhead tank from where water flows under gravity to the experimental channels. Adjustable vertical gates along with flow strengtheners were provided in the upstream section sufficiently ahead of rectangular notch to reduce turbulence and velocity of approach in the flow near the notch section. An adjustable tailgate at the downstream end of the flume helps to maintain uniform flow over the test reach. Water from the channel was collected in a volumetric tank of fixed area that helps to measure the discharge rate by the time rise method. From the volumetric tank water runs back to the underground sump by the valve arrangement. For present work the experimental data Rezaei (2006) have been used. Rezaei (2006) have also used converging compound channels of angles 11.31°, 3.81°, 1.91° giving the same subcritical flow and smooth surfaces. They have found the depth-averaged velocity and boundary shear distribution of the same channels under

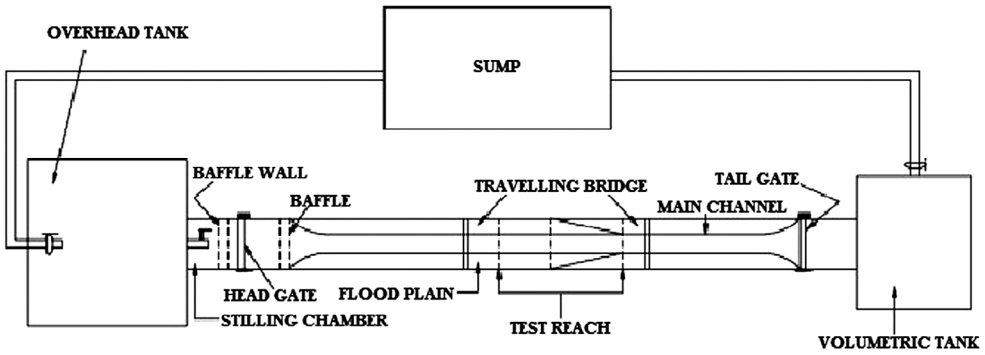

Figure 1a. Plan view of experimental setup.

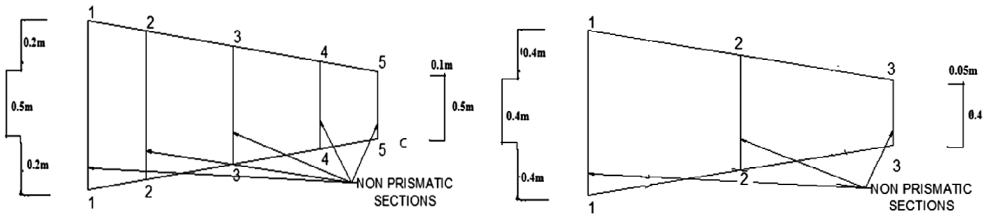

Figure 1b. Plan view of different test reaches with cross-sectional dimensions of non-prismatic compound channel from both NITR & Rezaei (2006) channels.

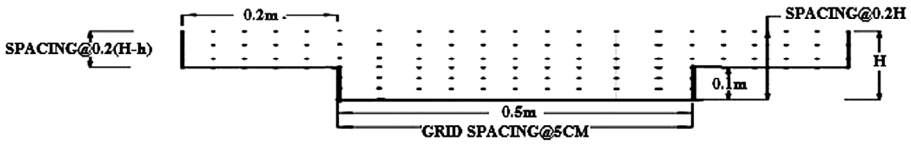

Figure 1c. Typical grid showing the arrangement of velocity measurement points at the test sections (1-1,2-2,3-3,4-4 & 5-5).

different flow conditions. Figure 1(a) shows the plan view of experimental setup. Figure 1(b) shows the plan view of different test reach with cross-sectional dimensions of both NITR and Rezaei (2006) channels. Figure 1(c) shows the typical grid showing the arrangement of velocity measurement points along horizontal and vertical direction in the test section.

A movable bridge was provided across the flume for both span-wise and stream-wise movements over the channel area so that each location on the plan of compound channel could be accessed for taking measurements. Water surface depths were measured directly with a point gage located on an instrument carriage. The flow depth measurements were taken along the center of the flume at an interval of 0.5 m both in upstream and downstream prismatic parts of flume and at every 0.1 m in the converging part of the flume. A micro-Pitot tube of 4.77 mm external diameter in conjunction with suitable inclined manometer and a 16-MHz Micro ADV (Acoustic Doppler Velocity-meter) was used to measure velocity at these points of the flow-grid. In some points, micro-ADV cannot take the velocity reading (up to 50 cm from the water surface). In such points Pitot tube was used to take the velocity. The Pitot tube was physically rotated with respect to the main stream direction until it gave maximum deflection of the manometer reading. A flow direction finder having a minimum count of 0.1° was used to get the direction of maximum velocity with respect to the longitudinal flow direction. The angle of limb of Pitot tube with longitudinal direction of the channel was noted by the circular scale and pointer arrangement attached to the flow direction meter. The overall discharge obtained from integrating the longitudinal velocity plot and from volumetric tank collection was found to be within ±3% of the observed values. Using the velocity data, the boundary shear at various points on the channel beds and walls were evaluated from a semi log plot of velocity distribution.

3. Numerical modeling

A number of CFD packages (Fluent, CFX, Star-CD, and others) are now available and have been used for research in water flows van Hooff and Blocken (2010). In recent past, a good number of researchers have used these software packages for prediction of different aspects of 3D flow fields e.g. Sahu et al. (2011). They detected that flow features in compound channels are dependent on topography of the channel, surface roughness etc. However, the flow behavior changes are still an unresolved phenomenon and attempts are underway to address this problem. These researchers attempted to predict the flow behavior using different numerical models as it is difficult to capture all flow features experimentally but still a lot of work is to be done. This is due to various problems which are encountered in numerical modeling such as grid generation, choice of turbulence model, discretization scheme, specifying the boundary, and initial conditions.

In this work, an attempt has been made to improve the understanding of 3D flows in converging compound channels. For this purpose, a 3D numerical code FLUENT has been tested for its suitability for simulation of flood flows. Initially, the closure problem of governing equations was considered as

there is no universal closure model which is acceptable for all flow problems. Each has its own advantages and disadvantages. Therefore, some consideration must be taken when choosing a turbulence model including, physics encompassed in the flow, level of accuracy, and computation resources available one has to attempt different models and then to choose the one producing best results. The models tested here were standard k-ε, LES, and *k-ω*. The one with best output (standard *k-ω* in this case) was then used for all simulation works. The *k-ω* model is chosen on the basis of the computational time and resource availability. Besides the fact that k-ϵ more or less produce same results as that of the *k-ω* model but the other two-equation model 'k-ω' performs better near the wall region and k-ϵ performs better in the fully turbulent region (Filonovich 2015). On the other hand, LES partially resolves the turbulence and give good results when compared to experimental data (Kara et al. 2012). The overall idea of modeling through sub grid model for small time and length scale (Kolmogorov scales i.e. ratio of small eddies to large eddies lengthwise as well as time wise) and resolving the large scale through governing equation needs an exceptionally high computation effort. To optimize such computational resource and time requirement, *k-ω* model is chosen even though compromises are made over the results which are acceptable than spending high in computational resources and time. It was used for prediction of resultant velocity contours on free surface, pressure, turbulence intensity, and secondary flow velocities at different sections along the converging length.

Generally FLUENT involves three stages. The first stage is the pre-processing, which involve geometry creation, setting of grid, and defining the physics of the problem. The second stage involves the application of solver to generate a numerical solution. In the third stage post-processing takes place, where the results are visualized and analyzed.

3.1. Geometry

The first step in CFD analysis is the explanation and creation of computational geometry of the fluid flow region. A consistent frame of reference for coordinate axis was adopted for creation of geometry. Here in coordinate system, x-axis corresponded the lateral direction which indicates the width of channel bed. Y-axis aligned stream-wise direction of fluid flow and Z-axis represented the vertical component or aligned with depth of water in the channel. The origin was placed at the upstream boundary and coincided with the base of the center line of the channel. The water flowed along the positive direction of the y-axis. The simulation was done on a non-prismatic compound channel with a converging flood plain. The setup of the compound channel is shown in Figure 2.

To identify the domain six different surfaces are generated. Figure 3 shows the different Geometrical entities used in a non-prismatic compound channel

- Inlet
- Outlet
- Free Surface
- Side Wall
- Channel Bottom
- Center line

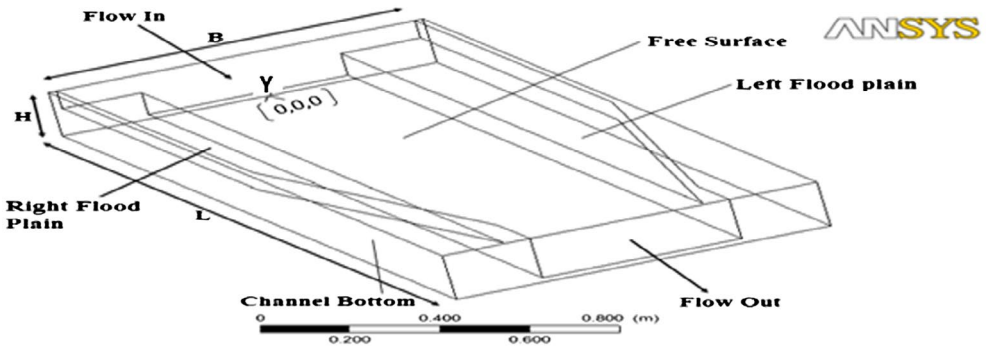

Figure 2. Geometry setup of a compound channel with converging flood plains.

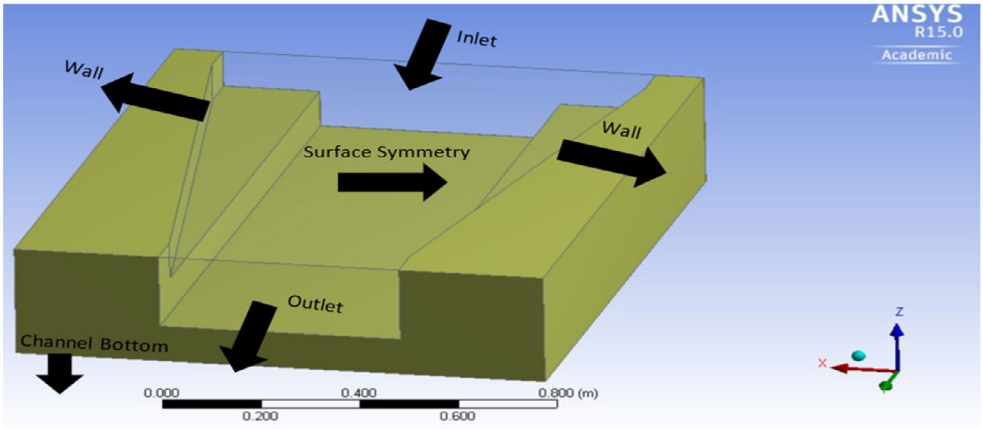

Figure 3. Different geometrical entities used in a compound channel with converging flood plain.

3.2. Mesh generation

The second and very important step in numerical analysis is setting up the discretized grid associated with the geometry. Construction of the mesh involves discretizing or subdividing the geometry into the cells or elements at which the variables will be computed numerically. Using the Cartesian co-ordinate system, the fluid flow governing equations i.e. momentum equation, continuity equation are solved based on the discretization of domain. The meshing divides the continuum into a finite number of nodes. Generally, one of three different methods, i.e. Finite Element, Finite Volume, and Finite Difference, can discretize the equations. Fluent uses Finite Element (FE)-based Finite Volume Method (FVM). This alternative uses the control volume analysis, which is vertex-centered, i.e. the solution correlation variables are saved at the nodes (vertices) of the mesh. The concept of FVM is used to convert the partial differential equation into system of algebraic equation, which can be solved through closure. Two prominent discretization steps involved at this stage are discretization of the computational domain and discretization of the equation. The discretization of the computational domain is done through mesh generation, which can be identified later through control volume constructions. However, a very dense mesh of nodes causes excess computational time and memory. For CFD analysis, more nodes are required in some areas of interest, such as near wall and wake regions, in order to capture the large variation of fluid properties. Thus, the structure of grid lines causes further unnecessary use of computer storage due to further refinement of mesh. In this study, the flow domain is discretized using an unstructured grid and body-fitted coordinates. Unstructured grid is used so that intricacies can be covered under the grid which is left over in structured one. The detailed meshing of the flow domain is shown in Figure 4.

3.3. Solver setting

3.3.1. Setup

After the meshing part is completed, various inputs are given in the Setup section. **VOF** (volume of fluid) model is the only model available for open channel flow simulation in ANSYS-FLUENT, which is based on the idea of volume fraction (Hirt and Nichols 1981). In this method, a transport equation is solved for the volume fraction at each time step whereupon the shape of the free surface is reconstructed explicitly using the distribution of the volume fraction function. The 'reconstruction' of the free surface can be explained more clearly through the concept of water volume fraction. Free surface is defined as the cell, which takes the value of the water volume fraction as non-zero while a zero value indicates that no fluid is present in the cell. The value of 0.5 for the water volume fraction is indicative of the fact that free surface position is detected. This method can define sharp interfaces and is robust. VOF is capable of calculating time-dependent solutions. Flow in an open channel is generally bound by channel from all directions except for the upward free surface. To achieve a free surface zero friction interface, a command called 'surface_symmetry' is given in named selection. Velocity inlet for inlet and pressure outlet for outlet is defined and the roughness coefficient is added to the walls for 'no slip' condition. Transient flow was chosen because the flow parameters were varied in time in the experiment. Gravity is check marked and the value for Z-axis is given as −9.81 because gravity acts downward opposite to the z-direction vector. As mentioned earlier, the turbulence model was chosen as k-ω model. PISO was selected for solving the pressure equation, as it is generally a pressure-based segregated algorithm recommended for transient flow conditions (Issa 1986). Also, PISO scheme may aid in accelerating convergence for many

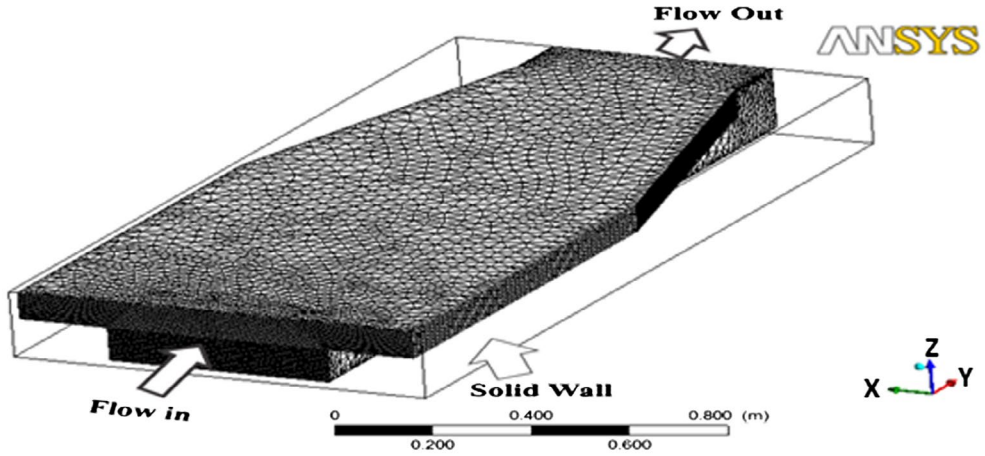

Figure 4. A schematic view of the grid used in the numerical model.

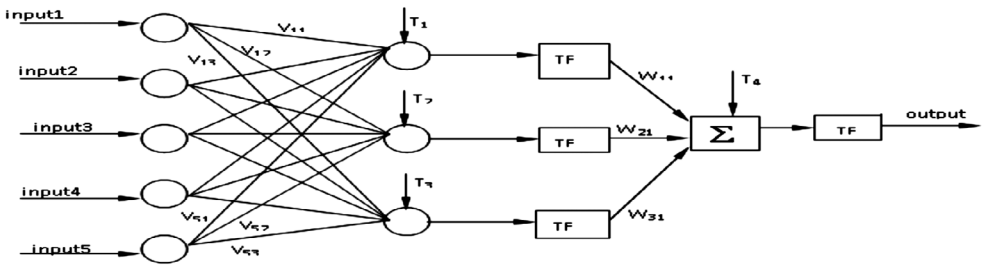

Figure 5. The architecture of back propagation neural network model.

unsteady flows. Finally, solver is patched and run to apply all the settings as well as conditions mentioned above. It's just finalizing and complying the settings. The equation solved in the CFD are usually iterative and starting from initial approximation, they iterate to a final result. However, these iterations are terminated at some step to minimize the numerical effort. This termination are done on the basis of normalized residual target which is by default is set to 10^{-4}, which leads to loose convergence target. For problems like compound channel in order to obtain more accuracy residual target should be placed a value near around 10^{-6}. Time step size was set to 0.001s and number of iteration given was 1000 for better accuracy and convergence of the iteration. Time step size, Δt, is then set in the Iterate panel, Δt must be small enough to resolve time-dependent features; making sure that the convergence is reached within the number of max iterations per time step. The order of magnitude of an appropriate time step size can be estimated as ratio of typical cell size to the characteristic flow velocity. Time step size estimate can also be chosen so that the unsteady characteristics of the flow can be resolved (e.g. flow within a known period of fluctuations). To iterate without advancing in time, use zero time steps.

3.3.2. Governing equations

ANSYS Fluent uses the finite volume method to solve the governing equations for a fluid. It provides the capability to use different physical models such as incompressible or compressible, inviscid or viscous, laminar or turbulent etc. The most practical and still the most popular method of dealing with turbulence is that based on the RANS method. With this method, all scales of turbulence are modeled. Several models were studied to compare the effect of turbulent modeling in the converging compound channel, including the following: (1) k-Epsilon, (2) k-ω, and (3) Large Eddy Simulation (LES) model. Here, k-ω model is used for turbulence modeling. The k-ω model solves the k-transport equation and a transport equation for ω. The k-transport equation and the transport equation for ω can be written (Wilcox 1988) as:

$$\frac{\partial k}{\partial t} + U_i \frac{\partial k}{\partial x_i} = \frac{\partial}{\partial x_i}\left(\frac{\nu_t}{\sigma_k}\frac{\partial k}{\partial x_i}\right) + P - \beta' k\omega \tag{1}$$

$$\frac{\partial \omega}{\partial t} + U_i \frac{\partial k}{\partial x_i} = \frac{\partial}{\partial x_i}\left(\frac{\nu_t}{\sigma_\omega}\frac{\partial k}{\partial x_i}\right) + \alpha\frac{\omega}{k}P - \beta\omega^2 \tag{2}$$

and the eddy viscosity is given by:

$$\upsilon_t = k/\omega \tag{3}$$

P is the turbulence kinetic energy production rate. The turbulence equation was suggested by Menter (1994) as:

$$P = \min(P, 10\beta' k\omega) \tag{4}$$

It represents the rate at which the energy is fed from the mean flow to each stress component. The estimation of the production term can be done directly from the stress and the men flow strain rate components and thus, needs no modeling other than this all other terms need modeling (Table 1).

The k-ω model involves five empirical constants β', β, α, σ_k, and σ_ω. They have their universal constant values, which have been derived on the basis of high-quality data. Their values vary from one turbulence model to another. For any particular turbulence model, the values of these constants remain same for all simulation purposes. For standard k-ω, their values are presented in Table 2.

Table 1. Hydraulic parameters for the experimental channel data.

Sl. No	Item description	Converging compound channel
1	Geometry of main channel	Rectangular
2	Geometry of flood plain	Converging
3	Main channel width (b)	0.5 m
4	Bank full depth of main channel	0.1 m
5	Top width of compound channel (B1)	Before convergence 0.9 m
6	Top width of compound channel (B2)	After convergence 0.5 m
7	Converging length of the channels	0.84 m, 1.26, 2.26 m
8	Slope of the channel	0.0011
9	Angle of convergence of flood plain (^{o})	12.38,9, 5
10	Position of experimental section 1	Start of the converging part
11	Position of experimental section 2	Middle of converging part
12	Position of experimental section	End of converging part

Table 2. Values of the constants in the k-ω model (Wilcox 1988).

β'	β	α	σ_k	σ_ω
0.09	0.075	5/9	2	2

3.3.3. Boundary conditions

Four different types of boundary condition were considered in this study. These are (i) inlet, (ii) outlet, (iii) water surface, and (iv) walls of the geometry

(i) Inlet

The velocity distribution at the upstream cross-section was taken as inlet boundary condition. At the inlet, turbulence properties i.e. k (turbulence kinetic energy) and (ω turbulence dissipation rate) must be specified. These were calculated as (Filonovich 2015)

$$k = IU^2 \tag{5}$$

$$\omega = \frac{k^{1/2}}{l} \tag{6}$$

where I is the turbulence intensity and U is the mean value of stream-wise velocity. l is the turbulence length scale.

(ii) Outlet

At the outlet, the pressure condition was given as the boundary condition and pressure was fixed at zero. Importance of the outflow boundary at an appropriate location can be explained through the influence of the downstream condition. Thus, it makes extremely imperative to put the downstream end far enough to prevail the fully developed state.

(iii) Channel and Floodplain Boundaries

A no-slip boundary condition was considered at the walls. This means that the velocity components should be zero at the walls. The no-slip condition is the default, and it indicates that the fluid sticks to the wall and moves with the same velocity as the wall, if it is moving. The wall is the most common boundary condition in bounded fluid flow problem. Setting the velocity near wall as zero under no-slip condition is appropriate condition for the solid boundary. The wall boundary condition in the turbulent flow is implemented and initiated by evaluating the dimensionless distance 'z$^+$' from the wall to the nearest boundary node. This dimensionless distance is the function of the near wall node to the solid boundary, friction velocity and the kinematic viscosity. The near wall treatment will depend on

the position of the nearest to the boundary node. If $z^+ \leq 11.06$, the nearest to boundary node will lie in the viscous sub-laminar layer where profile is linear and very fine meshing is required. This will tend to intensify the computation effort, which is being dedicated for near wall treatment. In another case where $z^+ > 11.06$, the nearest boundary node will lie in the buffer layer which is the transition region from viscous sublayer and the log law region. The main shortcoming of the wall function approach is their dependability on the nearest node distance from the wall, which cannot be overcome through refining since it does not guarantees high accuracy. Nevertheless, the problem of discrepancy in the wall function approach can be subsidized through Scalable wall function where limiting the z^+ value to not fall below 11.06 (the intersection of linear profile and log-law) is concentrated. Therefore, all mesh points are made to lie outside the viscous sublayer and all fine mesh discrepancies are circumvented.

Thus, standard wall function which uses log-law of the wall to compute the wall shear stress is used (Spalding 1980). Fluid flows over rough surfaces are encountered in diverse situations. If the modeling is a turbulent wall-bounded flow in which the wall roughness effects are considered significant, it can include the wall roughness effects through the law-of-the-wall modified for roughness.

(iv) Free Surface

The water surface was defined as a plane of symmetry which means that the normal velocity and normal gradients of all variables are zero at this plane. Free surface, in the present study, is modeled through VOF for estimating the domain for air and water (multiphase problem).

3.4. Results

A variety of flow characteristics can be considered in the post-processing software of CFD packages. This work has been concerned with the velocity distribution and the results are compared with experimental measurements. In general, the user should make an attempt to validate the CFD results with known data so that there can be some confidence in the solution. In the case of open channel flow, the validation is most likely to take the form of a comparison against physical measurements and a qualitative understanding of what features should be present in the flow. As part of the analysis, the user may also wish to perform a sensitivity study and vary any parameters (such as roughness here) which have a degree of uncertainty, and determine what influence they have on the solution.

4. Prediction using ANN

ANN is a new and rapidly growing computational technique and an alternative procedure to tackle complex problems. In recent years, it has been broadly used in hydraulic engineering and water resources (Bilgil and Altun (2008), Sahu et al. (2011)). It is a highly self-organized, self-adapted, and self-trainable approximator with high associative memory and non-linear mapping. ANNs may consist of multiple layers of nodes interconnected with other nodes in the same or different layers. Various layers are referred to as the input layer, the hidden layer, and the output layer. The inputs and the inter connected weights are processed by a weight summation function to produce a sum that is passed to a transfer function. The output of the transfer function is the output of the node. In this paper multi-layer perception network is used. Input layer receives information from the external source and passes this information to the network for processing. Hidden layer receives information from the input layer and does all the information processing, and output layer receives processed information from the network and sends the results out to an external receptor. The input signals are modified by interconnection weight, known as weight factor W_{ij} which represents the interconnection of ith node of the first layer to the jth node of the second layer. The sum of modified signals (total activation) is then modified by a sigmoidal transfer function (f). Similarly, output signals of hidden layer are modified by interconnection weight (W_{ij}) of kth node of output layer to the jth node of the hidden layer. The sum modified k signal is then modified by a pure linear transfer function (f) and output is collected at output layer.

Let $I_p = (I_{p1}, I_{p2}, \ldots, I_{pl})$, $p = 1,2, \ldots, N$ be the pth pattern among N input patterns. W_{ji} and W_{kj} are connection weights between ith input neuron to jth hidden neuron and jth hidden neuron to kth output neuron, respectively.

Output from a neuron in the input layer is:

$$O_{pi} = I_{pi},\ i = 1,\ 2 \ldots\ l \tag{7}$$

Output from a neuron in the hidden layer is:

$$O_{pj} = f(\mathrm{NET}_{pj}) = f\left(\sum\nolimits_{(i=0)}^{l} W_{ji} O_{pi}\right), j = 1,\ 2.\ m \tag{8}$$

Output from a neuron in the hidden layer is:

$$O_{pk} = f(\mathrm{NET}_{pk}) = f\left(\sum\nolimits_{(i=0)}^{l} W_{kj} O_{pj}\right), k = 1,\ 2.\ n \tag{9}$$

4.1. Sigmoidal function

A bounded, monotonic, non-decreasing, S Shaped function provides a graded non-linear response. It includes the logistic sigmoid function

$$F(x) = \frac{1}{1 + e^{-x}} \tag{10}$$

where x = input parameters taken

The architecture of back propagation neural network (BPNN) model, that is the l-m-n (l input neurons, m hidden neurons, and n output neurons) is shown in the Figure 5.

4.2. Learning or training in BPNN

Batch mode type of supervised learning has been used in the present case in which interconnection weights are adjusted using delta rule algorithm after sending the entire training sample to the network. During training the predicted output is compared with the desired output and the mean square error is calculated. If the mean square error is more, then a prescribed limiting value, it is back propagated from output to input and weights are further modified till the error or number of iteration is within a prescribed limit.

Mean Squared Error, E_p for pattern is defined as:

$$E_p = \sum\nolimits_{(i=1)}^{n} \frac{1}{2}\left(D_{pi} - O_{pi}\right)^2 \tag{11}$$

Where D_{pi} is the target output, O_{pi} is the computed output for the ith pattern.

Weight changes at any time t, is given by:

$$\Delta W(t) = -nE_p(t) + \alpha \times \Delta W(t-1) \quad (12)$$

n = learning rate i.e. $0 < n < 1$; α = momentum coefficient i.e. $0 < \alpha < 1$

4.3. Source of data

The data are collected from research work done in Hydraulic and Fluid Mechanics Laboratory, NIT Rourkela, Rezaei (2006) data, available at the laboratory of University of Birmingham, Wallingford and also generated data using ANSYS-15 .The descriptions of geometrical parameters of above data are mentioned in Table 3.

4.4. Selection of hydraulic parameters

Flow hydraulics and momentum exchange in converging compound channels are significantly influenced by both geometrical and hydraulic variables, the computation become more complex when the floodplain width contracted and become zero. The flow factors responsible for the estimation of depth-averaged velocities are

(i) Converging angle denoted as θ
(ii) Width ratio (α) i.e. .ratio of width of floodplain to width of main channel
(iii) Aspect ratio (σ) i.e. ratio of width of main channel (B) to depth of main channel (h)
(iv) Depth ratio (β) = (H-h)/H, where H = height of water at a particular section and, h = height of water in main channel
(v) Relative distance (X_r) i.e. of point velocity in the length wise direction of the channel)/total length of the non-prismatic channel. Total five flow variables were chosen as input parameters and depth-averaged velocity as output parameter.

Table 3. Input and output data used for the present analysis.

Sl. No	Converging angles	Flood plain type	Converging length
1	1.91	Convergent	6 m
2	3.81	Convergent	6 m
3	11.31	Convergent	2 m
4	5	Convergent	2.26 m
5	9	Convergent	1.28 m
6	12.38	Convergent	0.84 m
8	2.5	Convergent	4.58
9	3	Convergent	3.82
10	4	Convergent	2.86
11	7	Convergent	1.64
12	10	Convergent	1.15
13	14	Convergent	0.8
14	15	Convergent	0.77
15	17	Convergent	0.68
16	20	Convergent	0.58

5. Results

5.1. Results of ANSYS and CES

5.1.1. Verification

The values of depth-averaged velocity distributions of different cross-sections of the non-prismatic compound channel are achieved from the numerical models like CES (Conveyance Estimating System) and ANSYS then the results from the experimental data of both NITR and Rezaei (2006) channels were compared in Figures 6–11. As illustrated in Figures 6–10, the numerical model was in good agreement with experimental results but the results of the CES model have some differences with experimental results. The Conveyance and Afflux Estimation System (CES/AES) is a software tool for the improved estimation of flood and drainage water levels in rivers, watercourses, and drainage channels. The software development followed recommendations by practitioners and academics in the UK Network on Conveyance in River Flood Plain Systems, following the Autumn 2000 floods, that operating authorities should make better use of recent improved knowledge on conveyance and related flood (or drainage) level estimation. This led to a Targeted Program of Research aimed at improving conveyance estimation and integration with other

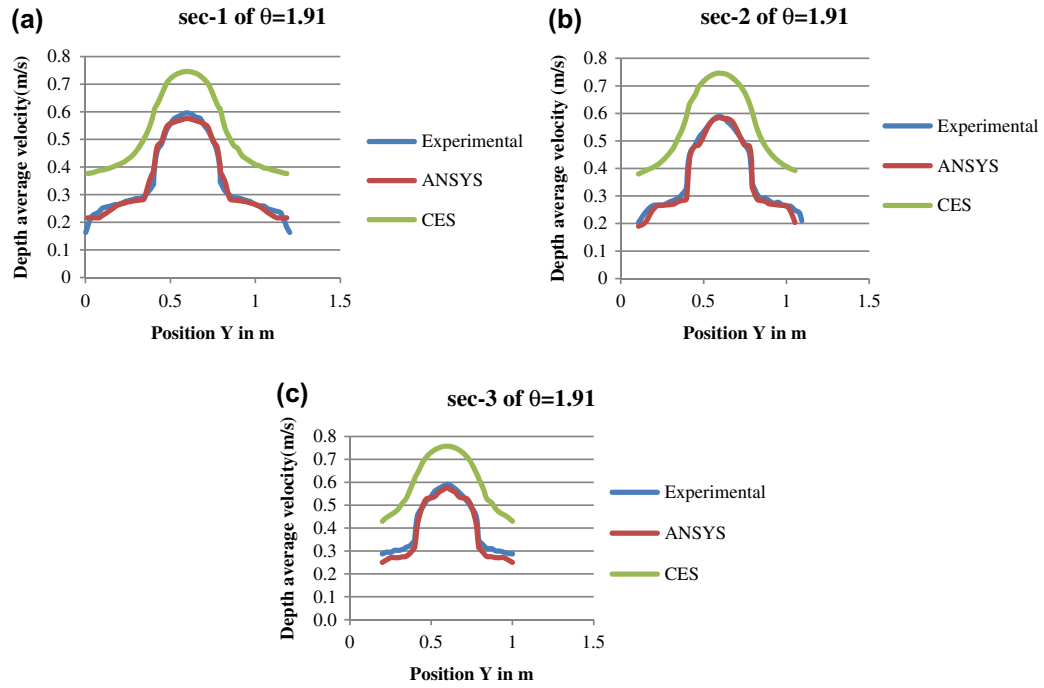

Figure 6. (a), (b), (c) Depth-averaged velocity of Sec 1, Sec 2, Sec 3 of $\theta = 1.91°$.

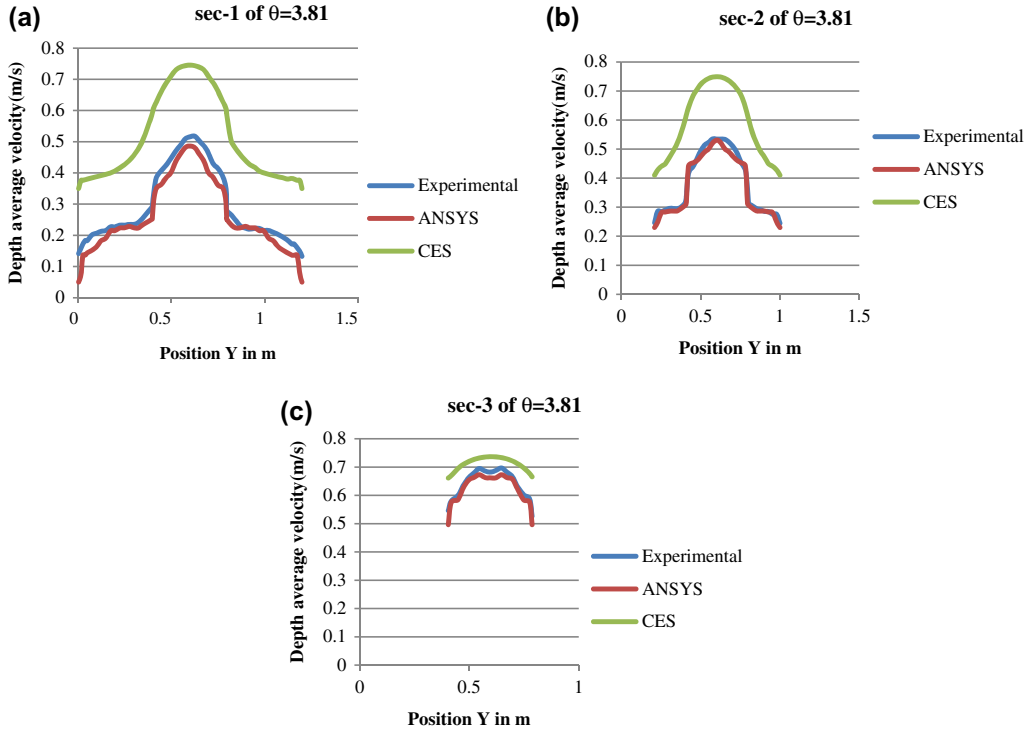

Figure 7. (a), (b), (c) Depth-averaged velocity of Sec 1, Sec 2, Sec 3 of $\theta = 3.81°$.

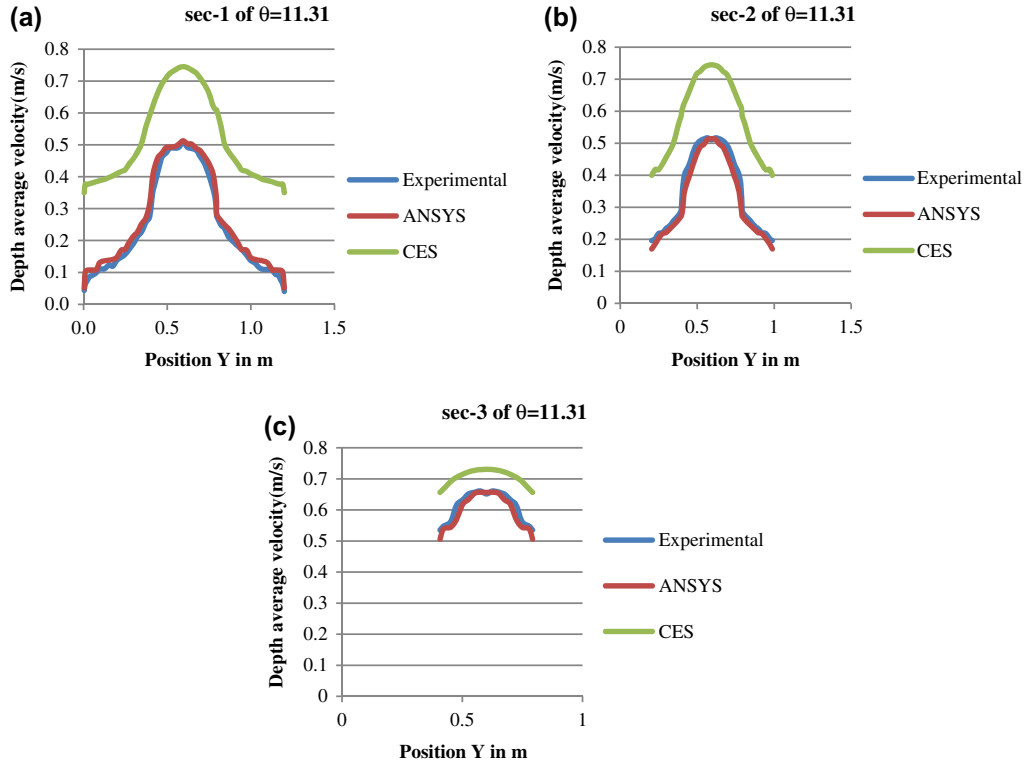

Figure 8. (a), (b), (c) Depth-averaged velocity of Sec 1, Sec 2, Sec 3 of $\theta = 11.31°$.

research on afflux at bridges and structures at high flows. The CES/AES software tool aims to improve and assist with the estimation of:

- hydraulic roughness
- water levels (and corresponding channel and structure conveyance)
- flow (given slope)
- section-average and spatial velocities
- backwater profiles upstream of a known flow-head control e.g. weir (steady)
- afflux upstream of bridges and culverts
- uncertainty in accuracy of input data and output

Conveyance Estimation System (CES) is developed by joint Agency/DEFRA research program on flood defense, with contributions from the Scottish Executive and the Northern Ireland Rivers Agency, HR Wallingford. CES is based on

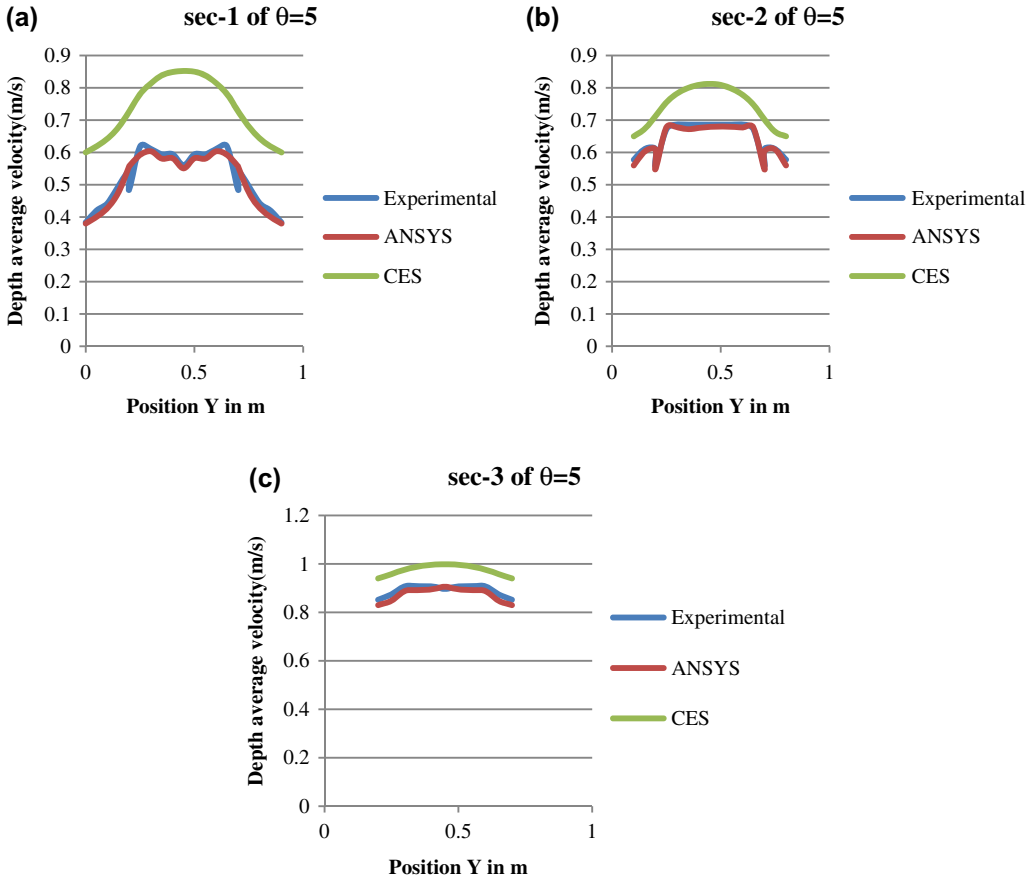

Figure 9. (a), (b), (c) Depth-averaged velocity of Sec 1, Sec 2, Sec 3 of $\theta = 5°$.

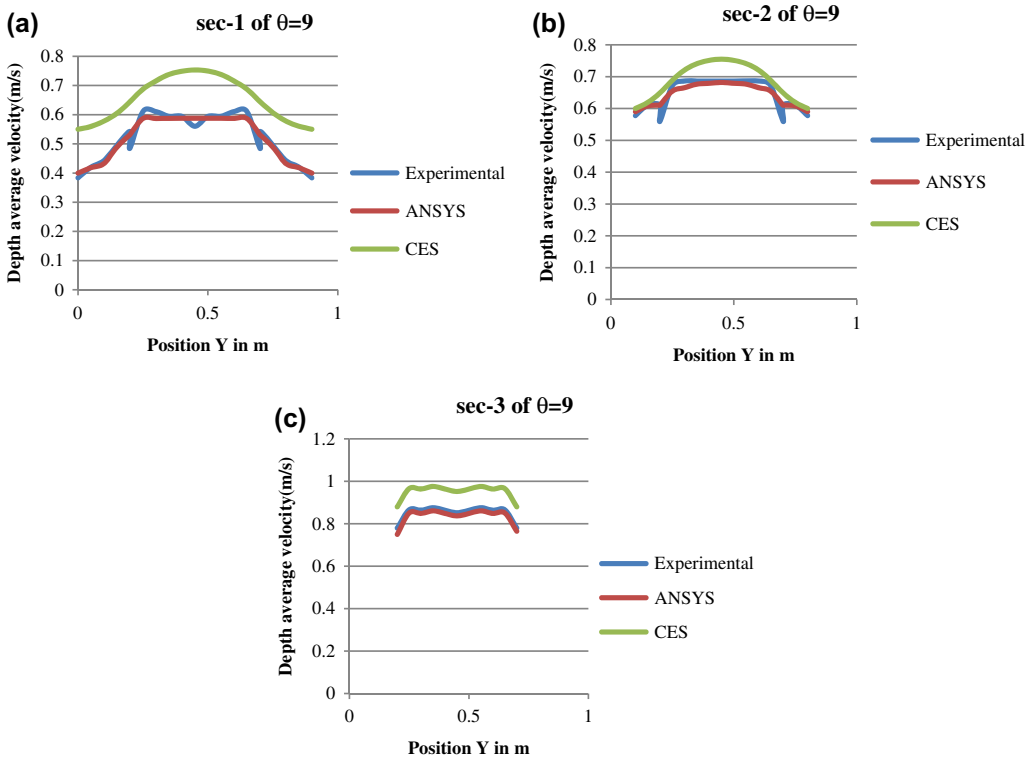

Figure 10. (a), (b), (c) Depth-averaged velocity of Sec 1, Sec 2, Sec 3 of $\theta = 9°$.

Reynolds-averaged Navier-Stokes (RANS) approach as the solution basis for estimation of conveyance. RANS equation of CES has been solved analytically by Shiono and Knight method. In this solution, the converging fluid plain effect has not been considered which is reflected by the results of depth-averaged velocity and giving much error However, Fluent k-ω model take care of converging effect as well as interaction effect of geometry of converging compound channel.

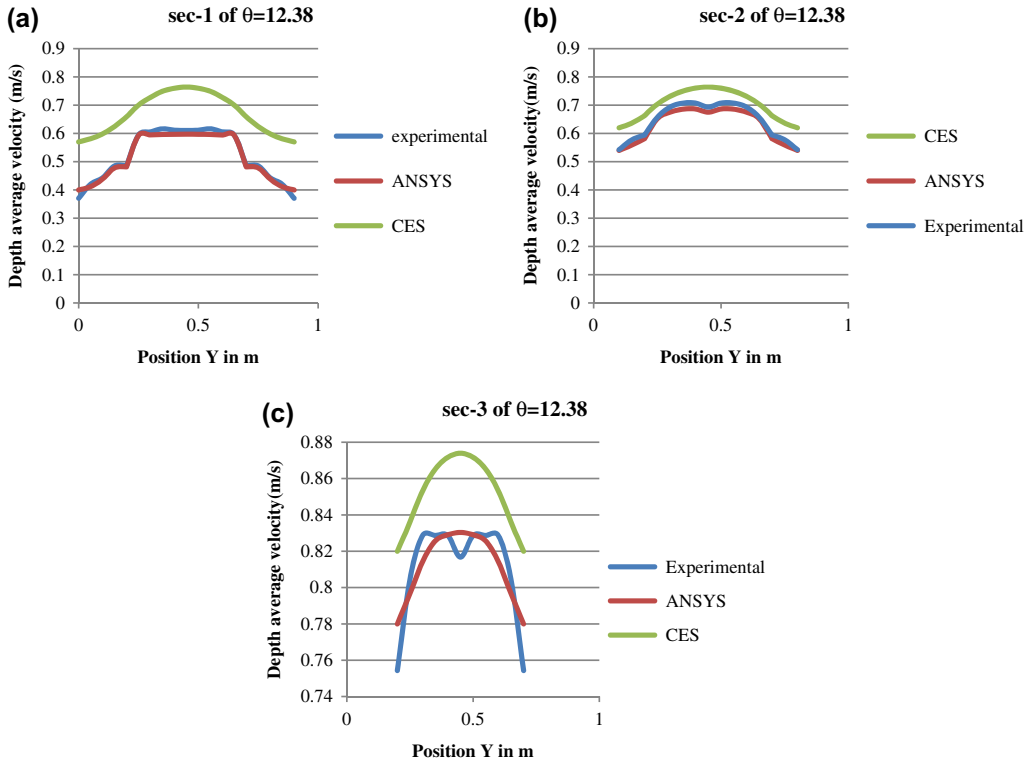

Figure 11. (a), (b), (c) Depth-averaged velocity of Sec 1, Sec 2, Sec 3 of $\theta = 12.38°$.

5.2. Results of ANN

5.2.1. Testing of BPNN

Determination of depth-averaged velocity distribution of compound channel with converging flood plain is an important task for river engineer. Due to non-linear relationship between the dependent and independent variables any model tools to provide the accurate depth-averaged velocity distribution. Numerical approach has also consumed more memory and time. So in the present work the ANN has been tested. The total experimental data-set is divided into training set and testing set. For depth-averaged velocity calculations 32,321 data are used among which 70% are training data and 30% are taken as testing data. The number of layers and neurons in the hidden layer are fixed through exhaustive experimentation when mean square error is minimized for training data-set. It is observed that minimum error is obtained for 5-7-1 architecture. So the BPNN used in this work has three layered feed forward architecture. The model was run on MATLAB commercial software dealing with trial and error procedure.

A regression curve is plotted between actual and predicted depth-averaged velocity of testing data which are shown in Figure 12. It can be observed that data are well fitted because a high degree of coefficient of determination R^2 of 0.91. Figure 13 shows the error histogram plot of the model.

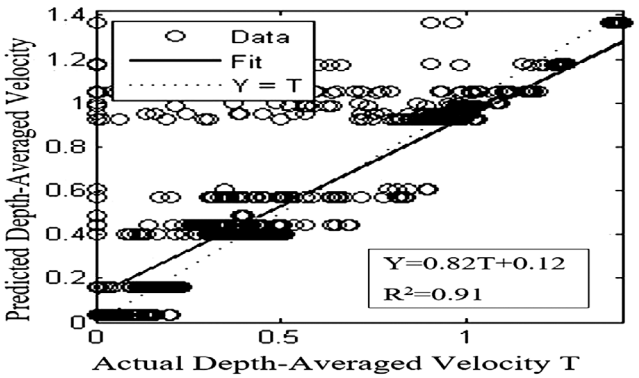

Figure 12. Correlation plot of actual depth-averaged velocity and predicted depth-averaged velocity.

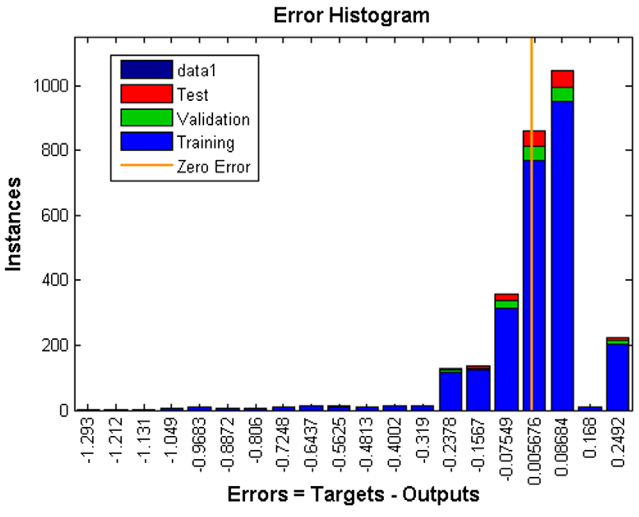

Figure 13. Error histogram.

6. Error analysis

To check the strength of the model, with the result from CES error analyses have been done. Mean Absolute Error (MAE), the Mean Absolute Percentage Error (MAPE), Mean Squared Error (MSE), the Root Mean Squared Error (RMSE) for all the converging compound channels for different geometry and flow conditions have been estimated. Efficiency criterion like R^2, Nash-Sutcliffe efficiency (E) have also been estimated

Table 4. Different error analysis.

	ANN	CES
MSE	0.0004	0.008
RMSE	0.02	0.08
MAE	0.033	0.2
MAPE	3.29	20
E	0.95	0.70
R^2	0.99	0.75

to provide more information on the systematic and dynamic errors present in the model simulation. The definitions of error terms are described below. The detailed results of the error analysis have been presented in Table 4. The expression used to estimate errors in different forms are

(1) Mean Absolute Error (MAE)

The Mean Absolute Error has been evaluated as,

$$\mathrm{MAE} = \frac{1}{n}\sum_{i}^{n}\left|\frac{P_i - O_i}{O_i}\right| \tag{13}$$

where P_i = predicted values, O_i = observed values

(2) Mean Absolute Percentage Error (MAPE)

Mean Absolute Percentage Error also known as Mean absolute Percentage Deviation. It was usually expressed as a percentage, and was defined by the formula:

$$\mathrm{MAPE} = \frac{1}{n}\sum_{i}^{n}\left|\frac{O_i - P_i}{O_i}\right| \tag{14}$$

(3) Mean Squared Error (MSE)

Mean Squared Error measures the average of the squares of the errors. It is computed as:

$$\mathrm{MSE} = \frac{1}{n}\sum_{i}^{n}\left(P_i - O_i\right)^2 \tag{15}$$

(4) Root Mean Squared Error (RMSE)

Root Mean Squared Error or Root Mean Squared Deviation is also a measure of the differences between values predicted by model or an estimator and the actually observed values. These individual differences are called as residuals when the calculations are performed over the data sample that is used for estimation, and are known as estimation errors when computed out of the sample. The RMSE is defined as,

$$\mathrm{RMSE} = \sqrt{\mathrm{MSE}} \tag{16}$$

(5) Coefficient of correlation R^2

The coefficient of correlation R^2 can be expressed as the squared ratio between the covariance and the multiplied standard deviations of the observed and predicted values. The range of R^2 lies between 0 and 1.0 which describes how much of the observed dispersion is explained by the prediction. A value of zero means no correlation at all whereas a value of 1 means that the dispersion of the prediction is equal to that of the observation.

(6) Nash–Sutcliffe efficiency E

The efficiency E proposed by Nash and Sutcliffe (1970) is defined as:

$$E = 1 - \frac{\sum_{i}^{n}\left(O_i - P_i\right)^2}{\sum_{i}^{n}\left(O_i - \bar{O}\right)^2} \tag{17}$$

Where $\bar{O}$ represents the mean of calculated values. The range of E lies between 1.0 (perfect fit) and $-\infty$.

7. Conclusions

In this study, numerical analysis for prediction of depth-averaged velocity for compound channel with converging flood plain using ANN was presented. In the first part of the paper, a 3D model of turbulence stream pattern in compound channel with converging flood plains were simulated using a numerical model. Using experimental and numerical analysis, variation of velocity components for compound channel with converging flood plains were studied. The other part of this paper dealt with the prediction of the depth-averaged velocity field using ANN. In the prediction part, at first, BPNN neural networks were created. Then coordinates of different points were applied as input values and corresponding velocity as target outputs to create ANNs. Some experimental data were used to train the ANNs and some experimental data were used to test the trained ANNs based on BPNN techniques. Finally, the results of ANN and CES methods were compared in sections. The main conclusions of this study are as follows:

(1) ANSYS shows a good conformity with the experimental results for predicting the depth-averaged velocity.
(2) Results of numerical model showed that the CES was not in good agreement with experimental results for predicting the depth-averaged velocity. Since the one-dimensional model of CES is incompetent when it comes to more realistic results.
(3) Results of ANNs that had been trained using BPNN indicated that the velocity field was predicted with good approximation in both training and testing methods and it was concluded that the proposed procedures are useful for velocity prediction in non-prismatic compound channel with converging flood plain.
(4) Different error analyses are performed to test the strength of the present ANN model. It is found that MAE as 0.033,MAPE as 3.29 which less than 10%,MSE as 0.0004, RMSE as 0.02, E as 0.0.95, R^2 as 0.99 where as CES gave MAE as 0.2, MAPE as 20, MSE as 0.008, RMSE as 0.08, E as 0.75, R^2 as 0.7.
(5) The main advantage of ANN is the prediction of the approximate velocity at points where experimental data are not available. Also the presented procedure can be used in predicting some other properties of flow besides velocity, such as shear stresses, depth of water or variations of channel bed. In addition, the presented procedure can be applied to prediction and analysis of the properties of other types of channels and other structures across the flow.

Acknowledgments

The author wish to acknowledge the support from the Institute and the UGC UKIERI Research project (ref no UGC-2013 14/017) by the second authors for carrying out the research work in the Hydraulics Laboratory at National Institute of Technology, Rourkela.

Disclosure statement

No potential conflict of interest was reported by the authors.

References

Abdeen, M.A.M. (2008). "Predicting the impact of vegetations in open channels with different distributaries' operations on water surface profile using artificial neural networks." *J. Mech. Sci. Technol.*, 22, 1830–1842.

Bhattacharya, B., and Solomatine, D.P. (2005). "Neural networks and M5 model trees in modelling water level–discharge relationship." *Neurocomputing*, 63, 381–396.

Bilgil, A., and Altun, H. (2008). "Investigation of flow resistance in smooth open channels using artificial neural networks." *Flow Measure. Instrument.*, 19, 404–408.

Cater, J.E., and Williams, J.J. (2008). "Large eddy simulation of a long asymmetric compound open channel." *J. Hydraul. Res.*, 46 (4), 445–453.

Cheng, C.T., Ou, C.P., and Chau, K.W. (2002). "Combining a fuzzy optimal model with agenetic algorithm to solve multi-objective rainfall–runoff model calibration." *J. Hydrol.*, 268, 72–86.

Cokljat, D. (1993). "Turbulence models for non-circular ducts and channels." PhD thesis, City University London, London.

Ervine, D.A., Koopaei, K.B., and Sellin, R.H.J. (2000). "Two dimensional solution for straight and meandering over-bank flows." *J. Hydraul. Eng., ASCE*, 126(9), 653–669.

Filonovich, M. (2015). "Numerical modelling of compound channel flow."

Gandhi, B.K., Verma, H.K., Abraham, B. (2010). "Investigation of flow profile in open channels using CFD." 8th Int. Conf. on Hydraulic Efficiency Measurement, 243–251.

Ghosh, S., and Jena, S.B. (1971). "Boundary shear stress distribution in open channel compound." *Proc. Inst. Civil Eng.*, 49, 417–430.

Ghosh, S., Pratihar, D.K., Maiti, B., and Das, P.K. (2010). "Optimum design of a two step planar diffuser: a hybrid approach." *Eng. Appl. Comput. Fluid Mech.*, 4(3), 415–424.

Hirt, C.W., and Nichols, B.D. (1981). "Volume of fluid (VOF) method for the dynamics of free boundaries." *J. comp. phys.*, 39(1), 201–225.

Hodges, B.R., and Street, R.L. (1999). "On simulation of turbulent nonlinear free-surface flows." *J. Comp. Phys.*, 151, 425–457.

Hodskinson, A. (1996). "Computational fluid dynamics as a tool for investigating separated flow in river bends." *Earth Surface Processes Landforms*, 21, 993–1000.

Hodskinson, A., and Ferguson, R. (1998). "Numerical modelling of separated flow in river bends: model testing and experimental investigation of geometric controls on the extent of flow separation at the concave bank." *Hydrol. Processes*, 12, 1323–1338.

Van Hooff, T., and Blocken, B. (2010). "Coupled urban wind flow and indoor natural ventilation modelling on a high-resolution grid: A case study for the Amsterdam ArenA stadium." *Environ. Model. Software*, 25(1), 51–65.

Hsu, T.Y., Grega, L.M., Leighton, R.I., and Wei, T. (2000). "Turbulent kinetic energy transport in a corner formed by a solid wall and a free surface." *J. Fluid Mech.*, 410, 343–366.

Issa, R.I. (1986). "Solution of the implicitly discretised fluid flow equations by operator-splitting." *J. Comput. Phys.*, 62(1), 40–65.

Jain, S.K. (2008). "Development of integrated discharge and sediment rating relation using a compound neural network." *J. Hydrol. Eng.*, 13, 124–131.

Kara, S., Stoesser, T., and Sturm, T.W. (2012). "Turbulence statistics in compound channels with deep and shallow overbank flows." *J. Hydraul. Res.*, 50(5), 482–493.

Kawahara, Y., & Tamai, N. (1988). Numerical calculation of turbulent flows in compound channels with an algebraic stress turbulence model. In: *Proc. 3rd Symp. Refined Flow Modeling and Turbulence Measurements*, Tokyo, Japan, pp. 9–17.

Khatua, K.K., and Patra, K.C. (2008). "Boundary shear stress distribution in compound open channel flow." *J. Hydraul. Eng. ISH*, 12(3), 39–55.

Khatua, K.K., Patra, K.C., and Mohanty, P.K. (2012). "Stage discharge prediction for straight and smooth compound channels with wide floodplains." *J. Hydraul. Eng., ASCE*, 138(1), 93–99.

Knight, D.W., Wright, N.G., and Morvan, H.P. (2005). "Guidelines for applying commercial CFD software to open channel flow." Report based on the research work conducted under EPSRC Grants GR/R43716/01 and GR/R43723/01.

Krishnappan, B.G., and Lau, Y.L. (1986). "Turbulence modelling of flood plain flows." *J. Hydraulic Eng., ASCE*, 112(4), 251–266.

Lane, S.N., Bradbrook, K.F., Richards, K.S., Biron, P.A., and Roy, A.G. (1999). "The application of computational fluid dynamics to natural river channels: three-dimensional versus two dimensional approaches." *Geomorphology*, 29, 1–20.

Lin, J.Y., Cheng, C.T., and Chau, K.W. (2006). "Using support vector machines for long-term discharge prediction." *Hydrol. Sci. J.*, 51(4), 599–612.

Menter, F.R. (1994). "Two-equation eddy-viscosity turbulence models for engineering applications." *AIAA*, 32(8), 1598–1605.

Moharana, S., and Khatua, K.K. (2014). "Prediction of roughness coefficient of a meandering open channel flow using Neuro-Fuzzy Inference System." *Measure.*, 51, 112–123.

Morvan, H.P. (2001). "Three-dimensional simulation of river flood flows." PhD thesis, University of Glasgow, Glasgow.

Muzzammil, M. (2008). "Application of neural networks to scour depth prediction at the bridge abutments." *Eng. Appl. Comput. Fluid Mech.*, 2(1), 30–40.

Myers, W.R.C., and Elsawy, E. M. (1975). "Boundary shear in channel with floodplain." *J. Hydraul. Eng., ASCE*, 101(HY7), 933–946.

Nakayama, A., and Yokojima, S. (2002). "LES of open-channel flow with free-surface fluctuations." *Proc. Hydraul. Eng. JSCE.*, 46, 373–378.

Nash, J.E., and Sutcliffe, J.V. (1970). "River flow forecasting through conceptual models, Part I. A discussion of principles." *J. Hydrol.*, 10, 282–290.

Pan, Y., and Banerjee, S. (1995). "Numerical investigation of free-surface turbulence in open-channel flows." *Phys. Fluids*, 113(7), 1649–1664.

Rezaei, B. (2006). "Overbank flow in compound channels with prismatic and non-prismatic floodplains." PhD thesis, Univ. of Birmingham, UK.

Rhodes, D.G., and Knight, D.W. (1994). "Distribution of shear force on boundary of smooth rectangular duct." *J. Hydral. Engg.*, 120-7, 787–807.

Safikhani, H., Khalkhali, A., and Farajpoor, M. (2011). "Pareto based multi-objective optimization of centrifugal pumps using cfd, neural networks and genetic algorithms." *Eng. Appl. Comput. Fluid Mech.*, 5(1), 37–48.

Sahu, M., Khatua, K.K., and Mahapatra, S.S. (2011). "A neural network approach for prediction of discharge in straight compound open channel flow." *Flow Measure. Instrument.*, 22, 438–446.

Shiono, K., and Knight, D.W. (1988). "Refined modelling and turbulance measurements." Proc. of 3rd Int. Symp., IAHR, Tokyo, Japan, July 26–28.

Shiono, K., and Knight, D.W. (1991). "Turbulent open-channel flows with variable depth across the channel." *J. Fluid Mech.*, 222, 617–646.

Sinha, S.K., Sotiropoulos, F., and Odgaard, A.J. (1998). "Three-dimensional numerical model for flow through natural rivers." *J. Hydraul. Eng.*, 124(1), 13–24.

Spalding, D.B. (1980). *Genmix: a general computer program for two-dimensional parabolic phenomena*, Pergamon Press, Oxford.

Speziale, C.G., Sarkar, S., and Gatski, T.B. (1991). "Modelling the pressure-strain correlation of turbulence: an invariant dynamical systems approach." *J. Fluid Mech.*, 227, 245–272.

Thomas, T.G., and Williams, J.J.R. (1995a). "Large eddy simulation of turbulent flow in an asymmetric compound channel." *J. Hydraul. Res.*, 33(1), 27–41.

Unal, B., Mamak, M., Seckin, G., and Cobaner, M. (2010). "Comparison of an ANN approach with 1-D and 2-D methods for estimating discharge capacity of straight compound channels." *Adv. Eng. Software*, 41, 120–129.

Wang, W.C., Chau, K.W., Cheng, C.T., and Qiu, L. (2009). "A comparison of performance of several artificial intelligence methods for forecasting monthly discharge time series." *J. Hydrol.*, 374, 294–306.

Wilcox, D.C. (1988). "Reassessment of the scale-determining equation for advanced turbulence models." *AIAA*, 26, 1299–1310.

Wu, C.L., Chau, K.W., and Li, Y.S. (2009). "Predicting monthly streamflow using data-driven models coupled with data-preprocessing techniques." *Water Resources Res.*, 45, 1–23.

Xie, Z., Lin, B., and Falconer, R.A. (2013). "Large-eddy simulation of the turbulent structure in compound open-channel flows." *Adv. Water Resources*, 53, 66–75.

Yuhong, Z., and Wenxin, H. (2009). "Application of artificial neural network to predict the friction factor of open channel flow." *Commun. Nonlinear Sci. Num. Simulation*, 14, 2373–2378.

DIGITALIZATION OF FINANCIAL SERVICES

Mrs. G. Madhavi*

ABSTRACT

Today most of the Consumer Markets are Digitalized, marketers are faced with new challenges and opportunities within this digital era. Digital marketing is the process of utilization of electronic media by the marketers to promote the products or services into the market. The main objective of digital marketing is attracting customers and allowing them to interact with them through digital media. This article focuses on the importance of digitalization of Financial Services. We examine the various Digital strategies available for effective Financial Services. This study has described various forms of digital marketing strategies, its effectiveness and its impact on Financial Service firms. Digital Marketing helps in saving fuel, energy and most importantly time of the customers in a way contributing to the society. Consumers now expect their experience with Financial Services to be just as simple and enjoyable as other high end products or services. Digitalization has raised the bar for brands, but complexity, compliance, and competition present major barriers to Financial Institutions. Evolve your marketing strategy for this digital age.

****

Introduction

The world of digital media is changing at a phenomenal pace. Its constantly evolving technologies, and the way people are using them, are transforming not just how we access our information, but how we interact and communicate with one another on a global scale.

Digitalization is one type of marketing strategy which is being widely used to promote products or services and to reach consumers through digital channels. Digital marketing extends beyond internet marketing including channels that do not require the use of Internet. It includes mobile phones (both SMS and MMS), social media marketing, display advertising, search engine marketing and many other forms of digital media. With the help of digital media, consumers can access information at any time and from any place where they want to.

As we are already aware of how powerful is "Word of Mouth" marketing communication and this takes places very often in the presence of digital media, as consumers do not just rely on what the company says about their brand but also they can see the reviews of the people who have already experienced the particular service, with the help of media, friends, peers etc .This has huge impact on consumers compare to advertising. Main advantage of social media is that it can enable companies to increase reach and reduce costs (Watson et al. 2002; Sheth & Sharma 2005).

McDonald's uses online channel to reinforce brand messages and relationships. They have built online communities for children, such as the Happy Meal website with educative and entertaining games to keep customers always close to themselves (Rowley 2004). Reinartz and Kumar (2003) found that the number of mailing efforts by the company is positively linked with company profitability over time. Digital technologies are no longer the preserve of tech-savvy early adopters, and today ordinary people are integrating them seamlessly

* Assistant Professor, Methodist College of Engineering and Technology, Abids, Hyderabad-01. E-mail: mgattoju@gmail.com

into their everyday lives.

Objectives

- To differentiate between Traditional Marketing and Digital Marketing.
- To study the various modes of digitalization
- To show various advantages to the customers through Digitalization.

Research Methodology

It is a descriptive study in which only secondary data is used for the study. The secondary data is collected from sources like Publications, Websites, Books, and Newspapers.

Strategies of Digitalization

Online Marketing

Internet marketing, or online marketing, refers to advertising and marketing efforts that use the Web and email to drive direct sales via electronic commerce, in addition to sales leads from Web sites or emails. Internet marketing and online advertising efforts are typically used in conjunction with traditional types of advertising such as radio, television, newspapers and magazines.

TRADITIONAL VS DIGITALIZATION	
Traditional Marketing	**Digital Marketing**
Traditional marketing includes print-Newspaper Magazines Journals etc Broadcast –Television Radio, Direct mail, and Telephone.	Digital marketing includes online Advertising, Email marketing, Social media, Text messaging, affiliate marketing, Facebook, Twitter, Mobile App search engine optimization, pay per click
One Way Communication – No immediate Feedback	Two Way Communication – Immediate Feedback
Demand forecast may not be accurate	Demand forecast accurate to a greater extent.
Advertising campaigns are planned for a long period of time	Advertising campaigns are planned for short period of time
Expensive and time-consuming process	Reasonably cheap and quick way to promote the products &Services
Not so Flexible - One campaign prevails for a long time	Flexible - Campaigns can be easily changed with ease and innovations can be introduced within any campaign
Limited reach to the customer due to limited number of customer technology	Wider reach to the customer because of the use of various modes of customers technology
Round the Clock availability is not possible	Available round the Clock
No ability to go viral	Ability to go viral
Responses can only occur during work hours	Response or feedback can occur anytime

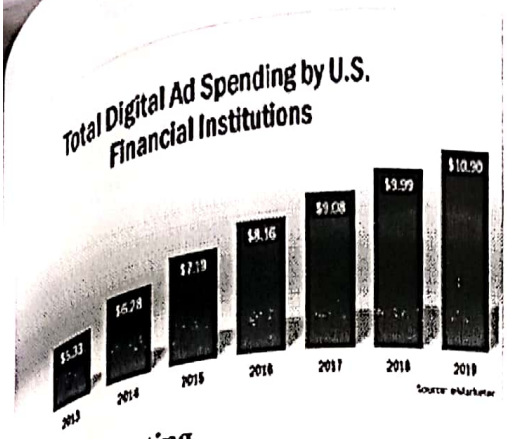

Mobile Marketing

Mobile marketing consists of ads that appear on mobile smart phones, tablets, or other mobile devices. Mobile marketing ad formats, customization, and styles can vary, as many social media platforms, websites, and mobile apps offer their own unique and tailored mobile ad options. Business needs a mobile marketing strategy for the same reason as we need a computer and wi-fi access – this is the age in which we live. If we walk around any major city and we will find majority of people faces glued to their smart phone screens. According to recent reports, 40% of users' internet time is spent on mobile devices. Mobile marketing is crucial for connecting with consumers on the go, engaging them from offline to online touch points as part of an integrated marketing strategy.

Types of Mobile Marketing Strategies

Google AdMob help advertisers create mobile ads that appear within third-party mobile apps.

Facebook also allows advertisers to create ads that are integrated into Facebook's mobile app. Facebook's mobile Promoted Post ads integrate so seamlessly with Facebook's news feed that users often don't realize they're looking at ads.

In-game mobile marketing: In-game mobile marketing refers to mobile ads that appear within mobile games In-game ads can appear as bannerpop-ups, full-page image ads or even video ads that appear between loading screens.QR codes: QR codes are scanned by users, who are then taken to a specific webpageLocation-based marketing: Location-based mobile ads are ads that appear on mobile devices based upon a user's location relative to a specific area or businessMobile search ads: These are basic Google search ads built for mobile, often featuring extra add-on extensions like click-to-call or maps.Mobile image ads: Image-based ads designed to appear on mobile devices.SMS: SMS marketing involves capturing a user's phone number and sending them text offers.

Email Marketing

It involves both advertising and promotional marketing efforts via e-mail messages to current and prospective customers. Financial Institutions communicate with their customers through this media. All the details and updates are communicated to the customers through Email from time to time. E-statements and E-certificates are also sent thorough this mode. Time and Energy saving. Environment friendly as it paper less.

Search Engine Optimisation

As a financial institution, your goal should be to be on the first page of Google search results when someone searches for banks or any type of Financial requirement. To get a website to rank highly on search engines, we need to communicate that our website provides value for customers. The language we use in our content should match the vocabulary employed by our consumer base.

Company's Website

Most millennials will begin a purchase decision with a web search. If people land on a website which is difficult to navigate, then they have a significantly harder time in becoming a customer. Website should be designed in such a way that it is an extension of sales team. It will often serve as the first point of contact between customers interested in your products and services and your brand. It is key to landing new customers.

Social Media

Social media marketing refers to the process

Banks	No of Channels	Social Grades
HDFC BANK	8	3.06
ICICI BANK	8	2.81
AXIS BANK	5	2.28
CITI BANK	5	2.02
YES BANK	6	1.97
KOTAK MAHINDRA	5	1.62
STANDARD CHARETERED	4	1.8
INDUS IND BANK	4	1.24
ING VYSYA BANK	3	0.79
SOUTH INDIAN BANK	3	0.72
KARNATAKA BANK	3	0.57
BANK OF PUNJAB	2	0.36

The Social Media Grades shows how active the banks are in the social media space

Calculated on a scale of 5, the Interactivity level of the banks in Facebook, Twitter, LinkedIn, YouTube and Blogs are taken into consideration

No of channels represents the bank's presence in any social networking sites

Social Media Grades for the Private Sector Banks in India

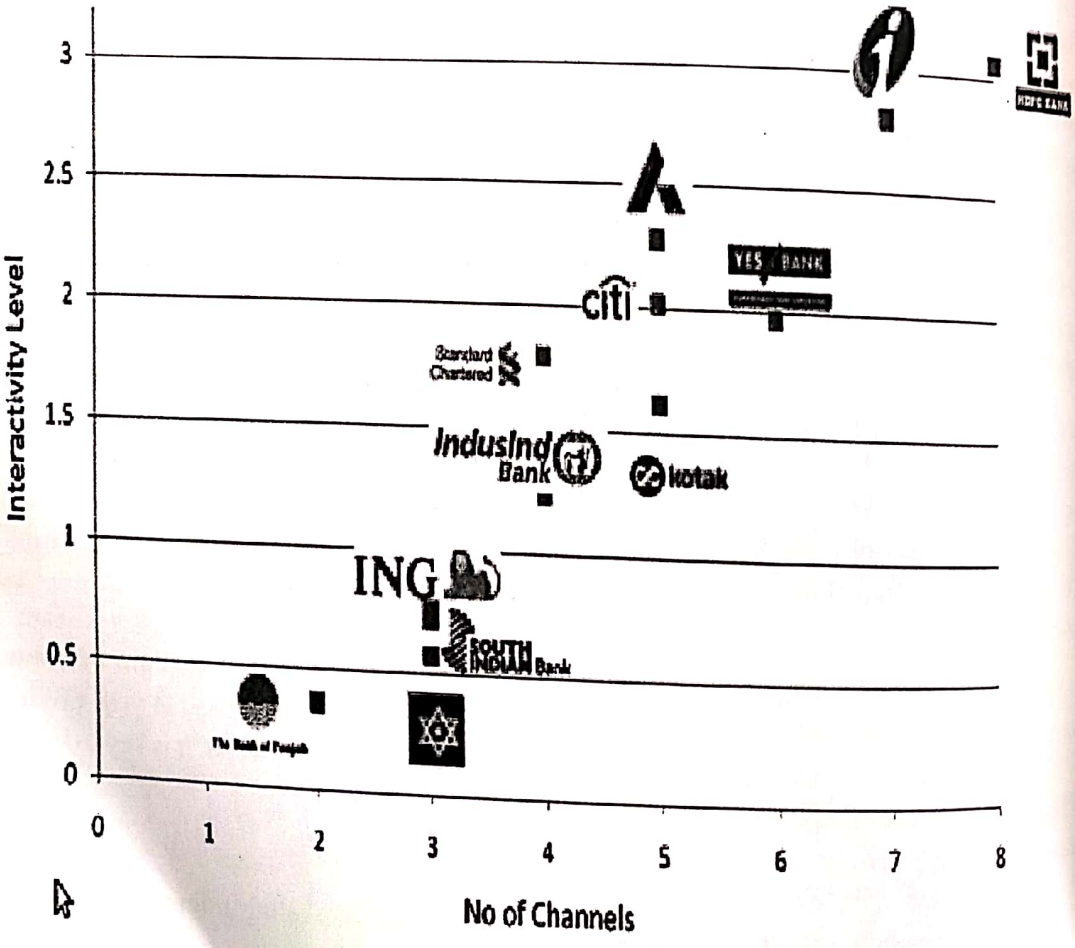

of gaining traffic or attention through social media sites. Such as Facebook, LinkedIn, Google+, YouTube, Del.icio.us, Twitter, Digg, blogs and other sites that have content based on user participation and user-generated content (UGC).It is computer based tool that allows people to create, exchange ideas, information and pictures about the company's offerings. Company can promote events concerning about products and services, explore new opportunities.

Twitter is all about discovering what's going on right now. As Bain notes, many users return to Twitter's homepage a few times per day just to see what's trending. Promoted Trends leverage that phenomenon by giving advertisers a premium position on the page.

Content Marketing

In Financial services Content Marketing plays a vital role. Content marketing is a strategic marketing approach focused on creating and distributing valuable, relevant, and consistent content to attract and retain a clearly-defined audience — and, ultimately, to drive profitable customer action. Content is key to driving inbound traffic and leads.

Advantages of Digitalization

- Purchase and Selling of Shares online
- Making Fixed Deposit sitting at home
- Transferring Funds online and through mobile as well.
- All banking transactions are click away
- Increased use if Digital Wallets
- Making payments and getting updates at our comfort
- Cashless transactions
- Paperless transactions at Stock Markets
- Getting personal with more personalization
- Staying updated with any updates through emails by the company
- Scope for online query resolution
- Big data will help financial marketers turn analytics into profit, minimizing costs, mitigating risks and recognizing Opportunities.

Conclusion

Financial institutions need to grow beyond old forms of advertising, such as TV or newspaper advertisements. Customers are online, and banks need be there to engage them and build the relationships that lead to brand loyalty and growth. Digital Marketing has no boundaries. Its very Cost effective. Companies should create innovative customer experiences and specific strategies of media to find the best path for gearing up Digitalization.

References

1. Digital Marketing - Damian Ryan and Calvin Jones
2. Digital Marketing -Godfery Parkin
3. http://www.digitalvidya.com/blog/digital-marketing-for-finance-industry/
4. http://contentmarketinginstitute.com/what-is-content-marketing/
5. http://www.webopedia.com/TERM/D/digital_advertising.html

ISH Journal of Hydraulic Engineering

ISSN: 0971-5010 (Print) 2164-3040 (Online) Journal homepage: http://www.tandfonline.com/loi/tish20

Flow resistance in gravel bed open channel flows case: intense transport condition

S. Banerjee, B. Naik, P. Singh & K. K. Khatua

To cite this article: S. Banerjee, B. Naik, P. Singh & K. K. Khatua (2018): Flow resistance in gravel bed open channel flows case: intense transport condition, ISH Journal of Hydraulic Engineering, DOI: 10.1080/09715010.2017.1422189

To link to this article: https://doi.org/10.1080/09715010.2017.1422189

Published online: 12 Jan 2018.

ISH JOURNAL OF HYDRAULIC ENGINEERING, 2018
https://doi.org/10.1080/09715010.2017.1422189

Flow resistance in gravel bed open channel flows case: intense transport condition

S. Banerjee, B. Naik, P. Singh and K. K. Khatua

Department of Civil Engineering, National Institute of Technology Rourkela, Rourkela, India

ABSTRACT

Gravel bed can be categorised into three bed load conditions, i.e. no load, moderate and intense. An experimental investigation was carried out in an open channel flow with gravel bed surface of grain size of D_{50} values 6.5 mm intense load conditions. The investigation of the roughness characteristics of gravel bed open channel flows under intense load conditions over various discharges and flow depths are presented. Variation of friction factor for the roughness conditions for different flow depths is estimated. The intensity of the bed load is calculated with the help of sediment transport rate. The bed load transport rate for the intense load conditions is also determined from experimentation on gravel beds of 6.5 mm gravel size for different flow depths. Using the data-set of other researchers and present experimental data, a new model as a function of intensity of the bed load transport with respect to Shield's parameter is formulated. The modified model gives satisfactory results as compared to previous works, which is displayed through error analysis.

ARTICLE HISTORY
Received 18 January 2017
Accepted 23 December 2017

KEYWORDS
Gravel bed open channel; Darcy–Weisbach friction factor; bed load; sediment transport; Shield's parameter; boundary shear stress

1. Introduction

Sediments can be identified as a fragmentary part of the earth material eroded, transported and deposited elsewhere naturally by causes like water and air. Sediment process is a natural occurring process and hence control over it is quiet convoluted. The effects of bed load on the estimation of friction factor *f*, is possible because of low sediment transport rates (Hey 1979; Van Rijn 1984; Whiting and Dietrich 1990). The bed load is commonly taken into account only in terms of the additional resistance caused by bed forms in the case of sandy rivers (Einstein and Barbarossa 1951; Van Rijn 1984; Wu and Wang 1999). Yet evidence does exist from earlier studies that bed load may have, at least under some conditions, a substantial impact on the friction factor. Long ago, proposed correction factor to take into account such effects including flatbed problems (Wong and Parker 2006). By comparing resistance produced by flow over a mobile bed, Bathurst et al. (1982) described a sharp increase in flow resistance with a slope (varying from 3 to 9%) as a direct consequence of the bed load concentration. Wiberg and Rubin (1989) observed that in upper plane bed conditions, the friction factor associated with sediment transport could reach much higher value than those measured with clear water flows. More generally, it is largely accepted that the introduction of suspended sediment into a clear flow can either amplify or dampen turbulence depending on the relative magnitude of flow and sediment transport variables (Carbonneau and Bergeron 2000). It is only in the last few decades researchers have taken a clear interest in the effects of bed load on the estimation of friction factor.

All experimental procedures have compared the resistance of a clear water flow with that caused by the injection of sediments. Injection of sediment into a clear water flow increases the resistance gradually with the quantity injected until it attains a plateau when the sediment rate is close to equilibrium conditions (Bergeron and Carbonneau 1999; Campbell et al. 2005; Carbonneau and Bergeron 2000; Mahdavi and Omid 2004; Omid et al. 2003). The effect of bedload on the friction factor in equilibrium flow conditions has received only very little attention in the literature. A few studies (Song et al. 1998) have shown that under such conditions the friction factor increases with the sediment concentration. A step has been taken to study experimentally the friction factor and intensity of bed load in a gravel bed carried by a trapezoidal channel for D_{50} sediment diameters of 6.5 mm.

2. Previous investigations

The most widely used flow resistance models (Manning, Chezy and Darcy–Weisbach equation) shows the relation between the linear energy losses to the mean flow velocity. All these models are semi-empirical and validation of these are done on experimental or field data. Consequently, literature had already proposed a wide range of calibration coefficients.

It was observed that bed load has a significant relation over the large increment in resistance in terms of friction factor *f*. Observations suggest that to properly model flow resistance in a gravel bed channel for a wide range of slopes and relative depths, it is required to identify three flow regimes: no, low and high sediment transport.

In this present study, a high/intense load is considered, which is suggesting high sediment transport flows. These transport flow condition can be characterised by a resistance coefficient *f* that decreases as the relative depth decreases.

CONTACT P. Singh prateek.k.singh1992@gmail.com

We have seen that for a uniform flow in open channel systems, the friction factor f can be expressed by Darcy–Weisbach relation given below:

$$\sqrt{\frac{8}{f}} = \frac{u}{\sqrt{gRS}} = \frac{u}{u*} \tag{1}$$

For rough flows, the friction coefficient f is not related on the basis of Reynolds number and a linear relation is usually expressed between $(8/f)^{1/2}$ and corresponding $\log(R/D)$ values. The friction factor f is reported in the Darcy form of $(8/f)^{1/2}$.

With the help of the experimental data of this present work, a simple graphical representation has been made between $(8/f)^{1/2}$ and relative depth, R/D Figure 2.

For a two-dimensional turbulent flow for the condition of Roughness Reynolds number, R_e^* is greater than 70, Keulegan (1938) had expressed u/u^* by integrating the formerly given logarithmic velocity distribution by Karman–Prandtl in (Equation 2):

$$\frac{u(z)}{u*} = \frac{1}{k} ln \frac{z}{z_0} \tag{2}$$

where u is channel velocity, u^* is the shear velocity, k is von Karman coefficient, z is the height above the bed and z_0 is the height where velocity is zero according to the law of the wall.

A good approximation has been obtained by taking over entire flow depth assuming logarithmic profile (Cardoso et al. 1989; Nikora and Smart 1997; Smart 1999; Song et al. 1995) and that $R >> z_o$ (where velocity tends to zero). Smart et al. (2002) reported that until the relative depth R/D was higher than 1, $(8/f)^{1/2}$ can be expressed as in Equation (3) (for $k = 0.4$):

$$\sqrt{\frac{8}{f}} = \frac{U}{u^*} = \frac{1}{k}\left[\left(\frac{R}{R - z_o}\right)\ln\left(\frac{R}{z_o}\right) - 1\right] \approx 5.75 \log \frac{0.368R}{z_o} \tag{3}$$

Nikuradse (1933) first suggested calculating z_o as a fraction of the bed roughness, K_s by taking $z_o = D/30$. Using this classification, $(8/f)^{1/2}$ can be written as:

$$\sqrt{\frac{8}{f}} = E + 5.75 \log\left(\frac{R}{D}\right) \tag{4}$$

where E is a constant, which is dependent upon the channel cross sections. Keulegan (1938) presented that E may marginally differ with the natures of the canal between 6 for wide rectangular channels and 6.25 for the trapezoidal open channel.

Cao (1985) observed that in a 0.6-m wide flume a 10% of error matches to minimum R/D values of 2, 2.5 and 9 for 44-, 22- and 11-mm grain diameters, respectively. There had been only a few attempts made, essentially on steep slopes, to amend flow resistance laws by adding slope as a parameter. Moreover, this was usually done by a general curve fitting processes without any physical consideration of the effects of slope, even if discussions regarding slope-induced additional resistance through surface instabilities and waves at high Froude numbers still exists. From this point of view, introducing a parameter like a slope, which is responsible for the incipient motion of sediments, is a new approach. The semi-logarithmic model proposed by Cao et al. (2006) as:

$$\sqrt{\frac{8}{f}} = 3.75 + 5.91 \log\left(\frac{R}{D}\right) \tag{5}$$

The Manning-Strickler equation given is:

$$u = K_s R^{\frac{2}{3}} S_0^{\frac{1}{2}} \tag{6}$$

where K_s is the grain resistance Manning-Strickler coefficient. From the definition of K_s which is:

$$K_s = \frac{21.1}{D^{1/6}} \tag{7}$$

It becomes

$$\sqrt{\frac{8}{f}} = 6.74\left(\frac{R}{D}\right)^{\frac{1}{6}} \tag{8}$$

Recking (2006) observed that for $2 < R/D < 8.6$, the resistance equation could not be fully derivative for flows without sediment transport from the law of the wall. Rather an empirical law was suggested, essentially affecting the slope of the logarithmic law. For significantly higher relative depths, the Keulegan law was effective for flows without sediment transport, which fall within the small-scale roughness series. Thus, the bed roughness was nearly taken as the grain diameter. The semi-logarithmic model proposed by Recking (2006) as:

$$\sqrt{\frac{8}{f}} = 2.5 + 9.5 \log\left(\frac{R}{D}\right) \tag{9}$$

Recking (2006) saw that when flow increases, the value of friction factor, f decreases with respect to relative depth R/D, whatever the slope will be. In his study first, it can be observed that all data chosen as high sediment rate regime were lined up with the sheet flow regime data, which he suggestively named regime 3 and which was similar to sheet flow regime. The model concerned with the intermediate-scale roughness ($R/D < 17$) must be modelled with the slope coefficient of 9.5. The semi-logarithmic model proposed by Recking (2006) as:

$$\sqrt{\frac{8}{f}} = -1 + 9.5 \log\left(\frac{R}{D}\right) \tag{10}$$

Julien (2002) proposed a model for bed load sediment transport rate, $q_b > 0.1$ and which was falling under regime 3,

$$\sqrt{\frac{8}{f}} = 5.75 \log\left(\frac{2R}{D}\right) \tag{11}$$

There were two common methods used towards the theory of bed load transport. One of the most popular method was based on variables such as stream power, shear stress, discharge, velocity. In this method, basic assumption was that until or unless the critical variable exceeds the flow conditions there was no bed load transport occurred and by exceeding the critical variable of the flow condition the bed load transport rate increases too. There were several studies based on this concept, both for natural channels and for flumes, which can be exhibited through number of equations presented below. Dependability for the usage of these equations was on the

assumptions of the existing models. The second method was a probabilistic method (Einstein 1950). A new perception to this method had been offered into bed load transport processes. However, the level of complexity made by this application to natural channels was intricate and challenging (Yang 1996).

The sediment particles on the bed start to transport when incipient motion happened and this was the basic assumption made. The tractive force or bed shear stress acting on the bed was a responsible factor for the transport of bed particles in a stream. Shields (1936) first gave two major parameters to determine the bed load intensity, which is θ and $\theta_{c.}$ The movement of bed particles indicate that the Shield's parameter θ which when exceed the critical value called as θ_c (for regime 2), which is:

$$\theta = \frac{\tau}{(\gamma_s - \gamma)D} \tag{12}$$

$$\theta_c = \frac{\tau_c}{(\gamma_s - \gamma)D} \tag{13}$$

where τ is bed shear stress, D is particle diameter and τ_c is critical bed shear stress

$$\theta_c = \frac{0.273}{1 + 1.2d*} + 0.046\left(1 - 0.576e^{-0.05d*}\right) \tag{14}$$

where d^* is:

$$d_* = D\left[\frac{s-1}{v^2}\right]^{.33} \tag{15}$$

Shields (1936) was the first investigator, who described the critical shear stress as a function of different particles sizes, D (irrespective of uniform or non-uniform shape) which supervises the threshold motion by a uniform flow and expressed as:

$$\frac{q_b \gamma s}{q\gamma S} = 10\,\frac{\tau_0 - \tau_c}{(\gamma_s - \gamma_0)D} \tag{16}$$

The solid discharge was expressed in a non-dimensional form (Einstein 1942) as:

$$\Phi = \frac{q_b}{\sqrt{\left(\frac{\rho_s}{\rho} - 1\right)gD^3}} \tag{17}$$

Following approaches and the developed equations by the previous researchers are given in the Table 1.

3. Experimental set-up

Experiments were conducted under controlled laboratory conditions in the Fluid Mechanics Laboratory of the Civil Engineering Department at the National Institute of Technology, Rourkela, India in order to find out the impact of friction factor, velocity distribution, bed load intensity and boundary shear stress on various hydraulic characteristics of open channel flow. For the study, a straight simple trapezoidal channel in the form of a tilting flume having dimensions of length 10 m, top width 0.9 m, bottom width 0.65 m and depth of 0.125 m is used. The tilting flume is made of a metal frame with glass walls at the test reach. At the starting of the flume after inlet and before the head gate, a baffle wall is fitted for the reducing the turbulence and make a uniform flow throughout the channel section. Head gate reduces the waves if formed in the water body before it passes over the channel and in this way, head gate plays a vital role in maintaining uniform flow. For measuring the bed slope tailgate was fitted at the end of the flume. There was the provision of an over bridge platform in the flume which helps in experimental works. The flume was supported on a hinge at the centre and by hydraulic jack provision flume can be pivoted over the centre in lengthwise direction to provide bed sloping. The plan view of the experimental channel used in the present study is shown in Figure 1. Experiments are conducted in a straight simple trapezoidal channel with uniform cross section built inside a metallic flume for intense load conditions. The whole channel is fabricated using D_{50} value of gravel size 6.5 mm for the intense load condition over bed. The roughness height is found to be 2.5 cm, which is estimated approximately from the number of layer (i.e. four in this case) of gravel, covered one upon another over bed. The slope of the flume is fixed at 0.0025 (0.25%) for all runs. Refer Table 2 for description of the bed load characteristics. Water for the experiment is provided from an overhead tank to which a water level indicator is attached for maintaining constant water level for test run discharge. Two parallel pumps are installed for pumping water from an underground sump to the overhead tank. Water delivers to the stilling chamber from the overhead tank, passing over the experimental channel under gravity and is made to fall into the volumetric tank situated at the end of the flume. From the volumetric tank, water is allowed to flow into an underground sump. The water is recirculated back from the sump.

Main parameters to be measured during the present experiment are discharge, bed slope, depth of flow and the velocity of flow and boundary shear stress. The measurement procedure of these parameters is briefly described as follows. The depth of flow in the channel is measured using a point gauge fixed into the travelling bridge and operated manually. Point velocities are measured using a Micro-Pitot tube of 4.77 mm external diameter with a suitable inclined manometer at a number of locations across the predefined channel section. Guide rails are provided at the top of the experimental flume on which a travelling bridge is moved in the longitudinal direction of the entire experimental channel. The point gauge attached to the travelling bridge can also move in both longitudinal as well as in the transverse direction of the experimental channel. The Micro-Pitot tube is also attached to the bridge on the other side of the point gauge. The Pitot tube is physically rotated normally to the mainstream direction until it gives a maximum deflection of manometer reading.

Table 1. Different approaches for determining bed load intensity for intense load condition used in the present work.

Sl. no.	Approaches	Developed equations
1.	Ashmore (1988)	$\Phi = 3.11(\theta - 0.045)^{1.37}$
2.	Wong and Parker (2006a)	$\phi = 4.93(\theta - 0.047)^{1.6}$
3.	Wong and Parker (2006b)	$\phi = 3.97(\theta - 0.0495)^{3/2}$
4.	Graf and Suszka (1987)	$\phi = 10.4\theta^{2.5}$ when $\theta \geq 0.068$
5.	Recking (2006)	$\phi = 14\theta^{2.45}$ when $0.08 < \theta < 0.25$

4. Model development

The measured values of geometric and hydraulic parameters are mentioned in Table 3 For all the experimental runs, the diameter of gravel was kept constant as 0.0065 m. Moreover, a constant bed slope of the channel (0.25%) maintain the subcritical flow conditions, which was used for all the runs. Total

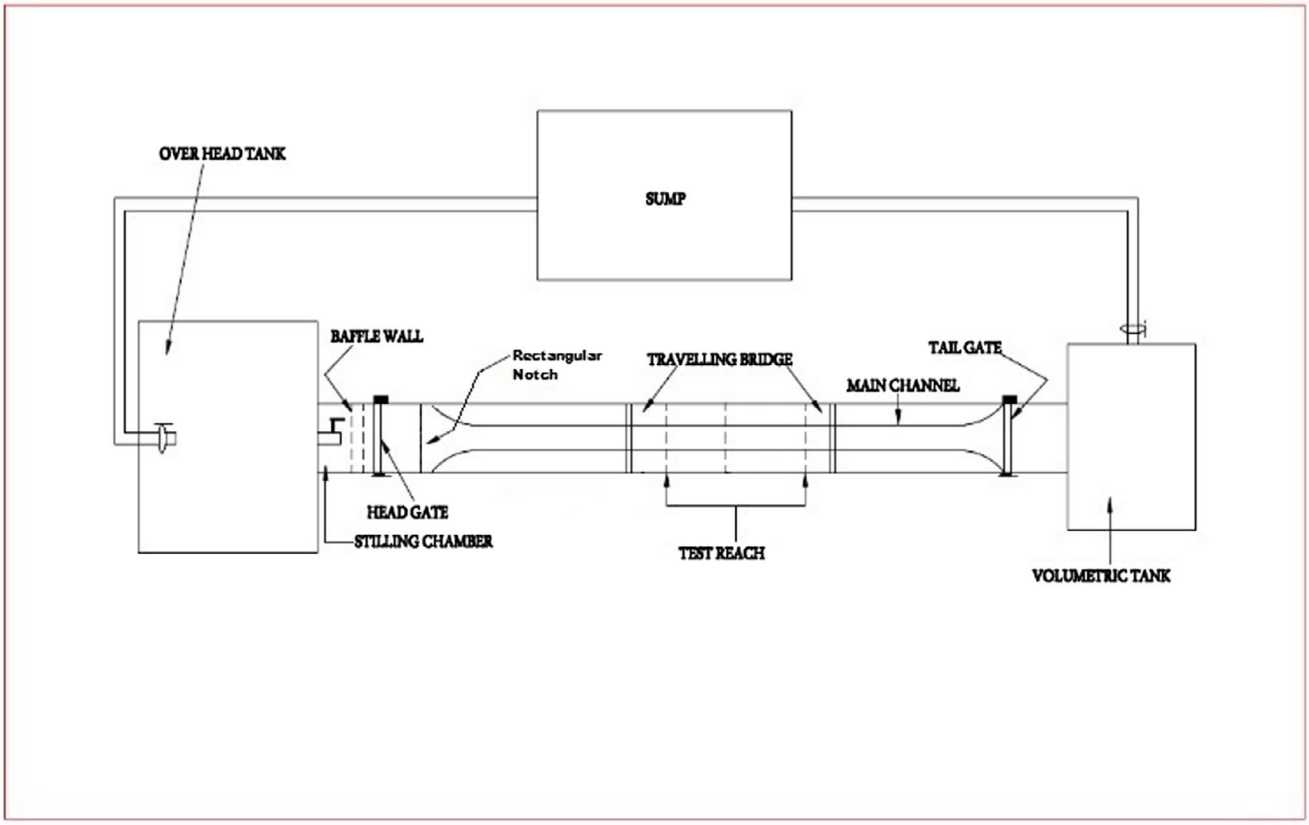

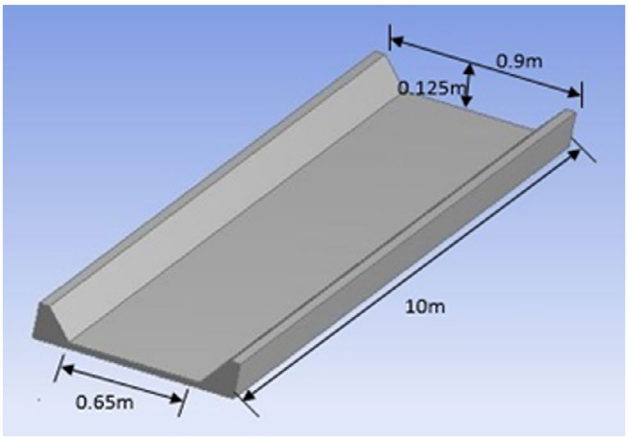

Figure 1. Plan view of the experimental channel and overall view of the flume with experimental set up.

Table 2. Detailed geometrical features for both the load conditions.

Sl no.	Bed loads characteristics	Description
1	Material	Gravel
2	Diameter of gravel (d)	6.5 mm
3	Sediment density (ρ_s)	1220 kg/m^3
4	Height of roughness	0.025 m
5	Distribution pattern	Normal
6	Test reach	6 m

18 experimental runs for uniform flow conditions were taken for the study.

A linear regression model is developed to predict friction factor, f for gravel bed under uniform flow condition with the intense load Figure 2. Recking (2006) developed a model for predicting friction factor, f for the intense load. This model was supposedly valid for relative depth (R/D) ranging from 2 to 16.9.

The present model is also developed for the range of R/D value less than 16.9 with values even lower than 2. The Shield's parameter θ, which is of assistance in finding out the bed load intensity Φ, is also a contributing factor for carrying out the new set of experimentations. Recking used θ values in the range of 0.08–0.25, while the present set of experimental data-sets have θ values less than 0.15. In total, 90 data-sets from the experimental observation, including that of Recking (2006) have been utilised in developing the new model.

Figure 2 illustrates a semi-logarithmic relationship between R/D and friction factor in terms of $(8/f)^{1/2}$ for uniform flow case for intense load condition. The linear regression curve shows a higher value of correlation coefficient, indicating a satisfactory relation between the two.

The linear regression model developed for the determination of friction factor, f is given as:

$$\sqrt{\frac{8}{f}} = 3.55 \ln\left(\frac{R}{D}\right) + 0.2 (R^2 = 0.92) \tag{18}$$

Table 3. Experimental data-set for intense load condition.

Discharge Q (m^3/sec)	Flow depth h (m)	Cross section area A (m^2)	Wetted perimeter P (m)	Hydraulic radius $R = A/P$	Mean channel velocity u (m/sec)	Relative Depth (R/D)	u/u^*
1	2	3	4	5	6	7	8
0.030	0.1004	0.075	0.93	0.080	0.405	12.41	9.11
0.028	0.095	0.071	0.91	0.077	0.39	11.85	9.06
0.026	0.0916	0.068	0.90	0.074	0.38	11.49	8.97
0.023	0.086	0.063	0.89	0.070	0.36	10.90	8.83
0.020	0.08	0.058	0.87	0.066	0.35	10.25	8.71
0.018	0.074	0.0531	0.85	0.062	0.33	9.59	8.59
0.016	0.07	0.050	0.84	0.059	0.32	9.14	8.49
0.014	0.065	0.046	0.83	0.055	0.30	8.57	8.21
0.012	0.06	0.042	0.81	0.051	0.29	7.99	8.13
0.011	0.057	0.040	0.81	0.049	0.27	7.64	7.98
0.009	0.05	0.035	0.79	0.044	0.25	6.80	7.77
0.007	0.046	0.032	0.78	0.041	0.24	6.31	7.62
0.006	0.04	0.027	0.76	0.036	0.22	5.56	7.33
0.005	0.037	0.025	0.75	0.033	0.19	5.11	6.77
0.003	0.031	0.021	0.73	0.029	0.16	4.40	6.07
0.002	0.025	0.017	0.72	0.023	0.14	3.60	5.95
0.001	0.022	0.014	0.71	0.021	0.09	3.19	4.09
0.0006	0.014	0.009	0.68	0.013	0.07	2.07	3.94

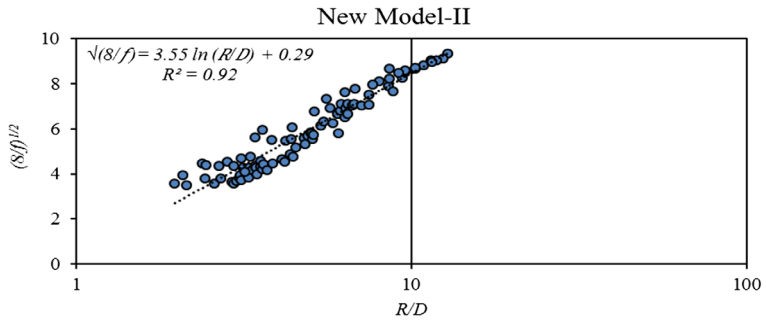

Figure 2. New friction factor model for intense load condition.

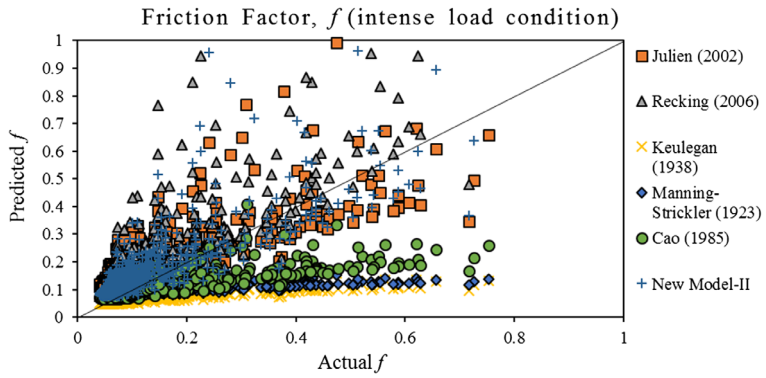

Figure 3. Validation of friction factor model for intense load condition with other author data.

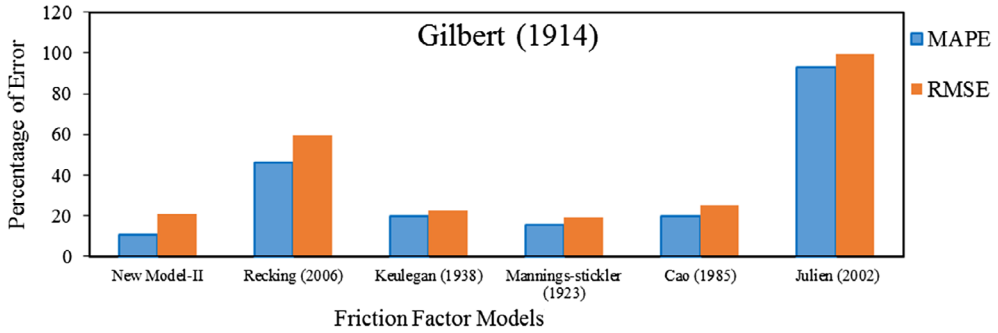

Figure 4a. Error analysis of friction factor model for intense load condition with Gilbert (1914) data.

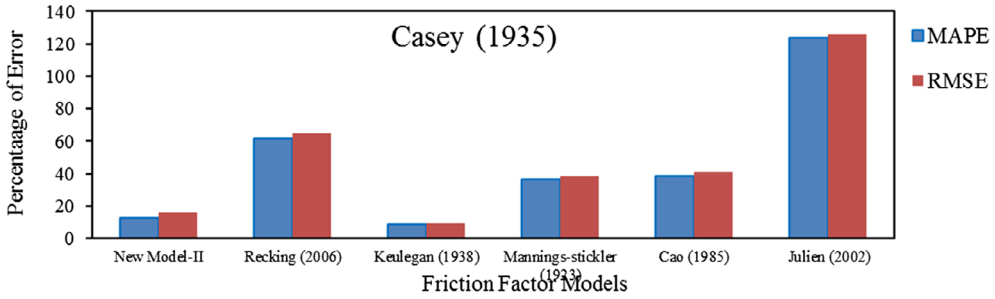

Figure 4b. Error analysis of friction factor model for intense load condition with Casey (1935) data.

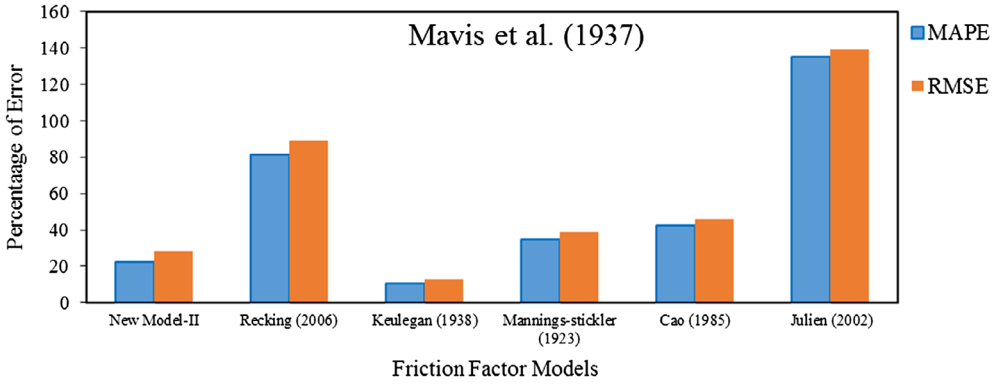

Figure 4c. Error analysis of friction factor model for intense load condition with Mavis et al. (1937) data.

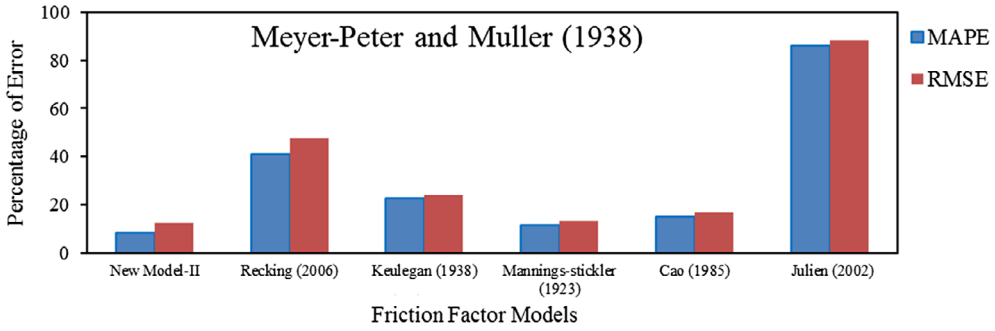

Figure 4d. Error analysis of friction factor model for intense load condition with Meyer-Peter and Muller (1948).

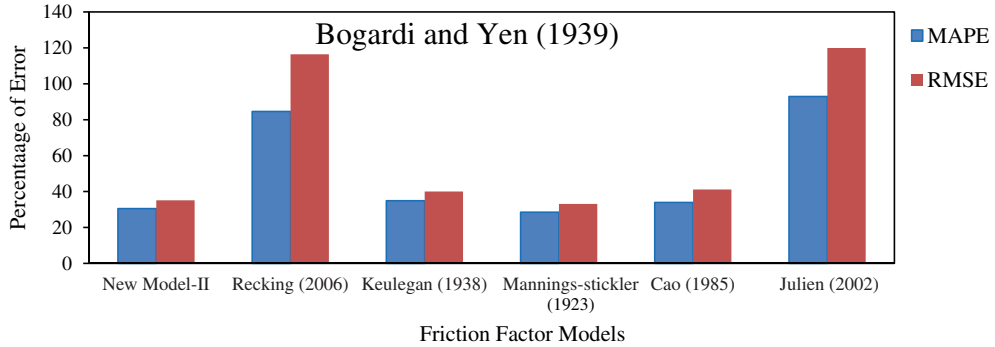

Figure 4e. Error analysis of friction factor model for intense load condition with Bogardi and Yen (1939).

The Equation (18) established above is verified with the data-sets of other investigators such as Bogardi and Yen (1939), Casey (1935), Gilbert (1914), Graf & Suzuka (1987), Ho (1939), Mavis et al. (1937), Paintal (1971), Recking (2006), Rickenman (1990), Smart and Jaeggi (1983) along with the experimental observations of present study. The total number of data-sets being 666 taken with experimentation as well as from other authors.

The functionality of the models suggested by previous researchers has also been evaluated for all of the available data-sets. Figure 3 shows the contrast between different models through predicted values of friction factor versus the

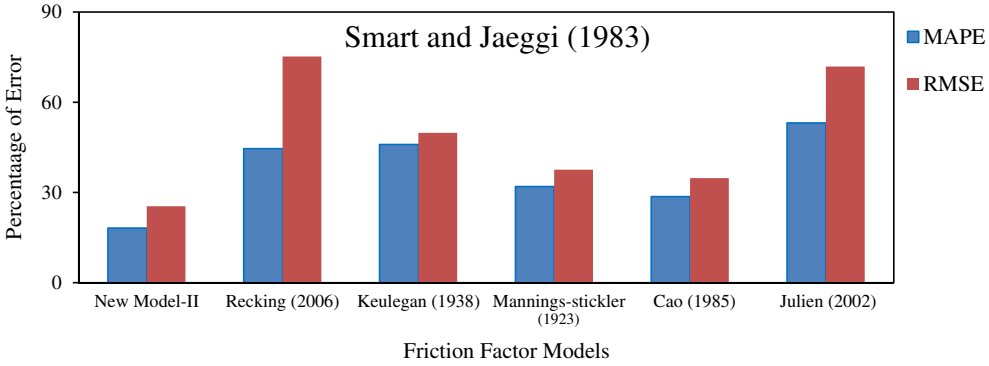

Figure 4f. Error analysis of friction factor model for intense load condition with Ho (1939).

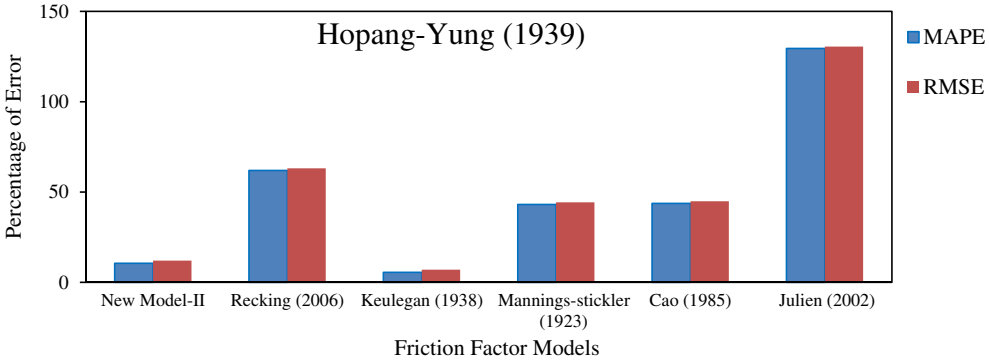

Figure 4g. Error analysis of friction factor model for intense load condition with Smart and Jaeggi (1983) data.

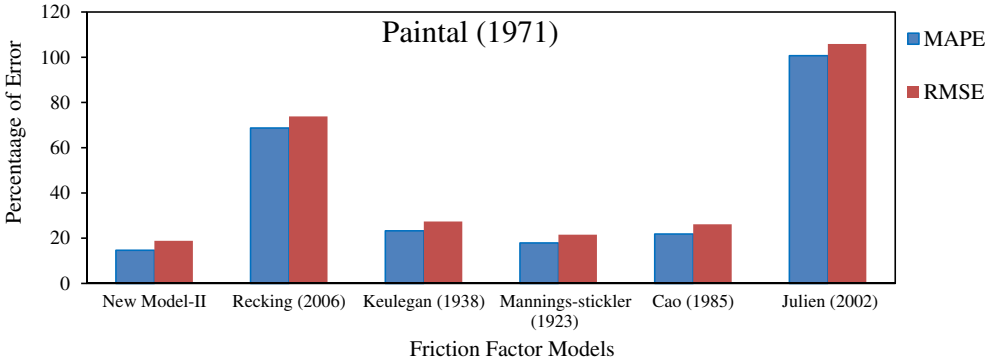

Figure 4h. Error analysis of friction factor model for intense load condition with Paintal (1971).

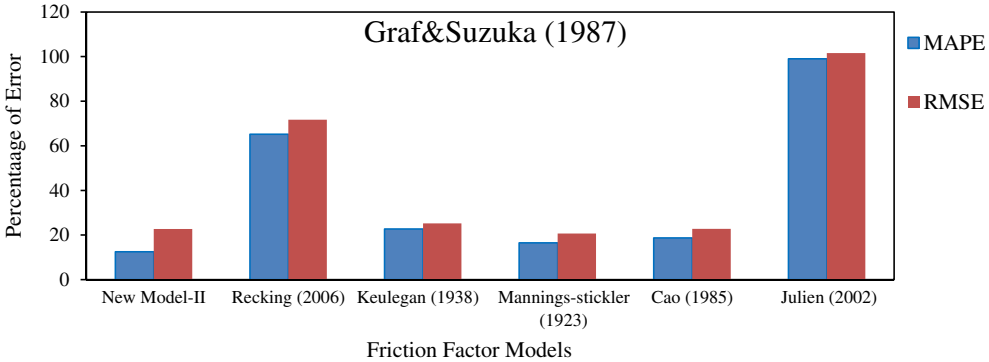

Figure 4i. Error analysis of friction factor model for intense load condition with Graf & Suzuka (1987) data.

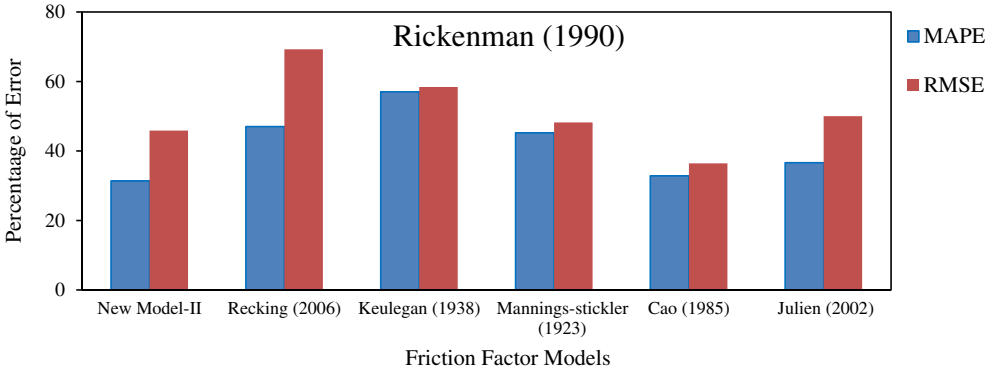

Figure 4j. Error analysis of friction factor model for intense load condition with Rickenman (1990) data.

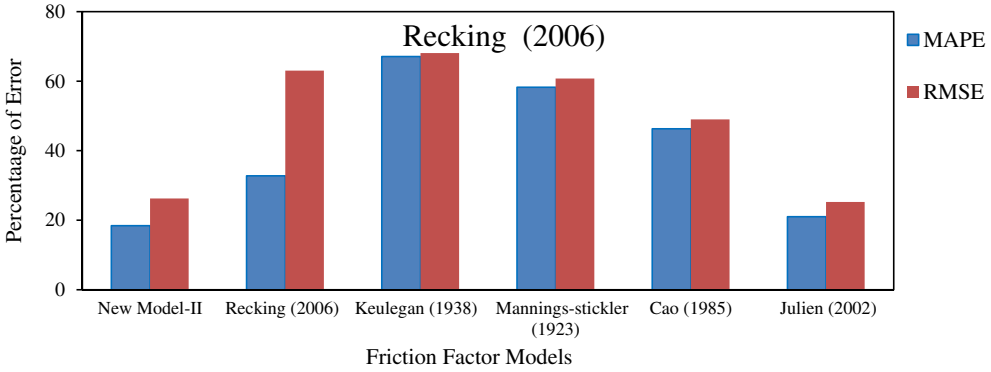

Figure 4k. Error analysis of friction factor model for intense load condition with Recking (2006) data.

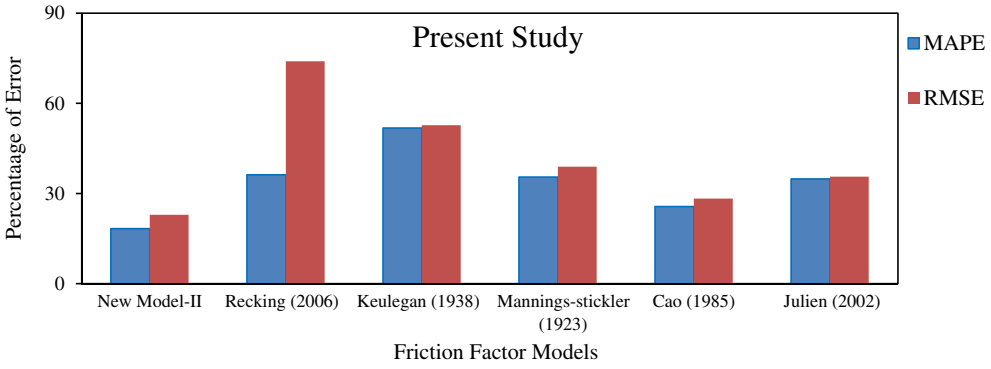

Figure 4l. Error analysis of friction factor model for intense load condition with Present study data.

measured value of friction factors. The present model on whole is observed to provide better predictions.

4.1. Error analysis of friction factor model for intense load flow condition

The error analysis of the different models is carried out for 12 data-sets of intense load conditions given in Figure 4(a)–(l). In almost all the sets of data, the developed expression is observed to provide with lower values of mean absolute percentage error (MAPE) as well as root-mean-square error (RMSE) in comparison to the other models.

The model suggested by the Keulegan (1938) provides significantly lower values of MAPE as well as RMSE for the data-sets of Casey (1935), Mavis et al. (1937), Ho (1939) but concurrently gives higher values for the other data-sets. The above observations are probably because the gravel size used by all the three investigators was less than 6 mm and even the Shield's parameter values less than 0.05. Therefore, in general, the newly developed expression can be accepted to give a satisfactory prediction of friction factor for intense load conditions.

4.2. Bed load intensity for intense load flow condition

In the present study, two parameters are very important, one is Shield's parameter, θ and another was intensity of bed load, Φ. To determine the Shield's parameter, boundary shear stress had to be calculated. Thus to determine the boundary shear stress energy gradient method had been used. In addition, another part of this present study was bed load intensity, which is calculated with the help of bed load sediment transport rate.

All the remaining parameters were same and taken from the stage-discharge data of intense load conditions. For all the experimental runs, the D_{50} diameter of gravel was kept constant

Table 4. Experimental data-set of bed load intensity for intense load condition.

Q (m^3/sec)	Flow depth h (m)	Cross section area A (m^2)	Wetted perimeter P (m)	Hydraulic radius $R = A/P$	Mean channel velocity V (m/sec)	Relative depth (R/D)	u/u^*	Shields parameter θ	Φ^*
1	2	3	4	5	6	7	8	9	10
0.031	0.10	0.075	0.934	0.081	0.405	12.41	9.11	0.141	0.102
0.029	0.095	0.071	0.919	0.078	0.394	11.85	9.06	0.137	0.095
0.026	0.092	0.068	0.910	0.075	0.384	11.50	8.97	0.1347	0.090
0.023	0.086	0.063	0.893	0.071	0.368	10.90	8.84	0.129	0.082
0.021	0.08	0.058	0.876	0.067	0.352	10.25	8.71	0.124	0.074
0.018	0.074	0.054	0.859	0.062	0.336	9.59	8.59	0.119	0.066
0.016	0.07	0.050	0.848	0.059	0.324	9.14	8.49	0.115	0.061
0.014	0.065	0.047	0.834	0.056	0.304	8.57	8.21	0.109	0.052
0.012	0.06	0.043	0.820	0.052	0.290	8.00	8.13	0.104	0.048
0.011	0.057	0.040	0.811	0.050	0.279	7.64	7.98	0.101	0.042

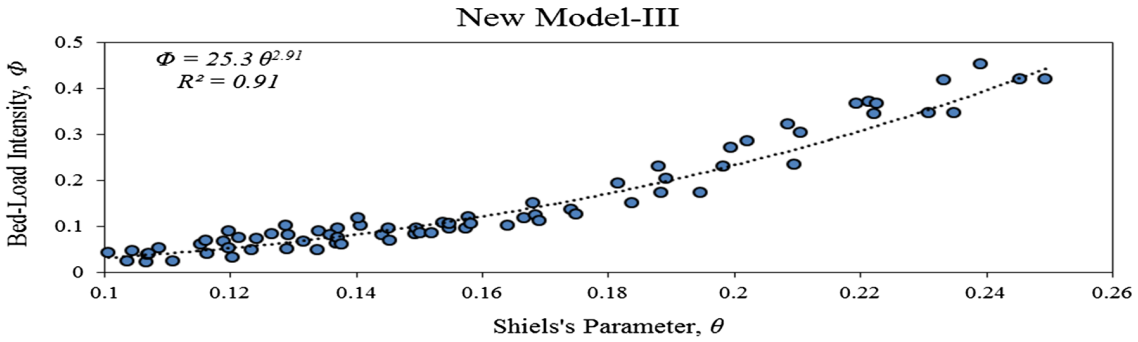

Figure 5. Bed load intensity model for intense load condition.

as 0.0065 m. Moreover, a constant bed slope of the channel (0.25%) was used for all the runs. Total 18 experimental runs for uniform flow conditions were taken for the study. Table 4 shows the experimental results. Graph between bed load intensity and Shield's parameter is plotted which best fit on power law shown in Figure 5. The bed load intensity model by Recking (2006) for intense load condition was apparently valid for relative depth (R/D) ranging from 2 to 16.9, with θ values ranging from 0.08 to 0.25. The present model is developed for the range of R/D values less than 16.9 with data even lower than 2. The Shield's parameter for the present set of experimentation ranges from 0.1 to 0.15. In total, 77 data-sets from the experimental observation, including that of Recking (2006) has been utilised in developing the new model.

$$\Phi = 25.3\,\theta^{2.91}\left(R^2 = 0.91\right) \tag{19}$$

Figure 5 illustrates a graphical relationship between Shield's parameter, θ and Bed Load Intensity, Φ for intense bed load condition. The power law curve shows a higher value of correlation coefficient, indicating a satisfactory relation between the two. The linear regression model developed for the determination of bed load intensity Φ is given as Equation (19). The model developed in the previous section is validated with the data-sets of other researchers such as Wong and Parker (2006), Ashmore (1988), Recking (2006), Graf and Suzuka (1987) etc. along with the present experimental observations. The number of data-sets being 253 in total. The performance of models suggested by previous investigators has also been analysed for the above data-sets.

Figure 6 shows the performance of different models through predicting the bed load intensity, Φ for intense load condition for all the available data-sets. The present model is observed to give better predictions as shown in Figure 7.

4.3. Error analysis of bed load intensity model for intense load flow condition

Bed load intensity is calculated using different models developed by the researchers and the values of MAPE and RMSE

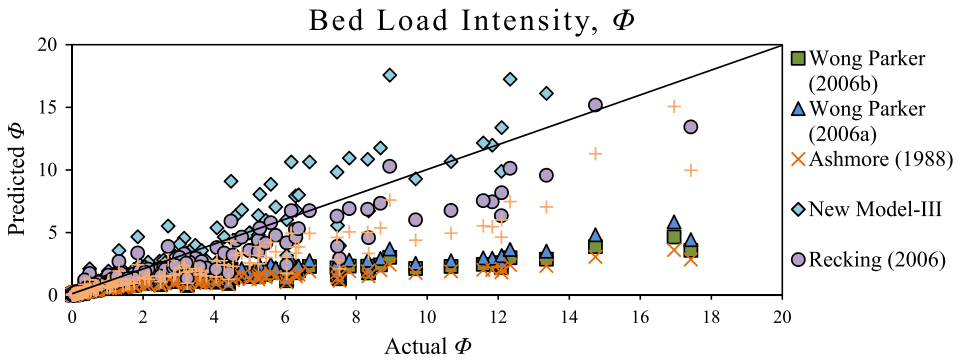

Figure 6. Validation of bed load intensity model for intense load condition with other author data.

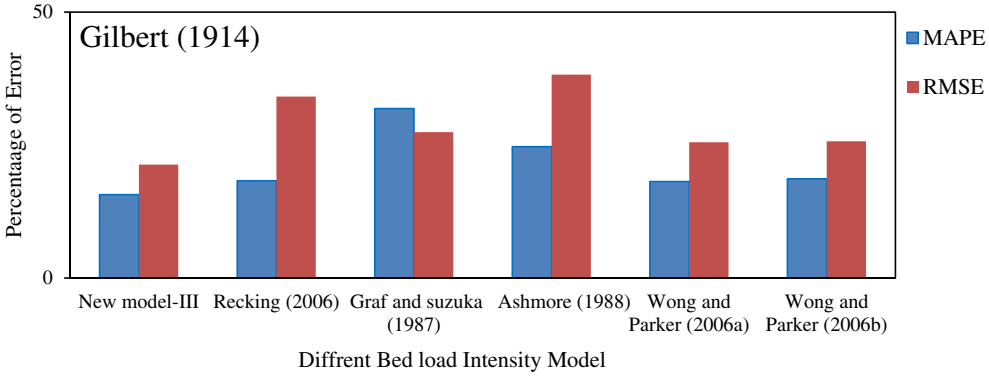

Figure 7a. Error analysis of bed load intensity model for intense load condition with Gilbert (1914) data.

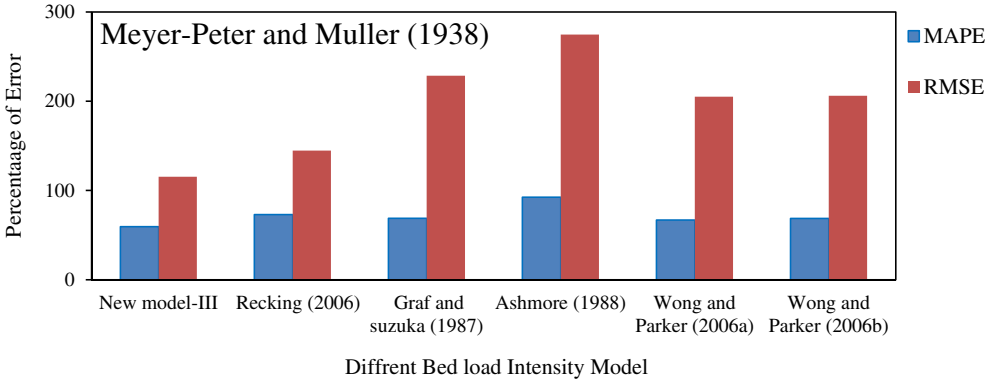

Figure 7b. Error analysis of bed load intensity model for intense load condition with Meyer-Peter and Muller (1948) data.

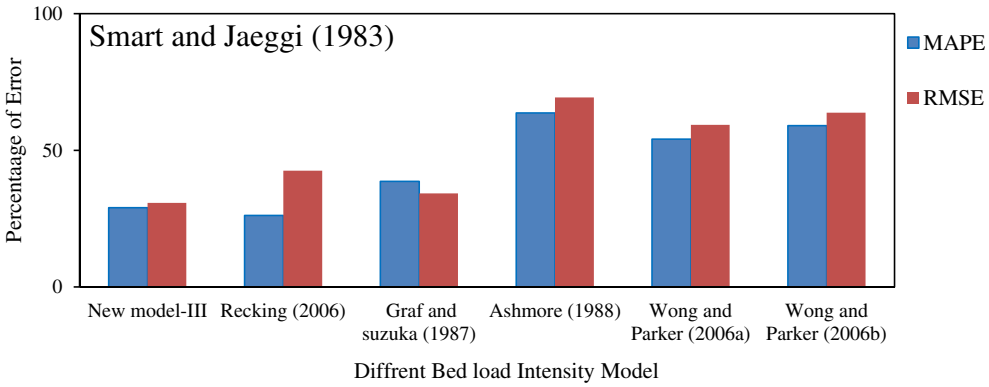

Figure 7c. Error analysis of bed load intensity model for intense load condition with Smart and Jaeggi (1983) data.

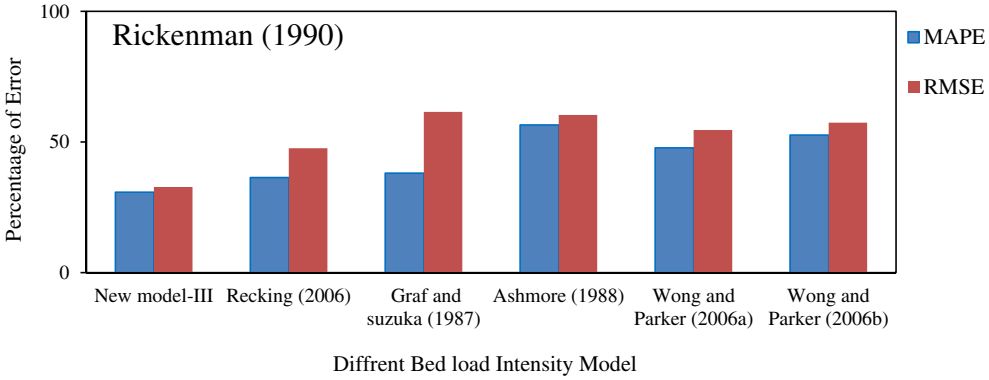

Figure 7d. Error analysis of bed load intensity model for intense load condition with Rickenman (1990) data.

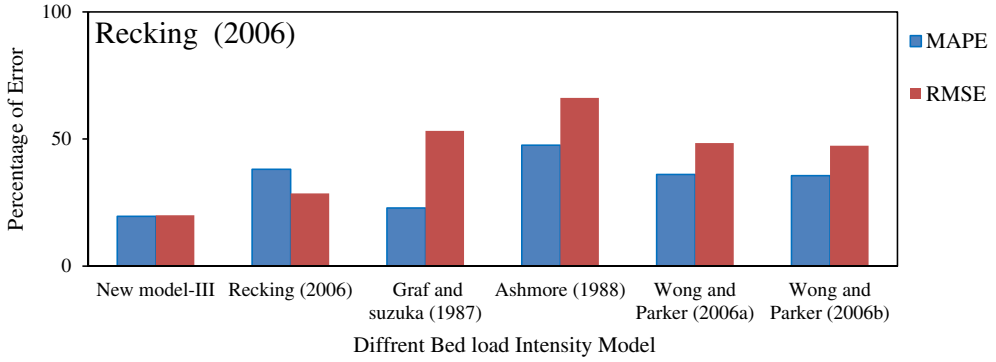

Figure 7e. Error analysis of bed load intensity model for intense load condition with Recking (2006) data.

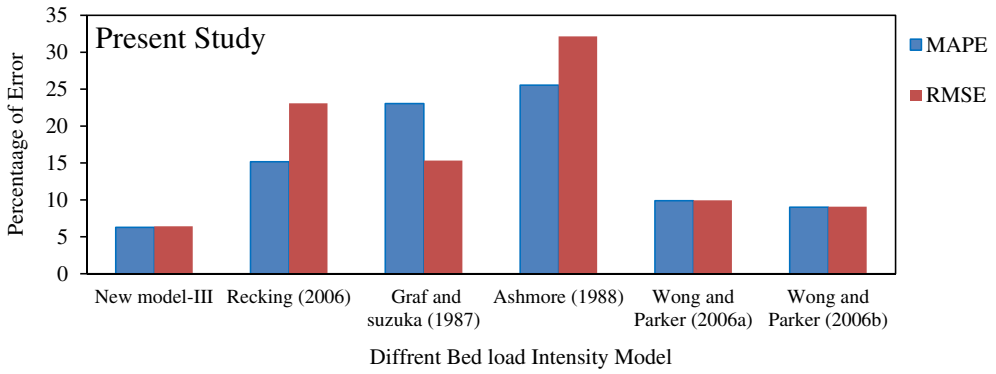

Figure 7f. Error analysis of bed load intensity model for intense load condition with present study data.

are demonstrated in Figure 7(a)–(f). The models developed are a power function of the shield's parameters, θ that depend on the boundary shear stress.

Total six number of data-sets are used for this analysis including the present experimental results with θ values less than 0.1, which indicates an intense load condition. In the error analysis figures demonstrated below, it is clearly observed that the developed expression by the other authors in Equation (19) gives lower values of MAPE and RMSE for all the available data. The values of RMSE and MAPE for the case of, is quite high for all the prediction models, it is because of the higher range of gravel size used i.e. 1.4–28.65 mm for a mild slope of 0.1–0.5%. The data-sets of Smart and Jaeggi (1983), Rickenman (1990), and Recking (2006) have steep slopes while that of Gilbert and the present experimental data-sets have mild bed slope. Hence, this might be an explanation for different ranges of values, where the former have the values in the range of 100 while the later gives better results with values below 35. Therefore, it can be concluded, that all the bed load and intensity models are quite suitable for predicting bed load intensity, Φ for the lower size of gravel weight with a mild slope, with the present expression provided the better results.

5. Conclusions

Types of sediment are considered for the purpose of the present study is smaller. Following salient findings are obtained from the present research work.

- Bed load intensity and friction factor are found to be functions of boundary shear stress, sediment transport rate, velocity, discharge, shear velocity, hydraulic radius, grain size diameter, the slope of the channel and Shield's parameter.
- The model developed for friction factor under intense load conditions when validated with others model, is found to give comparatively less erroneous values than previous models.
- A bed load intensity model established for the case intense bed load transport condition is observed to provide better results in comparison to that of the other models.
- The linear regression curve shows a higher value of correlation coefficient, indicating a satisfactory relation between the two in friction factor calculation of intense load.
- The power law curve shows a higher value of correlation coefficient, indicating a satisfactory relation between the two for bed load intensity and Shield parameter.

Notations

d Diameter of the Preston tube
d^* Dimensionless particle parameter
D Diameter of the gravel
D_{50} 50% grain size diameter at
f Darcy–Weisbach's friction factor
g Acceleration due to gravity
q_b Bed load sediment transport rate
Q Channel discharge
R Hydraulic radius, defined as flow area/wetted perimeter
R^2 Coefficient of Determination
S Channel bed slope

u Measured velocity by the manometer
u^* Shear velocity
θ Shields parameter for bed shear stress
θ_c Critical Shields parameter for bed shear stress
τ Boundary shear stress of the channel
τ_c Critical Boundary shear stress of the channel
ν Kinematic viscosity of water
z Distance between the free surface with arbitrary datum
z_0 Fraction of the bed roughness
ρ Density of water
Φ Dimensionless intensity of the bed load rate
γ Specific weight of water
γ_s Specific weight of sediment

Acknowledgement

The encouragement and assistance from the Institute and the Research project by the second authors for carrying out the research work in the Hydraulics laboratory at National Institute of Technology, Rourkela is gratefully acknowledged.

Disclosure statement

No potential conflict of interest was reported by the authors.

References

Ashmore, P.E. (1988). "Bed load transport in braided gravel bed stream models." *Earth Surface Proc. Landforms*, 13, 677–695.
Bathurst, J.C., Graf, W.H., and Cao, H.H. (1982). "Initiation of sediment transport in steep channels with coarse bed material." *Euromech 156: Mech. Sediment Transport, Istanbul*, 207–213.
Bergeron, N.E., and Carbonneau, P. (1999). "The effect of sediment concentration on bedload roughness." *Hydrol. Proc.*, 13, 2583–2589.
Bogardi, J., and Yen, C.H. (1939). "Tractation of pebbles by flowing water." *State Univeristy of Iowa*.
Campbell, L., McEwan, I., Nikora, V.I., Pokrajac, D., Gallagher, M., and Manes, C. (2005). "Bed-load effects on hydrodynamics of rough-bed open-channel flows." *J. Hydraul. Eng.*, 131(7), 576–585.
Cao, H.H. (1985). "Resistance hydraulique d'un lit à gravier mobile à pente raide; étude expérimentale." PhD thesis. Ecole PolytechniqueFederale de Lausane, Lausanne.
Cao, Z., Pender, G., and Meng, J. (2006). "Explicit formulation of the shields diagram for incipient motion of sediment." *J. Hydraul. Eng.* 132(10), 1097–1099.
Carbonneau, P., and Bergeron, N.E. (2000). "The effect of bed load transport on mean and turbulent flow properties." *Geomorphology*, 35, 267–278.
Cardoso, A.H., Graf, W.H., and Gust, G. (1989). "Uniform flow in s smooth open channel." *J. Hydraul. Res.*, 27(5), 603–616.
Casey, H.J. (1935). "Uber Geschiebebewegung, Preuss." *Versuchsanst. fur Wasserbau und Schifibau, Berlin*, 19, 86 pp.
Einstein, H.A. (1942). "Formulas for the transportation of bed-load." *Trans. Am. Soc. Civ. Eng.*, 107, 561–597.
Einstein, H.A. (1950). *The Bed-Load function for sediment transportation in open channel flows*, United States Department of Agriculture – Soil Conservation Service, Whashington, DC, 71.
Einstein, H.A., and Barbarossa, N.L. (1951). "River Channel Roughness." *Am. Soc. Civil Eng.*. Paper N°2528, 1121–1146.
Gilbert, G.K. (1914). "The transportation of Debris by running water." *US Geological Survey*, No. 86.
Graf, W.H., and Suszka, L. (1987). "Sediment transport in steep channels." *J. Hydrosci. Hydraul. Eng.*, 5(1), 11–26.
Hey, R.D. (1979). "Flow resistance in gravel bed rivers." *J. Hydraul. Div.*, 105(4), 365–379.
Ho, P.Y. (1939). "Dependence of the sediment movement on the grain shape and the temperature." *Preuss. Versuchsanst. fur Wasserbau und Schifibau, Berlin*, 37, 43 pp.
Julien, P.Y. (2002). "River mechanics." *Cambridge University Press*, 434.
Keulegan, G. B. (1938). "Laws of turbulent flows in open channels." *J. Res. Natl. Bureau Stand.*, 21, 707–741.
Mahdavi, A., and Omid, M. (2004). "The effect of bed roughness on velocity profile in open channels." *River Flow Naples Italy*, 295–300.
Mavis, F. T., Liu, T., and Soucek, E. (1937). "The transportation of detritus by flowing water." *IIHR Bull.* 11, University. of Iowa, Iowa City.
Meyer-Peter, E., and Muller, R. (1948). "Formulas for Bed-Load Transport." *IAHSR, Stockholm*, 39–64.
Nikora, V.I., and Smart, G.M. (1997). "Turbulence characteristics of the New Zealand gravelbed rivers." *J. Hydraul. Eng.*, 123(9), 764–773.
Nikuradse, J. (1933). "Strömungsgesetze in rauhen Rohren. Forsch." *Arb. Ing. - Wes*, 361.
Omid, M., Mahdavi, A., and Narayanan, R. (2003). "Effects of bed load transport on flow resistance in rigid boundary channels." *IAHR, Tessalonic*, IAHR, ed., 641–646.
Paintal, A.S. (1971). "Concept of critical shear stress in loose boundary open channels." *J. Hydraul. Res.*, 1, 90–113.
Recking, A. (2006). "An experimental study of grain sorting effects on Bedload." Ph.D. thesis, French engineering university INSA Lyon.
Rickenmann, D. (1990). Bed load transport capacity of slurry flows at steep slopes." *Versuchsanstalt für Wasserbau, Hydrologie und Glaziologie der Eidgenössischen, Zurich*.
Sheilds, A. (1936). "Anwendung der Ahnlichkeitsmechanik undTurbulenz-forschung auf Geschiebebewegung." *Mitteilungender Preuss. Versuchsanst. f. Wasserbau u, Schiffbau, Heft, Berlin*, 26.
Smart, G. (1999). "Turbulent velocity profiles and boundary shear in gravel bed rivers." *J. Eng.*, 125(2), 106–116.
Smart, G., and Jaeggi, M. (1983). "Sediment transport on steep slopes." *Nr.64, Mitteilungen der Versuchsanstalt für Wasserbau, Hydrologie und Glaziologie, Zurich*, 191.
Smart, G.M., Duncan, M.J., and Walsh, J.M. (2002). "Relatively rough flow resistance equations." *Journal of Hydraulic Engineering*, 128(6), 568–578.
Song, T., Graf, W.H., and Lemmin, U. (1995). "Uniform flow in open channels with a movable gravel bed." *J. Hydraul. Res.*, 32(6), 861–875.
Song, T., Chiew, Y.M., and Chin, C.O. (1998). "Effects of bed-load movement on flow friction factor." *J. Hydraul. Eng.*, 124(2), 165–175.
Van Rijn, L.C. (1984). "Sediment transport, Part I: Bed load transport." *J. Hydraul. Eng.*, 110(10), 14311457.
Whiting, P.J., and Dietrich, W.E. (1990). "Boundary shear stress and roughness over mobile Alluvial beds." *Journal of Hydraulic Engineering*, 116(12), 1495–1511.
Wiberg, P., and Rubin, D.M. (1989). "Bed roughness produced by saltating sediment." *J. Geophys. Res.*, 94(C4), 5011–5016.
Wong, M., and Parker, G. (2006). "Re-analysis and correction of bed load relation of Meyer-Peter and Muller using their own database." *J. Hydraul. Engng.*, 132, 1159–1168.
Wong, M., and Parker, G. (2006a). "One-dimensional modeling of bed evolution in a gravel bed river subject to a cycled flood hydrograph." *J. Geophys. Res.*, 111, F03018.
Wong, M., and Parker, G. (2006b). "One-dimensional modeling of morphodynamic bed evolution in a gravel-bed river subject to a cycled flood hydrograph." *J. Geophys. Res.*, 111.
Wu, W., and Wang, S.Y. (1999). "Movable bed roughness in Alluvial rivers." *J. Hydraul. Eng.*, 125(12), 1309–1312.
Yang, C.T. (1996). *Sediment transport theory and practice*, McGraw-Hill Series in Water Resources and Environmental Engineering, Singapore. ISBN 0-07-114882-5.

Demonetization - Challenges and Opportunities for Transforming India into Cashless Economy

K.V. Pavan Kumar

Associate Professor, Department of Business Management, Methodist College of Engineering & Technology.

Rationale Behind the Government to Demonitise the High Value Notes:

Prime Minister Narendra Modi's demonetization maneuver was a "shock doctrine" tactic to dismantle the cash-centric black market, to cleanse the country of counterfeit notes, to further digitize the economy, and to get more of the population onto the formal, taxable economic grid. Modi's plan called for the canceled notes to be replaced by new 500 and 2,000 denomination notes, but these were slow to be circulated, and India - the most cash-dependent country in the world - suddenly found itself without enough cash to run its economy.

Due to this cash crunch, India ground to a halt. Businesses shut down, farmers couldn't buy seeds, taxi and rickshaw drivers didn't have any way to receive payments, employers had no way to pay their employees, hospitals were refusing patients who only had old banknotes, fishermen watched their catch wither up and rot, some families had difficulty buying food, and weddings throughout the country were canceled.

The people of India were given 50 days to redeem their canceled banknotes, after which they would become as worthless as the paper they're printed on, which caused hundreds of millions of people to rush to banks, jewelry shops, foreign-exchange counters, and ATMs. Serpentine lines often stetched outside of such enterprises for blocks, where people would stand for hours just to re-validate their wealth.

This redemption period for the old notes came to an end on Friday December 30th - and, surprisingly, nearly the entire stock of 500 and 1,000 rupee notes were recovered by the central bank. But India's demonetization transition is far from being over. While the currency supply is still not completely restored and cash is still being rationed (there are strict bank withdrawal limits of 24,000 rupees a week ($350) or 2,500 rupees ($36) per day from ATMs), India is moving through the demonetization transition.

OBJECTIVES OF THE STUDY:

The following are the objectives of the Study:

1. To Study the reasons behind Demonetization
2. To study the various issues involved in the process of Demonetization.
3. To study the Impact of Demonetization on various sectors.
4. To study the Challenges and Opportunities for Transforming India towards Cashless Economy.

ISBN : 978-93-85101-54-0

RESEARCH METHODOLOGY:

The data in the study was mostly collected from the Secondary sources such as - News Articles, Information Bulletins from RBI, Experts opinion and also from different websites etc depicting the research topic.

IMPACT OF DEMONETIZATION ON VARIOUS SECTORS:

Effect on parallel economy: Cash Economy to Witness Contraction

The currency of the aforementioned denominations constitutes around 86% of the total value of the currency in circulation. It is expected to remove black money from the economy as they will be blocked considering the holders will not be in a position to deposit the same in the banks, temporarily halt the circulation of large volumes of counterfeit currency and curb the funding for anti-social elements like smuggling, terrorism, espionage, etc.

Effect on GDP: Downward Bias to GDP Growth

The sudden decline in money supply and simultaneous increase in bank deposits is going to adversely impact consumption demand in the economy in the short term. This, coupled with the adverse impact on real estate and informal sectors may lead to lowering of GDP growth.

Lower Money Supply has a Deflationary Effect: With the older 500 and 1000 Rupees notes being scrapped, until the new 500 and 2000 Rupees notes get widely circulated in the market, money supply is expected to be reduced in the short run. Reduction in money supply can also have a deflationary effect in the economy. However, whether the impact of the reduced money supply will lead to deflation or contraction in demand or a mix of both will vary from sector to sector depending on the nature of goods & services.

Impact on Bond Markets: Surge in deposits will create more demand for government bonds and other high rated bonds in a situation of tepid demands for credit, leading to lower bond yields especially in the shorter end of the curve. At the same time, a reduction in leakages in systemic liquidity will reduce the scope for open market operation purchases in the coming days. We believe that the RBI will continue to sterilize excess liquidity from the banking system to keep the short term rates aligned with the policy rate.

Credit Impact across Sectors: Impact of this policy measure will flow to the economy mainly through the Real Estate sector, which has strong linkages with sectors such as cement and steel and which will turn credit negative in the short-run. A significant impact in the short-run will be on the daily/weekly wage employment in the informal sector. The construction sector has one of the highest employment multipliers. The key segments of the economy where cash transactions play a vital role are real estate, gold and the informal sectors, which may face near term contraction.

Effect on Banks

As directed by the Government, the 500 and 1000 Rupee notes, which now cease to be legal tender are to be deposited or exchanged in banks (subject to certain limits). This will automatically lead to more amounts being deposited in Savings and Current Accounts of commercial banks. This, in turn, will enhance the liquidity position of the banks, which will be later utilized further for lending purposes. However, to the extent that households have held on to these funds for emergency purposes, there are expected to be withdrawals at the second stage.

ISBN : 978-93-85101-54-0

Effect on Online Transactions and alternative modes of payment:

With cash transactions facing a reduction, alternative forms of payment will see a surge in demand. Digital transaction systems, E wallets and apps, online transactions using E banking, usage of Plastic money (Debit and Credit Cards), etc. will definitely see substantial increases in demand. This should eventually lead to strengthening of such systems and the infrastructures required.

Bank Deposit Rates to Soften:

We can expect a large amount of cash in circulation to be brought within the purview of the formal banking system by way of deposits. This is structurally positive for banks, as part of this cash gets deposited as current account and savings account (CASA) deposits, reducing banks dependence on higher cost borrowing. Deposit deployment remains a challenge in the short to medium term due to the current tepid demand for credit, subsequently pushing deposit rates lower.

NBFC's Asset Quality Faces Pressure: We believe in the asset quality of Retail Asset Lenders, especially NBFC's which have developed expertise in the credit assessment of the informal segment and have built models around it to stay under pressure in the short term. Within NBFC's, asset quality of lenders with a large dependence on cash collection remain vulnerable in the short term. In the longer term the implications could be a risk profile shift for the NBFCs, as the stronger borrower profile could potentially migrate to banks.

Payment Banks to Benefit: Payment banks and others entities which are part of the transaction ecosystem are likely to be long term beneficiaries, as more and more cash finds its way into the formal banking channels. We believe the cumulative measures taken to reign in black money will improve banking habits, create financial and transactional history of the informal & cash dependent segments and could, over the long term, make them 'bankable'.

Investment in Financial Products: Investors in the short term will now believe that Cash is not the safest asset and there is little point in hoarding it. This will shift them from physical asset to financial assets where returns are also higher

Impact on Consumption Sectors

Agreement Cost of Real Estate May Rise: We expect that the real estate demand from end users is unlikely to be impacted, since a majority of them are backed by funding from bank loans. Demand from investors for real estate however may come down since in some cases, investors prefer cash transactions. If the proportion of earlier transactions in the real estate sector, which were allegedly done through partial cash payment reduces, the registered prices for real estate will go up. We expect the supply of real estate in the secondary market, which is strongly rumoured to have a large cash component involved, to suffer in the short term, which may in turn improve demand for residential real estate in the primary market.

In the medium term, the prices in this sector could regain on many fronts as developers rebalance their prices (probably charging more on cheque payment).

Used car Sales May Fall: Sales of vehicles in the second hand market for original equipment manufacturers will get impacted, which will cause a ripple effect on New Car sales, as buyers will not be able to dispose of their old vehicles easily.

ISBN : 978-93-85101-54-0

Slowdown in Discretionary Spending to Hurt Consumer Durable Sales: Sales of White Goods like TV, Refrigerator & Washing Machine could slump as much as 70% as a good portion of the market is driven by Cash. This may continue for next Six Months till the dust settles down and there is adequate circulation of the new currencies.

Prices are expected to fall only marginally, due to moderation in demand, as use of cards and cheques could compensate for some purchases.

Demand for Gems and Jewellery to Decline: We can expect the demand for gems and jewellery to decline in the next two to three quarters. This would result in a weakening in the credit profile of industry players due to the high working capital cycles and high operating leverage. The unorganised segment will be hit particularly hard, given the large proportion of unaccounted inventory and high proportion of cash sales. Over the medium-term the organised industry players will benefit at the cost of the unorganised players. Gold imports through the unofficial channels are likely to reduce. There will be no significant impact on jewellery exporters because it is mostly an organised market and sales are against invoices.

High End Retail Demand to fall: We expect the impact on high end fashion retail and luxury goods to be more pronounced as discretionary demand in this segment will be curtailed. In case of Quick Service Restaurants, although 60%-70% of the transactions are currently in cash, the impact is likely to be moderate due to the low ticket size of purchases and high likelihood of patrons adapting to plastic money. We expect a limited impact to be caused on the food and grocery retail sub-segment, given the non-discretionary nature of purchases in this segment, since the buying cycle for the current month would have been largely influenced.

Private Educational Institutions: Since Private Educational Institutions take huge amounts of donations in Cash which is 40 % to 50%, we expect that this move will impact the Private Education Institutions receipts.

Medical Institutions (Both Hospitals & Medical Colleges): Again, as Medical Institutions like Hospitals and Colleges take huge amounts of donations in Cash which are more than 100 % of fees, we can keep on expecting that this move will impact not only the admissions but also the receipts.

Political Parties: Elections & Political Parties are major sources of Black Money transactions. Most of the funding of National Political Parties is in Cash which is 40% to 50%, and when it comes to Regional Parties it goes upto 50% to 60%. The sources of more than 90% of such funds are never disclosed. Candidates as well as their donors even the Political Parties will feel cash strapped. An assembly seat candidate spent on an average Rs. 4-5 Crores on Campaigning that is likely to go down drastically.

This is going to cause huge craters on their funding and will reduce their funds drastically. It is going to deal a major blow to political parties fattening their coffers with cash contributions in anticipation of high stakes electoral battles in UP, Punjab, Uttarakhand, Goa and Manipur. This stroke is bound to leave big players hamstrung and suddenly resource-poor.

Dabba Trading (Bucketing): It may kill Dabba Trading. Trades done outside bourses, Satta Bazaar & Illegal Betting market may die a natural death as currency gets a new face. Demonetization was a jolt for Dabba traders, who were thriving in equity markets for many years now.

ISBN : 978-93-85101-54-0

Effect on various economic entities:

The key segments of the economy where cash transactions play a vital role are real estate / construction, gold and the informal sectors as such. The role of cash transactions in case of real estate and gold is mostly dubious, however in case of the informal sectors it is the lifeline. For example, small and marginal farmers in the fruits and vegetables category typically require off-loading of their produce in the local Mandi in cash and could see an immediate impact. A sudden demonetization will adversely impact this segment of the economy and it will witness immediate contraction, though this impact will diminish over time.

With cash transactions lowering in the short run, until the new notes are naturalized widely into circulation, certain sections of the society could face short term disruptions in facilitation of their transactions. These sections are:

- Agriculture and related sectors
- Small traders
- SME
- Services Sectors
- Households
- Professionals like doctors, carpenters, utility service providers, etc.
- Retail outlets

The nature, frequency and amounts of the commercial transactions involved within these sections of the economy necessitate cash transactions on a more frequent basis. Thus, these segments are expected to have the most significant impact post this demonetization process and the introduction of new notes in circulation.

Others Severely Hit:

Hawala Traders, Bookies, & Scrap Dealers.

Challenges and Opportunities for the Govt. for Cashless Economy:

Greater usage of digital payments will save trillions of rupees for the Indian economy as it will help bring down the cost of cash according to a report by payments company Visa Inc Titled "Accelerating the Growth of Digital Payments in India: A five-years Outlook". The report looks at the challenge of transitioning India to a less-cash society over the next five years and outlines an action roadmap for lowering the cost of cash to 1.3% of Gross Domestic Product from 1.7% now.

Increasing the Volume of Electronics Payments Provides numerous benefits to the government such as -

Drives Economic Growth:

Increased card penetration can increase GDP;

Shift from cash payment reduces social costs.

ISBN : 978-93-85101-54-0

Increases Financial Inclusion:

Greater acceptance of e-payments provides an on-ramp to financial inclusion.

Requires an enabling regulatory framework.

Reduces the Shadow Economy:

Cash enables and perpetuates shadow economies.

Electronic payment penetration correlates to size of shadow economy.

Enables Digital Commerce:

Electronic payments facilitate trusted transactions online.

Reduction in Cash Payments, enables e-Commerce growth, although in India Cash-on-delivery played an important role.

Benefits of Going Cashless Economy:

An investment of about Rs.60,000 crores over 5 years, India could reduce its cost of cash from 1.7% to 1.3% of GDP.

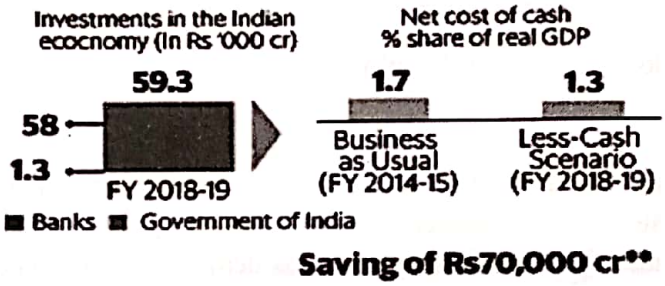

For the purposes of calculating the savings, we only count the additional mPOS and customer and merchant acquisition costs as the remaining capital cost is likely to be incurred by banks in the business-as-usual scenario. FY 2018-19 GDP estimate, Rs.132 trillion.

A 0.4% reduction in the cost of cash could provide India with additional saving of Rs.4 tn by FY 2024-25.

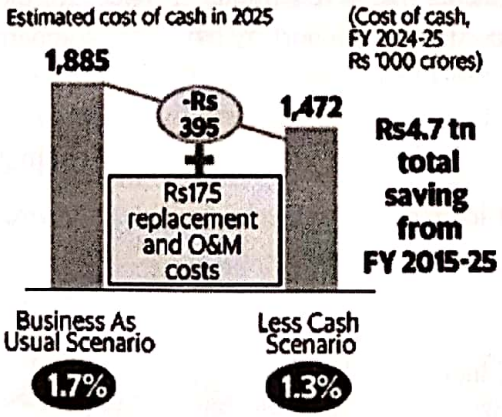

ISBN : 978-93-85101-54-0

Major Observations Post Demonetization:

The following are the major observations post Demonetization:

1. Banks have pumped in more cash deposits with the effect of demonetization of the higher denominations.
2. Jan Dhan accounts are filled with money, Government started this scheme for financial inclusion purpose, but people were reluctant to keep money in the bank, but after demonetization started, citizens are ready to come back to the banking network and thereby our banking system strengthened, citizens will be the beneficiaries of financial inclusion!
3. Many businessmen in India are declaring their black money as income and paying advance tax, we have seen many such examples in the recent days as many of them are coming forward and declaring cash lying with them as black money and paying taxes!
4. The fake currency is 100% out of circulation in one stroke! This is probably one of the greatest changes that are taking place.
5. All business men are depositing cash lying with them as current year income with Advance Tax which is a boon for the Indian Economy.
6. All jewellers are being issued forms to declare their Gold stock on day to day basis!
7. Defaulters of bank, property tax, electricity bills, and telecom bills have taken full advantage by clearing their long pending bills.
8. Defaulters of all kind of taxes have cleared their dues and are upto date, with the effect of the government's Demonetization scheme.
9. Small vendors started going digital and already using APPS, digital forms of transactions and digital wallets!
10. Cash to create chaos and terror lying with terrorists, Maoists, Naxalites, Jihadis gone waste!
11. Hawala sources dried up for funding of terrorists, Maoists, Naxalites, conversion lobby and Jihadis. As we know there is a considerable decrease of violence in Kashmir after this decision. Once the funding stopped, there won't be any riots in the valley and we are already witnessing the live effect!
12. Kashmir back to normal, schools are opened, normalcy in the valley, no schools burnt, you won't find any stone pelters these days!
13. More than 55 lakh money disputes settled in one day in Lok Adalats
14. Fiscal deficit of India has drastically reduced as compared to the previous years.

CONCLUSION:

The government more of demonetization of the high value currencies i.e. currency notes of 500 and 1000 with an objective to unearth the black money, and to curb the corruption, counterfeit currency as well as terror financing, was considered as biggest cleanliness drive against the black money in the history of Indian economy. But there is other view of experts on demonetization, as some argues that it will hit the black money and others argued in negative.

ISBN : 978-93-85101-54-0

Currently high-value currency notes accounts for the value of 86% of the notes in circulation in India. Central government's recent decision to demonetize the high value currency is one of the major step towards the eradication of black money in India. The demonetization drive will affect some extent to the general public, but for larger interest of the country such decisions are inevitable. Also it may not curb black money fully, but definitely it has major impact in curbing black money to large extent.

Key Suggestions to The Government for Cashless Economy:

The following key suggestions will be useful to the government to Penetrate the growth of Digital Payments:

1) Expand Acceptance:

A country's approach to expanding acceptance will depend upon its readiness for electronic payments

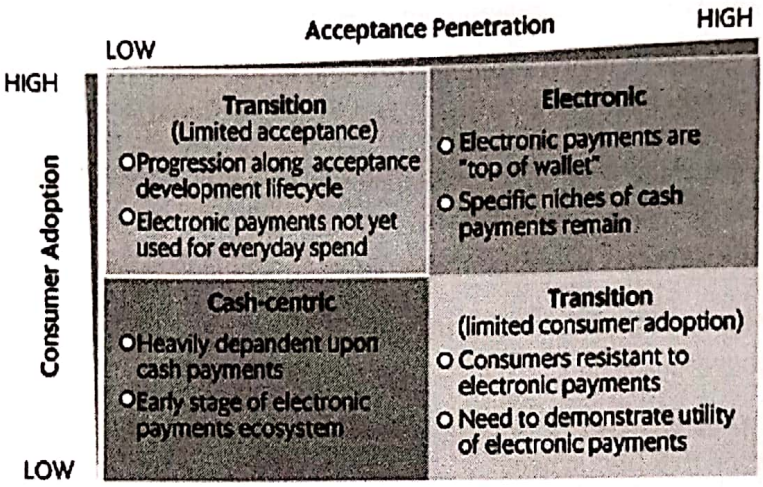

Source:http://www.livemint.com/r/LiveMint/final-digital-payments_web.jpg

Market readiness can be classified according to levels of:

a) Number of accepting Merchants

b) Number of acceptance points (per population).

Consumer Adoption:

Access to electronic payments

Frequency of usage

2) Energize Innovation:

a) Establish an acceptance development fund of around Rs.1000 crore to increase acceptance of digital payments in under-penetrated categories.

b) Provide Fiscal Incentives for promoting digital payments.

c) Introduce new regulations on mandatory digital payments in certain cases, reduce import duties on payments infrastructure; and make digital payments of salaries mandatory.

d) Allow foreign companies to participate in the digital payments ecosystem independently and develop a repository to track payment history of customers.

ISBN : 978-93-85101-54-0

3) Bolster Financial Participation:

a) Facilitating inter-ministerial collaboration at the centre and engagement with states to leverage existing programmes and platforms, for example, mKisan.

b) Designing programmes tailored to meet the needs of various types of underserved segments such as women and farmers.

c) Strengthening efforts to promote financial participation at the last mile, working in collaboration with existing microfinance institutions in different states.

d) Crafting approaches to inculcate financial literacy programmes at the school level and in higher education, and as part of public service education.

e) Introducing Certification standards and constructing innovating models for business correspondents.

References:

Accelerating the Growth of Digital Payments in India: a five-year outlook'

www.forbes.com

http://economictimes.indiatimes.com/news

http://www.jrfinancial.in/blog/impact-demonetization-rs-500-rs-1000-note-various-sectors-economy

http://www.ucnews.in/news/2101-3212217754017578/15-mind-blowing-immediate-benefits-of-demonetization-.html

http://www.livemint.com/r/LiveMint/Period2/2016/10/06/Photos/Processed/g_final-digital-payments_web.jpg

http://www.drishtiias.com/editorial-analysis-demonetisation-and-black-money

ISBN : 978-93-85101-54-0

International Journal of Ethics in Engineering & Management Education
Website: www.ijeee.in (ISSN: 2348-4748, Volume 4, Issue 3, March 2017)

Depressed Power Utilization on 3T Gain Cell EDRAM

[1] B. Sateesh
Research Scholar
JNTU Hyderabad
Telangana, India
basateesh27@gmail.com

[2] Dr. Prabhu G Benakop
Principal
Indur Institute of Engineering and Technology
Ponnala (v) Siddipet,Medak,TS,India
pgbenakop@ieee.org, pgbenakop@rediffmail.com.

Abstract: **Logic compatible gain cell (GC)-embedded DRAM (eDRAM) arrays are considered an alternative to SRAM because of their small size, non rationed operation, low static leakage, and two-port functionality. But traditional GC-eDRAM implementations require boosted control signals in order to write full voltage levels to the cell to reduce the refresh rate and shorten access times. The boosted levels require an extra power supply or on-chip charge pumps, as well as nontrivial level shifting and toleration of high voltage levels. In this paper, we present a novel, logic compatible, 3T GC-eDRAM bit cell that operates with a single-supply voltage and provides superior write capability to the conventional GC structures. The proposed circuit is demonstrated in 0.25µm CMOS process targeted at low power, energy efficient application.**

Keywords: **DRAM, GC, VLSI, SRAM, 3T, Cell**

I. INTRODUCTION

Memories have occupied large proportion of the die area of VLSI system-on chips in recent years. Major reason for this is increasing number of components as in case of 6T SRAM it has large 6-transistor the various other reasons are area-consuming, peripheral circuitry. Embedded memories have turned to be an important one in the long standby mode it continues to leak more power which characterize the system performance.

Initially SRSAMs are used for storing data bits in memory. But it has some of the disadvantages like large area, more power consumption even though it has been the traditional choice for the implementation of embedded memories due to its high-access speed and refresh-free data retention time. It also has some other disadvantages like static leakage of current, under voltage scaling and large transistor count. These limitations can be overcome by usage of gain-cell (GC)-embedded DRAM (eDRAM) such as circuit in Fig. 2 and Fig. 3 [3]-[8]. Which provides full CMOS logic compatibility of 2-transistor (2T) or 2-transistor (3T) GC-eDRAMS resulting in nonratioed operation and low static leakage currents from VDD to GND. Inspite of overcoming most of the disadvantages of static memories GC-eDRAM requires periodic refreshing operation. However, as opposed to static memories the data retention time of GC-eDRAM depend on dynamically stored charge.

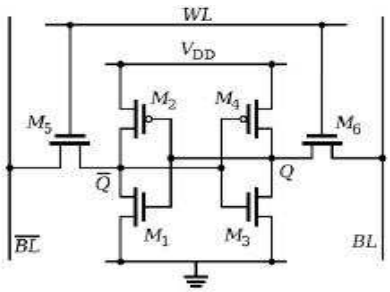

Fig.1 6T SRAM

II. EXISTING METHOD

A. 6T SRAM

Basic static RAM circuits can be viewed as vibrations on the designs used for latches and flip-flops more aggressive static RAMs make use of design tricks originally developed RAMs to speed up the system. The value is stored in the middle four transistors, of Fig.1 which form a pair on inverters connected in a loop. The other two transistors control access to the memory cell by the bit lines. When select = 0, the inverters reinforce each other to store the value. A read or write is performed when cell is selected.

To read, bit and bit are pre charged to before the select line is allowed to go high. One of the cell's inverters will have its output at 1, and the other at 0, which inverter is 1 depends on the value stored. The right hand inverter's pull down and the bit line will be drained to through that inverter's pull down and the bit line will remain high. If the opposite value is stored in the cell, the bit lines will be pulled own while bit remains high. To write, the bit and bit lines are set to the desired value, then select is set to 1.charge sharing forces the inverters to switch values, if necessary, to store the desired value. The bit lines have much higher capacitance than

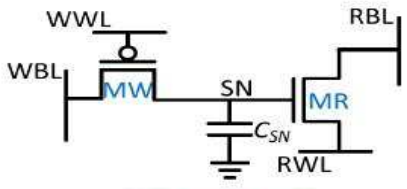

Fig.2. 2T Mixed Gain Cell

International Journal of Ethics in Engineering & Management Education
Website: www.ijeee.in (ISSN: 2348-4748, Volume 4, Issue 3, March 2017)

For a read operation a PMOS MR requires a pre-discharge of the parasitic RBL capacitance followed by raising the read word line (RWL). If the selected bitcell's storage mode (SN) holds a loop value, MR is
the inverters, so the charge on the bit lines is enough to overwhelm the inverter pair and cause it to flip state.

B. 2T Mixed Gain Cell

2T mixed GC can be implemented with either an NMOS or a PMOS device as shown in Fig.2. Moreover, both MW (write transistor) and MR (read transistor) can be implemented with standard threshold voltage core or high threshold voltage I/O devices in the considered CMOS technology. Due to the voltage drop across MW, a boosted write word line (WWL)voltage is required during write access above $|V_{DD}|$ for NMOS operation and below V_{ss} for PMOS operation. conducting and charges RBL post a detectable sensing threshold. If SN holds value MR is cut-off such that RBL remains discharged below the sensing threshold. For the NMOS implementation of MR, the
operation is exactly opposite i.e. RBL is precharged and RWL is lowered to initiate a read.

III. PROPOSED METHOD

In this brief, we present a new topology for a 3TGC, featuring a complementary transmission gate in the write port. While the proposed solution is quite straight forward it is novel and its impact in very high. We demonstrate the functionality of the proposed system used in ultra-low power applications such as biomedical sensor nodes and implants. The proposed 3T GC-eDRAM macro is shown to be fully functional with a supply voltage ranging from 600mv to 2.5v.

A. 3T Gain Cell eDRAM

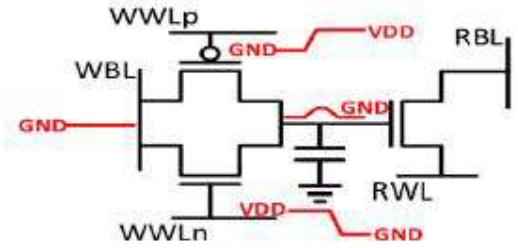

Fig.3. 3T Gain Cell eDRAM

3T GC consists of write port featuring a complementary transmission gate PMOS write (PW) and NMOS write (NW) a storage node (SN) composed of the three transistors, a read port based on NMOS read (NR) and the metal interconnect as in Fig 3. the GC is built that all the transistors operates with standard voltage and is fully compatible with standard digital CMOS technologies. The gates of PW and NW are connected to the world line of PMOS and NMOS WWLp and WWLn. A common write bit line is used to drive the data to the transmission gate during write operations. When the full-swing is given to the cells transmission gate enables the propagation of strong levels to the SN without any need for boosted world line. RBL capacitances or blocking the discharge path if SN is low. IN order to achieve a tradeoff between speed, area, power and reliability, a dynamic sense amplifier can be used to improve the read operation and its performance as described in [5],[6].

B. Operation

The circuit is described with = 900 mv. This voltage was chosen as a good medium voltage between and since the data retention time (DRT) is proved to be efficient in. GC-eDRAM design [8] at this voltage starting with charged WBL is driven low and the world lines WWLp is set to 0 and WWLn is set to . Then a strong 0 level is passed to the SN, during standby, the level on SN deteriorates due to leakage currents dominated by the sub threshold leakage of PW and NW in mature CMOS nodes. Hence in order to extend the retention time WBL is driven to during standby and read cycles thereby significantly reducing the sub threshold leakage through the transmission gate for both stored low and high values compared with the condition where WBL is either driven to either or GND. The write circuitry and read circuitry are described in section IV.A. During readout the 0 level blocks the discharge paththrough NR, maintaining the precharged voltage on RBL. During the next write operation WBL is driven high, resulting in a strong 1 stored on the SN. The subsequent read operation
provides a strong gate overdrive to transistor NR, thereby discharging RBL toread a 1. It should be noted that during this operation (Read 1), bitcells storing 1 and sharing thesame column turn on when RBL discharges by more than the of NR, causing it to saturate before it can completely discharge. This phenomenon is common to many GC-eDRAM configurations, as discussed in[8].

C. Data Retention Time

The data retention time (DRT) of GC embedded DRAMS is the time interval for writing a data level in the bit cell to the last moment the data can still correctly read out the stored information. For 2T and 3T cells methodology which are affected by the initially degraded voltage level corresponding to the data values due to the threshold voltage () drop across the write transistor DRT is primarily limited by the initial charge stored on the internal bit cell capacitance and the leakage currents that degrade the stored voltage level over time. In order to describe this issue a boosted write world line (WWL) voltage is usually employed to pass a full swing level to the storage capacitance. Any how this requires the generation of boosted on-chip voltage, which entails substantial overhead [1]. The magnitude of the voltage boost is set not only to overcome the drop, but also to achieve short write access time which otherwise are typically longer than 6T SRAM implementation. The proposed bitcells provides strong initial data levels for enhanced DRT and robust operation as well as for fast write access time.

International Journal of Ethics in Engineering & Management Education
Website: www.ijeee.in (ISSN: 2348-4748, Volume 4, Issue 3, March 2017)

IV. MEMORY

MACRO PERIPHERALS

To improve the array performance in terms of access time and power consumption several peripheral techniques were integrated into the designed memory macro in the proposed technique single supply voltage is provided to the circuit which simplifies the implementation of a full memory macro. This is the significant advantage over the other GC eDRAMS that uses conventional bit cells. These bit cells require the use of level shifters to create the desired boosted or negative voltage supply depending on the types of MOS write. The peripheral circuit which is designed for this memory macro and their techniques are described as follows.

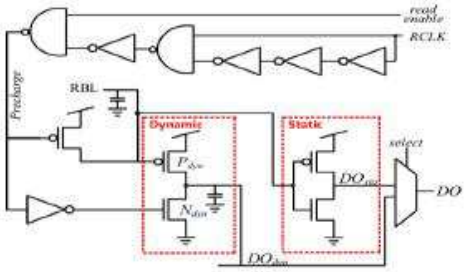

Fig.4.ReadOut Circuitry

A. Readout Circuitry

Large number of ultra low power systems comprising of low voltage embedded memories consists of simple sense inverter. This sense inverter is used for the purpose of reduction in area, robust and low power readout operation however this inverter suffers from very slow data readout as it requires RBL to be discharged or charged for PMOS read device switching the threshold of the inverter.

GC-eDRAM macro cell has two sensing node 1). A faster dynamic sensing mode but it is potentially more error-phrone which acts in dynamic readout mode 2). A slightly slower static mode but more reliable. In both the sensing modes however threshold device PMOS transistors were used in order to allow a faster read access time due to the above mentioned problem the read out circuitry is provided the supply voltage through the read enable signal in order to save substantial static power because of the leaky low voltage threshold devices the schematic diagram with the two sensing nodes of static and dynamic are shown in Fig. 4.RBL saturation during readout that slows down the charging and discharging operation as the RBL voltage increases and decreases The raising edge of the read clock (RCLK) creates a precharge pulse that charges the parasitic capacitance of RBL and discharges the dynamic sense inverter output capacitance through the discharge transistor, . Subsequently RBL is conditionally discharge during read operation turning on to complement the output if high value is stored in the selected cell. Therefore an RBL swing of only one threshold voltage is required to complete a read operation.

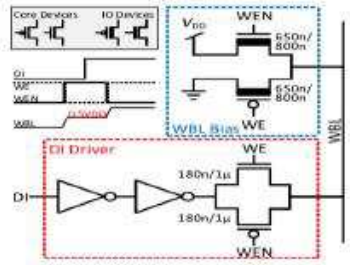

Fig.5. Write Circuitry

B. Write Circuitry

The proposed single supply 3T bit cell provide a significant improvement in write time when compared to the read time, which means it has fast access time, when compared to the readout circuitry. It also has an initial SN level improvement over standard GC implementation the dual transistor write port built by means of transmission gate provides a leakage path to or from the storage node. The write circuitry to implement the median WBL bias during standby and read cycle is shown in Fig.5.

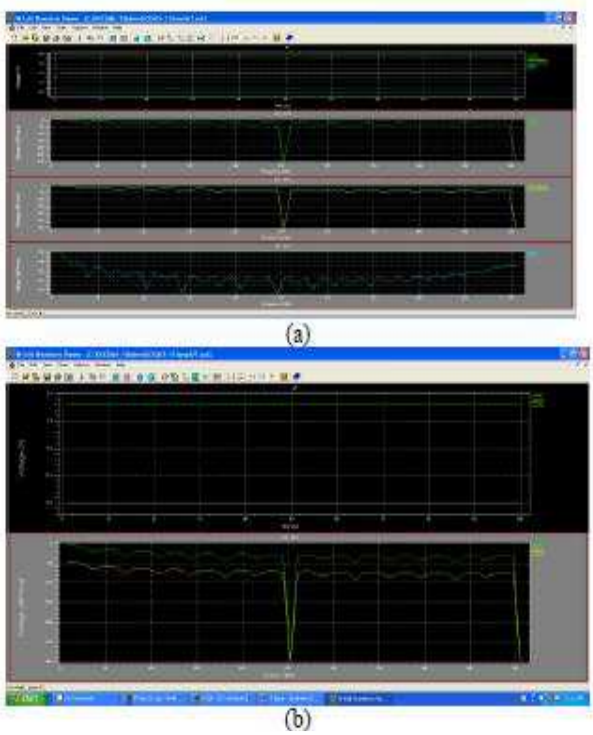

(a)

(b)

addition, several previous works have shown that the data dependent, asymmetric DRT (for data 0 and 1) of standard GCs can be manipulated to overall enhance DRTs by biasing the WBL at the best case voltage for the weaker data level during standby and read operations . For the proposed 3T configuration, the worst case DRTs of the 1 and 0 levels are similar, and significant deterioration of the stored levels occurs for both extreme values of WBL bias (VDD and GND). A standard inverter chain conditionally drives the data-in level on to the WBL through a TG, controlled by complementary

International Journal of Ethics in Engineering & Management Education
Website: www.ijeee.in (ISSN: 2348-4748, Volume 4, Issue 3, March 2017)

write enable signals Write Enable (WE) and Write Enable Negative (WEN). In parallel, a pair of long-channel I/O devices drives WBL during non-write cycles.

These devices create a short-circuit path between VDD and GND when WE is low, providing a median potential (VDD/2) at WBL. Due to the thick oxides and long channel-lengths of the I/O devices, process variations are significantly reduced, and the static current is extremely low compared to the readout circuit.

V. RESULTS AND DISCUSSIONS

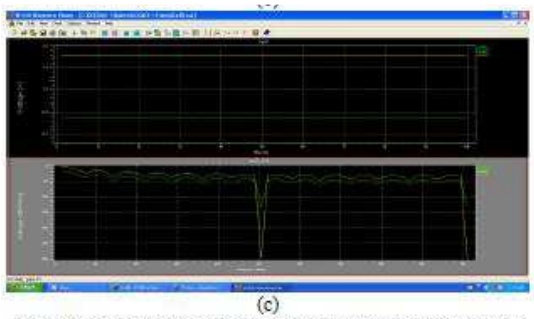

(c)

Fig.6. The functionality of the memories at different frequencies for various voltage range (a)6T SRAM. (b) 2T Mixed GC. (c) 3T GC-eDRAM

The functionality of the memories at different frequencies for various voltage range are shown in Fig. 7 and their corresponding power consumptions results are discussed as follows. The main aim of the proposed techniques is that 3T GC-eDRAM should consume less power than that of the other memories such as static RAM (SRAM) designed with 6 transistors and 2T mixed GC DRAM architecture 3T GC-eDRAM has a average power consumption of 12.71μW which is less when compared to other existing memories 6T SRAM and 2Tmixed GC which consumes average power of 36.85μW and 13.2μW respectively. The result shows that the proposed technology consumes very less power than that of static memory. For a dynamic memory relevant metric for static power consumption is retention power, composed of the sum of leakage and refresh power. Hence it is essential to be much more low so that the power consumption due to leakage and refreshing operation get reduced. The data retention power of 3T GC-eDRAM is

4.66nW where for the 2T mixed GC is 5.98nW. It shows that proposed technique has less leakage power and power required for refresh than 2T mixed GC as shown in TABLE 1. The memory frequency is limited by the read access time during readout, RBL needs to discharge in order to flip the sense inverter the operation strongly depends on the parasitic capacitance of RBL. Hence it consumes more power than the write architecture. The readout circuit consumes an average power of 35.11μW and write circuitry consumes an average power of 18.49μW. Hence naturally readout circuit has more read access time than that of the write access time of write circuitry. The read access time is 2.1ns whereas the write access time is 1.8ns respectively.

POWER CONSUMPTION OF MEMORIES

S.No	Power Consumption		
	Various Memories	Average Power Conumption (Mw)	Data Retention Power (Nw)
1. 2. 3.	6T SRAM 2TMIXED GAIN CELL 3T GC-eDRAM	36.85 13.20 12.70	- 5.98 4.66

VI. FUTURE WORK

This brief proposes a novel 3T GC eDRAM microcell targeted at ULP systems and providing high storage density. The proposed GC is operated from a single-supply voltage, eliminating the need for boosted voltages, commonly found in prior-art implementations. When compared with 6T SRAM technology and 2T mixed gain cell technology it has less consumption of power and becomes fully functional at the voltage range of 600mv to 2.5v showing a worst case Data Retention power of 4.6 nW at 900mv.The proposed cell exhibits faster write-access than conventional GC circuits, thereby increasing DRTs and reducing refresh power consumption. The average power consumption at write access time is less than that of read access time. Measurement resultsshow full functionality at voltages ranging from 600 mv to 2.5 V with power as much as lower than apreviously reported 6T SRAM in the same technology node. Testing is the major issue in eDRAM technology. So in future various testing method can be used to check the better performance of the circuit.

VII. CONCLUSION

This brief proposes a novel 3T GC eDRAM microcell targeted at ULP systems and providing high storage density. The proposed GC is operated from a single-supply voltage, eliminating the need for boosted voltages, commonly found in prior-art implementations. When compared with 6T SRAM technology and 2T mixed gain cell technology it has less consumption of power and becomes fully functional at the voltage range of 600mv to 2.5v showing a worst case Data Retention power of 4.6 nW at 900mv.The proposed cell exhibits faster write-access than conventional GC circuits, thereby increasing DRTs and reducing refresh power consumption. The average
power consumption at write access time is less than that of read access time. Measurement results show full functionality at voltages ranging from 600 mv to 2.5 V with power as much as lower than a previously reported 6T SRAM in the same technology node. Testing is the major issue in eDRAM

technology. So in future various testing method can be used to check the better performance of the circuit.

REFERENCES

[1]. Raychowdhuryet al., "PVT-and-aging adaptive word line boosting For 8T SRAM power reduction," in Proc. IEEE ISSCC, Feb. 2010, pp. 352353.

[2]. A. Teman, P. Meinerzhagen, R. Giterman, A. Fish, and A. Burg, "Replica Technique for adaptive refresh timing of gain-cell-embedded DRAM,"IEEE Trans. Circuits Syst. II, Exp. Briefs, vol. 61, no. 4, pp. 259–263, Apr2014

[3]. D. Somasekharet al., "2 GHz 2 Mb 2T gain cell memory macro with 128 GBytes/sec bandwidth in a 65 nm logic process technology,"IEEE J. Solid-State Circuits, vol. 44, no. 1, pp. 174–185, Jan. 2009.

[4]. G. M. S. Reddy and P. C. Reddy,"Design and implementation of 8k-bits Low power SRAM in 180nm technology," in Proc. IMCECS, vol. 2. 2009, K. C. Chun, P. Jain, T.-H. Kim, and C.

[5]. H. Kim, "A 667 MHz logic compatible embedded DRAM featuring an asymmetric 2T gain cell for high speed on-die caches," IEEE J. Solid-State Circuits, vol. 47, no. 2 pp. 547–559, Feb. 2012.

[6]. K. C. Chun, P. Jain, J. H. Lee, and C. H. Kim, "A 3T gain cell embedded DRAM utilizing preferential boosting for high density and low power on die Caches," IEEE J. Solid-State Circuits, vol. 46, no. 6, pp. 1495–1505, Jun. 2011.

[7]. K. C. Chun, W. Zhang, P. Jain, and C. H. Kim, "A 2T1C embedded DRAM macro with no boosted supplies featuring a 7T SRAM based Repair and a cell storage monitor," IEEE J. Solid-State Circuits, vol. 47,no. 10, pp. 2517–2526, Oct. 2012.

Impact of Demonetization: Short Run Vs Long Run effects

G.Madhavi
Assistant Professor, Methodist College of Engineering and Technology, Abids, Hyderabad-01.
Email: mgattoju@gmail.com

Abstract

Demonetization is the act of stripping a currency unit of its status as legal tender. The old unit of currency will be replaced with a new currency unit. The currency was demonetized for the first time in 1946 and second time in 1978. Third time on Nov 8th 2016 the 500 and 1000 rupee note currency is demonetized and replaced with new 500 and 2000 rupee note by the present Modi Government.

This is the bold step taken by the Government for the betterment of the economy and country. In this paper I would like to discuss the impact of recent demonetization in the short run as well as Long run effect in India. The move was targeted towards to put a check against Fake currency, Black money, Corruption and Terrorism. Unbanked villages, small businesses badly hit as currency crisis continues.

Introduction

The Government of India announced that the 500 and Rs. 1000 denominated currency notes will not cease to be legal tender from 8th November 2016 midnight 12.00 pm . The move was targeted towards tackling black money, corruption and terrorism. After initial euphoria, questions began to emerge. How does this demonetization affect the economy? How does GDP get affected with this move? What is its effect in the short run as well as Long run? Will the Black Money be completely eradicated? Does the Black turns into White? Is the pain of Demonetization worth the gain we get from it ? Is it a unplanned decision of central Government? Is it a process of cleaning up the country's financial system.

History

Demonetization took for first time in the year 1946 January of 1000 and 10000 rupee notes which were reintroduced again in the year 1954 in 1000, 5000 and 10000 denomination. Subsequently in the year 1978 Government demonetized 1000,5000 and 10000 notes from economy.

Objective of the Study

The main objective of this Paper is to know the effect of Demonetization on 8th November by the present government in the Short Run as well as Long Run.

Methodology of the Study

Data has been collected from various secondary sources. It was collected from various published sources like News Gazette, magazines, journals, newspapers and Media etc.

Short Run Effects

Sudden decline in paper Cash in the Economy which effect demand of Goods and Services as the flow

ISBN : 978-93-85101-54-0

Money comes down which is directly linked to GDP will also come down in short run. Demonetization sulted in short-run disruptions in economic activity in cash-intensive sectors like Retail, Trade, Hotels, Restaurants, Transportation and the unorganized sector. Hit on Hotels, Restaurants and Food ints which do not have swipe machines.Tourism and Travel Industry hit as bookings has come by 70% to 80% and plans cancelled. Shortage of Working Capital was majorly felt by small and Medium Entrepreneur.

Diesel and petrol use, which account for more than half of India's oil demand, has slowed down during the first quarter of Demonitisation. Several Corporate Hospitals refused to accept banned notes and instead asked patients to extend their stay during first two weeks of post demonetization. No money and No Medicines for some.

Anakapalli Jaggery market which has annual turnover of 150 crore has shut down temporarily during demonetization due to crunch of Hard cash. Lost 2 crore just in two days. During the period of Nov 10th to Nov 30th 1.77 lakh borrowers has repaid loans over 25lakhs using old currency repayment which added upto nearly 50000 Crore.

Income earning departments like Registration, Excise & Prohibition, Commercial taxes and other Tax collecting wings are reporting a steep fall in revenue. When Government said no Black money through Demonetization people started converting it into Gold Overnight in Crores which resulted in inflated increased demand for Gold. Nearly 1.5 lakh Small and Medium industrial units like Plastics, Manufacturing, Steel and Cement along with the Hyderabad City's belt have now stopped production due to severe Cash Crunch. While some are operating 10% to 20% of its Capacity.

- Small traders and Kirana store owners have witnessed a huge drop in Business. People stuck to minimum purchase even when it comes to basic necessities. People surviving on daily wages got affected badly
- Activities of Naxals and Terrorists has come down due to non availability of Cash
- Temporary suspension of Toll in Major Highways
- Limit on number of withdrawals in ATMs have been waived temporarily during this period
- SBI has waived charges on Rupay cards which usually range from 0.75 % to 2.95% during this period to subside the problems faced due to non available of cash.
- Many of the Banks and ATMs running out of cash by forenoon.
- A lot of Entrepreneurs are sending out employees to exchange cash and some of Labourers were paid in old currency even after demonetization.
- 90 people lost their life standing in queues near Banks and ATMs for cash and some committing suicide due unexpected move of central Government.
- Entertainment Industry is no escape as Movie theatres being empty in the initial days of Demonetization.
- Some People postponed weddings due to non-availability of cash though Government gave limit of 250000 to withdraw.

Effect on Auto Industry

The Government decisions to ban 500 and 1000 notes have cripped sales of Cars and Two

ISBN : 978-93-85101-54-0

wheelers. Luxury makers such as Mercedes Benz and BMW are feeling the pinch as there has been a slowdown in inquiries and even cancellation of bookings.

Drop in sales 20%-30% in mid segment cars which range from 6 lakh to 25 lakh and 60%-70% drop in high segment which range from 26lakhs to 1.5 Crore.

Revenue of RTA 77.83Cr in October month has come down to 45.81 Cr in November 40% decrease. Registration of vehicles down by 80% in Hyderabad city.1000 registrations per day has come down to 200-250 registrations per day.

India's second largest two-wheeler manufacturer Bajaj Auto Ltd said its local sales fell 10.3% in November, while sales at India's largest sport utility vehicle-maker Mahindra & Mahindra Ltd declined 22% in November.

Most affected vehicles Luxury Cars, Mid segment Cars, High End super bikes and Cruiser bikes.

Banks Marginal Cost of lending rate

Bank	MCLR %	Old Rate
SBI	8	8.9
Union Bank	8.65	9.3
IDBI Bank	9.15	9.3
SBT	9.2	9.45
IOB	9.15	9.5
PNB	8.45	9.15

Three Municipal corporations in Delhi have collected over 7 crores in the form of property tax and conversion charge paid by property owners, in demonetized high value bank notes.

Hyderabad tops in Municipal Tax Collections among 22 cities.

GHMC topped in nationed wide earnings

Survey City	Nov 2015 in Cr	Nov 2016 in Cr
Hyderabad	8	193
Kakinada	2	20
Guntur	1	6
Vijayawada	2	12
Vishakhapatnam	3	15
Tirupathi	1.22	4.43

A report by Union Ministry of Urban Development

Long Run Effect

- Increase in Bank Deposits and decrease in Bank Interest Rate.
- Banks lending rate will come down as Banks have enough money now.
- Inflation will come down as there is less liquidity of Cash.
- Digitalization of Economy will take place.
- New borrowers may get loans at cheap rates, more lending may boost economic growth.

ISBN : 978-93-85101-54-0

- Boost in demand for consumer durables and automobiles.
- Increase in Point of Sale machines.
- Increase in micro ATM's in rural areas

Though the market goes down in the short run it will move to positive side in the long run which will build confidence of overseas investors in Indian Stock Market.

The Sectors or Schemes expected to affect severely are Major & Medium irrigation, Mission Kakatiya, Mission Bhagiratha, Roads and Building, Housing, Social Welfare schemes such as Aasara Pension, Shaadi Mubarak, Kalyana Lakshmi, Pre & post matric scholarships, Fee reimbursement, Partial Waiver of farm loans, Power Subsidy for Farm Sector, release of funds for Panchayat Raj and Urban local bodies, interest payments & servicing of debts etc.

Conclusion

It's a Remedy and not a tragedy!!! Though its hurting comman man hard. It's a process to clean up the country's financial system. Demonetization will have a "negative" impact on growth in the short run but for the full fiscal, the GDP decline would be "relatively moderate", the impact on GDP growth is clearly going to be negative in the short run and depends to a large extent on how long the cash crunch is going to take. Demonetization was done for a " along term structured transformation" it's a step towards organizing the Economy. It's a short-term pain but long term gain. Its Boom time for swipe machine makers. Transaction fee on debit and credit cards should be waived off to encourage digitalization.

Digitalization is going to happen ,Cyber security is a major concern in transactions we should take measures to avoid cyber crime like Pharming (fake website that seems similar to orginal) Keystroke Logging, Malware etc. One of the challenge to the Government is 76% of Indians are not on Internet.

In any value chain, the last link is mostly cash. There has been slowdown in the off take of the Goods because cash has not been immediately available. But the fact is its temporary in nature. Demand still exists in the country. As there is demand still people will readjust their models, come back and do their business. The amount that is coming into the bank will not remain fully with the bank, around 10% to 15% of it will remain in the bank and rest will have to go back in the Economy not as cash but as transfer transactions.

References

http://www.catchnews.com/national-news/deaths-due-to-demonetisation-since-8-nov-here-s-a-list-of-the-casualties-of-pm-modi-s-note-ban-1480484645.html

https://housing.com/news/demonetisation-hyderabad-tops-municipal-tax-collections-among-22-cities/

Times of India News Papers from 10th November to 30th December 2016.

ISBN : 978-93-85101-54-0

International Journal of Advanced Research Foundation
Website: www.ijarf.com, ISSN: 2394-3394, Volume 4, Issue 6, June 2017

Composition of 4:2 Compressor using XOR-XNOR Sections for Gassed-Up Computation Bound

[1] B. Sateesh
Research Scholar
JNTU Hyderabad
Telangana, India
basateesh27@gmail.com

[2] Dr. Prabhu G Benakop
Principal
Indur Institute of Engineering and Technology
Ponnala (v) Siddipet,Medak,TS,India
pgbenakop@ieee.org, pgbenakop@rediffmail.com.

Abstract: **A low-power high speed 4:2 compressor circuit is proposed for fast digital arithmetic integrated circuits. The 4:2 compressor has been widely employed for multiplier realizations to based on a new exclusive OR (XOR) and exclusive NOR (XNOR) module, a 4:2 compressor circuit has been designed. The Proposed circuit shows power consumption is very less. Power consumption and delay of proposed 4-2 compressor circuit have been compared with earlier reported circuits and proposed circuit is proven to have the minimum power consumption and the lowest delay. Simulations have been performed by using verilog HDL.**

Keywords: **Full-Adder (FA), XOR-XNOR, MUX, XILINX10.1ISE,VERILOG &MODEL SIM 6.3.**

I. INTRODUCTION

Multipliers are one of the most significant blocks in computer arithmetic and are generally used in different digital signal processors. There is growing demands for high speed multipliers in different applications of computing systems, such as computer graphics, scientific calculation, image processing and so on. Speed of multiplier determines how fast the processors will run and designers are now more focused on high speed with low power consumption. The multiplier architecture consists of a partial product generation stage, partial product reduction stage and the final addition stage. The partial product reduction stage is responsible for a significant portion of the total multiplication delay, power and area. Therefore in order to accumulate partial products, compressors usually implement this stage because they contribute to the reduction of the partial products and also contribute to reduce the critical path which is important to maintain the circuit's performance.

First all the eight inputs are fed as input to the AND gates which form sixteen products as shown in the fig and form a tree like structure. Then these inputs are further fed to half adders, full adders and compressors to reduce the partial products. This is accomplished by the use of 3-2, 4-2 compressor structures. A 3-2 compressor circuit is also known as full adder cell. Since these compressors are used repeatedly in larger systems, so improved design will contribute a lot towards overall system performance.

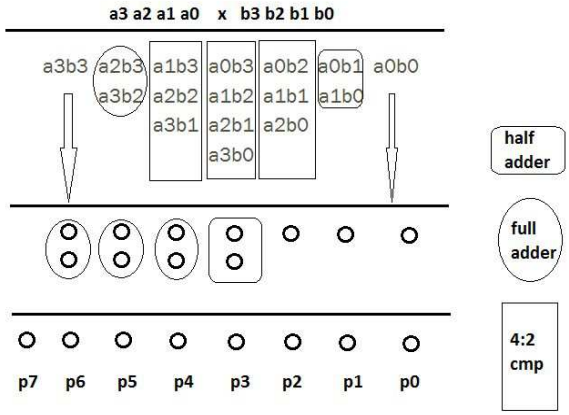

Fig.1. Structure of 4:2 Compressor.

The internal structure of compressors is basically composed of XOR-XNOR gates and multiplexers. The XOR-XNOR circuits are also building blocks in various circuits like arithmetic circuits, multipliers, compressors, parity checkers, etc. Optimized design of these XOR-XNOR gates can improve the performance of multiplier circuit. In present work, a XOR-XNOR module has been proposed and 4-2 compressor has been implemented using this module. By using partial product accumulation in proposed circuit reduces power consumption. following circuit shows compressor circuit is formed by xor-xnor gates.

II. COMPRESSOR

One of the major speed enhancement techniques used in modern digital circuits is the ability to add numbers with minimal carry propagation. The basic idea is that three numbers can be reduced to 2, in a 3:2 compressor, by doing the addition while keeping the carries and the sum separate. This means that all of the columns can be added in parallel without relying on the result of the previous column, creating a two output "adder" with a time delay that is independent of the size of its inputs. The sum and carry can be recombined in

International Journal of Advanced Research Foundation
Website: www.ijarf.com, ISSN: 2394-3394, Volume 4, Issue 6, June 2017

a normal addition to form the correct result. This process may seem more complicated and pointless, but the power of this technique is that any amount, number of additions can be added together in this manner. It is only the final recombination of the final carry and sum that requires a carry propagating addition. 3:2 compressor is also known as full adder. It adds three one bit binary numbers, a sum and a carry. The full adder is usually a component in a cascade of adders. The carry input for the full adder circuit is from the carry output from the cascade circuit. Carry output from full adder is fed to another full adder.

III. 4:2COMPRESSOR

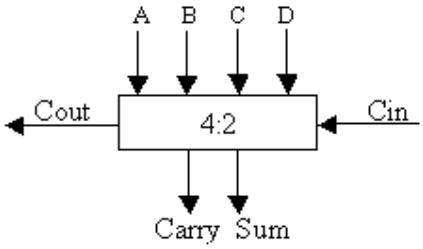

Fig.2. High level view of the 4:2 compressor.

The characteristics of the 4:2 compressor are:

- The outputs represent the sum of the five inputs, so it is really a 5 bit adder as shown in Fig.2.
- Both carries are of equal weighting (i.e. add "1" to the next column)
- To avoid carry propagation, the value of C_{out} depends only on A, B, C and D. It is independent of C_{in}.
- The C_{out} signal forms the input to the C_{in} of a 4:2 of the next column.

The common implementation of a 4-2 compressor is accomplished by utilizing two full-adder (FA) To add binary numbers cells.4:2 compressor is composed of two serially connected full adders. With minimal carry propagation we use compressor adder instead of other adder. Compressor is a digital modern circuit which is used for high speed with minimum gates requires designing technique. This compressor becomes the essential tool for fast multiplication adding technique on fast processor and lesser area.

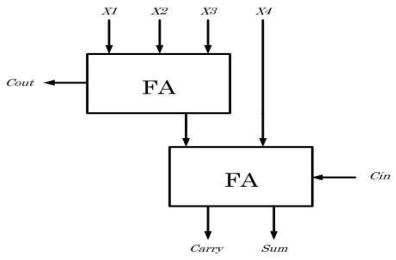

Fig.3. Structure of 3 bit

4:2 compressors are capable of adding 4 bits and one carry, in turn producing a 3 bit output. The 4-2 compressor has 4 inputs X1, X2, X3 and X4 and 2 outputs Sum and Carry along with a Carry-in (C_{in}) and a Carry-out (C_{out}). The input C_{in} is the output from the previous lower significant Compressor. The C_{out} is the output to the compressor in the next significant stage. The critical path is smaller in comparison with an equivalent circuit to add 5 bits using full adders. However, like in the case of 3-2 compressor, the fact that both the output and its complement are available at every stage is neglected. Thus replacing some XOR blocks with multiplexer's results in a significant improvement in delay as shown in Fig.4. Also the MUX block at the SUM output gets the select bit before the inputs arrive and this minimizes the delay to a considerable extent.

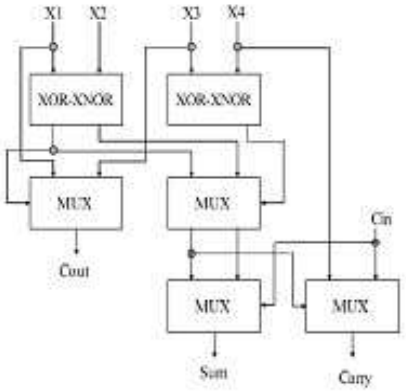

Fig.4. 4:2 compressor using xor xnor.

IV. VHDL SIMULATION RESULTS

The proposed 4:2 compressor using xor-xnor gates and mux has been simulated using Xilinx and results shown in Figs.5 to8.

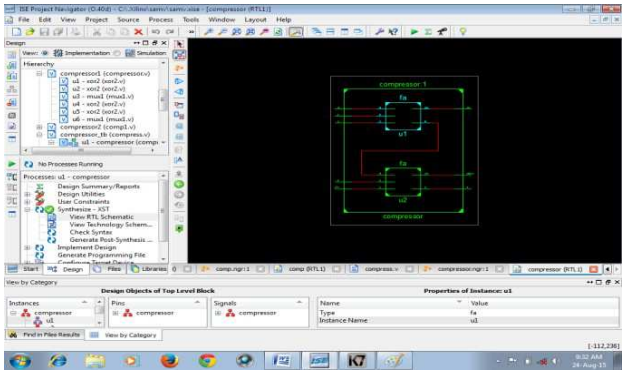

Fig.5. Compressor using full adders.

International Journal of Advanced Research Foundation
Website: www.ijarf.com, ISSN: 2394-3394, Volume 4, Issue 6, June 2017

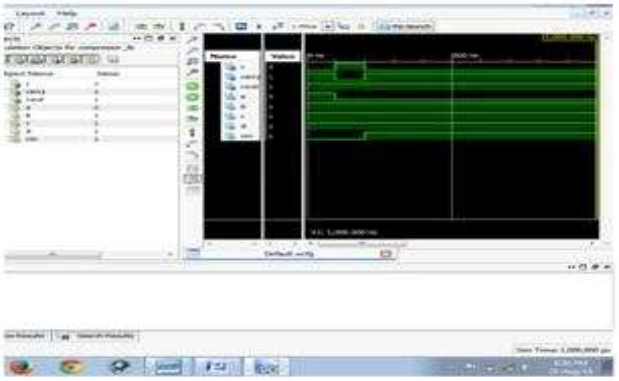

Fig.6. Schematic of 4;2 compressor using two full adders.

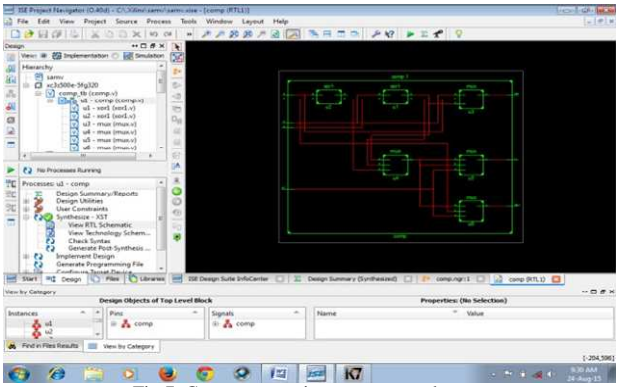

Fig.7. Compressor using xor-xnor and mux.

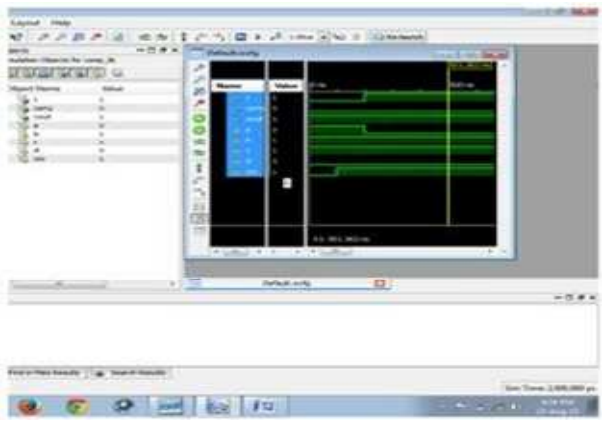

Fig.8. Schematic of 4:2 compressor using xor-xnor and mux.

TABLE I: Performance Analysis

Power Consumption	Using full adder	Using XNOR and MUX
	0.088pw	0.081pw
Area(UsedLUT)	2µm	1 µm
delay	6.837ns	5.776ns

V. CONCLUSION

A 4-2 compressor circuit based on a new XOR-XNOR designed provide better performance. The proposed XOR-XNOR design shows power consumption. The XOR provide maximum output delay of and XNOR shows delay. The performance of this circuit have been compared to earlier reported circuits in terms of power consumption, maximum output delay. The proposed circuit result shows better performance than existing circuits in all aspect.

REFERENCES

[1]. J. Liang, J. Han, F. Lombardi, "New Metrics for the Reliability of Approximate and Probabilistic Adders," IEEE Transactions on Computers,vol. 63, no. 9, pp. 1760 - 1771, 2013. and L.N. Chakrapani, "A probabilistic CMOSswitch and its realization by exploiting noise," in Proc. IFIP-VLSI SoC, Perth, Western Australia, Oct. 2005.

[2]. H.R. Mahdiani, A. Ahmadi, S.M. Fakhraie, C. Lucas, "Bio-Inspired Imprecise Computational Blocks for Efficient VLSI Implementation of Soft-Computing Applications," IEEE Transactions on Circuits and Systems I: Regular Papers, vol. 57, no. 4, pp. 850-862, April 2010.

[3]. M. J. Schulte and E. E. Swartzlander,Jr., "Truncated multiplication with correction constant," VLSI Signal Processing VI, pp. 388–396, 1993.

[4]. E. J. King and E. E. Swartzlander, Jr., "Data dependent truncated scheme for parallel multiplication," in Proceedings

[5]. V. Gupta, D. Mohapatra, S. P. Park, A. Raghunathan, K. Roy, "IMPACT: MPrecise adders for low-power approximate computing," Low Power Electronics and Design (ISLPED) 2011 International Symposium on. 1-3 Aug. 2011.

[6]. S. Cheemalavagu, P. Korkmaz, .V.Palem, B.E.S. Akgul, of the Thirty First Asilomar Conference on Signals, Circuits and Systems, pp. 1178–1182, 1998.

[7]. P. Kulkarni, P. Gupta, and MD Ercegovac, "Trading accuracy for power in a multiplier architecture", Journal of Low Power Electronics, vol. 7, no. 4, pp. 490--501, 2011.

[8]. C. Chang, J. Gu, M. Zhang, "Ultra Low-Voltage Low- Power CMOS 4-2 and 5-2 Compressors for Fast Arithmetic Circuits," IEEE Transactions on Circuits & Systems, Vol. 51, No. 10, pp. 1985-1997, Oct. 2004.

[9]. D. Radhakrishnan and A. P. Preethy, "Low-power CMOS pass logic 4-2 compressor for high-speed multiplication," in Proc. 43rd IEEE Midwest Symp. Circuits Syst., vol. 3, 2000, pp. 1296–1298.

[10]. Z. Wang, G. A. Jullien, and W. C. Miller, "A new design technique for column compression multipliers," IEEE Trans. Comput., vol. 44, pp. 962–970, Aug. 1995.

Author's Details:

B.Sateesh is working as Assistant Prof in the Dept of ECE, Vaagdevi College of Engineering, Warangal. Email:basateesh27@gmail.com.

Dr. Prabhu Benakop is working as Principal at Indore Institute of Engineering and Technology. in the ECE Department. Email: pgbenakop@ieee.org, pgbenakop@rediffmail.com.

ADMITTANCE RESPONSE OF PZT TRANSDUCERS BONDED TO A STRUCTURAL MEMBER SUBJECTED TO EXTERNAL LOADING

[1]Akshay S. K. Naidu, [2]Karthik Reddy Awala
[1]Associate Professor, [2]Research Student
Department of Civil Engineering,
Methodist College of Engineering and Technology, Hyderabad, India 500001

Abstract*—In the Electro Mechanical Impedance method (EMI) for structural health monitoring (SHM), a piezoelectric ceramic transducer (PZT) is bonded on to the structure to be regularly monitored. There exists a dynamic coupling between the mechanical impedance of the structure and the mechanical impedance of the bonded PZT transducer, which is reflected in the electrical admittance response of the PZT to frequency of its actuation, popularly called as the admittance signature. Damage or deterioration in the structure affects the mass, stiffness and damping parameters locally, which alters the mechanical impedance of the structure. This change reflects in the admittance signature of the PZT transducer by which the structural health can be assessed. External loads can also induce mass and stiffness changes locally and thus alter the admittance signature. The load induced changes in the admittance signatures have to be filtered out to get factual damage induced changes for reliable SHM. This paper presents the results of a numerical study, carried out to understand the influence of external loading on the PZT admittance signature, using coupled field FE analysis in ANSYS™.

***Index Terms*—Electromechanical Impedance (EMI), Piezoelectric transducers, Lead Zirconate Titanate (PZT), Structural Health Monitoring (SHM), Admittance Signatures, Coupled Field FE Analysis. (key words)**

I. INTRODUCTION

The structures performance assessment in terms of its service life, durability, sustaining any failure conditions has always been important criteria. The purpose of the early detection of the defects in the structures is to ensure that the structure does not disintegrate and extends its service life without much efforts investing in repairs. The conventional methods of the structural condition assessment by visual inspections and localized NDT techniques are inefficient for determining incipient damages and give early warning to the user. Especially for massive public structures, to ensure structural integrity and safety, it is essential to continuously monitor the structure at periodic intervals without much human interference. Thus, the concept of structural health monitoring (SHM) is conceived [1].

The SHM process involves (a) generation of diagnostic signals, by using passive or active sensors mounted at critical locations of the structure, (b) transmission of the signals through reliable electronic communication systems without deterioration and noise (c) analysis of the diagnostic signal to derive meaningful assessment criteria for the structure (d) structural damage and assessment metric to quantify the damage and (e) generating an alarm to give timely warning to the user. SHM technology aims at full automation of all these components without active human interference [2], [3]. Extensive research is being carried out throughout the world to achieve this goal of the SHM philosophy. Numerous techniques in SHM have been developed in each of these components [4].

The electromechanical impedance (EMI) method which utilizes the electric impedance characteristics of the piezoelectric ceramic transducers bonded to the structure has potential applications for structural health monitoring technology. Piezoelectric materials deform (strain) when an electric field is applied across their electrodes and conversely produce voltage across their electrodes due to an applied mechanical strain. This phenomenon is most prominently observed in piezoelectric ceramics, such as Lead Zirconate Titanate (PZT). This bifunctional property makes the PZT be used both as actuators and sensors. Many methods involving the PZT transducer chips use two chips, one as an actuator to generate a wave and the other as a receiver to sensor the incident wave for diagnosis. However, in the EMI method, a single PZT transducer is used to simultaneously actuate and sense the signal. Thus, in the EMI technique, the PZTs are used as self-sensing actuators [5].

To assess the structure, the diagnostic signal generated in the EMI method is the admittance signature of the PZT transducer surface-bonded to the structure, or sometimes, embedded within the concrete matrix of a structural element. The admittance signature is the electrical admittance of the PZT over a frequency range of excitation, which shall be elaborated more in the next section. Occurrence of damages in the structure, changes the pattern of the admittance signature of the PZT which is in the vicinity of the damage location. Numerous proof-of-the-concept tests have been successfully reported, and many of the technical aspects for implementation of this technique have been investigated over the past two decades[5]–[7].

For research purposes, towards understanding of the technical parameters involved in the EMI technique, many analytical or semi-analytical models have been derived and tested against the experimental investigations [8], [9]. Researchers have also demonstrated that the EMI technique can be numerically simulated by adopting the coupled field finite element analysis in ANSYS™ [9], [10]. Using this numerical simulation, the admittance signatures can be directly obtained just as we get in the experimental results. Further, by adjusting the various parameters, particularly damping parameters, a close match of the pattern of admittance signatures generated numerically with the experimentally generated signatures, has been achieved [10]. Thus, the coupled field FE simulations help in investigating the EMI technique without the need of complex experimental set-up.

In this paper, the coupled field FE analysis of the EMI technique is adopted to study the influence of loading on the admittance signature. This is so as to differentiate the admittance signature changes due to the presence of excessive load and load induced stresses, as opposed to those due to factual damages in the structure. The FE models are chosen to study the effect of induced longitudinal stresses and flexural stresses on the admittance signatures of the PZT transducer.

II. METHODOLOGY

Electromechanical Impedance Method

In the electromechanical impedance (EMI) method, the PZT transducer is excited through an alternating voltage signal using an impedance analyzer or an LCR meter, over a frequency range within 10 - 200 kHz. This induces a high frequency vibration in the PZT. The PZT, which is surface-bonded onto or embedded within the structural element, induces actuation in the structure, locally. The PZT actuates the structure at any particular frequency and the structural response is simultaneously sensed by the PZT. If the bond between the PZT and the structure is strong, there exists a coupling between the mechanical impedance of the structure and the mechanical impedance of the PZT. This coupling is reflected in the electrical admittance response of the bonded PZT at each frequency. The frequency response curve or the admittance response versus the excitation frequency range is called as the electromechanical admittance signature. The electromechanical admittance of the PZT is measured directly by the impedance measuring instrument, such as the impedance analyzer (HP 4192/4194 A) or an LCR meter (Agilent E4980A Precision LCR meter) [3], [11].

Any damage, such as a crack, debond or corrosion in the structure, alters the mass, stiffness and damping parameters locally around the damage. The mechanical impedance of the structure is dependent on the mass, stiffness and damping parameters. Thus, any damage alters the mechanical impedance of the structure locally, in the near vicinity of the damage location. Due to the impedance coupling that exists between the PZT and the structure, the changes in mechanical impedance reflects in the change in the electrical admittance of the PZT attached to the structure. Thus, change in the pattern of the admittance signature serves as the damage indicator. The changes in the admittance signatures can be statistically quantified or measured by parameter-based damage metrics [3], [11].

Numerical Simulation

Many analytical models in 1D, 2D and 3D have been developed for the EMI impedance techniques and experimentally verified. A summary of these models and their resultant equations can be obtained in the literature [5], [9], [12].

The analytical models, however, are limited to simple structures with simple geometries and boundary conditions. When the structure to be studied is relatively complex or with complicated boundary conditions, or when the targeted model involves a system of structures interacting with each other, analytical modeling is usually impossible.

Numerical models turn up to be a viable option, which often provide close enough approximation to the exact solution, satisfactory for engineering applications. Recent developments of various finite element method (FEM) based software package and advancement in computer hardware render the numerical modeling technique more attractive option.

Researchers have proposed a semi-analytical modeling approach incorporating the FE model and the impedance based model, commonly known as finite element analysis (FEA)-based impedance model. This model enables the modeling of PZT-structure interaction without the presence of PZT patch in the model, as it has been simplified and represented by a force or moment. This approach retains the simplicity of the impedance based model while utilizes the strength of FEM including the ability in modeling generic distributed structures possessing anisotropic material, mass loading and non-uniform boundary conditions.

Liu and Giurgiutiu [13] compared the real part of the impedance from both the FEA-based impedance model (non-coupled) and coupled field model of a 1-D narrow beam structure to those of the experimental tests. The coupled field model exhibited closer agreement to the experimental results.

Yang and co-researchers [9] studied the ability of coupled-field FE model in simulating the PZT-structure interaction. PZT patch surface-bonded onto aluminium structures of various shapes were simulated and compared with the experimental counterparts. The overall outcome of the numerical simulation showed excellent agreement with the experimental tests up to a frequency as high as 1000 kHz.

Advantages of FE simulation using coupled elements include: results in terms of electrical admittance can be readily obtained and compared with the experimental counterparts, higher accuracy can be achieved as the entire PZT patch can be simulated instead of being replaced by a force or moment, local modes omitted in the analytical model can be excited in the coupled field model, and the bonding layer and shear lag effect can be physically simulated.

Lim and Soh [10] showed that by adjusting material parameters and choosing an appropriate Damping Model the results obtained from the couple field. FE Simulations can have very close arrangement with the experimentally obtained signatures.

In this work we adopted the simulation method by using Lim and Soh [10].

Coupled Field Finite Element Simulation

In ANSYS™, piezoelectric analysis comes under the category of coupled field analysis. Coupled-field analysis considers the interaction or coupling between two or more disciplines of engineering. Piezoelectric analysis caters for the interaction between structural and electric fields.

Coupled-field analysis derives solutions to problems not possible with the usual FEM, by simplifying the modeling of coupled-field problems. Piezoelectric analysis makes use of direct coupling method, which involves only one analysis with the use of one coupled-field element containing all necessary degrees of freedom.

This formulation is very convenient for evaluating the admittance signatures used in the EMI technique. The complex electrical admittance signature, which is the ratio of electric current to voltage, can be expressed as:

$$\bar{Y} = \frac{\bar{I}}{\bar{V}}$$

where $\bar{Y}$ is complex electrical admittance of the PZT, $\bar{V}$ is the sinusoidal voltage applied and $\bar{I}$ is the modulated current in the PZT, with the bars above indicating complex terms. When the voltage is taken as $\bar{V} = 1 + 0i$, the output current directly gives the electrical admittance.

By performing Harmonic Analysis and extracting the current as output we can obtain the admittance signature. The details of the steps involved in modeling and harmonic analysis were similar to those used in the literature [10], [14].

III. FE SIMULATIONS AND CASES

Two simple models are considered in this study with the aim of understanding the influence of loading on the admittance signatures. A prismatic member is considered of dimensions: L= 0.3 m; b = 0.02m; h = 0.002m {30cm x 2cm x 0.2cm}.

Two cases of loading are considered:

a) Axially loaded member: Fixed support at the top of the member, which is acting under gravity and subjected to loading at the bottom. The loading is simulated by varying the density at the last 1 cm strip of the beam. The densities were increased to a limit below the yield

strength of the material. This beam would experience axial stresses. The PZT is located at one-third of the length of the member and at the center of the width, as shown in Figure 1(a).

b) Simply supported beam subjected to flexural stress: The same prismatic member is subjected to flexural loading. The load is induced by placing a block of mass at the centre of the span. Increasing the densities of the mass simulates increase in the load. Two PZTs are bonded at 1/3rd length from the end, one on top layer which can determine the compression stresses and one at the bottom layer for determining the tensile stresses. Densities for the mass block are varied below the yield strength of the material of the beam. This beam would experience flexural stresses. The illustrations are shown in Figure 1(b).

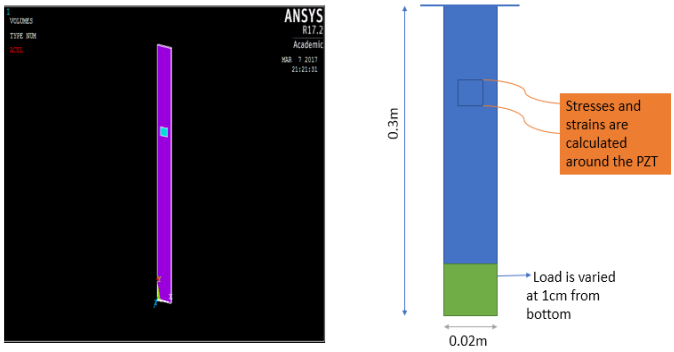

(a) Axial loading on a prismatic member

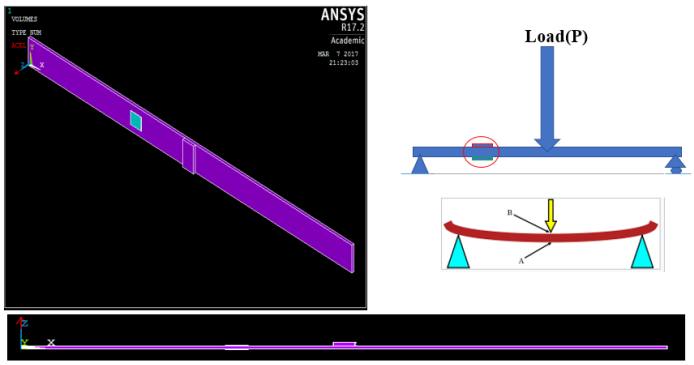

(b) Flexural loading on a beam member

Figure 1 Ansys Modelling of the (a) Axial Load on the Member (b) Flexural Load on the Member

Details of the FE model

Some features of the FE model are as follows:

Element Types Used:

(a) Solid 45 for material of the beam:

This is a 3D 8-noded brick element having three degrees of freedom at each node: translations in the nodal x, y, and z directions.

(b) Solid 45 for piezoelectric material:

This is a 3D 8-noded coupled field element with multi-physics capabilities in particular piezoelectric properties.

Material Properties

(a) Structural Material Properties: The material used for the prismatic member or the beam was metallic with the following material properties as given in Table 1.

Table 1 Properties for the Structural Material

Property	**Notation & Value**
Young's Modulus	$E = 6.89 \times 10^{10}$ N/m^2
Density	$\rho = 2600$ kg/m^3
Poisson's ratio	$\nu = 0.3$
Hysteretic damping ratio	$\xi = 0.0005$

(b) Piezoelectric Material Properties: The material used for the PZT is based of PI 155 of the PI Ceramic, a German company, which has been used by earlier researchers, with the following material properties as given in Table 2

Table 2 Properties for the PZT material

Parameters	**Symbols**	**Values**	**Units**
Density	ρ	7800	kg/m^3
Compliance	$s_{11} = s_{22}$	15	10^{-12} m^2/N
	s_{33}	19	
	$s_{12} = s_{21}$	-4.5	
	$s_{13} = s_{31}$	-5.7	
	$s_{23} = s_{32}$	-5.7	

	$s_{44}= s_{55}$	39	
	s_{66}	49.4	
Electric permittivity	ε^T_{11}	1980	
(Relative values)	ε^T_{22}	1980	
	ε^T_{33}	2400	
Piezoelectric strain coefficients	d_{31}	-210	10^{-12} C/N
	d_{32}	-210	
	d_{33}	500	
	d_{24}	-	
	d_{15}	580	
Mechanical quality factor	Q_m	100	
Damping ratio (Hysteretic)	$\xi_{PZT} = (2Q_m)^{-1}$	0.005	

FE Meshing

Mesh used: Hexagonal meshing type. Cube shaped meshes of dimension 1 mm. Both the PZT and the structural beam were meshed with the same mesh for compatibility.

Loading

As presented earlier, long prismatic beam subjected to axial loading and a simply supported beam subjected to flexural loading are considered for this numerical study.

The axial load in the cantilever beam is induced by increasing the density of the bottom segment of the beam, which is subjected to gravity. Whereas, in simply supported beam, flexural load is induced by placing a mass block at the center, and increasing the density of that block. The thickness of the block is taken as h, same as the thickness of the beam. The width of the block is same as the width

Thus, the various values of densities to increase the mass of the block for simulating loading are as follows in Table 3:

Table 3 Load Cases Considered in terms of densities of the loading block

Load Case	1	2	3	4	5
Density (in kg/m^3)	2600	10000	25000	50000	75000

The maximum limit for the densities is calculated from the yield point as follows:

Bending equation,

$$\frac{M}{I} = \frac{f}{y} = \frac{E}{R} \quad (1)$$

where,

M = bending moment; I = moment of inertia; f = bending stress; E= Young's modulus; R= radius of curvature; y = perpendicular distance from the neutral axis;

Consider,

$$M = \frac{I}{y} f = Z f_{\max} = \frac{bd^2}{6} f_{\max} \quad (2)$$

$$f_{\max} = \frac{6M}{bd^2} \le f_y \quad (3)$$

Equating to the extreme value to the yield point, and writing the bending moment M, in terms of the density ρ and dimensions of the loading block, we get

$$\rho \le \frac{2}{3} \frac{f_y}{Lhg} bd^2 \quad (4)$$

Taking the yield point of Aluminium from standard values of the texts, the density was calculated and the maximum limit was restricted to the above below.

$$\rho = 75025 \text{ kg/m}^3 \quad (5)$$

This is done to ensure that the flexural loading stresses the beam within its elastic limit of the material of the beam.

Analysis Types

Three different analyses were performed:

(i) Static analysis: This was done to calculate the stresses and strains developed in the beam at the location where the PZT is bonded. Three points under the beam were selected, two at the edges and one at the centre, and the stresses and strains were noted at these points an average was calculated.

(ii) Modal analysis: This was done to identify the natural frequencies of the beam mounted with the PZT, and to study the changes in the natural frequencies due to changes in the load condition. First twenty modal frequencies were considered for this purpose and compared. Block Lancoz eigen value extraction method was adopted in ANSYS™.

(iii) Harmonic analysis: The harmonic signature of admittance (real or imaginary) vs frequency is what is typically obtained in a real experimental set-up. Studying the changes in the harmonic admittance signature with various load cases is the key objective for the purposes of Structural Health Monitoring. The peaks in the signatures obtained from Harmonic analysis occur at points, corresponding to the natural frequencies of the system. Changes in the location of the peak in these signatures, are indicative of natural frequency shifts, which in turn gives insight into structural integrity.

IV. Results and Discussion

For Axial Loading Case

Static Analysis:

Static analysis was used for correlating load conditions to stresses developed below the PZT transducer in structural components caused by only steady-state inertial forces such as gravity. The axial stresses increase in magnitude as shown in Figure 2.

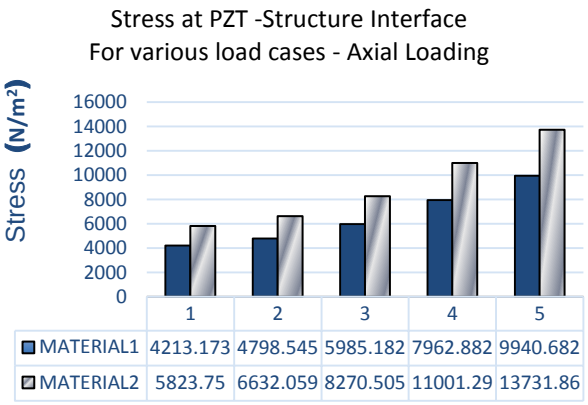

Figure 2: Axial stresses in the prismatic member at the PZT bottom – structure interface
Material 1 is for the PZT and Material 2 is the structural material (Aluminium)

Modal Analysis:

Modal frequency for any structure is certain natural frequency at which it vibrates freely without any external force. It is observed that natural frequency reduces when the load increases. The values of the first 20 modal frequencies for various loads is presented in Table 4. It can be noted for the same amount of load the changes in frequency in the higher modes is greater. This change in the frequencies of load cases 2, 3, 4 and 5 as compared with the load case 1 (which is the case of no external load) is shown in Table 5. Higher frequency modes are capable of notifying any changes or damages in the structure more effectively as compared to the lower frequency modes. As EMI method typically operates in the order of kHz, it is very sensitive in detecting even small changes.

Table 4 Natural Frequencies of the member with PZT for various axial loading cases

	Load Cases (as per Table 3)				
	1	2	3	4	5
Mode	Structural Natural Frequencies (in Hz)				
1	18.6	15.9	12.8	10.2	8.7
2	116.0	104.0	95.3	90.4	85.9
3	184.4	157.9	127.0	100.6	88.4
4	325.0	299.4	285.3	278.6	275.7
5	526.8	480.9	412.3	340.9	296.4
6	638.2	599.2	581.2	572.2	567.7
7	1055.7	1004.0	928.1	879.7	858.7
8	1126.8	1013.1	981.9	968.6	959.8
9	1572.6	1446.4	1306.9	1213.4	1172.9
10	1577.8	1513.9	1485.8	1463.5	1445.0
11	2205.6	2129.7	2091.8	2052.1	2014.9
12	2650.1	2457.8	2309.9	2237.9	2210.5
13	2938.2	2819.0	2679.8	2602.4	2430.9
14	3055.0	2849.6	2795.7	2726.0	2561.7
15	3742.2	3516.8	3372.0	2793.6	2660.2
16	3776.3	3672.7	3386.4	3329.2	3304.8
17	4291.9	3925.2	3594.0	3480.1	3383.4
18	4719.4	4571.3	4456.3	4315.6	4201.1
19	4819.4	4597.6	4480.6	4401.5	4366.7
20	5767.9	5436.9	5243.9	5104.9	5000.9

Table 5: Natural Frequency reduction values of the structure for load cases as compared to the first load case (axial loading).

	Load Cases (as per Table 3)			
Mode	2	3	4	5
	Frequency Reductions (in Hz)			
1	2.7	5.8	8.5	10.0
2	11.9	20.7	25.6	30.1
3	26.5	57.4	83.7	95.9
4	25.5	39.6	46.4	49.2
5	45.9	114.5	185.9	230.5
6	39.0	57.0	66.0	70.5
7	51.7	127.6	176.0	197.0
8	113.7	144.9	158.2	167.0
9	126.2	265.7	359.2	399.7
10	63.9	92.0	114.3	132.8
11	75.9	113.8	153.5	190.7
12	192.3	340.2	412.2	439.6
13	119.2	258.4	335.8	507.3
14	205.4	259.3	329.0	493.3
15	225.4	370.2	948.6	1082.0
16	103.6	389.9	447.1	471.5
17	366.7	697.9	811.8	908.5
18	148.1	263.1	403.8	518.3
19	221.8	338.8	417.9	452.7
20	331.0	524.0	663.0	767.0

Harmonic Analysis:

Harmonic response analysis gives the forced vibration response of the electrical admittance of the surface-bonded PZT transducer with the exciting frequency. The idea is to calculate the structures response at several frequencies (0 to 5 kHz) and obtain a graph of some response quantities versus frequency. We considered the real admittance (conductance) versus frequency, as this is the most commonaly used in the EMI method.

From these conductance signatures, the "peak" responses are then identified on these graphs for further study analysis. The peaks correspond to the resonance of the exiciting frequency with the structural natural frequency. Thus, the frequencies of the peaks can be correlated with the natural frequencies in the Table 4. The conductance signatures are extracted from 0-5000 Hz frequency values. For clear and a closer view representation, few sets of the graphs of conductance signatures are considered over a limited frequency range. Figure 3 shows the conductance signature for axially loaded prismatic member for the frequency range of 1400 – 1600 kHz. Figure 4 shows the conductance signature for axially loaded prismatic member for the frequency range of 1400 – 1600 kHz.

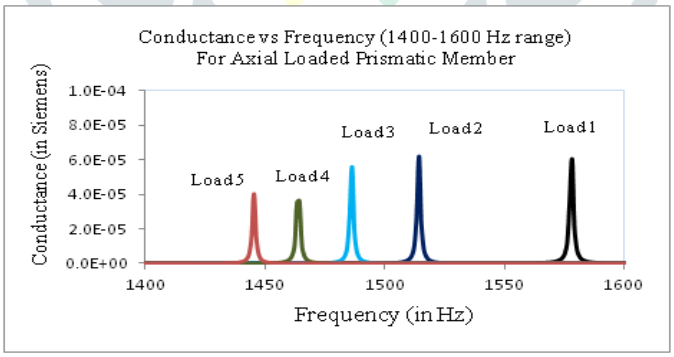

Figure 3: Conductance Signature for axially loaded prismatic member (1400-1600 Hz frequency range)

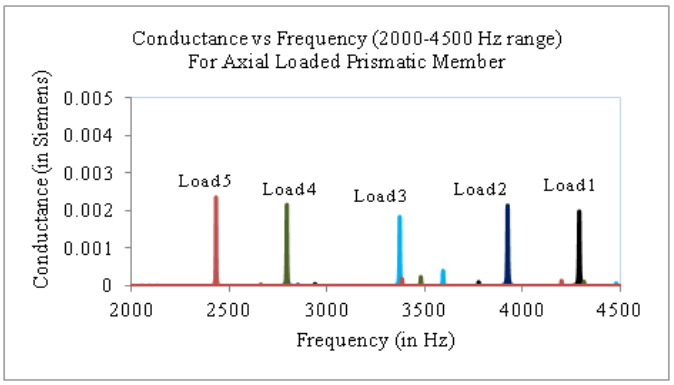

Figure 4: Conductance Signature for axially loaded prismatic member (2000-4500 Hz frequency range)

From both the figures, we can observe that with increase in load the conductance signatures shift leftwards, that is for the same mode the natural frequency values of the structure are reducing. These natural frequencies correspond to the peaks in the conductance signature. From the basic structural dynamics, we know that the natural frequency of a system is directly proportional to the square rooot of the stiffness and is inversely proportional to the square rooot of the lumped mass. Although the load increases the axial stress in the member, and tends to increase the dynamic stiffness, the natural frequencies do not increase. Here the load is induced by increasing the mass and not just applying the force. Thus, with increase in mass the natural frequencies reduce in values. This trend shown here is opposed to the trends seen in the works of [15]–[17].

For Flexural Loading Case

In similar lines as in the axial loading case, the flexural loading case results are also observed.

Static Analysis:

From static analysis, the stresses developed at the PZT-structure interface, both on the PZT transducer and the structure, are observed. In this case, however, there are two PZTs, one on the compression layer and the other on the tension layer. The axial stresses developed at the PZT-structure interface for both these cases are shown in Figures 5 and 6, respectively. Clearly, the magnitude of flexural stresses in increasing with the increase in the load.

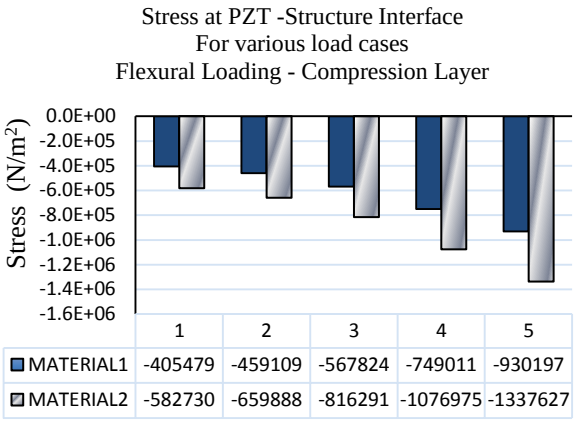

Figure 5: Flexural stresses in the compression layer of the simply supported beam member at the PZT – Structure Interface for various load cases Material 1 is for the PZT and Material 2 is the structural material (Aluminium)

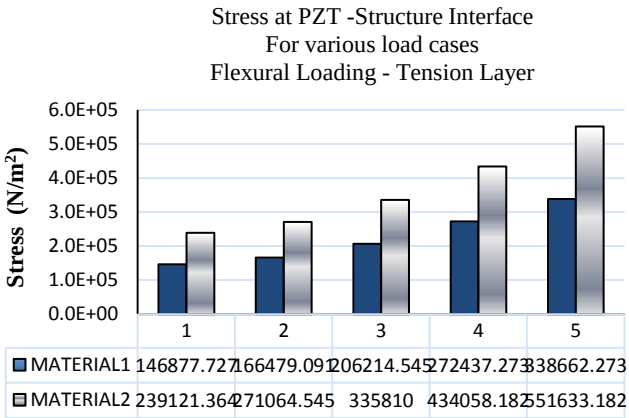

Figure 6: Flexural stresses in the tension layer of the simply supported beam member at the PZT – Structure Interface for various load cases Material 1 is for the PZT and Material 2 is the structural material (Aluminium)

Although the signs of the stresses are different in both the cases of compression and tension, as expected, we can see the increase in the magnitudes of the stresses in both the cases with the increase in loading. Another, observation is that the magnitudes of the compressive and tensile stresses are different, which is usually not the case in flexural stresses in beams. This might be due to the difference in the stiffness effects produced by the PZT under tension and in compression. This, however, is not fully understood and needs further investigation.

Modal Analysis:

Similar to the axial loading case, the modal analysis results for the flexurally loaded simply supported beam is presented herein. It is again observed that natural frequency reduces when the load increases. The values of the first 20 modal frequencies for various loads is presented in Table 6. It can be again noted that for the same amount of load the changes in frequency in the higher modes is greater. This change in the frequencies of load cases 2, 3, 4 and 5 as compared with the load case 1 (which is the case of no external load) is shown in Table 7. In some cases such as mode numbers 2, 4, 8, 9 and 11, and so on, we find that the frequency reduction values are extremely less compared to the other modes. This is because of the presence of vibrational nodes at the location of the load, either in the flexural or torsional modes of vibration. These observations are also helpful in identifying damage locations [3].

Table 6: Natural Frequencies of the member with PZT for various axial loading cases

	Load Cases as per Table 3				
	1	2	3	4	5
Mode	Structural Natural Frequencies (in Hz)				
1	81.718	75.044	65.324	55.091	48.513
2	207.17	207.09	206.92	206.64	206.37
3	512.83	484.86	453.96	430.45	418.92
4	829.09	826.75	732.75	599.09	517.14
5	908.56	846.64	787.99	675.1	601.75
6	1027	916.53	822.01	814.09	806.18
7	1361.9	1303	1249.3	1215.1	1200
8	1867.6	1861.4	1848.8	1827	1804.5
9	2152.4	2151.9	2150.8	2149	2147.1
10	2619.1	2528.6	2457.8	2417.5	2400.8
11	2682.4	2677.3	2654.9	2494	2418.9
12	3093.4	2882.1	2667.2	2650.4	2633.7
13	3304.6	3264.8	3179.9	3031.9	2887.3
14	4331.4	4212.9	4129.7	4085.5	4021.3
15	4438.9	4436.9	4279.2	4106.2	4067.7
16	4854.2	4540	4434.7	4429	4423.1
17	5133.9	5096.4	4977.7	4814.1	4653.8
18	5440.5	5214.9	5019.1	4888.6	4741.9
19	6425.9	6279.5	5826.5	5089.8	4778.9
20	6871.3	6532	6185.6	6137.9	6118.7

Table 7: Natural Frequency reduction values of the structure for load cases as compared to the first load case (flexural loading).

	Load Cases (as per Table 3)			
	2	3	4	5
Mode	Frequency Reductions (in Hz)			
1	6.7	16.4	26.6	33.2
2	0.1	0.3	0.5	0.8
3	28.0	58.9	82.4	93.9
4	2.3	96.3	230.0	312.0
5	61.9	120.6	233.5	306.8
6	110.5	205.0	212.9	220.8
7	58.9	112.6	146.8	161.9
8	6.2	18.8	40.6	63.1
9	0.5	1.6	3.4	5.3
10	90.5	161.3	201.6	218.3
11	5.1	27.5	188.4	263.5
12	211.3	426.2	443.0	459.7
13	39.8	124.7	272.7	417.3
14	118.5	201.7	245.9	310.1
15	2.0	159.7	332.7	371.2
16	314.2	419.5	425.2	431.1
17	37.5	156.2	319.8	480.1
18	225.6	421.4	551.9	698.6
19	146.4	599.4	1336.1	1647.0
20	339.3	685.7	733.4	752.6

Harmonic Analysis:

The conductance signatures obtained for the PZTs located in the compression layer and the tension layer, for a small frequency range of 2800-3400 Hz, is shown in Figures 7 and 8, respectively. The frequencies of the peaks can be correlated with the natural frequencies in the Table 6. The conductance signatures are extracted from 0-5000 Hz frequency values.

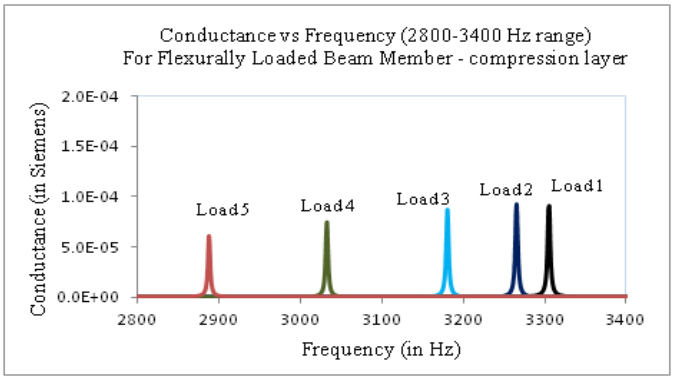

Figure 7: Conductance Signature for flexurally loaded simply supported beam member for PZT in the compression layer (2800-3400 Hz frequency range)

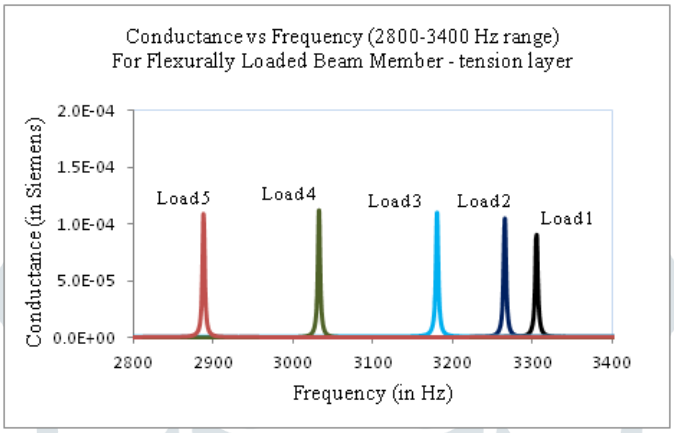

Figure 8: Conductance Signature for flexurally loaded simply supported beam member for PZT in the tension layer (2800-3400 Hz frequency range)

From both the figures, it can be observed that with increase in load the conductance signatures shift leftwards, that is for the same mode the natural frequency values of the structure are reducing. The values of the peaks seam to decrease in the compression zone while these peak values seem to increase in the tension zone. The values of the peaks are closely related to the damping parameters locally, study and discussion of which is beyond the scope of this work.

Again we observe that as the load increases the flexural stresses in the member, the natural frequencies do not increase, rather thet decrease. Again, the load is induced by increasing the mass and not just applying the force. Thus, with increase in mass the natural frequencies reduce in values. This trend shown here is opposed to the trends seen in the previous works as aforementioned.

It is also note that the compression and tension zone give same pattern shifts, that the frequency reduction values is the same. Thus, by this analysis presented in this paper, the compressive or tensile nature of the stresses cannot be distinguish using the PZT admittance signatures.

It may be noted that on occurrence of a damage the pattern of frequency shifts for various modes is not uniform, as it can be seen in the case of the pattern seen for the loading case[11], [18]. This difference can be utilized for identifying pattern changes for induced load versus factural; structural damage cases.

V. CONCLUSIONS

In this work, the coupled field FE modeling of the EMI technique is adopted to study the influence of loading on the admittance signature. The FE models of a prismatic member are chosen with axial and flexural loading to study the effect of induced longitudinal stresses and flexural stresses on the admittance signatures of the PZT transducer bonded on to the member.

For both the models, as load is increased, the resultant stress increased at the PZT-structure interface. An important observation is that for the same amount of load, the higher modes result in a larger frequency reduction shifts when compared to the lower modes. This result concurs with the findings of the previous researchers that the higher frequency modes are more sensitive to changes in the structural parameters. Thus, the EMI technique using PZT sensors, which typically operates at ultrasonic frequencies actuating the higher modal frequencies, is more sensitive for SHM purposes than the conventional vibration based NDT methods, where only the first three or four modes are only considered.

Usually, we may expect that axial load will increase the stiffness of a structural member and thus, natural frequencies may increase. However, as loads are induced by gravity applied on the mass blocks, increase in the mass results is decrease in frequencies, as observed in this investigation. Thus, it can be said that the structural member response is dominated by mass over the stiffness parameter.

In the case of flexural loading, since the load is concentrated at the center and applied on the top surface, the stresses on the top compression layer was observed to be higher compared to the bottom tension layer. In modal analysis, we observe that for certain modes there are negligible natural frequency shifts with increasing loads. This is because for those modes, the vibration nodes (points of zero displacement) coincide with the position of load. resulting in low frequency shifts.

For the same loading condition, the shift in compression and tension have similar peak pattern. Essential conclusion is that natural frequencies correlate with the stresses, but does not indicate whether the beam surface is in compression or in tension.

The results presented in this paper shall be useful to the researchers who would be interested in further analysis of the EMI method, especially in the area of pattern recognition of the changes in the admittance signatures due to structural damage identification and induced stress.

REFERENCES

[1] C. R. Farrar and K. Worden, "An introduction to structural health monitoring," *Philos. Trans. R. Soc. Lond. Math. Phys. Eng. Sci.*, vol. 365, no. 1851, pp. 303–315, 2007.

[2] S. Bhalla, "Smart system based automated health monitoring of structures," M.Engg. Thesis, Nanyang Technological University, Singapore, 2001.

[3] A. S. K. Naidu, "Structural damage identification with admittance signatures of smart PZT transducers.," PhD Thesis, Nanyang Technological University, Singapore, 2004.

[4] H. Sohn *et al.*, *A review of structural health monitoring literature: 1996-2001*. Los Alamos National Laboratory Los Alamos, NM, 2004.

[5] V. G. M. Annamdas and C. K. Soh, "Application of electromechanical impedance technique for engineering structures: review and future issues," *J. Intell. Mater. Syst. Struct.*, vol. 21, no. 1, pp. 41–59, 2010.

[6] G. Park, H. Sohn, C. R. Farrar, and D. J. Inman, "Overview of piezoelectric impedance-based health monitoring and path forward," *Shock Vib. Dig.*, vol. 35, no. 6, pp. 451–464, 2003.

[7] V. G. Annamdas and M. A. Radhika, "Electromechanical impedance of piezoelectric transducers for monitoring metallic and non-metallic structures: A review of wired, wireless and energy-harvesting methods," *J. Intell. Mater. Syst. Struct.*, vol. 24, no. 9, pp. 1021–1042, 2013.

[8] Y. Yang, Y. Y. Lim, and C. K. Soh, "Practical issues related to the application of the electromechanical impedance technique in the structural health monitoring of civil structures: I. Experiment," *Smart Mater. Struct.*, vol. 17, no. 3, p. 35008, 2008.

[9] Y. Yang, Y. Y. Lim, and C. K. Soh, "Practical issues related to the application of the electromechanical impedance technique in the structural health monitoring of civil structures: II. Numerical verification," *Smart Mater. Struct.*, vol. 17, no. 3, p. 35009, 2008.

[10] Y. Y. Lim and C. K. Soh, "Towards more accurate numerical modeling of impedance based high frequency harmonic vibration," *Smart Mater. Struct.*, vol. 23, no. 3, p. 35017, 2014.

[11] A. S. K. Naidu and C. K. Soh, "Identifying damage location with admittance signatures of smart piezo-transducers," *J. Intell. Mater. Syst. Struct.*, vol. 15, no. 8, pp. 627–642, 2004.

[12] Y. Y. Lim, W. Y. H. Liew, and C. K. Soh, "A Parametric Study on Admittance Signatures of a PZT Transducer Under Free Vibration," *Mech. Adv. Mater. Struct.*, vol. 22, no. 11, pp. 877–884, 2015.

[13] W. Liu and V. Giurgiutiu, "Finite element simulation of piezoelectric wafer active sensors for structural health monitoring with coupled-filed elements," in *The 14th International Symposium on: Smart Structures and Materials & Nondestructive Evaluation and Health Monitoring*, 2007, p. 65293R–65293R.

[14] S. Moharana and S. Bhalla, "Numerical investigations of shear lag effect on PZT-structure interaction: review and application," *Curr. Sci.*, vol. 103, no. 6, pp. 685–696, 2012.

[15] C.-W. Ong, Y. Yang, A. S. Naidu, Y. Lu, and C. K. Soh, "Application of the electro-mechanical impedance method for the identification of in-situ stress in structures," in *SPIE's International Symposium on Smart Materials, Nano-, and Micro-Smart Systems*, 2002, pp. 503–514.

[16] Y. Y. Lim and C. K. Soh, "Effect of varying axial load under fixed boundary condition on admittance signatures of electromechanical impedance technique," *J. Intell. Mater. Syst. Struct.*, p. 1045389X12437888, 2012.

[17] V. G. M. Annamdas, Y. Yang, and C. K. Soh, "Influence of loading on the electromechanical admittance of piezoceramic transducers," *Smart Mater. Struct.*, vol. 16, no. 5, p. 1888, 2007.

[18] A. S. K. Naidu and C. K. Soh, "Damage severity and propagation characterization with admittance signatures of piezo transducers," *Smart Mater. Struct.*, vol. 13, no. 2, p. 393, 2004.

International Journal of Emerging Technology and Advanced Engineering
Website: www.ijetae.com (ISSN 2250-2459, ISO 9001:2008 Certified Journal, Volume 7, Special Issue 2, December 2017)

Design and Examination of 6T SRAM Operation and Its Architecture

[1]B. Satheesh
Research Scholar, Dept. of ECE
JNTU Hyderabad
Telangana, India
basateesh27@gmail.com

[2]Dr. Prabhu Benakop
Principal
Indur Institute of Engineering &Technology
Siddhipet, Telangana, India
pgbenakop@ieee.org

Abstract: **Today's' natural philosophy worlds ask for towards additional and additional low power and high speed performance. So, SRAM is embedding in each integrated circuit(IC) for higher performance. This paper explores the look of 256 bit Static Random Access Memory (SRAM) with facilitate of 6-T cell in 65nm and 45nm CMOS technology node, specializing in optimizing delay and average power dissipation, and conjointly compared in terms of write interval, browse interval and average power dissipation mistreatment LT spice IV and layout of 1bit memory has been performed. Low power memory is given most priority in VLSI style. The facility is most significant facet for today's technology. Therefore the power reduction for one cell is that the important role in memory style techniques. Because the technology growing moveable device (e.g. Cell phone, PDA) will increase, the Static Power Consumption (Leakage Power) became a major issue. Leak current in standby mode is that the major a part of power loss. We have a tendency to focus on the technique that to cut back the leak current in standby mode. The one CMOS semiconductor device leak current owing to varied parameters is that the essential role of power consumption. The CMOS leak current to the method level may be attenuated by mistreatment sleepy headed keeper technique. The benefits during this technique area unit ultra-low leak with twin 5th, state-saving, less space penalty and quicker than alternative techniques like sleepy headed stack approach, sleep, Zig Zag.**

Keywords: **6-T SRAM cell, 65-45nm, layout, write interval, browse interval, power dissipation**

1. INTRODUCTION

From the 20th century to up to these days, semiconductor natural philosophy becomes additional and additional dominates in each space. Nowadays, it's become a world trade value billions of bucks. Up to date society uses all manner of electronic devices in-built machine-driven or semi-automated factories operated by the trade. Our daily lives area unit considerably full of natural philosophy, electronics technology. This is often true on the domestic scene, in our everyday life.

Indeed, there's little question that revolutionary changes have taken place in a very comparatively short time and it's conjointly bound that even additional dramatic advances are going to be created within the next decades. This sort of domination of industry has been arisen as a result of fast advancement and drastically improvement in integration technology. Over the past 3 decades, CMOS technology scaling has been a primary driver of the industry and has provided a path toward each denser and quicker integration. The transistors factory-made these days area unit twenty times quicker and occupies but a hundred and twenty fifth of the world of these engineered twenty years past. Because the channel length is reduced, the performance improves, the facility per shift event decreases, and therefore the density improves. Domination of digital VLSI styles, on chip memory is additional essential. Mostly, SRAM is employed as a cache memory in trendy SoCs and it's used SRAM memory is employed in a very heap of devices wherever speed is additional crucial than capability. Here SRAM enforced through deep submicron CMOS technology as a result of its low static power consumption quick shift and its noise immunity.

Semiconductor memory technology is an important part of today's natural philosophy. Ordinarily primarily based around semiconductor technology, memory is employed in any instrumentality that uses a processor of 1 type or another. So as processors became additional standard and therefore the range of microchip controlled things has inflated therefore has the need for semiconductor memory. An extra driver has been the very fact that the package related to the processors and computers has become additional refined and far larger, and this too has greatly inflated the need for semiconductor memory. in sight of the pressure on memory, new and improved semiconductor memory technologies area unit being researched and development may be terribly fast. Even so, the additional mature semiconductor memory technologies area unit still in widespread use and can stay therefore for several years to return.

International Journal of Emerging Technology and Advanced Engineering
Website: www.ijetae.com (ISSN 2250-2459, ISO 9001:2008 Certified Journal, Volume 7, Special Issue 2, December 2017)

Additionally to those new applications like digital cameras, PDAs and plenty of additional applications have given rise to the requirement to recollections. Consequently it's not uncommon to examine semiconductor recollections of eight GB and far additional needed for varied applications. With the zoom within the demand for semiconductor recollections there are variety of technologies and kinds of memory that have emerged. Names like store, RAM, EPROM, EEPROM, non-volatile storage, DRAM, SRAM, SDRAM, and therefore the terribly new MRAM will currently be seen within the natural philosophy literature. Each has its own benefits and space within which it's going to be used.[1] [2]

Previously several works had been wiped out the sector of leak Current reduction mistreatment completely different techniques like Sleep, Sleep, Zigzag, Stack, Sleepy-Stack, leak feedback in numerous circuits.

Here we have a tendency to gift a replacement VLSI technique to cut back leak power, the sleepy headed Keeper Technique provides associate degree economical thanks to cut back leak power, however disadvantage of this method increase the delay because the semiconductor device area unit inflated. during this paper 6TSRAM cell was designed with sleepyheaded Keeper technique and analyze the leak, Dynamic power consumption and Static power consumption in numerous topology.

2. GENERALIZED SRAM ARCHITECTURE

Conceptually, SRAM design is drawn below. It consists memory cell array, write driver and precharge circuit, raw and column decoder, sense electronic equipment, knowledge lines-data in and out. If numbers of address lines area unit m and numbers of information lines area unit n, then total size of memory may be obtained as 2m+n.where standard numbers of m and n area unit eight, 16, 32, 64, 256 etc. during this design, rows denote word lines that indicate for choosing explicit memory cell and column denote bit and bit-bar lines for inserting and retrieving knowledge from it. Separate write driver and sense electronic equipment area unit dedicated to every column for quick browse and write operation. This design possesses quick write and skim operation owing to its differential writing and sensing theme.

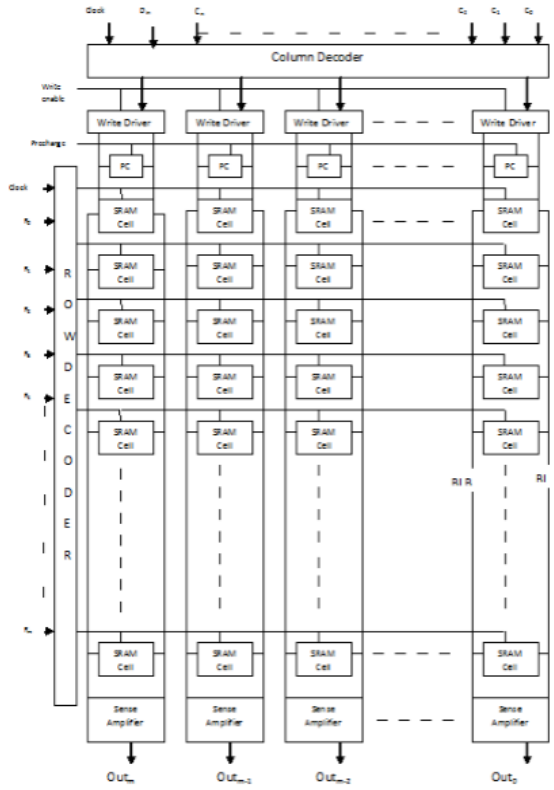

Fig.1 Detailed SRAM Architecture

Memory cell is an important part of SRAM that stores digit voltage level. A 6T CMOS SRAM cell is that the hottest SRAM cell owing to its superior hardiness, low power and low-tension operation. SRAM uses bistable latching electronic equipment to store every bit. The six-transistor (6T) SRAM cell is shown in fig. 2, within which Q3 and this autumn PMOS area unit pull up transistors, Q1 and Q2 NMOS area unit driver transistors. Access to the cell is enabled by the word line that controls the 2 access transistors Q5 and Q6 (NMOS as a pass transistor) that, in turn, management whether or not the cell ought to be connected to the bit lines: BL and BLB. They accustomed transfer knowledge for each browse and write operations. though it's not strictly necessary to possess 2 bit lines, each the signal and its inverse area unit usually provided so as to boost noise margins. The bilateral structure of SRAM memory cells conjointly permits for differential signaling, that makes tiny voltage swings additional simply detectable. this sort of memory cell retains state either zero or one as long as power activate that doesn't refresh sporadically as DRAM cell.

International Journal of Emerging Technology and Advanced Engineering
Website: www.ijetae.com (ISSN 2250-2459, ISO 9001:2008 Certified Journal, Volume 7, Special Issue 2, December 2017)

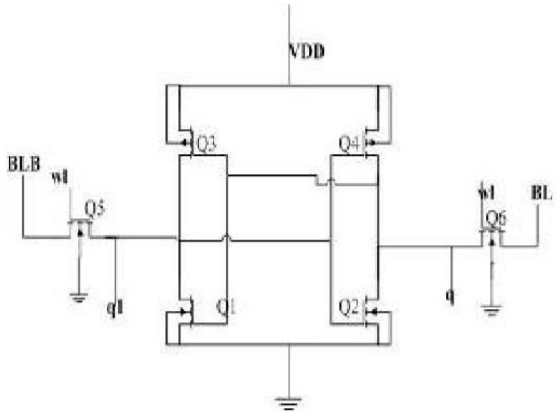

Fig.2 6-transistor memory cell

3. SRAM WITH VARIOUS DESIGN TECHNIQUES

3.1. SPRAM Design

A 32-mb spin-transfer torque RAM (SPRAM) with 2TIR memory cell, an access time of 32 ns and cell write-time of 40 ns at a supply voltage of 1.8V. This SPRAM has three circuit technologies used for the design of large-scale array [24], 1) Two transistors and one resistor
(2T1R) type memory cell are used to design a small size memory cell at sufficiently large write current despite. 2) A separate read/write compact hierarchy of bit/source-line structure is used with a localized bi-directional write driver for the efficiency of distribution write current. 3) It is used for the performance of stable read operation to design a scheme of '17 'O' dual- array equalized reference.

3.2. Charge-Recycling SRAM Design

A low-power SRAM using bit-line can be used for charge-recycling, and for performing read and write operation. This charge-recycling SRAM (CR-SRAM) technique reduces the power of read/write by recycling the charge in bit-lines. When N-bit-lines recycle their charge, the voltage of bit-lines is reduced to 1/N and the power of bit-lines is reduced by 1/N respectively. Byung-Do Yang et al, proposed Charge-recycling SRAM. This technique utilizes hierarchical bit-line architecture to perform charge-recycling without using static noise margin degradation in memory cell [25],

3.3. Adaptive Dynamic Word-Line under Drive Design

A 32 nm high-K metal gate SRAM with adaptive dynamic stability enhancement for low- voltage operation on word-line under drive (ADWLUD) scheme uses a bit, cell-based sensor to dynamically optimize the strength of WLUD for each die. Pramod Kolar et al, introduced sensor tracks process corners and temperature shifts allowing dynamically adjusting WLUD. The sensor area overhead is limited to 0.02% and power overhead is limited to 2% for a 34 mb SRAM array [26],

3.4. Data-Aware-Feedback-Cutoff Design

A 9T-SRAM cell with a data-aware-feedback-cutoff (DAFC) scheme is used to increase the write margin and a dynamic-read-decoupled (DRD) scheme in order to prevent read-disturb,
for achieving the deep sub-threshold operation. Upto 30 mV, a negative-pumped voltage is applied to the unselected word lines to suppress the bit-line leakage current. The 32 kb, 9T SRAM cells are stable for performing read and write operation at 105 mV. The shorter bit¬line length overcomes the bit-line leakage issue [27], This 9T SRAM cell is enabled at low- VDDmin sub-threshold chip feasibility for ultra-low-power application as well as energy harvesting based low-voltage systems.

5. SRAM OPERATION

Basically, SRAM operations area unit synchronous with its peripherals and given as knowledge write, browse and hold.

Write operation

The write operation means that no matter knowledge write into the SRAM cell. The write operation is similar to a reset operation of associate degree SR latch.. once one in every of the bit lines, BL in fig. 2, is driven from pre-charged worth (VDD) to the bottom potential by a write driver through semiconductor device Q6. If transistors this autumn and Q6 area unit properly sized, then the cell is flipped and its knowledge is effectively overwritten. For a regular 6T SRAM Cell, writing is completed by lowering one in every of the bit lines to
ground whereas declarative the word line at this point. Normally, to reduce the cell space and thence, increase the packing density, the sizes of the pull-up and access transistors area unit chosen to be marginal and some identical. However, stronger access transistors and/or weaker pull-up transistors is also required to make sure a sturdy write operation underneath the worst method conditions e.g., within the quick PMOS and slow NMOS method skew corner.

Read operation

A browse operation means that no matter knowledge store in SRAM Cell, that is browse by the sense electronic equipment. once applying browse modify at access semiconductor device of sense electronic equipment, same input at native pre-charge, and insertion of word line to memory cell, no matter knowledge in memory cell seems at sense electronic equipment output node. For this operation

standing of memory has been explained. In browse operation, the bit lines area unit precharged to VDD. once these pre-charged lines connect with memory cell to sense electronic equipment, sense electronic equipment detects tiny distinction of bit and bit-bar lines voltages and amplifies it through regeneration. Here, 6T SRAM Cell includes a differential browse operation. This means that that each the keep worth and its inverse area unit used in analysis to verify the keep worth. The browse operation is initiated by enabling the word line (WL) and connecting the pre-charged bit lines, BL and BLB, filler of Q1 and Q5 ought to make sure that electrical converter Q2−Q4 doesn't switch inflicting a harmful browse. .A most popular filler resolution may be to use a minimumwidth access transistors with a rather larger than the marginal length channel and a bigger than marginal dimension with a marginal length driver transistors.

Data hold operation

If the word line isn't declared, the access transistors are going to be isolated the cell from the bit lines. the 2 cross coupled electrical converters fashioned the 2 inverter connected back to back reinforce one another as long as they're disconnected from the skin world. and that they can retain the info that they need already keep within the memory cell. during this state, pre-charge is activated.

REFRENCES

[1]. AMINUL ISLAM and MOHD. HASSAN, "VARIABILITY ANALYSIS OF 6T AND 7T SRAM CELL IN SUB-45NM TECHNOLOGY", IIUM Engineering Journal, Vol. 12, No. 1, 2011.

[2]. Andrei S. Pavlov, "Design and test of embedded SRAMS" ,phd thesis,waterloo,Ontario,Canada,2005.

[3]. Arash Azizi-Mazreah, Mohammad T. Manzuri Shalmani, Hamid Barati, and Ali Barati,"Delay and Energy Consumption Analysis of Conventional SRAM" ,International Journal of Electronics, Circuits and Systems Volume 2 Number 1.

[4]. Bharadwaj S. Amrutur, "Design And Analysis Of Fast Low Power SRAMs" , August 1999.

[5]. C.M.R. Prabhu and Ajay Kumar Singh, "A proposed SRAM cell for low power consumption during write operation", Faculty of Engineering and Technology, Multimedia University, Melaka, Malaysia

[6]. G. Razavipour, A. Afzali-Kusha, and M. Pedram, "Design and Analysis of Two Low Power SRAM Cell Structures", IEEE Transactions on VLSI Systems

[7]. Kevin Zhang, Senior Member, Fatih Hamzaoglu, and Yih Wang, "Low-Power SRAMs in Nanoscale CMOS Technologies" IEEE TRANSACTIONS ON ELECTRON DEVICES, VOL. 55, NO. 1, JANUARY 2008

[8]. Mr. Viplav A. Soliv, Dr. Ajay A. Gurjar, "AN ANALYTICAL APPROACH TO DESIGN VLSI IMPLEMENTATION OF LOW POWER, HIGH SPEED SRAM CELL USING SUB-MICRON TECHNOLOGY", International Journal of Enterprise Computing and Business Systems, Vol. 2 Issue 1 January 2012

[9]. Martin Margala, "Low Power SRAM Circuit Design", University of Alberta, Canada Pankaj Prajapati, Chintan Patel, Kirit Patel, Parul Panchal, "Low Power SRAM cell Using 0.18µm Technology" , National Conference on Recent Trends in Engineering & Technology.

[10]. Ravi Kumar. K. I, Vijayalaxmi. C. Kalal, Rajani. H. P, Dr.K. Dhanumjaya, M. Sudha, Dr.MN.Giri Prasad ,Dr.K.Padmaraju "CELL STABILITY ANALYSIS OF CONVENTIONAL 6T DYNAMIC 8T SRAM CELL IN 45NM TECHNOLOGY" VLSICS Vol.3, No.2, April 2012

[11]. Ramnath Venkatraman, Olga Kobozeva, Franklin L. Duan, Arvind Kamath, S. T. Sabbagh,Miguel A. Vilchis-Cruz, Member, Jhon Jhy Liaw, Jyh-Cheng You, and Subramanian Ramesh , "The Design, Analysis, and Development of Highly Manufacturable 6-T SRAM Bitcells for SoC Applications", IEEE TRANSACTIONS ON ELECTRON DEVICES, VOL. 52, NO. 2, FEBRUARY 2005

[12]. S. Y. Kulkarni, "Design and Verification of Low Power 64bit SRAM System using 8T SRAM:Back-End Approach" , IJEIT, Volume 1, Issue 6, June 2012

[13]. Sampath Kumar, Sanjay Kr Singh, Arti Noor, D. S. Chauhan & B.K. Kaushik, "COMPARATIVE STUDY OF DIFFERENT SENSE AMPLIFIERS IN SUBMICRON CMOS TECHNOLOGY", IJAET Nov 2011.

[14]. Simran Kaur,Ashwani Kumar, "Analysis of Low Power SRAM Memory Cell using Tanner Tool", IJECT Vol. 3, Issue 1, Jan. – March 2012

[15]. Sung-Mo Kang and Yusuf Leblebici, "CMOS Digital Integrated Circuits", TMH, 2003

[16]. Sreerama Reddy G.M, P. Chandrashekara Reddy, "Design and VLSI Implementation of 8 Mb Low Power SRAM in 90nm",European Journal of Scientific Research

[17]. Tegze.P.Haraszti, "CMOS Memory Circuits", Kluwer Academic Publishers, 2002

[18]. Benton Highsmith Calhoun and Anantha P Chandrakasan, "A 256 kb 65-nm sub-threshold SRAM design for ultra-low-voltage operation", IEEE Journal of Solid-State Circuits, vol. 42, no.3, pp. 680-688, 2007.

[19]. Navid Azizi, Farid N.Naim and Andreas Moshovos, "Low-Leakage Asymmetric-cell SRAM", IEEE Transitions on VLSI Systems, vol. 11, no. 4, pp. 701-715, 2003.

[20]. Yinhui Chen, Zhiyuan Yu, Haiqing Nan and Ken Choi, "Ultralow Power SRAM Design in Near Threshold Region using 45 nm CMOS Technology", Proc. of IEEE International Conference on Electro/Information Technology (EIT-2011), pp.1-4, 2011.

[21]. Atsushi Kawasumi, Yasuhisa Takeyama, Osamu Hirabayashi, Keiichi Kushida,Yuki Fujimura and Tomoaki Yabe, "A low-Supply-Voltage-Operation SRAM with HCI Trimmed Sense Amplifiers", IEEE Journal of Solid-State Circuits, vol. 45, no. 11, pp.2341-2347, 2010.

[22]. A., Goel, R.K., Sharma, and A.K., Gupta, "Process variations aware area efficient negative bit-line voltage scheme of improving write ability of SRAM in nanometer technologies", IET Journal vol. 6, no. 1, pp. 45-51, 2012.

[23]. Wen-Tsong Shiue, "Low power memory design", Proc. of IEEE Inti, conference on Application Specific Systems, Architecture and Processor, pp 55-64, 2002.

[24]. Riichiro Takemura, Takeyuki Kawahara, Katsuya Miura, Hiroyuki Yamamoto, Jun Hayakawa, Nozomu Mastsuzaki, Kazuo Ono, Michihiiko Yamanouchi, Kenchi Ito, Hiromasa Takahashi, Shoji Ikeda, Haruhiro Hasegawa, Hideyuki Matsuoka and Hideo Ohno, "A 32- Mb SPRAM with 2T1R Memory cell localized Bi-directional Write Driver and '17 'O' Dual- Array Equalized Reference Scheme", IEEE Journal of Solid- State Circuits, vol. 45, no.4, pp. 869-879, 2010.

[25]. Byung-Do Yang, "A low-Power SRAM using bit-line charge-Recycling for read and write operations", IEEE Journal of Solid-State Circuits, vol. 45, no.10, pp. 2173-2183, 2010.

[26]. Pramod Kolar, Eric Karl, Uddalak Bhattacharya, Fatih Hamzaoglu, Henry Nho,Yong- Gee Ng, Yih Wang and Kevin Zhang, " A 32 nm High-k Metal Gate SRAM with Adaptive Dynamic Stability Enhancement for Low-Voltage Operation", IEEE Journal of Solid-State Circuits, vol. 46, no.l,pp. 76- 84, 2011.
[27]. Meng-Fan Chang, Shi-Wei Chang, Po-Wei Chou and Wei-Cheng Wu, "A 130 mV SRAM with Expanded Write and Read Margins for Sub-threshold Applications", IEEE Journal of Solid-State Circuits, vol. 46, no.2, pp. 520- 529, 2011.
[28]. Myoung Jin Lee, " A Sensing Noise Compensation Bit-line Sense Amplifier for Low Voltage Applications", IEEE Journal of Solid-State Circuits, vol. 46, no.3, pp. 690- 694, 2011.
[29]. Kochi Takeda, Toshio Saito, Shinobu Asyama, Yoshiharu Aimoto, Hiroyuki Kobatake, Shinya Ito, Toshifumi Takahashi, Masahiro Nomura, Kiyoshi Takeuchi and Yoshihiro Hayashi, " Multi-Step Word-Line Control Technology in Hierarchical Cell Architecture for Scaled-Down High-Density SRAMs", IEEE Journal of Solid-State Circuits, vol. 46, no.4, pp. 806-814, 2011.
[30]. Takashi Ohsawa, Kosuke Hatsuda, Katsuyuki Fujita, Fumiyoshi Matsuoka and Tomoki Higashi, "Generation of Accurate Reference Current for Data Sensing in
[31]. Elaine Ou and S. Simon Wong, "Array Architecture for a Nonvolatile 3-Dimensional Cross-Point Resistance-Change Memory", IEEE Journal of Solid-State Circuits, vol. 46, no.9, pp. 2158-2170, 2011.
[32]. Kousuke Miyaji, Shuhei Tanakamaru, Kentaro Honda, Shinji Miyano and Ken Takeuchi, "Improvement of Read Margin and its distribution by Mismatch Self- Repair in 6T-SRAM with Asymmetric Pass Gate Transistor Formed by post-Process Local Electron Injection", IEEE Journal of Solid-State Circuits, vol. 46, no.9, pp. 2180-2188, 2011.
[33]. Vibhu Sharma, Stefan Cosemans, Maryam Ashouei, Jos Huisken, Francky Catthoor and Wim Dehaene, "A 4.4 pJ/Access 80 MHz, 128 Kbit Variability Resilient SRAM with Multi-Sized Sense Amplifier Redundancy", IEEE Journal of Solid-State Circuits, vol. 46, no. 11, pp. 2416-2430, Oct. 2011.
[34]. Satyanand Nalam and Benton H. Calhoun, "5T SRAM with Asymmetric Sizing for Improved Read Stability", IEEE Journal of Solid-State Circuits, vol. 46, no. 10, pp. 2431-2442, 2011.

Available online at www.sciencedirect.com

ScienceDirect

Materials Today: Proceedings 4 (2017) 746–751

materialstoday: PROCEEDINGS

www.materialstoday.com/proceedings

5th International Conference on Materials Processing and Characterization (ICMPC 2016)

A Hybrid Neural Network - Genetic Algorithm for Prediction of Mechanical Properties of ASS-304 at Elevated Temperatures

Lakshmi Kanumuri[a,*], D V Pushpalatha [b], Akshay S.K. Naidu[c] Swadesh Kumar Singh[c]

[a*]*Department of CSE, GRIET, Hyderabad-500090, Telangana, India*
[b]*Department of EEE, GRIET, Hyderabad-500090, Telangana, India*
[c]*Department of CIVIL ENGINEERING, IARE, Hyderabad-500090, Telangana, India*
[d]*Department of MECHANICAL ENGINEERING, GRIET, Hyderabad-500090, Telangana, India*

Abstract

In the present work, genetic algorithm is implemented, to optimize the artificial neural networks used, to predict the mechanical properties of Austenitic Stainless Steel 304 (ASS-304) at elevated temperatures. ASS-304 is a very important alloy used in various applications involving high temperatures which make it very important to study the mechanical properties at elevated temperatures. The dynamic neural networks have been employed first for predicting the mechanical properties such as Ultimate Tensile Strength (UTS), Yield Strength (Ys), % elongation, Strain Hardening Exponent (n) and Strength Coefficient (K) at elevated temperatures. Genetic algorithm was then integrated with the neural network model for optimization, to achieve better regression statistics, taking the mean square error as the fitness function. The results show that the proposed hybrid, neural network - genetic model is more accurate and effective method for predicting the mechanical properties of ASS-304 at elevated temperatures.

Selection and peer-review under responsibility of the Conference Committee Members of the 5th International conference on Materials Processing and Characterization (ICMPC 2016)

Keywords: ASS-304; Material Properties; Artificial Neural Network; Genetic Algorithm

1. Introduction

Austenitic Stainless Steel is very important alloy used in various high temperature applications, include: as fuel cladding, core structural elements in nuclear industries due its high corrosion resistance in seawater environment because of the addition of molybdenum which prevents chloride corrosion[1]. Since it has very less carbon content,

* Corresponding author. Tel.: +91-9000005181;
*E-mail address:*lakshmi.kanumuri@yahoo.com.

2214-7853
Selection and peer-review under responsibility of Conference Committee Members of 5th International conference on Materials Processing and Characterization (ICMPC 2016).

wear resistance, friction properties are adequate in the heat effected zone and during welding there is very less susceptibility to intergranular corrosion[2]which make it important to study their mechanical properties at elevated temperatures[3].Austenitic stainless steels (300-series), when subjected to high temperatures and loads, there is a martenstic transformation involved plastic deformation which depends on several parameters: chemical composition, mechanical stress and magnetic behavior[4].The martenstic transformation at room and low temperature, which mostly depend on microstructural aspects, influence the drawability of the materials. The drawability of the 304 ASS is very much steady when compared to the 316 ASS. In balance biaxial test, there is a decreased strain hardening rate due to the increase of the volume fraction of the induced martensite when compared to the uniaxial test[5].The ASS 304 material is very much suitable structural element at elevated temperatures and in nuclear reactors the temperature is very high therefore its tensile properties at elevated temperatures needs to be analysed with the knowledge of constitutive modes among which ANN is famous for its simplicity and accuracy.

The trained ANN model gives an excellent correlation coefficient and absolute average error values which represents a good accuracy of the model. The Artificial Neural Network (ANN) to predict the mechanical properties of AZ61 Mg alloy fabricated by equal channel angular pressing (ECAP)[6]. A back-propagation (BP) algorithm is used to train the neural network prediction models. Grain size, yield strength, and tensile strength of the alloy are predicted based on the number of ECAP passes[7]. The ANN predictions are shown to be in excellent agreement with experimental results, and the prediction error is shown to be minimal. These models can also be extended in the future to predict other properties, and possibly characterize other alloys.

Genetic Algorithm (GA) is a search algorithm based on the mechanics of natural selection and genetics and they combine survival of the fittest among string structures to form a search algorithm[8]. GA is particularly suitable for multi-parameter optimization problems with an objective function subject to numerous hard and soft constraints. The main idea of GA is to start with a population of solutions to a problem, and attempt to produce new generations of solutions which are better than the previous ones. GA operates through a simple cycle consisting of the following four stages: initialization, selection, crossover, and mutation. Fig.1. shows the basic steps of the basic genetic algorithm model[9].

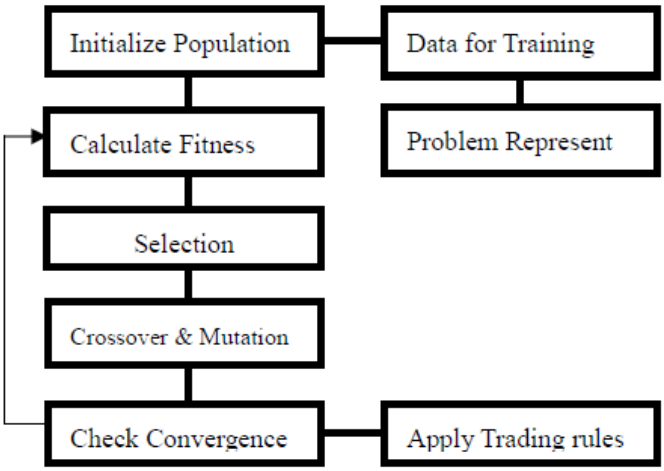

Fig.1. Basic Steps of the GA Model

Genetic algorithms are proven, theoretically and empirically, to provide a robust search in complex spaces, thereby offering a valid approach to problems requiring efficient and effective searches. To execute a particular optimization task using GA, it requires to address a genetic representation of candidate solutions, a way to create an initial population of solutions, an evaluation function which describes the quality of each individual, genetic operators that generate new variants during reproduction, and values for the parameters of the GA, such as population size, number of generations and probabilities of applying genetic operators.

In the initialization stage, a population of genetic structures (called chromosomes) that are randomly distributed in the solution space is selected as the starting point of the search. These chromosomes can be encoded using a variety of schemes including binary strings, real numbers or rules. After the initialization stage, each chromosome is evaluated using a user-defined fitness function. The goal of the fitness function is to numerically encode the performance of the chromosome. For real- world applications of optimization methods such as GA, the choice of the fitness function is the most critical step. The mean squarederror (MSE), which is the error between the desired and the predicted outputs as given by the equation (1)[10], is considered as the fitness function in the genetic algorithm.

$$MSE = \frac{1}{N}\sum_{i=1}^{patterns\ number}(y_i^{desired\ output} - y_i^{predicted\ output})^2 \qquad (1)$$

In the present study, ANN-GA model is initially trained with one input neuron, representing the temperature and six output neurons, corresponding to the mechanical properties and twenty hidden neurons. The model has been trained with the desired value of MSE using the genetic algorithm for predicted the desired value of the output values.

2. Implementation

2.1. Experimentation on UTM Machine:

In this work, the material tested was Austenitic Stainless Steel 304 (ASS-304). In the previous study of author ["Study the Effect of Temperature on the Properties of ASS-304 Using ANN", 23rd International Conference on Processing and Fabrication of Advanced Materials, 1186-1192, Dec 2014, IIT Roorkee], the specimens of ASS-304 steels were tested on a 5 ton UTM machine (Fig.2.) to calculate the material properties like Ultimate Tensile Strength (UTS), Yield Strength (YS), % Elongation, Strength Coefficient (K) and Work Hardening Exponent (n). The experiments were conducted from temperature 50^0C to 650^0C in the interval of 50^0C. It was found out that as the temperature increases, there is a decrease in the values of YS, UTS, K and n values. But at 350^0C these values starts increasing again due to blue brittle phenomenon which occurs due to impurities of Cr, Ni and other impurity materials. After 450^0C these properties again starts decreasing due to material being in the plastic region.

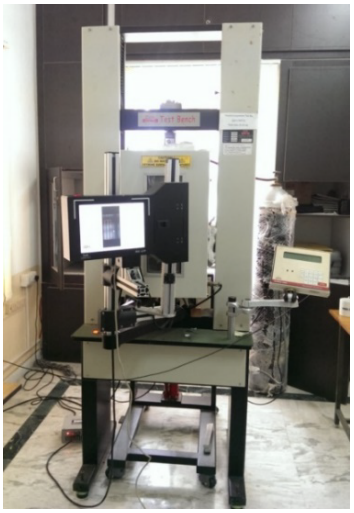

Fig.2. Universal Testing Machine

2.2. Development of ANN- GA Model:

The experimental data (Table 1.) was trained using Artificial Neural Network (ANN) model at unknown temperature with Back Propagation (BP) algorithm. 13 samples of input data i.e. temperature and 13 samples of 6 target data i.e. n, K, UTS, YS, Youngs, %elon were taken to train the network. This training stops when the validation error increased for six iterations, which occurred at 6th iteration. The performance plot which shows the training errors, validation errors and testing errors is shown in Fig.3. The network response is very promising; hence a new input of unknown temperature can be given to the network to predict the properties of the material as the outputs.

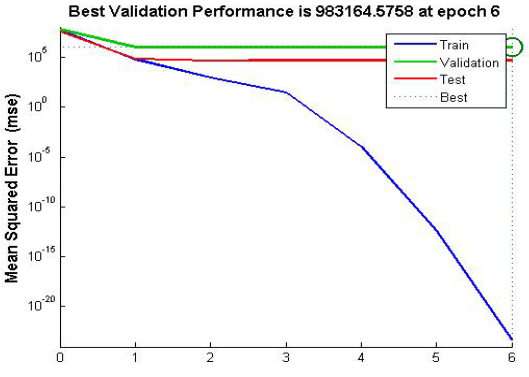

Fig.3. Performance plot

Table 1. Trained data Set

Temperature	N	K	UTS	YS	Youngs	%elon
50^0C	0.3706	1085.925	675	275.36	20652	58.3531
100^0C	0.3394	1029.912	636.6667	299.404	17612	56.93569
150^0C	0.3629	1032.048	578.3333	266.46	17764	42.52202
200^0C	0.3972	1000.691	516.6667	214.3147	20092	37.6805
250^0C	0.4184	1043.758	518.3333	225.72	15048	36.30065
300^0C	0.4474	1159.044	526.6667	221.2	13825	33.25284
350^0C	0.4932	1204.759	520	215.3503	10591	32.8554
400^0C	0.4119	1056.331	471.6667	231.3373	15773	36.96493
450^0C	0.3797	950.3859	500	203.895	22655	32.07232
500^0C	0.3751	848.985	458.3333	193.336	13182	34.00373
550^0C	0.3957	887.9735	440	195.0643	14273	33.90331
600^0C	0.3862	855.6576	395	184.31	15360	37.59177
650^0C	0.3942	675.6161	320	156.144	13012	30.86086

The BP algorithm employed in the training of the neural network derived from the gradient method requires an objective function which is continuously differentiable[11]. This might cause some problems in the learning process, such as the slow convergence, oscillation effect etc., which are due to the random selection of weight and threshold values. Hence, the genetic algorithm is used to optimize the artificial neural network by minimizing the mean squared error which is considered as the fitness function. A function can be written to accept the network, weights and biases, inputs and targets. This function may return the mean squared error based on the outputs and the targets as GA requires a function handle that only returns a scalar value. A basic BP neural network model is created with the definition of a MSE function handle to be passed to GA.

3. Results and Discussion

The concrete steps in implementing the ANN-GA algorithm are as follows:

(i) Create the neural network model.
(ii) Initialize the population.
(iii) Compute the fitness value, MSE of the present population MSE can be considered as the count of fitness value.
(iv) Chromosomes are generated. The encoded chromosomes are searched to minimize the fitness function.

In this phase, GA operates the process of crossover and mutation on initial chromosomes and iterates until the stopping conditions are satisfied. The population size is set to 20 organisms and the crossover and mutation rates are varied to prevent ANN from falling into a local minimum. The range of the crossover rate is set to 0.8 while the mutation rate ranges from 0.05 to 0.1. As the stopping condition, only 50 trials are permitted. The performance plots of the ANN-GA algorithm are shown in Fig.4. and Fig.5.

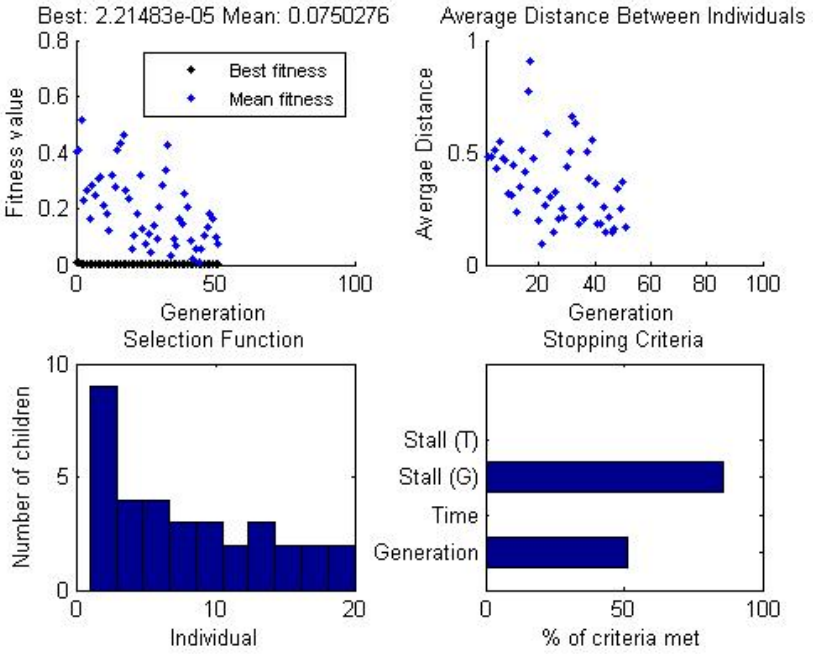

Fig. 4. Performance Plots of the Fitness, Distance, Selection and Stopping

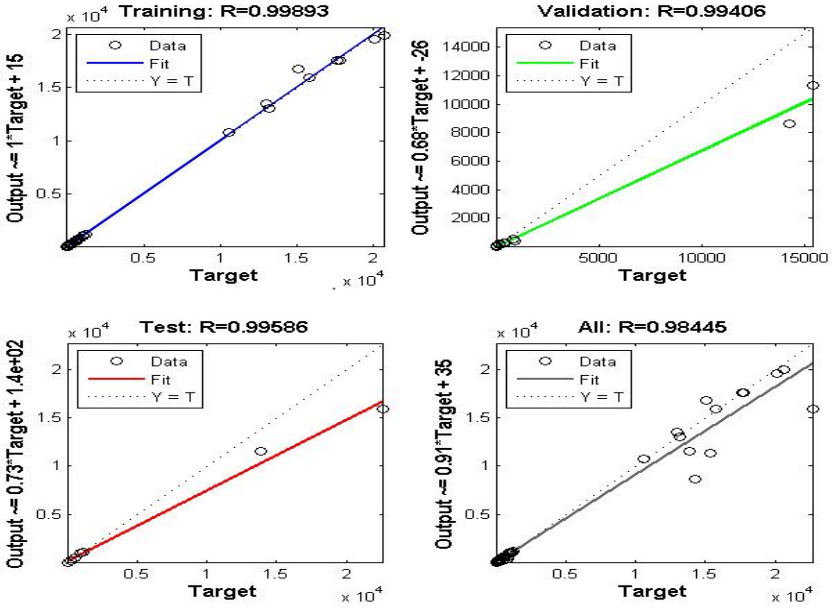

Fig.5. Performance Plots of the ANN-GA Algorithm

The proposed ANN-GA model is tested for new values of the temperature for predicting the mechanical properties of the ASS-304. The test results show that the hybrid ANN-GA model is more accurate, fast and effective method for prediction applications.

4. Conclusions

In this work, the MSE values of the neural network model were minimized using GA. The accurate results show that the proposed ANN-GA model can be considered a robust tool for prediction applications and is an effective mathematical model for assessing the mechanical properties of ASS-304 at elevated temperatures. The hybrid ANN-GA model is validated based on the statistical parameters like the mean square error and the convergence speed.The simulation results show that ANN-GA model gets great improvement in generalization ability, and has higher reliability in prediction when compared to ANN models. The results also show that genetic algorithm can be very good at speeding up convergence speed and solving the problem of local minimum to realize the global search.

5. Acknowledgment:

The financial support received for this research work from University Grants Commission, Government of India, MRP-4587/14 (SERO/UGC) is gratefully acknowledged.

References

[1] A. K. Gupta, H. N. Krishnamurthy, Y. Singh, K. M. Prasad, and S. K. Singh, "Development of constitutive models for dynamic strain aging regime in Austenitic stainless steel 304," *Mater. Des.*, vol. 45, pp. 616–627, 2013.
[2] X. Y. Wang and D. Y. Li, "Mechanical , electrochemical and tribological properties of nano-crystalline surface of 304 stainless steel," vol. 255, pp. 836–845, 2003.
[3] M. Kaur, H. Singh, and S. Prakash, "A survey of the literature on the use of high velocity oxy-fuel spray technology for high temperature corrosion and erosion-corrosion resistant coatings," *Anti-Corrosion Methods Mater.*, vol. 55, no. 2, pp. 86–96, 2008.
[4] M. Fujiwara, K. Yamazaki, M. Okamoto, J. Todoroki, T. Amano, T. Watanabe, T. Hayashi, H. Sanuki, N. Nakajima, and K. Itoh, "Large helical device (LHD) program," *J. fusion energy*, vol. 15, no. 1–2, pp. 7–153, 1996.
[5] Z. Tourki, H. Bargui, and H. Sidhom, "The kinetic of induced martensitic formation and its effect on forming limit curves in the AISI 304 stainless steel," vol. 166, pp. 330–336, 2005.
[6] L. Singaram, "Ann prediction models for mechanical properties of AZ 61 mg alloy fabricated by equal channel angular pressing," *Int. J. Res. Rev. Appl. Sci.*, vol. 8, no. 3, 2011.
[7] F. Djavanroodi, B. Omranpour, and M. Sedighi, "Artificial neural network modeling of ECAP process," *Mater. Manuf. Process.*, vol. 28, no. 3, pp. 276–281, 2013.
[8] L. D. Davis and M. Mitchell, "Handbook of Genetic Algorithms," pp. 1–6, 1991.
[9] R. Naik, D. Ramesh, B. Manjula, and A. Govardhan, "Prediction of Stock Market Index Using Genetic Algorithm," *Comput. Eng. ...*, vol. 3, no. 7, pp. 162–172, 2012.
[10] M. A. Mohandes, T. O. Halawani, S. Rehman, and A. A. Hussain, "Support vector machines for wind speed prediction," *Renew. Energy*, vol. 29, no. 6, pp. 939–947, 2004.
[11] V. G. Gudise and G. K. Venayagamoorthy, "Comparison of particle swarm optimization and backpropagation as training algorithms for neural networks," in *Swarm Intelligence Symposium, 2003. SIS'03. Proceedings of the 2003 IEEE*, 2003, pp. 110–117.

NOVATEUR PUBLICATIONS
International Journal of Research Publications in Engineering and Technology [IJRPET]
ISSN: 2454-7875
VOLUME 3, ISSUE 7, July-2017

OPTIMIZED SNR FOR INTERSYMBOL INTERFERENCE REDUCTION OVER MODIFIED DFZF EQUALIZER FOR PACKET ERASURE NETWORK

ARJUN GHULE
Research Scholar, Department of ECE, Jawaharlal Nehru Technological University, Kukatpally, Hyderabad, India

DR. PRABHU BENAKOP
Principal, Indur Institute of Engineering & Technology, Siddipet, Telangana, India

ABSTRACT:

A novel technique presented in this paper is used to find an optimal signal to noise ratio (SNR) for maximizing overall data throughput and system performance for Automatic speech Recognition (ASR) applications. In speech data transmission over communication channels inter symbol Interference (ISI) will occur. In this paper the major problem faced while implementation is loss of data due to inter symbol Interference. By changing multiplying factor at feedback filter coefficients & Optimizing the signal to noise ratio, receiver errors can be minimized. DFZFE is used to combat ISI in wireless channels. In literature, purpose of designing the feed forward equalizer in the channel is treated linear. .A drawback of this method is error propagation due to the feedback.[15]. Feedback angle is found to maximize the output signal-to-noise ratio (SNR) [17]. Algorithm that achieves the same equalization performances at a reduced complexity are used [18]. Inter symbol Interference problem is faced in many applications such as cognitive radio, robotics, and sensor networks [19]

KEYWORDS: Data communication, system performance, Intersymbol Interference (ISI), interference constraints, degradation, Signal to Noise Ratio(SNR) , Decentralized feedback zero forcing equalizer (DFZFE): Automatic speech Recognition(ASR) etc.

INTRODUCTION:

In literature it is suggested that data accuracy can be comprised because the loss due to absence of optimal feedback, as well as the gain obtained from limited feedback with local channel knowledge compared to preceding without feedback [16].In this paper optimized SNR and feedback filter coefficients are recommended at Decentralized feedback zero forcing equalizer (DFZFE)

DECENTRALIZED FEEDBACK ZERO FORCING EQUALIZER (DFZFE):

This technique is widely used in combat internal interference [1]. It is used to combat (inter symbol interference) ISI in wireless channels [2]. Codes are designed in such a way that, it will generate random symbols that which will be sent through a channel with ISI (inter symbol interference) with AWG noise [3]. Then in Next step DFZFE is applied to for decoding.

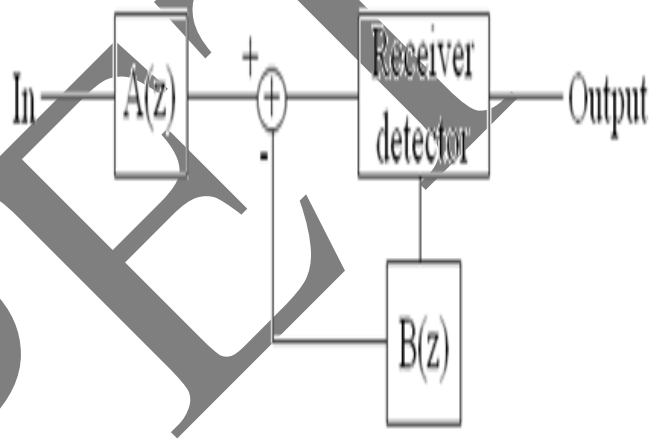

Fig. No.1. Typical DFZFE system

The main cause of inter symbol interference is time depressiveness the signal environment [4]. E.g. multipath scattering environment, delayed versions of a symbol transmission is received at receiver end this may lead to interference with other symbols transmission.

IMPLEMENTED ALGORITHM:

- Defining length of transmitting sequence.
- Convolution of channel impulse response with transmitting sequence.
- Addition of SNR.
- Modified filter with Multiplication factor of half & one fourth.
- Computing Inverse impulse Response.
- Hard decision decoding.

RESULTS & DISCUSSION:

ZF DFE solution and as such can be viewed as a generalization of an existing work. We demonstrate the effectiveness of the proposed solution through simulation [20] for zero-forcing decision feedback equalization (ZF-DFE) on fast fading channels. We present an error propagation framework in ZF-DFE [21]

Table No.1 Results of modified DZFZ equalizer

SR. No	No. of Bits	Xh for SNR (db)					Xh/2 for SNR (db)					Xh /4 for SNR (db)				
		5	20	30	40	80	5	20	30	40	80	5	20	30	40	80
1	8	2	1	0	0	0	4	0	0	0	0	1	0	0	0	0
2	10	0	0	0	0	0	3	0	0	0	0	1	0	0	0	0
3	12	10	0	0	0	0	4	1	0	0	0	3	2	0	0	0
4	14	7	0	0	0	0	4	1	0	0	0	7	0	0	0	0
5	16	5	1	0	0	0	7	0	0	0	0	11	0	0	0	0
6	18	8	0	0	0	0	7	2	0	0	0	6	1	0	0	0
7	20	10	1	0	0	0	8	2	0	0	0	0	2	0	0	0
8	22	11	1	0	0	0	7	0	0	0	0	8	0	0	0	0
9	24	11	1	0	0	0	6	0	0	0	0	9	0	0	0	0
10	26	10	1	0	0	0	7	2	0	0	0	10	0	0	0	0
11	28	12	1	0	0	0	7	3	0	0	0	10	0	0	0	0
12	30	15	0	0	0	0	8	1	0	0	0	7	0	0	0	0
13	32	12	2	0	0	0	9	1	0	0	0	10	0	0	0	0
14	34	13	0	0	0	0	7	1	0	0	0	12	0	0	0	0
15	36	14	0	0	0	0	8	0	0	0	0	11	1	0	0	0
16	38	18	0	0	0	0	12	1	0	0	0	19	1	0	0	0
17	40	17	1	0	0	0	8	0	0	0	0	11	0	0	0	0
Avg	**24**	**22.529**	**0.588**	**0**	**0**	**0**	**6.823**	**0.882**	**0**	**0**	**0**	**30.235**	**0.411**	**0**	**0**	**0**

In table no.1 modified DZFZ observations are for different number of bits are transmitted at the transmitter and same can be decoded at the equalizer output in the receiver end. Readings are obtained for different SNRs as shown .It is also observed for modified filter coefficients such as multiplying factor of 0.5 and 0.25.

As shown in the table no.2 averaging of number of bits at the transmission and corresponding average errors are obtained.

Table No:-2 averaging of different errors received through DFZF.

Sr.No.	SNR(db)	xh	xh/2	xh/4
1	5	22.5294	6.82353	30.23235
2	20	0.58824	0.88235	0.41176
3	30	0	0	0
4	40	0	0	0
5	80	0	0	0

As shown in the Table no.3 averaging of the errors when SNR is maintained for 5db.Results are further obtained for modified filter that is with multiplying facto of 0.5 & 0.25 respectively.

Table No.3 Average Errors received for 5db SNR.

Sr.No.	SNR(db)	xh	xh/2	xh/4
1	5	22.5294	6.82353	30.23235

In fig no.2 It is observed that errors are minimum if filter coefficients are multiplied by 0.5 and such errors are maximum at such filter coefficients are 0.25. for of SNR of 5db.

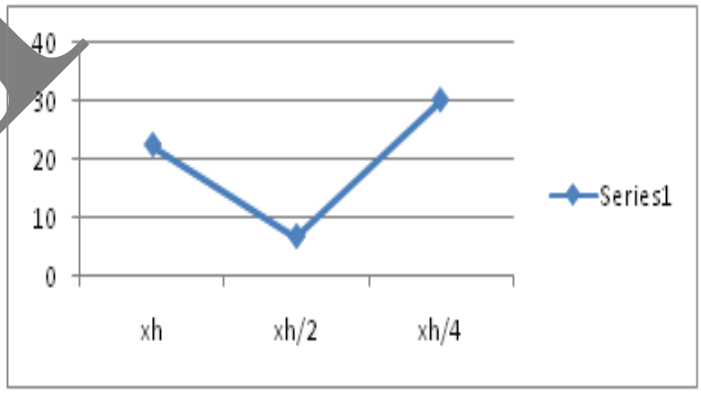

Fig. No.2. SNR = 5db , Average Number of bits for transmission = 24 bit X-axis , Xh is feedback filter coefficients at receiver Y-axis average number of bits for transmission

In table number 4 above process is repeated for SNR OF 20 db at equalizer .i.e. at receiver. Here it is observed that error are minimum at maintenance of filter coefficients are multiplied by 0.25.

Table No.4 :-Average Errors received for 20db SNR

Sr.No.	SNR(db)	xh	xh/2	xh/4
1	20	0.58824	0.88235	0.41176

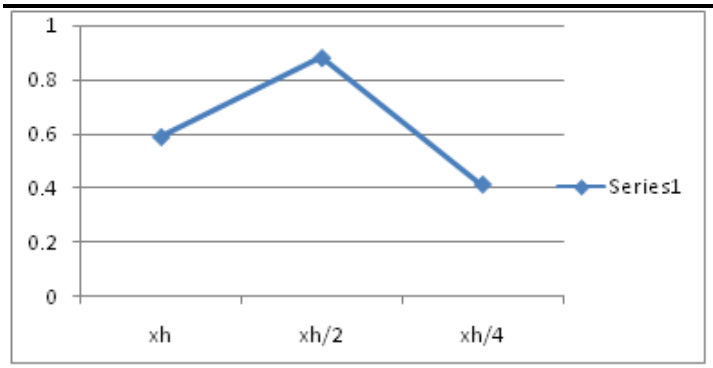

Fig no.3. SNR = 20db , Average Number of bits for transmission = 24 bits. X-axis , Xh is feed back filter coefficients at receiver Y-axis is error rate.

In table number 5. above process is repeated for SNR OF 30 db at equalizer .i.e. at receiver. Here it is observed that error are zero at maintenance of filter coefficients are multiplied by 0.5 & 0.25. But overall errors are zero for 30db SNR.

Table No.5:- Average Errors received for 30db SNR

Sr.No.	SNR(db)	xh	xh/2	xh/4
1	30	0	0	0

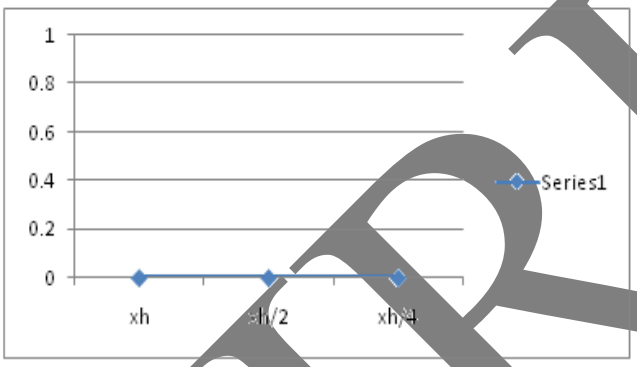

Fig no.4. SNR = 40db, Average Number of bits for transmission = 24 bits X-axis , Xh is feedback filter coefficients at receiver , Y-axis is error rate

From the simulated results we have observed that:

- Error occurred in the received signal can be minimized or made to zero by maintaining optimized Signal to Noise power Ratio (SNR).
- (Fig no.2. and Table No.3) Average Symbol errors are minimum i.e. 6.82353 for SNR 5db with average number of bits considered are 24.with modified filter coefficients are multiplied by multiplying factor of 0.5.
- (Fig no.3. and Table No.4) Average Symbol errors are minimum i.e. 0.41176for SNR 20db with average number of bits considered are 24.with modified filter coefficients are multiplied by multiplying factor of 0.25.
- (Fig 4. and Table No.5) Average Symbol errors are minimum i.e. 0.00for SNR 30db & above i.e.30 db, 40db & 80 db. With average number of bits considered are 24.with modified filter coefficients are multiplied by multiplying factor of 0.5 & 0.25 etc.

CONCLUSION:

Experimented results suggest that optimization of SNR & filter coefficients in the feedback will increase the accuracy in the speech data transmission. It can be used when ever recognizing accuracy demanded. In this paper a new algorithm for reduction in inter-symbol interference is developed by using modified DFZF equalizer packet erasure network. Few important points observed here are, average symbol errors are minimum (6.82353 multiplying factor 0.5, 0.41176 multiplying factor 0.25). Also it is observed that average symbol errors are minimized at 30db. In the implemented system, is designed to have an equipartition of energy over the entire used transmission band at the input to the channel. Moreover the actual performance degradation is negligible proposed method is designed to make errors negligible. In this paper optimized SNR and feedback filter coefficients are recommended at Decentralized feedback zero forcing equalizer (DFZFE).Optimized SNR suggested is 30 Db and above. Equalizer performance is optimized for optimized filter coefficients i.e.05 and 0.25.

REFERENCES:

1) Farhang-Boroujeny, B., *Adaptive Filters: Theory and Applications*, Chichester, England, Wiley, 1998.
2) Haykin, Simon, *Adaptive Filter Theory, Third Ed., Upper Saddle River*, N.J., Prentice-Hall, 1996.
3) Kurzweil, Jack, An Introduction to Digital Communications, New York, Wiley, 2000.
4) J. W. Lechleider, "*High Bit Rate Digital Subsciber Lines: A Review of HDSL Progress",* IEEE Journal on Selected Areas in Communications, vol. 9, no. 6, pp. 769-784, August 1991.
5) J. Salz, "*Optimum Mean-Square Decision Feedback Equalization*", The Bell System Technical Journal, vol. 52, no. 8, pp. 1341-1373, October 1973.
6) D. D. Falconer, G. J. Foschini, "*Theory of Minimum Mean-Square-Error QAM Systems Employing Decision Feedback Equalization",* The Bell System Technical Journal, vol. 52, no. 10, pp. 1821-1849, December 1973.
7) J. A.C. Bingham, *"Multicarrier Modulation for Data Transmission: An Idea Whose Time Has Come",* IEEE Communications Magazine, vol. 28, no. 5, pp. 5-14, May 1990.

8) I. Kalet, "*The Multitone Channel"*, IEEE Transactions on Communications, vol. 37, no. 2, pp. 119-124, February 1989.
9) R. G. Gallager, *Information Theory and Reliable Communication*, NY, New York: Wiley, 1968.
10) N. A. Zervos, I. Kalet, "*Optimized Decision Feedback Equalization Versus Optimized Orthogonal Frequency Division Multiplexing for High-Speed Data Transmission Over the Local Cable Network*", International Conference on Commumcations, pp. 1080-1085, 1989-June.
11) J. C. Tu, J. M. Cioffi, *"A Loading Algorithm for the Concatenation of Co-set Codes with Multichannel Modulation Methods*", Global Telecommunications Conference, pp. 1183-1187, 1990-December.
12) A. Ruiz, J. M. Cioffi, S. Kasturia, "*Discrete Multiple Tone Modulation with Co-set Coding for the Spectrally Shaped Channel"*, IEEE Transactions on Communications, vol. 40, no. 6, pp. 1012-1029, June 1992.
13) J. M. Cioffi, G. P. Dudevoir, M. V. Eyuboglu, G. D. Forney, "*MMSE Decision-Feedback Equalizers and Coding - Part I: Gerneral Results",* IEEE Transactions on Commumcations.
14) S. Kasturia, J. Aslanis, J. M. Cioffi, "*Vector Coding for Partial-Response Channels*", IEEE Transactions on Information Theory, vol. 36, no. 4, pp. 741-762, July 1990.
15) *Decision feedback equalization in channels with signal-dependent media noise* IEEE Transactions on Magnetics > Volume: 37 Issue: 4 Page(s): 1909 – 1911 Date of Publication: Jul 2001
16) P*ersonal, Indoor, and Mobile Radio Communications (PIMRC)*, 2015 IEEE 26th Annual International Symposium on. Date of Conference: 30 Aug.-2 Sept. 2015 Date Added to IEEE Xplore: 03 December 2015.
17) *Closed-Loop Space Time Block Coding for High Data Rate with Angle Feedback Published in: Communications (ICC), 2011* IEEE International Conference on ,Date of Conference: 5-9 June 2011 ,Date Added to IEEE Xplore: 29 July 2011
18) *"Complexity reduced blind multichannel equalization* "Signal Processing Conference, 2004 12th European Date Added to IEEE Xplore: 06 April 2015 ,Print ISBN: 978-320-0001-65-7.
19) *"Stability of distributed adaptive algorithms I: Consensus algorithms* "Decision and Control (CDC), 2015 IEEE 54th Annual Conference on IEEE Xplore: 11 February 2016.
20) *ZF DFE transceiver design for MIMO relay systems with direct source-destination link Signal Processing Conference,* 2011 19th European .Date of Conference: 29 Aug.-2 Sept. 2011 Date Added to IEEE Xplore: 02 April 2015.
21) "*An exact SER analysis of ZF-DFE for M-QAM on fast*" Personal Indoor and Mobile Radio Communications (PIMRC), 2010 IEEE 21st International Symposium on Date of Conference: 26-30 Sept. 2010 Date Added to IEEE Xplore: 17 December 2010

PREDOMINANCE OF BLOWFISH OVER TRIPLE DATA ENCRYPTION STANDARD SYMMETRIC KEY ALGORITHM FOR SECURE INTEGRATED CIRCUITS USING VERILOG HDL

V. Kumara Swamy[1] Prabhu Benakop[2]

[1]Dept of ECE, Sreenidhi Institute of Science and Technology,Yamnampet, Ghatkesar, Hyderabad, Telangana, India

[2]Dept of ECE, Indur Institute of Engineering and Technology, Siddipet Dist, Telangana, India

ABSTRACT

Computer data communication is the order of the day with Information Communication Technology (ICT) playing major role in everyone's life, communicating with smart phones, tabs, laptops and desktops using internet. Security of the data transferred over the computer networks is most important as for as an organization is concerned. Hackers attempt hard to crack the software key and indulge in cyber crimes. In this paper, the main concern is not only to provide security to the data transferred at the software level but it provides the security at hardware level by the modified Blowfish Encryption and Decryption Algorithms. It results minimum delay, high speed, high throughput] and effective memory utilization compared to Blowfish (BF) and Triple Data Encryption Standard (TDES) algorithms. The implementation of Blowfish with modulo adder and Wave Dynamic Differential Logic (WDDL) is to provide security against Differential power analysis (DPA). In the proposed four implementations, BF with constant delay n-bit adder (BFCDNBA) yielded minimum delay, maximum frequency, high memory utilization and high throughput compared to BF with modulo adder and WDDL logic (BFMAWDDL), BF with modulo adder (BFMA) and TDES algorithms. The VLSI implementation of Blowfish and TDES algorithms is done using Verilog HDL.

KEYWORDS:

BF, TDES, WDDL, DPA, BFMA, BFCDNBA, BFMAWDDL, HDL.

1. INTRODUCTION

Many encryption algorithms have come into an existence for information confidentiality, authenticity, integrity, non repudiation and access control such as DES, TDES, Advanced Encryption Standard (AES) and Blowfish [4, 10] etc. This research work analyzes the merits and demerits of Blowfish compared to TDES algorithm in terms of their operation, propagation delay, memory utilization and throughput of the algorithms considered. The brief information about following algorithms is explained below:

1.1. DATA ENCRYPTION STANDARD (DES)

Data Encryption Standard encrypts 64-bit block plain text with 56- bits key length. It is a fiestel network. After initial permutations, it undergoes 16- rounds of processing steps. It can operate in Cipher Block Chaining (CBC), Electronic Code Book (ECB), Cipher Feedback (CFB) and Output Feedback (OFB) modes [10] [12]. It is prone to Brute Force attack in which hacker attempts to break the key by applying all possible combinations of inputs. It's a popular and most widely used algorithm before TDES, AES, and BF algorithms. It's an insecure algorithm [23] [10]

DOI: 10.5121/ijnsa.2017.9603

1.2. TRIPLE DATA ENCRYPTION STANDARD (TDES)

It is also known as Triple Data Encryption Algorithm (TDEA) which is triplication of Data Encryption Standard (3DES) applied to every 64-bits data block, came into an existence to overcome the brute force attacks commonly suffered by DES algorithm. It has 48 rounds of operations. In this method, three keying options are there:

- Three keys k1,k2 and k3 are independent
- Keys k1 and k2 are independent and k3 = k1.
- All three keys are equal, i.e., k1= k2 =k3.

Thus option-1 is the strongest among all three. It has 168 bits of independent key bits where as option-2 has 112 key bits which are moderately secured compared to the option-1. The last option is having 56 key bits as same as DES but used thrice in the algorithm because of all three keys are equal and prediction can be done easily. It is a symmetric key block cipher [16]. It is less secured than AES.

1.3. ADVANCED ENCRYPTION STANDARD (AES)

AES is a block cipher with variable key length. The block length is 128 bits and key length may be 128/192/256 bits with 9/11/13 rounds respectively. Each processing round consists of four steps, i.e., substitute bytes, shift rows, mix columns and add round key. AES encryption is flexible, more secured and fast [14] [20] [16]. It is a popular and secured encryption algorithm in the industry compared to DES [9] [12], but it is prone to side channel attacks.

1.4. BLOW-FISH (BF)

Blowfish is a symmetric block cipher with variable key length. The plain text is in 64-bit blocks but the key length varies from 32 to 448 bits. The data encryption occurs through 16-round fiestel network. Each round consists of plain text and key dependent operations such as XOR, ADD AND SUBSTITUTE etc. It's faster than TDES and AES [15] [17]. It's a replacement for DES algorithm [16] [4] [10]. Blowfish algorithm is used more than AES due to its large key length and high security. It provides high throughput compared to other algorithms considered in this research work [18, 21]

1.5. RELATED RESEARCH REVIEW

Literature review reveals that Blowfish Algorithm implemented using Verilog HDL gave better results in terms of reduced delay and increased throughput. To mention a few, the jest of few papers referred is given below:

Performance of blowfish algorithm based on field programmable gate array (FPGA) is analyzed in terms of speed, rate of encrypting the given data and power. Results indicate that the proposed Blowfish algorithm reduced delay and increases throughput with low power consumption compared to AES. This paper focused on small high-speed security architectures and systems with low power consumption for mobile devices [1].

The amalgamation algorithm consists of both Blowfish and Rivest Cipher 6 (RC6) to solve the security problems and maintains the efficiency. It provides faster data transfer and high security, both are very important for Wi-Fi applications. The collision attack problem is eliminated using S-Box overlapping process and Brute Force attack is eliminated using Sub key generation process. It decreases delay time and frequency [2].

Cloud computing needs secure, fast and area efficient cryptographic techniques. Blowfish cryptosystem is one of the strong and fast algorithms used for cryptography. It uses hybrid algorithm consists of RSA and blowfish algorithms and implemented using VHDL. It has

symmetric and asymmetric properties. Thus, it is more useful for cloud computing applications [3]

Various range application of blowfish algorithm can be implemented for data encryption sent from an Internet of Things physical network which has IP-based data. Performance metrics are analyzed such as Security, Complexity, propagation delay, and throughput of Blowfish Algorithm. Hardware implementation of blowfish algorithm on FPGA using VHDL which yielded reduced propagation delay and enhanced throughput [6, 18]

Conjugate- structure algebraic CELP coding method is used in speech encryption using Blowfish algorithm. A new method for generating S-boxes and P-arrays which are the main building blocks of the Blowfish algorithm is proposed which reduces time, complexity and provides more security [8].

Performance of symmetric encryption algorithms on power consumption for wireless devices is studied and analyzed to have less battery power consumption. The algorithms considered are DES, 3DES, AES, Blowfish, Rivest Cipher2 (RC2), and RC6. Energy efficiency is the main focus of this design [15, 19].

Blowfish has better performance than other commonly used encryption algorithms. Blowfish can be considered as an excellent standard encryption algorithm than AES. AES requires more processing power and more processing time than Blowfish algorithm [20].

Performance analysis of DES and Blowfish is done for wireless networks to provide security to the information. It presented about security, speed and power consumption. Results confirm that Blowfish algorithm runs faster than DES but power consumption is almost same even though blowfish has 448-bit key length and more number of iterations/operations [23].

2. THEORETICAL ANALYSIS OF BLOW-FISH ALGORITHM

Blowfish is a block cipher; encryption and decryption is performed in the block sizes of 64-bits. It is a 16-round fiestel network and symmetric algorithm. The plain text of 64-bits separated as two halves, 32 bit each (LE and RE). We perform 16-rounds of operations during encryption and decryption processes as shown in equation 1 and 2 respectively which involve XOR, Fiestel function (F), XOR and SWAP LE and RE operations in each round as shown in flowchart fig no.1. Fiestel function (F) involves XOR and modulo addition operation [7] [11].

The Encryption operation equation is given below in equation (1).

$$\begin{aligned} &\text{For } i=1 \text{ to } 16 \text{ do} \\ &RE_i = LE_{i-1} \oplus P_i; \\ &LE_i = F[RE_i] \oplus RE_{i-1}; \\ &\qquad LE_{17} = RE_{16} \oplus P_{18}; \\ &\qquad RE_{17} = LE_{16} \oplus P_{17} \quad \ldots\ldots\ldots (1) \end{aligned}$$

The Decryption operation equation is given below in equation (2).

$$\begin{aligned} &\text{For } i=1 \text{ to } 16 \text{ do} \\ &RD_i = LD_{i-1} \oplus P_{19-1}; \\ &LD_i = F[RD_i] \oplus RD_{i-1}; \\ &\qquad LD_{17} = RD_{16} \oplus P_1; \\ &\qquad RD_{17} = LD_{16} \oplus P_2 \quad \ldots\ldots\ldots (2) \end{aligned}$$

The flowchart depicts Encryption process of converting plaintext in to Cypher text as shown below

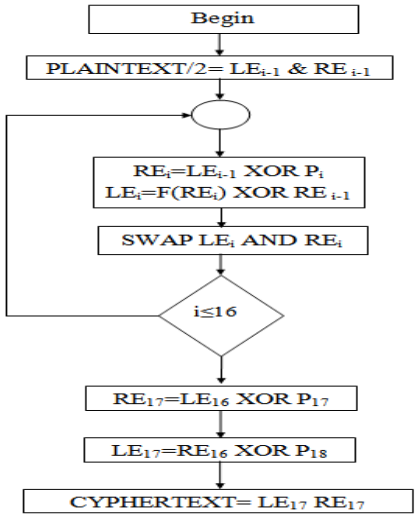

Fig.1.0: Encryption Process Flowchart

Fig. 1.0 indicates the complete process of LE and RE generations in every round of operation which includes XOR, Fiestel Function (F) and Swapping operation. Every round is supported by P-array elements.. After completion of 16-rounds of operations, LE_{16} and RE_{16} are XORed with P_{17} and P_{18} to generate RE_{17} and LE_{17}. LE_{17} and RE_{17} are concatenated to get the 64-bit Cyphertext as an output. Reverse operation is performed in the decryption process.

3. ARCHITECTURAL DESIGN OF PROPOSED BLOWFISH ALGORITHM

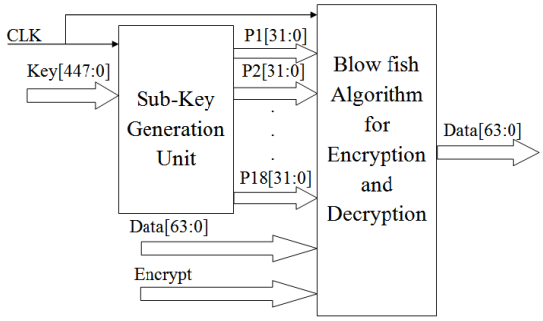

Fig.2.0: Top level Design module of Blowfish Algorithm

As shown in fig.2.0 above, Blowfish algorithm [5, 13] is divided in to two parts: Encryption & Decryption unit for data processing and Sub-key generation Unit for generation of sub-keys to be used in each round of operation. In the data encryption and Decryption block, input 64-bit data block is divided in to two halves as 32-bit Left Encryption (LE) and 32-bit Right Encryption (RE). In each round of operation, the algorithm will perform RE and LE operations as shown in equation (1) for encryption and equation (2) for Decryption which is also shown in fig.1.0 for Encryption process. The Fiestel function (F) in each round consists of combination of substitution, addition/modulo addition, XOR and addition/modulo addition operations. Thus, the algorithm follows the procedure for 16-rounds. RE_{16} and LE_{16} are XORed with P_{17} and P_{18} respectively to generate RE_{17} and LE_{17}. Reverse operation is performed for the decryption operation [7] [11] [22].

The sub-key generation unit is to generate 18- sub-keys (P-Array) from 448-bit input key, i.e., K-array has 14 input sub-keys of 32-bit each, can be used in generating P-Array of P1 to P18 initial sub-keys as shown in fig.2.0, each one is 32-bit in width which is updated as per the following equations (3):

P1=P1^K1, P2=P2 ^K2…P14=P14^K14,
P15=P15^K1, P16=P16 ^K2,
P17=P17^K3, P18=P18 ^K4; (3)

Where K1 to K14 (32-bits each) are generated from 448-bit input key.

3.1. MODULO- M-BIT ADDER:

In the encryption or decryption operation, modulo-addition operation [24] with and without WDDL logic is shown in fig.3.0. For increasing the speed of series adders in this figure can be operated in parallel. one adder adds Two h-bit residues, X and Y to form their sum $S_1+2^hC_{out1}$.Another one is 3-operand adder that computes "X+Y+m". Note that if $m=2^n+1$, we have h=n+1.It has been reported that if either Cout1 or Cout2 of this addition is '1' then the output is X+Y+m instead of X+Y. However, in the following we illustrate that only if the carry of "X+Y+m" is '1', it is sufficient to select it as the final output.

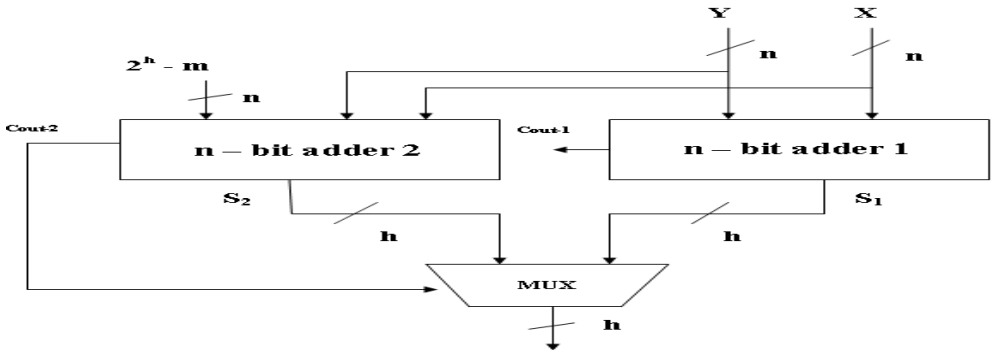

Fig.3.0: Modulo M –bit adder

3.2. CONSTANT DELAY N-BIT ADDER:

Constant Delay n-bit adder is adder is used to perform two array addition operations as shown in fig.4.0. The main advantage of this adder is irrespective of input the delay is constant so it's called Constant Delay n-bit adder.

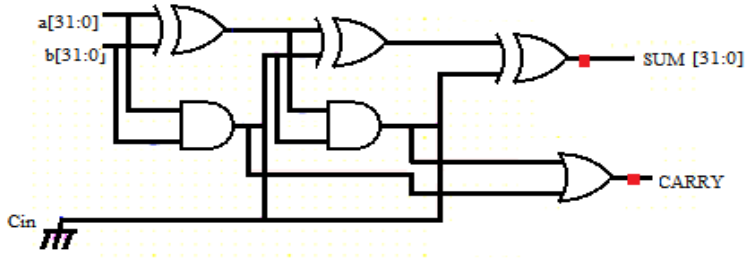

Fig.4.0: Constant Delay n-Bit Adder

The constant delay n-bit adder consists of three n-bit XOR gates, two n-bit AND gates, one n-bit OR gate. In this the input arrays are Xored in XOR n-bit gate and AND operation is performed in AND n-bit gate. The Output of AND n-bit gate is performed left shift operation and the resulted value XORed with output of XOR n-bit gate and AND operation with AND n-bit gate. Again the Output of AND gate is performed left shift operation and the resulted value XORed with output of present XOR n-bit gate. The output of XOR n-bit adder is declared as sum of constant delay n-bit adder. The MSB bit of each AND n-bit gate output before shift, is performed OR operation with OR gate and output is declared as carry bit output.

4. RESULTS AND DISCUSSION

The implementation of Blowfish Algorithm is done in three methods which are compared with Triple DES Algorithm. The implementation of the design followed bottom up approach. The test bench is written in Verilog HDL for every module of the design to provide 100% code coverage of the design. Top level Test Bench (TB) of the design is instantiated with top module of the design which consists of all the sub modules instantiated in it. Test cases are generated, applied to the Design Under Test (DUT) and results are generated for further verification of functionality, Delay estimation, frequency of the design and Throughput calculation. Mentor Graphics ModelSim is used for simulation. Xilinx ISE Design Suite14.2 is used to implement the design on Altera 6.3g_p1 (Quartus II 8.1). The synthesis tool Xilinx ISE 14.2 generated the RTL circuit, Memory Utilization, Propagation delay and even the percentage of area utilized by the design. The Comparison of the four implementations is given in the table.1. This paper compares delay, frequency, memory utilization and throughput of the four implementations listed in the table. 1.

Table.1 Comparison Of BFMAWDDL, BFMA, BFCDNBA And Triple DES Implementations

S NO	Crypto processor algo/parameter	Delay (ns)	Freq(10KHz)	Memory Utilization (Mb)	Throughput (Mbps)
1	Triple DES	197.241	506	294.74	320
2	BF with modulo adder and WDDL logic (BFMAWDDL)	112.566	888.4	469.384	570
3	BF with modulo adder (BFMA)	99.395	1006	460.808	640
4	BF with constant delay n-bit adder and WDDL Logic (BFCDNBA)	76.337	1309	520.584	840

In the delay comparison shown in fig.5.0, Blowfish with constant delay n-bit adder and WDDL logic implementation produces constant delay irrespective of number of stages of adders in the parallel adder design. Constant delay adder makes lot of difference in hardware implementation compared to modulo adder with and without WDDL gates. Hence, it resulted in lowest delay (76.337ns) compared to other implantations.

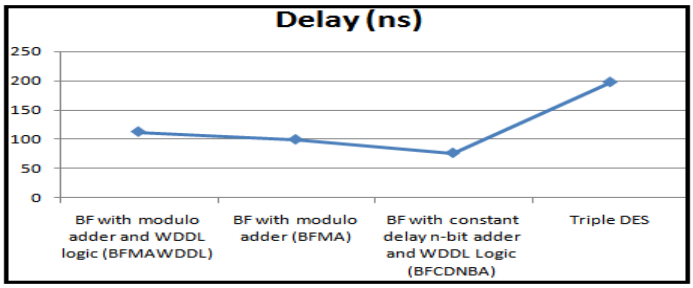

Fig.5.0: Delay comparison of BFMAWDDL, BFMA, BFCDNBA and Triple DES implementations

As the delay is less for Blowfish with constant delay n-bit adder and WDDL logic because of parallelism in implementing the hardware design,the frequency is more (13.09MHz) for

BFCDNBA implementation compared to TDES, Blowfish with modulo adder implementations as shown below in fig.6.0. As the frequency of design is high which can convert plaintext to ciphertext at faster rate. Triple DES , Blowfish with modulo adder with and without WDDL logic implementations are more of sequential implementations. Hence, they are slow. Critical path delay is reduced with effective implementation and thus the frequency is improved for constant delay n-bit adder approach.

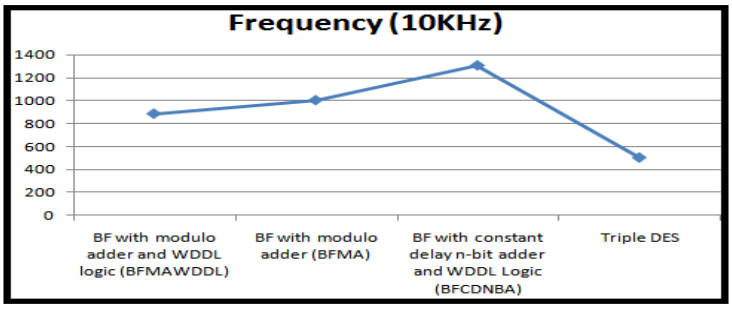

Fig.6.0: Frequency comparison of BFMAWDDL, BFMA, BFCDNBA and Triple DES implementations

As per fig.7.0 shown below, the memory utilization of BFCDNBA is more (520.584Mb) because more of parallelism in implementing the hardware design, data related to more number of operations and more iterations are to be stored than other implementations for high speed of Encryption and Decryption processes. S-Boxes are also called as Look Up Tables (LUTs) contains large number of data items to be stored in for future substitutions. Intermediate P-array keys are also requires more memory utility to generate sub-keys for every round of encryption and decryption operations.

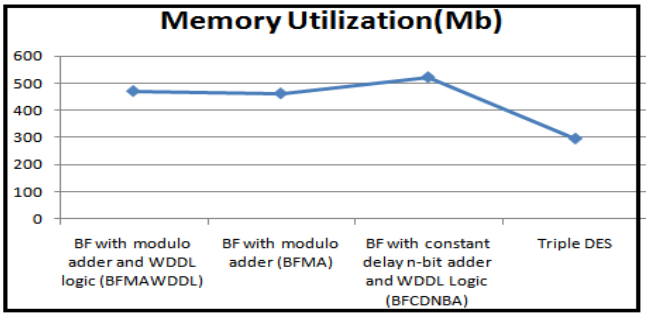

Fig.7.0: Memory Utilization comparison of BFMAWDDL, BFMA, BFCDNBA and Triple DES implementations

Throughput is defined as the ratio of number of bits Encrypted/Decrypted to the time taken by the algorithm. As per the results obtained shown in fig.8.0, BFCDNBA implementation yielded best throughput (840Mbps) compared to other implementations considered. As explained with respect to fig.5.0, the delay is very less in BFCDNBA implementation compared to other implementations considered in this research work. Hence throughput is very good in the BFCDNBA implementation.

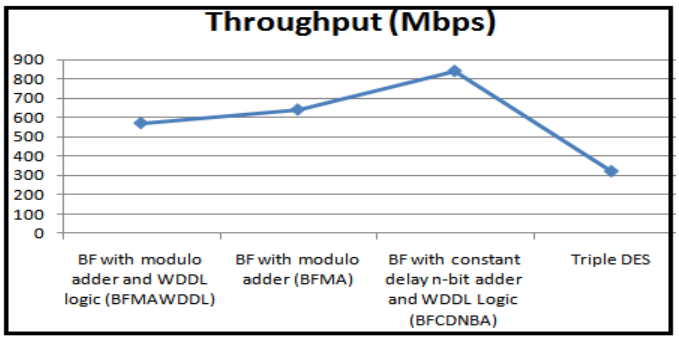

Fig.8.0: Throughput comparison of BFMAWDDL, BFMA, BFCDNBA and Triple DES implementations

As shown in fig. 9.0, delay of the Blowfish with constant delay n-bit adder and WDDL logic implementation is less and thus throughput of the same is more than the other implementations considered in this research paper. Even though the number of bits of the adder is increasing, the delay is constant and thus the throughput is increased with this approach.

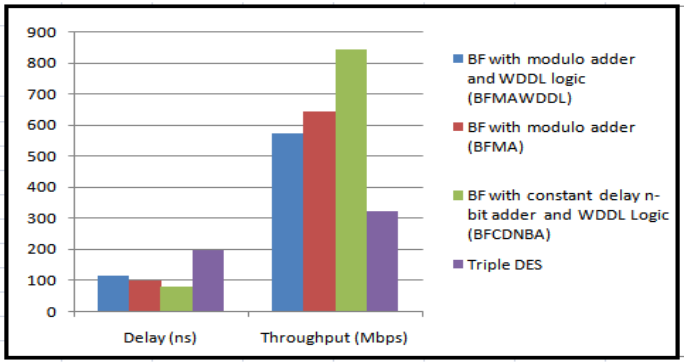

Fig.9.0: Delay and Throughput comparison of BFMAWDDL, BFMA, BFCDNBA and Triple DES implementations

5. CONCLUSIONS

As discussed in the results and discussion that BFCDNBA implementation gave better results compared to other implementations. Constant delay n-bit adder circuit used in the Blowfish Algorithm which reduced the delay to 76.337ns, increased frequency to 13.09MHz and thus increased throughput to 840Mbps compared to BFMAWDDL, BFMA and Triple DES implementations. It is providing more security because of 448 bit key length and incorporating WDDL logic in the Encryption and Decryption process of Crypto-processor digital design flow. However, the memory utilization is more (520.584Mb) for BFCDNBA implementation compared to other implementations considered in this research paper because of its complexity, more number of iterations/operations and more key length to provide at most security to the plaintext. Blowfish algorithm is developed in Verilog HDL and implemented it on ModelSim-Altera 6.3g_p1 (Quartus II 8.1) Web Edition and Xilinx ISE Design Suite14.2. This was run on a Windows 7 Home Basic (64-bit) Operating System, Intel® Core(TM) i3-2350M Processor @ 2.30 GHz clock rate with an internal Memory of 4 GB and 500 GB Hard Disk.

Future scope of this research work is to decrease the delay, improve the frequency and yielding better throughput compared to BFCDNBA implementation. This research work is also expected extend it analysis to compare the area utilization of the crypto algorithms considered in this design.

ACKNOWLEDGEMENT

The author would like to thank Dr. Prabhu Benakop for his continuous guidance and support to carry out this research work and present it in a systematic way.

REFERENCES:

[1] Rafidah Ahmad, AsrulnizamAbd. Manaf, "Development of an Improved Power-Throughput Blowfish Algorithm on FPGA", 2016 IEEE 12th International Colloquium on Signal Processing & Its Applications (CSPA),Vol 12, 06 March 2016.

[2] Nusrat Jahan Oishi, Arafin Mahamud, Asaduzzaman, "Enhancing Wi-Fi Security Using a Hybrid Algorithm of Blowfish and RC6",2016 International Conference on Networking Systems and Security (NSysS), 7-9 Jan, 2016..

[3] Viney Pal Bansal,Sandeep Singh, "A Hybrid Data Encryption Technique using RSA and Blowfish for Cloud Computing on FPGAs", 2015 2nd International Conference on Recent Advances in Engineering & Computational Sciences (RAECS), 21-22 Dec. 2015

[4] Ashraf Odeh, Shadi R.Masadeh, Ahmad Azzazi, "A Performance Evaluation of Common Encryption Techniques with Secure Watermark System (SWS)", International Journal of Network Security & Its Applications (IJNSA), Vol.7, No.3, May 2015, DOI : 10.5121/ijnsa.2015.7303

[5] Vaibhav Poonia, Dr.Narendra Singh Yadav, "Analysis of modified Blowfish Algorithm in different cases with various parameters", International Journal of Engineering Research and General Science Volume 3, Issue 1, January-February, 2015 ISSN 2091-2730.

[6] Kurniawan Nur Prasetyo, YudhaPurwanto, Denny Darlis, "An implementation of data encryption for internet of things using Blowfish algorithm based on FPGA", Vol 2, 2014.

[7] V .Kumara Swamy, Dr Prabhu G Benakop, "High Throughput and High Speed Blowfish Algorithm for Secure Integrated Circuits", Ana le. Seria Informatică. Vol. XII fasc. 1 – 2014, Annals. Computer Science Series. 12th Tome 1st Fasc. – 2014

[8] Amaal A. Abd El-Sadek, Talaat A. El-Garf, Mohammed M.Fouad, "Speech Encryption Applying a Modified Blowfish Algorithm", October 2014.

[9] Meenakshi Shankar, Akshaya.P, "Hybrid Cryptographic Technique using RSA Algorithm and Scheduling Concepts", International Journal of Network Security & Its Applications (IJNSA) Vol.6, No.6, November 2014, DOI : 10.5121/ijnsa.2014.6604.

[10] Ranjeet Masram, Vivek Shahare, Jibi Abraham, Rajni Moona," Analysis and Comparison of Symmetric Key Cryptographic Algorithms based on various file features", International Journal of Network Security & Its Applications (IJNSA), Vol.6, No.4, July 2014, DOI : 10.5121/ijnsa.2014.6404.

[11] V .Kumara Swamy, Dr Prabhu G Benakop, "Performance Analysis of Secure Integrated Circuits using Blowfish Algorithm", Global Journal of Computer Science and Technology Network, Web & Security, Volume 13, Issue 17, Version 1.0,Page no.10-15, December 2013, Global Journals Inc (USA), Online ISSN. 0975-4172, Print ISSN.0975-4350.

[12] Kuo-Tsang Huang , Jung-Hui Chiu1 and Sung-Shiou Shen, "A Novel Structure with Dynamic Operation Mode for Symmetric-Key Block Ciphers", International Journal of Network Security & Its Applications (IJNSA), Vol.5, No.1, January 2013, DOI : 10.5121/ijnsa.2013.5102

[13] Monika Agrawal, Pradeep Mishra, "A Modified Approach for Symmetric Key Cryptography Based on Blowfish Algorithm", International Journal of Engineering and Advanced Technology (IJEAT) ISSN: 2249 – 8958, Volume-1, Issue-6, August 2012.

[14] M.Chandra Mohan, V.Kumara Swamy, Dr. T.Srinivasulu, "Design of High Speed AES Algorithm", International Conference on Electronics and Communication Engineering (ICECE-2012),GNIT, Hyderabad, Andhra Pradesh, India, 19-20,July 2012

[15] Monika Agrawal, Pradeep Mishra, 'A Comparative Survey on Symmetric Key Encryption Techniques', International Journal on Computer Science and Engineering (IJCSE), ISSN : 0975-3397, Vol. 4, No. 05, pp.877, May 2012

[16] Gurjeevan Singh, Ashwani Kr. Singla, K.S. Sandha, "Superiority of Blowfish Algorithm in Wireless Networks", International Journal of Computer Applications, ISSN: 09758887, Volume 44– No11, April 2012

[17] Walied W. Souror, Ali E. Taki el-deen, Rasheed Mokhtar-awady Ahmed, Adel Zaghlul Mahmoud - An Implementation of High Security and High Throughput Triple Blowfish Cryptography Algorithm, International Journal of Research and Reviews in Signal Acquisition and Processing (IJRRSAP) Vol. 2, No. 1, March 2012, ISSN: 2046-617X.

[18] Gurjeevan Singh, Ashwani Kumar Singla, K. S. Sandha - Through Put Analysis of Various Encryption Algorithms, IJCST Vol.2, Issue3, September 2011.

[19] Diaa Salama, Hatem Abdual Kader and Mohiy Hadhoud (2011), "Studying the Effects of Most Common Encryption Algorithms", International Arab Journal of e-Technology, Vol. 2, No. 1, January 2011, pp 1-10.

[20] SimarPreet Singh, and Raman Maini (2011), "Comparison of Data Encryption Algorithms", International Journal of Computer Science and Communication Vol. 2, No. 1, January-June 2011, pp. 125-127.

[21] A.Rathika, Parvathy Nair and Parvathy Nair (2011), "A High Throughput Algorithm for Data Encryption" International Journal of Computer Applications (0975 – 8887) Volume 13, No.5, January 2011 pp 13-16.

[22] V.Kumara Swamy, Dr Prabhu G Benakop and P.Sandeep, "Implementation of a digital design flow for DPA secure WDDL Cryptoprocessor using Blowfish Algorithm", Libyan Arab International Conference on Electrical and Electronic Engineering(LAICEEE-2010), Tripoli, Libya, October 23-26, 2010, pp.565-73

[23] Tingyuan Nie, Chuanwang Songa and Xulong Zhi (2010), "Performance Evaluation of DES and Blowfish Algorithms", Proceedings of 2010 IEEE International Conference on Biomedical Engineering and Computer Science (ICBECS- 2010), 23-25 Apr 2010. pp 1-4.

[24] Somayeh Timarchi, Keivan Navi - Improved Modulo 2n +1 Adder Design, International Journal of Computer and Information Engineering 2:7 2008.

AUTHORS BIBLIOGRAPHY:

V. Kumara Swamy completed his B.E (ECE) in1998 from Osmania University, Hyderabad and his M.Tech (DSCE) in 2005 from JNTUH, Hyderabad and pursuing PhD in the area of VLSI Design from JNTUH, Hyderabad. His areas of research include VLSI Design, advanced Digital Design, Cryptography and Computer Networks and Applications. He has published 8 research papers in international journals and conference proceedings. He has expertise in industry standard EDA tools such as Cadence, Mentor Graphics and Xilinx Tools etc. He has 20 years of teaching and research experience in India and abroad. He is currently working as an Associate Head, Department of ECE in Sreenidhi Institute of Science and Technology, Hyderabad, Telangana, India

Dr. Prabhu G Benakopis a renowned educationalist and he is currently working as Principal in INDUR Institute of Engineering & Technology, Telangana State, India. Formerly he held the positions of PRINCIPAL in Aurora's Engineering College, Director in Aurora's Technological and Research Institute, Hyderabad. He has 28years of teaching and research experience. Senior Member, IEEE, Member, International Biomedical Engineering, Life Member of Indian Society for Technical Education, Life Member of CSI, Life Member of Instrument Society of India. Guided/Guiding 11 research scholars under JNTUH, Hyderabad and VTU Bangalore for PhD programme. His areas of research include VLSI System Design, Embedded Systems, Computer Networks, and Biomedical Signal Processing. He has published more than 90 research papers in national, international journals and conference proceedings.

International Journal of Civil Engineering and Technology (IJCIET)
Volume 8, Issue 4, April 2017, pp. 339–353 Article ID: IJCIET_08_04_040
Available online at http://www.iaeme.com/IJCIET/issues.asp?JType=IJCIET&VType=8&IType=4
ISSN Print: 0976-6308 and ISSN Online: 0976-6316

STUDY ON DUCTILITY BEHAVIOR OF DIFFERENT TYPES OF SHEAR CONNECTORS IN COMPOSITE STRUCTURAL ELEMENTS

P. Sai Shraddha
Post Graduate Student, Structural Engineering, SRM University,
Chennai, TamilNadu, India

C. Sudha
Assistant Professor, Civil Engineering Department, SRM University,
Chennai, TamilNadu, India

Dr. M. Lakshmipathy
Professor, Civil Engineering Department, SRM University,
Chennai, TamilNadu, India

ABSTRACT

Composite Structures have several advantages over traditional reinforced concrete which incorporate high strength to weight ratios, dimensional stability and structural integrity. Late years have seen a considerable increment in the utilization of composite structures and improved research went for creating new strategies for combining steel and concrete. composite structures result in efficient design and economy in construction time hence used especially in construction of building floors and bridges. Wide construction practices involve connecting Concrete slab and hot rolled steel beam sections by shear connectors. Shear Connectors are used to enhance proper connection and resist horizontal shear forces. A Composite member has to be designed in such a way that before composite structural element reaches ultimate capacity, shear connectors should not fail due to lack of ductility. In this study Finite Element Analysis has been done on four types of shear connectors for ductility criteria. Push-out test Specimen and Composite beam modeling with four different types of shear connectors is done in ANSYS and are analyzed. The Analytical results are presented and focused on the study of ductility behavior and load slip behavior of connectors of varying height in composite beams.

Key words: Shear connectors, Push-out test, Composite beam, Ductility, Load slip behavior.

Cite this Article: P. Sai Shraddha, C. Sudha and Dr. M. Lakshmipathy, Study on Ductility Behavior of Different Types of Shear Connectors in Composite Structural Elements. *International Journal of Civil Engineering and Technology*, 8(4), 2017, pp. 339–353.
http://www.iaeme.com/IJCIET/issues.asp?JType=IJCIET&VType=8&IType=4

1. INTRODUCTION

Since 1920 there has been an incredible increment in the usage of composite structures in Bridge and tall building construction. Generally the construction strategy employs connecting a Concrete slab and Steel beam sections by different types of connectors to suite the purpose. Resistance offered in compression and tension by Concrete and Steel respectively is completely utilized by connecting them properly through Shear connectors. Shear connectors which are generally welded to the flange of steel section resist the horizontal Shear forces present at the interface of concrete and steel and also ensures a legitimate bond between them.

Shear connectors are of various sorts and depending upon the purpose of use, quality, strength and deformation they can be divided as Rigid and Flexible shear connectors. If the failure of the connector occurs by front side shearing and there is an accumulation of stress in the surrounding concrete then the connector can be called as rigid shear connector. This type of connector results in concrete area failure or failure by cracking of weld. If the failure of connector is by shearing of connector at the root or connection point and if it undergoes plastic deformation then the connector can be called as flexible connector. Flexible connectors are more ductile connectors. Different types of shear connectors have been developed in accordance with time and use.

1.1. Headed Studs

Headed stud is a short round piece of cold drawn steel which is welded to the beam at one edge and has a greater diameter head at the other end in to the concrete slab which helps in uplifting of concrete slab from the steel beam. It is the most commonly used connector because of its ease in placing and welding. They prove to be non ductile connectors and result in large interfacial slip. They go in coherence when used with concrete of low strength. Breakdown of shear connection can occur by stud shearing failure or crushing of concrete.

1.2. Perfobond Shear connector

In recent years (1980) a connector called perfobond shear connector was developed by Leonhardt, Andra and partners to overcome the fatigue issues caused by stud connectors when used in bridges. Generally a steel plate with a number of circular openings welded to beam flange can be called as perfobond connector. The concrete which flows through these connector holes helps in creating a dowel action amongst concrete and connector. Thus it improves the bondage property and offers good resistance in both horizontal and vertical directions. The structural behavior of these connectors is highly impacted by its dimensional properties, number of holes, diameter of holes, thickness, length and height of plate.

1.3. Channel Connectors

When one flange of rolled Channel section is welded to steel beam flange, it can be called as Channel connector. Channel connectors are rarely used where field installations are required and are generally shop welded. A very small number of channel connectors can supplant a large number of headed studs because of their expected higher load carrying capacity. Inspection procedures required for channel connectors are low because of high reliable and dependable welding system adopted.

1.4. I-shape Shear Connectors

Various reasons like monetary contemplations and strength aspects has persuaded in development of I-shape shear connector. Due to its symmetry in both the axes, it offers more resisting in bending. Similar to channel connector, connection is established by welding one flange of rolled I section to flange of steel beam.

Connectors are those with adequate deformation capacity to legitimize any inelastic redistribution of shear assumed in design can be called as ductile connector. A Shear connector can be called as ductile connector if its characteristic slip is at least 6mm [Euro code 4]. In this paper an attempt has been made to study about ductility and load slip behavior of different shear connectors analytically by nonlinear static analysis and the results are compared by software package ANSYS.

2. ANALYTICAL STUDY

Ductility, bondage and shear strength of a connector can be discovered from the push-out test. Properties of connector like height of connector, embedded depth of connector, modulus of elasticity etc., influences it's behavior under load. Behavior of Shear connectors is also influenced by grade of concrete and the reinforcement provided in the concrete slab.

2.1. Finite Element Analysis in ANSYS

Push-out test specimen is modeled in ANSYS. Concrete is modeled using SOLID 65 element and BEAM 189 element is used for modeling Steel. SOLID 65 is a eight node element with six degrees of freedom at each node. This element is used for Reinforced or plain concrete models. When considered in structural analysis point of view, this element has large deflection and stress stiffening capabilities. Geometry, node locations and coordinate system of this element are shown below.

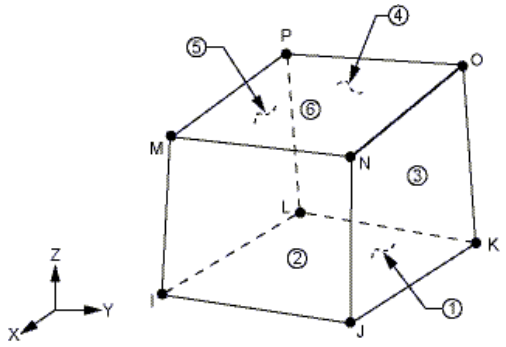

Figure 1 Solid 65 Element

BEAM189element is suitable for analyzing slender to moderately thick beam structures. This element has six degrees of freedom at each node which include translations and rotations in the x, y, and z directions. An additional option of restrained and unrestrained warping is also available with this element. When considered in structural analyses point of view, this element has large rotation, stress stiffness and large-strain nonlinear applications. Geometry, node locations and coordinate system of this element are shown below.

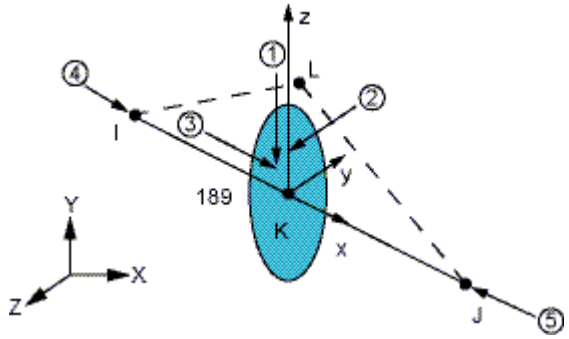

Figure 2 BEAM 189 Element

M 40 and Fe 250 are the grades of concrete and steel used for modeling respectively. The material properties adopted for the different elements in analysis are given in table below.

Table 1 Material Properties

Material	Poisson ratio	Young's modulus of Elasticity(N/mm^2)
I beam	0.3	200000
Shear connectors	0.3	200000
Concrete slab	0.17	31620

Uniformly distributed load is applied and increased at the rate of 50kN for each load step. The loading conditions are applied on the nodes of steel beam at the top until 6mm slip is observed at the base. The load and support conditions are maintained same in all models with different connectors.

2.2. Description of Push-Out Test Specimen

The Push-out specimen comprises of hot rolled steel section with concrete slab and shear connectors attached to both of its flanges. The push-out test specimens are modeled according to Eurocode 4 specifications with only the variation made in its dimensions. The dimensional properties of push-out specimen are given below.

Hot rolled Steel beam section: ISMB 200 @ 25.4 kg/m

Width of concrete slab on either side of flange: 100 mm

Breadth of Concrete slab: 250 mm

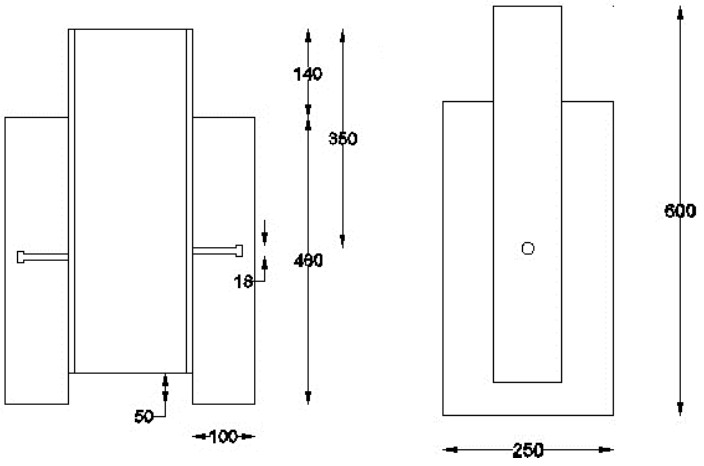

Figure 3 Details of push-out specimen used for analysis

Four of different types of Shear connectors are modeled and their load slip behavior is analyzed under load. The length and thickness of connectors is taken as 80mm and 10mm and are maintained constant for all these connectors. The Dimensional details of these connectors are given as follows.

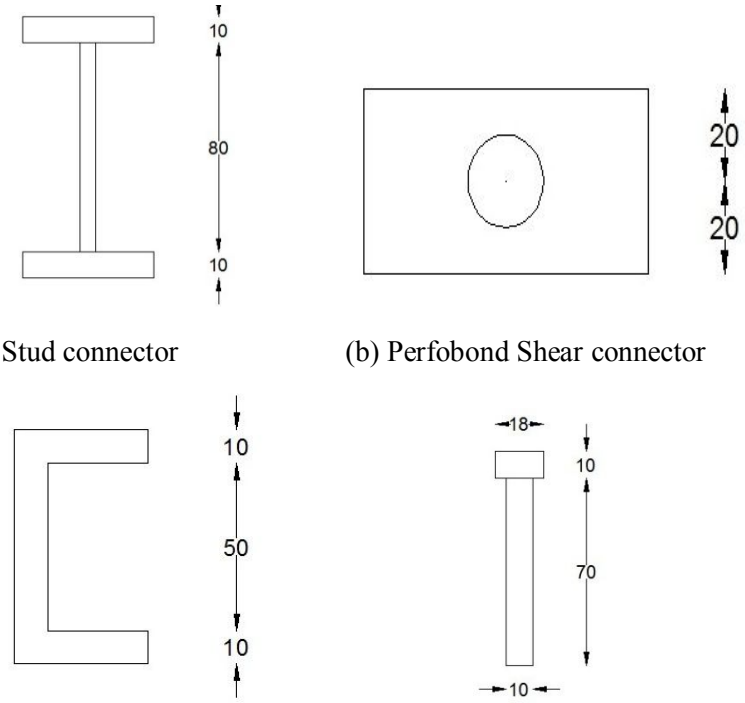

(a) Headed Stud connector (b) Perfobond Shear connector

(c) Channel Shear connector (d) I shape Shear connector

Figure 4 Details of Shear connectors used for analysis

2.2.1. Push-Out Test Analysis with Stud Connector

The Push-out test specimen is modeled with stud connector and meshing is done using a free mesh. The model consists of 5832 nodes and 25438 elements. Fixed end conditions are adopted to the nodes of concrete at the bottom of slab restraining all the degrees of freedom. The model, meshing, support conditions and the analytical results for stud connector specimen are as shown in figure 5.

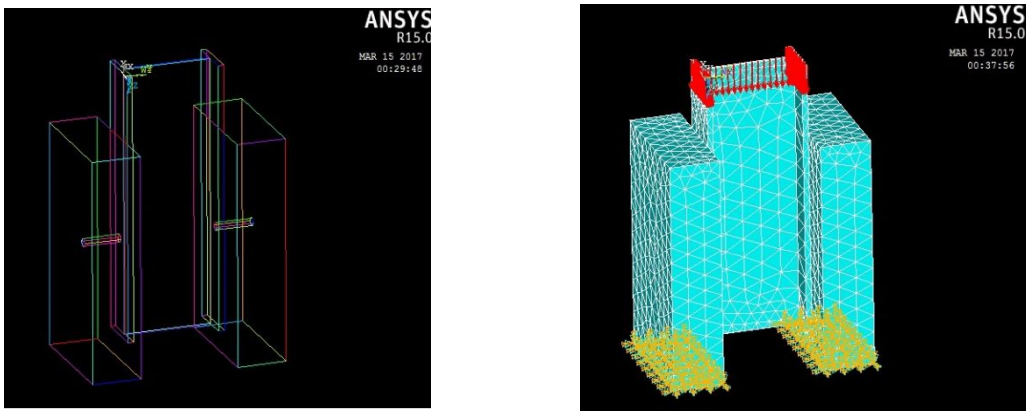

(a) Model of Push-out test specimen (b) Meshing of Push-out test specimen

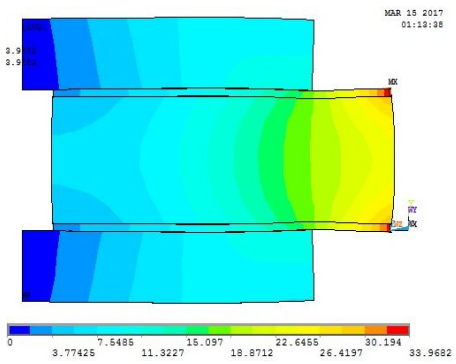

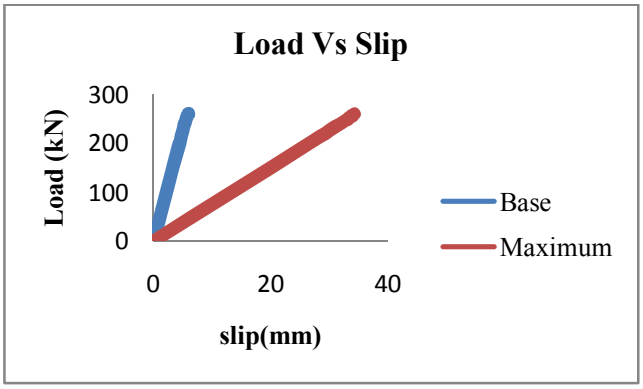

(c) Nodal displacement of push-out test specimen (d) Load Vs Slip behavior

Figure 5 Push-out test specimen with Stud connector

2.2.2. Push-Out Test Analysis with Perfobond Connector

The model consists of 6380 nodes and 26905 elements. The model, and the analytical results for perfobond connector specimen are as shown in figure 6

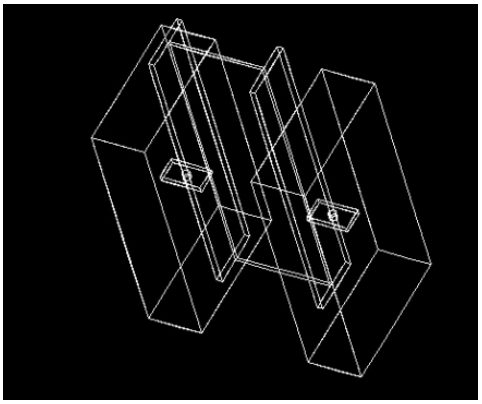

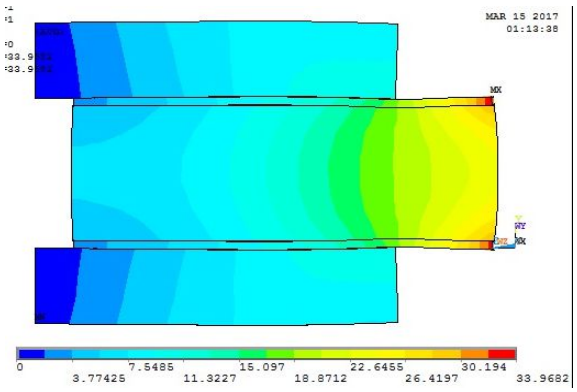

(a) Modeling of push-out test specimen (b)Nodal displacement of push-out specimen

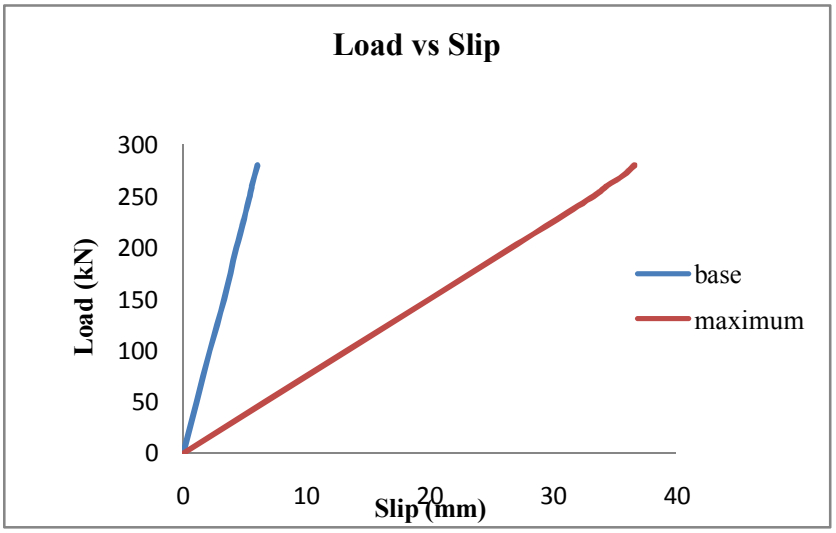

(c) Load Vs Slip behavior

Figure 6 Push-out test specimen with Perfobond connector

2.2.3. Push-Out Test Analysis with Channel Connector

The model consists of 9192 nodes and 38201 elements. The model and the analytical results for channel connector specimen are as shown in figure 7.

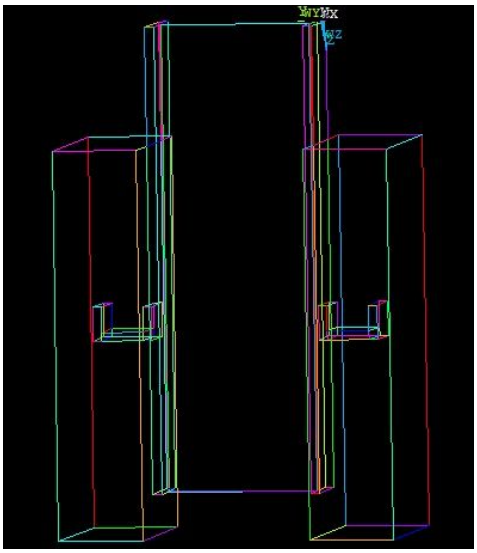

(a) Modeling of Push-out test specimen

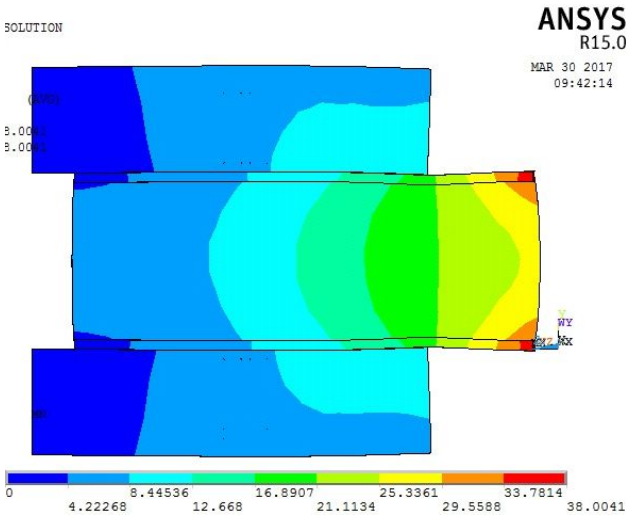

(b) Nodal displacement of push-out specimen

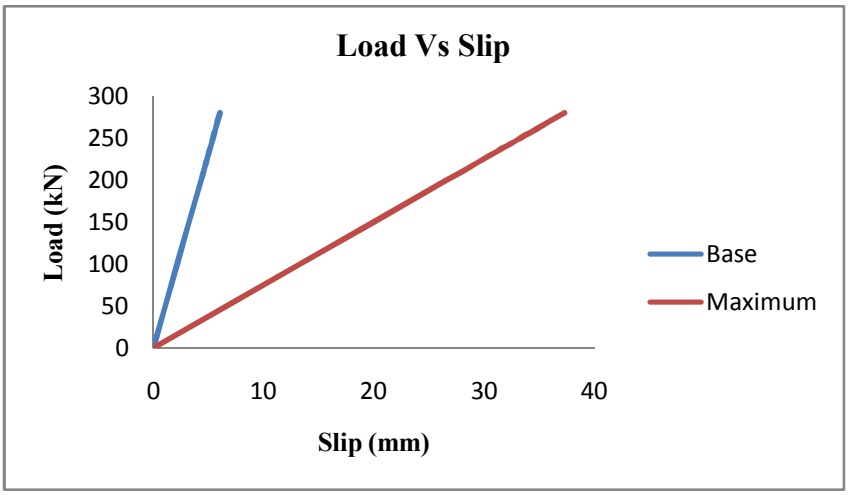

(c) Load Vs Slip behavior

Figure 7 Push-out test specimen with channel connector

2.2.4. Push-Out Test Analysis with I-Shape Shear Connector

The model consists of 9192 nodes and 38201 elements. The model and the analytical results for I-shape shear connector specimen are as shown in figure 8

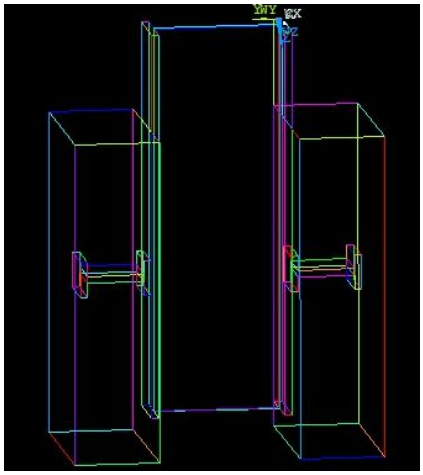

(a) Modeling of Push-out test specimen

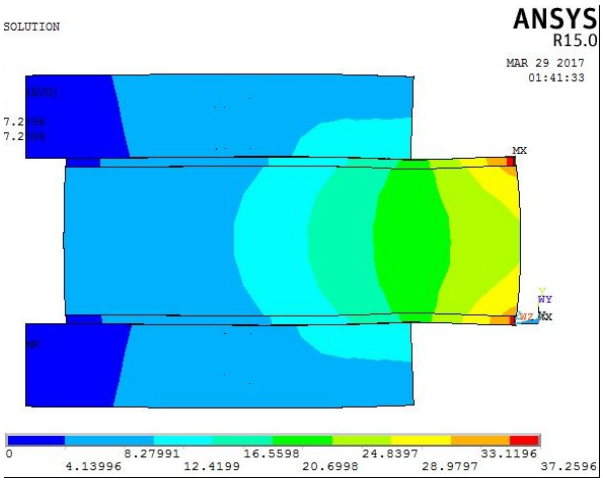

(b) Nodal displacement of push-out specimen

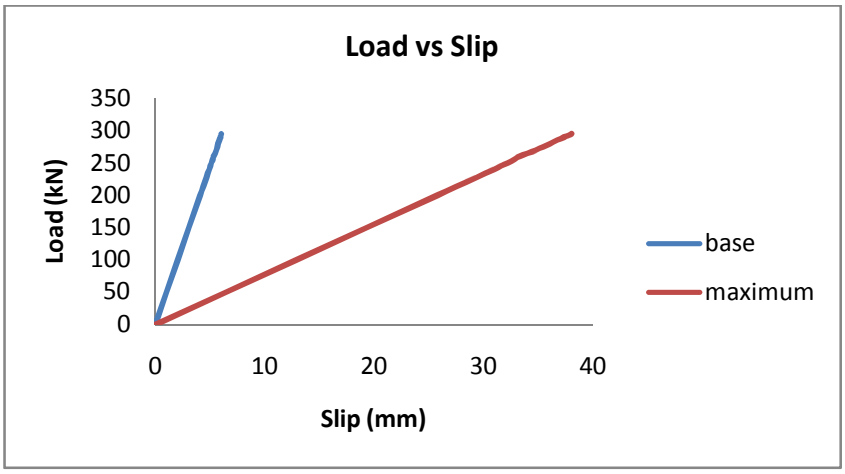

(c) Load Vs Slip behavior

Figure 8 Push-out test specimen with I shape shear connector

The displacement of the nodes at the base of I beam is calculated. The Nodal displacement at the base and the maximum displacement are as follows in Table 2.

Table 2 Slip values of different shear connectors

LOAD (kN)	SLIP (mm)							
	STUD		PERFOBOND		CHANNEL		I-SHAPE	
	Base	Max	Base	Max	Base	Max	Base	Max
50	1.12	6.66	1.08	6.66	1.07	6.65	0	6.44
100	2.24	13.32	2.16	13.32	2.15	13.3	2.05	12.88
150	3.36	19.98	3.32	19.99	3.23	19.96	3.08	19.32
200	4.48	26.64	4.32	26.65	4.32	26.61	4.11	25.76
250	5.6	33.3	5.4	33.31	5.4	33.27	5.14	32.2
260	6.02	34.36	5.57	34.38	5.61	34.6	5.35	33.24
270			5.79	35.71	5.81	35.93	5.59	34.78
280			6.02	36.63	6.04	37.26	5.76	36.07
290							5.97	37.36
295							6.04	38.04

2.3. Description of Composite Beam Specimen

A Composite Beam consists of hot rolled steel beam section connected to concrete slab by shear connectors .Composite beams specimens are analysed with different shear connectors and load slip behavior is studied. Uniformly Distributed load is applied at the rate of 50 kN for each load step up to 450kN. The dimensional details of beam are maintained constant when analysed with different types of shear connectors. Dimensional properties of Composite beam are as follows

Length of beam: 1500mm

Depth of concrete slab: 150mm

Width of concrete slab: 400mm

Distance between supports: 1300mm

2.3.1. Composite Beam with Stud Connectors

Stud connectors of 75mm length and a diameter of 16mm are modeled in the beam and load-slip behavior is analysed. The element and material properties are adopted as stated above. Modeling, meshing, support conditions and the analytical results for stud connector beam specimen are as shown below.

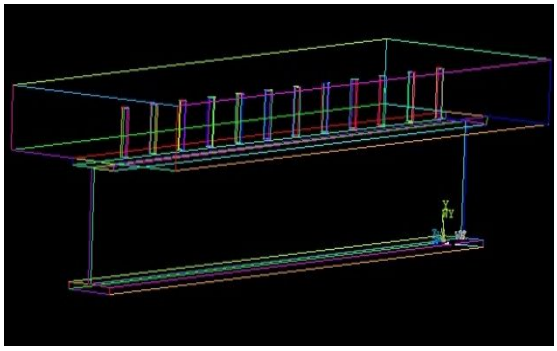

(a). Modeling of composite beam

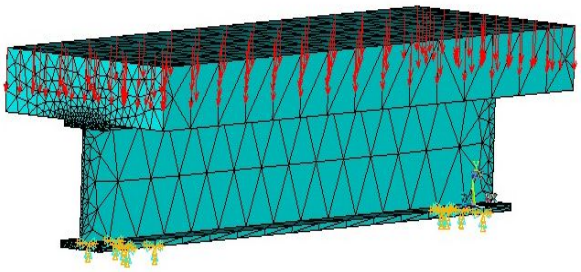

(b) Meshing of composite beam

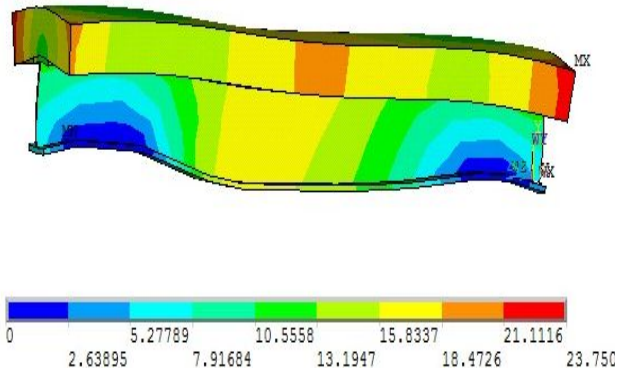

(c). Nodal Displacement

Figure 9 Composite beam with Stud connector

The composite beam is analysed with stud connectors of different heights namely 65mm,75mm and 100mm and load slip behavior is observed. Dimensions of beam, Material and element properties are maintained as above.

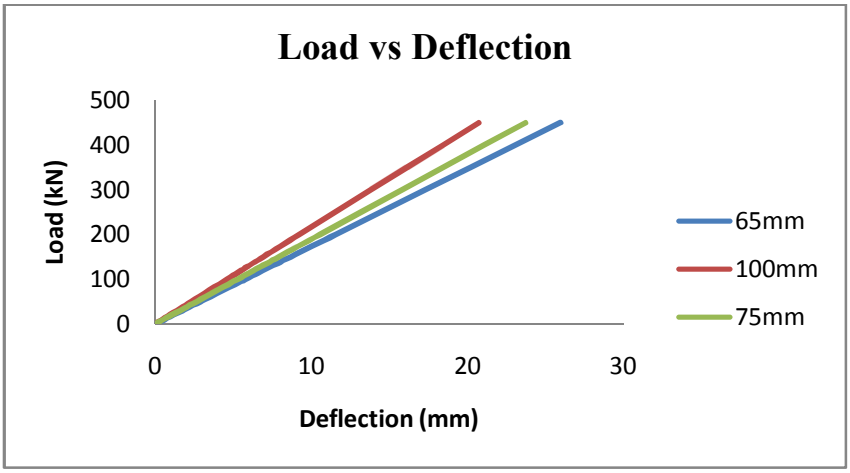

Figure 10 Load Vs Deflection behavior for varying height of stud connectors

2.3.2. Composite Beam with Perfobond Connectors

Perfobond connectors of 75mm height and 300mm length are modeled in the beam and load-slip behavior is analysed. The element and material properties are adopted as above. The model and the analytical results for perfobond connector beam specimen are as shown .in figure 11.

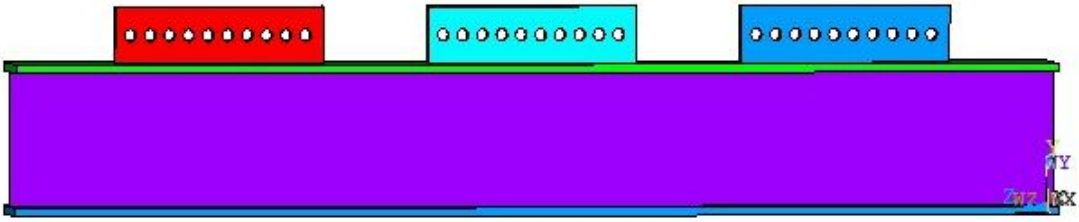

(a) Modeling composite beam

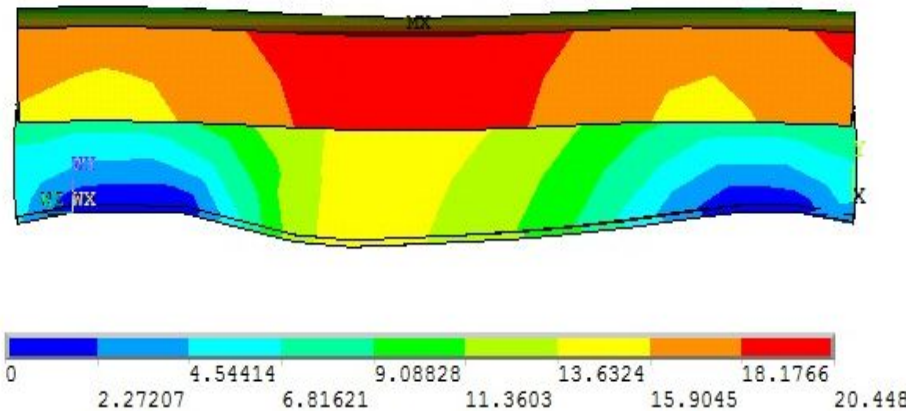

(b) Nodal displacement

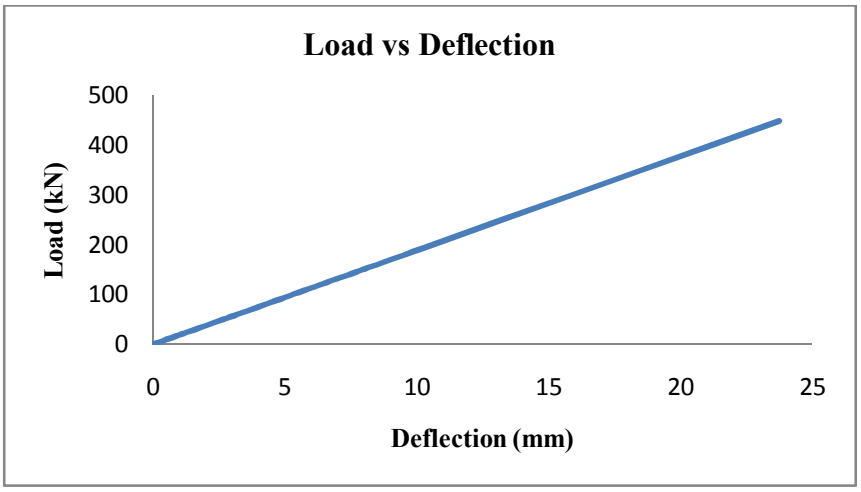

(c) Load Vs Deflection behavior

Figure 11 Composite beam with Perfobond connector

The composite beam is analysed with Perfobond connectors of different heights namely 75mm,85mm and 100mm and load slip behavior is observed.

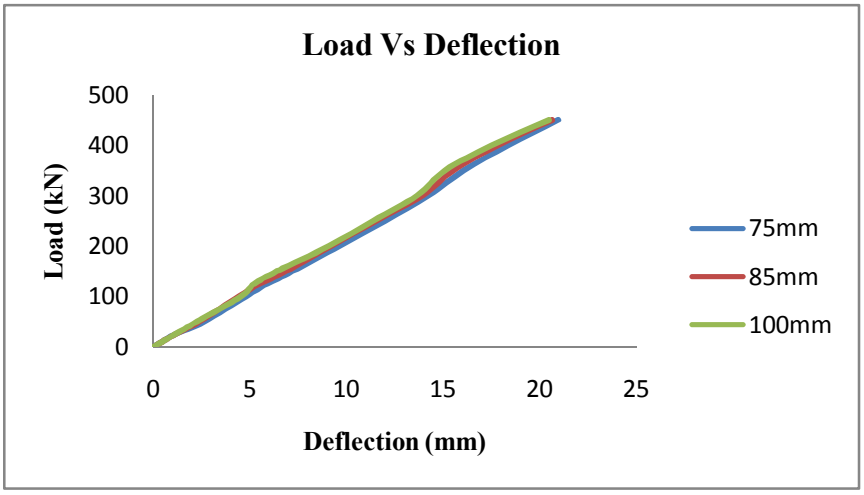

Figure 12 Load Vs Deflection behavior for varying height of Perfobond connectors

2.3.3. Composite Beam with Channel Connector

Channel connectors of 75mm height and 100mm length are modeled in the beam and load-slip behavior is analysed. The model and the analytical results for Channel connector beam specimen are as shown in figure 13.

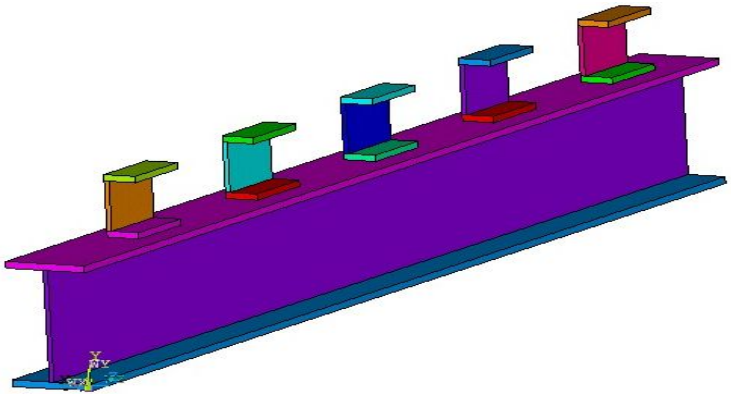

(a) Modeling of composite beam

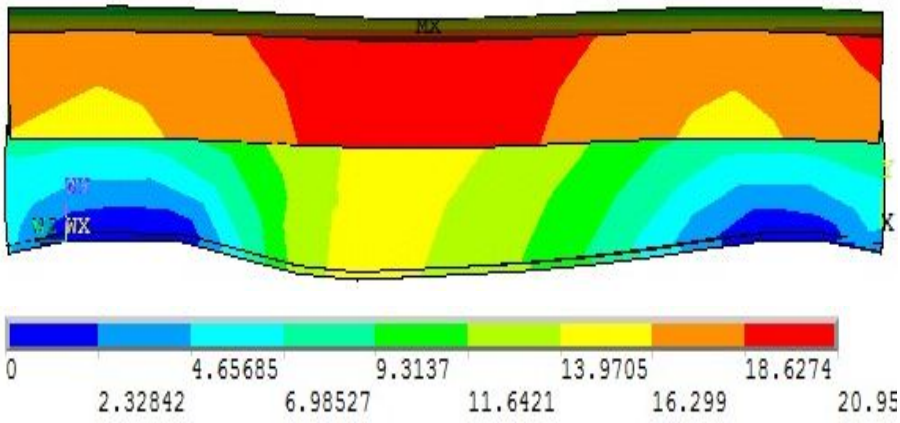

(b) Analytical result of composite beam

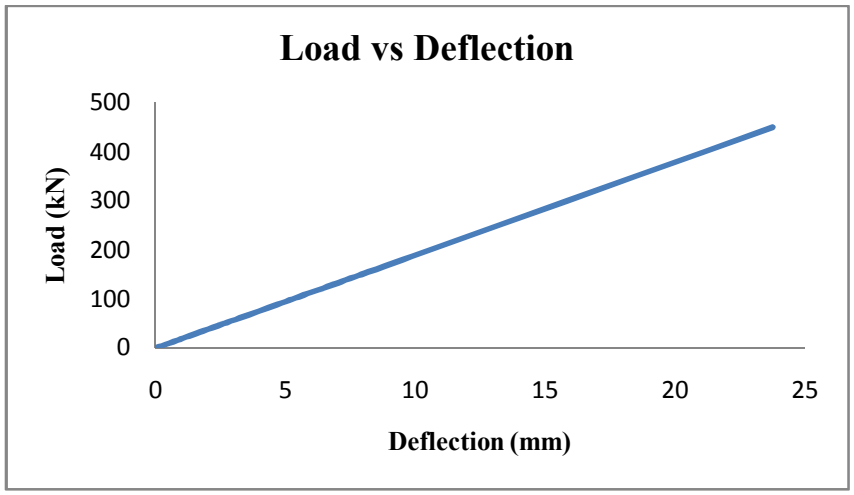

(c) Load Vs Deflection behavior

Figure 13 Composite beam with Channel connector

The composite beam is analysed with Channel connectors of different length namely 75mm,100mm and 125mm and load-slip behavior is observed.

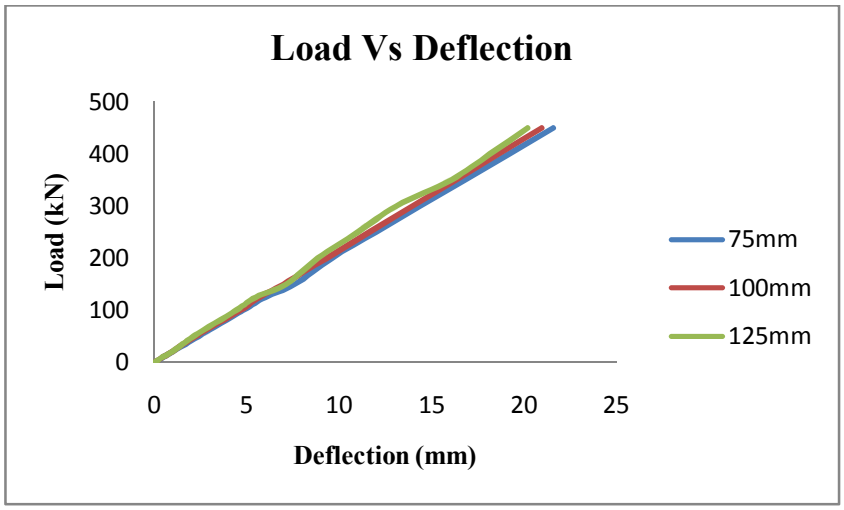

Figure 14 Load Vs Deflection behavior for varying height of Channel connectors

2.3.4. Composite Beam with I Shape Shear Connector

I shape shear connector of 75mm height and 100mm length are modeled in the beam and load-slip behavior is analysed. The model and the analytical results for I Shape shear connector beam specimen are as shown in figure 15.

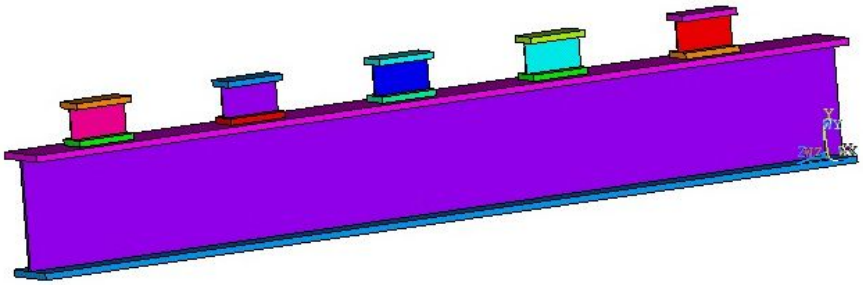

(a) Modeling of composite beam

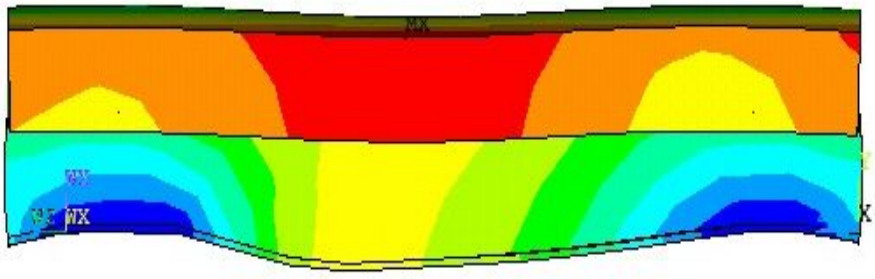

(b). Analytical result of composite beam

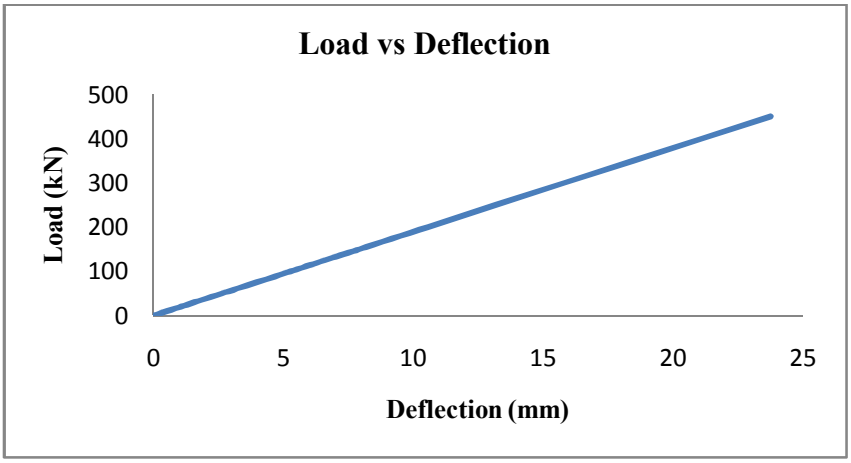

(c) Load Vs Deflection behavior

Figure 15 Composite beam with I shape shear connector

The composite beam is analysed with Channel connectors of different heights namely 75mm,100mm and 125mm and load-slip behavior is observed.

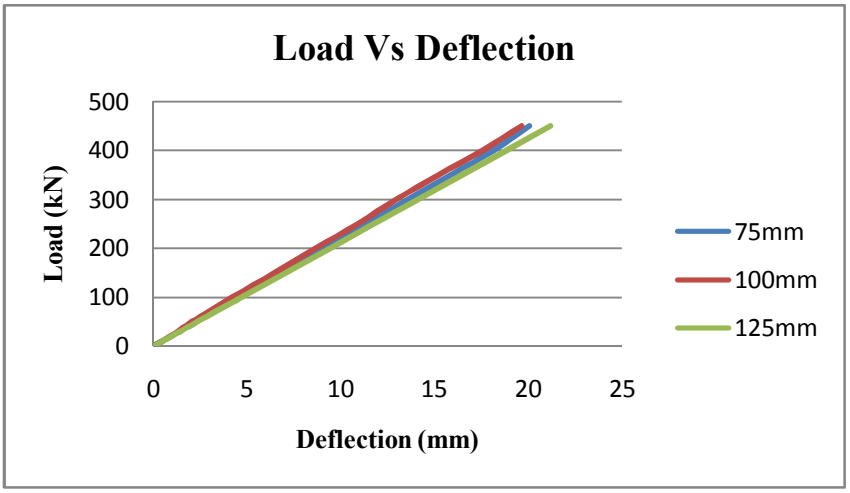

Figure 16 Load Vs Deflection behavior for varying height of I Shape connectors

3. CONCLUSION

According to Eurocode 4 if a shear connector allows at least a displacement of 6mm before failure it can be called as ductile shear connector. Finite element analysis of push-out test specimen is done and load-slip behavior is plotted for four different types of shear connectors. It is observed that the load at which Stud and Perfobond connectors reach a slip of 6mm is higher than the load carrying capacity of these connectors. This indicates that Stud and Perfobond connectors fail before reaching a slip of value 6mm. Channel and I shape connectors reach the slip value of 6mm within their load carrying capacity. According to the results obtained it can be observed that the channel and I shape connectors are ductile whereas Stud and Perfobond connectors are non ductile connectors.

When the same connectors are used in beams channel and I shape connectors show higher load carrying capacities with lesser deformations. With the increase in height of Stud connectors within range of 65mm to 100mm and Perfobond connectors in range of 75mm to 100mm the load carrying capacity of beam is increased with reduction in deformation.

Increase in height beyond 100mm both Stud and Perfobond connectors show an increase in deflection values.

With the increase in height of Channel connectors within range of 75mm to 125mm the load carrying capacity of beam is increased with reduction in deformation. Increase in height beyond 125mm channel connector show an increase in deflection values. With the increase in height of I shape connector within range of 70mm to 125mm the load carrying capacity of beam is increased with reduction in deformation. Increase in height beyond 125mm I shape connector show an increase in deflection values.

REFERENCES

[1] Eurocode 4 (2005). Eurocode 4: Design of composite steeland concrete structures - Part 1-1: General rules and rules for buildings.

[2] Deepika Ramesh, Jonnalgadda Sadhana, Bhargavi Ganesh, Umarani Gunasekaran (2015), *Enchancement of Shear connectors for steel-concrete composite structures*, Department of civil engineering, Anna University.

[3] Aida Mazoz, Abdelkader Benanane, Messaoud Titoum (2013) *Push-out Tests on a new Shear connector of I-shape,* Laboratory of materials and processes of construction, University of Mostaganem.

[4] Ali Shariati, N.H.Ramilsulong, Meldisuhatril and Mahdi Shariati (2012),*Various types of shear connectors in structures*, Department of civil engineering, University of Malaya.

[5] Anju. T, Smitha. K *Finite Element Analysis of Composite Beam with Shear Connectors* Department of Civil Engineering, KMEA Engineering College, Ernakulam, Kerala,

[6] J. da. C. Vianna, S.A.L. de Andrade, P.C.G. da S. Vellasco, L.F. Costa-Neves (2012)*Experimental study of Perfobond shear connectors incomposite construction*, PUC-Rio, Civil Engineering Department, Pontifical Catholic University of Rio de Janeiro, Brazil.

[7] Ali Shariati, Mahdi Shariati, N. H. Ramli Sulong, Meldi Suhatril, M. M. Arabnejad Khanouki, (2014*), Experimental analysis of angle shear connectors under monotonic and fully reversed cyclic loading in high strength concrete*, Department of civil engineering, University of Malaya.

[8] IS 11384-1985 Indian Standard Code Of Practice For Composite Construction In Structural Steel and Concrete.

[9] Pashan, A. (2006).MSc. Thesis, *Behaviour of channel shear connectors: push-out tests* Department of Civil Engineering, University of Saskatchewan, Canada.

[10] Jayas, B. S. and Hosain, M. U. (1988*). Behaviour of headed shear studs in composite beams: push-out tests Canadian J.* Civil Engineering

[11] Vidula S. Sohoni, Dr. M.R. Shiyekar. Concrete–Steel Composite Beams of a Framed Structure for Enhancement in Earthquake Resistance. *International Journal of Civil Engineering and Technology*, 3(1), 2012, pp. 99–110.

[12] Dr. Laith Khalid Al- Hadithy, Dr. Khalil Ibrahim Aziz and Mohammed Kh. M. Al-Fahdawi. Flexural Behavior of Composite Reinforced Concrete T-Beams Cast in Steel Channels with Horizontal Transverse Bars as Shear Connectors. *International Journal of Civil Engineering and Technology*, 4(2), 2013, pp. 215–230.

International Journal for Research in Applied Science & Engineering Technology (IJRASET)
ISSN: 2321-9653; IC Value: 45.98; SJ Impact Factor: 6.887
Volume 5 Issue VII, July 2017- Available at www.ijraset.com

Empirical Analysis of Mccall's Quality Factors Using Analytic Hierarchy Process Agile Perception

Dr.V. Padmakar[1], Dr.B.V. Ramana Murthy[2], Jogannagari Malla Reddy[3]
[1]*Professor, Dept. of. CSE, Visvesvaraya College of Engineering and Technology, Hyderabad, Telangana State, India,*
[2]*Professor, Dept. of. CSE, AAR Mahaveer Engineering College, Hyderaba, Telangana State, India,*
[3]*Research Scholar, Dept. of. CSE, Lingaya's University, Faridabad, Haryana State, India*

Abstract: Software Quality is the degree of which a system components and process meets the system requirements, in other words software quality is user satisfaction, in this paper, we are trying to find out weightages of McCall quality factors, which are applied on development process using agile methodology. An empirical analysis has been found out using Analytic Hierarchy Process on McCall factors with reference to agile methodology applications has been carried out. The process of empirical techniques provides the weightages of McCall factors, which provides insights to the work flow, work process required to attain quality standards

Keywords: Quality Assurance, Quality factors, Quality Model, Analytic Hierarchy Process

I. INTRODUCTION

Software quality is the degree of which a system components, process, meets, specified requirements and customer or user needs or expectations requirements [1]. The question, Quality is a complex concept, it means different things to different people and it is highly context dependent. Gravin has analysed how software quality is perceived in different ways in different domains, such as philosophy, economics, marketing, and management. The software quality is difficult to define, it depends on the viewpoint of the observer. Kitchenham and Pfleeger's emphasizes the views in comprehensive manner as follows[13].

Transcendental view: it visualizes quality as something that can be recognized but is difficult to define. The transcendental view is not specific to software quality alone but has been applied in other complex area of everyday life.

User View: It perceives quality as fitness of purpose. According to this view, while evaluating the quality of a product, one must ask the key question " Does the product satisfy user needs and expectations?

Manufacturing View: here quality is understood as conformance to the specification. The quality level of a product is determined by the extent to which the product meets it specifications.

Product View: in this case, quality is viewed is viewed as coupled to the inherent characteristics of the product. A product's inherent characteristic that is internal qualities determines its external qualities.

Value-Based View: quality in this perspective depends on the amount a customer is willing to pay for it.

The connect of software quality and the effort to understand it in terms of measurable qualities date back to the mid -1970. McCall, Richards, and Walters were the first to study the concept of software quality in terms of quality factors and quality criteria

Usually a quality factor represents a behavioural characteristic of a system. Some examples of high level quality factors are correctness, reliability, efficiency, testability, maintainability and reusability. A quality criterion is an attribute of a quality factor[2] that is related to software development. For example, modularity is an attribute of the architecture of a software system[5]. Highly modular software allows designers to put cohesive components in one module thereby improving the maintainability of the systems.

II. SOFTWARE QUALITY FACTORS

A. The software industry have been anxiously targeted for improve the product quality with innovative methods. Software quality plays the vital role in the software development in the various phases of the software development life cycle. The faulty software products has significant cost to the suppliers and unsatisfaction to end-users which fails to meet their goals. Any system behavioural characteristic represent quality factors [13][14]. The Jim McCall developed the model for US Air Force identified with following three main perspective for characterizing the quality attributes of software product of the following.

ISSN: 2321-9653; IC Value: 45.98; SJ Impact Factor: 6.887
Volume 5 Issue VII, July 2017- Available at www.ijraset.com

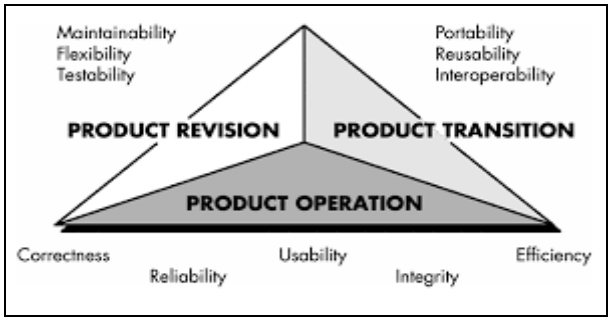

Figure 1. McCall's Quality factors of the software product

1) *Product Operation:* The product operational characteristics shows the operational behaviour of the software product like Correctness, Reliability, Usability, Integrity and Efficiency.
2) *Product Revision:* The product revision is ability to Change, test and maintain the software product as per change management . Example : Testability, Flexibility, Maintainability.
3) *Product Transition:* The product transition have the adaptability and comfortably features with the new environments.. Example. interoperability, portability, and reusability etc

B. Software developers and quality assurance engineering are interested in different quality factors to a different extent. For example customer may want efficient and reliable software with less portability[15]. The developers are required to meet customer needs by plan their system efficient and reliable for the same time making the product portable and reusable to reduce the cost of software development. The software quality assurance team is interested in the testability of a system so that some other factors such as correctness, reliability and efficiency can be easily verified through testing. The testability factor is important to developers and customers as well[9].

1) *Correctness:* **S**oftware systems satisfy all the functional requirements the system is said to be correct. A correct software system may still be unacceptable to customer if the system fails to meet unstated requirements such as stability performance and scalability[7].
2) *Reliability:* It is difficult to construct large software systems which are correct. But the software may still be acceptable to customers because the execution scenarios causing the system to fail may not frequently occur when the system is deployed. Reliability is a customer perception and incorrect software can still be considered to be reliable.
3) *Efficiency*: Efficiency concerns to what extent a software system utilizes resources such as computing power memory disk space communication bandwidth and energy. A software system must utilize as little resources as possible to perform its functionalities[16]. For example by utilizing less communication bandwidth base station in a cellular telephone network can support more users.
4) *Integrity*: A system is integrity refers to its ability to withstand attacks to its security integrity refers to the extent to which access to software or data by unauthorized persons or programs can be controlled. Integrity has assumed a prominent role in today's network based application.
5) *Usability*: A software systems is considered to be usable if human users find it easy to use. User put much stress on the user interface of software systems. Software fails too often no good user interface can keep it in the market.
6) *Maintainability*: In general maintenance refers to the upkeep of products in response to deterioration of their components due to continued use of the products. Maintainability known to how easily and inexpensively the maintenance task can be performed.
7) *Testability*: It is important to be able to verify every requirement both explicitly stated and simply expected. Testability means the ability to verify requirements. At every stage of software development it is necessary to consider the testability aspect of a product.
8) *Flexibility*: Flexibility is reflected in the cost of modifying an operational system. As more and more changes are effected in a system throughout its operational phase subsequent changes may cost more and more. It the initial design is not flexible it is highly likely that subsequent changes are every expensive in order to measure the flexibility of a system[17] and easily one can add a new feature to a system.

9) *Portability:* Portability of a software system refers to how easily it can be adapted to run in a different execution environment. Is a board term encompassing hardware platform operating system distributedness and heterogeneity of the hardware system to name a few. Portability is important for developers because a major adaptation of a system can increase its market potential.
10) *Reusability:* Reusability means if a significant portion of one product can be reused may be with minor modification in another product economically it may not be viable to reuse small components. Reusability saves the cost and time to develop and test the component being reused.
11) *Interoperability*: Interoperability feature can binds different type of environments with the computer networking.

III. ANALYTICAL HIERARCHY PROCESS

The Analytic Hierarchy Process considers a set of evaluation criteria, and a set of alternative options among which the best decision is to be made. It is important to note that, since some of the criteria could be contrasting, it is not true in general that the best option is the one which optimizes each single criterion,[20] rather the one which achieves the most suitable trade-off among the different criteria.

The Analytic Hierarchy Process generates a weight for each evaluation criterion according to the decision maker's pair wise comparisons of the criteria[21]. The higher the weight, the more important the corresponding criterion. Next, for a fixed criterion, the Analytic Hierarchy Process assigns a score to each option according to the decision maker's pair wise comparisons of the options based on that criterion. The higher the score, the better the performance of the option with respect to the considered criterion. Finally, the Analytic Hierarchy Process combines the criteria weights and the options scores, thus determining a global score for each option, and a consequent ranking[22]. The global score for a given option is a weighted sum of the scores it obtained with respect to all the criteria.

A. *Implementation of the Analytic Hierarchy Process*

The Analytic Hierarchy Process can be implemented in simple consecutive steps:

1) Prepare the table
2) Fill the pair wise comparison table
3) Summation of columns
4) Each column Summation
5) Repeat for all other columns.
6) Each entry I divided by summation of columns i
7) Repeat for all entries
8) Summation of rows
9) Summation of rows divided by no of columns equal to weight ages of attributes.
10) Summation of weight ages of attributes equal to 1

TABLE I
PAIR WISE COMPARISON TABLE

Agile	C	Re	E	I	U	M	T	F	P	R	Io
C	1.0	0.3	5.0	0.3	5.0	6.0	0.2	3.0	4.0	4.0	4.0
Re	3.0	1.0	4.0	0.3	0.3	3.0	0.2	5.0	6.0	5.0	5.0
E	0.2	0.3	1.0	0.3	4.0	3.0	0.2	4.0	3.0	3.0	3.0
I	3.0	4.0	4.0	1.0	5.0	3.0	3.0	7.0	6.0	7.0	7.0
U	0.2	0.3	0.3	0.3	1.0	0.3	0.2	3.0	3.0	3.0	3.0
M	0.2	0.3	5.0	0.3	4.0	1.0	0.3	4.0	5.0	4.0	6.0
T	0.2	5.0	5.0	0.3	5.0	3.0	1.0	4.0	6.0	5.0	6.0
F	0.3	0.2	0.3	0.1	0.3	0.3	0.3	1.0	3.0	5.0	5.0
P	0.3	0.2	0.3	0.2	0.3	0.2	0.2	0.3	1.0	3.0	3.0
R	0.3	0.2	0.3	0.1	0.3	0.3	0.2	0.2	0.3	1.0	0.3
Io	0.3	0.2	0.3	0.1	0.3	0.2	0.2	0.2	0.3	3.0	1.0

ISSN: 2321-9653; IC Value: 45.98; SJ Impact Factor: 6.887
Volume 5 Issue VII, July 2017- Available at www.ijraset.com

TABLE II
PAIR WISE COMPARISON TABLE AND SUMMATION OF COLUMN

Agile	C	Re	E	I	U	M	T	F	P	R	Io
C	1.0	0.3	5.0	0.3	5.0	6.0	0.2	3.0	4.0	4.0	4.0
Re	3.0	1.0	4.0	0.3	0.3	3.0	0.2	5.0	6.0	5.0	5.0
E	0.2	0.3	1.0	0.3	4.0	3.0	0.2	4.0	3.0	3.0	3.0
I	3.0	4.0	4.0	1.0	5.0	3.0	3.0	7.0	6.0	7.0	7.0
U	0.2	0.3	0.3	0.3	1.0	0.3	0.2	3.0	3.0	3.0	3.0
M	0.2	0.3	5.0	0.3	4.0	1.0	0.3	4.0	5.0	4.0	6.0
T	0.2	5.0	5.0	0.3	5.0	3.0	1.0	4.0	6.0	5.0	6.0
F	0.3	0.2	0.3	0.1	0.3	0.3	0.3	1.0	3.0	5.0	5.0
P	0.3	0.2	0.3	0.2	0.3	0.2	0.2	0.3	1.0	3.0	3.0
R	0.3	0.2	0.3	0.1	0.3	0.3	0.2	0.2	0.3	1.0	0.3
Io	0.3	0.2	0.3	0.1	0.3	0.2	0.2	0.2	0.3	3.0	1.0
∑ Columns	8.9	11.9	25.6	3.3	25.6	20.1	5.9	31.7	37.7	43.0	43.3

TABLE III
SUMMATION OF ROWS

	C	R	E	I	U	M	T	F	P	R	Io	∑ Row
C	0.11	0.03	0.20	0.10	0.20	0.30	0.03	0.09	0.11	0.09	0.09	1.35
Re	0.34	0.08	0.16	0.07	0.01	0.15	0.03	0.16	0.16	0.12	0.12	1.40
E	0.02	0.02	0.04	0.07	0.16	0.15	0.03	0.13	0.08	0.07	0.07	0.84
I	0.34	0.34	0.16	0.30	0.20	0.15	0.51	0.22	0.16	0.16	0.16	2.69
U	0.02	0.02	0.01	0.07	0.04	0.01	0.03	0.09	0.08	0.07	0.07	0.53
M	0.02	0.03	0.20	0.10	0.16	0.05	0.06	0.13	0.13	0.09	0.14	1.09
T	0.02	0.42	0.20	0.10	0.20	0.15	0.17	0.13	0.16	0.12	0.14	1.79
F	0.04	0.02	0.01	0.04	0.01	0.01	0.04	0.03	0.08	0.12	0.12	0.52
P	0.03	0.01	0.01	0.05	0.01	0.01	0.03	0.01	0.03	0.07	0.07	0.33
R	0.03	0.02	0.01	0.04	0.01	0.01	0.03	0.01	0.01	0.02	0.01	0.21
Io	0.03	0.02	0.01	0.04	0.01	0.01	0.03	0.01	0.01	0.07	0.02	0.26

TABLE IV
WEIGHTAGES OF ATTRIBUTES

	C	Re	E	I	U	M	T	F	P	R	Io	∑ Row	Weightages = ∑Rows/no of attributes
C	0.11	0.03	0.20	0.10	0.20	0.30	0.03	0.09	0.11	0.09	0.09	1.35	0.12
Re	0.34	0.08	0.16	0.07	0.01	0.15	0.03	0.16	0.16	0.12	0.12	1.40	0.13
E	0.02	0.02	0.04	0.07	0.16	0.15	0.03	0.13	0.08	0.07	0.07	0.84	0.08
I	0.34	0.34	0.16	0.30	0.20	0.15	0.51	0.22	0.16	0.16	0.16	2.69	0.24
U	0.02	0.02	0.01	0.07	0.04	0.01	0.03	0.09	0.08	0.07	0.07	0.53	0.05
M	0.02	0.03	0.20	0.10	0.16	0.05	0.06	0.13	0.13	0.09	0.14	1.09	0.10
T	0.02	0.42	0.20	0.10	0.20	0.15	0.17	0.13	0.16	0.12	0.14	1.79	0.16
F	0.04	0.02	0.01	0.04	0.01	0.01	0.04	0.03	0.08	0.12	0.12	0.52	0.05
P	0.03	0.01	0.01	0.05	0.01	0.01	0.03	0.01	0.03	0.07	0.07	0.33	0.03
R	0.03	0.02	0.01	0.04	0.01	0.01	0.03	0.01	0.01	0.02	0.01	0.21	0.02
Io	0.03	0.02	0.01	0.04	0.01	0.01	0.03	0.01	0.01	0.07	0.02	0.26	0.02
													1.00

ISSN: 2321-9653; IC Value: 45.98; SJ Impact Factor: 6.887
Volume 5 Issue VII, July 2017- Available at www.ijraset.com

B. Analysis of Results

From the above table it has been determined that the integrity have much significance of 24% followed by testability(16%), Reliability(13%), Correctness(12%), Maintainability(10%), Efficiency(8%) and portability(3%). The remaining quality factors usability and flexibility occupies the equal significance of 5% similarly other quality factors reusability and interoperability with less significance of 2% in the product.

C. Interpretation of Results

The results shows the pair wise comparison of attributes using AHP which gives sound and strong empirical relation to map into real world, the weightages given the insights of the business objection work flows to be carried out while developing application using agile method and to attain quality standards, focus of work weightages in terms of product perceptive must be given in the following order to attain McCall Factors.

TABLE IV
WEIGHTAGES OF ATTRIBUTES IN ORDER OF SEQUENCE WITH PRIORITY IN PERCENTAGE

Sl. No	Quality factor	Significance	Weightages in %
1	Integrity	0.24	24
2	Testability	0.16	16
3	Reliability	0.13	13
4	Correctness	0.12	12
5	Maintainability	0.10	10
6	Efficiency	0.08	8
7	Usability	0.05	5
8	Flexibility	0.05	5
9	Portability	0.03	3
10	Reusability	0.02	2
11	Interoperability	0.02	2

From the research findings concludes that, the quality significance in the software product can be visualize with the following bar graph figure.2

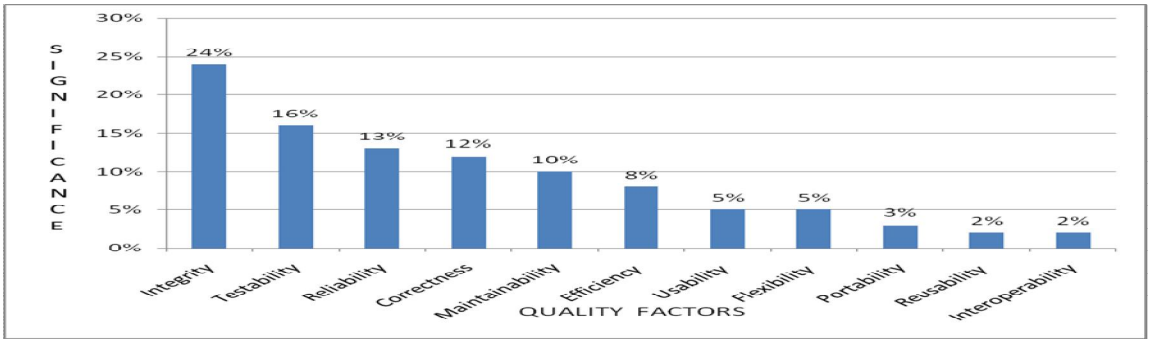

Fig 2 Quality significance in the software product

IV. CONCLUSIONS AND FUTURE SCOPE

An prototype of one sample taken from industry project manager, the process can be consolidation and further research can be done by framing a questioner and getting sample from medium scale industry. Quality is always depends on the design of the product. Any product is designed it is very important to develop to have primary knowledge of factors which will affect the quality of the product. The paper is the study and comparison of quality models as it tells the factors and criterion. Along with this AHP is to the developer for developing a quality product. The Analytical Hierarchy process is effective decision making method for multi criteria

problems.. There are many inherent complexities in the prioritization. With the numerical example. the authors suggest that when some alternatives to be very close to other with sensitive. The decision maker needs to very cautious in prioritization. There is a need of extensive research in area of Multi Criteria Decision Making methods which is useful for scientific and Software engineering applications.

V. ACKNOWLEDGEMENT

We sincerely acknowledge to all the faculty of the department of Computer Science & Engineering, Mahaveer group of Institutions, Hyderabad for their support, guidance, and cooperation during the period of study

REFERENCES

[1] Software Engineering - Product Quality, Part 3, 4, Version 1.0 (ISO/IEC TR 9126), url:http://www.iso.org/iso/home/store /catalogue_tc/, visited:7th July, 2012 .
[2] Al-Qutaish, R. E., "Qualit y Models in Software Engineering Literature: An Analytical and Comparative Study," Journal of American Science , 2010. Vol. 6, no. 3, pp. 166 - 175.
[3] Kitchenham, B., Pfleeger, S. L. "Software Quality: the Elusive Target,"1996. IEEE Software , vol. 13, no. pp. 12-21.
[4] Wirth, N. "A Brief History of Software Engineering,"IEEE Annals of the History of Computing, 2008. Vol. 30 no.3, pp. 32- 39.
[5] Boehm, B. W.; Brown, J. R.; Kaspar, H.; Lipow, M.; McLeod, G.; and Merritt, M., "Characteristics of Software Quality, "North Holland Publishing, Amsterdam, The Netherlands, 1978, vol., no., pp.
[6] Deissenboeck, F.; Juergens, E.; Lochmann, K.; and Wagner, S. 2009. Software quality models: purposes, usage scenarios and requirements. In Proceedings of the 7th ICSE conference on Software quality (Munich, Germany, 2009).
[7] Dromey, R. G., "A Model for Software Product Quality," IEEE Transactions on Software Engineering, 1995, vol. 21, no., pp 146 - 162.
[8] History of Software Engineering. In Wikipedia . Retrieved June 27 2012, from http://en.wikipedia.org/wiki/History_of_software_engineering.
[9] Software Engineering - Product Quality, Part 3, 4, Version 1.0 (ISO/IEC TR 9126), url:http://www.iso.org/iso/home/store/ catalogue_tc/, visited: 7th July, 2012
[10] Bawane Neelam and Srikrishna, C.V. 2010. A Novel Method for Quantitative Assessment of Software Quality. International Journal of Computer Science and Security 3, 6, 508 - 517
[11] Alvaro Alexandre, E.S. de Almeida and S.R. deLemos Meira 2010. A Software Component Quality Framework. ACM SIG SOFT SEN 35, 1(Nov. 2010), 1 – 18.
[12] Kalaimangal Sivamuni and Srinivasan Rengaramanujam 2011. Q'Facto12 - An improved quality model for COTS Components. ACM SIGSOFT SEN 35, 2(Mar. 2010), 1 – 4.
[13] Upadhyay Nitin, Despande, Bharat M. and Agrawal, Vishnu P. 2011. Towards a Software Component Quality Model . Springer Press CCIS ACST .131, 3 , 398 – 412 DO I: 10.1007/978 -3 – 642 – 17857 - 3_40
[14] Bassem Anas AL-Badareen 2011. Software Quality Evaluation: User's View. International Journal of applied mathematics and informatics 5, 3(2011), 200-207
[15] Bawane, Neelam and Srilrishna, C.V, "A Novel Method for Quantitative Assessment Of software Quality", international Journal of Computer Science and Security, Vol 3,Issue 6,2011.
[16] Wu,B.H "An evolutionary approach to evaluate quality of software systems", 2011
[17] A. P. Mathur, Foundations of Software Testing, Second. Pearson, 2013.
[18] P. R. Suri and H. Singhani, "Object Oriented Software Testability Survey at Designing and Implementation Phase," International Journal of Science and Research, vol. 4, no. 4, pp. 3047– 3053, 2015.
[19] P. R. Suri and H. Singhani, "Object Oriented Software Testability (OOSTe) Metrics Analysis," International Journal of Computer Applications Technology and Research , vol. 4, no. 5, pp. 359–367, 2015.
[20] . Khanna, "Testability of Object- Oriented Systems : An AHP -Based Approach for Prioritization of Metrics," in International Conference on Contemporary Computing and Informatics(IC3I) , 2014, pp. 273 – 281.
[21]] P. K. Singh, O. P. Sangwan, A. Pratap, and A. P. Singh, "Testability Assessment of Aspect Oriented Software Using Multicriteria Decision Making Approaches, World Applied Sciences Journal, vol. 32, no. 4, pp. 718–730, 2014.
[22]] P. K. Singh, O. P. Sangwan, A. P. Singh, and A. Pratap, "A Quantitative Evaluation of Reusability for Aspect Oriented Software using Multi-criteria Decision Making Approach," World Applied Sciences Journal, vol. 30, no. 12, pp. 1966–1976, 2014.

Mark Twain's the Adventures of Huckleberry Finn: A Study of Expressions, Feelings and Emotions of Children

LINGAMURTHY MUKKERA
Assistant professor
Department of English
Methodist College of Engineering & Technology
(Hyderabad) India

Abstract:
Children's literature is written exclusively for the children to read. Children select variety of books among which comics are favoured by them. Some of the critics opined that, the books written for children may not be considered as a literature in the traditional sense. But, this concept cannot be consented by literary figures because children's books speak on multiple levels besides literature. The term children's literature is used in senses excluding young adult fiction, comic books. Books for children, specifically written even in seventeenth century. Knowledge on children's literature includes professional organizations, dedicated publications and University courses. It is beneficially matched to analyze the novel by using the sociological approach to comprehend the social phenomena of social and cultural pattern of family of a member of society. The present article attempts to understand the role of children and their feelings. It also expresses, understanding how children see life and their feelings.

Keywords: *Children's life, Expressions, Feelings and emotions of children, Social phenomena*

1. Introduction

The present article attempts to understand the role of children and their feelings. It also expresses, understanding how children see life and their feelings. Nancy Anderson, defines children's literature;

> "As all books written for children
> excluding works such as comic books, joke books,
> cartoon books and non-fiction works that are not
> intended to be read from front to back, such as
> dictionaries, encyclopaedias and other reference
> material"[1]

Children's literature consists of literary genres such as picture books, comic books, fiction, non-fiction, biography and poetry. Children's literature can be considered as didactic literature. Since, it tries to make the children better. A scholar views that;

> " No one needs to be ashamed to say that children's literature is
> didactic literature. Its intention is to be make our children better,
> to in still noble ideals in them and to lovingly mould them into men
> and women of character"[2]

J.K. Rowling's Harry Potter is originally written for children and marketed for children, but it was equally popular among children and adults. It was the best seller in 1997 as listed by the New York Times.

There are quite a number of writers who have written books for children they are Johanna spyri, carlo collodi, Robert louis Stevenson, Rudgard Kipling, L. Frank Baum, Beatrix Potter, Kenneth Grahame, J.M. Barrie A.A.Milne, Laura Ingalls wilder, C.S.Lewis, Dr. Seuss Roald Dahl, J.K. Rowling, Eoin colfer and Mark Twain.

Mark Twain, the pen name Samuel Langhorne Clemens was one of the best humorous writers in America who wrote two books 'THE ADVENTURES of TOM SAWYER' & 'THE ADVENTURES OF HUCKLEBERRY FINN' which attracted both children and adults equally. Mark Twain wrote adventures of HUCKLEBERRY FINN were originally intended to write for adults but it is widely read as a part of children's curriculum. Since its first publication in 1884, Mark Twain's masterpiece The Adventures of Huckleberry Finn has proven to be one of history's most controversial novels; especially recently, the novel has often been banned by schools and censored by libraries. Characters in the book are constantly using disparaging language toward slaves, and the repeated use of the word "nigger" makes many sensitive and offended. Critics denounce the novel and Mark Twain as racist for this word being insulting and politically incorrect and for its depiction of black people and how they are treated.
Huck & Jimm were young boys, this novel is a sequence of earlier novel 'The adventures of Tow Sawyer' , at the end of which two boys find a treasure trove, a tidy sum of twelve thousand dollars, each of them share six thousand dollars.

Huck's father was a confirmed drunkard. Huck was treated as an outcaste of the village, clothed in racks and sleeps in hegsheads. A sudden change comes among the villagers when they come to know that Huck is a owner of six thousand dollars. One widow Douglas comes forward to adopt the boy in order to civilize him. Meanwhile, the boy invests the money with Judge Thatcher which provides him one dollar a day. The widow neatly dresses the boy, sends him to school and teaches him manners. This kind of environment doesn't sui9t Huck. So, he thinks of enjoying, he used to do it earlier In order to get some relief, he whishes to join Tom'[s gang once again, when he was explained that they are going to undertake certain adventures, Huck's expression of joy is boundless. He feels elated, when Tom unfolds his plan to rob the caravan of Arabs and to keep their men and women imprisoned till they are 'ransomed'. These adventures are purely the activities to be done by the children. The whole business of robbing the Caravan appeared to be a Sunday school picnic of children, chasing the little boys and girls. Other feet that Huck tried to get a genie by rubbing an old lamp but nothing happened. He comes to a conclusion that Tom's adventures had 'all the marks of a Sunday school' children so, he decided to quiet childish adventures.

His father comes to know about the wealth of Huck. So, he tortures him to extract money from Huck. Pap tries to get the custody of boy. Even as a father he criticizes Huck's going to the school. The cruel mentality on the child like Huck is reflected here one day; his father drags him to a far-off place & imprisons him in a log cabin. Mark Twain perhaps intended to curb the ill treatment of children by the parents by narrating such incidents. The parent should try to comprehend the mindset of the children. Huck is in trouble and planned to escape. Due to his childish mentality, he contrived the drama of 'Self- murder', stained his clothes with the blood of a pig he had killed and made an escape in a canoe to the Jackson's island. There he meets Jim who is a slave, he runs away from Miss. Watson who tried to sell him for 800 dollars. Jim is also an innocent boy and they are good friends. Jim is a Negro who is illiterate and Superstitious. He is domesticated, docile and highly skilled in manual tasks. Jim believes that white men are superior to him. Jim & Huck resort to many adventures in the Jackson's island. Mark Twain advocates for the rights of Slaves and one should have mercy towards others. Once Huck says that:

> "Necessary for everybody to ------
> feel right and kind toward the other "[5]

2. Conclusion

Mark Twain pleases for humanistic attitude of the people towards children. The novel dramatizes man and deals directly with a virtue and depravity of man's heart. The writer introduces vision of an ideal society. Mark Twain attacks the evils of society and he is a social rebel who could not stand hypocritical models of conduct and behavior. He rejects the social morality so cruelly formalized that it had last all touches of human values. Especially towards children and he tries to uphold individual morality.

"a particular moral reference to the United States in the period after the civil war"[6]

He attacks all kinds of institutionalisms and evils of contemporary society. The activities of Tom & Huck appear to be romantic illusions for the children as popularized by Scott. Mark Twain fights for the rights of the slaves. Mark Twain however exhibits sympathetic attitude towards children like Huck & Jimm who are required to be taken care of not only by the parents but also by the Society in general. Compassion and pity should be showered on the children. Because they are the future citizens who can shape the country into a moralistic society.

References

1. Anderson, Nancy. Elementary children's literature. Boston: Pearson education.2006.
2. Extracted from an article on Indian Children's literature.
3. Johanna Spyri, Heidi, published in New review of children's literature and librarianship, Volume16, issue 1 April 2010
4. Johanna Spyri, Heidi, published in New review of children's literature librarianship, Volume16, issue 1 April 2010
5. Lionell Trilling- Extracted from net sources.
6. Mark Twain, Adventures of Huckleberry Finn,

UGC Approved Journal

IJELLH

International Journal of English Language, Literature in Humanities

Indexed,Peer Reviewed (Refereed) Journal

ISSN-2321-7065

Impact Factor : 5.7

Editor-in-Chief

Volume V, Issue XI
November 2017
www.ijellh.com

About Us | Editorial Board |Submission Guidelines |Call for Paper

Paper Submission | FAQ |Terms & Condition | More…….

Lingamurthy Mukkera

Assistant professor

Dept. of English

Methodist College of Engineering & Technology

Hyderabad

Telangana 500008

THE HAIRY APE- A SEARCH FOR IDENTITY

Abstract:

Eugene O'Neill continues his dramatization of the American identity in his works. In *Anna Christie*, he presented an important type of the American identity, the irresponsible, careless, lost, disintegrated and doomed to suffer character. O'Neill is still engaged with the sea plays but this time the journey is from the sea to the land not the opposite. In 1922 O'Neill presents his play *The Hairy Ape.* In this play O'Neill exposes and important problem that was common in the world in general and in the American society in particular. It discusses the alienation of the American individual in the modern technological age and the lost identity of that individual. O'Neill in this play shows the lost identity of the modern American man and his futile attempts in regaining it. *The Hairy Ape* is a one character play which shows the reality and the bad conditions of the American society.

Key words: American identity, social outcaste, reality of working class, modern American man

In this play O'Neill symbolizes the relationship between the modern man and his universe, a universe in which the desires of men to "belong" are mere playthings in the hands of a capricious deterministic force and the capitalists who do not care for the desires of those people. O'Neill focuses his attention on the social outcast, whose rootless and bitter struggle against a hostile society is symbolic of the position of mankind in an indifferent universe (Clark and Roberts: 52).

The play talks about the reality of the working class. Yank, Paddy, and Long are the central characters with Mildred, the representative of the upper class. Yank is the leader of the firemen on a steamship. Early in the play Yank is strong, powerful and confident of himself and his existence. He glorifies himself and his strength; he resembles himself with the machines that he serves. He thinks of himself as the leader and the prime mover of all machinery, he is the maker of the steel. He 'belongs', of course that is his favorite word. He has found a place for him and he is satisfied with it (Ranald : 24).

O'Neill's dramatization of Paddy as animal–like man and his desperate and hopeless condition shows the reality of the American character. Paddy goes to alcohol in order to forget his sorrows and shortcomings. He says that he sings when he is dead to the world, when he is hopeless and desperate. When they ask him to sing he replies "I'm never too drunk to sing. Tis only when I'm dead to the world I'd be wishful to sing at all"(Scene One :144). This means that alcohol is their shelter from the bitter reality of their existence, the means to forget the hard and desperate reality is to escape to the world of unconsciousness, to live in the dreams and illusions. Paddy sings when he is drunk, and he is drunk when he is dead to the world, he drinks to forget his miseries and sorrows.

O'Neill uses characters in the plays without names , he just calls them Voices on purpose in order to suggest their minimumity in their society. These characters where lost underworld and society is ignorant of their being and that is why O'Neill called them mere voices to suggest their loss in life. They are like machines, after each utterance by them O'Neill comments suggestively: "The chorused word has a brazen metallic quality as if their throats were phonograph horns. It followed by a general uproar of hard, barking laughter" (Scene One :145). This shows their mechanized being, they are treated like machines, they have the same voice, the same laugh and the same qualities .

The Hairy Ape dramatizes the bewilderment of a powerful stoker when his naïve confidence in himself is shaken. Yank expresses his futile attempts to find a place for himself in this world, he symbolizes man's search for a meaning for his life and his alienation in the world. O'Neill's play talks about Yank in relation to his surroundings and

environments, his relation to other characters in the play, and his attempts to find meaning for his reality.

The Hairy Ape dramatizes the theme of alienation and loss of identity. O'Neill draws a character, Yank, a stoker who lives in the bellow deck in the stokehole of an ocean liner. Yank, after he left his home when he was a child, becomes homeless, an outcast; he thinks that he has finally found his warm home which is the stokehole. In this work Yank thinks that he has found his real place in the world and he can achieve something valuable for himself and for society. Having this feeling Yank thinks that he belongs to his society and he is important and counted. O'Neill puts those stokers in the bellow deck and at the bottom of the social ladder and even so they are satisfied and convinced in their lives and positions because they think that they do something for society and society is grateful in return. Yank confirms this illusion to his fellow men
when he says:

We ‘re better men dan dey are, ain’t we? Sure! One Of us
guy could clean de whole mob wit mit. Put one of dem
down here foe one watch in de stokwhole, what’d happen
? Dey’dcarry ‘himoffon a Stretcher. Dem biods don’t
amount to nothing dey’re just baggage. Who make dis old
tub run? Ain’t it us guys well den, we belong, don’t we?
We belong and dey don’t dat’s all(Scene One: 147).

Yank has this idea in his mind; he thinks that he and his fellow men are more important and stronger than the others and they can achieve many things for their society, for that reason he thinks that he belongs and has his real and valuable identity. This gives the audience an important clue to O'Neill's vision of the American character at that time. Long, on the one hand supports Yank's ideas that they are better guys and they belong, their real home is the stoker and they have no home other than this one. He says; "Listen 'er, Comrades! Yank 'er is right.'E says this stikin' ship is our 'ome. And 'e says as 'ome is 'ell. And 'e s right. This is 'ell. We lives in 'ell, Comrades" (SceneOne:146).

O'Neill’s dramatization of Yank is not individual but there are millions of men and women who are blood relations of Yank in this modern industrial world. Those people, the Yanks of

the world, all their lives think that they belong, counted and have their dignity and human qualities. They feel that they are necessary to their society, a respected and important part of their social ladder. In the first scene of the play Yank appears to have self confidence and satisfaction of his position in the social ladder. Yank tells his friends that this stokehole is their real home, they have no home but this one. Yank considers this stokehole as his real home and he is glad of it. When his friends sing their song about home he tells them that this is their home and they have no home as he says:

Shut up, yuh lousy boob. Where d'yuh get dat tripe?
Home? Home, hell! I'll make home for yuh! I'll 'knoc
yuh head. Home! …dis is home, see? What d' yuh want
wit home? I runned away from mine when I was a kid.
on'y too glad to beat it, dat was me (Scene One: 145).

O'Neill dramatizes Yank as a man who deludes himself of belonging.
Yank thinks that he belongs to the stokehole, he is proud of himself, he thinks that all the work in these engines depends on him. He feels that he is the force that makes the entire mechanized society moves, that is his credo. He is the man who runs all the works and all the steel that is produced is by his hand. This feeling of pride gives Yank the sense of belonging and contempt of his life in the stokehole. He expresses a satisfaction for the noise that the other men make, he condemns home, women, religion and all these things.

O'Neill here dramatizes Yank as a man who belongs to the world, a
man who needs nothing , he is proud of himself because he thinks that he is the provider of the energy and steel of all the world. Yank argues with Paddy saying that he is part of the engines and he likes to be down in the stokehole for, as he puts it, he can eat coal, "…I eat it up! I get fat on it! It's me makes it hot! It's me makes it roar! It's me makes it move" (Scene One :151). Yank sees that all the works of the engines and all the steel produced is by his hand. In the stokehole Yank is stripped to the waist with all his mates, he can outfight, outcurse and outfeel them all, he is proud of himself, of his power and his job as a stoker at the heart of the ship. He lives through the illusions of his own making. He feels glory when he thinks that he is steel and coal and motion (Eaton: 4). "….Dey 're speed , ain't dey! Dey smash trou, don't dey? Twenty –five knots a hour !...Dat's belong"(Scene One :150).

Through the words of Paddy O'Neill draws and dramatizes a specific

portrait of the American society, Paddy cannot face the bitter life and wrongs done to him and his people, he escapes to the past of the beautiful days. He does not think that he belongs to this life and this world, he is unlike Yank; he belongs to the past. Paddy symbolizes another type of the American character which is the nostalgic character. Even the song of Paddy is intended by O'Neill to reveal the real picture of the American society, Paddy sings; "I care for nobody, no, not I, and nobody cares for me" (Scene one:152) .This shows O'Neill's dramatization of the American character, he uses many ways and techniques to reveal his ideas and feelings.

O'Neill's dramatization of the American character appears sometimes in his comments on the characters and the dialogues, in Mildred's conversation with the Second Engineer O'Neill shows the class conflict and the carelessness of the American people for each other.

SECOND ENGENEER --- Hum, excuse me, ma'am, but are you
intending to Wear that dress?
MILDRED--- Why not ?
SECOND ENGENEER--- you 'll likely rub against oil and dirt.
It can't be helped .
MILDRED --- it doesn't matter. I have lots of white dresses.
SECOND ENGENEER---I have an old coat you might throw over
MILDRED--- I have fifty dresses like this. I will throw this one in
into the sea when I come back, that ought to wash it clean
Don't you think? (Scene Two : 158).

In Scene Three, Yank's world is turned upside down and he loses all
his illusions about himself. O'Neill introduces another important character in the play which is Mildred the daughter of the president of all the steel. Mildred has an important purpose in the play, she resembles a turning point in the world of Yank. Mildred wants to know how the other half lives so that she goes down below the deck and then she sees Yank's face as O'Neill describes him, he says: "he branches his shovel murderously over his head, pounding on his chest, gorilla-like...he whirls defensively with a snarling, murderous growl …his lips drawn back over his teeth, his small eyes gleaming furiously" (Scene Three:163).

Yank realizes that he is no more than a filthy beast in the eyes of

Mildred and her class. He falls under the curse of consciousness, he is conscious of who is he in their eyes. He knows his real value in society and what is his position in the ladder of evaluation. He falls under the curse of bewilderment, despair and hopelessness. He even ceases to think as a man and a meaningful creature, but he despises himself being a hairy ape. Yank now is left to no one, he is abandoned by every one, society, and even his friends mock him being insulted by a woman.

O'Neill intentionally brings Mildred to the stage though he knows that her role is limited and minimal. Mildred's importance in the play lies in her few words that are intended by O'Neill to awake Yank from his illusion. She was a catalyst to shake Yank from within, to make him realize his reality and his value in society. Mildred's appearance represents an awakening from the lethargy and the dormancy of Yank. She shocked him down and forced him to wake up and to reevaluate his existence.

Yank is shocked by this situation when Mildred calls him the filthy
beast in front of his friends. He works for society, for Mildred's father but there is no gratitude and no appreciation even. Yank works hard and he is near to the fire that makes him look like an ape. His face is black and he is half naked because he works hard and near the fire. He looks like an ape because he is caged below the deck, the workers cannot stand even because the ceiling is too low, they are caged inside the stokehole and Mildred ignores all that, not only Mildred but all her class because she is a representative of her class as O'Neill intends. For that reason no wonder if Yank questions his existence and his worth in society. He should reconsider his place in the world and his being.

The first thing that Yank wants to do after his insult is to "think". He begins to question himself; he tries to think who is he, "Can't yuose see I'm tryin' to tink?" .Then he begins to hate, he falls in hate as he puts it "I've fallen in hate, get me?". Yank feels himself insulted so that he wants to avenge himself and his fellow men also "I'll brain her! I'll brain her yet, wait 'n' see! Say , is dat what she called me –hairy ape?"(Scene Four :169). Now Yank reevaluates himself and his worth in society, he realizes how people looks at him, "hairy ape so dat's me, huh?....i'll show yuh who's ape!... I'll fix her…(Scene Four:170) .

In Scene Four when Yank starts his journey looking for his identity in the Fifth Avenue, it's the first time for him to see people since months or years. O'Neill describes Yank and Long in the street, he says:

Long is dessed in shore clothes, wear a black Windsor tie
cloth up. Yank is in his dirty dungarees. A fireman's cap
with black peak on his head…around his fierce resentful
eyes—as around those of Long—the black smudge of coal
dust stills like make-up(Scene Five : 173).

This shows and discloses Yanks reality, how he speaks, how he wears and how he behaves with other people. He tries to attack men and women, he just wants to fight anybody but their reactions shock him severely because no one seems to see or hear him. He begins to speak about his glories and his work in the stokehole; "Sure! I'm steel and steam and smoke and de rest of it! It moves –speed…."(scene Five : 179).

Then he begins to insult them; "Youse simps don't move. Yuh're on'y dolls I winds up to see 'm spin. Yuh 're de garbage, get me- de leavins – de ashes we dump over de side! Now, what 'a' yuh gotta say? (Scene Four: 179). Even his way of talking with others is intended by O'Neill to suggest his primitivism and to reflect his identity. Yank was living down in the stokehole for a long period, he even cannot talk like other people; and his way of talking is not polite with others, his language is intended by O'Neill to suggest his ape-like state.

Yank tries to attack people in his way but they seem even not seeing him and unaware of his existence, they ignore him and just passed him, they seem neither to see nor to hear him. This negative reaction of those people annoys Yank so much so he jumps into fury and begins to insult them; "Bums! Pigs ! Tarts! Bitches!... Git off de oith! G'wan, yuh bum! Look where yuh're goin', can't yuh ? Git outa here! Fight , why don't yuh? Put up yer mits! Don't be a dog! Fight or I'll knock yuh dead! (Scene Five :179).

O'Neill dramatizes the people who are exiting from the church in a
very expressive way. He envisions the real picture of the American

society, the rich people move like robots, they even do not see Yank or care about him. They even have no reaction to Yank's insults because they do not count him as human as O'Neill intends. This picture shows the rich people's indifference to the poor .

Yank is taken to the prison for misbehaviour and there O'Neill draws an ironic picture of the American character. Yank is the maker of the steel and it's him "who makes it move, roar"….etc. Now he is imprisoned and he is taken behind the steel that he produces. He spends a month in the prison and he never felt that he belonged to this place either, this is the second time that society rejected him, first Mildred and then people. He still wants to avenge himself from that harsh ungrateful society. He tries to find someone who can understand him in this society .

Yank at this moment realizes that steel has betrayed him. He thinks of himself as the personification of steel, but as a result of his experience he now sees steel as something that imprisons him in some kind of a cage, whether it is the cage of the stoker's forecastle, the cage of prison, or the cage of social injustice.

In prison Yank learns about the Industrial Workers of the World (IWW). Then when he gets out of the prison Yank still has the idea of revenge, he joins this organization in an attempt to avenge himself upon Mildred by blowing up the steel company of her father. However Yank's suggestion is too violent even for the IWW, they think that he is a spy, they just give him another name, a brainless ape, and then he is thrown unto the street. In Yank's conversation with the secretary of the IWW the difference of languages between them appears. The language of Yank is abrupt, fragmentary and full of mistakes and errors. This language is intended by O'Neill to reveal Yank's identity and reality .

In the street Yank is shocked by the other reality, not only Mildred rejects him but even the IWW which is supposed to serve and help the people like Yank. O'Neill here tries to dramatize not only Yank but his surroundings also, the people around him, the social system because the play is not about Yank as an individual but about his world, the Yanks of the world, the surroundings and the social factors who gave Yank his lost identity. O'Neill's criticism is for the government, for the social system like that, what was his fault to be rejected by all people!. O'Neill through this dialogue gives his audience a silent but very expressive picture of the reality of the

American Eden:
POLICEMAN -- what you been doing
YANK -- Enuf to gimme life for! I was born, see? Sure, dat's de charge. Write it in de blotter. I was born, get mee!
POLICEMAN -- God pity your old woman! But I've no time for kidding. You're soused. I'd run you in but its long walk to the station, come on now, get up, or I'll fan your ears with this club. Beat it now!
YANK: Say where do I go from here?
POLICEMAN: Go to hell (Scene Eight :197)

O'Neill dramatizes the American society and the American character in that society in a way that shows him lost and belonging to nothing, no one care for him; his proper place is hell as the policeman suggests. O'Neill shows the reality of being American inside this mechanical revolution. The American society and the social system do not care for their citizens, they are indifferent to their lives, as did the policeman to Yank. The American individual has no room inside his house, he is dismissed because it's not his house anymore. Their only fault is that they were born, so this is the charge as Yank says, and the sentence for this fault is hell. Hell is the only shelter that is offered by society. But O'Neill's characters never give up to their shortcomings, Yank is convinced that he does not fit in this world, so he moves to another world in an attempt to find out his lost identity.

When Yank realizes that his search to belong to somewhere has been futile, and he has been rejected by all segments of society, the wealthy represented by Mildred, the imprisoned in the prison and the representatives of the masses, the IWW, Yank is confused and bewildered, where should he go and what should he do in this cruel society?. He realizes that he has no place in this mechanized society and this world is not for him. He remembers Mildred's words and applies her theory and goes to the zoo.

In the final scene, Yank visits the gorilla in the zoo. He looks at the beauty of sunrise and realizes that he does not belong to that, now he comes to see how it is with a real hairy ape. Everyone thinks that he is an ape, Mildred has called him "filthy beast" so he might be one. When he approaches the gorilla, he sees the real hairy ape and he realizes the ugliness that Mildred has seen in him. He starts talking to the gorilla, he envies it because,

he says, gorilla can think of the past and should not have to question its being. He envies the gorilla because it has a place and he does not; the gorilla belongs and he does not "you belong! Yuh 're de on'y one in de woild dat does, yuh lucky stiff!"(Scene Eight : 197).

In Yank's conversation with the gorilla, he remembers Mildred's words, he questions his value in her eyes. He considers himself as an ape, he says:

Ain't we both members of de same club- de hairy apes.
So yuh're what she seen when she looked at me, de white face tart. I was you to her, get me? On'y outa de cage—broke out free to moider her, see? Sure! Dat's what she tought. She…wasn't wise dat I was in a cage too—worser'nyours (Scene Eight:196).

Yank envies the gorilla because it does not belong to human beings, he reveals his bitter experience with the human beings so that he envies the gorilla, he says " on'y yuh're lucky, see? Yuh don't belong wit 'em and yuh know it. But me, I belong wit 'em but I don't, see? Dey don't belong wit me…." (197). Yank justifies his envy for the gorilla that it has a past to think of, but he does not have any. " youse can sit and dope dreams in de past, green woods, de jungle and de rest of it.… but me – I ain't got no past to tink in , no nothin' dat comin', on'y now and dat don't belong"(Scene Eight :197) Yank envies the gorilla's ability to avoid thinking and examining his place in the world(Krasner :63).

O'Neill suggests that man becomes equal to animals yet sometimes even the animal is better than man, says Yank to his "brother" ; "Sure yuh're de best off! I ain't on oith and ain't on heaven, get me?…you belong! Sure yuh're de on'y one in de woild dat does..."(Scene Eight :197).

Yank realizes that man is not his brother but an ape is. He wants to take the gorilla in a walk to Fifth Avenue, he replace man with an ape so he wants to shake hands with his new brother. But the gorilla is not convinced of this brotherhood because it is not reasonable, a man becomes a gorilla's brother!. The gorilla rejects Yank and hugs him murderously and Yank dies at the cage ending his quest for identity.

O'Neill's dramatization of the American character is revealed in this scene. Society is not the only one that rejects Yank, but even the animals do. The gorilla, Yank's brother, also rejects him. The American individual, according to O'Neill, has no place neither

with the humans nor with the animals. "Where do I fit in? Even him didn't tink I belong. Christ, where do I get off at?"(Scene Eight : 197). This is the question of the modern American man, he does not fit in society, he cannot live with animals even, so what is the answer of Yank's question? Might be hell as the policeman tells him.

In this way O'Neill dramatizes another type of the American identity, Yank is like Anna; he revolutionizes against the social system in order to have his own identity after he has lost it. Anna moves from the land to the sea to find her identity, she has lost her identity in the land , she comes to the sea in attempt to regain it. But Yank has lost his identity on the sea and he moves to the land seeking for his identity. In both cases the American man fails to find his own identity. Anna suffers in her life and Yank is shocked by reality that he is nothing and belongs to nothing. Yank found belonging and identity in death as O’Neill suggests at the end of the play.

References

O'Neill, E., 1932. Nine plays. New York: Modern Library Random House.

Winther, S, K., 1961. Eugene O'Neill: A Critical Study .New York: Random House.

Cargill, O. et al, ed 1962. Eugene O'Neill and his plays. New York: New York University Press.

Bogard, T., 1972. Contour in Times: The Plays of Eugene O'Neill. New York: Oxford University Press.

International
Journal
Of Advanced Research in Engineering & Management (IJAREM)
ISSN: 2456-2033 || PP. 01-06

LAND USE LAND COVER CHANGE DETECTION USING GEOSPATIAL TECHNOLOGIES-A CASE STUDY FROM RAMAGUNDAM

A. Nihaarika,
Research Scholar, Centre for Environment, Jawaharlal Nehru Technological University Hyderabad.

Dr. K.Santosh Kumar,
Associate Professor, Methodist College of Engineering & Technology, Hyderabad.

Dr. M. Anji Reddy,
Professor of Environment & Director R & D, Jawaharlal Nehru Technological University Hyderabad, Kukatpally, Hyderabad

Abstract: Land use/ land cover is an important component in understanding the interactions of the human activities with the environment and thus it is necessary to monitor and detect the changes to maintain a sustainable environment. In this project an attempt has been made to study the changes in land use and land cover patterns. This project examines the use of Geographic Information System (GIS) and Remote Sensing in mapping Land Use Land Cover change detection in study area between 2012 and 2013, so as to detect the changes that has taken place in this status between these periods. Subsequently, an attempt was made at projecting the observed land use land cover in the 2-years. In achieving this, Land Consumption Rate and Land Absorption Coefficient were introduced to aid in the quantitative assessment of the change. Suitable change detection techniques were developed for the study area by taking into account its physical and cultural conditions, there by optimising use of information in the land cover maps. The result of the work shows a rapid growth in built-up, land between 2012 and 2013. Suggestions were therefore made at the end of the work on ways to use the information as contained therein optimally.

1. GENERAL:

The land use/land cover pattern of a region is an outcome of natural and socio– economic factors and their utilization by man in time and space. Land is becoming a scarce resource due to immense agricultural and demographic pressure. Hence, information on land use / land cover and possibilities for their optimal use is essential for the selection, planning and implementation of land use schemes to meet the increasing demands for basic human needs and welfare. This information also assists in monitoring the dynamics of land use resulting out of changing demands of increasing population.

Land use and land cover change has become a central component in current strategies for managing natural resources and monitoring environmental changes. The advancement in the concept of vegetation mapping has greatly increased research on land use land cover change thus providing an accurate evaluation of the spread and health of the world's forest, grassland, and agricultural resources has become an important priority.

Viewing the Earth from space is now crucial to the understanding of the influence of man's activities on his natural resource base over time. In situations of rapid and often unrecorded land use change, observations of the earth from space provide objective information of human utilization of the landscape. Over the past years, data from Earth sensing satellites has become vital in mapping the Earth's features and infrastructures, managing natural resources and studying environmental change.

Remote Sensing (RS) and Geographic Information System (GIS) are now providing new tools for advanced ecosystem management. The collection of remotely sensed data facilitates the synoptic analyses of Earth - system function, patterning, and change at local, regional and global scales over time; such data also provide

an important link between intensive, localized ecological research and regional, national and international conservation and management of biological diversity (Wilkie and Finn, 1996).
Therefore, attempt will be made in this study to map out the status of land use land cover of Hyderabad District between 2005 and 2008 with a view to detecting the land consumption rate and the changes that has taken place in this status particularly in the built-up land so as to predict possible changes that might take place in this status in the next 14 years using both Geographic Information System and Remote Sensing data.

2. STUDY OBJECTIVES

The following specific objectives will be pursued in order to achieve the aim above.

- To create a land use land cover classification scheme
- To determine the trend, nature, rate, location and magnitude of land use land cover change.
- To forecast the future pattern of land use land cover in the area.
- To develop land use/ land cover details of the Core Zone (Mine lease area) and the buffer zone (10km radius from the Mine lease area boundary) using latest possible satellite imageries.
- To evaluate the socio – economic implications of predicted change.

3. PROJECT DESCRIPTION

Physiography & Drainage:

a) Core zone Physiography:

The Core zone area is 2070.10 Ha. This is a plain terrain and gently slopes towards northeast. The topographic elevation varies from 140 m. to 180 m. above mean sea level. The area is covered by Sandy clay soils. In this area north and north western part is covered by RG - OC III Project up to a depth of 140 m and western portion is covered by OB dumps of the existing project to the height of 240 m. above MSL..

4. RESULTS AND DISCUSSION

A) PRE PROCESSING OF DATA

The Digital Image Processing has been performed using ERDAS Imagine software tools and Garmin handled GPS has been used for Ground truthing.

The IRS R2 Liss IV Multispectral Imageries Kharif and Rabi seasons have been geometrically corrected with respect to Survey of India Toposheets. To carry out the geo-referencing, ground control points (GCPs) were identified on the maps and raw satellite data. The coefficients for two co-ordinate transformation equations were computed based on polynomial regression between GCPs on map and satellite data. Alternate GCPs were generated till the Root Mean Square (RMS) error was less than 0.5 pixels and then both the images were co-registered.

This IRS R2 Liss IV Multispectral satellite data of Kharif and Rabi season has been used for the Land Use Land Cover Analysis of Buffer Zone. The satellite imageries were analyzed digitally by the method of supervised classification with necessary Ground truthing using the reference map as well as GPS instrument.

IRS PV Cartosat-1 Pan F data (of Core Zone) is geo-referenced data supplied by NRSC, Hyderabad. This For better spatial resolution of multi-spectral, the satellite datasets - IRS Resourcesat 2 Liss IV and IRS PV Cartosat-1 Pan F have been merged for Core Zone to achieve better spatial resolution.

The hybrid method of Digital Interpretation and visual interpretation has been used to classify the Core Zone to achieve accuracy levels.

The coordinates of the boundary were collected using the GPS for geo-referencing the boundary, during Ground truthing phase.

The topography of the buffer zone has been studied using the Survey of India Toposheets considering the elevations and the drainage pattern including drainage orders.

B) TOPOGRAPHY

i) Source of Information

Survey of India Toposheets 56N/5, 56N/6, 56N/9 and 56N/10 SOI has been used for the study of the topography. In topography map of buffer zone has been shown elevation and drainage pattern including drainage order in Pic 3.1.

ii) Study Results

The 10km buffer zone from the core zone boundary i.e. mine lease area of Ramagundam Open Cast-I Expansion (Phase-II) Project is mostly pediment area, the elevation contour values ranges between 140m–540m from amsl. There is hilly terrain only in the Southern part of the buffer zone. The mine has the elevation contour values within the range of 140-180m from amsl.

South-West area of the buffer zone covered with reserve forests namely Begumpet, Ramgir and kamanpalli Reserve Forests. Bokkala Vagu, Jallaram Vagu and Godavari River are passing through the buffer zone. The buffer zone is covered with 1-5th order streams. Industrial Area of Ramagundam Open Cast-I Expansion (Phase-II) Project contains NTPC, RTPS and FCI. NTPC Reservoir also covered in this buffer zone. Godavarikhani, Ramagundam urban Settlements covered this buffer zone

C) PREPARING SPATIAL DATA

The step-by-step procedure for preparing the spatial data for the entire study area is discussed below:

Step I: Satellite data was processed using image processing software

Step II: Generation of thematic maps such as land use / land cover, hydro geomorphology, groundwater prospect map and soil map.

Step III: Generation of topographical maps showing physical characteristics of the study area. The topographical maps extracted from SOI toposheets are drainage, physiography and basemap.

Step IV: Generation of maps derived from hydro geomorphology map and land use map.

Satellite Data Processing

In this study, the Remote Sensing data is used in the digital mode and is obtained by LISS III and PAN of Indian Remote Sensing (IRS - ID). More details of IRS-ID and its sensor characteristics are discussed by Anji Reddy (2001).

Map of 1:50,000 scale obtained from SOI covering the entire study area is used to extract the Ground Control Points (GCPs) and to demarcate the boundary of study area. This information is then used for image registration of LISS III and PAN digitally using EASI/PACE software.

D) HARDCOPY GENERATION

In order to derive spatial thematic data, a hardcopy of satellite image is generated through the following steps:

i) Acquisition of satellite data from National Remote Sensing Centre (NRSC), Balanagar, Hyderabad and toposheets from Survey of India (SOI) Hyderabad.
ii) Geo-coding and geo-referencing of LISS III and PAN digital data by extracting the Ground Control Points (GCPs) from SOI toposheets.
iii) Digital image enhancement and application of correction models for making the digital data free from errors and distortions both radiometry and geometry of the satellite data.
iv) Fusion of PAN and LISS III for merged product preparation of a mosaic (Plate 3.1), which shows the continuous imagery of two study areas.
v) A satellite hard copy of this fused data is generated for subsequent analysis.
vi) Preparation of Land use / Land cover map of sites 1 and 2 using visual interpretation technique.
vii) Preparation of cartographic output of visual interpretation for making the data layer ready for scanning for further GIS analysis.
viii) Scanning of cartographic output using A0 colour Abacus scanner, digitization of this hard copy using AUTOCAD software and editing the digitized data compatible to ARC/INFO GIS software.
ix) GIS data manipulation and analysis, linking the spatial data file and attribute data file for the creation of topology.
x) GIS output in the form of land use/land cover map showing various land use/land cover patterns of the study area.

International
Journal
Of Advanced Research in Engineering & Management (IJAREM)
ISSN: 2456-2033 || PP. 01-06

E) LAND USE / LAND COVER CLASSIF ICATION OF OR BUFFER ZONE

Digital image processing was carried out to delineate various land use / land cover categories in 10km buffer Zone viz. built up area, crop areas, forests, scrubs, land with or without scrub, water bodies by assigning necessary training sets, which were identified based on tone, texture, size, shape pattern and location information. Necessary care has been taken to identify proper land use class, where there is conflict between signatures of various classes. The interpreted map was verified on ground at limited points and final land use / land cover map was prepared.

(i) Various Land Use Classes Identified:

The buffer zone can be broadly identified into forest areas, built-up areas, agriculture areas and other land with or without Scrub. The definitions of various land use classes are given below. Forest Blank and Forest Plantation are additional classes shown in the classification compared to the classes followed by Forest Survey of India (FSI).

(ii) Forest Cover:

All the areas declared as reserve forest areas are shown in this class. The forests can be classified based on density into following classes:

Very Dense Forest:	Forests with tree canopy coverage above 70%
Moderate Dense Forest:	Forests with tree canopy coverage between 40%-70%
Open Forest:	Forests with tree canopy coverage between 10%-40%
Scrub Forest:	Forests with tree canopy coverage between 1%- 10%.
Forest Blanks:	Forests with tree canopy coverage less than 0%. Forest encroachments and illegal agriculture also will be shown in this class.
Plantations:	The plantations raised with in the reserve forest boundaries are shown in these classes.

(iii) **Agriculture Area:**

Single Crop Land:	The areas where farmers practice cultivation for single season (Kharif) in a year.
Double Crop Land:	The areas where farmers practice cultivation for two seasons (Kharif & Rabi) in a year.
Fallow Land:	The areas not cultivated in current year/ years.
Plantations:	The private areas with horticulture/ other plantations

(iv) Waste Lands:

Areas with/ without Scrub: Generally waste lands-non agriculture, non forest areas covered with or without scrubs.

Barren lands:	Land without any usage and without scrubs and sometimes they are rocky exposed areas.
Built-up Area:	The habitations are villages/ colonies/ Industries will be shown in this class.
Mining Areas:	The areas, where the mining activity is being carried out/ has been done are shown in this class.
Industrial Area:	The industrial Establishments will be shown in this class.
Water Bodies:	The oceans, rivers, streams, lakes, tanks, reservoirs, canals etc will be identified in this class.

(v) Land Use Land Cover Details of Buffer Zone

The image of the study area around 10 Km. from mine site (Core zone boundary) as captured by satellite is presented in figure 1.2 and 1.3. The Land use land cover in this study area is depicted in figure 2.1. Total 9.75% of the buffer zone is covered in Reserve Forest area under various density categories and 53.08% of the area is under cultivation.

(vi) Land Use Land Cover Study of Core Mine Area

The Satellite data of the core zone of 923.88 Ha has been presented in fig 1.4, 1.5, and 1.6 (IRS R2 Liss IV, Cartosat Pan F and Cartosat Pan F + IRS R2 Liss IV Merged data respectively). The IRS R2 Liss IV and Cartosat Pan merged data has been interpreted to delineate various land use classes in core zone.

International
Journal
Of Advanced Research in Engineering & Management (IJAREM)
ISSN: 2456-2033 || PP. 01-06

The hybrid method of digital and visual interpretation procedures was followed for Core mine area on the merged data of Liss IV and Pan Datasets for identifying various classes.

5. CHANGE DETECTION:

The land use studies for Core and Buffer zones of Ramagundam Open Cast-I Expansion (Phase-II) Project comparative statement of land use land cover studies of 2010-11 and 2012-13 are given below.

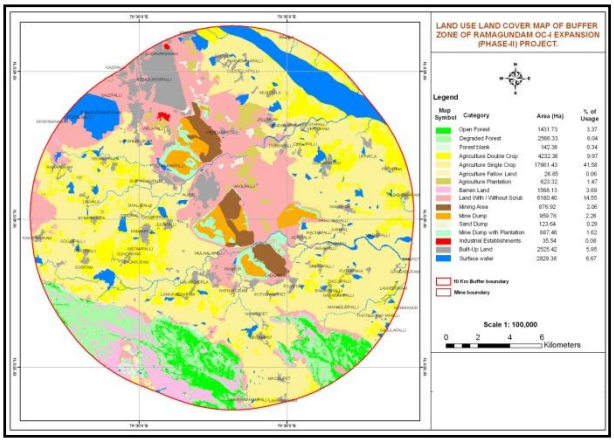

Figure 1.1 Land Use/ Land Cover pattern map of the Core zone

Tab: 1.1 Table showing land use comparative area statement of Buffer zone

Land Use Land Cover Class	**2013**		**2012**	
	Area in ha	**Area in%**	**Area in ha**	**Area in%**
Open forest	1431.73	3.37	414.22	0.98
Degraded forest	2566.33	6.04	4714.39	11.1
Forest blank	142.38	0.34	661.14	1.56
Agriculture - Double Crop	4232.36	9.97	6613.6	15.57
Agriculture - Single Crop	17661.43	41.58	16802.55	39.56
Agriculture - Fallow Land	26.85	0.06	988.42	2.33
Agriculture - Plantation	623.32	1.47	16.17	0.04
Barren land	1568.13	3.69	23.57	0.06
Land With/ Without Scrub	6180.40	14.55	5398.52	12.71
Mine area	876.92	2.06	739.93	1.74
Mine Dump	959.76	2.26	1343.93	3.16
Dump with plantation	687.46	1.62	0	0
Sand dump	123.64	0.29	0	0
Industry	35.54	0.08	115.79	0.27
Built Up Land	2525.42	5.95	2295.27	5.40
Water body	2829.36	6.67	2343.53	5.52
Total Area	**42471.03**	**100**	**42471.03**	**100**

The Land use / Land cover categories of Agriculture plantation, Barren land, Coal Dump are not classified in previous study. Mine pit, Dump with plantation, road, water body, Built up Land has been increased in Current year Core study. OB Dump and land with/without scrub are decreased in current study.

The Land use / Land cover categories of Dump with plantation and Sand dump are not observed in the previous study Buffer zone, these categories are classified in the current study. Open forest, single crop and plantation, barren land, mine area, water body are increased. In current buffer area forest blank, fallow land, mine dump, degraded forests are decreased in current study.

REFERENCES:

[1]. Land Use Land Cover Management Pratices In India by N.C.Gautam;V.Raghavswamy-B.S.Publications
[2]. Anji Reddy, M., Textbook Of Remote Sensing And Geographical Information Systems, B. S. Publications, Hyderabad, 2001.
[3]. District Census Handbook of Statistics, Chief Planning Officer, Prakasham District, Ongole, Andhra Pradesh, Census of India 2004-2005.
[4]. Thomas M. Lillesand and Ralph W. Keifer, Remote Sensing And Image Interpretation, Fourth Edition, John Wiley and Sons, Inc, New York, 2000.
[5]. FAO, 1989 : Guidelines of Land Use Planning.
[6]. FAO of the united Nations, Rome.uis, Vol. 5, pp. 23-34, 1988.
[7]. Comellia O. Kuntze Modelling tea yield using satellite derived LAI, Land use and meteorological data. GIS development ACRS 2000.
[8]. Yujiro Hirano, Shiroochi and Ryosukeshibasaki, Estimation of agricultural productivity distribution in India Institute of Industrial Science, University of Tokyo, Japan.

RESEARCH ARTICLE OPEN ACCESS

Simulation of Flow and Structural Analysis of Industrial Blower

Rakesh Mididoddi*, A. Raja Sekhar**
**(M.E (CAD/CAM) Scholar, Department of Mechanical Engineering, Methodist College of Engineering and Technology, Hyderabad-500001 Email: rakeshmididoddi@gmail.com)*
*** (Professor, Department of Mechanical Engineering, Methodist College of Engineering and Technology, Hyderabad-500001 Email: arsekhar06@gmail.com)*
Corresponding author: Rakesh Mididoddi

ABSTRACT
Industrial Blowers are used to transport air to different upward/downward components in power/process equipment assembly. However performance degradation during operation concerns designers for plant efficiency. To this effect performance analysis is aimed in three dimensional environments. The basic approach followed to obtain three dimensional CAD model of blower comprises suction duct, volute chamber, impeller and exit duct. The CAD model in the form of IGES format has been imported in Altair Hyper Mesh pre-processor for surface repair and fluid/solid domain extraction. The fluid domain has been further discretized in the form of unstructured and structured grids so as to generate tetrahedral and hexahedral elements respectively which in turn was imported in Ansys Fluent Software. With the prescribed boundary conditions such as inlet velocity, exit pressure and blade rotation, CFD simulation is performed to visualize the velocity and pressure distribution. Solid domain of blower impeller was imported in Ansys Mechanical to map pressure load from fluid simulation to compute deformations and principal stresses.
Keywords: Ansys, Blade rotation, Blower, CFD.

Date of Submission: 26 -07-2017 Date of acceptance: 05-08-2017

I. INTRODUCTION

Blowers are widely used in several engineering applications including process and power generation, refinery, petrochemical, pharmaceutical, heating, ventilating and air-conditioning applications. For the design and development of turbo machinery components like pumps, blowers, fans, turbines, etc., multi-disciplinary analysis is critical before development of prototype models [1]. During the operation of turbo machinery components the fluid dynamic perturbations are produced which may also alter vibration and noise levels. One of the major problems with the impeller blade design is whether the impeller blades are strong enough to withstand the hydrodynamic load. Some impeller blades have suffered failures, possibly due to the inadequate use of material and geometries or because the design load was not correctly estimated. When the internal pressure load acted on the blade reaches or exceeded the yield stress of the material, yielding and deformation occurred. Most frequently impeller blades yield and deform at the highly stressed region. This type of failure has critical importance because yield of impeller blades decreases the blade performance.

So the component develops performance degradations which are planned to be addressed in the proposed research investigation using three dimensional modeling and simulation techniques. In order to understand flow behavior and pressure rise parameters, CFD simulation is performed on the complete geometry involving blower casing as well as impeller blades. Structural simulation is also performed on the impeller blades to understand deformations and structural stresses.

The casing of the blower under consideration is of volute type and the impeller blades are of backward aero foil shape. The fluid enters at the centre of the impeller, turns through a right angle and as it moves outwards radially, is subjected to centrifugal force resulting increase in its static pressure. The airflow tends to drop drastically, as the system pressure increases is one of characteristic of centrifugal fan. Pressure Volume characteristic curve for a backward bladed centrifugal blower represents losses in the blowers [2]. Though the design and development of blowers with different configurations are discussed in the literature using advanced CFD techniques, they lack fluid-solid interaction effects [3-6]. Blowers can get failure due to vibration, lack of performance, excessive noise and premature component failure.

1.1 Experimentation and Methodology

CFD provides the fundamental improvements by simulating the performance of the turbo machinery component with the account of complete geometry. It also helps to reduce the design lead time by performing design cycles in software rather than hardware and improves the product performance by evaluation of more design alternatives in shortest time.

The first step in performing a CFD analysis is called pre-processing. This involves identifying the flow region of interest, geometrically representing the region, meshing and defining the flow physics. Once the region is defined, computer model of the geometry is created. Computational domain can be discretized with the choice of elements like tetra, hexahedral elements in "Altair Hyper Mesh". The mesh generation concepts were discussed, reviewed and resulted to several commercial softwares which are being extensively used for several industrial components [7-9]. Unstructured grid methods [10] utilize an arbitrary collection of elements to fill the domain automatically requires the volume bounded by error free surfaces. Structured grid generation of CFD simulation is explained by Bhasker [11]. The appropriate boundary conditions are applied to define the regions of inflow, outflow and moving walls. Physical models within the software are activated to simulate the flow physics especially turbulent flows can be done in "Ansys Fluent Solver". After initialization of flow field variables, the problem is submitted to solver. Solution is converged or stopped when the equation residuals are meeting the specified values and writes the result file.

This result file can be loaded in post-processing to visualize the flow characteristics in terms of vector plots, contour plots and streamlines. The post processor also provides fluxes and averaged quantities across the computational domain. Solid domain of blower impeller was imported into "Ansys Mechanical" to map pressure load from fluid simulation to compute deformations and principal stresses.

II. BLOWER MODEL FOR ANALYSIS

The blower is shown in Fig.1 comprises the casing with supports. The casing is of volute type with exit duct and inlet is on the suction plate which is placed on top of the blower casing. The impeller was designed with seven aero foil backward blades whose leading and trailing edges are filled with fillets.

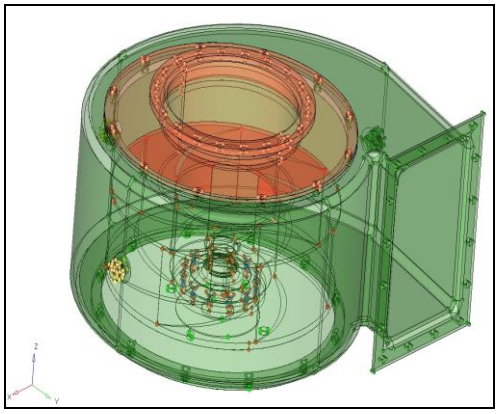

Fig 1 Blower model.

Table 1 Dimensions of blower.

1	Casing height	:	239.4 mm
2	Casing dia	:	360 mm
3	Inlet dia	:	212.0 mm
4	Inlet height	:	34.8 mm
5	Impeller height	:	98.4 mm
6	Impeller dia	:	354 mm
7	No.of aero foil blades	:	7
8	Pitch angle	:	56.429^0

The solid model used for flow simulation was comprises thickness, plugs, lining washers, casing bushes, casing lining washers, whose presence is not effected for the flow simulation. Hence, surfaces associated with these supports are deleted. As a result pin holes are present on casing at several locations need to be filled.

2.1 CFD Analysis:

Pre-processing: Pre-processing consists of the following steps. From the blower model configuration (fig.1):

Step 1: Extraction of casing from blower model.

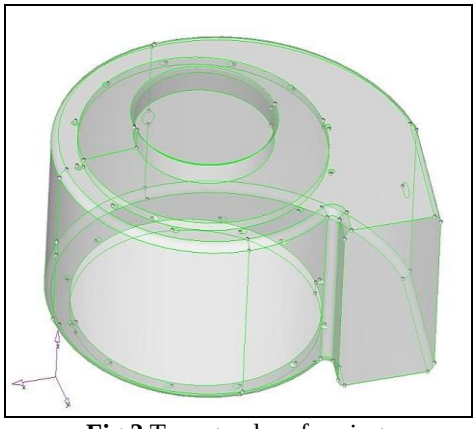

Fig.2 Topography of casing.

Step 2: Extraction of impeller from blower model.

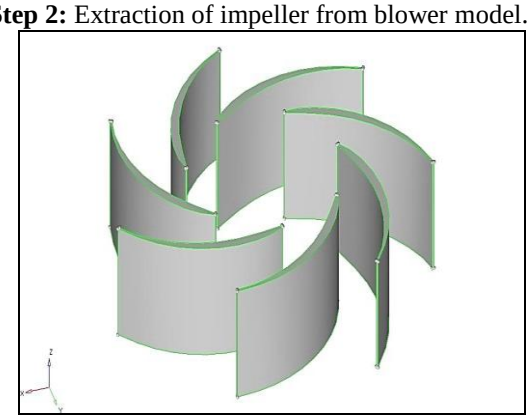

Fig.3 Topography of impeller.

Step 3: In separate group collector, using bounding surfaces, casing and blower are grouped together to form complete geometry of blower model.

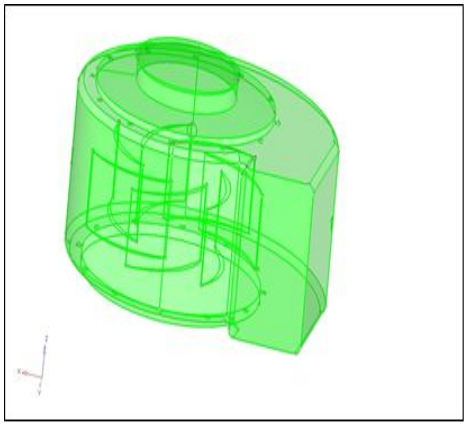

Fig.4 Grouping of casing and impeller.

Step 4: Unstructured grid mesh with boundary conditions.

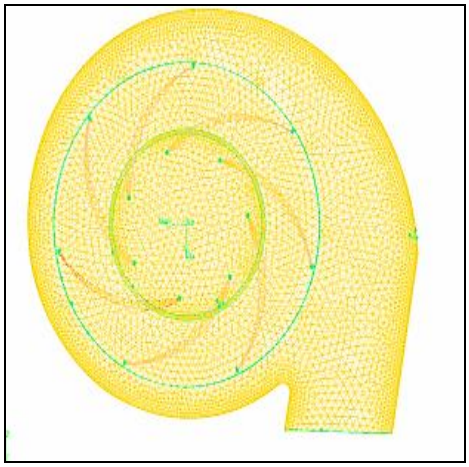

Fig.5 Unstructured grid mesh model with boundary conditions.

Step 5: Structured grid mesh of complete geometry with boundary conditions.

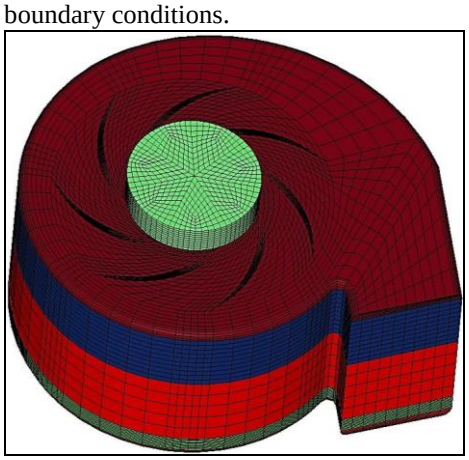

Fig.6 Structured grid mesh with Boundary Conditions.

Step 6: Simulation of blower model with unstructured grid.

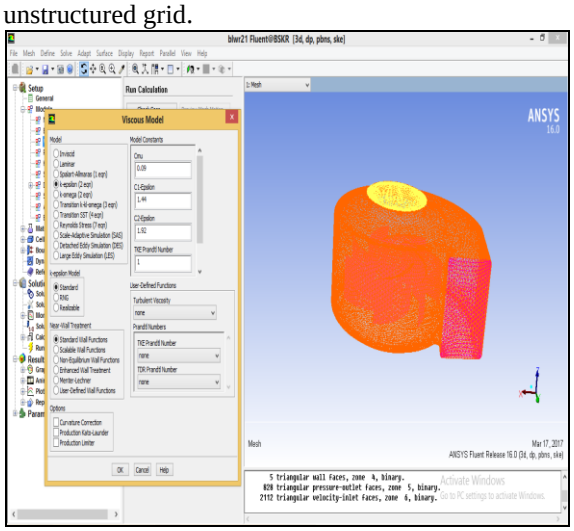

Fig.7 Critical parameters applied to the model.

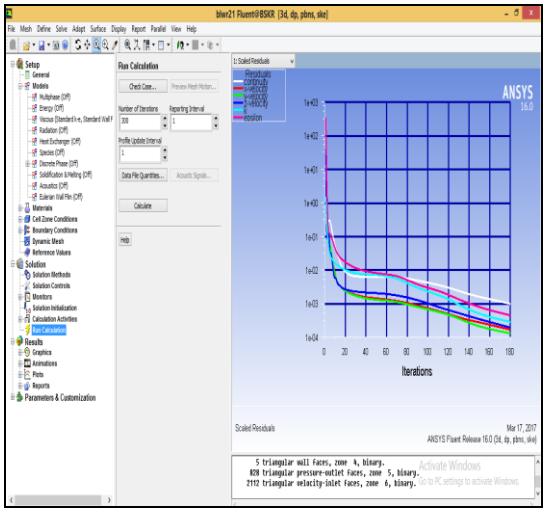

Fig.8 Convergence history of unstructured grid model.

The material considered is air. Generally operating pressures are 1 atm and its value in the "pressure out boundary condition" should be mentioned as zero. Under run calculations, mention about 300 iterations and profile update interval has made as 1. The unstructured grid with tetrahedral elements generated for blower model has taken 180 iterations to obtain numerical results for flow and pressure parameters when the blades are rotating with 2800 rpm along z direction.

Step 7: Simulation of blower model with structured grid.

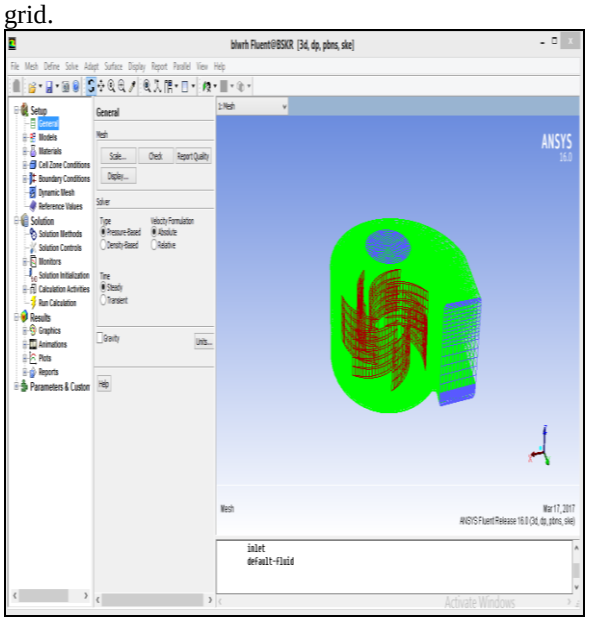

Fig.9 Structured grid model into Ansys Fluent Solver.

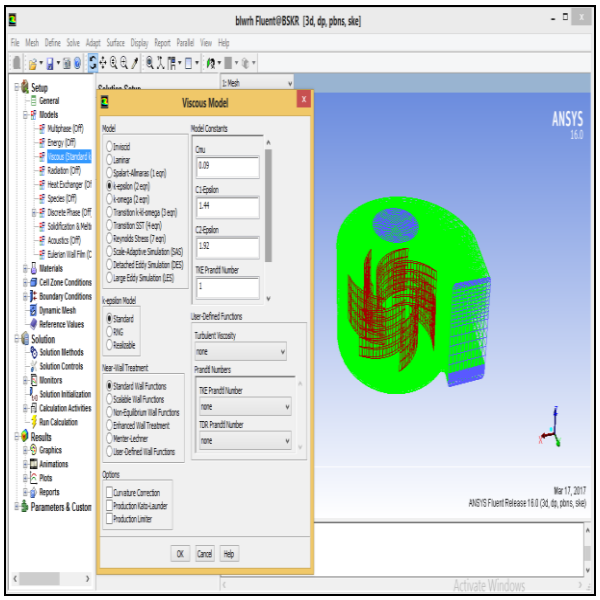

Fig.10 Critical parameters applied to the model.

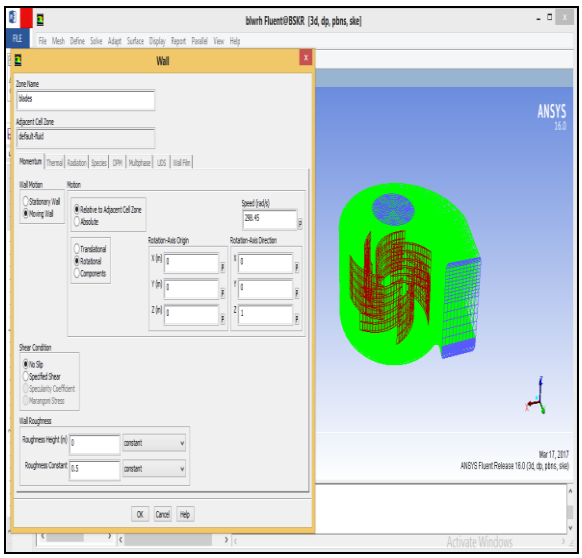

Fig.11 Boundary conditions (wall) applied to model.

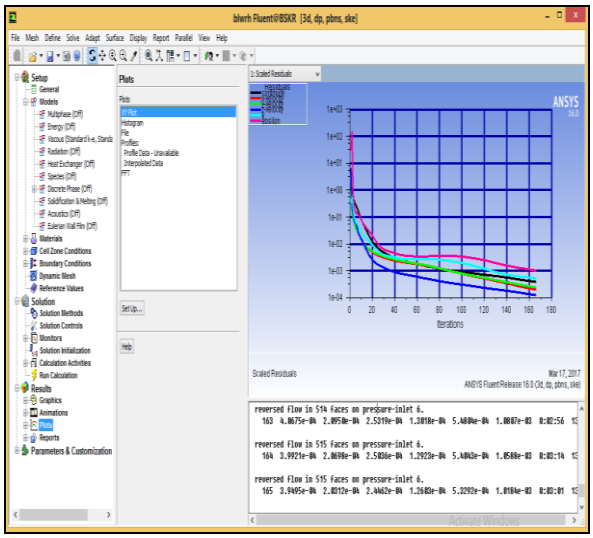

Fig.12 Convergence history of structured grid model.

The working fluid considered is air. Inlet velocity 9 m/sec, working pressure will be 1 atm and blades are rotating about z direction with 2800 rpm. When assigning the boundary conditions, the wall motion considered is as moving wall and blade motion considered is as rotatory. The convergence history of equation residuals in case of structured multi-block grid is faster than unstructured grid and took only 166 iterations.

Post-processing:
Discussion of results from CFD simulation:

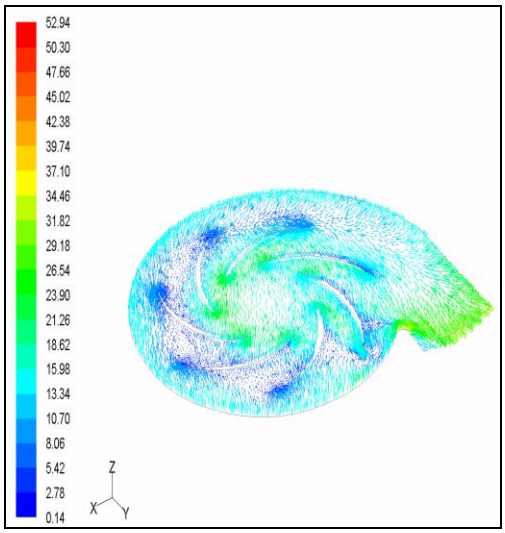

Fig.13 Describing velocity vectors in the middle plane of the impeller section.

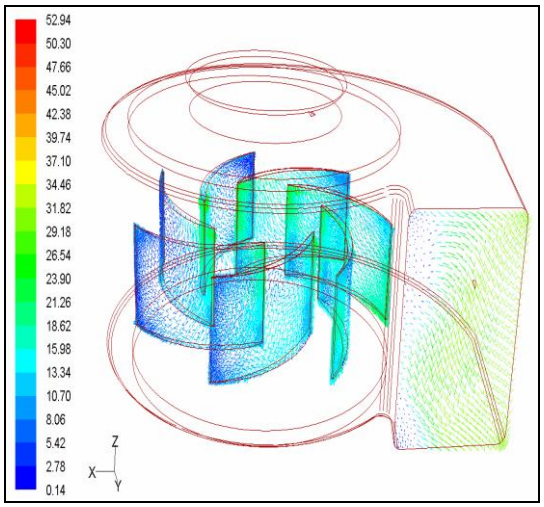

Fig.14 Velocity vector plots drawn on full blade surfaces to understand its effect on exit.

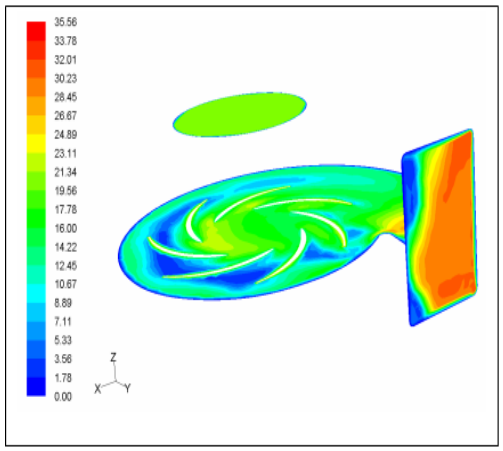

Fig.15 Contour plot indicating flow non-uniformity.

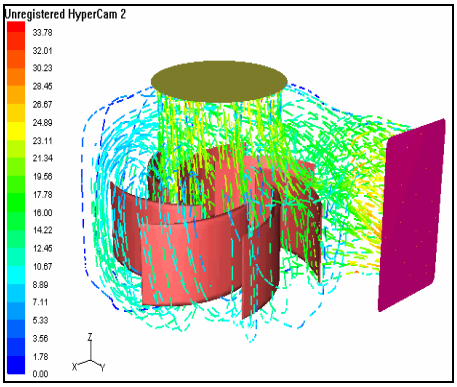

Fig.16 Flow path in the blower casing in the form of animated streams from inlet to exit.

Maximum velocity is taking place at blade leading edge and the minimum velocity is at blades trailing edges (fig.13) and is observed that low velocity of flow taking place on blades trailing edges side away from the exit location (fig.14). The flow through blade channels indicates low velocities and higher pressure drop. This kind of flow will have effect on the exit location which indicates flow non-uniformity is more clearly observed in contour plot (fig.15). Fluid flow from inlet to exit in the form of animated streams is representing the centrifugal forces due to rotation of blades changes the flow to move upwards and then leaves to exit location (fig.16). The flow also fluctuates with turbulent eddies near blade channels away from exit causing higher pressure drop and influence non-uniform flow at the exit location.

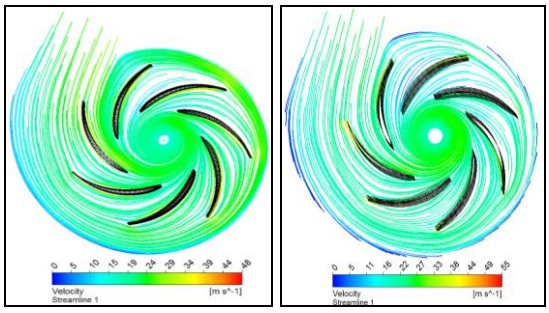

Fig.17 Surface Streamlines on the velocity scale from the suction to exit via impeller blades.

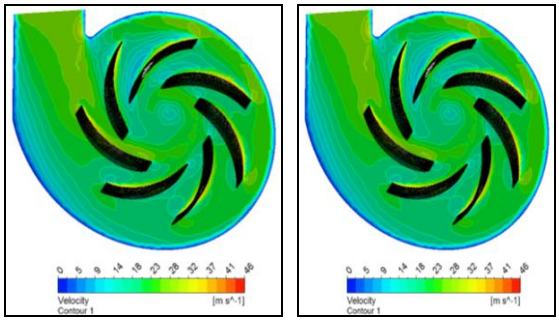

Fig.18 Flow recirculation in the blade passage away from exit.

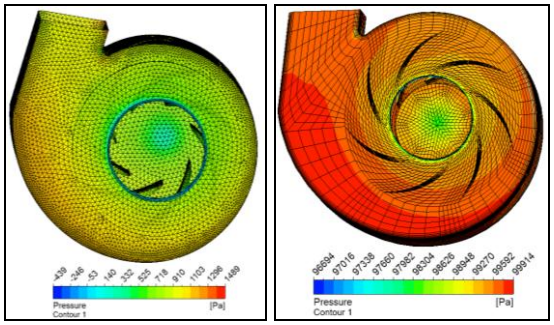

Fig.19 Contours of pressure distribution on the blade middle span and wall surfaces.

From the plots (fig.17 & fig.18), high velocity is noticed near the blade surfaces in impeller and low velocity in the volute area because the velocity is converting into pressure. The contours on velocity scale exhibit the non-uniform flow in cross section plane blade span along volute casing. The contours also reveal the high velocity regions near the impeller due to rotation of blades. As the flow moves away from the rotating wall, this high velocity however reduces. It is also observed that as the flow moves from suction to exit along the volute casing static pressure is increasing due to conversion of velocity into pressure (fig.19).

2.2 Ansys Mechanical Analysis:

Step 1: Mesh generation of impeller.

After creating the three-point spline curves for blade and tip, volumes created for blade surfaces. Then meshing has done, generally mapped mesh is preferred for impeller blade surfaces.

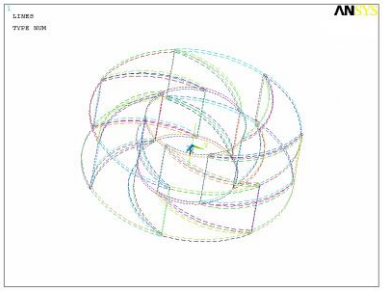

Fig.20 3-point spline curves for blade tip and hub.

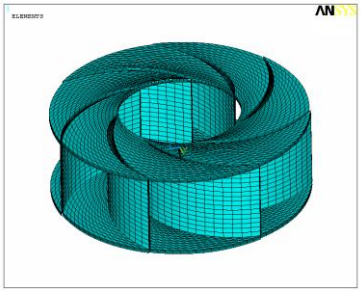

Fig.21 Mesh Generation for Impeller Blades.

Step 2: Structural simulation of blower impeller.

The geometry has to be scaled in SI units and preferences for linear structural analysis have to define with proper material properties like poisson ratio, young's modulus and density. The objective is to study the effect of internal pressure load and displacement constraints on impeller for stress analysis.

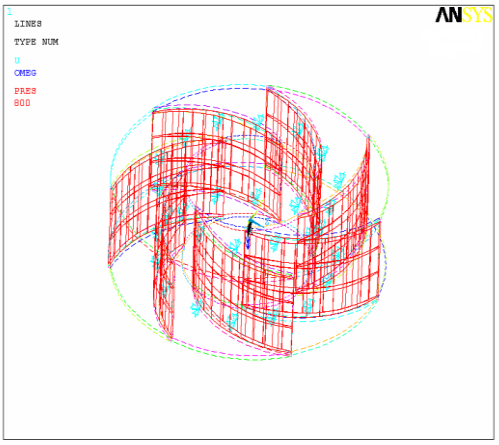

Fig.22 Critical parameters applied to impeller blades.

From the fluid flow analysis, on the blade surfaces, it is found that the average pressure load acting on the blades is about 800 Pascals.

Results from Ansys Mechanical:

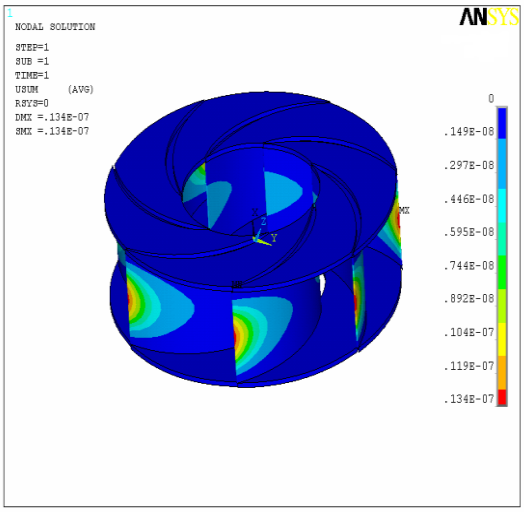

Fig.23 Deformed model with color map indicates highest displacement while blue shows the least.

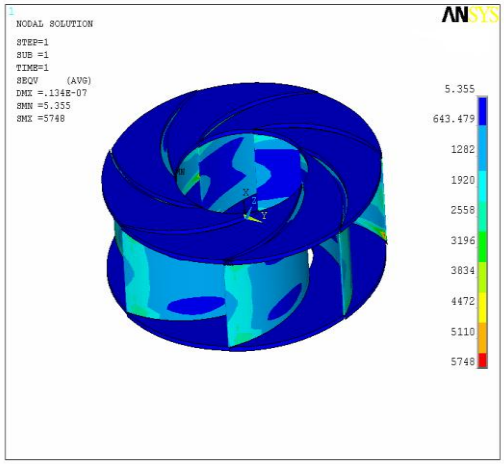

Fig.24 Equivalent stresses on blade surfaces shows maximum stress at blade trailing edges symmetrically on all blades.

It is observed that blades are deforming very small and maximum displacement is taking place at mid-section of blade towards trailing edge which decreases towards leading edge. The stress distribution on rest of the blade section and pressure surfaces is small and appears to be in limits.

III. MATHEMATICAL FORMULATION OF FLUID MECHANICS

The transport of fluid comprises gases/liquid from one component to other in power/process equipment are described through mass, moment and energy conservation principles. The Navier Stokes (transport) equations are derived from these principles are discussed and represented mathematically as [12]:

$$\frac{\partial}{\partial t}\int_V \rho\varphi dV + \oint_A \rho\varphi V.dA = \oint_A \Gamma\nabla\varphi.dA + \int_V S_\varphi dV \quad (1)$$

Where ϕ describes the transport equation for x, y, z momentum when this variable assigns u, v, w in the above equation. If φ takes 1, equation (1) becomes continuity equation. The acceleration of fluid depends on the inertia, diffusion and sources terms. The equation (1) is further discretized into:

$$\sum_f \rho_f V_f . A_f \varphi_f - \sum_f \Gamma_f (\nabla\phi)_f . A_f = \bar{S}_f \Delta V \quad (2)$$

Wherein diffusion term on right hand side of equation (1) is volume integral and is converted into surface integral using Green-Gauss theorem. Equation (2) after its reconstruction from cell centers forms the set of algebraic equations and can be solved for the variable φ iteratively. During the iteration process, imbalance of flow variables between left and right hand side of an equation is called Residual error (R) will minimizes to specified target, if the following criterion is satisfied:

$$R \equiv \sqrt{\frac{\sum_{i=1}^{N}(\varphi_i - \varphi_g)^2}{N}} \quad (3)$$

Where φ with subscript g and i are assumed and currently calculated value; N is of Number of iterations.

3.1 Finite Element Method of Solids:

Finite element analysis is a computer based numerical technique for calculating the strength and behavior of engineering structures [13]. Structural analysis was carried using commercial solver Ansys Mechanical for which following mathematical relations are employed:

$$[K]\{u\} = \{F\} \quad (4)$$

Where K is the system stiffness matrix; F load vector and u is displacement vector. The system stiffness matrix is obtained by assembling the element stiffness matrices consistent with the compatibility requirements between the global and local displacements. The state of stress of the idealized structure is obtained by compiling the results for the states of stresses of individual elements. The state of stress of an individual element is obtained by solving equation (8) for the system displacements. The compatibility equations between the system and element nodal displacements:

$$\{\delta\}_i = [\beta]_i\{u\} \quad (5)$$

Where δ nodal displacement is vector and β is the compatibility matrix for the element I. The equation for the strains:

$$\{\epsilon\}_i = [B]_i\{\delta\}_i \quad (6)$$

Where B is the strain displacement matrix and ε strain vector for the element i. The relation for computation of stresses:

$$\{\tau\}_i = [C]\{\epsilon\}_i \quad (7)$$

Where C is the elastic constants matrix and τ is the stress vector for the element i.

IV. CONCLUSIONS

The simulation using structured grid data provides better insights (took 166 iterations) than the same observed in the simulation using unstructured grid (took 180 iterations).

The simulation results in both unstructured and structured grid method cases relatively addressed the non-uniform flow in blower volume with the flow velocity near impeller blades shows high and lower in volute section. Lower velocity in volute section converts into pressure and hence pressure rise takes place across exit and entry location.

The mechanical simulation of impeller blades with the average pressure load suggests (800 Pascals) that the component is structurally safe, as the deformations are small and equivalent stress determined on blades are within the acceptable limits.

REFERENCES

[1]. Process design of Fans and Blowers, Design document, KLM Technology, April, 2001.
[2]. Takahashi, Characteristics of Centrifugal Blowers and its effective use in high static Pressure Area, Oriental Motor Co Ltd, 2002.
[3]. Tremmel M, Taulbee DB Calculation of the Time Averaged Flow in Squirrel Cage Blowers by Substituting Blades with Equivalent Forces, ASME Jr of Turbo machinery, Vol 130 PP 1-12,2008.
[4]. Huang C-K, Hsich M-E, Performance analysis and optimized Design of Backward-Curved Aerofoil Centrifugal Blowers, HVAC&R Research Magazine, Vol 15, pp 461-488,2009.
[5]. Pathak Y, Baloni D B and Channiwala SA, Numerical simulation of Centrifugal Blower using CFX, Intl.Jnl. of electronics, April, 2012.
[6]. Hsia S-Y, Chiu, S-M and Cheng J-W, Sound field analysis and simulation of fluid machines, Adv.in Engg.software, Vol.40, 2009.
[7]. Thomson, J.F et.al Numerical Grid Generation – Foundations and Applications, North Holland, Amsterdam, 1985.
[8]. Shekar Majumdar Pressure based finite volume algorithm for viscous flow computation, Lecture Notes, CFD Advances and Applications, NAL, Bangalore, India, 1994.
[9]. Bhasker C CFD applications for Industrial Flow Simualtions – Invited talk, SONIC-10 Conference, International Institute of information Technology, Pune, India, 2010(a).
[10]. Shevare, G Issues in Unstructured Mesh Generation, Lecture notes, 1994.
[11]. Bhasker, C,Simulation of Three Dimensional Flows in Industrial Components using CFD Techniques, chap-8, Computational Fluid Dynamics Technologies/Applications Editedby Igor V. Minin and Oleg V. Minin, InTech, Rijeka, Croatia.
[12]. Hoffman, K.A et al Computational Fluid Dynamics for Engineers, in two volumes, Engineering Education System, Wichita, KS, 67208-1078. 1993.
[13]. Mohd Zubair Nizami, et al Evaluation of static and dynamic analysis of centrifugal blower using FEA. Procgs of International Journal of Advanced Trends in Computer Science and Engineering, Vol.2 , No.1, Pages : 316 - 321 (2013).

ACKNOWLEDGEMENT

The authors would like to thank **Dr C.BHASKER**, (MD/Ex.sr Mgr (BHEL, R&D, Hyderabad) for his support in this work.

International Journal of Engineering Research and Applications (IJERA) is **UGC approved** Journal with Sl. No. 4525, Journal no. 47088. Indexed in Cross Ref, Index Copernicus (ICV 80.82), NASA, Ads, Researcher Id Thomson Reuters, DOAJ.

Rakesh Mididoddi " Simulation of Flow and Structural Analysis of Industrial Blower" International Journal of Engineering Research and Applications (IJERA) 7.8 (2017):82-89

International Journal of Engineering Science Invention
ISSN (Online): 2319 – 6734, ISSN (Print): 2319 – 6726
www.ijesi.org ||Volume 6 Issue 11|| November 2017 || PP. 50-55

Optimization of Process Parameters in Abrasive Jet Drilling Of Hastelloy Using Taguchi Method

Prerna Ramagiri[1], Rajasekhar Adula[2] , D.V.Srikanth[3]
[1,] *Department of Mechanical Engg., Methodist College of Engg & Tech.,Abids, Hyderabad, Telangana, India-500001 Mobile No 9885002036; e-mail: prernar009@gmail.com*
[2]*Department of Mechanical Engg., Methodist College of Engg & Tech.,Abids, Hyderabad, Telangana, India-500001Mobile No 9989421206; e-mail: arsekhar06@gmail.com*
3Department of Mechanical Engg., St.Martin College of Engg. & Tech., Hyderabad Telangana, India: Mobile No 9703050004: e-mail: dvsk75@gmail.com

Abstract: *Machining of nickel base Hastelloys is considered as moderate to difficult. During machining, these alloys work harden rapidly, generate high heat during cutting, weld to the cutting tool surface and offer high resistance to metal removal because of their high shear strengths. Abrasive jet machining (AJM) is a non-conventional machining process which is effective in machining hard and brittle materials. Hence to overcome the difficulties in machining of hastelloy by conventional machining process, Abrasive jet machining is employed. During AJM, the influence of process parameters on machining characteristics were studied using Taguchi method and the results were compared using ANOVA technique. The process parameters chosen were air pressure, standoff distance (SOD) and nozzle diameter. AJM performance was measured in terms of MRR and Kerf. In the Taguchi analysis it is observed that the air pressure has largest effect and nozzle diameter has the smallest effect on the material removal rate whereas the Standoff distance (SOD) has large effect and nozzle diameter has the least effect on Kerf. Similar kinds of results were observed when analyzed by ANOVA.*

Key Words: *Abrasive Jet Machining, MRR, Kerf, Hastelloy, Taguchi, ANOVA*

Date of Submission: 15-11-2017 Date of acceptance: 28-11-2017

I. Introduction

In abrasive jet machining, a stream of fine abrasive particles carried by compressed air (or) gas focused through a nozzle and strikes the target surface. The particles coming out of the nozzle with high velocities impinges on the work surface and removes the material from the surface by mechanical erosion. The air (or) gas stream carries both the abrasive particles and the fractured material away from the work area [1-2]. AJM is an effective process for machining hard and brittle metals, alloys, and non-metallic materials (e.g., germanium, silicon, glass, ceramics, and mica). The various operations performed on AJM are drilling, deburring, polishing, etching, and cleaning. In addition to its wide applications at the macro-scale, it has a significant role in micro-machining, especially micro-channels and micro-holes in the manufacture of micro-devices.

A number of experimental investigations have been carried out on AJM process to determine the effect of various input parameters on material removal rate, penetration rate, kerf and on surface finish [3-6]. The experimental research has also involved use of various optimizing techniques [7-11]. The work materials used by various researchers for AJM machining are Alumina Ceramics [11], Glass [12],[6],[4], Silicon Nitride [5] Zirconium dioxide [6], EDM die material [6], Quartz [14], PMMA [14], plaster-of-paris [10], stainless steel [15].

HASTELLOY C276 is a Nickel based super alloy with an addition of chromium, molybdenum and tungsten designed to have excellent corrosion resistance in a wide range of severe environments. The high nickel and molybdenum contents make the alloy resistant to pitting and crevice corrosion in reducing environments while chromium improves resistance to oxidizing media. This alloy is resistant to the formation of grain boundary precipitates in the weld heat-affected zone, thus making it suitable for most chemical process applications in as welded condition. Due to its high temperature strength, resistance to neutron radiation, and perfect anti-oxidation ability, it is widely used in the most severe environments such as chemical processing, pollution control, pulp and paper production, industrial and municipal waste treatment, and recovery of sour natural gas.

Machining of nickel base corrosion and temperature resistant alloys are considered as moderate to difficult. Machining of this alloy through notching is a prominent failure due to high mechanical properties of work piece

which results in short tool life and low productivity. During machining these alloys work harden rapidly, generate high heat during cutting, weld to the cutting tool surface and offer high resistance to metal removal because of their high shear strengths.

A review of the literature shows that the great majority of published work is focused on AJM of different materials; however till date hastelloy was not included. Hence the usage of AJM to machine Hastelloy is being done to prevent the excessive heat production and wastage of the material which occur during the conventional methods of machining. The parameters like MRR and Kerf are mostly influenced by process parameters like SOD, ND and Pressure. Hence, AJM has been used for machining of Hastelloy and the MRR and Kerf are optimized by using Taguchi Techniques.

II. Experimentation

2.1 Experimental set up

The experimental work was carried on AJM test rig. The set up is shown in Figure 1**.** Atmospheric air was used as a medium of carrier gas and a compressor with a maximum pressure of 10 bar was used to achieve the desired range of pressure. The silicon carbide abrasives with an average grit size of 60 μm were mixed with an air stream and allowed to pass through the nozzle. The abrasive flow rate was kept constant throughout the machining process. Nozzles were made using Tungsten Carbide material with three different bore diameters of 2mm, 3mm, and 4mm and experiments were conducted at three levels of Pressure and SOD using all three nozzles. Hastelloy C 276 sheets were used as work material whose chemical composition is given in the Table1. The specimen after experimentation is shown in Figure 2.

Table 1. Chemical composition of Hastelloy

Element	Ni	Mo	Cr	Fe	W	Co	Mn	V	Si	P	S	C
%	57	15-17	14.5-6.5	4-7	3-4.5	2.5	1	0.35	0.08	0.025	0.01	0.01

Figure 1. AJM Test Rig

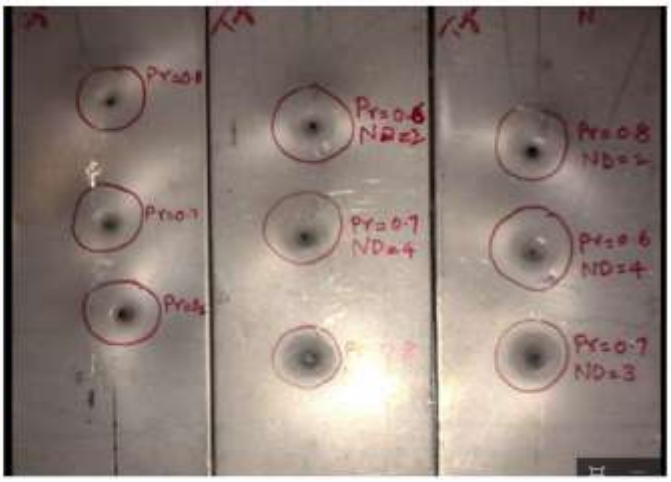

Figure 2. Taguchi Test Specimen (Hastelloy C-276)

2.2 Design of experiments

Design of experiments (DOE) using Taguchi method was used to conduct experiments. L9 orthogonal array was selected for this purpose. Three parameters namely air pressure, nozzle diameter and nozzle tip distance (stand off distance-SOD) at three different levels were considered to conduct a total of 9 experiments. These values are given in Table 2.

Table 2. Process parameters and their levels

S. No	Parameters	Levels		
		1	**2**	**3**
1	Pressure (kg/cm^2)	6	7	8
2	Stand of Distance (SOD) (mm)	7	8	9
3	Nozzle diameter (mm)	2	3	4

2.3 Response Variables

The performance of the process was measured in terms of material removal rate (MRR) and kerf. The initial and final weight of the work piece along with drilling time for each hole were noted for finding the Metal removal rate (MRR). Difference in diameters of top and bottom surface of the drill was measured to find the Kerf values.

III. Results And Analysis

3.1 Analysis of the S/N Ratio

Taguchi method stresses the importance of studying the response variation using the signal – to – noise (S/N) ratio. The term "signal" represents the desirable value and the "noise" represents the undesirable value. The formulae for signal-to-noise are designed in such a way that results in optimization of quality characteristic variation due to uncontrollable parameter. Therefore, the method of calculating the signal-to-noise ratio depends on whether the quality characteristic has smaller-the-best, larger the- better or nominal-the-better formulation [16].

The metal removal rate was considered as the quality characteristic with the concept of "the larger-the-better" and Kerf with the concept of "the smaller-the-better". The S/N ratios for "the larger the better" and "the smaller-the-better" are calculated as per equation (1) and equation (2) respectively [17].

$$\text{S/N Ratio } \eta = -10 \text{ Log10 } (1/n \, \Sigma \, 1/Y_i^2) \qquad (1)$$

$$\text{S/N Ratio } \eta = -10 \text{ Log10 } (1/n \, \Sigma \, Y_i^2) \qquad (2)$$

Where n = no of measurements in a Trail and Yi = Ith value in a run/row.

Table 3. Experimental Design Matrix and Results

SNo	Pressure (kg/cm^2)	SOD (mm)	Nozzle dia. (mm)	MRR (g/sec)	PSNRA1	Kerf (mm)	PSNRA2
1	6	7	2	0.018580	-32.9273	6	-14.2373
2	6	8	3	0.041790	-28.4974	3.5	-10.9980
3	6	9	4	0.073560	-23.4401	3	-10.7515
4	7	7	3	0.041890	-28.3307	5	-15.1884
5	7	8	4	0.055800	-23.3755	4	-10.7155
6	7	9	2	0.064600	-24.7142	2.5	-08.0755
7	8	7	4	0.077530	-23.1295	5	-14.0961
8	8	8	2	0.064585	-24.5703	2	-7.2296
9	8	9	3	0.081940	-20.0383	3	-8.2167

The results of MRR and Kerf values of the 9 experiments with S/N ratios are given in Table 3. The maximum material removal rate i.e.; MRR observed is 0.081940 gm/s which is at pressure 8 kg/cm^2, SOD 9 mm and 3 mm nozzle diameter. The lowest kerf value is 2 mm which is at pressure 8 kg/cm^2, SOD 8mm and 2 mm nozzle diameter.

Table 4 shows Taguchi Analysis Response Table for Signal to Noise Ratios for MRR (Larger is better). Here the pressure is most dominating factor i.e. has large effect on MRR. Nozzle diameter has the smallest effect on the material removal rate. Figure 3 shows the effect of parameters on Mean of S/N ratio (left side) & Mean of Means of MRR. The increase in pressure causes an increase in the MRR. This may happen because with an increase in the pressure there is an increase in the kinetic energy of the abrasive particles coming out of the nozzle. Similar kinds of results were reported by the earlier researchers. [18-20]

Table 4. Response table for signal to noise ratio for MRR (Larger is better)

Level	Pressure (kg/cm^2)	SOD (mm)	Nozzle dia. (mm)
1	-28.29	-28.13	-27.40
2	-25.47	-25.48	-25.62
3	-22.58	-22.73	-23.32
Delta	5.71	5.4	4.09
Rank	1	2	3

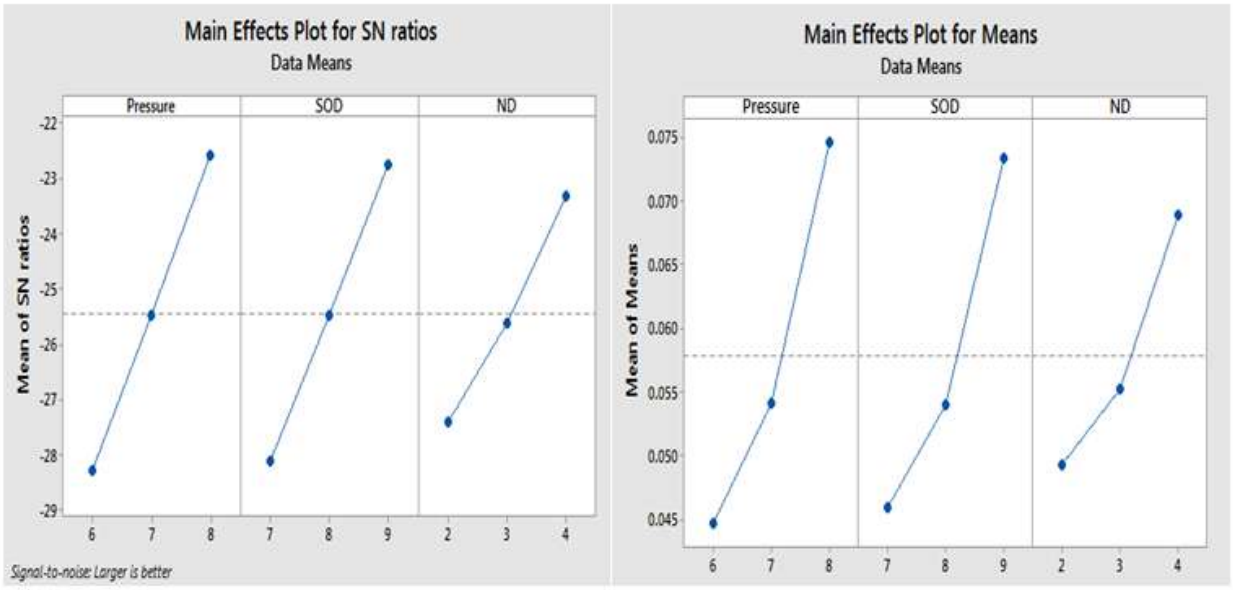

Figure 3: Effect of Parameters on Mean of S/N ratio (left side) & Mean of Means of MRR (right side)

Taguchi Analysis Response Table for Signal to Noise Ratios for Kerf (Smaller is better) is shown in Table 5. Here the Standoff distance (SOD) is most dominating factor i.e. has large effect and Nozzle diameter has the smallest effect on Kerf.

3.2 Validation for Optimization Using ANOVA

Though Taguchi Method is used in reducing the number of experiments, the effect of individual parameter on entire process is not effectively rated. By using ANONA the influence of individual parameters on process characteristics can be well determined [22]. Hence to determine the contribution of individual parameters on MRR and Kerf and to detect any differences in average performances of tested parameters, a general linear model of ANOVA was employed. The software used for executing the validation is Minitab 17. The optimized values produced in Taguchi are validated by using ANOVA. Table 6 shows the general linear model for MRR and Kerf versus parameters.

Table 5. Response table for signal to noise ratio for Kerf (Smaller is better)

Level	Pressure (kg/cm^2)	SOD (mm)	Nozzle dia. (mm)
1	-11.996	-14.507	-9.847
2	-11.326	-9.648	-11.468
3	-9.847	-9.015	-11.854
Delta	2.148	5.493	2.007
Rank	2	1	3

Table 6. General linear model: MRR and Kerf vs. Pressure, SOD, Nozzle Diameter

Factor	Type	Levels	Values
Pressure	Fixed	3	6,7,8
SOD	Fixed	3	7,8,9
ND	Fixed	3	2,3,4

Table 7. Analysis of variance for MRR using ADJSS for TESTS

Source	DF	Adj SS	Adj MS	F-Value	P-Value
Pressure	2	0.001416	0.000708	9.51	0.095
SOD	2	0.001187	0.000593	7.97	0.111
ND	2	0.000613	0.000307	4.12	0.195
Error	2	0.000149	0.000074		
Total	8	0.003364			

S =0.0086257 R-sq=95.58%; R-sq(adj) =82.31%

Table 8. Analysis of variance for Kerf using ADJSS for TESTS

Source	DF	Adj SS	Adj MS	F-Value	P-Value
Pressure	2	1.0556	0.5278	0.68	0.596
SOD	2	11.0556	5.5278	7.11	0.123
ND	2	0.3889	0.1944	0.25	0.800
Error	2	1.5556	0.7778		
Total	8	14.0556			

S =0.881917 R-sq=90.93% R-sq(adj) =55.73%

Table 7 shows Analysis of Variance for MRR. F Value (9.51) of the parameter indicates the Air Pressure is significantly contributing more towards cutting performance. F value (4.12) of parameter indicates the contribution of Nozzle diameter is less.
Table 8 shows Analysis of Variance for Kerf. F Value (7.11) of the parameter indicates that SOD is significantly contributing more towards cutting performance. F value (0.25) of parameter indicates the contribution of Nozzle diameter is less.

IV. Conclusions

This paper discussed the influence of process parameters on machining characteristics of hastelloy. Taguchi optimization and ANOVA techniques were employed for this purpose. The process parameters chosen were Nozzle pressure, SOD and Nozzle diameter and AJM performance was measured in terms of MRR and Kerf.
From the Taguchi technique the following conclusions were drawn:

- The pressure has largest effect and Nozzle diameter has the smallest effect on the material removal rate.
- The maximum material removal rate is occurred at pressure 8 kg/cm^2, SOD 9 mm and 3 mm nozzle diameter.
- The Standoff distance (SOD) has large effect and Nozzle diameter has the least effect on Kerf.
- The lowest kerf value is observed at pressure 8 kg/cm^2, SOD 8mm and 2 mm nozzle diameter.

From ANOVA the following conclusions were drawn.

- The Air Pressure is significantly contributing more towards cutting performance and nozzle diameter has least contribution on MRR.
- SOD is significantly contributing more towards cutting performance and nozzle diameter has least contribution on Kerf.

From the above it is concluded that both Taguchi method and ANOVA techniques drew similar results.

Acknowledgements

The authors would like to thank the Department of Mechanical Engg., St.Martin College of Engg. & Tech., Hyderabad for their support and permitting to utilize the test facilities.

References

[1] Marinov, V. Manufacturing process design (2012). (pp. 129– 148). Kendall/Hunt. Retrieved , from http:// www.amazon.com July 17, 2015

[2] Jagadeesha, T. (2015). Non traditional machining. Mechanical Engineering Department, National Institute of Technology, Calicut. Retrieved July 22, 2015, from http:// www.nitc.ac.in

[3] Ghobeity, A H. Getu, M. Papini and J. K. Spelt. Surface evolution models for abrasive jet micromachining. Elsevier Wear, Feb. 2008. Vol. 264; pp.185–198,.

[4] D. S. Park, M. W. Cho, H. Lee and W. S. Cho. Micro-grooving of glass using micro-abrasive jet machining. Journal of Materials Processing Technology, 2004. Vol. 146; pp. 234–240

[5] M. Wakuda , Y. Yamauchi and S. Kanzaki. Effect of workpiece properties on machinability in abrasive jet machining of ceramic materials. Precision Engineering Journal of the International Societies for Precision Engineering and Nanotechnology, 2002.Vol. 26; pp.193-198

[6] V. C. Venkatesh, T. N. Goh, K. H. Wong and M. J. Lim. An empirical study of parameters in abrasive jet machining. Int. J Mach Tools and Manufacturing, 1989. Vol.29; No.4, pp.471-479

[7] R. Balasubramaniama, J. Krishnan, and N. Ramakrishnan. An experimental study on the abrasive jet deburring of cross-drilled holes. Journal of Materials Processing Technology, 1999. Vol. 91; pp. 178–182

[8] D.V. Srikanth and M. SreenivasaRao. Metal removal and kerf analysis in abrasive jet drilling of glass sheets. Procedia Materials Science, 2014. Vol. 6; pp. 1303–1311.

[9] N. Jagannatha, S.S. Hiremath and K. Sadashivappa. Analysis and parametric optimization of abrasive hot air jet machining for glass using taguchi method and utility concept. International Journal of Mechanical and Materials Engineering (IJMME), 2012. Vol. 7, No. 1; pp. 9–15

[10] R. Balasubramaniam, J. Krishnan and N. Ramakrishnan. An empirical study on the generation of an edge radius in abrasive jet external deburring (AJED). Journal of Materials Processing Technology, 2000. Vol. 99; pp. 49-53

[11] M. Wakuda , Y. Yamauchi and S. Kanzaki. Material response to particle impact during abrasive jet machining of alumina ceramics. Journal of Materials Processing Technology, Jan' 2003. Vol.132; pp. 177-183

[12] J. M. Fan, C. Y. Wang, J. Wang. Modeling the erosion rate in micro abrasive air jet machining of glasses. Wear, 2009. Vol. 266; pp. 968-974

[13] K. Abhishek and S.S. Hiremath. Improvement of geometrical accuracy of micro holes machined through micro abrasive jet machining. Procedia CIRP, 2016. Vol. 46; pp. 47-50

[14] H. Getu, A. Ghobeity, J.K. Spelt and M. Papini. Abrasive jet micromachining of acrylic and polycarbonate polymers at oblique angles of attack. Wear, March. 2008. Vol. 265; pp. 888–901

[15] S. Ally, J.K. Spelt and M. Papini. Prediction of machined surface evolution in the abrasive jet micro-machining of metals. Wear, June. 2012.Vol. 292–293; pp. 89–99

[16] N. Muthukrishnana, J.P.D. Optimization of machining parameters of Al/Sic-MMC with ANOVA and ANN analysis. Journal of materials processing technology, 2009. Vol 209; p. 225-232

[17] Taguchi G, Hocheng, Taguchi methods of orthogonal arrays and linear graphs, tools for quality engineering, (Dearborn, MI: American Supplier Institute, 1987, 35–38)

[18] Jukti Prasad Padhy. Optimization and effect of controlling parameters on AJM using Taguchi technique. Int. Journal of Engineering Research and Applications, 2014. Vol. 4, Issue 3 (Version 1), pp.598-604

[19] Rajeev Kumar[a] , Gurdeep Singh Deol[b], C. S. Kalrac, Vijay Kr Sharmad. Analysis on Performance of Different Parameters during Abrasive Jet Machining by Taguchi Method. International Journal of Emerging Research in Management &Technology, Aug'2014. (Volume-3, Issue-8); pp.35-41

[20] Mr. Bhaskar Chandra. A Study of effects of Process Parameters of Abrasive jet machining. International Journal of Engineering Science and Technology, Jan' 2011.vol.3; pp.504-513

[21] Roy, R.K. Design of experiments using the Taguchi approach: 16 steps to product and process improvement. John Wiley & science, New York, 2001

International Journal of Engineering Science Invention (IJESI) is UGC approved Journal with Sl. No. 3822, Journal no. 43302.

Prerna Ramagiri Optimization of Process Parameters in Abrasive Jet Drilling Of Hastelloy Using Taguchi Method." International Journal of Engineering Science Invention(IJESI), vol. 6, no. 11, 2017, pp. 50-55.

International Journal of Power Electronics Controllers and Converters
eISSN: 2456-1614
Vol. 3: Issue 2
www.journalspub.com

Multifunctional Shunt Hybrid Power Filter and Thyristor Controlled Reactor for Distributed Generation Integration and Power Quality Improvement

*Sandeepthi Nandhyala[1], A.N.V.J. Rajagopal[1], *R.C. Garimella[2]*
1Department of EEE, BVC Institute of Technology and Science, Batlapalem, Amalapuram, AP, India
2Department of EEE, Madanapalle Institute of Technology and Science, Angallu, Chittoor District, India

ABSTRACT

This project presents a multifunctional PV fed SHPF-TCR compensator for achieving maximum benefits from these grid-interfacing inverters. The inverter is controlled to perform as a multi-function device by incorporating active power filter functionality. An inverter can be used as power converter to insert the power created from RES to the grid, and shunt APF to reimburse load current harmonics. A SHPF-TCR compensator of a TCR and a SHPF has been proposed to achieve harmonic elimination. A proposed nonlinear control scheme of a SHPF-TCR compensator has been established and simulated. The shunt active filter and SPF have a complementary function to advance the performance of filtering and to diminish the power rating supplies of an active filter. It has been found that the SHPF-TCR compensator can effectively eliminate current harmonic and reactive power compensation during steady and transient operating conditions for a variety of loads. It has been shown that the system has a fast dynamic response, has good performance in both steady-state and transient operations, and is able to reduce the THD of supply currents well below the limit of 5% of the IEEE-519 standard.

Keywords: *Dynamic response, harmonics, power, thyristor*

Corresponding Author
***E-mail**: raghuchandhra@gmail.com*

INTRODUCTION

Electrical energy is the most efficient and popular form of energy and the modern society is heavily dependent on the electric supply. The life cannot be imagined without the supply of electricity. At the same time the quality of the electric power supplied is also very important for the efficient functioning of the end user equipment.

The term power quality became most noticeable in the power sector and both the electric power supply company and the end users are fretful about it. The quality of power delivered to the consumers depends on the voltage and frequency ranges of the power. If there is any deviance in the frequency and voltage of the electric power delivered from that of the standard values then the quality of power delivered is affected [1].

Now-a-days with the advancement in technology there is a drastic improvement in the semi-conductor devices. With this development and advantages, the semi-conductor devices got a permanent place in the power sector helping to ease the control of overall system. Moreover, most of the loads are also semi-conductor based equipment. But the semi-conductor devices are non-linear in nature and draws non-linear current from the source. And also, the semiconductor devices are involved in power conversion, which is either AC to DC or from DC to AC [2]. This power conversion contains lot of switching operations which may introduce discontinuity in the current. Due to this non-linearity and discontinuity, harmonics

exists which affect the quality of power delivered to the end user. In order to maintain the quality of power delivered, the harmonics should be filtered out. Thus, a device named filter is used which serves this purpose.

There are several filter topologies in the literature like- passive, active and hybrid. In this project the use of shunt hybrid power filters and thyristor controlled reactor for the improvement of electric power quality is studied and analyzed [3–5].

Non-linear loads cause significant harmonic currents with poor input power factor, which creates serious problems at the power supply system.

Traditionally, passive filters have been used to eliminate current harmonics of the supply network. However, these devices suffer from resonance. Recently, thyristor-switched filters (TSFs), which contain several groups of passive filters, have been used to compensate reactive power. The compensation amount of TSFs can be adjusted with the variation of load power. However, the parallel and the series resonance could occur between TSF and grid impedance. Active filters were developed to mitigate problems of passive filters. They are more effective in harmonic compensation and have good performance [6, 7].

However, the costs of active filters are relatively high for large-scale system and require high power converter ratings. Hybrid filters efficiently soften the problems of the passive filter and an active filter solution and provide profitable harmonic compensation, mainly for high-power nonlinear [8]. Many control techniques such as instantaneous reactive power theory, synchronous rotating reference frame, sliding-mode controllers, neural network techniques, nonlinear control feed forward control lyapunov function-based control, etc. have been used to improve the performance of the active and hybrid filters [9]. Several filter topologies for compensating harmonics and reactive power have been reported in the literature in a multi-converter conditioner topology formed by an active conditioner operating in parallel with a hybrid conditioner has been proposed. The hybrid conditioner consists of one or more passive filters in series with a low-rated active power filter (APF). The conditioner compensates harmonic distortion, imbalance, and reactive power in three-phase four-wire systems [10]. This topology constitutes an effective solution at high-power levels, which is cost-effective because of the kilovolt-ampere rating reduction of the inverters [11].

A hybrid configuration based on the combination of a three-phase three-level neutral point clamped (NPC) inverter and a series connection of a three-level H-bridge inverter with a novel control scheme to control the floating voltage source of the H-bridge stage has been presented [12]. In this topology, the NPC inverter is used to supply the total active power while the H-bridges operate as series active filters for the harmonic compensation of the NPC output voltage. The rating of the series active filter is reduced because the latter provides only the reactive power for the operation of the floating capacitor. In a combination of a resonant impedance-type hybrid APF and a thyristor-controlled reactor (TCR) for harmonic cancellation, reactive power compensation, and load balancing has been proposed. The control strategy of the system is based on the voltage vector transformation for compensating the negative-sequence current caused by the unbalance load without using phase-locked loops [13, 14]. A predictive current controller based on Smith predictor is suggested to compensate the widespread current delay. A combined system of a static var compensator (SVC) and a small-rated APF for harmonic suppression and reactive power compensation have been reported in ref. [15]. The SVC consists of a Y-connected passive power filter and a delta-connected TCR.

The APF is used to eliminate harmonic currents and to avoid resonance between

the passive power filters and the grid impedance.

System Description

In this project, a new combination of a shunt hybrid power filter (SHPF) and a TCR (SHPF-TCR compensator) is proposed to suppress current harmonics and compensate the reactive power generated from the load. The hybrid filter consists of a series connection of a small-rated active filter and a fifth-tuned LC passive filter. In the proposed topology, the major part of the compensation is supported by the passive filter and the TCR while the APF is meant to improve the filtering characteristics and damps the resonance, which can occur between the passive filter, the TCR, and the source impedance. The shunt APF when used alone suffers from the high kilovolt-ampere rating of the inverter, which requires a lot of energy stored at high dc-link voltage. On the other hand, as published by some authors, the standard hybrid power filter is unable to compensate the reactive power because of the behavior of the passive filter. Hence, the proposed combination of SHPF and TCR compensates for unwanted reactive power and harmonic currents [16].

In addition, SHPF-TCR reduces significantly the volt-ampere rating of the APF part. The control method of the combined compensator is presented. A control technique is proposed to improve the dynamic response and decrease the steady-state error of the TCR. It consists of a PI controller and a lookup table to extract the required firing angle to compensate a reactive power consumed by the load. A nonlinear control of SHPF is developed for current tracking and voltage regulation purposes. It is based on a decoupled control strategy, which considers that the controlled system may be divided into an inner fast loop and an outer slow one. The currents injected by the SHPF are controlled in the synchronous orthogonal dq frame using a decoupled feedback linearization control method. The dc bus voltage is regulated using an output feedback linearization control. The SHPF can maintain the low level of dc bus voltage at a stable value below 50 V. The proposed nonlinear control scheme has been simulated and validated experimentally to compute the performance of the proposed SHPF-TCR compensator with harmonic and reactive power compensation and analysis through the total harmonic distortion (THD) of the source and the load current [17]. The proposed methodology is tested for a wide range of loads as discussed further.

Simulation and experimental results show that the proposed topology is suitable for harmonic suppression and reactive compensation of a three-phase full-bridge voltage-source pulse width modulation (PWM) inverter with an input boost inductor (Lpf, Rpf) and a dc bus capacitor (Cdc). The APF sustains very low fundamental voltages and currents of the power grid, and thus, its rated capacity is greatly reduced. Because of these merits, the presented combined topology is very appropriate in compensating reactive power and eliminating harmonic currents in power system. The modified passive filter in parallel with TCR forms a shunt passive filter (SPF). This latter is generally for fifth harmonic compensation and PF correction. The small-rating APF is used to filter harmonics generated by the load and the TCR by enhancing the compensation characteristics of the SPF aside from eliminating the risk of resonance between the grid and the SPF. The TCR goal is to obtain a regulation of reactor power [18]. The set of the load is a combination of a three-phase diode rectifier and a three-phase star connected resistive inductive linear load.

PROPOSED SYSTEM

Here in this project, we developed a new combination of a TCR (SHPF-TCR compensator) and a shunt hybrid power filter (SHPF) is projected to suppress the current harmonics and to compensate the generated reactive power from the load. The hybrid filter consists of a series connection of a small-rated active filter

and a fifth-tuned *LC* passive filter. In the proposed topology, the major part of the compensation is supported by the passive filter and the TCR while the APF is meant to improve the filtering characteristics and damps the resonance, which can occur between the passive filter, the TCR, and the source impedance. The shunt APF when used alone suffers from the high kilovolt ampere rating of the inverter, which requires a lot of energy stored at high dc-link voltage. On the other hand, as published by some authors [15], the standard hybrid power filter is unable to compensate the reactive power because of the behavior of the passive filter. Hence, the proposed combination of SHPF and TCR compensates for unwanted reactive power and harmonic currents (Figure 1). In addition, it reduces significantly the volt ampere rating of the APF part. The control method of the combined compensator is presented. A control technique is proposed to improve the dynamic response and decrease the steady-state error of the TCR (Figure 2). It consists of a PI controller and a lookup table to extract the required firing angle to compensate a reactive power consumed by the load. A nonlinear control of SHPF is developed for current tracking and voltage regulation purposes. It is based on a decoupled control strategy, which considers that the controlled system may be divided into an inner fast loop and an outer slow one. The currents injected by the SHPF are controlled in the synchronous orthogonal *dq* frame using a decoupled feedback linearization control method. The dc bus voltage is regulated using an output feedback linearization control. The SHPF can maintain the low level of dc bus voltage at a stable value below 50 V. The proposed nonlinear control scheme has been simulated and validated experimentally to compute the performance of the proposed SHPF-TCR compensator with harmonic and reactive power compensation and analysis through the total harmonic distortion (THD) of the source and the load current. The proposed methodology is tested for a wide range of loads as discussed further. Simulation and experimental results show that the proposed topology is suitable for harmonic suppression and reactive compensation.

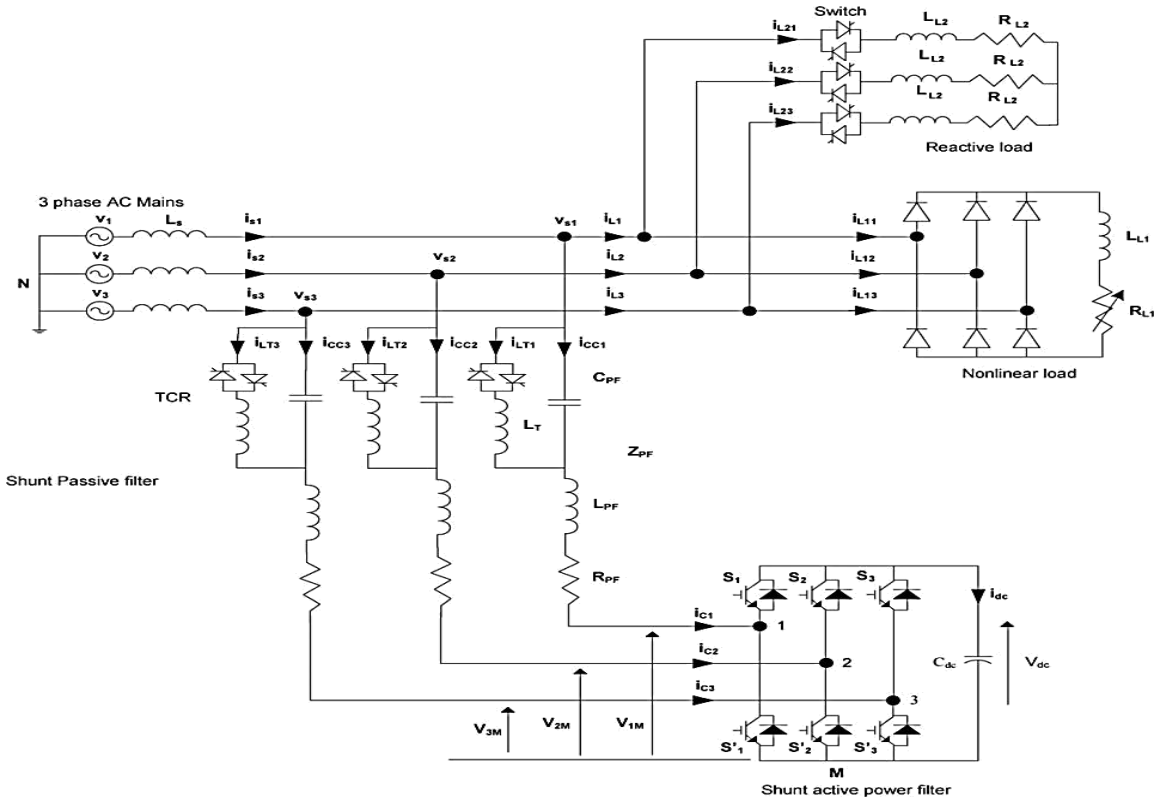

Fig. 1. *Basic circuit of the proposed SHPF-TCR compensator.*

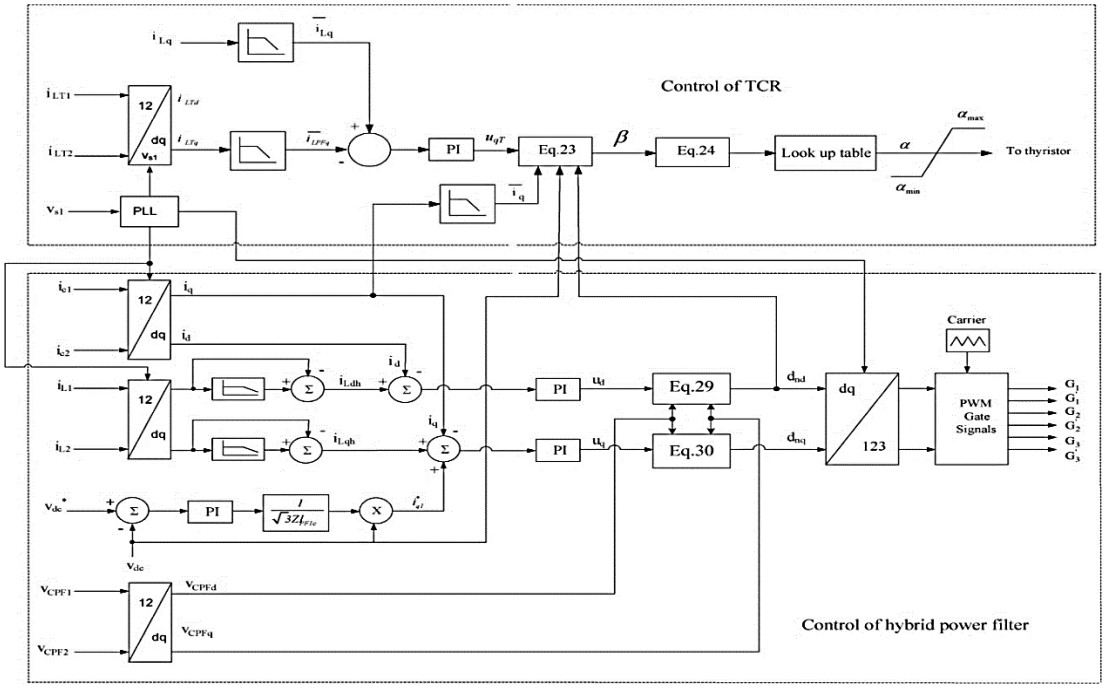

Fig. 2. *Control scheme of the proposed SHPF-TCR compensator.*

SIMULATION RESULTS

The total circuit configuration is simulated using MATLAB 2012a and it is analyzed in power graphical user interfacing environment and the total harmonic distortion is calculated by the use of the fast Fourier transformation technique. In POWERGUI, the following result represents the combined system of a thyristor-controlled reactor (TCR) and a shunt hybrid power filter (SHPF) for harmonic and reactive power compensation. The proposed device is tested under different case scenarios using MATLAB/Simulink to evaluate its capability to improve the PQ and reliability of the distribution network. A proportional–integral controller was used, and a triggering alpha was extracted using a lookup table to control the TCR. A nonlinear control of APF was developed for current tracking and voltage regulation. The following tabular form represents the different electrical parameters of the source, transmission and load end (Table 1).

Table 1. *Parameters used in simulation.*

Line to Line source voltage, and frequency	$V_{s\text{-}L\text{-}L}$=208 V, f_s=60 Hz
Line impedance	L_s=0.5 mH, R_s=0.1 Ω
Non linear load	L_{L1}=10 mH, R_{L1}=27 Ω,
Linear load	L_{L2}=20 mH, R_{L2}=27 Ω
Passive filter parameters	L_{pf}= 1.2 mH, C_{pf}=240 μF
Active filter parameters	C_{dc}=3000 μF , R_{dc}=1k Ω
DC bus voltage of APF of SHAF	V_{dc}=50 V
Switching frequency	1920 Hz
Inner controller parameters	K_{p1}= K_{p2}=43.38 ; K_{i1}= K_{i2}=37408
Outer controller parameters	K_1=0.26 ; K_2=42
Cut off frequency of the low pass filters	F_c=70 Hz
TCR inductance	L_T= 25 mH

Figure 3 represents the circuit configuration of the general circuit without shunt hybrid power filter and thyristor-controlled reactor in steady state condition and (Figures 4 and 5) represents the complete MATLAB-based results in POWERGUI environment.

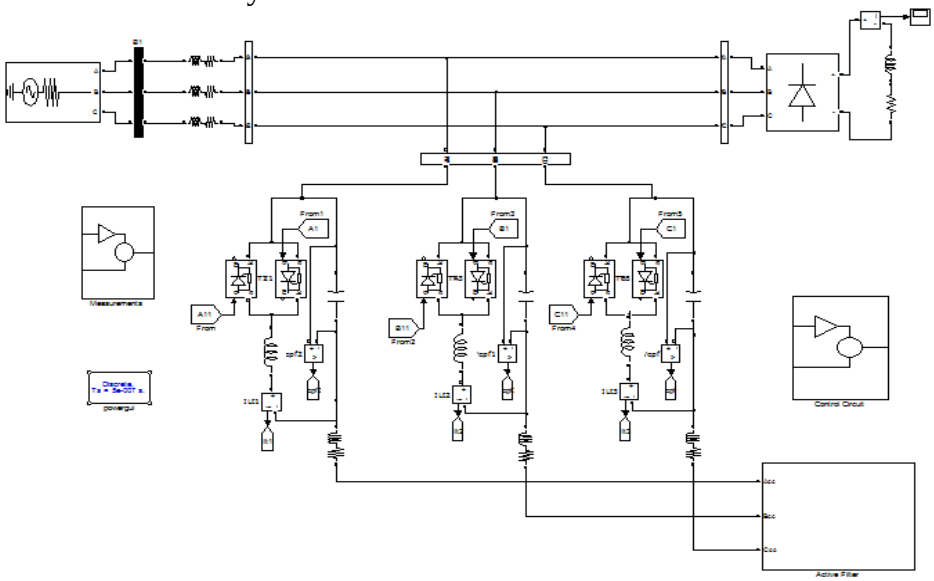

Fig. 3. *A combination of shunt hybrid power filter and thyristor-controlled reactor under normal load.*

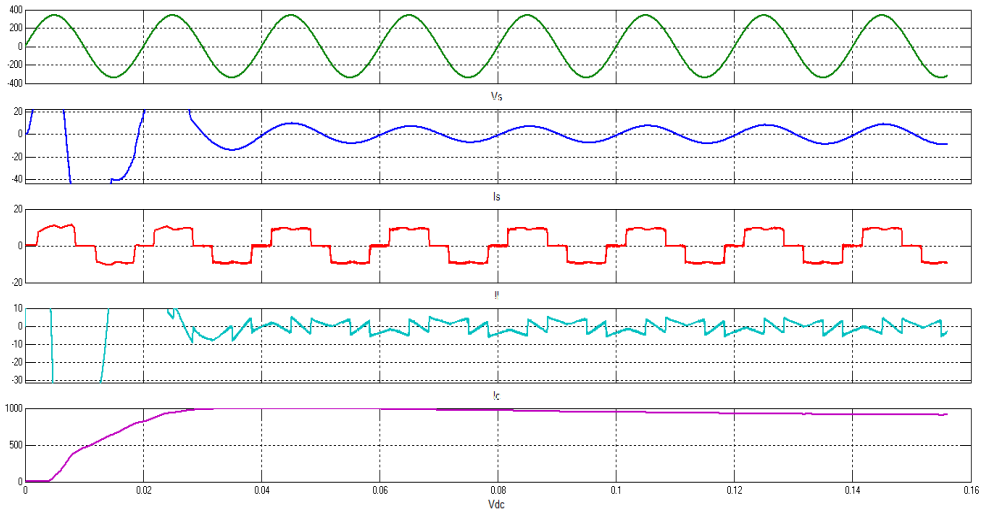

Fig. 4. *Wave form representation of a combination of shunt hybrid power filter and thyristor-controlled reactor under normal load.*

V(S)V the above waveform represent voltage at source side with represent time in Matlab software it shows no change in voltage at source because we are applied constant load so constant power required to drain load so that constant voltage will be applied from the source side.

I(S)A the waveform represents current source side and it all constant because constant load applied and steady-state configuration so the constant current from source.

I(L)A the above waveform represents load current with represent time and fast wave

from constant of load of harmonic it all constant because load is not in change under steady state constant.

I(C)A the above waveform represents capacitor charge with represent time and load current from steady state constant so that APF state charging and discharging that represent.

Vdc(V) Vdc voltage with represent time and steady-state constant from the perform load constant.

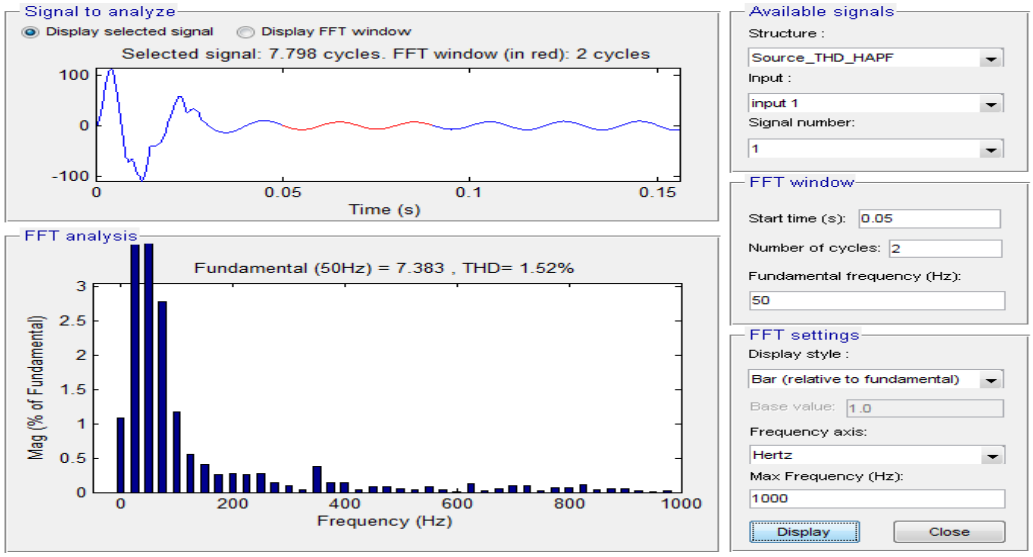

Fig. 5. *Harmonic order a combination of shunt hybrid power filter and thyristor-controlled reactor under normal load.*

Figure 6 represents the circuit configuration of the combination of shunt hybrid power filter and thyristor-controlled reactor in dynamic state condition and Figures 7 and 8 represent the complete MATLAB based results in POWERGUI environment.

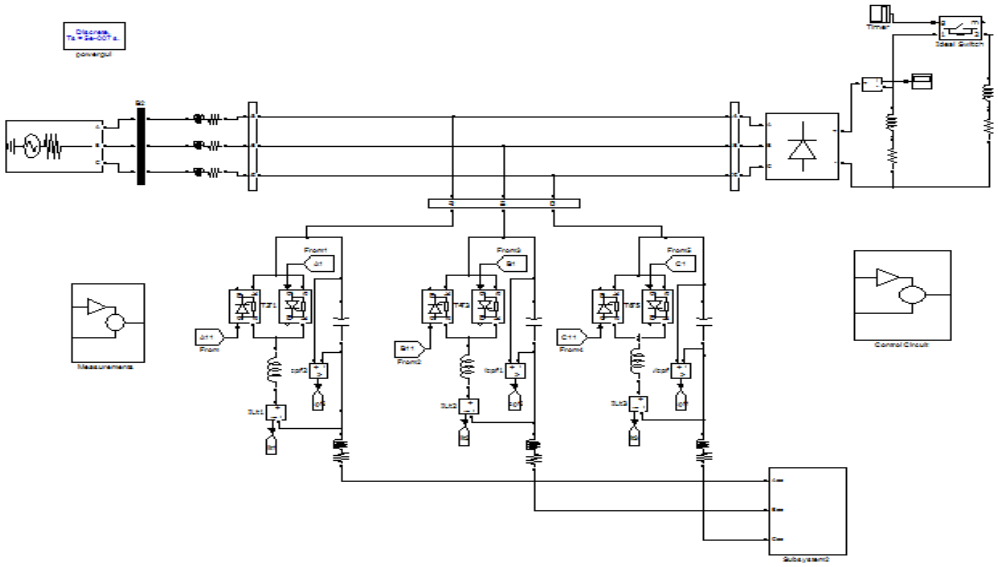

Fig. 6. *Circuit configuration of a combination of shunt hybrid power filter and thyristor-controlled reactor under sudden load (variation at DC load).*

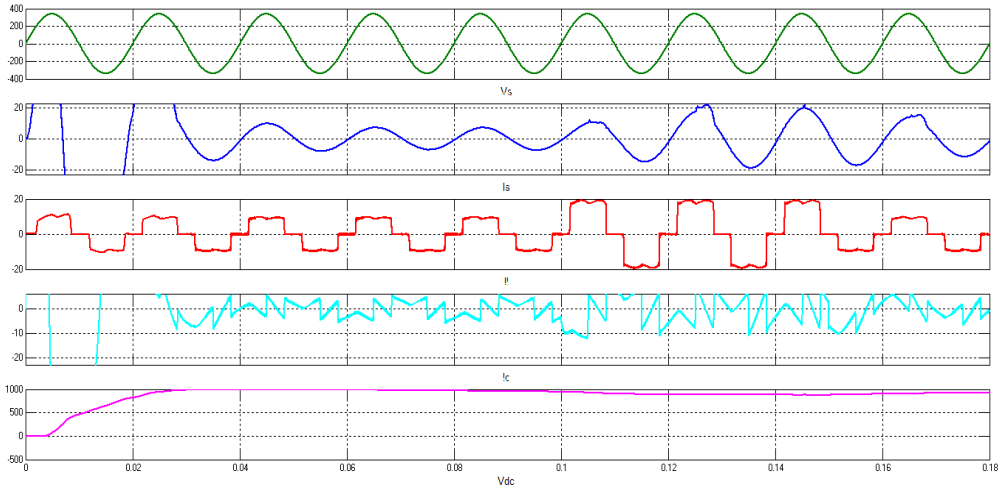

Fig. 7. *MATLAB-based waveforms of a combination of shunt hybrid power filter and thyristor-controlled reactor under sudden load (variation at DC load).*

V(S)V the above waveform represents voltage at source side with represent time in MATLAB software it shows no change in voltage at source because we are applied constant load so constant power required to drain load so that constant voltage will be applied from the source side.

I(S)A the waveform represents current source side and it all constant because constant load applied and Dynamic response configuration so the constant current from source.

I(L)A the above waveform represents load current with represent time and fast wave from constant of load of harmonic it all constant because load is not in change under Dynamic response constant.

I(C)A the above waveform represents capacitor charge with represent time and load current from dynamic response constant so that APF state charging and discharging that represent.

Vdc (V) voltage with represent time and Dynamic response constant from the perform load constant.

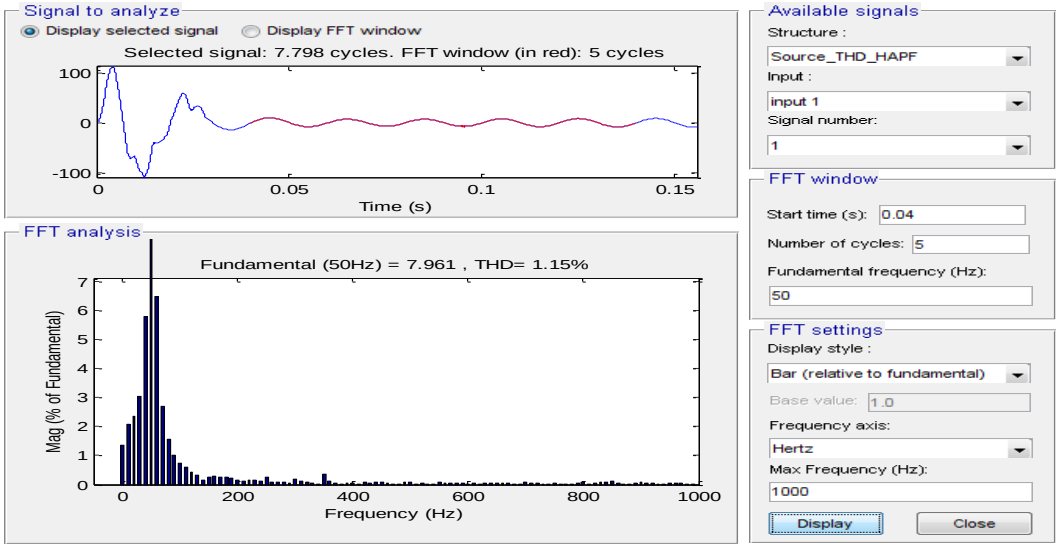

Fig. 8. *Harmonic order a combination of shunt hybrid power filter and thyristor-controlled reactor under sudden load (variation at DC load).*

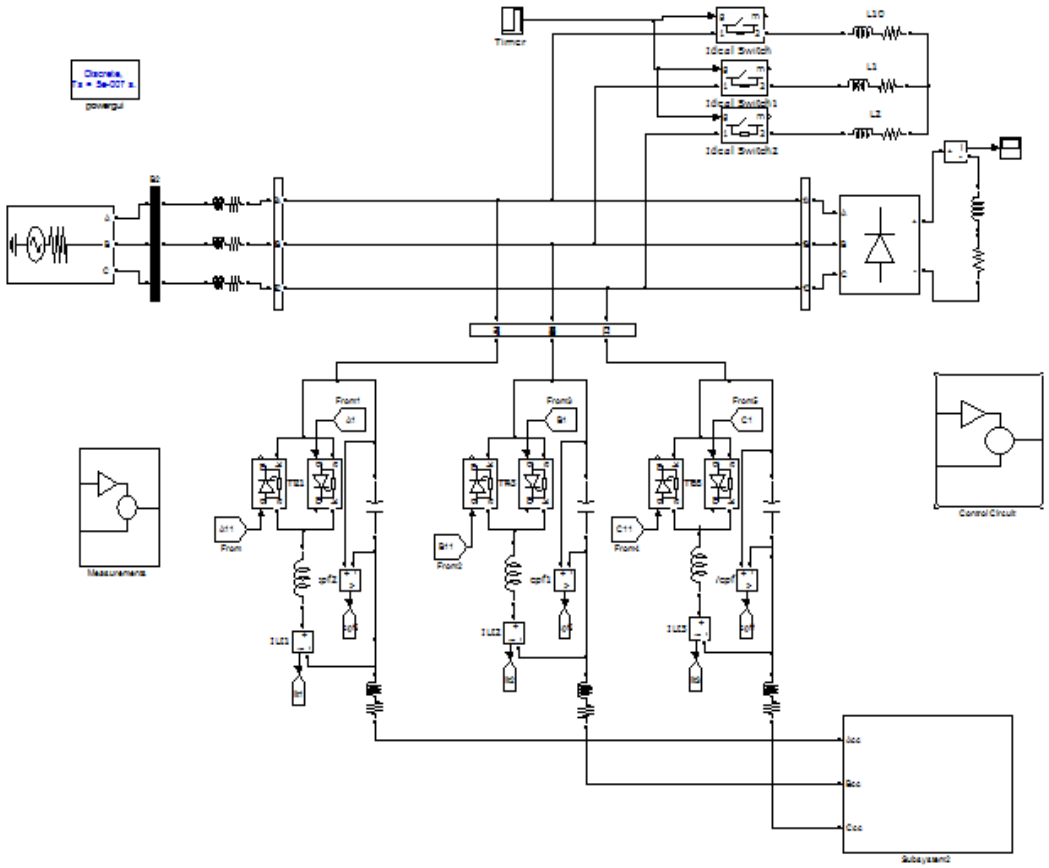

Fig. 9 *Circuit configuration of a combination of Shunt Hybrid Power Filter and Thyristor-Controlled Reactor with reactive load*

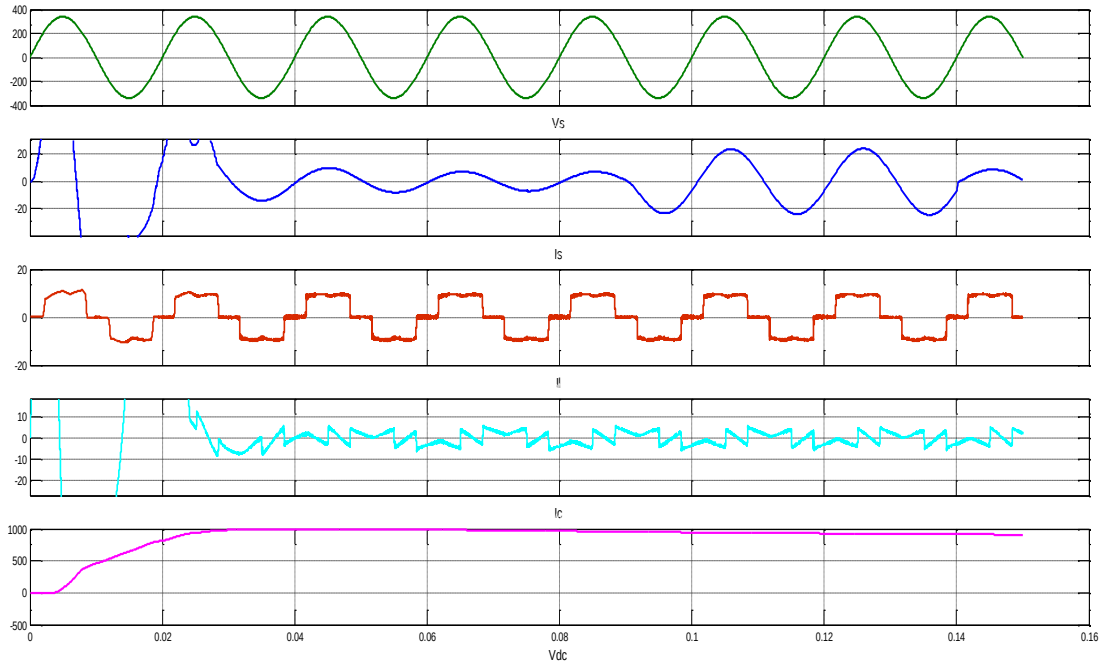

Fig. 10 *MATLAB based waveforms of A Combination of Shunt Hybrid Power Filter and Thyristor-Controlled Reactor with reactive load*

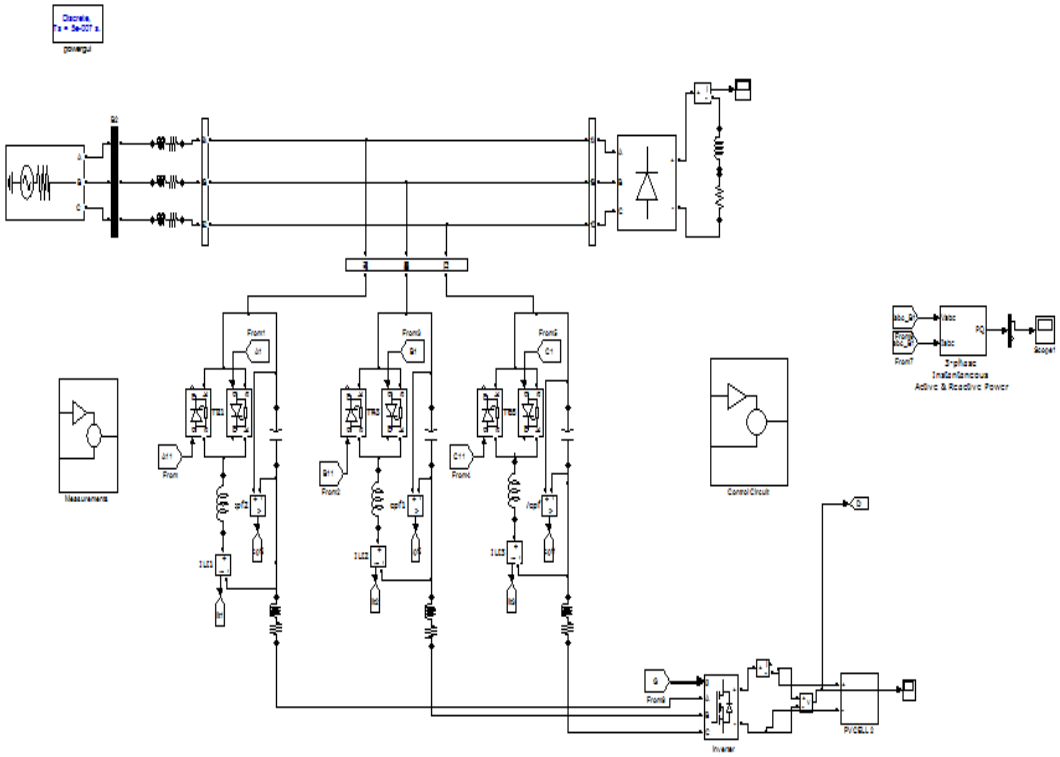

Fig. 11 *Circuit Configuration of PV fed Combined Shunt Hybrid Power Filter and Thyristor-Controlled Reactor with reactive load*

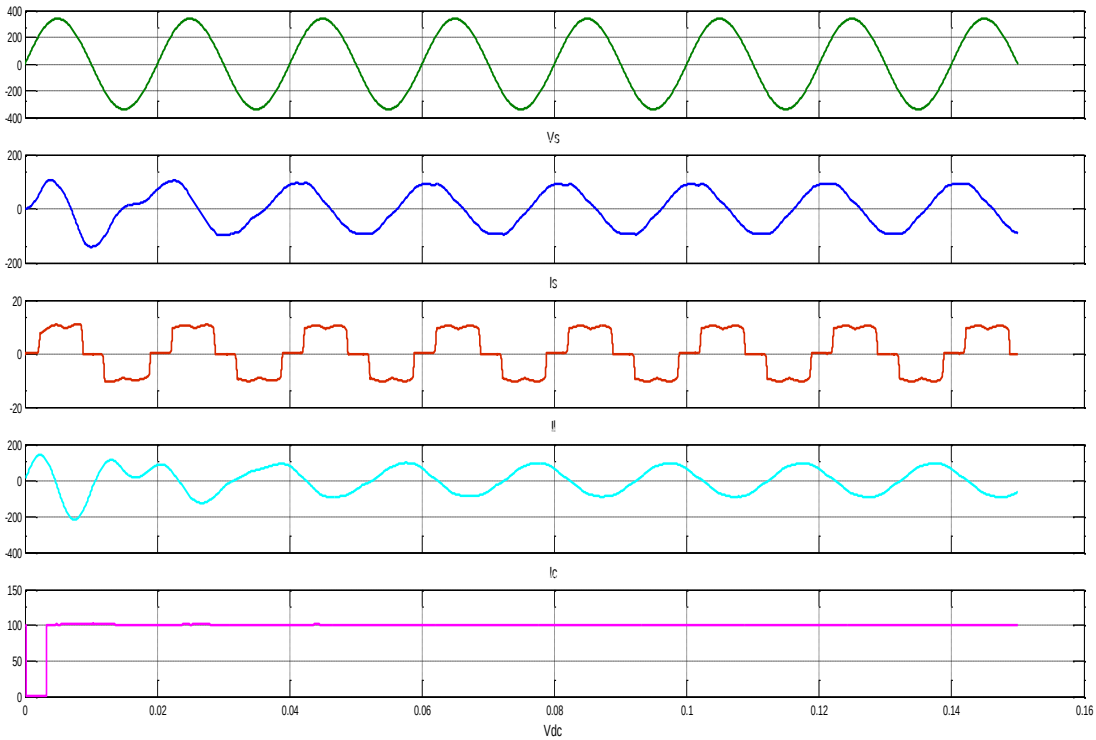

Fig. 12 *MATLAB based waveforms of PV fed Combined Shunt Hybrid Power Filter and Thyristor-Controlled Reactor with reactive load*

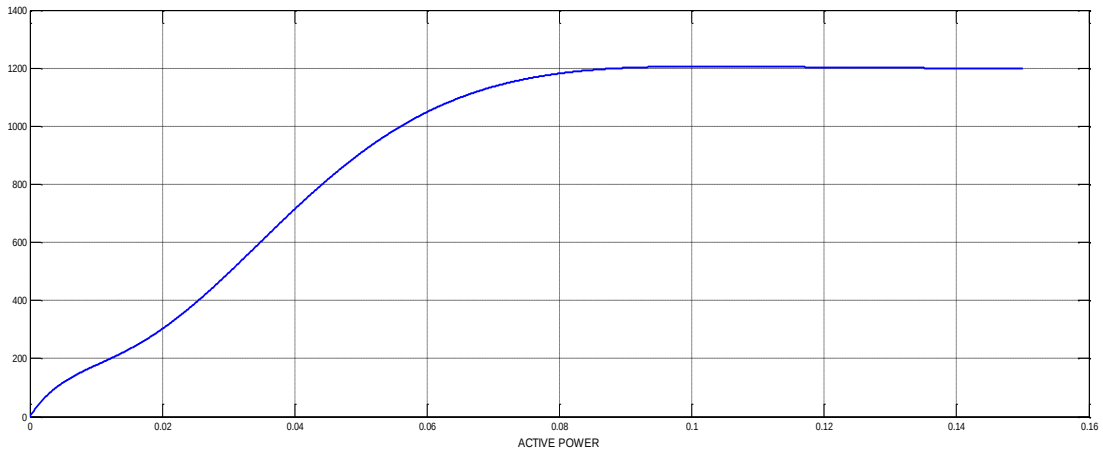

Fig. 13 *Instantaneous power injected from PV to grid*

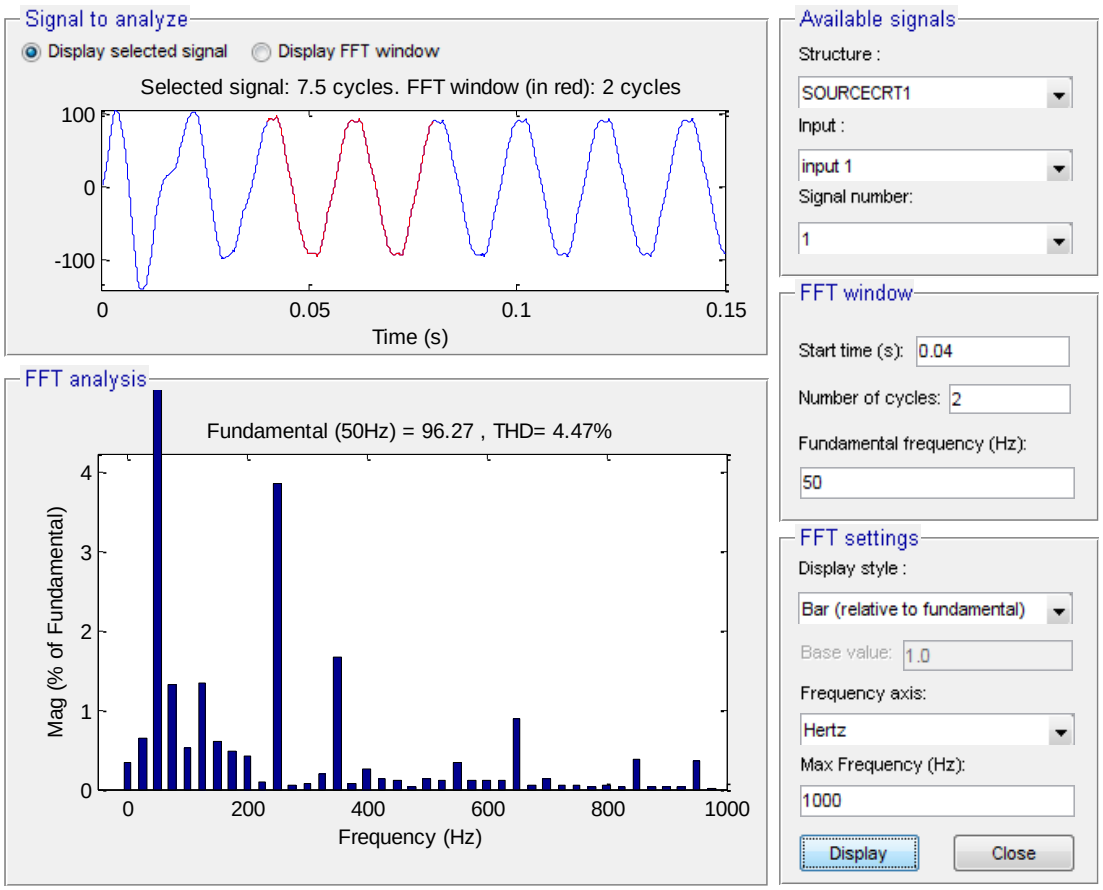

Fig. 14 *Harmonic order PV Fed Combined of Shunt Hybrid Power Filter and Thyristor-Controlled Reactor*

CONCLUSION

In this paper, an SHPF-TCR compensator of a TCR and an SHPF has been proposed to achieve harmonic elimination and PV Fed SHPF-TCR compensator is also proposed. It has been shown that the grid-interfacing inverter can be efficiently consumed for power conditioning without affecting its normal operation of real power transfer. A proposed nonlinear control scheme of an SHPF-TCR compensator has been established and simulated. It has been found that the SHPF-TCR compensator can effectually

eliminate current harmonic and reactive power compensation during both the steady as well as in the transient operating conditions for a variety of loads. It has been shown that the system has a fast-dynamic response, has good performance in both steady-state and dynamic operations. The simulation results obtained in this work and the current analysis serve as a fundamental step towards the design of control circuits for hardware implementation of the device in the future. In this paper, an SHPF-TCR compensator of a TCR and an SHPF has been proposed to achieve harmonic elimination and PV Fed SHPF-TCR compensator is also proposed. It has been shown that the grid-interfacing inverter can be efficiently consumed for power conditioning without affecting its normal operation of real power transfer. A proposed nonlinear control scheme of an SHPF-TCR compensator has been established and simulated. It has been found that the SHPF-TCR compensator can effectually eliminate current harmonic and reactive power compensation during both the steady as well as in the transient operating conditions for a variety of loads. It has been shown that the system has a fast-dynamic response, has good performance in both steady-state and dynamic operations. The simulation results obtained in this work and the current analysis serve as a fundamental step towards the design of control circuits for hardware implementation of the device in the future.

REFERENCES

[1] A. Hamadi, S. Rahmani, K. Al-Haddad. A hybrid passive filter configuration for VAR control and harmonic compensation, *IEEE Trans Ind Electron*. 2010; 57(7): 2419–34p.

[2] P. Flores, J. Dixon, M. Ortuzar, R. Carmi, P. Barriuso, L. Moran. Static Var compensator and active power filter with power injection capability, using 27-level inverters and photovoltaic cells, *IEEE Trans Ind Electron*. 2009; 56(1): 130–8p.

[3] H. Hu, W. Shi, Y. Lu, Y. Xing. Design considerations for DSP controlled 400 Hz shunt active power filter in an aircraft power system, *IEEE Trans Ind Electron*. 2012; 59(9): 3624–34p.

[4] X. Du, L. Zhou, H. Lu, H.-M. Tai. DC link active power filter for three-phase diode rectifier, *IEEE Trans Ind Electron*. 2012; 59(3): 1430–42p.

[5] M. Angulo, D.A. Ruiz-Caballero, J. Lago, M.L. Heldwein, S.A. Mussa. Active power filter control strategy with implicit closed loop current control and resonant controller, *IEEE Trans Ind Electron*. 2013; 60(7): 2721–30p.

[6] X. Wang, F. Zhuo, J. Li, L. Wang, S. Ni. Modeling and control of dual-stage high-power multifunctional PV system in d-q-0 coordinate, *IEEE Trans Ind Electron*. 2013; 60(4): 1556–70p.

[7] J.A. Munoz, J.R. Espinoza, C.R. Baier, L.A. Moran, E.E. Espinosa, P.E. Melin, D.G. Sbarbaro. Design of a discrete-time linear control strategy for a multicell UPQC, *IEEE Trans Ind Electron*. 2012; 59(10): 3797–807p.

[8] L. Junyi, P. Zanchetta, M. Degano, E. Lavopa. Control design and implementation for high performance shunt active filters in aircraft power grids, *IEEE Trans Ind Electron*. 2012; 59(9): 3604–13p.

[9] Y. Tang, P.C. Loh, P. Wang, F.H. Choo, F. Gao, F. Blaabjerg. Generalized design of high performance shunt active power filter with output LCL filter, *IEEE Trans Ind Electron*. 2012; 59(3): 1443–52p.

[10] Z. Chen, Y. Luo, M. Chen. Control and performance of a cascaded shunt active power filter for aircraft electric power system, *IEEE Trans Ind Electron*. 2012; 59(9): 3614–23p.

[11] S. Rahmani, A. Hamadi, K. Al-Haddad, A.I. Alolah. A DSP-based implementation of an instantaneous current control for a three-phase shunt hybrid power filter, *J Math Comput Simul Model Simul Elect Mach Convert Syst*. 2013; 91: 229–48p.

[12] C.S. Lam, W.H. Choi, M.C. Wong, Y.D. Han. Adaptive dc-link voltage-controlled hybrid active power filters for reactive power compensation, *IEEE Trans Power Electron*. 2012; 27(4): 1758–72p.

[13] A. Hamadi, S. Rahmani, K. Al-Haddad. Digital control of hybrid power filter adopting nonlinear control approach, *IEEE Trans Ind Informat*. to be published.

[14] A. Bhattacharya, C. Chakraborty, S. Bhattacharya. Parallel connected shunt hybrid active power filters operating at different switching frequencies for improved performance, *IEEE Trans Ind Electron*. 2012; 59(11): 4007–19p.

[15] S. Rahmani, A. Hamadi, N. Mendalek, K. Al-Haddad. A new control technique for three-phase shunt hybrid power filter, *IEEE Trans Ind Electron*. 2009; 56(8): 2904–15p.

[16] A. Luo, X. Xu, L. Fang, H. Fang, J. Wu, C. Wu. Feedback feedforward PI-type iterative learning control strategy for hybrid active power filter with injection circuit, *IEEE Trans Ind Electron*. 2010; 57(11): 3767–79p.

[17] S. Rahmani, A. Hamadi, K. Al-Haddad. A Lyapunov-function-based control for a three-phase shunt hybrid active filter, *IEEE Trans Ind Electron*. 2012; 59(3): 1418–29p.

[18] M.I. Milanés-Montero, E. Romero-Cadaval, F. Barrero-González. Hybrid multiconverter conditioner topology for high-power applications, *IEEE Trans Ind Electron*. 2011; 58(6): 2283–92p.

International Journal of Geological and Geotechnical Engineering
Vol. 3: Issue 2
www.journalspub.com

Application of High Speed Videography and Digital Image Processing Software to Assess Performance of Blasts In Opencast Mines: A Case Study

T. Murali Naik, V.R. Sastry*, G. Raghu Chandra, S. Kuili*
Department of Mining Engineering, National Institute of Technology Karnataka, Surathkal, India

ABSTRACT

Rock mass can be fragmented by the process of blasting in which a known volume of the yield is obtained by using a calculated quantity of explosive. The explosive selected for blasting depends on factors like rock mass parameters, blasting economics and blast design. Assessment of the performance of a given blast is essential in the larger economics of the mining project. A study was conducted to know the blast performance at two different mines. High speed videography was used to assess blast performance and wastage of gaseous energy. With the increase in stemming height from 1.0m to 3.5m, it was found that there is decrease in the escape of gas energy ejection from 7.42m height to 3.5m, which was almost half the height of ejection. The analysis showed that the maximum velocity of rock movement was found to be 8.97m/s in Mine-A and 12.40m/s in Mine-B with varying strength of intact rock mass. Wipfrag digital image processing software was used to determine the fragment size distribution, which gives quick and accurate measurements. Blast-4 of Mine-A with explosive charge of about 33.36kg/hole produced finer fragmentation compared to Blast-4 in Mine-B with same explosive charge, clearly showing influence of strength of rock mass.

Keywords: fragmentation assessment, high speed videography, rock mass movement, Wipfrag

****Corresponding Authors***
E-mail: muralinaikt@gmail.com, vedala_sastry@yahoo.co.in

INTRODUCTION

Rock blasting is carried out to fragment and displace the rock mass in mines and quarries. In order to achieve the desired objective to be performed in the field, precise engineering application of blasting operation is required. In civil engineering projects like construction of dams, tunnels or caverns, hard rock mass has to be removed, using blasting process. Blasting process takes place in a fraction of second to few seconds and it is not possible to assess the performance of the blast with naked eye. To view and analyze the performance of mine blasts and subsequently design the blasts, high speed video camera is used, which can capture images and can be played back to view in slow motion for further analysis [1]. In increasing the cast blasting benefit, the high-speed videography is used. Fragmentation in blasted muck piles was analyzed by Wipfrag digital image processing based software [2].

This paper presents a part of the research work carried out for assessing the blast performance using High Speed Video Camera of AOS Technologies, Switzerland, in two different opencast limestone mines located in Southern India. Studies were conducted at limestone Mine-

A in Tamil Nadu and other limestone Mine-B in Andhra Pradesh as shown in Figure 1.

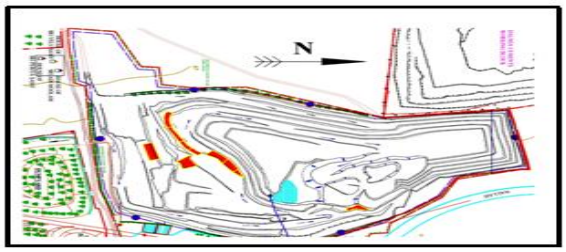

Mine-A

Mine-B

Fig. 1. *View of limestone mines.*

METHODOLOGY

In total, 22 blasts were conducted in the two mines to assess the performance of the blast. High speed video videography was used to record all the blasts (Figure 2).

The parameters used in blast studies are listed in Table 1. Blastholes were of 115 mm diameter in both mines A and B. Depth of blast holes was varying from 5 to 10 m in Mine-A [3], 2m to 9.5m in Mine-B [4].

Slurry explosive available in the form of cartridges was used as primer and column charge in Mine-A, whereas in Mine-B slurry explosive available in the form of cartridges was used as primer and ANFO was used as column charge.

Table 1. *Summary of blast studied limestone mine-A.*

Limestone mine-A					
Specifications	**Blast number**				
	1	**2**	**3**	**4**	**5**
Bench height (m)	5.0	6.0	7.0	7.5	10.0
Burden (m)	2.5	2.5	2.5	2.5	2.5
Spacing (m)	3.0	3.0	3.0	3.0	3.0
No. of blastholes	13	24	23	18	20
Explosive/hole (kg)	19.25	25.02	29.37	33.36	40.03
Total exp. charge (kg)	250.20	600.48	675.54	600.48	800.64
Stemming (m)	1.5	1.4	1.5	1.4	1.0
Limestone mine-B					
Specifications	**Blast number**				
	1	**2**	**3**	**4**	**5**
Bench height (m)	2.0	3.5	5.0	8.0	9.5
Burden (m)	2.0	2.0	3.0	2.5	3.0
Spacing (m)	3.0	3.0	5.0	5.0	6.0
No. of blastholes	17	12	10	27	15
Explosive/ hole (kg)	03.82	07.00	09.40	33.33	48.21
Total exp. charge (kg)	65.00	85.00	94.00	900.00	723.00
Stemming (m)	1.6	2.7	3.5	3.5	3.7

The information obtained from the high-speed videography with a capacity of 1000 frames per second was used to understand the dynamics involved in the blasts, which in turn reduce the costly trials that are necessary for optimizing the blast design. The camera provides results on the spot and recorded video is played using imaging studio software.

Fig. 2. *High speed video camera of 1000fps capacity.*

Pro-analyst software provides a series of video processing and motion analysis that can be applied to any video or image sequence which will allow users to measure the displacement and velocity of the moving fragments. It is also used to track the particles and to know the ejection of gas energy from the stemming zone of blasthole. The velocity of burden rock increases with the increase in bench height to burden ratio [5]. The sequence of blasts with specific time intervals from the time of initiation in limestone Mine-A and Mine-B are shown in Figures 3 and 4.

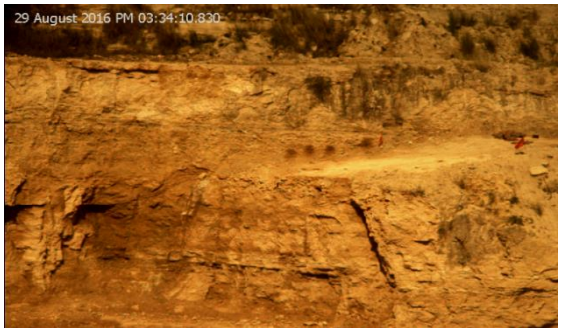

0 ms

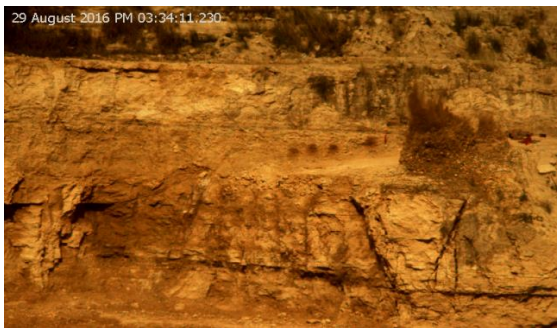

400ms

600ms

800ms

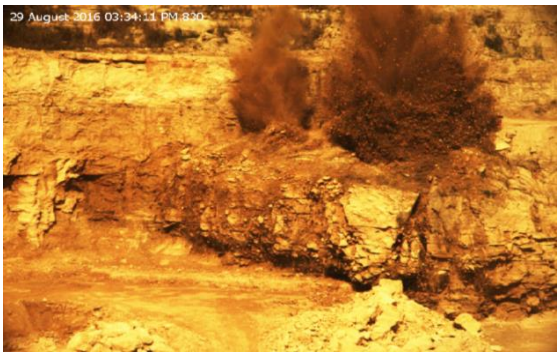

1000ms

1200ms

Fig. 3. *Sequence of progress of a typical blast in Mine-A.*

0ms

400ms

600ms

800ms

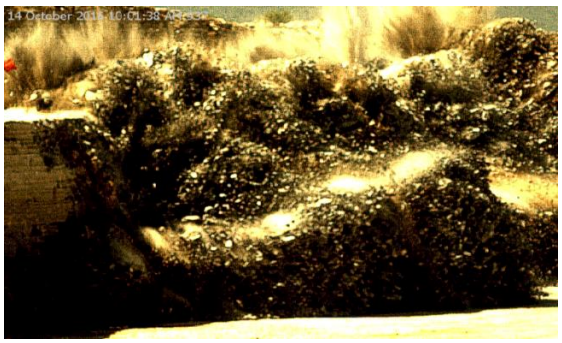

1000ms

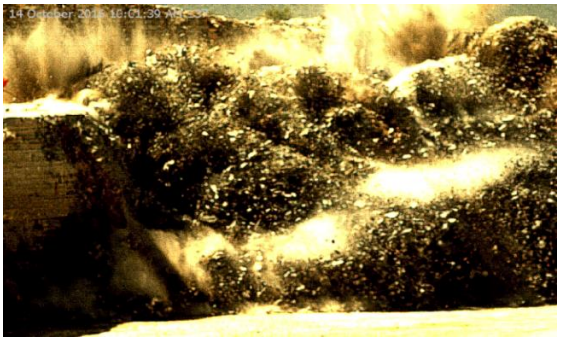

1200ms

Fig. 4. *Progress of a typical blast in mine-B.*

Fragmentation resulting from the blasts can be assessed by taking the photos of the muck piles generated. After the blasts, photos were taken covering various layers of the entire muck pile during the process of shoveling at regular intervals till the entire muck pile was excavated. Wipfrag software was used to analyze the fragmentation. Wipfrag software uses the technique that analyze the digital image of blasted rock to predict the grain size distribution in the muck pile. Scale device was used to view the reference of each sizing zone. The muck pile was photographed and image is then transferred to Wipfrag system. Typical muck piles generated from different production scale blasts are shown in Figure 5.

Mine-A

Mine-B

Fig. 5. *Typical muck piles obtained from the blasts.*

RESULTS AND DISCUSSION

To track down the rock movement of bench face and to find out the escape of gaseous energy, Pro-analyst software was used. Study carried out revealed that the bench height of 10m in Mine-A resulted in gas ejection of 7.42m height (on average), whereas the bench height of 7.5m in the same mine resulted in gas ejection of 8.73m. Thus, it may be interpreted that wastage of gas energy was lesser in taller benches. Figure 6 shows typical case analysis in Mine-A, and Figure 7 for Mine-B.

The comparison of gas ejection from Mine-A and Mine-B revealed that the gas ejection was found to be more in Mine-A. This may be due to lesser stemming in Mine-A compared to Mine-B. The stemming height of 1.0m in Mine-A resulted in gas ejection of 7.42m, whereas the stemming height of 3.5m in Mine-B resulted in gas ejection of 3.82m, which was almost half the height in Mine-B.

Height of bench

Escape of gas energy

Tracking of burden rock mass

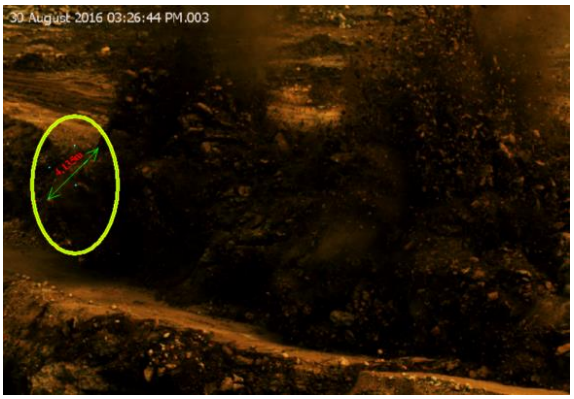

Displacement of rock mass

Fig. 6. *Analysis of a typical blast in Mine-A.*

Height of bench

Escape of gas energy

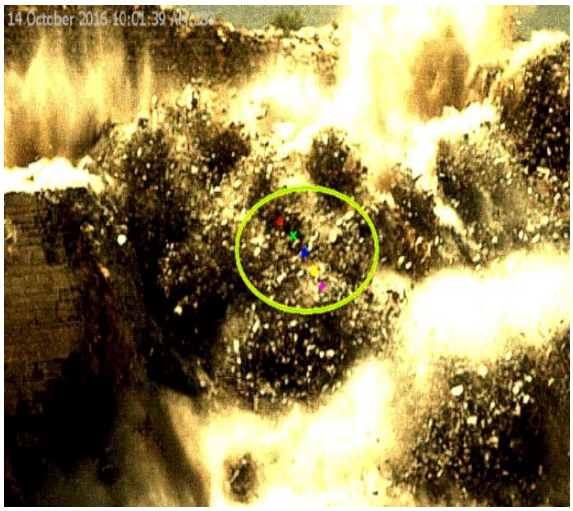

Tracking of burden rock mass

Displacement of rock mass

Fig. 7. *Analysis of a typical blast in Mine-B.*

The velocity of the burden rock was varying from 6.58m/s to 8.97m/s in Mine-A and 8.34m/s to 12.4m/s in Mine-B. The burden rock movement was found to be increase in both the mines with increase in Bench Height/Burden ratio. Velocity of 6.58m/s resulted with charge factor of 0.28kg/m^3 and velocity of 8.97m/s resulted with charge factor of 0.41kg/m^3 in Mine-A. In Mine-B, a burden rock velocity of 8.34m/s resulted with charge factor of 0.18kg/m^3 and 12.4m/s with charge factor of 0.25kg/m^3. Thus, in both Mine-A and Mine-B, the velocity of the burden rock was found to increase with increase in charge factor. The observed readings are tabulated in Tables 2 and 3.

Table 2. *Comparison of velocity of rock movement with BH/B ratio.*

Limestone mine-A					
Parameters	**Blast number**				
	1	2	3	4	5
Time (s)	1.2	1.1	0.9	0.8	0.8
Velocity (m/s)	6.58	7.68	7.95	8.29	8.97
BH/B ratio	2.0	2.4	2.8	3.0	4.0
Limestone mine-B					
Parameters	**Blast number**				
	1	**2**	**3**	**4**	**5**
Time (s)	0.9	0.8	0.8	0.7	0.7
Velocity (m/s)	8.34	9.26	8.76	9.57	12.4
BH/B ratio	1.0	1.75	1.67	3.2	3.16

Table 3. *Comparison of Velocity of rock movement with charge factor.*

Limestone mine-A					
Parameters	**Blast number**				
	1	2	3	4	5
Volume (m^3)	900	1620	1800	1500	1950
Velocity (m/s)	6.58	7.68	7.95	8.29	8.97
Charge factor (kg/m^3)	0.28	0.37	0.38	0.40	0.41
Limestone mine-B					
Parameters	**Blast number**				

	1	2	3	4	5
Volume (m^3)	360	425	450	3750	2892
Velocity (m/s)	8.34	9.26	8.76	9.57	12.4
Charge factor (kg/m^3)	0.18	0.20	0.21	0.24	0.25

Output of the fragmentation analysis obtained from Wipfrag software consists of a cumulative size in both the limestone mines and results are shown in Figures 8 and 9.

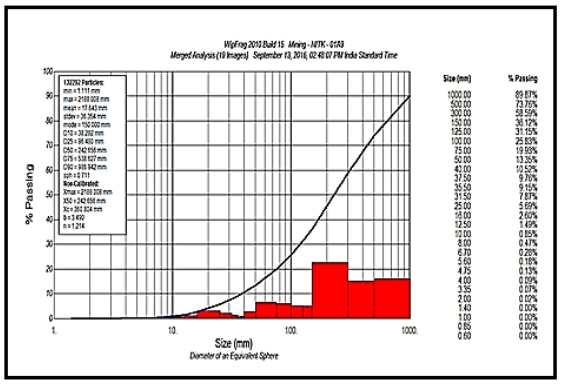

Blast-1

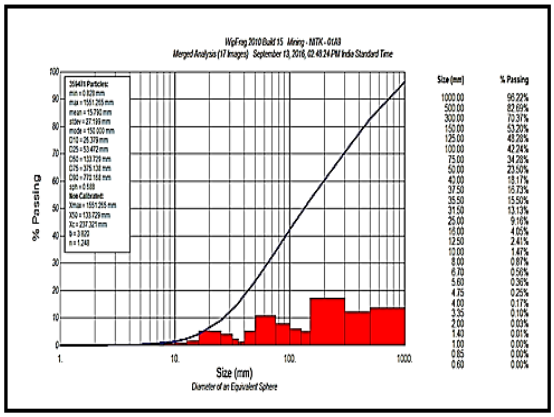

Blast-2

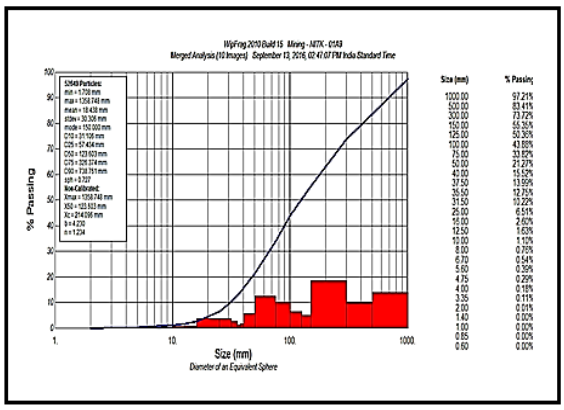

Blast-3

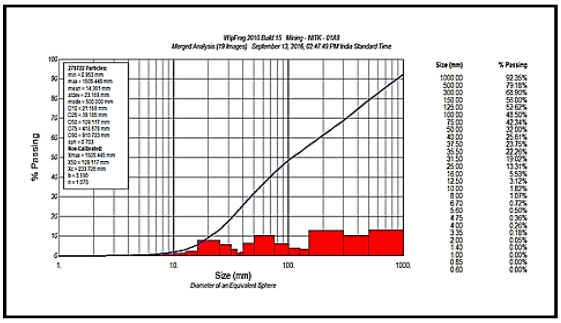

Blast-4

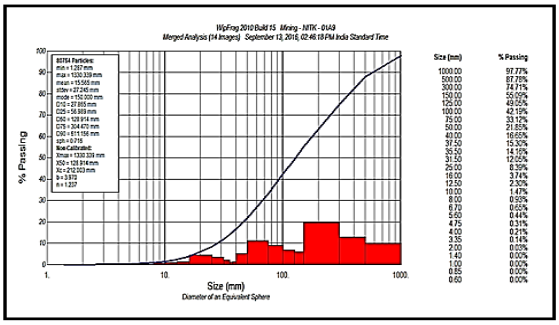

Blast-5

Fig. 8. *Fragmentation analysis of different blasts in mine-A.*

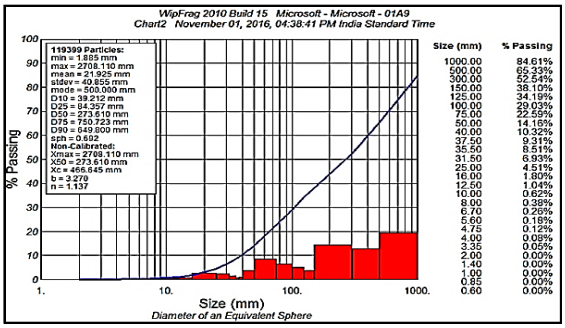

Blast-1

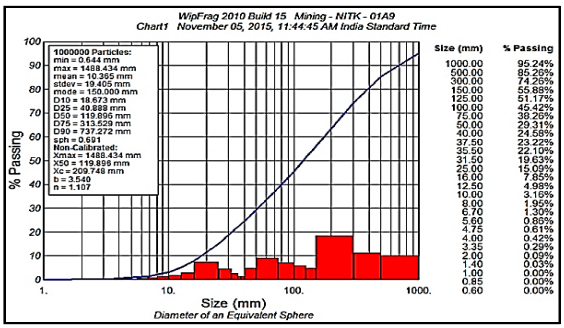

Blast-2

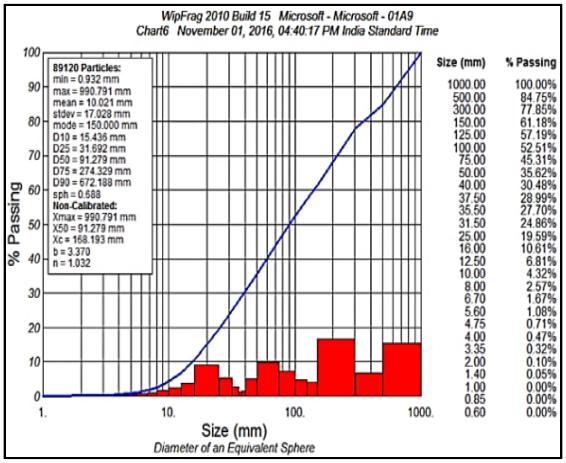

Blast-3

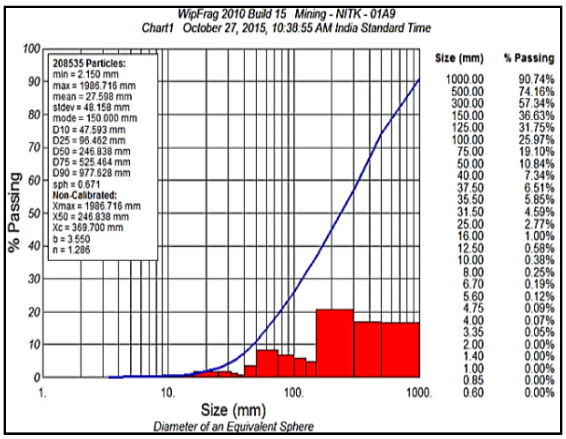

Blast-4

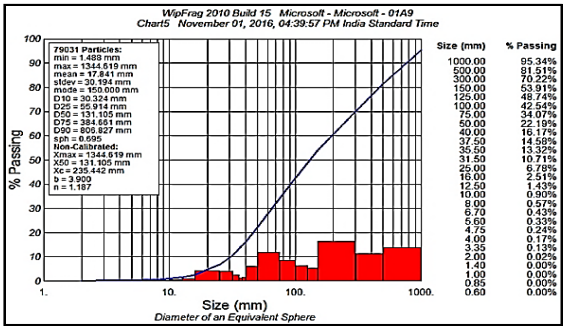

Blast-5

Fig. 9. *Fragmentation analysis of different blasts in mine-B.*

In Mine-A, Blast-4 with explosive charge of about 33.36kg/hole produced coarser fragmentation compared to Blast-5 with explosive charge of about 40.03kg/hole. In mine-B, Blast-4 with explosive charge of about 33.33 kg/hole produced coarser fragmentation compared to Blast-5 with explosive charge of about 48.21 kg/hole.

In Mine-A, Blast-4 with explosive charge of about 33.36 kg/hole produced finer fragmentation compared to Blast-4 in Mine-B with similar explosive charge. The observed fragmentation values of Mine-A and Mine-B are tabulated in Tables 4 and 5.

Table 4. *Fragmentation values obtained from blasts in mine-A.*

Blast number	Number of holes	Percentage passing				
		1000 (mm)	500 (mm)	300 (mm)	150 (mm)	100 (mm)
1	13	89.87	73.76	58.59	36.12	25.83
2	24	96.22	82.69	70.37	53.20	42.24
3	23	97.21	83.41	73.72	55.35	43.88
4	18	92.35	79.18	68.90	56.00	52.62
5	20	97.77	87.78	74.71	55.09	42.19

Table 5. *Fragmentation values obtained from blasts in mine-B.*

Blast number	Number of holes	Percentage passing				
		1000 (mm)	500 (mm)	300 (mm)	150 (mm)	100 (mm)
1	17	84.61	65.33	52.54	38.10	29.03
2	12	95.24	85.26	74.26	55.88	45.42
3	10	100.00	84.75	77.85	61.18	52.51
4	27	90.74	74.16	57.34	36.63	25.97
5	15	95.34	81.51	70.22	53.91	42.54

CONCLUSIONS

High speed videography is a very good tool for analyzing the performance of blast in mines and quarries, in terms of tracking down the burden rock movement, behavior of bench with different explosive loading and initiation pattern, ejection of stemming from stemming zone and role of structural discontinuities, etc. Similarly, the digital image processing techniques predicts the fragmentation size resulting from blasts quite effectively. Following are the major conclusions from the study carried out in two limestone mines.

- From the analysis made, it was observed that bench height of 10m resulted in 7.42m of stemming ejection (on average) and bench height of 7.5m resulted in 8.73m of stemming ejection (on average). Hence, it may be concluded that increase in bench height results in lesser stemming ejection, and better utilization of explosive energy. This is due to the fact that taller benches result in lesser stiffness coefficient.
- Results have clearly indicated higher burden rock movement with increase in charge factor. Velocity of 6.58m/s resulted with a charge factor of 0.28kg/m^3, whereas velocity of 8.97m/s resulted with increased charge factor of 0.41kg/m^3. This indicates that any increase in explosive charge results in finer fragmentation.
- Velocity of rock mass movement increased clearly with increase in bench height, due to more flexibility in the bench. BH/B ratio of 2.0 resulted in burden movement of 6.58m/s, whereas BH/B ratio of 2.8 resulted in increased burden rock movement of 7.95m/s.

It is expected that more similar studies involving advanced instrumentation and softwares will improve the blasting results leading to better project economics.

REFERENCES

[1] V.R. Sastry, K. Ramchandar. Assessment of performance of explosives/blast results based on explosive energy utilization, *R&D Project Report*. 2014.

[2] N.H. Maerz, T.C. Palangio, J.A. Franklin. WipFrag image based granulometry system, In: *Proceedings of the FRAGBLAST 5 Workshop on Measurement of Blast Fragmentation*. Montreal, Quebec, Canada 1996 Aug 23, 91–9p. AA Balkema.

[3] V.R. Sastry. Scientific study of the impact of blasting operations carried out in Pathapadu Limestone Mine of Sree Jayajothi Cements Limited on the surrounding village structures, Unpublished *Technical Report* submitted to My Home Industries Private Limited. 2016.

[4] V.R. Sastry. Study of the effect of blasting operations in Periyanagalur Limestone Mine, Ariyalur district, on nearby village structures, Unpublished *Technical Report* submitted to M/S The Ramco Cements Limited. 2017.

[5] S. Bhandari. On the role of stress waves and quasi-static gas pressure in rock fragmentation by blasting, *Acta Astronautica*. 1979; 6(3-4): 365–83p.

World Journal of Engineering

Investigations on performance of diesel engine by varying injection timings with design modification on piston crown

Vijaya K., Shailesh Palaparty, Raghavan Srinivasa, Ravi Kumar Puli,

Investigations on performance of diesel engine by varying injection timings with design modification on piston crown

Vijaya K.
National Institute of Technology Warangal, India
Shailesh Palaparty and Raghavan Srinivasa
Methodist College of Engineering and Technology, Hyderabad, India, and
Ravi Kumar Puli
National Institute of Technology, Warangal, India

Abstract

Purpose – Investigations are carried out with the aim of improving performance of a diesel engine with the design modification on piston crown to stimulate the uniform combustion by inducing turbulence in the incoming charge.

Design/methodology/approach – A stirrer is introduced at the top of the piston so as to inculcate more turbulence to the incoming charge by improving the rate of fuel vaporization. Whirling motion is created in the combustible mixture by providing rotating blades on the cavity/bowl of the reciprocating piston head. By putting a simple link mechanism, the oscillatory motion of connecting rod will rotate the blade by an angle of 60°.

Findings – The investigations are carried out with and without swirl piston at 17.5 compression ratio and 200 bar injection pressure by varying injection timings.

Originality/value – Finally, the result shows that by using the modified piston, nearly 3 per cent of efficiency increased and 31 per cent of NOx emissions are reduced compared to that of a normal piston with 80 per cent load at standard injection timing.

Keywords Turbulence, Piston, Diesel engine, Diesel

Paper type Research paper

Nomenclature

CR = Compression ratio;
BSFC = Brake specific fuel consumption;
HC = Hydrocarbons;
A = Advanced injection timing;
R = Retard injection timing;
SP = Swirl piston;
BTE = Brake thermal efficiency;
CO = Carbon monoxide;
NO_x = Oxides of nitrogen;
S = Standard injection timing; and
NP = Normal piston.

1. Introduction

Internal combustion engines have become an important part of our day-to-day life, and it plays a major role in the field of automobile sector and agricultural sectors. Diesel engines are used in large numbers, and they offer a lot of opportunities to researchers to study them from the perspective of enhancing their performance and reducing emissions. The in-cylinder fluid motion in internal combustion engine is one of the most important factors controlling the combustion process. It governs the fuel-air mixing and burning rates in diesel engines. The fluid flow prior to combustion in internal combustion engines is generated during the induction process and developed during the compression stroke. Therefore, a better understanding of fluid motion during the induction process is critical for developing engine designs with the most desirable operating and emission characteristics. To obtain a better combustion with lesser emissions in direct -injection diesel engines, it is necessary to achieve a good spatial distribution of the injected fuel throughout the entire space. This requires matching of the fuel sprays with combustion chamber geometry to effectively make use of the gas flows. In other words, matching the combustion chamber geometry, fuel injection and gas flows is the most crucial factor for attaining a better combustion. In this scenario, Prasad *et al.* (2011, 2013a, 2013b) investigated the impact of swirling of the incoming charge on the emission and performance of the DI diesel engine. The more turbulence is induced in the charge by modifying the design of the piston head, that is, modification of combustion chamber to enhance the turbulence in the cylinder. The swirl is intensified by cutting grooves on the piston crown.

The current issue and full text archive of this journal is available on Emerald Insight at: **www.emeraldinsight.com/1708-5284.htm**

World Journal of Engineering
15/5 (2018) 562–566
 [ISSN 1708-5284]
[DOI 10.1108/WJE-11-2017-0348]

Received 1 November 2017
Revised 8 January 2018
Accepted 9 January 2018

Heywood (1988) studied the performance of 1.8 L single-cylinder diesel engine with an additional attachment of the swirl rate controller. This attachment allowed variation of the mean swirl ratio. Swirl level has a significant influence on the combustion process and exhaust emissions. When the swirl ratio increased to certain level, more intense premixed combustion phase is improved. By increasing the swirl ratio, pressure and temperature of the charge are increased because of premixed and controlled combustion in the engine cylinder which results the promotion of NOx formation and also reduces the soot production and increases the soot oxidation. The overall combustion duration was also shortened with reduced fuel consumption. Singh (2005) modified the combustion chamber by creating grooves on it, which will in turn improve the turbulence to the charge. They created a possibility of multiple flame fronts so as to improve the combustion efficiency and reduce the heat losses. Jeng *et al.* (1999) experimentally investigated the quality of the tumbling motion, especially for the engine with a bowl in the piston. It is observed that a small-scale vortex will be reserved inside the bowl in the piston. In their further investigation, the quality of the vertical flow in the axial plane with the generation of turbulence during the compression stroke is strongly recommended. The researchers (Yun and Lee, 2000) discussed the collective effect of tumble and swirl flows of charge at the inlet port. They noticed that swirl and tumble motions together are induced in the combustion chamber, and it is difficult to separate the influence of each on combustion and they also proposed new evaluation index to characterize the in-cylinder flow. Suzuki (1988) proposed baseline modifications in piston and cylinder liners to enhance mechanical and thermal loading on vital engine parts. Hard anodizing of the piston head, reinforcing the piston head with SiC whisker. He proposed a new process for improving the surface lubrication by introducing numerous finely distributed micro-pits. The researchers (Dembinski and Angstrom, 2012) studied by applying different inlet port designs and valve seat making, swirl and tumble. In their study, they measure the flow of charge at the TDC by capturing the combustion images by renounced software called velocimetry. They also estimated the swirl number from the same data. They concluded that swirling motion is progressed from compression to combustion process, whereas tumble motion plays a vital role at the final phase of combustion. However, this tumble effect will influence the swirl motion and offset its location during combustion.

Turbulence of charge plays a crucial role in the combustion in IC engines. Flame speed, mixing of unburned charge is relatively poor in case of transition and low-turbulent mixtures. However, homogeneous combustion can be attained by inducing turbulence either by changing the flow pattern or by changing the geometry of the combustion chamber. This will improve the performance of the engine. A higher turbulence in the charge can be created by changing the geometry of the combustion chamber that can be carried out either by changing the design of cylinder head or the piston crown. At a particular operating pressure, piston speed would proportionally increase the turbulence induced in charge. However, excessive turbulence is also undesirable. The effects of turbulence can be summarized as turbulence accelerates chemical action, so that the combustion time is reduced and hence minimizes the tendency to detonate. Even though the turbulence gives uniform combustion, higher turbulence may lead to flame extinguish. In the present work, experiments are conducted at a constant speed, with and without piston modification, 200 bar injection pressure and various injection timings at four different loads levels namely, 20, 40, 60 and 80 per cent of full load with 17.5 CR.

2. Experimental setup

To induce the turbulence in charge, piston crown in re-designed and experiments are conducted to evaluate the performance. Schematic representation of the experimental test setup is presented in Figure 1. Experiments are conducted to study the influence of swirl and tumble on the performance of diesel engine. The engine specifications are presented in Table I. It is a computerized single-cylinder, four-stroke, water-cooled CI engine with an eddy current dynamometer. The engine is provided with chromium–aluminum thermocouples to measure the jacket water inlet and outlet (T1 and T2), calorimeter water inlet and outlet (T3 and T4) and exhaust gas inlet and outlet (T5 and T6) temperatures.

Engine is also provided with pressure sensors, the dynamic pressure with water-cooled piezo sensor, combustion gas pressure with differential pressure transducers and fuel injection pressure with differential pressure unit. Flow rate of the cooling water is measured using a Rota meter with stainless steel float. An encoder is fixed for crank angle record. The signals from all the sensors are interface with a computer to display P-□, P-V and FIP-□ plots. A provision is also made in the measurement of volumetric fuel flow. A built-in program in the system calculates the indicated power, brake power and thermal efficiency.

2.1 Piston modification

Piston modification is an important strategy that has been followed since recent times by the research community owing to the performance of the diesel engine. Figures 2 and 3 show the normal piston and modified piston, respectively. In a

Figure 1 Schematic diagram of the experimental set-up

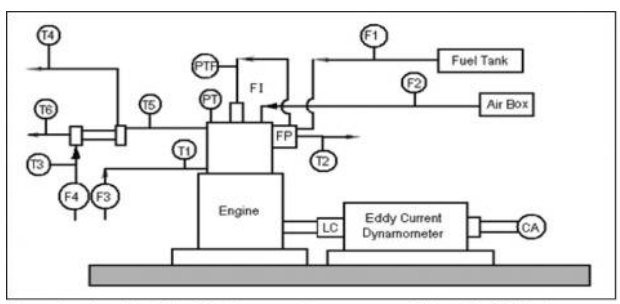

PT	Combustion Chamber Pressure Sensor	FI	Fuel Injector
PTF	Fuel Injection Pressure Sensor	FP	Fuel Pump
T1	Jacket Water Inlet Temperature	F1	Liquid fuel flow rate
T2	Jacket Water Outlet Temperature	F2	Air Flow Rate
T3	Inlet Water Temperature at Calorimeter	F3	Jacket water flow rate
T4	Outlet Water Temperature at Calorimeter	F4	Calorimeter water flow rate
T5	Exhaust Gas Temperature before Calorimeter		
T6	Exhaust Gas Temperature after Calorimeter	LC	Load Cell
EGC	Exhaust Gas Calorimeter	CA	Crank Angle Encoder

Table I Engine specifications

Sl. No.	Engine parameters	Specifications
1	Engine type	TV1(Kirloskar, Four stroke)
2	Number of cylinders	Single cylinder
3	Speed	1,500 rpm
4	Bore	87.5 mm
5	Stroke	110 mm
6	Swept volume	661 cc
7	Compression ratio	20.1:1
8	Dynamometer	Eddy current dynamometer
9	Type of cooling	Water cooling
10	Fuel injection pressure	300 bar
11	Fuel	Diesel

normal piston, piston crown has a simple bowl-shaped structure, while in the modified piston, it is made with three blades at 120° to each other. The same aluminum alloy is used in fabrication of chamber and 2-mm thick small strips are used to make the chamber. The modified piston assembly with the engine is as shown in Figure 4.

2.2 INDUS model PEA-205 five-gas analyzer

Emission analysis is carried out by using INDUS model PEA-205 five-gas analyzer is as shown in Figure 5. It has a provision

Figure 2 Normal piston

Figure 3 Swirl piston

Figure 4 Modified piston arrangement in-cylinder

Figure 5 INDUS model PEA205 five-gas analyzer

for monitoring five gases, namely, CO, CO_2, HC, O_2 and NOx from the engine exhaust. It is made such that it meets the OIML Class I specifications. CO, CO_2 and HC (Hydrocarbon residue) are measured by NDIR technology, and O_2 and NOx are measured by electrochemical sensors.

3. Results and discussions

The experiments are conducted on a diesel engine fueled with diesel by varying three injection timings and 200 bar injection pressure at 17.5 CR with and without design modification on piston crown. The influence of load on the brake specific fuel consumption (BSFC) by varying the injection timings with and without modified piston design is as shown in Figure 6. It can be observed that the BSFC of modified piston is reduced compared to normal piston at all injection timings. The results show that the BSFC is minimum at advanced injection timing for modified piston at 60 per cent load 0.231 kg/kW-h, and it is maximum for normal piston at retard injection timing with 20 per cent load 0.554 kg/kW-h. The BSFC of the swirl piston engine with 80 per cent is 5.07 per cent lesser than compared to normal piston at advanced injection timing may be because of the homogeneous combustion that occurred by increasing the turbulence of the air.

The variation of brake thermal efficiencies with respect to load for modified piston and normal piston is shown in Figure 7. It can be noticed that the brake thermal efficiency (BTE) of modified piston increases with increase in load at all injection timings compared to normal piston may be because of the increase in combustibility of the mixture which can be

Figure 6 Variation of BSFC with load

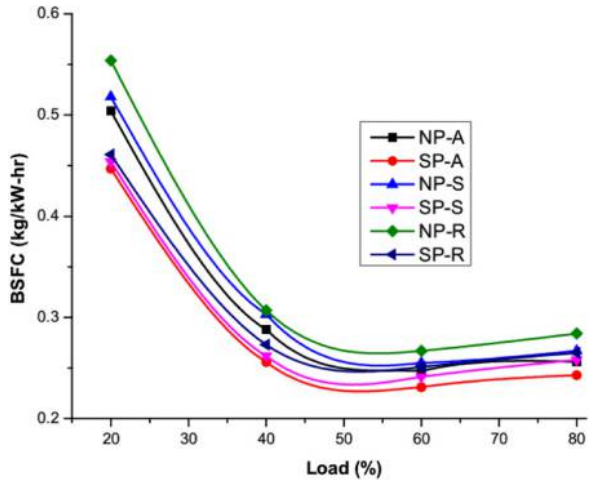

Figure 7 Variation of BTE with load

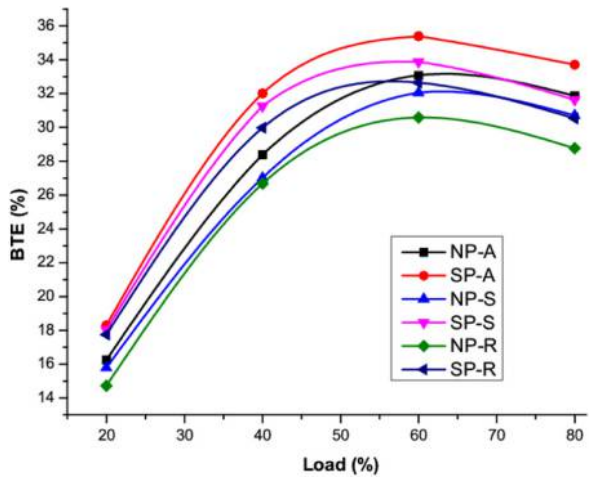

accomplished by turbulence in the engine. A similar trend in BTE can be noticed at all the loads. The results show that the BTE is minimum 16.25 per cent at advanced injection timing for the normal piston at 20 per cent load and maximum 35.39 per cent observed for the swirl piston with 80 per cent load at advanced injection timing.

Major constituents of engine emissions are CO, O_2, CO_2, unburned HC, NO_x and particulate matter. In Figure 8, it is observed that, as the emissions of carbon monoxide linearly decreased at all injection timings with respect to load, these emissions diminished with swirl piston compared to normal piston may be because of increasing turbulence because of which the more amount of oxygen will be available at the inlet of the engine. The results show that the CO emissions are minimum at standard injection timing for with and without modifying piston at 80 per cent of load, and it is maximum at retard injection timing for normal piston with 20 per cent of load. The effect of HC emissions using with and without modified piston is depicted in Figure 9. From the results, it can be observed that the unburnt hydrocarbons are diminished

Figure 8 variation of CO emissions with load

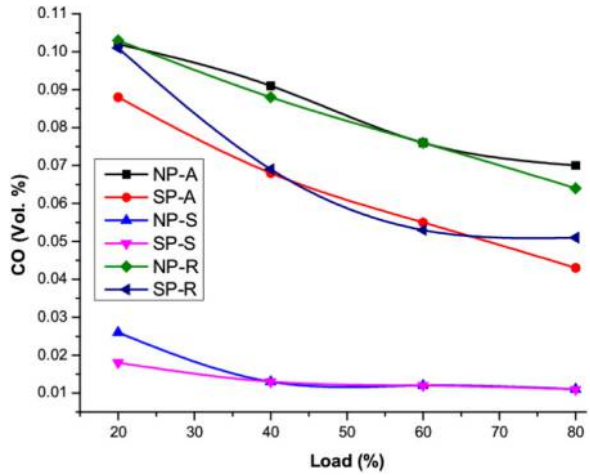

Figure 9 Variation of HC emissions with load

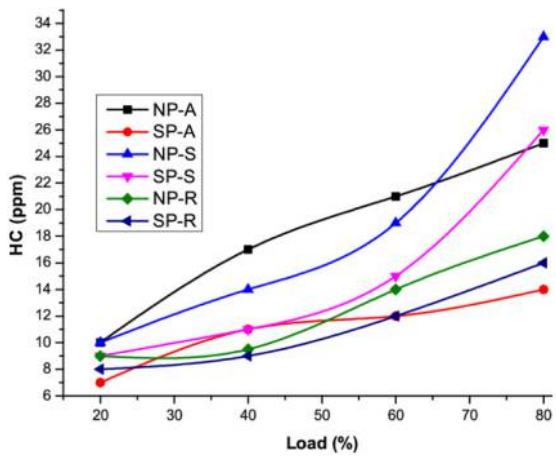

with swirls piston compared to normal piston at all loads because of uniform combustion of the charge by creating turbulence to the charge. From the results at full load, the HC emissions are decreased by 44 per cent with swirl piston compared to normal piston at advanced injection timing. This could be attributed to better air mixture formation, which resulted in ameliorated swirl motion within the combustion bowl.

The variation of oxides of nitrogen with respect to load can be observed for normal piston and modified piston is depicted in Figure 10. The NO_x emissions are increasing with uniform increase in the peak cylinder temperature by an increase in load for both swirl and normal pistons. It can be explained by higher mixing rate, which facilitates a better swirl motion and helps for better air-fuel mixture preparations, eventually leading to more complete combustion. It created higher engine cylinder temperatures which increases the NOx emissions with and without modified piston. From the results, it can be observed that at full load, the NO_x emissions are decreased with swirl piston compared to normal piston at all injection timings. The

Figure 10 Variation of NO_x emissions with load

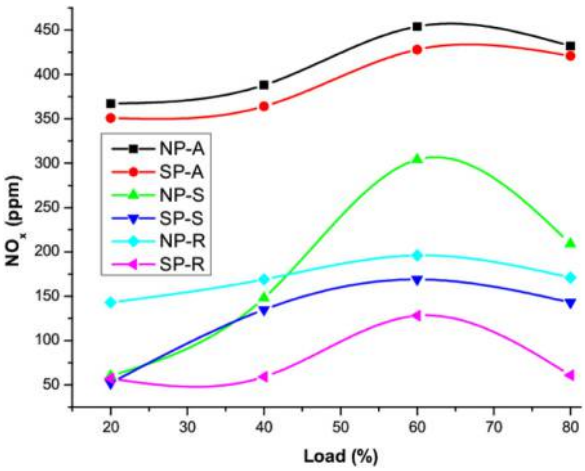

minimum NO_x emissions is 52 ppm at standard injection timing for the swirl piston at 20 per cent load and maximum 454 ppm is observed for normal piston with 60 per cent load at advanced injection timing.

4. Conclusions

To improve the performance of the engine, several active and passive alternative techniques are available. Piston modification is a one of the active techniques to induce more turbulence and minimize the emissions. In this connection, the geometry of the piston is modified by accommodating rotating blades in the piston crown to induce turbulence by means of swirl motion of charge. The results are as follows:

- From the results, it can be observed that at full load, decrement of the BSFC is 3.37 per cent observed for swirl piston compared to normal piston at standard injection timing.
- The BTE observed with 80 per cent load is 3.02 per cent increased for swirl piston compared to normal piston at standard injection timing.
- The engine exhaust CO emissions by using swirl piston with standard injection timing 78 per cent decreased compared to retard injection timing and 74 per cent decreased compared to advanced injection timing at 80 per cent load.
- The engine HC emissions by using swirl piston at standard injection timing 21.2 per cent decrement was noticed compared to normal piston with 80 per cent load.
- The engine NO_x emissions by using swirl piston at standard injection timing 31.5 per cent decrement was observed compared to normal piston with 80 per cent load.

From the above, it can be concluded that with the use of swirl piston, there has been an improvement in BTE and decrease of BSFC and have a remarkable decrease in exhaust emissions. Also, the results obtained for the modified piston at standard injection timing performance and emissions are better compared to other timing operations.

References

Dembinski, H.W.R. and Angstrom, H.-E. (2012), "Optical study of swirl during combustion in a CI engine with different injection pressures and swirl ratios compared with calculations," SAE Technical Paper 2012-01-0682.

Heywood, J.B. (1988), *Internal Combustion Engine Fundamentals*, McGraw-Hill International Edition, Automotive technology series.

Jeng, Y.-L., Chen, R.-C. and Chang, C.-H. (1999), "Studies of tumbling motion generated during intake in a Bowl-In-Piston Engine", *Journal of Marine Science and Technology*, Vol. 7 No. 1, pp. 52-64.

Prasad, S.L.V., Dr., Pandurangadu, V., Prof., Manoj Kumar, P., Dr. and Naga Malleshwara Rao, G. Dr. (2013a), "Reduction of emissions by enhancing air swirl in a diesel engine with grooved cylinder head", *International Journal of Innovative Research in Science, Engineering and Technology*, ISSN: 2319-8753, Vol. 2 No. 12.

Prasad, S.L.V., Dr., Pandurangadu, V., Prof., Manoj Kumar, P., Dr. and Naga Malleshwara Rao, G. Dr (2013b), "Enhancement of air swirl in a diesel engine with grooved cylinder head", *International Journal of Innovative Research in Science, Engineering and Technology*, ISSN: 2319-8753, Vol. 2 No. 8.

Prasad, S.L.V., Prof., Pandurangadu, V., Pratibha Bharathi, V. V. and Naga Deepthi, V.V. (2011), "Experimental study of the effect of in-cylinder air swirl on diesel engine performance", *International Journal of Engineering Science and Technology (IJEST)*, ISSN: 0975-5462, Vol. 3 No. 2, pp. 1571-1575.

Singh, S. (2005), "Design to improve turbulence in combustion chambers by creating a vortex", pure energy systems, 2005-10-13-9600187.

Suzuki, Y. (1988), "Surface modifications of pistons and cylinder liners", *Journal of Materials Engineering*, Vol. 10 No. 1, pp. 61-67.

Yun, J.-E. and Lee, J.-J. (2000), "A study on combine effects between swirl and tumble flow of intake port system in-cylinder head", Seoul 2000 FISITA World Automotive Congress, F2000A094, 12-15 June.

Corresponding author

Shailesh Palaparty can be contacted at: palapartyshailesh@gmail.com

International Journal of Analysis of Electrical Machines
Vol. 3: Issue 1
www.journalspub.com

Generation of Electrical Energy From Blast Induced Vibrations

Raghu Chandra Garimella, Rama Sastry Vedala*
Department of Mining Engineering, National Institute of Technology Karnataka, Surathkal, India

ABSTRACT

Generation of electrical energy has become a basic aspect in power system because of incremental demands from citizenry in electrical distribution system. Power may be generated in different ways. Numerous developments took place in power generation technology for the generation of electricity, but those are all dependent on conventional sources. In the present research, generation of electrical energy using piezo sensors was done by tapping electrical voltage from undesirable ground vibrations generated from blasts in mines.

Blasting operations in mines and quarries always result in ground vibrations, which are of major environmental concern, to be investigated by the researchers. Studies were carried out in three different limestone mines and two different sandstone bench formations of coal mines, situated in Southern India, to assess and analyze the seismic energy resulting from the blast induced ground vibrations. In total, 116 blast vibration events in limestone formation and 94 blast vibration events in sandstone formation were studied from various blasts. It was observed that there is a potential for tapping of electrical energy from the ground vibrations generated due to blasts carried out in mines and quarries, using piezo sensors. Piezo generator circuits were developed and used in addition to the seismographs at different distances ranging from the short to long range in all mining locations, to tap the ground vibrations. Electrical voltage was tapped from the blast induced ground vibrations during studies, which later was used for running low powered VLSI systems as ambient power source. Also, it was noticed that the obtained electrical potential is in direct proportion to the input vibration intensity.

The range of voltage tapped from ground vibrations is up to 4531.42mV in limestone and 4277.51mV in sandstone formations. Further, the amount of voltage acquired was used to obtain the intensity of blast vibrations. A very good correlation between seismic energy (obtained from ground vibrations using signal processing analysis) and electrical energy (obtained from piezo generator developed) was observed during the studies, i.e. about 99% in both formations. Results also indicated that the working of piezo sensor in tapping ground vibrations is as accurate as traditional ground vibration monitors.

Keywords: electricity generation, piezo generator, seismograph, seismic energy, signal processing

****Corresponding Author***
E-mail: raghuchandhra@gmail.com

INTRODUCTION

When the charge detonates in a blasthole under confinement, the chemical energy of the explosive is converted into heat and works to the surroundings with an enormous pressure according to the first principle of thermodynamics (Johansson and Persson [1]). Explosion of a spherical charge in an infinite rock medium results in three major zones: (1) Explosion cavity, where explosion energy is liberated and the process is hydrodynamic; (2) Transition

zone, where plastic flow, crushing and cracking occur; and (3) seismic zone, where strain waves travel as seismic waves (Atchison et al. [2]; Nicholls [3]; Sastry [4]).

The partition of the explosive energy in a blast depends on the end effects involved. For instance, part of the fracture work is in its first stage intimately connected to the shock wave flow in the locality of the hole and, in the later stages, also to the rock movement, which begins as the fractures burst open. All other energy transfer takes place obviously, as follows: (a) expansion work of the fractures, that is absorbed as elastic and plastic deformation of the rock in the surface of fractures as they are penetrated by the gases; (b) heat transferred to the rock from the hot detonation products; and (c) heat and work conveyed as enthalpy of the gases venting to the atmosphere through open fractures and stemming (Sanchidria´n et al. [5]).
Seismographs, high-speed video camera and fragmentation monitoring systems were used to measure the seismic field, the initial velocity of the blasted rock face and the fragment size distribution curve, respectively, from which the various energy terms are calculated.

PIEZO-GEN TECHNIQUE

Piezoelectricity is a phenomenon of electricity assembled in some solid materials (such as crystalline particles, certain ceramic substances, and biological composition for example bone, DNA and various proteins) due to applied mechanical stress. The electricity resulting from applied pressure is known as piezoelectricity. The word “piezo” derived from the Greek “piezein”, means to squeeze or press, and “electric” or “electron”, derived from “amber”, which is an ancient source of electric charge. Piezoelectricity was discovered in 1880 by French physicists Jacques and Pierre Curie (Anon [6]; Jacques and Curie [7]; Tingley [8]).

Piezoelectricity is the ability of some materials such as crystals and certain ceramics, to generate an electric potential in response to applied mechanical stress or heat (Jacques and Curie [7]; Pramethesth and Ankur [9]). However, piezoelectricity is not caused by a change in charge density on the surface, but by dipole density in the bulk. For example, a 1 cm^3 cube of quartz with 2kN of correctly applied force can produce a voltage of 12500 V (Jacques and Curie [10]). Mechanical compression or tension on a poled piezoelectric ceramic element changes the dipole moment, creating a voltage. Compression along the direction of polarization, or tension perpendicular to the direction of polarization, generates voltage of the same polarity as the poling voltage (Figure 1).

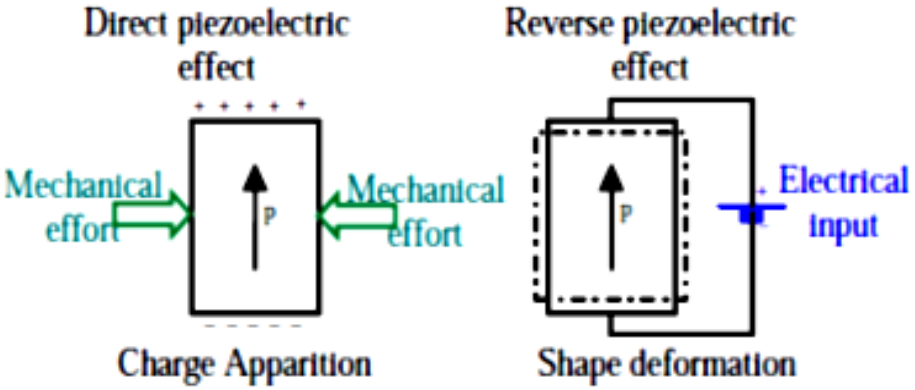

Fig. 1. *Working mechanism of simple piezo transducer (Anon [11]).*

VIBRATION MONITORING AND RECORDING INSTRUMENTS (SEISMOGRAPHS)

Many types of seismographs are available today. Each performs the basic function of measuring ground motion but supplies much additional information. Most seismographs are equipped with meters that register and hold the maximum value of the vibration components and the sound level. Other seismographs are equipped to produce a printout which gives a variety of information such as maximum value for each component, frequency of vibration for the maximum value, maximum displacement, maximum acceleration, vector sum, and sound level. Blast information such as date, blast number, time, location, job designation, and other pertinent information can also be added to the printout (Konya and Walter [12]).

SEISMIC ENERGY

The energy transferred into the strata in the form of seismic waves is calculated as the integral of the energy flow past a control surface at a given distance from the blast. The energy flux (power or rate of energy dissipated per unit area) is the scalar product of the stress at the surface and the particle velocity (Achenbach [13]). Calculations of seismic energy and its comparison with explosive energy have been reported by many researchers like Howell and Budenstein [14], Fogelson et al. [15], Berg and Cook [16], Nicholls [17], Atchinson [18], and more recently by Hinzen [19]. Berta [20] attempted to use some of the energy concepts in his principles of blast design, though this is seldom used in practice. The seismic energy dissipated by a ground vibration event at a given distance from blast site could be a critical component in assessing performance of blasts.

ASSESSMENT OF SEISMIC ENERGY

Ground Vibrations Monitoring

Intensity of ground vibrations generated due to blasting operations were monitored using 3 units of Minimate Plus, Instantel, Canada. These ground vibration monitors are of 8-Channeled instruments with six channels recording three mutually orthogonal ground vibration components, namely Transverse, Vertical and Longitudinal at two locations. The fourth and eighth channel records the noise level using microphone. Minimates with geophones and microphones connected are placed at different distances covering both short and long range distances, from the blast site. The vibration events were later transferred to a computer using advanced blastware software. Using the full wave forms, the seismic energy was estimated for all the signals in three directions, based on the principle that the area within the curve is ‘Seismic Energy Dissipated’ using DADiSP Signal Processing software. Care was taken to filter the noise.

DADiSP is a signal processing tool/software, using which shock energy dissipated in the form of waves is calculated. Longitudinal, transverse and vertical components of blast vibration events were imported from blastware software to digital signal processing software DADiSP in ASCII format. Fast Fourier transformation (FFT) was performed subsequently to find the frequency component of the time domain of blast wave signal as blast wave recorded by Minimate Plus and processed by Blastware falls in the category of random progressive signal. The estimation of absolute area describes the intrinsic energy of the blast wave signal distributed in various frequency bands. The energy of the signal x(t) is given by ∫_(-∞)^∞▒ 〖|x(t)|〗 2 dt (Sastry [21]).

FIELD INVESTIGATIONS AND RESULTS

Blasts were carried out in various mines for the extraction and assessment of seismic energy. Ground Vibration monitors were placed near blast field at various distances to find the impact of blast on nearby structures. Geophones were glued to the ground with the help of Plaster of Paris for proper contact. The piezo generator circuits were placed beside the conventional seismographs for maintaining accuracy in the obtained data. In total, 55 blasts were analyzed for the assessment of seismic energy based on electrical energy generation technique, out of which 10 blasts were carried out in Choutapalli limestone mine, 11 blasts were carried out in Yepalamadhavaram limestone mine and 34 blasts were carried out in coal mines of The Singareni Collieries Company Ltd. The following are some photographs depicting obtained electricity from undesirable seismic waves, extracted through piezo-gen circuit in various mine locations (Figure 2).

The various seismic data collected at various distances in different blasts were compared with the obtained electrical energy data as shown in Tables 1 and 2.

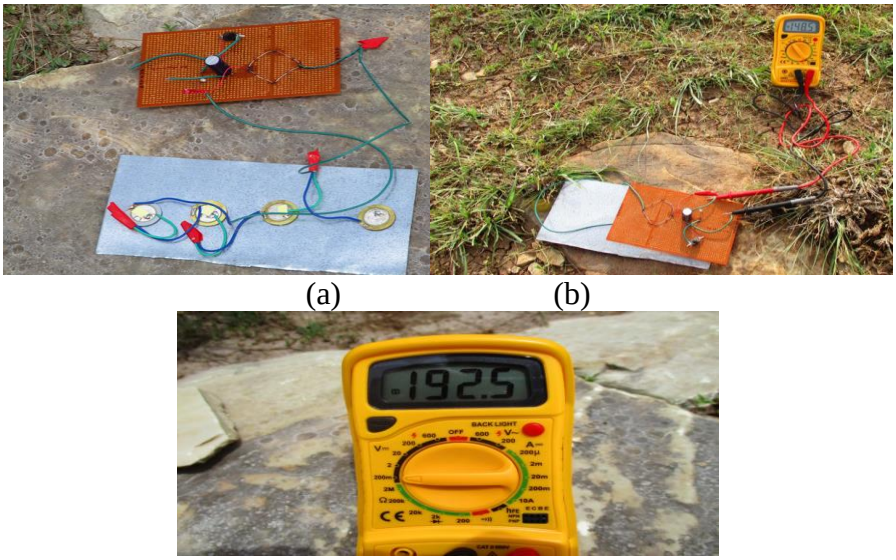

(a) (b)

(c)

Fig. 2. *(a) Piezo-Gen circuit. (b) Extraction of electricity using Piezo-Gen circuit from undesirable blast vibrations at limestone mine. (c) Observation of obtained voltage from the blast vibrations undesirable by multimeter for the assessment at limestone mine of seismic energy.*

Table 1. *Summary of seismic energy extracted as electricity from blasts conducted in limestone mines.*

Sl. no.	Distance (m)	MCD (kg)	PPV (mm/s)	Seismic energy from three mutually orthogonal ground vibrations (MJ)	Electrical energy extracted from blast vibrations (MJ)
1	30	38.33	64.4	42256215	4509139.6
2	40	38.33	39.2	18524598	1963630.3
3	45	38.33	37.5	17108152	1709115.6
4	50	38.33	26.3	6729443	299095.23
5	55	38.33	22.5	14013633	1526210.7
6	60	38.33	11.8	6377533	248069.74
7	40	37.5	55.6	26656654	2424915.1
8	50	37.5	35.6	11103330	1041516.2

9	55	37.5	29.3	5419536	234614.75
10	60	37.5	27.3	3903284	103863.11
11	65	37.5	26.4	18419851	1634399
12	65	37.5	22.7	7523677	460683.92
13	50	70.14	61	25837627	2571913.8
14	65	70.14	41.9	13666773	1407946
15	65	70.14	39.4	9824630	833789.96
16	70	70.14	32.5	2895806	64473.335
17	40	36.57	40	6548821	283286.87
18	50	36.57	30.1	4453486	123605.68
19	55	36.57	28.2	3232849	88722.367
20	70	36.57	16.1	712081	16118.334
21	75	36.57	10.4	964048	18693.452
22	80	36.57	3.43	306033	1931.3388
23	40	39.06	32.2	6893020	326396.26
24	50	39.06	28.2	6264554	243229.47
25	80	39.06	2.41	156568	95.374756
26	134	39.06	11.7	359719	3433.4912
27	40	39.28	171	59727766	7186831.2
28	50	39.28	181	99699604	11691266
29	55	39.28	68.8	27009086	3014047.3
30	75	39.28	10.3	2040307	40081.241
31	80	39.28	38.6	28970681	3120027.8
32	85	39.28	7.75	1901915	36266.251
33	50	51.4	118	21503717	2142627.3
34	60	51.4	126	111259278	13291238
35	65	51.4	91.4	58338415	6943699.5
36	90	51.4	38.1	5758561	262356.88
37	95	51.4	30.9	24691269	3269370.3
38	100	51.4	12.3	3366361	88722.367
39	30	24.58	44.7	23418621	2961119.1
40	38	24.58	42	38133182	4654974.8
41	50	24.58	23.7	9264400	633502.97
42	90	24.58	19.8	3331585	88722.367
43	95	24.58	18.4	4060162	110253.22
44	100	24.58	15	6492304	348280
45	40	14.35	34.8	3185760	80210.17
46	50	14.35	14.4	627148	13733.965
47	75	14.35	8.76	473566	8607.5717
48	80	14.35	8.13	240986	1168.3408
49	85	14.35	6.73	446799	6103.9844
50	40	30.36	34.4	12451737	1122775.5
51	50	30.36	23.1	8552912	550884.59
52	60	30.36	14.6	5350973	168241.07
53	70	30.36	11	1241977	24415.938
54	40	28.33	37.6	14565085	1699792.7
55	45	28.33	35.4	12675683	1164549.6
56	55	28.33	23.1	8573518	572844.63
57	70	28.33	15.5	4502870	137721.15

Typical sample event report and FFT reports generated from the blastware software (Figure 3). Seismic energy has obtained from the events recorded using signal processing tool, DADiSP. Sample of signal processing window is shown in Figure 4.

Table 2. *Summary of seismic energy extracted as electricity from blasts conducted in coal mine.*

Sl. no.	Distance (m)	MCD (kg)	PPV (mm/s)	Seismic Energy from three mutually orthogonal ground vibrations (MJ)	Electrical Energy Extracted from blast vibrations (MJ)
1	100	66	53.5	2738832.38	547766.476
2	110	66	33.8	1511665.32	151166.532
3	120	66	29.3	1470468.86	147046.886
4	150	66	18.92	6916156.65	4841309.66
5	160	66	17.4	5245447.1	3147268.26
6	170	66	17.3	8461652.43	7615487.19
7	184	50	5.33	1562458.55	1249966.84
8	178	88	22.61	9277651.8	7422121.44
9	188	88	20.2	4747405.68	2373702.84
10	200	88	17.9	366544.54	36654.454
11	292	88	4.06	376992.65	188496.325
12	150	85	19.81	10544797.7	10544797.7
13	209	85	10.7	2280225.67	456045.134
14	234	85	8.89	1055142.78	105514.278
15	295	85	3.3	134876.62	53950.648
16	696	450	3.56	513484.49	205393.796
17	719	450	1.52	136859.22	82115.532
18	750	450	1.52	171645.3	102987.18
19	800	450	1.02	1.836	1.836
20	603	460	7.11	1980472.55	594141.765
21	636	460	2.29	160142.93	112100.051
22	678	460	1.9	166647.59	66659.036
23	721	460	1.27	45698.08	45698.08
24	220	100	9.4	8769781.29	9646759.42
25	380	100	1.4	172599.58	172599.58
26	1591	1953	1.02	79583.75	79583.75
27	1856	1953	0.89	71031.38	71031.38
28	2033	1953	0.89	49481.5	49481.5
29	2121	1953	0.63	1.134	1.134
30	304	90	3.43	638174	638174
31	332	90	2.67	164876	98925.6
32	379	90	1.14	61901.33	111422.394
33	280	100	4.32	615873.463	123174.693
34	290	100	2.92	73406.109	44043.6654
35	300	100	2.03	402677.92	402677.92
36	440	100	1.27	108396.33	108396.33

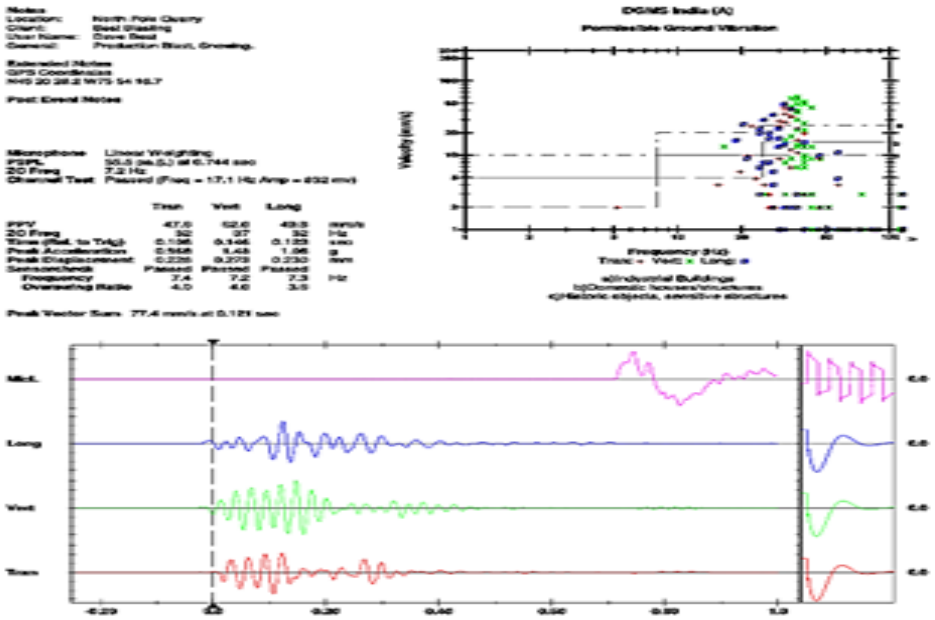

(a)

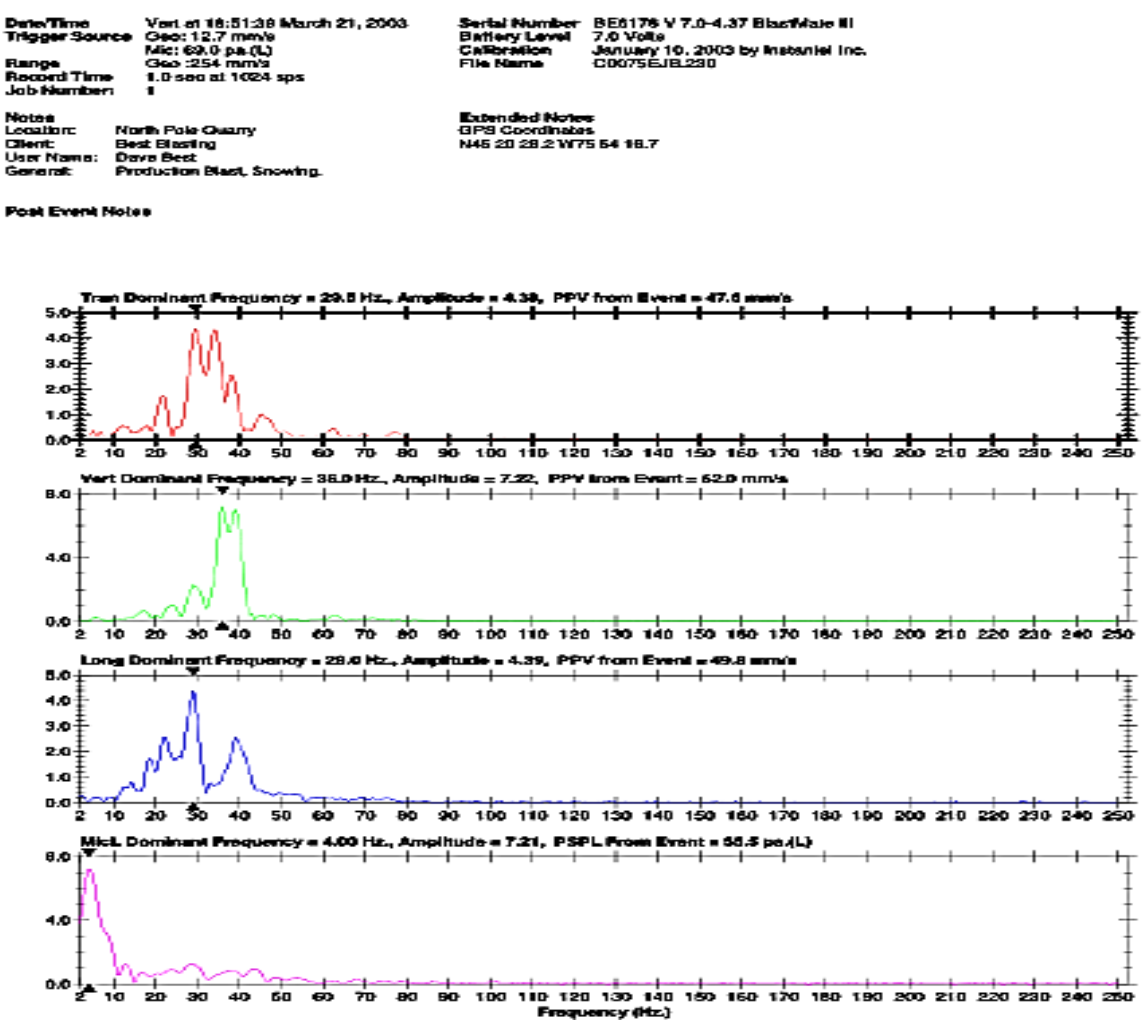

(b)

Fig. 3. *Screenshots of vibration events recorded by minimate plus. (a) Typical event report, (b) typical FFT report from blastware.*

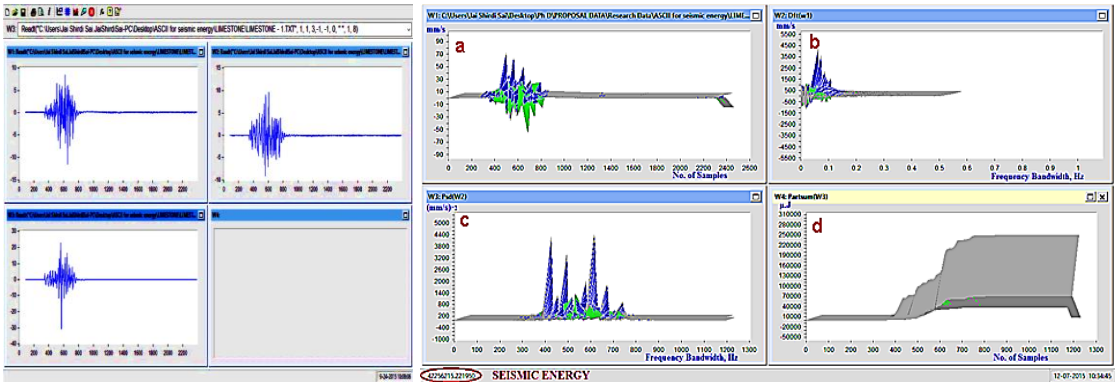

(a) (b)

Fig. 4. *Finding of shock energy dissipated using DADiSP. (a) Signal processing window, (b) estimation of seismic energy.*

Also, comparison of seismic energy with the generated electrical energy was made to observe the amount of undesirable vibrations which were converted to electricity (Figure 5). From the analysis, it was observed that amount of seismic energy extracted in the form of electricity is 80–90% of the total seismic energy in limestone mines and that is about 75–80% in the case of coal mines.

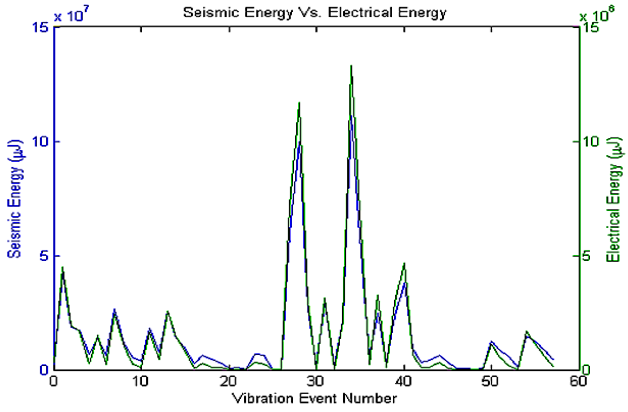

(a)

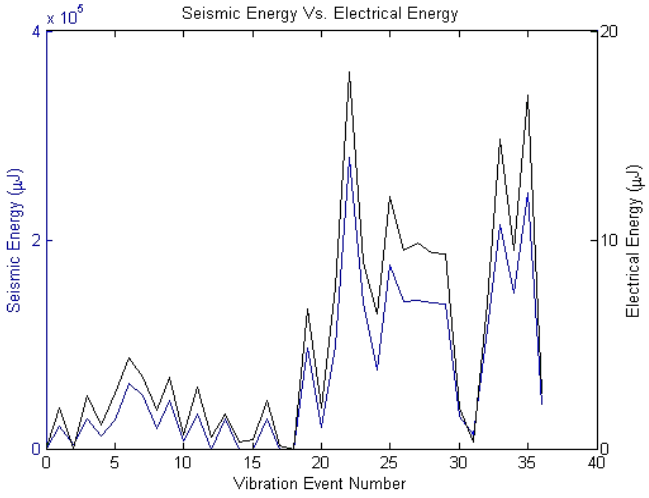

(b)

Fig. 5. *Amount of electrical energy extracted from blast induced vibrations with its corresponding seismic energy in various blasts. (a) In limestone mines, (b) in coal mine.*

CONCLUSIONS

Based on the study, the following conclusions are drawn:

- Studies indicated that the amount of seismic energy is increased with the increase in maximum charge per delay. Hence, the optimal usage of MCD improves the performance of blasts by reducing seismic energy loss and improving explosive energy utilization.
- Seismic waves in the form of ground vibrations induced due to blasts can be efficiently tapped and converted with the help of Piezo-Gen circuit into useful electrical energy.
- The amount of seismic energy obtained in case of limestone mines is higher than in coal mines.
- The Piezo-Gen circuit may become a renewable source for generation of electricity from ground vibrations caused by blasting operations and further will be more useful in assessing the seismic energy in blast field.

REFERENCES

[1] C.H. Johansson, P.A. Persson. *Detonics of High Explosives.* London: Academic Press; 1970.

[2] T.C. Atchison, W.I. Duvail, J.M. Pugliese. Effect of decoupling on explosion generated strain pulses in rock (USBM RI: 6333), 1964.

[3] H.R. Nicholls. Coupling explosive energy to rock, *J Geophys.* 1962; 27(3): 305–16p.

[4] V.R. Sastry. A study into the effect of some parameters on rock fragmentation by blasting, *PhD Thesis.* BHU, India, 1989.

[5] A. Sanchidrian Jose´, S. Pablo, L.M. Lopez. Energy components in rock blasting, *Int J Rock Mech Min Sci*. 2007; 44: 130–47p.

[6] Anon, 2015. All About Heven, web Site http://www.allaboutheaven.org/science /149/121/piezoelectricity. [Accessed August 28, 2015].

[7] J. Curie, P. Curie. On electric polarization in hemihedral crystals with inclined faces, 1880; 91: 383–6p.

[8] R. Tingley. Method and application of piezoelectric energy harvesting as a mobile power source, *Res Des Project.* 2013; New Hampshire.

[9] T. Pramethesth, S. Ankur. Piezoelectric crystals: future source of electricity, *Int J Sci Eng Technol.* 2013; 2(4): 260–2p.

[10] J. Curie, P. Curie. Contractions and expansions produced by voltages in hemihedral crystals with inclined faces, 1881; 93: 1137–40p.

[11] Anon, 2002. "Piezotronics", weblink https://en.wikipedia.org/wiki/Piezotronics. [Accessed Sept. 14, 2016].

[12] C.J. Konya, E.J. Walter. *Surface Blast Design*. USA: Prentice Hall Publishers; 1990.

[13] J.D. Achenbach. *Wave Propagation in Elastic Solids*. Amsterdam: Elesevier; 1975, 166p.

[14] B.F. Howell, D. Budenstein. Energy distribution in explosion generated seismic pulses, *Geophysics*. 1955; 20(1): 33–52p.

[15] D.E. Fogelson, T.C. Atchison, W.I. Duvall. Propagation of peak strain and strain energy for explosion-generated strain pulses in rock, In: *Proc. of the 3rd US Symp. on Rock Mechanics*. Colorado School of Mines, Golden, 1959, 271–84p.

[16] J.W. Berg, K.L. Cook. Energies, magnitudes and amplitudes of seismic waves from quarry blasts at Promontory and lakeside, Utah, *Seismol Soc Bull*. 1961; 51(3): 389–400p.

[17] H.R. Nicholls. Coupling explosive energy to rock, *Geophysics*. 1962; 27(3): 305–16p.

[18] T.C. Atchinson. Fragmentation principles, In: *Surf Mining*. E.P.

Pfleider, Ed., New York: The American Institute of Mining, Metallurgical and Petroleum Engineers; 1968, 355–72p.

[19] K.G. Hinzen. Comparison of seismic and explosive energy in five smooth blasting test rounds, *Int J Rock Mech Min Sci*. 1998; 35(7): 957–67p.

[20] G. Berta. *Lesplosivostrumento di Lavoro*. Milan: Italesplosivi; 1990, 31–64p.

[21] V.R. Sastry. *Assessment of Performance of Explosives/Blast Results Based on Explosive Energy Utilization.* Unpublished R&D Project Report, M/S Coal India Limited; 2014.

A hybrid artificial bee colony algorithm for the cooperative maximum covering location problem

International Journal of Machine Learning and Cybernetics

April 2017, Volume 8, Issue 2, pp 691–697 | Cite as

- B. Jayalakshmi (1)
- Alok Singh (1) Email author (alokcs@uohyd.ernet.in)

1. School of Computer and Information Sciences, University of Hyderabad, , Hyderabad, India

Original Article
First Online: 07 December 2015

Abstract

This paper proposes a hybrid artificial bee colony algorithm for the cooperative maximum covering location problem (CMCLP) on a network. In location covering problems, it is assumed that each facility generates a signal whose strength decreases with the increase in distance and a demand point is considered to be covered if the total signal strength received by it from various facilities exceeds a certain threshold. The objective of the CMCLP is to locate the facilities in such a way that maximizes the total demands covered. The proposed hybrid approach obtained better quality solutions in comparison to the methods available in the literature.

Acknowledgments

Authors would like to place on record their sincere thanks to Dr. Jörg Kalcsics for providing the CMCLP test instances and their solution values obtained by various approaches proposed in [1]. Authors are also grateful to two anonymous reviewers for their valuable comments and suggestions which helped in improving the quality of this manuscript.

References

1. Averbakh I, Berman O, Krass D, Kalcsics J, Nickel S (2014) Cooperative covering problems on networks. Networks 63(4):334–349
MathSciNet (http://www.ams.org/mathscinet-getitem?mr=3218450)
CrossRef (https://doi.org/10.1002/net.21549)
Google Scholar (http://scholar.google.com/scholar_lookup?title=Cooperative%20covering%20problems%20on%20networks&author=I.%20Averbakh&author=O.%20Berman&author=D.%20Krass&author=J.%20Kalcsics&author=S.%20Nickel&journal=Networks&volume=63&issue=4&pages=334-349&publication_year=2014)

2. Berman O (1994) The p maximal cover—p partial center problem on networks. Eur J Oper Res 72(2):432–442
MathSciNet (http://www.ams.org/mathscinet-getitem?mr=953621)
CrossRef (https://doi.org/10.1016/0377-2217(94)90321-2)
zbMATH (http://www.emis.de/MATH-item?0809.90092)
Google Scholar (http://scholar.google.com/scholar_lookup?title=The%20p%20maximal%20cover%E2%80%94p%20partial%20center%20problem%20on%20networks&author=O.%20Berman&journal=Eur%20J%20Oper%20Res&volume=72&issue=2&pages=432-442&publication_year=1994)

3. Berman O, Drezner Z, Krass D (2010) Cooperative cover location problems: the planar case. IIE Trans 42(3):232–246
CrossRef (https://doi.org/10.1080/07408170903394355)
Google Scholar (http://scholar.google.com/scholar_lookup?title=Cooperative%20cover%20location%20problems%3A%20the%20planar%20case&author=O.%20Berman&author=Z.%20Drezner&author=D.%20Krass&journal=IIE%20Trans&volume=42&issue=3&pages=232-246&publication_year=2010)

4. Berman O, Drezner Z, Krass D (2011) Discrete cooperative covering problems. J

Google Scholar (http://scholar.google.com/scholar_lookup?title=The%20maximal%20covering%20location%20problem&author=R.%20Church&author=C.%20ReVelle&journal=Pap%20Reg%20Sci%20Assoc&volume=32&issue=1&pages=101-118&publication_year=1974)

6. Drezner Z (1981) On a modified one-center model. Manag Sci 27(7):848–851
CrossRef (https://doi.org/10.1287/mnsc.27.7.848)
zbMATH (http://www.emis.de/MATH-item?0462.90027)
Google Scholar (http://scholar.google.com/scholar_lookup?title=On%20a%20modified%20one-center%20model&author=Z.%20Drezner&journal=Manag%20Sci&volume=27&issue=7&pages=848-851&publication_year=1981)

7. Drezner Z (1986) The p-cover problem. Eur J Oper Res 26(2):312–313
MathSciNet (http://www.ams.org/mathscinet-getitem?mr=852302)
CrossRef (https://doi.org/10.1016/0377-2217(86)90196-7)
zbMATH (http://www.emis.de/MATH-item?0597.90028)
Google Scholar (http://scholar.google.com/scholar_lookup?title=The%20p-cover%20problem&author=Z.%20Drezner&journal=Eur%20J%20Oper%20Res&volume=26&issue=2&pages=312-313&publication_year=1986)

8. Drezner Z, Suzuki A (2004) The big triangle small triangle method for the solution of nonconvex facility location problems. Oper Res 52(1):128–135
CrossRef (https://doi.org/10.1287/opre.1030.0077)
zbMATH (http://www.emis.de/MATH-item?1165.90552)
Google Scholar (http://scholar.google.com/scholar_lookup?title=The%20big%20triangle%20small%20triangle%20method%20for%20the%20solution%20of%20nonconvex%20facility%20location%20problems&author=Z.%20Drezner&author=A.%20Suzuki&journal=Oper%20Res&volume=52&issue=1&pages=128-135&publication_year=2004)

9. Drezner Z, Suzuki A (2010) Covering continuous demand in the plane. J Oper Res Soc 61(5):878–881
CrossRef (https://doi.org/10.1057/jors.2009.10)
zbMATH (http://www.emis.de/MATH-item?1193.90147)
Google Scholar (http://scholar.google.com/scholar_lookup?title=Covering%20continuous%20demand%20in%20the%20plane&author=Z.%20Drezner&author=A.%20Suzuki&journal=J%20Oper%20Res%20Soc&volume=61&issue=5&pages=878-881&publication_year=2010)

10. Karaboga D (2005) An idea based on honey bee swarm for numerical optimization. In: Technical report-TR06, Erciyes University, Engineering Faculty,

CrossRef (https://doi.org/10.1007/s10898-007-9149-x)
zbMATH (http://www.emis.de/MATH-item?1149.90186)
Google Scholar (http://scholar.google.com/scholar_lookup?title=A%20powerful%20and%20efficient%20algorithm%20for%20numerical%20function%20optimization%3A%20artificial%20bee%20colony%20%28ABC%29%20algorithm&author=D.%20Karaboga&author=B.%20Akay&journal=J%20Glob%20Optim&volume=39&issue=3&pages=459-471&publication_year=2007)

12. Karaboga D, Akay B (2008) On the performance of artificial bee colony (ABC) algorithm. Appl Soft Comput 8(1):687–697
CrossRef (https://doi.org/10.1016/j.asoc.2007.05.007)
Google Scholar (http://scholar.google.com/scholar_lookup?title=On%20the%20performance%20of%20artificial%20bee%20colony%20%28ABC%29%20algorithm&author=D.%20Karaboga&author=B.%20Akay&journal=Appl%20Soft%20Comput&volume=8&issue=1&pages=687-697&publication_year=2008)

13. Karaboga D, Akay B (2009) A comparative study of artificial bee colony algorithm. Appl Math Comput 214(1):108–132
MathSciNet (http://www.ams.org/mathscinet-getitem?mr=2541051)
zbMATH (http://www.emis.de/MATH-item?1169.65053)
Google Scholar (http://scholar.google.com/scholar_lookup?title=A%20comparative%20study%20of%20artificial%20bee%20colony%20algorithm&author=D.%20Karaboga&author=B.%20Akay&journal=Appl%20Math%20Comput&volume=214&issue=1&pages=108-132&publication_year=2009)

14. Karaboga D, Gorkemli B, Ozturk C, Karaboga N (2014) A comprehensive survey: artificial bee colony (ABC) algorithm and applications. Artif Intell Rev 42(1):21–57
CrossRef (https://doi.org/10.1007/s10462-012-9328-0)
Google Scholar (http://scholar.google.com/scholar_lookup?title=A%20comprehensive%20survey%3A%20artificial%20bee%20colony%20%28ABC%29%20algorithm%20and%20applications&author=D.%20Karaboga&author=B.%20Gorkemli&author=C.%20Ozturk&author=N.%20Karaboga&journal=Artif%20Intell%20Rev&volume=42&issue=1&pages=21-57&publication_year=2014)

15. Pan QK, Tasgetiren MF, Suganthan P, Chua T (2011) A discrete artificial bee colony algorithm for the lot-streaming flow shop scheduling problem. Inf Sci 181(12):2455–2468
MathSciNet (http://www.ams.org/mathscinet-getitem?mr=2784709)
CrossRef (https://doi.org/10.1016/j.ins.2009.12.025)
Google Scholar (http://scholar.google.com/scholar_lookup?

Google Scholar (http://scholar.google.com/scholar_lookup?title=The%20maximum%20capture%20or%20sphere%20of%20influence%20location%20problem%3A%20Hotelling%20revisited%20on%20a%20network&author=C.%20ReVelle&journal=J%20Reg%20Sci&volume=26&issue=2&pages=343-358&publication_year=1986)

17. Singh A (2009) An artificial bee colony algorithm for the leaf-constrained minimum spanning tree problem. Appl Soft Comput 9(2):625–631
CrossRef (https://doi.org/10.1016/j.asoc.2008.09.001)
Google Scholar (http://scholar.google.com/scholar_lookup?title=An%20artificial%20bee%20colony%20algorithm%20for%20the%20leaf-constrained%20minimum%20spanning%20tree%20problem&author=A.%20Singh&journal=Appl%20Soft%20Comput&volume=9&issue=2&pages=625-631&publication_year=2009)

18. Singh A, Sundar S (2011) An artificial bee colony algorithm for the minimum routing cost spanning tree problem. Soft Comput 15(12):2489–2499
CrossRef (https://doi.org/10.1007/s00500-011-0711-6)
Google Scholar (http://scholar.google.com/scholar_lookup?title=An%20artificial%20bee%20colony%20algorithm%20for%20the%20minimum%20routing%20cost%20spanning%20tree%20problem&author=A.%20Singh&author=S.%20Sundar&journal=Soft%20Comput&volume=15&issue=12&pages=2489-2499&publication_year=2011)

19. Suzuki A, Drezner Z (1996) The p-center location problem in an area. Locat Sci 4(1–2):69–82
CrossRef (https://doi.org/10.1016/S0966-8349(96)00012-5)
zbMATH (http://www.emis.de/MATH-item?0917.90233)
Google Scholar (http://scholar.google.com/scholar_lookup?title=The%20p-center%20location%20problem%20in%20an%20area&author=A.%20Suzuki&author=Z.%20Drezner&journal=Locat%20Sci&volume=4&issue=1%E2%80%932&pages=69-82&publication_year=1996)

20. Watson-Gandy C (1982) Heuristic procedures for the m-partial cover problem on a plane. Eur J Oper Res 11(2):149–157
CrossRef (https://doi.org/10.1016/0377-2217(82)90109-6)
zbMATH (http://www.emis.de/MATH-item?0495.52009)
Google Scholar (http://scholar.google.com/scholar_lookup?title=Heuristic%20procedures%20for%20the%20m-partial%20cover%20problem%20on%20a%20plane&author=C.%20Watson-Gandy&journal=Eur%20J%20Oper%20Res&volume=11&issue=2&pages=149-157&publication_year=1982)

Jayalakshmi, B. & Singh, A. Int. J. Mach. Learn. & Cyber. (2017) 8: 691. https://doi.org/10.1007/s13042-015-0466-y

- Received 27 July 2015
- Accepted 25 November 2015
- First Online 07 December 2015
- DOI https://doi.org/10.1007/s13042-015-0466-y
- Publisher Name Springer Berlin Heidelberg
- Print ISSN 1868-8071
- Online ISSN 1868-808X

- About this journal
- Reprints and Permissions

Personalised recommendations

Imperial Journal of Interdisciplinary Research (IJIR)
Vol-3, Issue-7, 2017
ISSN: 2454-1362, http://www.onlinejournal.in

Implementation of Adaptive Power Oscillation Damping Controller by STATCOM with Energy Storage

Ramesh Jatoth
Assistant Professor
EEE department, Methodist College of Engineering & Technology

Abstract: This *paper deals with the design of an adaptive power oscillation damping (POD) controller for a static synchronous compensator (STATCOM) equipped with energy storage. This is achieved using a signal estimation technique based on a modified recursive least square (RLS) algorithm, which allows a fast, selective, and adaptive estimation of the low-frequency electromechanical oscillations from locally measured signals during power system disturbances. The proposed method is effective in increasing the damping of the system at the frequencies of interest, also in the case of system parameter uncertainties and at various connection points of the compensator. First, the analysis of the impact of active and reactive power injection into the power system will be carried out using a simple two-machine system model. A control strategy that optimizes active and reactive power injection at various connection points of the STATCOM will be derived using the simplified model. Small-signal analysis of the dynamic performance of the proposed control strategy will be carried out. The effectiveness of the proposed control method to provide power oscillation damping irrespective of the connection point of the device and in the presence of system parameter uncertainties will be verified through simulation and experimental results.*

Index Terms—Energy storage, low-frequency oscillation, power oscillation damping (POD), recursive least square (RLS), static synchronous compensator (STATCOM).

I.INTRODUCTION

A D-STATCOM (Distribution Static Compensator), which is schematically depicted in Figure, consists of a two-level Voltage Source Converter (VSC), a dc energy storage device, a coupling transformer connected in shunt to the distribution network through a coupling transformer. The VSC converts the dc voltage across the storage device into a set of three-phase ac output voltages. These voltages are in phase and coupled with the ac system through the reactance of the coupling transformer. Suitable adjustment of the phase and magnitude of the D-STATCOM output voltages allows effective control of active and reactive power exchanges between the D-STATCOM and the ac system. Such configuration allows the device to absorb or generate controllable active and reactive power.

The VSC connected in shunt with the ac system provides a multifunctional topology which can be used for up to three quite distinct purposes:

1. Voltage regulation and compensation of reactive power;
2. Correction of power factor; and
3. Elimination of current harmonics.

Here, such device is employed to provide continuous voltage regulation using an indirectly controlled converter.

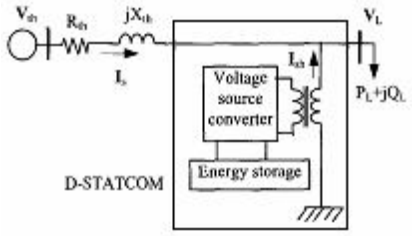

Figure- the shunt injected current I_{sh} corrects the voltage sag by adjusting the voltage drop across the system impedance Z_{th}. The value of I_{sh} can be controlled by adjusting the output voltage of the converter.

The shunt injected current I_{sh} can be written as,

$$I_{sh} = I_L - I_s = I_L - \frac{V_{Th} - V_L}{Z_{Th}}$$

$$I_{sh}\angle\eta = I_L\angle -\theta - \frac{V_{th}}{Z_{th}}\angle(\delta-\beta) + \frac{V_L}{Z_{th}}\angle -\beta$$

The complex power injection of the D-STATCOM can be expressed as,

$$S_{sh} = V_L I_{sh}^*$$

It may be mentioned that the effectiveness of the D-STATCOM in correcting voltage sag depends on the value of Z_{th} or fault level of the load bus. When the shunt injected current I_{sh} is kept in quadrature with $V_{L,}$ the desired voltage correction can be achieved without injecting any active power into the system. On the other hand, when the value of I_{sh} is minimized, the same voltage correction can be achieved with minimum apparent power injection into the system. The control scheme for the D-STATCOM follows the same principle as for DVR. The switching frequency is set at 475 Hz.

Figure shows the test system used to carry out the various D-STATCOM simulations.

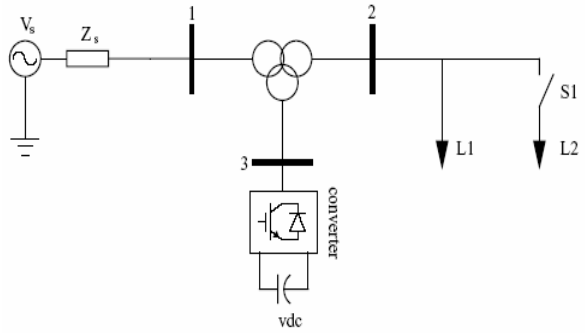

Fig. Single line diagram of the test system for D-STATCOM.

In this paper, a control strategy for the E-STATCOM when used for POD will be investigated. Thanks to the selected local signal quantities measured in the system, the control strategy optimizes the injection of active and reactive power to provide uniform damping at various locations in the power system. It will be shown that the implemented control algorithm is robust against system parameter uncertainties. For this, a modified recursive least square (RLS)-based estimation algorithm as described in [13], [14] will be used to extract the required control signals from locally measured signals. Finally, the effectiveness of the proposed control strategy will be validated via simulation and experimental verification.

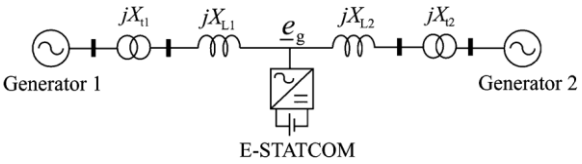

Fig. 1. Simplified two-machine system with E-STATCOM.

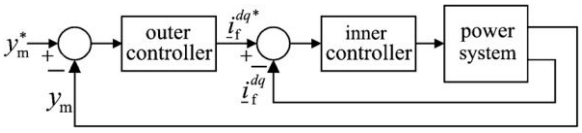

Fig. 2. Block diagram of the control of E-STATCOM

II.SYSTEM MODELING FOR CONTROLLER DESIGN

A simplified power system model, such as the one depicted in Fig. 1, is used to study the impact of the E-STATCOM on the power system dynamics. The investigated system approximates an aggregate model of a two-area power system, where each area is represented by a synchronous generator.

The synchronous generators are modeled as voltage sources of constant magnitude (Vg1,Vg2) nd dynamic rotor angles behind a transient reactance(X'd1,X'd2) . The transmission system consists of two transformers represented by their equivalent leakage reactance (Xt1,Xt2) and a transmission line with equivalent reactance (XL=XL1+XL2) The losses in the transmission system are neglected for simpler analytical expressions. If the mechanical damping in the generators is neglected, the overall damping for the investigated system is equal to zero. Therefore, the model is appropriate to allow a conservative approach of the impact of the E-STATCOM when used for stability studies [14]. For analysis purpose, the electrical connection point of the converter along the transmission line is expressed by the parameter as

$$a = \frac{X_1}{(X_1 + X_2)} \quad (1)$$

where

$$X_1 = X'_{d1} + X_{t1} + X_{L1}$$
$$X_2 = X'_{d2} + X_{t2} + X_{L2.}$$

The control of the E-STATCOM consists of an outer control loop and an inner current control loop, as shown in Fig. 2. The outer control loop, which can be an ac voltage, dc-link voltage or POD controller, sets the reference current for the inner

current controller. The generic measured signal Ym depends on the type of outer loop control. The control algorithm is implemented in dq -reference frame where a phase-locked loop (PLL) [15] is used to track the grid-voltage angle θg from the grid-voltage vector . By synchronizing the PLL with the grid-voltage vector, the - and -components of the injected current (and) control the injected active and reactive power respectively. In the notation in Fig. 2, the superscript "* " denotes the corresponding reference signals.

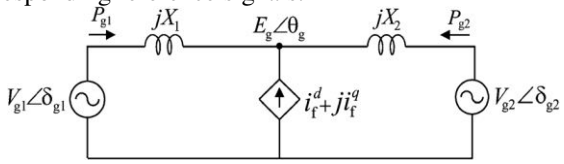

Fig. 3. Equivalent circuit for two-machine system with E-STATCOM

In this paper, the outer control loop is assumed to be a POD controller, and the detail of the block will be described in Section III. For this reason, we assume that the injected active and reactive powers in the steady state are zero. When designing a cascaded controller, the speed of outer control loop is typically selected to be much slower than the inner one to guarantee stability. This means that the current controller can be considered infinitely fast when designing the parameters of the outer controller loop. Therefore, the E-STATCOM can be modeled as a controlled ideal current source, as depicted in the equivalent circuit in Fig. 3, for analysis purpose.

The level of power oscillation damping provided by the converter depends on how much the active power output from the generators is modulated by the injected current, . For the system in Fig. 3, the change in active power output from the generators due to injected active and reactive power from the E-STATCOM is calculated as in

$$\begin{aligned}
&\Delta P_{g1,P} \approx -\Gamma_P P_{inj}, \quad \Delta P_{g2,P} \approx -(1-\Gamma_P)P_{inj} \\
&\Delta P_{g1,Q} \approx \left[\frac{V_{g1}V_{g2}\sin(\delta_{g10}-\delta_{g20})a(1-a)}{E_{g0}^2}\right] Q_{inj} \\
&\Delta P_{g2,Q} \approx -\left[\frac{V_{g1}V_{g2}\sin(\delta_{g10}-\delta_{g20})a(1-a)}{E_{g0}^2}\right] Q_{inj} \qquad (2)
\end{aligned}$$

where $(\Delta P_{g1,P}, \Delta P_{g2,P})$ and $(\Delta P_{g1,Q}, \Delta P_{g2,Q})$ represent the change in active power from the corresponding generators due to injected active power (P_{inj}) and reactive power (Q_{inj}), respectively. Γ_P, P_{inj}, and Q_{inj} are given by

$$\begin{aligned}
\Gamma_P &= \frac{\left([(1-a)V_{g1}]^2 + a(1-a)V_{g1}V_{g2}\cos(\delta_{g10}-\delta_{g20})\right)}{E_{g0}^2} \\
P_{inj} &\approx E_{g0} i_f^d \\
Q_{inj} &\approx -E_{g0} i_f^q. \qquad (3)
\end{aligned}$$

The initial steady-state PCC voltage magnitude Eg0 and generator rotor angles (δg10,δg20) correspond to the operating point.

It can be seen from (2) and (3) that the change in active power output from the generators depends on the location of the converter as well as on the amount of injected active and reactive power. Moreover, it can be understood from (2) that the effect of reactive power injection depends on the magnitude and direction of transmitted power from the generators.

III.POD CONTROLLER DESIGN

The derivation of the POD controller from locally measured signals will be made in this section.

A. Derivation of Control Input Signals

Considering the simplified two-machine system in Fig. 1, the active power output from each generator should change in proportion to the change in its speed to provide damping [9]. From (2), it can be observed that the effect of the power injected by the compensator on the generator active power output highly depends on the parameter , i.e., on the location of the E-STATCOM. Using the equivalent system in Fig. 3, a control input signal that contains information on the speed variation of the generators can be derived. When the E-STATCOM is not injecting any current, the variation of the locally measured signals,
Θg and Ptran at different E-STATCOM connection points using the dynamic generator rotor angles δg1 and δg2 is given by

$$\theta_g = \delta_{g2} + \tan^{-1}\left[\frac{(1-a)V_{g1}\sin(\delta_{g1}-\delta_{g2})}{(1-a)V_{g1}\cos(\delta_{g1}-\delta_{g2})+aV_{g2}}\right] \qquad (4)$$

$$P_{tran} = \frac{V_{g1}V_{g2}\sin(\delta_{g1}-\delta_{g2})}{X_1+X_2}. \qquad (5)$$

From a small-signal point of view and under the assumption that the PCC-voltage magnitude along the lineEg does not change significantly, the required control input signals can be derived from the PCC-voltage phase and transmitted active power as [14]

$$\frac{d\theta_g}{dt} \approx \Gamma_P\omega_{g0}\Delta\omega_{g1} + (1-\Gamma_P)\omega_{g0}\Delta\omega_{g2} \qquad (6)$$

$$\frac{dP_{tran}}{dt} \approx \left\{\frac{V_{g1}V_{g2}\cos(\delta_{g10}-\delta_{g20})}{X_1+X_2}\right\}\omega_{g0}[\Delta\omega_{g1}-\Delta\omega_{g2}] \qquad (7)$$

where the constantΓp has been defined in the previous section. The nominal system frequency is represented byWgo whereas ΔWg1andΔWg2 represent the speed variation of the generators in p.u.

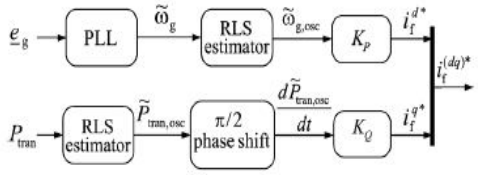

Fig. 4. Block diagram of the POD controller

B. Estimation of Control Input Signals

As described in the Introduction, effective power oscillation damping for various power system operating points and E-STATCOM locations require fast, accurate, and adaptive estimation of the critical power oscillation frequency component. This is achieved by the use of an estimation method based on a modified RLS algorithm. For reasons described in the previous subsection, the derivative of the PCC-voltage phase and the transmitted power should be estimated for controlling the active and reactive power injection, respectively.

IV. STABILITY ANALYSIS OF SYSTEM MODEL

The mathematical model of the system in Fig. 3 is developed in this section to investigate the performance of the POD controller using active and reactive power injection. Using the expressions in (6)–(7) for and , the injected currents are controlled as

$$i_f^d \approx K_P \omega_{g0} \left[\Gamma_P \Delta\omega_{g1} + (1-\Gamma_P)\Delta\omega_{g2}\right] \quad (\text{illegible})$$

$$i_f^q \approx K_Q \omega_{g0} \left\{\frac{V_{g1}V_{g2}\cos(\delta_{g10}-\delta_{g20})}{X_1+X_2}\right\} [\Delta\omega_{g1} - \Delta\omega_{g2} \quad (\text{illegible})$$

where the constant is Γp as defined in (3). Linearizing around an initial steady-state operating point, the small-signal dynamic model of the two-machine system with the E-STATCOM in per unit is developed as in

$$\frac{d}{dt}\begin{bmatrix}\Delta\omega_{g1}\\ \Delta\delta_{g12}\\ \Delta\omega_{g2}\end{bmatrix} = \begin{bmatrix}\beta_{11} & \beta_{12} & \beta_{13}\\ \omega_{g0} & 0 & -\omega_{g0}\\ \beta_{31} & \beta_{32} & \beta_{33}\end{bmatrix}\begin{bmatrix}\Delta\omega_{g1}\\ \Delta\delta_{g12}\\ \Delta\omega_{g2}\end{bmatrix} + \begin{bmatrix}\frac{1}{2H_{g1}} & 0\\ 0 & 0\\ 0 & \frac{1}{2H_{g2}}\end{bmatrix}\begin{bmatrix}\Delta T_{m1}\\ \Delta T_{m2}\end{bmatrix}$$

where representsΔδ12=Δδ1-Δδ2 the rotor angle difference between the two generators and other signals as defined previously. Assuming no mechanical damping and the initial steady-state speed of the generators set to Wg0 , the constants are derived as in

$$\begin{bmatrix}\beta_{11}\\ \beta_{12}\\ \beta_{13}\\ \beta_{31}\\ \beta_{32}\\ \beta_{33}\end{bmatrix} = \begin{bmatrix}\frac{\omega_{g0}\left(K_P E_{g0}\Gamma_P^2 + K_Q\Gamma_Q\right)}{2H_{g1}}\\ -\frac{V_{g1}V_{g2}\cos(\delta_{g10}-\delta_{g20})}{2H_{g1}(X_1+X_2)}\\ \frac{\omega_{g0}(K_P E_{g0}\Gamma_P(1-\Gamma_P)-K_Q\Gamma_Q)}{2H_{g1}}\\ \frac{\omega_{g0}(K_P E_{g0}\Gamma_P(1-\Gamma_P)-K_Q\Gamma_Q)}{2H_{g2}}\\ \frac{V_{g1}V_{g2}\cos(\delta_{g10}-\delta_{g20})}{2H_{g2}(X_1+X_2)}\\ \frac{\omega_{g0}\left(K_P E_{g0}(1-\Gamma_P)^2 + K_Q\Gamma_Q\right)}{2H_{g2}}\end{bmatrix}$$

where Γ_Q is given by

$$\Gamma_Q = \frac{[V_{g1}V_{g2}]^2 \sin\left(2(\delta_{g10}-\delta_{g20})\right) a(1-a)}{2E_{g0}(X_1+X_2)}.$$

The termsβ12 and β32 represent the synchronizing torque coefficients resulting from the selected operating point and the contribution of the E-STATCOM is zero. The termsβ11 and β33 determine the damping torque coefficient provided by the E-STATCOM with respect to the change in speed of the respective generator. To provide positive damping,

As an example for the analysis in this section, a hypothetical 20/230 kV, 900 MVA transmission system similar to the one in Fig. 1 with a total series reactance of 1.665 p.u. and inertia constant of the generatorsHg1=Hg2=6.5 s is considered. The leakage reactance of the transformers and transient impedance of the generators are 0.15 p.u. and 0.3 p.u., respectively. The movement of the poles for the system as a function of the E-STATCOM location is shown in Fig. 6.With the described control strategy, injected active power is zero at the point where the effect of active power injection on damping is zero. This is at the electrical midpoint of the line. On the other hand, at the same location damping by reactive power injection is maximum. The reverse happens at either end of the generators.

V. SIMULATION RESULTS

The POD controller described in Section III is here verified via PSCAD/EMTDC simulation using the well-known two-area four-machine system in Fig. 7. The implemented system is rated 20/230 kV, 900 MVA and the parameters for the generators and transmission system together with the loading of the system are given in detail in [9]. The system is initially operating in SteadyState with a transmitted active power Ptran= 400 MW from area 1 to area 2.

A three-phase fault is applied to the system on one of the transmission lines between bus 7 and bus 8. The fault
is cleared after 120 ms by disconnecting the faulted line. Due to the applied disturbance, a poorly damped oscillation is obtained after the fault clearing.

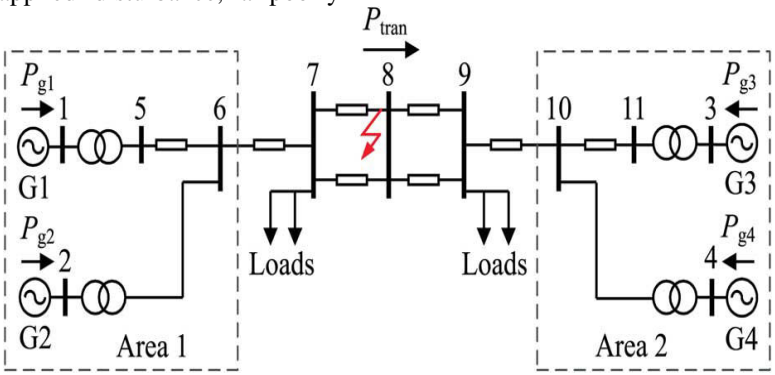

Fig. 7. Simplified two-area four machine power system

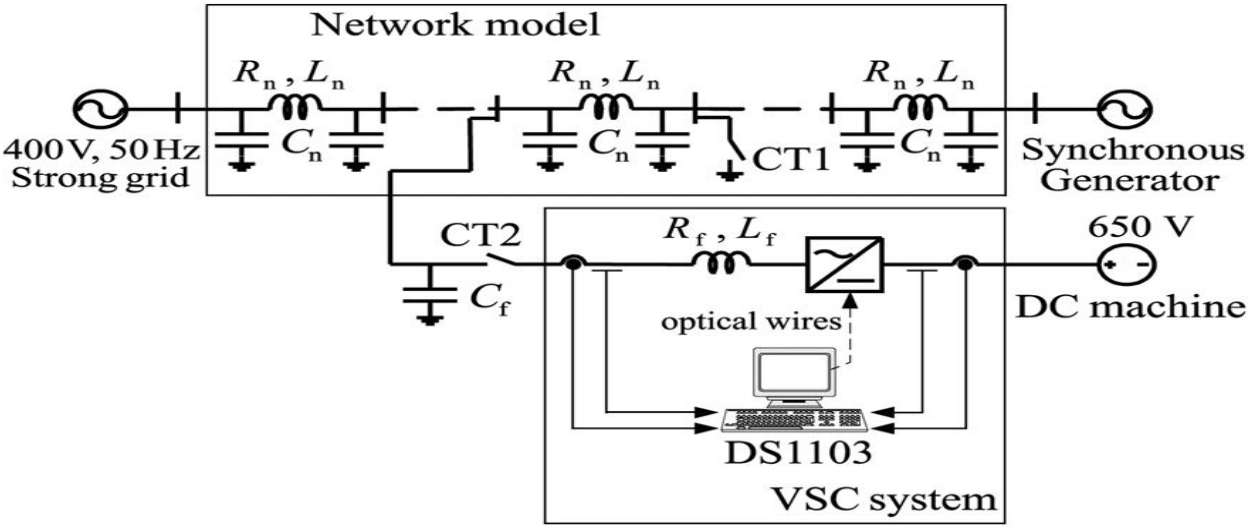

Fig. 9. Single-line diagram of the laboratory setup.

With the POD controller structure described in Fig. 4, the performance of the E-STATCOM following the fault at three different locations is shown in Fig. 8. As described in the small-signal analysis for two-machine system in Section IV, when moving closer to the generator units, a better damping is achieved by active power injection (see Fig. 8, black solid plots). With respect to reactive power injection, maximum damping action is provided when the E-STATCOM is connected close to the electrical midpoint of the line and the level of damping decreases when moving away from it (see Fig. 8, gray solid plots). Because of a good choice of signals for controlling both active and reactive power injection, effective power oscillation damping is provided by the E-STATCOM irrespective of its location in the line (see Fig. 8, black dashed plots).

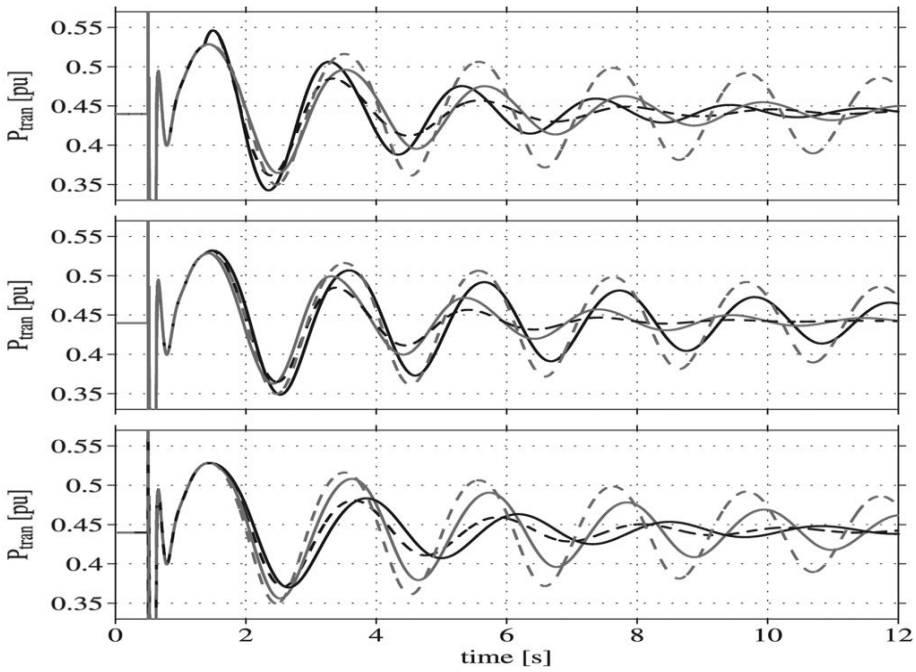

Fig. 8. Measured transmitted active power output following a three-phase fault with E-STATCOMconnected at bus 7 (top), bus 8 (middle), and bus 9 (bottom).

VI. CONCLUSION

An adaptive POD controller by E-STATCOM has been developed in this paper. For this, a modified RLS algorithm has been used for estimation of the low-frequency electromechanical oscillation components from locally measured signals during power system disturbances. The estimator enables a fast, selective and adaptive estimation of signal components at the power oscillation frequency. The dynamic performance of the POD controller to provide effective damping at various connection points of the E-STATCOM has been validated through simulation as well as experimental verification. The robustness of the control algorithm against system parameter changes has also been proven through experimental tests. Furthermore, using the frequency variation at the E-STATCOM connection point as the input signal for the active power modulation, it has been shown that active power injection is minimized at points in the power system where its impact on POD is negligible.

This results in an optimal use of the available energy source

REFERENCES

[1] N. G. Hingorani and L. Gyugyi, *Understanding FACTS. Concepts and Technology of Flexible AC Transmission Systems*. NewYork,NY, USA: IEEE, 2000.

[2] G. Cao, Z. Y. Dong, Y. Wang, P. Zhang, and Y. T. Oh, "VSC based STATCOM controller for damping multi-mode oscillations," in *Proc. IEEE Power and Energy Soc. General Meeting—Conversion and Delivery of Electrical Energy in the 21st Century*, Jul. 2008, pp. 1–8.

[3] M. Zarghami and M. L. Crow, "Damping inter-area oscillations in power systems by STATCOMs," in *Proc. 40th North Amer. Power Symp.*, Sep. 2008, pp. 1–6.

[4] Z. Yang, C. Shen, L. Zhang,M. L. Crow, and S. Atcitty, "Integration of a statcom and battery energy storage," *IEEE Trans. Power Syst.*, vol. 16, no. 2, pp. 254–260, May 2001.

[5] A. Arulampalam, J. B. Ekanayake, and N. Jenkins, "Application study of a STATCOM with energy storage," *Proc. Inst. Electr. Eng.—Gener., Transm. and Distrib.*, vol. 150, pp. 373–384, July 2003.

[6] N. Wade, P. Taylor, P. Lang, and J. Svensson, "Energy storage for power flow management and voltage control on an 11 kV UK distribution network," Prague, Czech Republic, CIRED paper 0824, Jun. 2009.

[7] A. Adamczyk, R. Teodorescu, and P. Rodriguez, "Control of full-scale converter based wind power plants for damping of low frequency system oscillations," in *Proc. IEEE PowerTech*, Trondheim, Norway, Jun. 2011, pp. 1–7.

[8] H. Xie, "On power-system benefits, main-circuit design, control of Statcoms with energy storage," Ph.D. dissertation, Dept. Electr. Energy Conversion, Royal Inst. Technol., Stockholm, Sweden, 2009.

[9] P. Kundur, *Power System Stability and Control*. New York, NY, USA: McGraw-Hill, 1994.
[10] K. Kobayashi, M. Goto, K. Wu, Y. Yokomizu, and T. Matsumura, "Power system stability improvement by energy storage type STATCOM," in *Proc. IEEE Power Tech Conf.*, Bologna, Italy, Jun.
2003, vol. 2, DOI 10.1109/PTC.2003.1304302.
[11] L. Zhang and Y. Liu, "Bulk power system low frequency oscillation suppression by FACTS/ESS," in *Proc. IEEE PES Power Syst. Conf. Exp.*, Oct. 2004, pp. 219–226.
[12] A. Arsoy, L. Yilu, P. F. Ribeiro, and F. Wang, "Power converter and SMES in controlling power system dynamics," in *Proc. Ind. Appl. Conf.*, Oct. 2000, vol. 4, pp. 2051–2057.
[13] M. Beza and M. Bongiorno, "A fast estimation algorithm for low-frequency oscillations in power systems," in *Proc. 14th Eur. Conf. Power Electron. Appl.*, Sep. 2011, pp. 1–10.
[14] M. Beza, "Control of energy storage equipped shunt-connected converter for electric power system stability enhancement," Licentiate Thesis, Dept. Energy and Environment, Chalmers Univ. of Technol., Gothenburg, Sweden, 2012, .
[15] L. Ängquist and M. Bongiorno, "Auto-normalizing phase-locked loop for grid-connected converters," in *Proc. IEEE Energy Conv. Congress Expo.*, Sep. 2009, pp. 2957–2964.
[16] M. Gustafsson and N. Krantz, "Voltage collapse in power systems," Licentiate thesis, Dept. Electr. Power Eng., Chalmers Univ. of Technol., Gothenburg, Sweden, Dec. 1995.

Int. J. Mach. Learn. & Cyber.
DOI 10.1007/s13042-015-0466-y

ORIGINAL ARTICLE

A hybrid artificial bee colony algorithm for the cooperative maximum covering location problem

B. Jayalakshmi[1] · **Alok Singh**[1]

Received: 27 July 2015 / Accepted: 25 November 2015

Abstract This paper proposes a hybrid artificial bee colony algorithm for the cooperative maximum covering location problem (CMCLP) on a network. In location covering problems, it is assumed that each facility generates a signal whose strength decreases with the increase in distance and a demand point is considered to be covered if the total signal strength received by it from various facilities exceeds a certain threshold. The objective of the CMCLP is to locate the facilities in such a way that maximizes the total demands covered. The proposed hybrid approach obtained better quality solutions in comparison to the methods available in the literature.

Keywords Artificial bee colony algorithm · Cooperative maximum covering location problem · Heuristic · Networks · Swarm intelligence.

1 Introduction

The cooperative maximum covering location problem (CMCLP) was introduced by [3]. In this problem, it is assumed that each facility generates a signal whose strength decreases over distance, according to some signal strength function. A demand point receives the signals from all the facilities and it is considered as covered, if the strength of the combined signal received by it from all the facilities exceeds a certain threshold. Hence, the CMCLP follows a cooperative coverage model, where all the facilities cooperate in providing the coverage. This coverage model differs from the one used in classical maximum covering location problem (MCLP) introduced by [5], where the signal received from the single closest facility determines whether a demand point is covered or not, thus it is referred as individual coverage model.

The individual coverage model may not always be appropriate as it may result in poor quality of solutions by underestimating the coverage provided by the group of facilities together. This will obviously result in deployment of more number of resources than actually needed. In fact, it was shown in [3], that the solution resulting from considering individual coverage only can be around twice as worse as the solution resulting from considering cooperative coverage.

Signal can be physical or non-physical. Physical signal such as radio signal propagates along the straight line path between two points, whereas a non-physical signal may not. An example of a non-physical signal is the service time of an ambulance to reach a particular point from its rest location. Rather than traveling on a straight line path, an ambulance has to make use of the road network to reach the desired point from its rest position.

The potential application for cooperative cover problems include situations, where the facilities are generally unreliable and the customer needs to be covered by multiple facilities in order to ensure a satisfactory coverage. Another application of cooperative cover includes models assuming partial coverage by the facilities, i.e., a single facility is not sufficient to provide the required coverage to any customer.

Application of both signal types, physical and non-physical, of the cooperative coverage models have been

✉ Alok Singh
alokcs@uohyd.ernet.in

B. Jayalakshmi
bjayalakshmi@uohyd.ac.in

[1] School of Computer and Information Sciences, University of Hyderabad, Hyderabad 500 046, India

Published online: 07 December 2015

discussed by [3]. For example, application such as, installation of light towers to provide adequate lighting to an area, location of warning sirens and location of cell phone towers belong to physical signal class. The main aspect of the physical signal class of cooperative cover models is—strength of the signal received by a particular demand point is the combined signal strength from all the facilities. In case of installation of light towers, a demand point is covered if the luminous intensity at that point exceeds a certain threshold value. Similarly, in case of installation of warning sirens, a demand point is covered if the intensity of the sound at that point exceeds a certain threshold. In case of location of cell towers, the demand point (mobile phone user) is considered as covered if the probability of establishing a successful connection exceeds a certain threshold value. On the other hand, applications such as emergency response system design, belong to non-physical signal class. In such systems, having a single facility within the coverage of demand point is not sufficient, to ensure the coverage all the time, because it may become busy at some point. To deal with these types of issues, the demand point must be within the coverage radius of several facilities.

Averbakh et al. [1] provided a practical example for cooperative coverage model on a network in the context of "Pizza Delivery System". Consider a set of pizza centres promoting their service as "Delivery in 30 Minutes Only". Suppose the pizza preparation time is distributed as a normal variable with the mean of 20 min and standard deviation of 2 min. Also suppose that the trading area is defined as the set of customers who can be served at least 75 % of time within 30 min. For an individual coverage model, the customers should be within the coverage of $30 - 20 - 0.7\times\ 2 = 8.6$ min (0.7 = 75 % of the standard normal distribution) to get the delivery within 30 min. For instance, a customer located at a distance of 15 min from the pizza centre has only 50 % chances to get the pizza delivery within 30 min time. Suppose this customer has another pizza center which is at a distance of 9 min away. The customer has only 69 % chance to get a pizza delivered within 30 min time from this alternate pizza center. So none of the centers cover this customers who is located outside the coverage areas of both centers. Assuming the existence of a dispatcher which has the ability to redirect the order to the center which is least busy at the moment and on-site preparation times at both the centers are independent of each other. Here in this particular situation, it is possible to deliver the order to the customer within 30 min time with the probability of $1 - (1 - 0.5)(1 - 0.69) = 0.84$, which meets the coverage standard. Hence, this example, clearly shows that the customer has better chances of being covered by assuming cooperative coverage rather than individual coverage. From this example, we can also conclude that if we need to determine the locations of some fixed number of pizza centres so as to cover as large an area as possible with required level of coverage, the area covered with cooperative coverage model will always be greater than or equal to the area covered by the individual coverage model. Likewise, location of emergency services such as fire stations and ambulances can be determined using cooperative coverage model on a network in a more efficient manner than using individual coverage model.

In the literature, covering problems are analyzed in plane by [6, 20] and [7] as well as for network topology by [16] and [2] assuming the discrete demand. Covering problems are also analyzed under the assumption of continuously distributed demand by [19] and [9]. The planar version of the CMCLP is solved using both optimal and heuristic algorithms by [3]. Berman et al. [3] proposed an algorithm which is based on the big triangle and small triangle approach [8] for the *2-facility* problem with the assumption that one of the facilities location is known. For more than *2-facilities* problem, they proposed a heuristic method. The discrete version of the CMCLP was considered by [4], where the location space is restricted to the nodes of the network. The discrete version allowing the facilities to be located at both the nodes and along the edges is solved by [1], where they proposed greedy methods and local search based heuristics to solve the *p-facility* problem.

In this paper, we have proposed an artificial bee colony algorithm based approach for solving the CMCLP for network version of *p-facility* problem where facilities can be located both at the nodes and along the edges. The artificial bee colony (ABC) algorithm is a recently developed population based meta-heuristic, proposed by [10]. ABC algorithm is inspired by foraging behaviour of real honey bee swarms. ABC algorithm has been successfully applied to solve numerous optimization problems in various domains. Motivated by the success of ABC algorithm in solving different optimization problems in various domains, we have designed an ABC algorithm to solve the CMCLP. We have compared the results obtained through our approach with two interchange heuristic methods proposed in [1]. In comparison to these methods, our approach obtained better quality results on most of the instances.

The remaining part of this paper is structured as follows: Sect. 2 defines the CMCLP formally. In Sect. 3, we provide a brief introduction to ABC algorithm. Section 4 presents our ABC approach for the CMCLP. Section 5 reports the computational results and compares our approach with other approaches available in the literature. Finally, Sect. 6 presents some concluding remarks and directions for future research.

Table 1 Summary of notations

n	The number of nodes or demand points, i.e., $n = \|V\|$
w_i	The weight associated with demand point $i \in V$
l_k	The length associated with each edge $e_k \in E$
X	The location space
p	The number of facilities to locate
$d_i(x_j)$	The distance between demand point $i \in N$ and facility j
$\phi(d)$	The strength of the signal at distance d from the facility, $\phi(d) = \max\{0, 1 - d/U\}$
$\Phi_i(x)$	The overall signal at point $i \in N$
U	The fraction of diameter of the network
T	The threshold for coverage

2 Formal problem definition

The CMCLP can be formally defined as follows: Let $G = (V, E)$ be an undirected network, with $V = (1, \ldots, n)$ be the set of demand points and $E = (e_1, \ldots, en)$ be the set of edges connecting various demand points. Each demand point i has a non-negative real weight w_i indicating the total demand at this point. Each edge e_k has a positive length l_k. p facilities need to be located on the edges (including end demand points) to cover these demand points. A demand point is said to be covered, if the combined strength of the signal received by it from all the facilities is not less than a threshold T. The CMCLP seeks a location vector X_p for these p facilities so as to maximize the sumtotal of the weights of the covered demand points.

$$f(X_p, T) = \sum\nolimits_{i:\Phi_i(X_p) \geq T} w_i$$

The signal strength function is defined as the sum of all signals received by a demand point $i \in V$ from p facilities.

$$\Phi_i(X_p) = \sum\nolimits_{k=1}^{p} \phi(d_i(x_k))$$

Location x of a facility along an edge e_k joining demand point j_1 with j_2 ($e_k = (j_1, j_2)$) is represented by an ordered pair (l_k, t) where t is the relative distance of x from j_1 with respect to l_k, i.e., $0 \leq t \leq 1$. The distance from a node $i \in V$ to this facility is defined as follows

$$d(i, x) = \min\{d(i, j_1) + t \times l_k, d(i, j_2) + (1 - t) \times l_k\}$$

where $d(i, j_1)$ and $d(i, j_2)$ are the lengths of the shortest paths connecting node i to node j_1 and node j_2 respectively. The notations used above are summarized in the Table 1.

To illustrate CMCLP, consider the network depicted in Fig. 1. Let p = 3, T = 0.5, and the signal strength function be defined as $\phi(d) = \max\{0, 1 - \frac{d}{10}\}$.

One possible solution that we can obtain by locating the facilities along the edges as well as on nodes is $X = \{(4), ([7, 8], 0.6), ([1, 2], 0.4)\}$, where the first point p_1 is located on node 4, the second point p_2 is located on edge [7, 8] at a relative distance of $t = 0.6$ from node 7, and the last point p_3 is located on edge [1, 2] at a relative distance of $t = 0.4$ from node 1. This solution produces an objective value of 29 covering all nodes. In this example, we have selected the points randomly. There might be a possibility of some other solutions existing for this network.

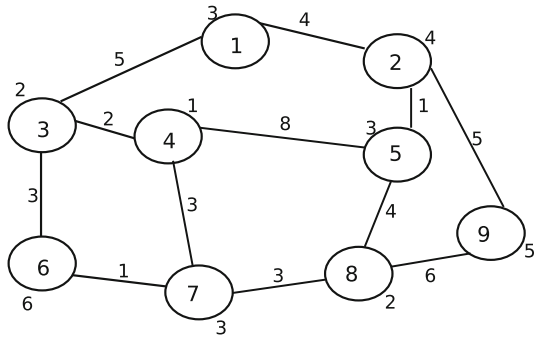

Fig. 1 Illustrating CMCLP

3 Overview of ABC algorithm

The artificial bee colony (ABC) algorithm proposed by Karaboga in 2005 is a population based meta-heuristic algorithm, which is inspired from the intelligent behavior of the foraging honey bees [10]. In a bee colony, there are three types of bees: employed, onlooker and scout. Employed bees are those bees which are currently exploiting a food source. The responsibility of the employee bees is to bring loads of nectar to the hive and share the information about their food sources with other bees waiting in the hive. The waiting bees are the onlookers. The onlookers then choose a food source with a probability directly proportional to its quality and becomes employed. Scout bees search for new food sources in the vicinity of the hive and they become employed as soon as they find a new food source. An employed bee whose food source becomes empty will abandons that food source and becomes either a scout or an onlooker.

Motivated by the foraging bees' behavior described above, Karaboga developed ABC algorithm. This

algorithm was originally developed for solving optimization problems in continuous domain only, later, it has been extended to solve discrete optimization problems also [10–13, 15, 17, 18]. For a recent survey on ABC algorithm and its applications, interested readers may refer to [14].

In ABC algorithm also there are three groups of bees, viz. employed, onlooker and scout with functions similar to their real counterparts. In ABC algorithm, the food sources represent the possible solutions to the problem under consideration and the quality of a food source represents the fitness of the represented solution. The employed bees are associated with food sources. Always, there is a one-to-one association between food sources and employed bees, which means, the number of food sources is equal to the number of employee bees. Usually, but not always, the number of onlooker bees is also taken to be equal to number of employed bees. The ABC algorithm is a iterative search process, which starts with initializing the employee bees, with randomly generated food sources (solutions), then repeats through the cycles of the employed bee and onlooker bee phases.

In the employed bee phase, each employed bee generates a food source in the proximity of its associated food source and evaluates its quality. The method of determining a new food source in the proximity of a particular food source depends on the problem under consideration. If the quality of the new food source is better than the current one then the employed bee moves to the new food source leaving the old one. Otherwise, it remains at the old food source. When all the employed bees finish this process, then employed bee phase ends and onlooker bee phase begins.

Onlooker bee phase starts with sharing of information by employed bees about their food sources with the onlookers. Onlookers select the food sources depending on their quality, i.e., higher the value of the fitness of the solution represented by a food source, higher will be the chances of its selection. As a result of such a selection, good quality food sources will get more chance for selection by the onlookers. After all onlookers select the food sources, they determine the food sources in the proximity of their selected food sources in a manner similar to the employed bees and evaluate their fitness. Among all the neighboring food sources generated by the onlookers who chose food source i and the food source i itself, the best quality food source is determined. This best food source will be updated as food source i for next iteration. The onlooker bee phase ends once all food sources are updated, and then the next iteration of the ABC algorithm begins. The algorithm is repeated until the termination condition is satisfied. If a solution associated with any employed bee does not improve over some specific number of iterations, then that food source is considered as exhausted and it is discarded by its associated employee bee and that employee bee becomes scout. Such scouts are converted back into employed bees by associating them with newly generated solutions. Usually, these new solutions are generated randomly in the same manner as initial employed bee solutions.

In the employed bee phase, every solution is given a fair chance to improve itself, whereas in the onlooker bee phase, because of the selection policy used by the onlookers as mentioned above good quality solutions get more chance to improve themselves in comparison to poor quality solutions. This inclination towards selecting good quality solutions may produce better quality solutions, as there will be higher chances of finding even better solutions within the proximity of good solutions. However, if a solution is locally optimal, then no better solution exists in its proximity and any attempt to improve it will always fail. The concept of scout bees helps in this situation. If a solution is not improved over certain number of iterations then it is assumed to be locally optimal and is discarded by making its associated employed bee a scout. A new solution is generated for this scout bee to make it employed again. This new solution is created either in the same manner as an initial solution or by perturbing an existing solution. Hence by utilizing the concept of scout bees, solutions which are not improved since long are replaced with new solutions. In a robust search process, the balance between the exploration and exploitation must be maintained. In the ABC algorithm, employed bees and onlooker bees carry out the exploitation, and scouts perform the exploration. A proper balance need to be maintained between exploration and exploitation by appropriately setting the number of iterations without improvement in the ABC algorithm after which an employed bee abandons a solution and becomes scout.

4 ABC approach for the CMCLP

This section presents salient features of our ABC approach for the CMCLP.

4.1 Fitness of a solution

We follow the same two level approach as used in [1] for determining the fitness of a solution. We say that a solution X' is better than another solution X, if solution X' either has a larger objective function value,

$$f(X', T) > f(X, T)$$

or, if solution X and solution X' have same objective function value, but solution X' provides larger total coverage.

$$\sum_{i \in V} \Phi_i(X') > \sum_{i \in V} \Phi_i(X)$$

4.2 Method for selecting a food source for an onlooker

We have used the binary tournament selection method for selecting a food source for an onlooker. In the binary tournament selection method, two food sources are selected uniformly at random, and their fitness is compared. The better of the two food sources is selected with the probability p_{onl}. Otherwise, the worse of the two food sources is selected, i.e., the probability of selection of the worst solution is $1 - p_{onl}$. The Pseudo code for the binary tournament selection method is as follows:

Algorithm 1: Binary tournament selection

```
Select two solutions e1 & e2 randomly form the employee bee solutions;
p := generate a random number between 0 and 1;
if p ≤ p_onl then
    return the best among e1 and e2
else
    return the worst among e1 and e2
```

4.3 Initial solution

To generate an initial solution, we have followed a method which is a mix of greediness and randomness. In this method one facility at a time will be added to the current partial solution starting with an empty solution. In each iteration, to add a facility to the current partial solution S, we compute the set Y of all points $x \in G$ (including nodes $\in V$) that provide exact or greater coverage for yet uncovered nodes V'. The x points are considered on edges at equal intervals separated by a relative distance of 0.1. The condition of exact or greater coverage is based on the signal strength function defined. With the choice of the signal strength function used and/or the way we are considering the points on the edges, it may happen during the iterations of the greedy method that there may not exist even one point which can provide exact coverage (specially in case of large instances). So we have chosen points providing either exact or greater coverage. Next, we evaluate the points based on how much coverage they are providing, then choose R best points from the set Y, and select one point randomly from R.

$$Y = V \cup \{x \in G | \phi_i(x) \geq T_i(X)\} \text{ for some } i \in V'$$

After locating a facility, the threshold is updated as follows:

$$T_i(S) = max\{0, T - \Phi_i((S)\} \quad \text{for} \quad i \in V$$

This process is repeated till the desired number of facilities are located.

4.4 Neighboring solution generation

To generate a solution X' in the neighborhood of solution X, we delete F facilities from X randomly. Then, F facilities are added one-by-one from the set F^{new} containing all points $x \in G$ (including nodes $\in V$) which provide exact coverage for at least one yet un covered node in V'. A formal definition of F^{new} is given below.

$$F^{new} = Z - X$$

where

$$Z = V \cup \{x \in G | \phi_i(x) = T_i(X)\} \quad \text{for some} \quad i \in V'$$

To add each facility, we first choose R best points from F^{new} and then choose one randomly from R. Once a facility has been added, F^{new} is updated. The manner in which facilities are added is similar to Greedy 1 heuristic of [1] except for the fact that Greedy 1 always choose the best point, whereas we choose randomly a point from among R best points.

4.5 Other features

We have used different number of employee bees and onlooker bees. If an employed bee solution does not improve for a specified number of iterations *limit* then the associated employed bee becomes scout. There is no restriction on the number of scout bees in an iteration. The number of scouts in a particular iteration depends on the number of employed bee solutions which have not improved for exactly *limit* number of iterations. The scout bee is again made employed by assigning it to a new solution which is generated in the same manner as one of our initial solution.

4.6 Local search

We have used a local search on the best solution obtained through ABC algorithm in a bid to improve it further. In this local search, each facility x in a solution S is considered one-by-one and the best point b_x to relocate it is determined. For this, we compute the set F^{new} for solution $(S \backslash \{x\}$ and find the best point b_x to locate the next facility. If the solution $(S \backslash \{x\}) \cup \{b_x\}$ is better than S then we replace S with this new solution. This process is repeated till each facility is considered once.

Algorithm 2 provides the pseudo-code for our hybrid ABC approach, where n_e and n_o are respectively the number of employed bees and number of onlooker bees. Generate_Neighbor(e_i) and Binary_Tournament($e_1, e_2, \ldots, e_n$) are two functions. The former function generates a solution in the neighborhood of solution e_i as per Sect. 4.4, whereas the

latter selects a solution for an onlooker bee from all employed bee solutions $e_1, e_2, \ldots, e_n$ as per Sect. 4.2.

Algorithm 2: Pseudo-Code of our Hybrid ABC Algorithm

```
Randomly generate n_e solutions e_1, e_2, ..., e_{n_e};
best_sol:= best solution among e_1, e_2, ..., e_{n_e};
while termination condition is not satisfied do
    for i = 1 to n_e do
        e' := Generate_Neighbor(e_i);
        if e' is better than e_i then
            e_i:=e'
        if e' is better than best_sol then
            best_sol:=e'
    for i = 1 to n_o do
        k_i := Binary_Tournament(e_1, e_2, ..., e_n);
        onl_i := Generate_Neighbor(e_{k_i});
        if onl_i is better than best_sol then
            best_sol:=onl_i
    for i = 1 to n_o do
        if onl_i is better than e_{k_i} then
            e_{k_i}:=onl_i
    for i = 1 to n_e do
        if e_i has not improved over limit iterations then
            replace e_i with a random solution;
best_sol := Local_search(best_sol);
return best_sol ;
```

5 Computational results

To test our ABC approach, we have used the same instances as used in [1]. These instances are generated randomly in the following manner: For each combination of (n, dgr) where n is the number of nodes and dgr is the average degree of nodes, five instances were generated by [1]. In these instances $n \in \{40, 60, 80, 100, 120, 140, 160, 180, 200\}$ and $dgr \in \{5, 6, 7\}$. Like [1], we have done all computational experiments by taking $p = 3, 4, 5$ for $n = 40$, 60, 80; $p = 4$, 5, 6 for $n = 100$, 120, 140; and $p = 5$, 6, 7 for $n = 160$, 180, 200. Three different values have been used for signal threshold values T, i.e., $T \in \{0.6, 0.8, 1.0\}$ and linear signal strength function $\phi(d) = \max\{0, 1 - d/U\}$ has been used like in [1]. The parameter U was determined in [1] as a fraction of the diameter of the network and $U_{\%} \in \{0.15, 0.25, 0.35\}$ for $T \in \{0.6, 0.8\}$ and $U_{\%} \in \{0.2, 0.3, 0.4\}$ for $T = 1.0$ were used. Overall, there are 3625 instances.

Our ABC approach has been implemented in C and executed on a Linux based Intel Core i5 2400 system with 4 GB memory running at 3.10 GHz. In all our computational experiments, the number of employed bees (n_e) is taken to be 10, the number of onlooker bees (n_o) is taken to be 20, *limit* is set to 50, p_{onl} is set to 0.9 for $U_{\%} = 0.15, 0.25, 0.35$ and $T = 0.6$, it is set to 0.8 for remaining combinations of U and T, and $R = 20$. We have taken $F = 2$ for $n = 40, 60, 80$ and $p = 3, 4, 5$, $F = 3$ for $n = 100, 120, 140$ and $p = 4, 5, 6$, $F = 4$ for $n = 160, 180, 200$ and $p = 5, 6, 7$. Our ABC approach terminates after 500 iterations. All these parameter values were chosen empirically after a large number of trials.

Table 2 Comparison between our ABC approach and I1 and I2 heuristics of [1]

T	$U_{\%}$	%(ABC, I1)	%(ABC, I2)	R(I1)	R(I2)	R(ABC)
0.6	0.15	1.28	1.21	42.36	25.28	351.62
0.6	0.25	12.84	12.76	99.99	67.21	253.26
0.6	0.35	1.1	1.07	80.61	104.49	244.21
0.8	0.15	4.88	4.71	39.07	28.93	366.45
0.8	0.25	22.36	21.98	84.42	78.00	271.49
0.8	0.35	5.34	5.06	118.80	141.13	257.82
1.0	0.2	35.98	35.52	36.26	29.48	263.43
1.0	0.3	25.15	24.86	122.42	108.10	278.56
1.0	0.4	12.08	12.09	82.56	153.21	206.29

We have compared the results of our ABC approach with interchange heuristics I1 and I2 proposed in [1]. Results are reported in the same format as used in [1]. Averbakh et al. [1] reported the average percentage improvement in solution quality by I2 with respect to I1 over all the instances with same T and $U_{\%}$. The percentage improvement in solution quality by method A over method B on a particular instance is $100 \times \frac{\Phi_i(S_A) - \Phi_i(S_B)}{\Phi_i(S_B)}$ where S_A and S_B are the solutions obtained by methods A and B respectively on the particular instance under consideration. However, average execution times are reported over all instances with $n = 200$ only, i.e., all instances having maximum number of nodes. Table 2 reports the results of I1, I2 and our ABC approach. Data for I1 and I2 have been obtained from the corresponding author of [1] through personal communication. The first column in Table 2 represents the thresholds (T value), second column represents $U_{\%}$ values, third column (%(ABC,I1)) reports the average percentage improvement of our ABC approach over I1, fourth column (%(ABC,I2)) reports the average percentage improvement of our ABC approach over I2. And the last 3 columns (R(.)) report the average execution times of various approaches on the largest instance (n = 200). There are 405 instances with same T and $U_{\%}$ and hence, reported average percentage improvements are averaged over these 405 instances. Similarly, reported execution times are averaged over 45 instances with 200 nodes.

The results shows that the performance of our ABC algorithm is better compared to the Interchange heuristics on all classes of instances with same T and $U_{\%}$ values. In fact, average percentage improvement in solution quality

by our approach over I1 and I2 is always positive. Our approach on an average provide larger coverage than already existing methods. I1 and I2 were executed on a system having 3.31 GHz AMD Phenom II processor and 16 GB RAM which is different from the system used to execute our ABC approach. Therefore, execution times can not be compared directly. However,it is clear that our approach is slower than interchange heuristics I1 and I2.

6 Conclusions

In this paper, we have proposed an ABC algorithm based approach for the CMCLP and compared it with two interchange based heuristic methods proposed in the literature. Our ABC algorithm outperformed these two methods in terms of solution quality. However, its slower than these methods.

Our ABC algorithm based approach is the first metaheuristic approach for the CMCLP. Averbakh et al. [1] also experimented with tabu search and variable neighborhood search, but results obtained by these approaches were only slightly better than those obtained by interchange heuristics and hence they did not present these metaheuristics. Therefore, population based metaheuristics seem more appropriate for this problem. As a future work, we intend to investigate this further by developing some other metaheuristics for the CMCLP and compare them with our ABC approach and two heuristics of [1]. Approaches similar to our ABC approach can be developed for other related problems employing cooperative coverage model.

Acknowledgments Authors would like to place on record their sincere thanks to Dr. Jörg Kalcsics for providing the CMCLP test instances and their solution values obtained by various approaches proposed in [1]. Authors are also grateful to two anonymous reviewers for their valuable comments and suggestions which helped in improving the quality of this manuscript.

References

1. Averbakh I, Berman O, Krass D, Kalcsics J, Nickel S (2014) Cooperative covering problems on networks. Networks 63(4):334–349
2. Berman O (1994) The p maximal cover—p partial center problem on networks. Eur J Oper Res 72(2):432–442
3. Berman O, Drezner Z, Krass D (2010) Cooperative cover location problems: the planar case. IIE Trans 42(3):232–246
4. Berman O, Drezner Z, Krass D (2011) Discrete cooperative covering problems. J Oper Res Soc 62(11):2002–2012
5. Church R, ReVelle C (1974) The maximal covering location problem. Pap Reg Sci Assoc 32(1):101–118
6. Drezner Z (1981) On a modified one-center model. Manag Sci 27(7):848–851
7. Drezner Z (1986) The p-cover problem. Eur J Oper Res 26(2):312–313
8. Drezner Z, Suzuki A (2004) The big triangle small triangle method for the solution of nonconvex facility location problems. Oper Res 52(1):128–135
9. Drezner Z, Suzuki A (2010) Covering continuous demand in the plane. J Oper Res Soc 61(5):878–881
10. Karaboga D (2005) An idea based on honey bee swarm for numerical optimization. In: Technical report-TR06, Erciyes University, Engineering Faculty, Computer Engineering Department, Turkey
11. Karaboga D, Akay B (2007) A powerful and efficient algorithm for numerical function optimization: artificial bee colony (ABC) algorithm. J Glob Optim 39(3):459–471
12. Karaboga D, Akay B (2008) On the performance of artificial bee colony (ABC) algorithm. Appl Soft Comput 8(1):687–697
13. Karaboga D, Akay B (2009) A comparative study of artificial bee colony algorithm. Appl Math Comput 214(1):108–132
14. Karaboga D, Gorkemli B, Ozturk C, Karaboga N (2014) A comprehensive survey: artificial bee colony (ABC) algorithm and applications. Artif Intell Rev 42(1):21–57
15. Pan QK, Tasgetiren MF, Suganthan P, Chua T (2011) A discrete artificial bee colony algorithm for the lot-streaming flow shop scheduling problem. Inf Sci 181(12):2455–2468
16. ReVelle C (1986) The maximum capture or sphere of influence location problem: Hotelling revisited on a network. J Reg Sci 26(2):343–358
17. Singh A (2009) An artificial bee colony algorithm for the leaf-constrained minimum spanning tree problem. Appl Soft Comput 9(2):625–631
18. Singh A, Sundar S (2011) An artificial bee colony algorithm for the minimum routing cost spanning tree problem. Soft Comput 15(12):2489–2499
19. Suzuki A, Drezner Z (1996) The p-center location problem in an area. Locat Sci 4(1–2):69–82
20. Watson-Gandy C (1982) Heuristic procedures for the m-partial cover problem on a plane. Eur J Oper Res 11(2):149–157

Imperial Journal of Interdisciplinary Research (IJIR)
Vol-3, Issue-8, 2017
ISSN: 2454-1362, http://www.onlinejournal.in

Control and Design of a Single-Phase Active Device for Power Quality Improvement of Electrified Transportation

Jatoth Ramesh
Assistant Professor, EEE Department
Methodist College of Engineering & Technology

Abstract—*A transformerless hybrid series active filter is proposed to enhance the power quality in single-phase systems with critical loads. This paper assists the energy management and power quality issues related to electric transportation and focuses on improving electric vehicle load connection to the grid. The control strategy is designed to prevent current harmonic distortions of nonlinear loads to flow into the utility and corrects the power factor of this later. While protecting sensitive loads from voltage disturbances, sags, and swells initiated by the power system, ridded of the series transformer, the configuration is advantageous for an industrial implementation. This polyvalent hybrid topology allowing the harmonic isolation and compensation of voltage distortions could absorb or inject the auxiliary power to the grid. Aside from practical analysis, this paper also investigates on the influence of gains and delays in the real-time controller stability. The simulations and experimental results presented in this paper were carried out on a 2-kVA laboratory prototype demonstrating the effectiveness of the proposed topology.*

Index Terms—*Current harmonics, electric vehicle, hybrid series active filter (THSeAF), power quality, real-time control*

I. INTRODUCTION

THE forecast of future Smart Grids associated with electric vehicle charging stations has created a serious concern on all aspects of power quality of the power system, while widespread electric vehicle battery charging units [1], [2] have detrimental effects on power distribution system harmonic voltage levels [3]. On the other hand, the growth of harmonics fed from nonlinear loads like electric vehicle propulsion battery chargers [4], [5], which indeed have detrimental impacts on the power system and affect plant equipment, should be considered in the development of modern grids. Likewise, the increased rms and peak value of the distorted current waveforms increase heating and losses and cause the failure of the electrical equipment. Such phenomenon effectively reduces system efficiency and should have properly been addressed [6], [7].

Moreover, to protect the point of common coupling (PCC) from voltage distortions, using a dynamic voltage restorer (DVR) function is advised. A solution is to reduce the pollution of power electronics-based loads directly at their source. Although several attempts are made for a specific case study, a generic solution is to be explored. There exist two types of active power devices to overcome the described power quality issues. The first category are series active filters (SeAFs), including hybrid-type ones. They were developed to eliminate current harmonics produced by nonlinear load from the power system. SeAFs are less scattered than the shunt type of active filters [8], [9]. The advantage of the SeAF compared to the shunt type is the inferior rating of the compensator versus the load nominal rating [10]. However, the complexity of the configuration and necessity of an isolation series transformer had decelerated their industrial application in the distribution system. The second category was developed in concern of addressing voltage issues on sensitive loads. Commonly known as DVR, they have a similar configuration as the SeAF. These two categories are different from each other in their control principle. This difference relies on the purpose of their application in the system.

The hybrid series active filter (THSeAF) was proposed to address the aforementioned issues with only one combination. Hypothetically, they are capable to compensate current harmonics, ensuring a power factor (PF) correction and eliminating voltage distortions at the PCC [11], [12]. These properties make it an appropriate candidate for power quality investments. The three-phase SeAFs are well documented [13], [14], whereas limited research works reported the single-phase applications of SeAFs in the literature. In this paper, a single-phase transformerlessTHSeAF is proposed and capable of cleaning up the grid-side connection bus bar from current harmonics generated by a nonlinear load [15]. With a smaller

rating up to 10%, it could easily replace the shunt active filter [16]. Furthermore, it could restore a sinusoidal voltage at the load PCC/

The advantage of the proposed configuration is that nonlinear harmonic voltage and current producing loads could be effectively compensated. The transformerless hybrid series active filter (THSeAF) is an alternative option to conventional power transferring converters in distributed generation systems with high penetration of renewable energy sources, where each phase can be controlled separately and could be operated independently of other phases [17]. This paper shows that the separation of a three-phase converter into single-phase Hbridge converters has allowed the elimination of the costlyisolation transformer and promotes industrial application for filtering purposes. The setup has shown great ability to perform requested compensating tasks for the correction of current and voltage distortions, PF correction, and voltage restoration on the load terminal [18].

The contemporary container crane industry, like many other industry segments, is often enamored by the bells and whistles, colorful diagnostic displays, high speed performance, and levels of automation that can be achieved. Although these features and their indirectly related computer based enhancements are key issues to an efficient terminal operation, we must not forget the foundation upon which we are building. Power quality is the mortar which bonds the Foundation blocks. Power quality also affects terminal operating economics, crane reliability, our environment, and initial investment in power distribution systems to support new crane installations. To quote the utility company newsletter which accompanied the last monthly issue of my home utility billing: 'Using electricity wisely is a good environmental and business practice which saves you money, reduces emissions from generating plants, and conserves our natural resources.' As we are all aware, container crane performance requirements continue to increase at an astounding rate. Next generation container cranes, already in the bidding process, will require average power demands of 1500 to 2000 kW – almost double the total average demand three years ago. The rapid increase in power demand levels, an increase in container crane population, SCR converter crane drive retrofits and the large AC and DC drives needed to power and control these cranes will increase awareness of the power quality issue in the very near future

POWER QUALITY PROBLEMS

For the purpose of this article, we shall define power quality problems as: 'Any power problem that results in failure or misoperation of customer equipment, Manifests itself as an economic burden to the user, or produces negative impacts on the environment.'

When applied to the container crane industry, the power issues which degrade power quality include:

- Power Factor
- Harmonic Distortion
- Voltage Transients
- Voltage Sags or Dips
- Voltage Swells

The AC and DC variable speed drives utilized on board container cranes are significant contributors to total harmonic current and voltage distortion. Whereas SCR phase control creates the desirable average power factor, DC SCR drives operate at less than this. In addition, line notching occurs when SCR's commutate, creating transient peak recovery voltages that can be 3 to 4 times the nominal line voltage depending upon the system impedance and the size of the drives. The frequency and severity of these power system disturbances varies with the speed of the drive. Harmonic current injection by AC and DC drives will be highest when the drives are operating at slow speeds. Power factor will be lowest when DC drives are operating at slow speeds or during initial acceleration and deceleration periods, increasing to its maximum value when the SCR's are phased on to produce rated or base speed. Above base speed, the power factor essentially remains constant. Unfortunately, container cranes can spend considerable time at low speeds as the operator attempts to spot and land containers. Poor power factor places a greater kVA demand burden on the utility or engine-alternator power source. Low power factor loads can also affect the voltage stability which can ultimately result in detrimental effects on the life of sensitive electronic equipment or even intermittent malfunction. Voltage transients created by DC drive SCR line notching, AC drive voltage chopping, and high frequency harmonic voltages and currents are all significant sources of noise and disturbance to sensitive electronic equipment

II. SYSTEM ARCHITECTURE

A. System Configuration

The THSeAF shown in Fig. 1 is composed of an H-bridge converter connected in series between the source and the load. A shunt passive capacitor ensures a low impedance path for current

harmonics. A dc auxiliary source could be connected to inject power during voltage sags. The dc-link energy storage system is described in [19]. The system is implemented for a rated power of 2200 VA. To ensure a fast transient response with sufficient stability margins over a wide range of operation, the controller is implemented.

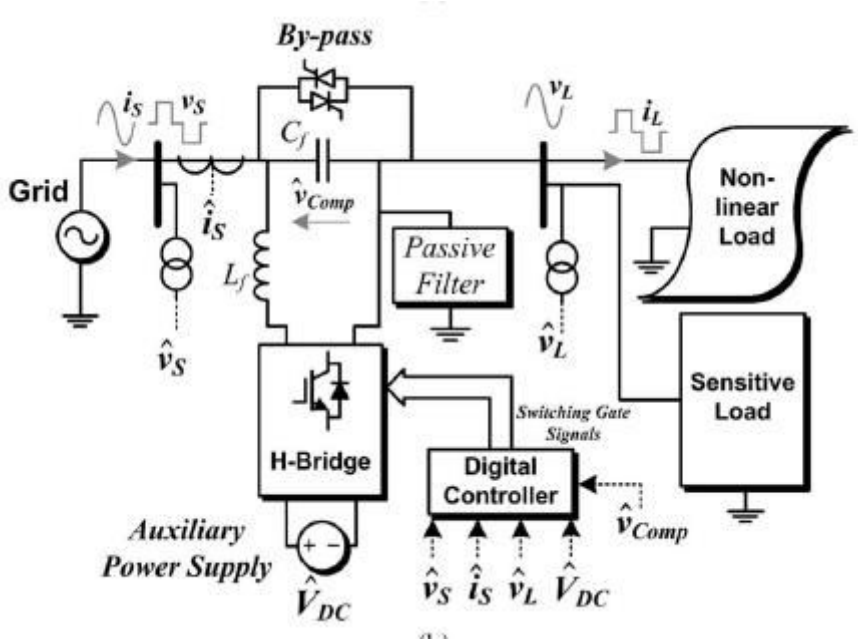

Fig.1.Electrical diagram of the THSeAF in a single-phase utility.

The system parameters are identified in Table I. A variable source of 120 Vrms is connected to a 1.1-kVA nonlinear load and a 998-VA linear load with a 0.46 PF. The THSeAF is connected in series in order to inject the compensating voltage. On the dc side of the compensator, an auxiliary dc-link energy storage system is installed. Similar parameters are also applied for practical implementation.

Symbol	Definition	value
Vs	Line phase to neutral voltage	120 Vrms
F	System frequency	60 hz
Rload	Load resistance	11.5 ohm
Lload	Load inductance	20mH
PL	Linear load power	1KVA
PF	Linear load power factor	46%
Lf	Switching ripple filterinductance	5mH
Cf	Switching ripple filter capacitance	2 microF
Ts	dSPACE synchronous sampling time	40 micro sec
Fpwm	PWM frequency	5Khz
G	Control gain for current hormonics	8ohm
VthseSf	VSI bus voltage of THSeAF	70V
Pig	Proportional gain integral gain	0.025(4*)

Table 1 Configuration parameters

THSeAFs are often used to compensate distortions of the current type of nonlinear loads. For instance, the distortedcurrent and voltage waveforms of the nonlinear system during normal operation and when the source voltage became distorted are depicted in Fig. 2. The THSeAF is bypassed, and current harmonics flowed directly into the grid. As one can perceive, even during normal operation, the current harmonics (with a total harmonic distortion (THD) of 12%) distort the PCC, resulting in a voltage THD of 3.2%. The behavior of the system when the grid is highly polluted with 19.2% of THD is also illustrated. The proposed configuration could be solely connected to the grid with no need of a bulky and costly series injection transformer, making this topology capable of compensating source current harmonics and voltage distortion at the PCC. Even if the number of switches has increased, the transformer less configuration is more cost-effective than any other series compensators, which generally uses a transformer to inject the compensation voltage to the power grid. The optimized passive filter is composed of 5th, 7th, and highpass filters. The passive filter should be adjusted for the system upon load and government regulations. A comparison between different existing

configurations is given in Table II. It is aimed to point out the advantages and disadvantages of the proposed configuration over the conventional topologies.

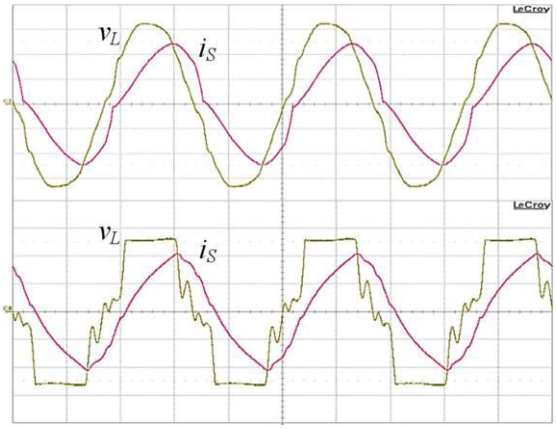

Fig. 2. Terminal voltage and current waveforms of the 2-kVA single phase system without compensator.

To emphasize the comparison table fairly, the equivalent single phase of each configuration is considered in the evaluation. Financial production evaluation demonstrated a 45% reduction in component costs and considerable reduction in assembly terms as well.

Definition	Proposed THSeAF	21	22	12
Injection transformer	Non	2 per phase	1 per phase	1 per phase
# of semiconductor devices	4	8	4	4
Dc link storage element	1+aux power	1	2	1+aux power
AF rating to the load power	10-30%	10-30%	10-30%	10-30%
Size and weight,regarding the transformer, power switches, dive circuit and heat sink	The lowest	High	good	good
Industrial production cost	The lowest	High	Low	low
Power losses including switching conduction and fixed losses	Low	better	Low	low
Reliability regarding independent operation capability	Good	low	Good	Good
Harmonic correction of current source load	Good	Good	Good	low
Voltage harmonic correction at load terminals	Good	better	Good	Good
Power factor correction	Yes	Yes	Yes	no
Power injection to the grid	Yes	No	No	yes

TABLE II SINGLE-PHASE COMPARISON OF THE THSeAF TO PRIOR THSeAF s

B. Operation Principle

The SeAF represents a controlled voltage source (VSI). In order to prevent current harmonics *iLh*to drift into the source, this series source should present low impedance for the fundamental component and high impedance for all harmonics as shown in Fig. 3. The principle of such modeling is well documented in [20]. The use of a well-tuned passive filter is then mandatory to perform the compensation of current issues and maintaining a constant voltage free of distortions at the load terminals. The behavior of the SeAF for a current control approach is evaluated from the phasor's equivalent circuit shown in Fig. 3. The nonlinear load could be modeled by a resistance representing the active power consumed and a current source generating current harmonics. Accordingly, the impedance *ZL* represents the nonlinear load and the inductive load.

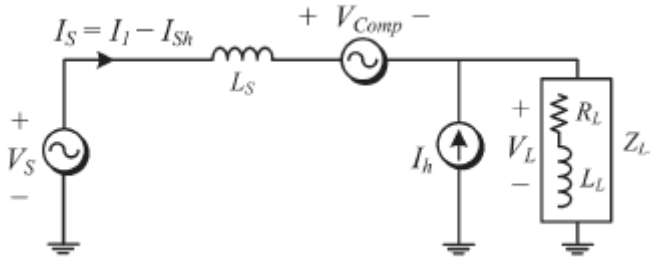

Fig. 3. THSeAF equivalent circuit for current harmonics

The SeAF operates as an ideal controlled voltage source (*V* comp) having a gain (***G***) proportional to the current harmonics (*Ish*) flowing to the grid (*Vs*)
*V*comp= *G.Ish*− *VLh*……. (1)
This allows having individual equivalent circuit for the fundamental and harmonics
*V*source= *Vs*1 + *Vsh, VL* = *VL*1 + *VLh*. ….(2)
The source harmonic current could be evaluated
Vsh= − *Zs.Ish*+ *V*comp+ *VLh*…… (3)
VLh=*ZL*(*Ih*− *Ish*). ……..(4)
Combining (3) and (4) leads to (5)
Ish=*Vsh*(*G* − *Zs*)……..(5)
If gain ***G*** is sufficiently large (*G*→∞), the source current will become clean of any harmonics (*Ish*→ 0). This will
help improve the voltage distortion at the grid side. In this approach, the THSeAF behaves as high-impedance open circuit for current harmonics, while the shunt high-pass filter tuned at the system frequency creates a low-impedance path for all harmonics and open circuit for the fundamental; it also helps for PF correction.

III. MODELING AND CONTROL OF THE SINGLE-PHASE THSeAF

a. *Average and Small-Signal Modeling*

Based on the average equivalent circuit of an inverter [23], the small-signal model of the proposed configuration can be obtained as in Fig. 4. Hereafter, *d* is the duty cycle of the upper switch during a switching period, whereas ¯*v* and ¯*i*denote the average values in a switching period of the voltage and current of the same leg. The mean converter output voltage and current are expressed by (6) and (7) as follows:
¯*vO*= (2*d* − _ __ 1_)*V*DC
……(6)
where the (2*d* − 1) equals to *m*, then ¯*i*
DC = *m*¯ *if* ……..(7)
Calculating the Thévenin equivalent circuit of the harmonic current source leads to the following assumption:
¯*vh*(*jω*) = −*j*¯ *ihCHPF* · *ωh* ……. (8)

If the harmonic frequency is high enough, it is possible to assume that there will be no voltage harmonics across the load. The state-space small-signal ac model could be derived by a linearized perturbation of the averaged model as follows:
$x^{\cdot} = Ax + Bu$…… (9)

Hence, we obtain

$$\frac{d}{dt}\begin{bmatrix} \bar{v}_{Cf} \\ \bar{v}_{CHPF} \\ \bar{i}_S \\ \bar{i}_f \\ \bar{i}_L \end{bmatrix} = \begin{bmatrix} 0 & 0 & \frac{1}{C_f} & \frac{1}{C_f} & 0 \\ 0 & 0 & \frac{1}{C_{HPF}} & 0 & -1/C_{HPF} \\ -1/L_S & -1/L_S & -r_c/L_S & -r_c/L_S & 0 \\ -1/L_f & 0 & -r_c/L_f & -r_c/L_f & 0 \\ 0 & \frac{1}{L_L} & 0 & 0 & -R_L/L_L \end{bmatrix} \times \begin{bmatrix} \bar{v}_{Cf} \\ \bar{v}_{CHPF} \\ \bar{i}_S \\ \bar{i}_f \\ \bar{i}_L \end{bmatrix} + \begin{bmatrix} 0 & 0 & 0 \\ 0 & 0 & 0 \\ \frac{1}{L_S} & 0 & \frac{1}{L_S} \\ 0 & \frac{m}{L_f} & 0 \\ 0 & 0 & -1/L_L \end{bmatrix} \times \begin{bmatrix} \bar{v}_S \\ V_{DC} \\ \bar{v}_h \end{bmatrix}. \quad (10)$$

Moreover, the output vector is
y = *Cx*+ *Du*…… (11)
or

$$\begin{bmatrix} \bar{v}_{comp} \\ \bar{v}_L \end{bmatrix} = \begin{bmatrix} 1 & 0 & r_c & r_c & 0 \\ 0 & 1 & 0 & 0 & 0 \end{bmatrix} \times \begin{bmatrix} \bar{v}_{Cf} \\ \bar{v}_{CHPF} \\ \bar{i}_S \\ \bar{i}_f \\ \bar{i}_L \end{bmatrix} + \begin{bmatrix} 0 & 0 & 0 \\ 0 & 0 & -1 \end{bmatrix} \times \begin{bmatrix} \bar{v}_S \\ V_{DC} \\ \bar{v}_h \end{bmatrix}. \quad (12)$$

By means of (10) and (12), the state-space representation of the model is obtained as shown in Fig. 4.

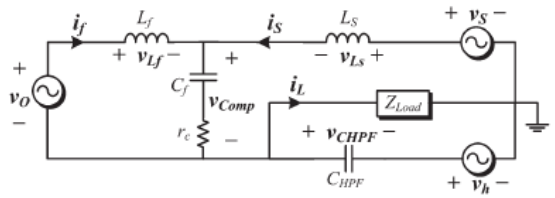

Fig. 4. Small-signal model of transformerlessTHSeAF in series between the grid and the load.

dc auxiliary source should be employed to maintain an adequate supply on the load terminals. During the sag or swell conditions, it should absorb or inject power to keep the voltage magnitude at the load terminals within a specified margin. However, if the compensation of sags and swells is less imperative, a capacitor could be deployed. Consequently, the dc-link voltage across the capacitor should be regulated as demonstrated in Fig. 5.

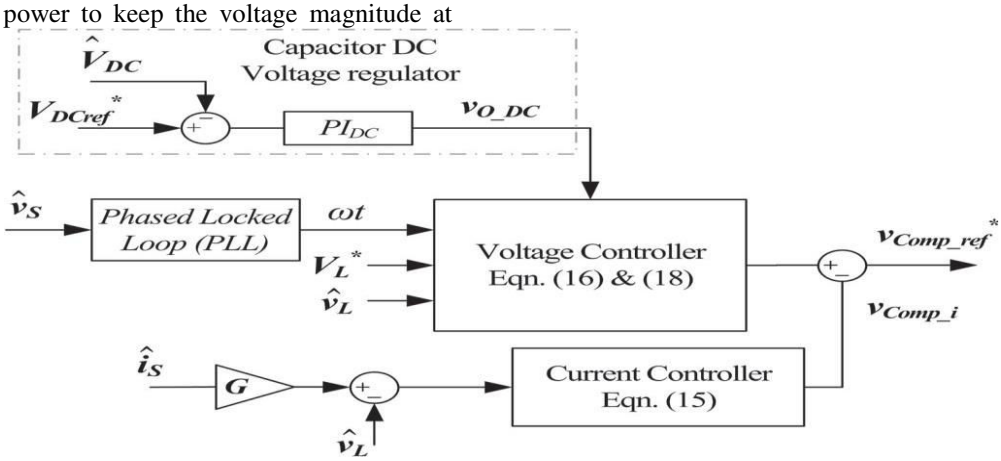

Fig. 5. Control system scheme of the active part.

B. *Voltage and Current Harmonic Detection*

The outer-loop controller is used where a capacitor replaces the dc auxiliary source. This control strategy is well explained in the previous section. The inner-loop control strategy is based on an indirect control principle. A fast Fourier transformation was used to extract the magnitude of the fundamental and its phase degree from current harmonics. The control gain ***G*** representing the impedance of the source for current harmonics has a sufficient level to clean the grid from current harmonics fed through the nonlinear load.

The second proportional integrator (PI) controller used in the outer loop was to enhance the effectiveness of the controller when regulating the dc bus. Thus, a more accurate and faster transient response was achieved without compromising the compensation behavior of the system. According to the theory, the gain ***G*** should be kept in a suitable level, preventing the harmonics from flowing into the grid [22], [24]. As previously discussed, for a more precise compensation of current harmonics, the voltage harmonics should also be considered

C. *Stability Analysis for Voltage and Current Harmonics*

The stability of the configuration is mainly affected by theintroduced delay of a digital controller. This section studies the impact of the delay first on the inclusive compensated system according to works cited in the literature. Thereafter, its effects on the active compensator is separated from the grid. Using purely inductive source impedance (see Fig. 4) and Kirchhoff's law for harmonic frequency components, (19) is derived.

A *PI* controller with system parameters described in Table I demonstrates a smooth operation in the stable region. By means of MATLAB, the behavior of the system's transfer function $F(s)$ is traced in Fig. 9. The root locus and the Bode diagram of the compensated open-loop system demonstrate a gain margin of 8.06 dB and a phase margin of 91◦.

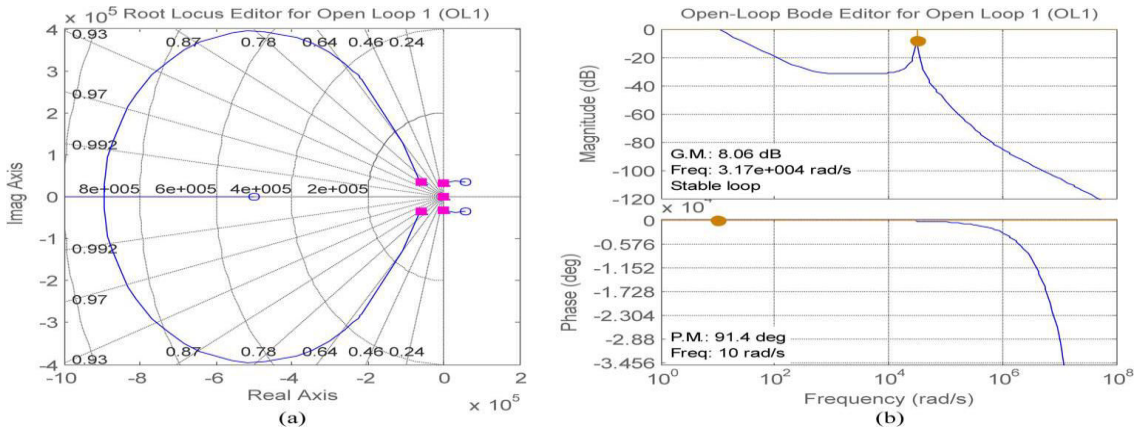

Fig. 9. Compensated open-loop system with delay time of 40 μs. (a) Root locus diagram. (b) Bode diagram.

IV.SIMULATIONS AND EXPERIMENTAL RESULTS

The proposed transformerless-THSeAF configuration was simulated in MATLAB/Simulink using discrete time steps of Ts= 10 μs. A dSPACE/dsp1103 was used for the fast control prototyping. To ensure an error-free and fast implementation, the complete control loop was executed every 40 μs. The parameters are identified in Table I.

The combination of a single-phase nonlinear load and a linear load with a total rated power of 2 kVA with a 0.74 lagging PF is applied for laboratory experiments and simulations. For experiments and simulations, a 2-kVA 120-Vrms 60-Hz variable source is used. THSeAF connected in series to the system compensates the current harmonics and voltage distortions. A gain $\boldsymbol{G}$ = 8 Ω equivalent to 1.9 p.u. was used to control current harmonics. As mentioned earlier, the capability of operation with low dc voltage is considered as one of the main advantages of the proposed configuration. For this experiment, it is maintained at 130 Vdc. During a grid's voltage distortion, the compensator regulates the load voltage magnitude, compensates current harmonics, and corrects the PF. The simulated results of the TTHSeAF illustrated in Fig. 11 demonstrates improvement in the source current THD. The load terminal voltage *VL* THD is 4.3%, while the source voltage is highly distorted (THD *VS* = 25%). The grid is cleaned of current harmonics with a unity power factor (UPF) operation, and the THD is reduced to less than 1% in normal operation and less than 4% during grid perturbation. While the series controlled source cleans the current of harmonic components, the source current is forced to be in phase with the source voltage. The series compensator has the ability to slide the load voltage in order for the PF to reach unity. Furthermore, the series compensator could control the power flow between two PCCs.

The THSeAF reacts instantly to this variation and does not interfere its operation functionality. Meanwhile, it is normal to observe a slight transient voltage variation depending on the momentum of the load disengagement or connection. To evaluate the compensator during utility perturbation, the power source became distorted as depicted in Fig. 12. The source current became cleaned of the majority of harmonics available in the load current and has a unity PF. The THSeAF prevents existing perturbation on the grid's voltage to propagate on the load PCC. It protects sensitive loads and maintains a sinusoidal and regulated voltage across the PCC of loads with a 3.9% of distortion. Moreover, in a worst possible scenario, the already distorted utility's voltage is subjected to voltage magnitude variation. Thus, the compensator should also inject power to maintain the load PCC voltage regulated at the desired level

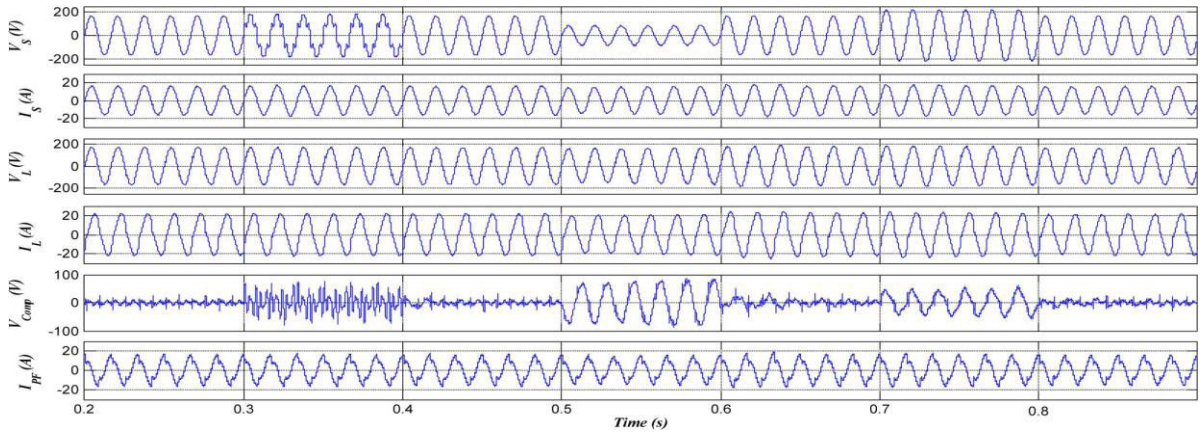

Fig. 11. Simulation of the system with the THSeAF compensating current harmonics and voltage regulation. (a) Source voltage *vS*, (b) source current *iS*, (c) load voltage *vL*, (d) load current *iL*, (e) active-filter voltage *V*Comp, and (f) harmonics current of the passive filter *I*pf

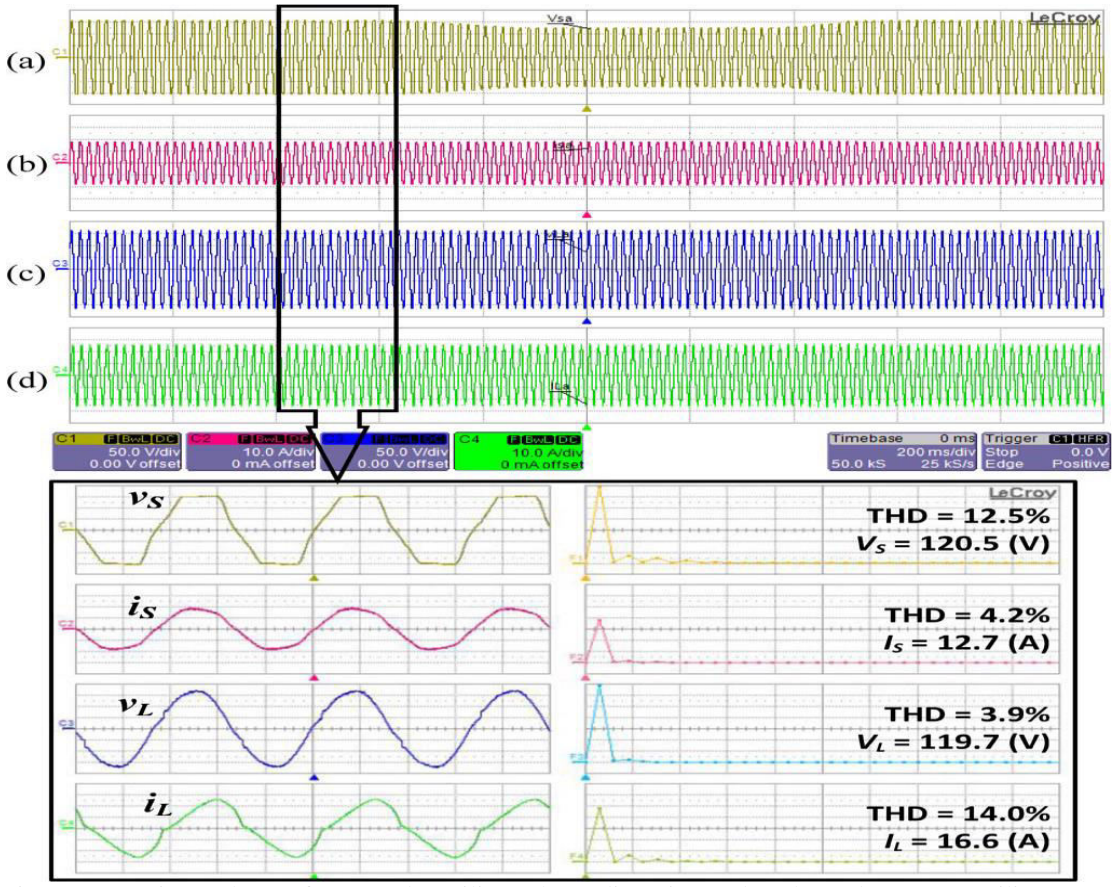

Fig. 12. Experimental waveforms under utility voltage distortion and prolonged sags. (a) Utility source voltage *vS*[50 V/div], (b) utility current *iS*[10 A/div], (c) load PCC voltage *vL*[50 V/div], and (d) load current *iL* [10 A/div]

During voltage sag and swell, the auxiliary source supplies the difference of power to maintain the magnitude of the load side voltage regulated. The harmonic content and THD factor of the source utility and load PCC presented show dramatic improvements in THD, while the load draws polluted current waveforms. Furthermore, although the grid's voltage is polluted, the compensator in a hybrid approach regulates and maintains a harmonic-free load voltage.

V. CONCLUSION

In this paper, a transformerlessTHSeAF for power quality improvement was developed and tested. The paper highlighted the fact that, with the ever increase of nonlinear loads and higher exigency of the consumer for a reliable supply, concrete actions should be taken into consideration for future smart grids in order to smoothly integrate electric car battery chargers to the grid. The key novelty of the proposed solution is that the proposed configuration could improve the power quality of the system in a more general way by compensating a wide range of harmonics current, even though it can be seen that the THSeAF regulates and improves the PCC voltage. Connected to a renewable auxiliary source, the topology is able to counteract actively to the power flow in the system. This essential capability is required to ensure a consistent supply for critical loads. Behaving as high-harmonic impedance, it cleans the power system and ensures a unity PF. The theoretical modeling of the proposed configuration was investigated. The proposed transformerless configuration was simulated and experimentally validated. It was demonstrated that this active compensator responds properly to source voltage variations by providing a constant and distortion-free supply at load terminals. Furthermore, it eliminates source harmonic currents and improves the power quality of the grid without the usual bulky and costly series transformer.

REFERENCES

[1] L. Jun-Young and C. Hyung-Jun, "6.6-kW onboard charger design using DCM PFC converter with harmonic modulation technique and two-stage dc/dc converter," *IEEE Trans. Ind. Electron.*, vol. 61, no. 3, pp. 1243– 1252, Mar. 2014.

[2] R. Seung-Hee, K. Dong-Hee, K. Min-Jung, K. Jong-Soo, and L. Byoung- Kuk, "Adjustable frequency duty-cycle hybrid control strategy for fullbridge series resonant converters in electric vehicle chargers," *IEEETrans. Ind. Electron.*, vol. 61, no. 10, pp. 5354–5362, Oct. 2014.

[3] P. T. Staats, W. M. Grady, A. Arapostathis, and R. S. Thallam, "A statistical analysis of the effect of electric vehicle battery charging on distribution system harmonic voltages," *IEEE Trans. Power Del.*, vol. 13, no. 2, pp. 640–646, Apr. 1998.

[4] A. Kuperman, U. Levy, J. Goren, A. Zafransky, and A. Savernin, "Battery charger for electric vehicle traction battery switch station," *IEEE Trans.Ind. Electron.*, vol. 60, no. 12, pp. 5391–5399, Dec. 2013.

[5] Z. Amjadi and S. S. Williamson, "Modeling, simulation, control of an advanced Luo converter for plug-in hybrid electric vehicle energy-storage system," *IEEE Trans. Veh. Technol.*, vol. 60, no. 1, pp. 64–75, Jan. 2011.

[6] H. Akagi and K. Isozaki, "A hybrid active filter for a three-phase 12-pulse diode rectifier used as the front end of a medium-voltage motor drive," *IEEE Trans. Power Del.*, vol. 27, no. 1, pp. 69–77, Jan. 2012.

[7] A. F. Zobaa, "Optimal multiobjective design of hybrid active power filters considering a distorted environment," *IEEE Trans. Ind. Electron.*, vol. 61, no. 1, pp. 107–114, Jan. 2014.

[8] D. Sixing, L. Jinjun, and L. Jiliang, "Hybrid cascaded H-bridge converter for harmonic current compensation," *IEEE Trans. Power Electron.*, vol. 28, no. 5, pp. 2170–2179, May 2013.

[9] M. S. Hamad, M. I. Masoud, and B. W. Williams, "Medium-voltage 12-pulse converter: Output voltage harmonic compensation using a series APF," *IEEE Trans. Ind. Electron.*, vol. 61, no. 1, pp. 43–52, Jan. 2014.

[10] J. Liu, S. Dai, Q. Chen, and K. Tao, "Modelling and industrial application of series hybrid active power filter," *IET Power Electron.*, vol. 6, no. 8, pp. 1707–1714, Sep. 2013.

[11] A. Javadi, H. Fortin Blanchette, and K. Al-Haddad, "An advanced control algorithm for series hybrid active filter adopting UPQC behavior," in *Proc.38th Annu. IEEE IECON*, Montreal, QC, Canada, 2012, pp. 5318–5323.

[12] O. S. Senturk and A. M. Hava, "Performance enhancement of the singlephase series active filter by employing the load voltage waveform reconstruction and line current sampling delay reduction methods," *IEEETrans. Power Electron.*, vol. 26, no. 8, pp. 2210–2220, Aug. 2011.

[13] A. Y. Goharrizi, S. H. Hosseini, M. Sabahi, and G. B. Gharehpetian, "Three-phase HFL-DVR with independently controlled phases," *IEEE Trans. Power Electron.*, vol. 27, no. 4, pp. 1706–1718, Apr. 2012.

[14] H. Abu-Rub, M. Malinowski, and K. Al-Haddad, *Power Electronics for Renewable Energy Systems, Transportation, Industrial Applications*. Chichester, U.K.: Wiley InterScience, 2014.

[15] S. Rahmani, K. Al-Haddad, and H. Kanaan, "A comparative study ofshunt hybrid and shunt active power filters for single-phase applications: Simulation and experimental validation," *Math. Comput. Simul.*, vol. 71, no. 4–6, pp. 345–359, Jun. 19, 2006.

[16] W. R. Nogueira Santos *et al.*, "The transformerless single-phase universal active power filter for harmonic and reactive power compensation," *IEEETrans. Power Electron.*, vol. 29, no. 7, pp. 3563–3572, Jul. 2014.

[17] A. Javadi, H. Fortin Blanchette, and K. Al-Haddad, "A novel transformerless hybrid series active filter," in *Proc. 38th Annu. IEEE IECON*, Montreal, QC, USA, 2012, pp. 5312–5317.

[18] H. Liqun, X. Jian, O. Hui, Z. Pengju, and Z. Kai, "High-performance indirect current control scheme for railway traction four-quadrant converters," *IEEE Trans. Ind. Electron.*, vol. 61, no. 12, pp. 6645–6654, Dec. 2014.
[19] E. K. K. Sng, S. S. Choi, and D. M. Vilathgamuwa, "Analysis of series compensation and dc-link voltage controls of a transformerlessselfcharging dynamic voltage restorer," *IEEE Trans. Power Del.*, vol. 19, no. 3, pp. 1511–1518, Jul. 2004.
[20] H. Fujita and H. Akagi, "A practical approach to harmonic compensation in power systems-series connection of passive and active filters," *IEEETrans. Ind. Appl.*, vol. 27, no. 6, pp. 1020–1025, Nov./Dec. 1991.
[21] A. Varschavsky, J. Dixon, M. Rotella, and L. Mora, "Cascaded nine-level inverter for hybrid-series active power filter, using industrial controller," *IEEE Trans. Ind. Electron.*, vol. 57, no. 8, pp. 2761–2767, Aug. 2010.
[22] X. P. n. Salmero and S. P. n. Litra, "A control strategy for hybrid power filter to compensate four-wires three-phase systems," *IEEE Trans. PowerElectron.*, vol. 25, no. 7, pp. 1923–1931, Jul. 2010.
[23] B. Singh, A. Chandra, and K. Al-Haddad, *Power Quality Problems and Mitigation Techniques*. Chichester, U.K.: Wiley, 2015.
[24] P. Salmeron and S. P. Litran, "Improvement of the electric power quality using series active and shunt passive filters," *IEEE Trans. Power Del.*, vol. 25, no. 2, pp. 1058–1067, Apr. 2010.
[25] S. Srianthumrong, H. Fujita, and H. Akagi, "Stability analysis of a series active filter integrated with a double-series diode rectifier," *IEEE Trans.Power Electron.*, vol. 17, no. 1, pp. 117–124, Jan. 2002.

AUTHOR'S PROFILE

Ramesh jatoth received hid btech degree in electrical and electronics engineering and m.tech in power system from NIT Calicut,kerala,india,in 2008 to 2010 respectively .2010 to 2014 he is asstistant professor in GIET and PBIT engineering colleges.Since 2014 he is assistant professor in methodist college of engineering and technology,Hyderabad,Telangana,india

Appl Intell
DOI 10.1007/s10489-017-0950-z

Hybrid artificial bee colony algorithm based approaches for two ring loading problems

Alok Singh[1] · **Jayalakshmi Banda**[1]

Abstract This paper presents hybrid artificial bee colony algorithm based approaches for two $\mathcal{NP}$-hard problems arising in optical ring networks. These two problems falls under the category of ring loading problems. Given a set of data transfer demands between different pair of nodes, the first problem consists in routing the demands on the ring in either clockwise or counter-clockwise directions so that the maximum data transmitted through any link in either directions is minimized. The second problem, on the other hand, discriminates between the data transmitted in one direction from the other and consists in minimizing the maximum data transmitted in one particular direction through any link. The first problem is referred to as weighted ring edge-loading problem in the literature, whereas the latter as weighted ring arc-loading problem. Computational results on the standard benchmark instances show the effectiveness of our approaches on both the problems.

Keywords Artificial bee colony algorithms · Communication networks · Ring loading · Swarm intelligence · Weighted ring arc-loading problem · Weighted ring edge-loading problem

✉ Alok Singh
alokcs@uohyd.ernet.in

Jayalakshmi Banda
bjayalakshmi@uohyd.ac.in

[1] School of Computer and Information Sciences, University of Hyderabad, Hyderabad 500046, India

1 Introduction

Synchronous Optical NETworking (SONET) in USA and Canada, and Synchronous Digital Hierarchy (SDH) in the rest of the world are the current standards for transmitting and multiplexing high speed signals over optical fibre communication networks. Basically, SONET/SDH enforce a ring based topology where nodes are connected via a ring of optical fibre cables. Each node is equipped with an Add-Drop-Multiplexer (ADM) that acts as an interface between the node and the ring and that performs the following functions

- It sends the message originating at its associated node over the ring
- It receives the message meant for its associated node over the ring and removes that message from the ring
- It relays all other messages

SONET/SDH rings are bi-directional, i.e., a message can be transmitted in either directions (clockwise or counter-clockwise) over the ring and the messages routed through clockwise direction compete with those messages routed through counter-clockwise direction for the common bandwidth. In addition to the type of optical fibre cable, the bandwidth available along any edge of SONET/SDH ring depends on the ADM [16]. The amount of data transmitting through an edge in either directions at a particular instant is called its load at that instant. Obviously, the load on any edge can not exceed the available bandwidth. Weighted Ring Edge-Loading Problem (WRELP) is an important problem in this context that seeks to minimize the maximum load on any edge. Given a set of communication

Published online: 22 May 2017

demands between various pairs of nodes, the WRELP consists in routing the demands on the ring in either clockwise or counter-clockwise directions so that the maximum load over all the edges is minimized.

IEEE 802.17 standard for Resilient Packet Ring (RPR) combines the benefits of SONET/SDH and Ethernet networks for significantly enhancing the performance of optical fibre ring networks with regard to data traffic [12, 30, 36]. Like SONET/SDH, RPR rings are also bidirectional. However, unlike SONET/SDH where there is a single bi-directional ring, RPR consists of two distinct uni-directional rings (one clockwise and another counter-clockwise) each with its own bandwidth and the messages sent through clockwise ring do not compete with those messages sent through counter-clockwise ring for the common bandwidth. So bi-directionality, RPR is achieved by making use of these two rings while sending the messages. Clearly, in RPR, we have to deal with directed edges or arcs, where an arc, depending on its direction, belongs to clockwise or counter-clockwise ring. The amount of data transmitting through an arc at a particular instant is called its load at that instant. Weighted Ring Arc-Loading Problem (WRALP) in RPR is equivalent of WRELP in SONET/SDH. Given a set of communication demands between various pairs of nodes, the WRALP problem consists in routing the demands either through clockwise ring or counter-clockwise ring so that the maximum load over all the arcs of both the rings is minimized.

Depending on whether demands can be split or not, there are two variants of WRELP and WRALP. In the first variant, demands can be split into two parts with each part routed through a different direction, whereas the second variant does not allow splitting of demands, i.e., each demand has to be routed into through one of the two directions. The first variant can be solved in polynomial time, whereas the latter variant is $\mathcal{NP}$-Hard. For those interested in the first variant may refer to [10, 26, 27, 35, 36]. In this paper, we have considered the second variant only. WRELP and WRALP with non-split demands are referred to as non-split WRELP and non-split WRALP respectively in the literature. Hereafter, in this paper, WRELP and WRALP will refer to their respective non-split variants only even if we don't use the qualifier "non-split".

In this paper, we present artificial bee colony (ABC) algorithm based hybrid approaches for WRELP and WRALP. The best solution obtained through ABC algorithm is improved further by two local searches which are applied one after the other. The ABC algorithm is same for WRELP and WRALP, but the two local searches differ according to the problem. We have compared the performance of our hybrid approaches with four state-of-the-art approaches available in the literature on the standard benchmark instances. Computational results show the superiority of our proposed approaches over these approaches. We have also evaluated the performance of our ABC approaches without the use of two local searches and found that they are capable of finding high quality solutions on their own and local searches improves the solution quality only slightly.

The remaining part of this paper is organized in the following manner: Section 2 provides an overview of ABC algorithm, whereas Section 3 defines the two ring loading problems in a formal manner. Section 4 provides a brief survey of related works in the literature. Our hybrid ABC approaches for WRELP and WRALP are presented in Section 5. Section 6 reports the computational results and provide a comparative analysis of our hybrid approaches vis-à-vis state-of-the-art approaches available in the literature. Finally, Section 7 outlines some concluding remarks and directions for future research.

2 Overview of ABC algorithm

The artificial bee colony (ABC) algorithm is a population based metaheuristic algorithm inspired from the intelligent foraging behavior of the honey bees. It is developed by D. Karaboga in 2005 [17]. There exist three groups of bees in a colony of real bees, viz. scout, employed and onlooker. Scout bees look for new food sources in the proximity of the hive. Their status is changed to employed at the moment new food sources are discovered by them. Employed bees are responsible for exploiting a food source. They bring loads of nectar to the hive and share the information about their food sources with onlooker bees which wait in the hive. This information is used by the onlooker bees in selecting the food sources which take into consideration the information shared by several employed bees. Each onlooker choose a food source with a probability directly proportional to the quality of that food source and then it becomes employed. An employed bee whose food source is exhausted will leave that food source and change its status to either scout or onlooker.

Motivated by this intelligent behavior of foraging bees, Karaboga developed ABC algorithm with the intention of solving optimization problems in continuous domain. Later, ABC algorithm was extended for solving discrete optimization problems also. Now, numerous variants of ABC algorithm exist in the literature [1, 9, 17–21, 28, 29, 32–34]. Karaboga et al. [21] provides a good survey on ABC algorithm and its applications.

In ABC algorithm, there are also three groups of bees, viz. employed, onlooker and scout with functions similar to real bees. In ABC algorithm, the food sources represent the solutions to the problem under consideration and the quality of a food source represents the fitness of the solution being represented by that food source. Every employed bee

is assigned an unique food source, which means, the number of food sources is equal to the number of employee bees. The number of onlooker bees is also taken to be equal to number of employed bees usually (but not always). Throughout this paper, we will use food source and solution interchangeably. The ABC algorithm starts with initialization, then iterates through the cycles of the employed bee and onlooker bee phases until some stopping criteria is met.

In the initialization, each employed bee is assigned a solution which is usually generated randomly. In the employed bee phase, each employed bee determines a new food source in the vicinity of its associated food source and evaluates its quality. The manner in which a new food source is determined depends on the problem under consideration. If the new food source determined by the employee bee is of better quality in comparison to its currently associated food source, then it leaves the currently associated food source and proceeds to the new food source. If the quality of the new food source is not as good as the current one, then the employee bee remains at the currently associated food source. Once all employee bees complete this process, they initiate the onlooker bee phase by sharing the information about their food sources.

In onlooker bee phase, onlookers select food sources (employed bee solutions) as per their quality. This selection is carried out in such a manner that solutions having higher fitness will have more chance of selection. Such a selection policy results in better chances of finding good quality solutions. Then, they determine the new food sources in the vicinity of their selected food sources and compute their fitness. The onlookers determine the new food sources in the same manner as employed bees. Next, the best food source among all the new food sources determined by all the onlookers who have selected food source i is found. If this food source is better than food source i, then this best food source will be the new location of food source i for the next iteration, otherwise there is no change in the location of food source i for the next iteration. Once all food sources are updated in this manner, the onlooker bee phase ends.

The ABC algorithm repeats itself through the cycles of the afore-mentioned two phases as long as the termination condition is not met. If a solution associated with an employed bee has not improved over certain number of iterations, then that solution is discarded by the associated employed bee and it becomes scout. Immediately this scouts is turned into an employed bee by associating it with a newly generated solution. This new solution is usually generated in the same manner as an initial employed bee solution.

The success of any metaheuristic algorithm will mainly depend on two factors: exploration and exploitation. A balance between these two need to be maintained to achieve good results. In the ABC algorithm, during employed bee phase, every employed bee solution is given a fair chance to improve itself. However, in the onlooker bee phase, owing to the selection policy used by the onlookers as described already, good quality solutions get more chance to improve themselves in comparison to poor quality solutions. This bias towards good quality solutions may produce better quality solutions, as there are higher chances of finding even better solutions in the proximity of good solutions. However, if a solution is locally optimal, then no better solution exists in its proximity and any attempt to improve it is futile. The concept of scout bees helps in such a situations. Instead of determining whether a solution is locally optimal or not which involves exploring the whole neighborhood and which can be computationally expensive, the ABC algorithm assumes a solution to be locally optimal when it has not improved over certain number of iterations. To get rid of this solution, its associated employee bee is made a scout. This is equivalent to the phenomenon of abandoning an exhausted food source by an employed bee associated with that food source in real bee colonies. A locally optimal solution is treated like an exhausted food source. However, unlike the real employed bee, in case of ABC algorithm, the employed bee of a locally optimal solution always becomes scout only, but never an onlooker. As explained already, a new solution is generated for this scout bee to turn it into an employed bee again. Hence by utilizing the concept of scout bees, solutions which have not improved since long are replaced with new solutions. Clearly, in case of the ABC algorithm, exploitation is carried out by employed bees and onlooker bees, whereas scouts do the job of exploration. A proper balance is maintained between exploration and exploitation by appropriately setting the number of iterations without improvement in the ABC algorithm after which an employed bee abandons a solution and becomes scout.

3 Problem formulation

Given a n node bi-directional ring $R_n = \{n_1, n_2, \ldots, n_n\}$ such that $e_i =< n_i, n_{i+1} > \forall i \in \{1, 2, \ldots, n-1\}$ and $e_n =< n_n, n_1 >$ are edges of this ring. Each edge $e_i =< n_i, n_{i+1} >$ corresponds to two directed edges or arcs represented by ordered pairs $e_i^+ = (n_i, n_{i+1})$ and $e_i^- = (n_{i+1}, n_i)$. Likewise $e_n =< n_n, n_1 >$ corresponds to two arcs $e_n^+ = (n_n, n_1)$ and $e_n^- = (n_1, n_n)$. The direction $n_1, n_2, \ldots, n_n$ corresponds to clockwise direction and $n_n, n_{n-1}, \ldots, n_1$ corresponds to counter-clockwise direction. So, e_i^+, $\forall i \in \{1, 2, \ldots, n\}$ are arcs in clockwise direction, whereas e_i^-, $\forall i \in \{1, 2, \ldots, n\}$ are arcs in counter-clockwise direction. A set of m demands is given where each demand j is represented by a triple (s_j, d_j, w_j) where s_j is the source node, $d_j \neq s_j$ is the destination

node and $w_j > 0$ is the weight associated with the demand j, which can be interpreted as the size of the data to be transmitted or amount of traffic generated to fulfil this demand. Demands can not be split, i.e., each demand needs to be routed into one of the two directions. By associating binary variables x_j with each demand j such that $x_j = 1$, means demand j is routed through clockwise direction and $x_j = 0$ means demand j is routed through counter-clockwise direction, the load $L(e_i)$ on an edge e_i can be determined as follows: Clearly, $L(e_i) = L(e_i^+) + L(e_i^-)$ where
$L(e_i^+) = \sum_{j=1}^{m} f(i,j) \times w_j$
and
$L(e_i^-) = \sum_{j=1}^{m} g(i,j) \times w_j$
The value of $f(i,j)$ and $g(i,j)$ can be determined in the following manner:

$$f(i,j) = \begin{cases} 0 \text{ if } x_j = 0 \\ 1 \text{ if } ((i < n) \text{ and } (x_j = 1) \text{ and } ((s_j \leq n_i \text{ and } d_j > n_i) \text{ or } (s_j > d_j \text{ and } s_j > n_{i+1} \text{ and } d_j > n_i))) \\ 1 \text{ if } ((i = n) \text{ and } (x_j = 1) \text{ and } (s_j > d_j \text{ and } s_j > n_1 \text{ and } d_j \geq n_1)) \\ 0 \text{ otherwise} \end{cases}$$

and

$$g(i,j) = \begin{cases} 0 \text{ if } x_j = 1 \\ 1 \text{ if } ((i < n) \text{ and } (x_j = 0) \text{ and } ((s_j > n_i \text{ and } d_j \leq n_i) \text{ or } (s_j < d_j \text{ and } s_j < n_i \text{ and } d_j \leq n_i))) \\ 1 \text{ if } ((i = n) \text{ and } (x_j = 0) \text{ and } (s_j < d_j \text{ and } s_j < n_i \text{ and } d_j \leq n_i)) \\ 0 \text{ otherwise} \end{cases}$$

The WRELP seeks a route for each of these m demands such that the maximum load over all the edges is minimized. In other words, the objective of WRELP is to find the values of m binary variables $x_1, x_2, \ldots x_m$ in such a manner that minimizes $max(L(e_1), L(e_2), \ldots, L(e_n))$

The WRALP seeks a route for each of these m demands such that the maximum load over all the arcs is minimized. In other words, the objective of WRELP is to find the values of m binary variables $x_1, x_2, \ldots x_m$ in such a manner that minimizes $max(\ell^+, \ell^-)$, where
$\ell^+ = max(L(e_1^+), L(e_2^+), \ldots, L(e_n^+))$
and
$\ell^- = max(L(e_1^-), L(e_2^-), \ldots, L(e_n^-))$.

For both WRELP and WRALP, the size of the search space is 2^m as each of m demands can be routed through one of the two possible directions. Please note that the size of the search space is independent of the number of nodes in the ring and depends only on the number of demands.

To illustrate WRELP and WRALP, let us consider the 8 nodes ring shown in Fig. 1. Suppose 10 communication demands occur between different pairs of nodes in this ring. These demands, along with their route and values of their associated variables x_i in a routing scheme (a feasible solution) are shown below:

$(1,5,4)$	*clockwise*	$x_1 = 1$
$(2,7,3)$	*counter-clockwise*	$x_2 = 0$
$(3,7,2)$	*clockwise*	$x_3 = 1$
$(4,8,5)$	*clockwise*	$x_4 = 1$
$(5,2,7)$	*counter-clockwise*	$x_5 = 0$
$(5,8,3)$	*clockwise*	$x_6 = 1$
$(6,1,5)$	*clockwise*	$x_7 = 1$
$(6,4,4)$	*counter-clockwise*	$x_8 = 0$
$(7,5,8)$	*counter-clockwise*	$x_9 = 0$
$(8,2,3)$	*clockwise*	$x_{10} = 1$

The route for each demand is also shown in Fig. 1. In this routing scheme, loads on various arcs and edges are as follows:

$L(e_1^+) = 7$	$L(e_1^-) = 3$	$L(e_1) = 10$
$L(e_2^+) = 4$	$L(e_2^-) = 7$	$L(e_2) = 11$
$L(e_3^+) = 6$	$L(e_3^-) = 7$	$L(e_3) = 13$
$L(e_4^+) = 11$	$L(e_4^-) = 11$	$L(e_4) = 22$
$L(e_5^+) = 10$	$L(e_5^-) = 12$	$L(e_5) = 22$
$L(e_6^+) = 15$	$L(e_6^-) = 8$	$L(e_6) = 23$
$L(e_7^+) = 13$	$L(e_7^-) = 3$	$L(e_7) = 16$
$L(e_8^+) = 8$	$L(e_8^-) = 3$	$L(e_8) = 11$

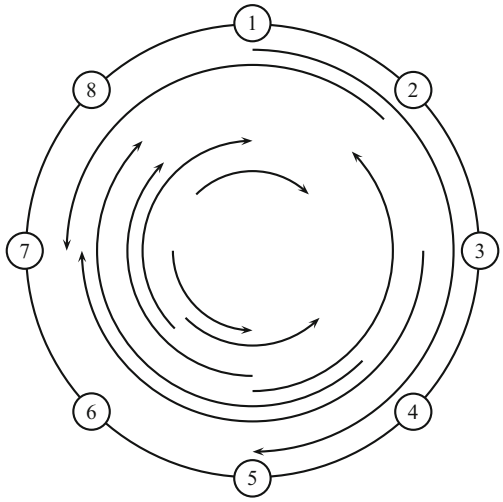

Fig. 1 Illustrating WRELP and WRALP

If the above routing scheme is used for WRELP then objective function value is 23. If the above routing scheme is used for WRALP then objective function value is 15 ($max(\ell^+, \ell^-)$, where $\ell^+ = 15$, $\ell^- = 12$).

4 Related work

Cosares and Saniee [11] introduced non-split WRELP and proved its $\mathscr{NP}$-hardness. This problem is known to be polynomially solvable only in cases where all demands are one [14]. The non-split WRALP was introduced and proved $\mathscr{NP}$-hard by Yuan et al. [36] and further studied in [10, 25].

Schrijver et al. [31] proposed a highly efficient greedy heuristic for WRELP, which returns a solution that can exceed the optimal by at most $\frac{3}{2}$ times the maximum demand and which performs much better in practice. Moreover, this heuristic finds the optimal solution when all demands are equal to one. Extending this work, Khanna [23] developed a polynomial time approximation scheme for this problem. Dell' Amico et al. [13] presented efficient lower and upper bounding procedures, and a branch-and-bound based exact algorithm for WRELP.

Among the metaheuristics techniques for WRELP and WRALP, Karunanithi and Carpenter [22] proposed a genetic algorithm for WRELP and solved the small instances of WRELP. Kim et al. [24] presented different variations of Ant Colony Optimization (ACO) Algorithm for WRELP. [2–6, 8] proposed several evolutionary algorithms based approaches and a tabu search based approach for WRELP and several evolutionary algorithms and swarm intelligence based approaches for WRALP. In particular, [5] describes an artificial bee colony algorithm based approach for WRALP. As explained in Section 5, our proposed ABC algorithm is altogether different from this ABC algorithm except for solution encoding. Further, unlike the ABC approach of [5], no local search is used inside the neighboring solution generation procedure in our ABC approach. Our neighboring solution generation procedure is based on a very simple, but effective strategy. Hence, our ABC approach is computationally more efficient.

Bernardino et al. [7] presented a genetic algorithm (GA), a hybrid differential evolution algorithm (HDEM) and a hybrid discrete particle swarm optimization algorithm (HDPSO) for WRELP and WRALP and compared the performance of these three approaches on both the problems with best performing previously proposed approaches mentioned above. The HDEM performed the best followed by ABC approach of [5] and HDPSO on both the problems. It is to be noted, that ABC approach was presented in [5] for WRALP. However, [7] presented the results of ABC approach for WRELP also. We have compared our proposed approaches with these four approaches, viz. GA, HDEM, HDPSO and ABC on the same benchmark instances as used in [7].

As mentioned already, we have applied the two local searches only on the best solution obtained through ABC algorithm. This strategy has already been used in the ABC literature, e.g. [29, 34]. However, this strategy deviates from the widely used strategy of combining local search with ABC algorithm where local search is used inside ABC algorithm to improve the neighboring solutions. Actually, applying a local search on every/some neighboring solutions inside ABC algorithm is computationally expensive in comparison to using it once on the best solution. This latter strategy is useful in circumstances where either the local search is computationally too expensive to be used inside ABC algorithm or the best solution produced by ABC algorithm without any local search is already closed to optimal/best known solution values and applying the local search only on the best solution can produce the results of desired quality. We have used the strategy of applying local search only on the best solution due to latter reason.

5 Hybrid ABC approaches for WRELP and WRALP

We have developed hybrid approaches combining artificial bee colony (ABC) algorithm with local search procedures for WRELP and WRALP. Except for fitness function, the

ABC algorithm is same for both the problems. The local search procedure consists of two local searches that are applied one after the other. These two local searches vary according to the problem. The local search procedure is applied only to the best solution obtained through ABC algorithm in a bid to further improve its quality. Hereafter, our hybrid approach for WRELP will be referred to as HABC-E, whereas our hybrid approach for WRALP will be referred to as HABC-A.

Following subsections describe other salient features of proposed approaches.

5.1 Solution encoding

We have used a bit vector of length m to represent a solution, where m is the total number of communication demands. A value of 1 at the i^{th} position indicates that demand i to be routed in clockwise direction, whereas a value of 0 at the same place indicates that demand i to be routed in counter-clockwise direction. Bernardino et al. [7] and [5] also used the same encoding.

5.2 Fitness

We have used the objective function as the fitness function. So, HABC-E uses objective function of WRELP as fitness function, whereas HABC-A uses objective function of WRALP as fitness function. As WRELP and WRALP are minimization problems, so for these problems, a lower value of the fitness function indicates a more fit solution.

5.3 Initial employed bee solutions

Among the initial employed bee solutions, the first solution is generated by following a shortest path strategy where each demand is routed through the direction where it has to traverse lesser number of links in comparison to the other direction (ties are broken arbitrarily). All other initial employed bee solutions are generated by following either a purely random strategy or a strategy that is a mix of greediness and randomness. The first strategy is used with probability ρ_{ir}, otherwise the second strategy is used. In the first strategy, each demand is routed uniformly at random in one of the two directions. In the second strategy, each demand is routed through shortest path with probability ρ_{ig}, otherwise it is routed uniformly at random in one of the two directions. ρ_{ir} and ρ_{ig} are two parameters whose values need to be determined empirically. The values for these parameters are chosen in such a manner so that the initial population of employed bee solutions is a proper mix of greediness and randomness.

The ABC approach of [5] generates initial employed bee solutions either in a completely random manner or in a completely deterministic manner. The deterministic strategy was again based on shortest path algorithm.

5.4 Policy used by onlookers to select a food source

We have used probabilistic binary tournament selection method to select a food source for each onlooker bee. This method works by choosing two different food sources uniformly at random and then comparing their fitness. With probability ρ_o, more fit food source is selected, otherwise the lesser fit food source is selected. ρ_o is a parameter to be determined empirically. The reason for using probabilistic binary tournament selection method in place of roulette wheel selection method, which is used commonly in ABC algorithm is that probabilistic binary tournament selection method performs better in general and at the same time computationally less expensive [15].

The ABC algorithm of [5] assigns $P_i \times NO$ onlookers to a food source i, where $P_i = \frac{\sum_{j=1}^{NE} F_j - F_i}{\sum_{j=1}^{NE} F_j}$, F_i is the fitness of food source i, and NE is the number of employed bees and NO is the upper limit on the number of onlookers that can be sent to any food source. Usually, $\sum_{j=1}^{NE} F_j$ is much larger than the fitness of any solution and hence P_i is near to 1 for all $i = 1, \ldots, NE$. NO is taken to be greater than NE in [5], so a large number of onlookers are deputed for every solution in their approach. In contrast, we have used total number of onlookers for all food sources to be twice as much as there are food sources.

5.5 Neighboring solution generation

Our neighboring solution generation method is based on the fact that if a demand is routed through a particular direction in one good solution, then it is highly likely that this demand is routed through the same direction in many good solutions. Hence, to generate a new solution X' in the neighborhood of a solution X, another solution Y is utilized. The solution Y is chosen randomly from all employed bee solutions other than X. Then to create X', each demand is considered one-by-one and it is routed in X' through the same direction as in Y with small probability ρ_{ns}, otherwise it is routed through the same direction as in X. Pseudo-code of neighboring solution generation process is given in Algorithm 1, where $X[i]$ refers to the i^{th} element (bit) of solution X which is a bit vector.

Algorithm 1 Pseudo-code of neighboring solution generation process

```
Input: A solution X
Output: A new solution X' in the neighborhood of X
Select a solution Y randomly from all employed bee solutions other than X;
for i ← 1 to m do
    if (u_01 < ρ_ns) then
        X'[i] ← Y[i];
    else
        X'[i] ← X[i];
return X';
```

We have applied the afore-mentioned neighboring solution generation method in both employed and onlooker bee phases. Bernardino et al. [5] used different neighboring solution generation methods in employed and onlooker bee phases. Unlike our neighboring solution generation method which does not use any form of local search, these methods do partial local search around a solution to generate its neighboring solution. Hence, all these methods are computationally much more expensive than our method. In the employed bee phase, two neighboring solution generation methods are used. In the first method called "Exchange Direction", some demand pairs are randomly selected and each pair is checked one-by-one to see whether the exchange of directions between the two demands in the pair can improve the original solution. If more than one such exchanges are possible, then the exchange which results in the solution of least cost is performed and solution thus obtained replaces the original solution. If no such exchange exists, then the original solution does not change. The second method called "Exchange Max Arc" randomly selects some demands routed through the arc having the highest load and tries to flip the direction of each of these demands one-by-one so as to improve the solution. Again the best improvement strategy is followed like the previous method. In onlooker bee phase, the neighboring solution generation method tries to improve a solution by changing the direction of a randomly chosen demand in the solution. With probability 0.5, the direction of the chosen demand is set to shortest path, otherwise the direction of the chosen demand is set to its direction in the best solution. If the solution improves, the methods stops, otherwise it repeats itself. The method stops only after some fixed number of unsuccessful attempts.

5.6 Other features

If an employed bee solution X has not improved over S_{it} number of consecutive iterations, then it is assumed to be locally optimal and replaced with a new solution X'. However, instead of generating X' like the initial population members, which is usually the case with most ABC algorithms including the one described in [5], we have generated X' by perturbing X. For perturbing X to generate X', each demand is considered one-by-one and its direction in X is flipped with probability ρ_s. We have followed this perturbation strategy because solution thus generated retains major part of the original highly fit solution, and as a result, it is expected to be of better quality in comparison to a solution generated in a manner similar to initial population members.

Unlike the traditional ABC algorithm where there is an upper limit of only one scout in an iteration, we have not imposed any limit on the number of employed bee solutions replaced in an iteration, i.e., number of scouts. This number can be more than one or can be zero depending on how many employed bee solutions in an iteration has not improved over last S_{it} number of consecutive iterations. This is also different from ABC approach of [5], where in every iteration, the number of scouts is equal to 10% of the number of employed bees. The solutions for these scouts bee are created in the same manner as the initial population members. Instead of replacing those employed bee solutions which has not improved since long, these scout bee solutions replace worst employed bee solutions in case scout bee solutions are better. However, this is a severe flaw because if an employed bee solution is locally optimal, it will forever remain in the population and waste computational efforts without offering any opportunity for further improvement.

5.7 Local search procedure

As mentioned already, our local search procedure is composed of two local searches which are applied one after the other on the best solution obtained through ABC algorithm. Our first local search repeatedly applies a direction flip based heuristic as long as there is improvement in solution quality. This heuristic considers each demand one-by-one in their natural order and flips its direction in the solution, if doing so reduces the objective function value. It is to be noted that in case of WRELP problem, flipping the direction of only those demands can possibly reduce the objective function value which are currently routed through the edge having the maximum load. Similarly, in case of WRALP problem, flipping the direction of only those demands can possibly reduce the objective function value which are currently routed through the arc having the maximum load. Hence, for efficiency considerations, only such potential demands should be tried for flipping.

Our second local search repeatedly applies a heuristic, which considers a pair of demands at a time, as long as there is improvement in solution quality. This heuristic considers each demand one-by-one in some random order (for implementing the random ordering, every time the heuristic begins execution, a random sequence of demands is generated) and if the demand under consideration, say i, contributes to the maximum load, then we try to pair it with some other demand so that flipping the directions of both the demands together reduces the objective function values. The demands are tried for pairing with demand i in their natural order. If such a pairing is found, then we immediately do the required flipping and then again all demands are tried one-by-one for pairing with i. Only when i can not be paired with any other demand to reduce the objective function value, next demand in the random sequence is considered. Demands in a pair can have the same direction or opposite directions. Again for efficiency considerations, we can curtail the number of demands that need to be tried for pairing

with i. Only those demands can possibly pair with i which does not contribute to the maximum load and which have weight less than that of i. In case of WRELP, a demand contributes to the maximum load if it is routed through the edge having the maximum load. In case of WRALP, a demand contributes to the maximum load if it is routed through the arc having the maximum load.

The pseudo-code of hybrid ABC approach is presented in Algorithm 2. In this algorithm, E_n and O_n are the number of employed bees and onlooker bees respectively. *DNS(X)* is a function that determines a new solution X' in the neighborhood of the solution X and returns X' (Section 5.5). Pseudo-code for *DNS(X)* is given in Algorithm 1. Function *PBTS*(e_1, e_2,...,e_E) implements the probabilistic binary tournament selection method (Section 5.4). This function returns the index of the solution selected. Function *Perturb(X)* perturbs a solution X to generate a new solution X' as per Section 5.6. *LS_1(best)* and *LS_2(best)* are two functions that implement the two local searches described in Section 5.7. These two local searches are applied once on the best solution returned by ABC algorithm.

Algorithm 2 Pseudo-code of hybrid ABC approach

```
Input: Set of parameters for ABC algorithm and a WRALP/WRELP instance
Output: Best solution found
Generate E_n initial employed bee solutions e_1, e_2, ..., e_{E_n};
best ← Best solution among e_1, e_2, ..., e_{E_n};
while best has improved over specified number of previous iterations do
    for i ← 1 to E_n do
        e_i' ← DNS(e_i);
        if e_i' is better than e_i then
            e_i ← e_i';
        else if e_i has not improved over last S_it iterations then
            e_i ← Perturb(e_i);
        if e_i is better than best then
            best ← e_i;
    for i ← 1 to O_n do
        j ← PBTS(e_1, e_2, ..., e_{E_n});
        o_i ← DNS(e_j);
        if o_i is better than e_j then
            e_j ← o_i;
            if o_i is better than best then
                best ← o_i;
best ← LS_1(best);
best ← LS_2(best);
return best;
```

6 Computational results

To evaluate the performance of HABC-A and HABC-E, we have used the same 19 instances as used in [7] and [5]. The number of nodes (n) in these instances vary from 5 to 30 and the number of demands (m) in these instances vary from 6 to 435. To generate these instances, six equally spaced values of n in the interval [5, 30] are considered, i.e., $n \in \{5, 10, 15, 20, 25, 30\}$. Hence, with respect to n, there are six cases which are called case 1 ($n = 5$), case 2 ($n = 10$) and so on. The rings with 5/10/15 nodes are characterised as ordinary sized rings and rings with 20/25/30 as extremely large rings. For a n node ring, $\frac{n(n-1)}{2}$ demand pairs are possible. So if the demand set contains all these pairs then the demand set is said to be complete, otherwise it is said to be partial. Four different cases are considered with respect to the type of demand set. The first three cases are applicable for all values of n, whereas the last case is applicable to only $n = 30$. The first case consists of complete set of demands, the second case consists of partial set of demands with $max(\lceil \frac{n(n-1)}{4} \rceil, 8)$ demand pairs randomly chosen from complete set of demands and the third case consists of partial sets of demands with $max(\lceil \frac{n(n-1)}{8} \rceil, 6)$ demand pairs randomly chosen from complete set of demands. The weights associated with demands is considered to be uniformly distributed in the interval [5, 100] in these three cases. For each combination of n and these three demand cases, a single instance is generated leading to a total of 18 instances. The last demand case is applicable for $n = 30$ only and consists of a complete set of demands with weights uniformly distributed in [1, 500]. Again, a single instance is generated for this case, thereby, leading to a grandtotal of 19 instances. These instances have the name of the form Cxy where $x \in \{1, 2, 3, 4, 5, 6\}$ is the case with respect to the value of n and $y \in \{1, 2, 3, 4\}$ is the case with respect to demand set. Please also note, that $y = 4$ only when $x = 6$. Except for larger ring sizes and higher variance in demand weights, these instances are similar to the instances used previously in the literature for ring loading problems. Table 1 presents the characteristics of these test instances along with their best known values (BKV) for WRALP and WRELP.

Table 1 Characteristics of test instances along with their best known values (BKV)

Instance	#Nodes(n)	#Demands(m)	BKV(WRALP)	BKV(WRELP)
C11	5	10	161	185
C12	5	8	116	137
C13	5	6	116	137
C21	10	45	525	583
C22	10	23	243	352
C23	10	12	141	199
C31	15	105	1574	1657
C32	15	50	941	941
C33	15	25	563	618
C41	20	190	2581	2745
C42	20	93	1482	1760
C43	20	40	612	683
C51	25	300	4265	4304
C52	25	150	2323	2488
C53	25	61	912	1015
C61	30	435	5762	5953
C62	30	201	2696	2901
C63	30	92	1453	1506
C64	30	435	27779	29245

We have implemented HABC-A and HABC-E approaches in C and executed them on a 2.83 GHz Intel Q9550 processor based system under Linux environment. In all our computational experiments with HABC-A, we have used $E_n = 100$, $O_n = 200$, $\rho_{ir} = 0.95$ if $m < 250$, otherwise $\rho_{ir} = 0.75$, $\rho_{ig} = 0.25$, $\rho_o = 0.8$, $\rho_{ns} = max(0.15, \frac{2}{m})$, $\rho_s = max(0.15, \frac{4}{m})$. If $m < 250$ then S_{it} is set to 60 and HABC-A terminates when best solution has not improved over 100 consecutive iterations, otherwise ($m \geq 250$) S_{it} is set to 90 and HABC-A terminates when best solution has not improved over 150 consecutive iterations. In all our computational experiments with HABC-E, we have used $E_n = 125$, $O_n = 175$, $\rho_{ir} = 0.75$, $\rho_{ig} = 0.25$, $\rho_o = 0.8$, $\rho_{ns} = max(0.15, \frac{2}{m})$, $\rho_s = max(0.1, \frac{4}{m})$. If $m < 250$ then S_{it} is set to 15 and HABC-E terminates when best solution has not improved over 100 consecutive iterations, otherwise ($m \geq 250$) S_{it} is set to 25 and HABC-E terminates when best solution has not improved over 150 consecutive iterations. These parameter values are chosen empirically after performing a large number of trials. Approaches proposed in [7] and [5] were designed with the intention of obtaining best known solution value in every run and their termination conditions were chosen accordingly. To allow a fair comparison with the approaches of [7] and [5], the termination conditions for HABC-A and HABC-E are chosen with the same intention. Please also note that HABC-E and HABC-A both use 300 bees in total ($E_n + O_n$) in an iteration, though the number of employed and the number of onlooker bees used by them differ, and hence, their termination conditions are equivalent in terms of total number of solutions generated without improvement in quality of best solution. Like the approaches of [7] and [5], HABC-A and HABC-E approaches are executed 100 times independently on each instance. As termination conditions are chosen for various methods to reach the best known solution value in every run, therefore, comparison is done on execution time. However, on instance C51, we found value of 4283 for WRELP which is better than BKV of 4304 and no matter how we tried, we failed to get this value of 4283 in every run. Please refer to Table 5 for average solution quality in case of this instance.

Table 2 compares the average execution time of HABC-A on WRALP instances with that of genetic algorithm (GA), hybrid differential evolution algorithm (HDEM), hybrid particle swarm optimisation algorithm (HDPSO) and artificial bee colony algorithm (ABC). The first three approaches are from [7], whereas the last approach is from [5]. Data for GA, HDEM, HDPSO and ABC approaches have been taken from [7] where all the approaches were executed on a 2.66 GHz Intel Q9450 processor based system and average time and iterations to reach the best solution were reported for each method. From average time and iteration to reach the best solution, we got average time per iteration and multiplying it with total number of iterations allotted yielded the execution time. This is done to follow the standard practice

Table 2 Execution times of various approaches in seconds on WRALP instances

Instance	GA	HDEM	HDPSO	ABC	HABC-A
C11	<0.10	<0.10	<0.10	<0.10	<0.10
C12	<0.10	<0.10	<0.10	<0.10	<0.10
C13	<0.10	<0.10	<0.10	<0.10	<0.10
C21	<0.10	<0.10	<0.10	<0.10	<0.10
C22	<0.10	<0.10	<0.10	<0.10	<0.10
C23	<0.10	<0.10	<0.10	<0.10	<0.10
C31	0.33	1.00	0.50	0.67	0.23
C32	<0.10	<0.10	<0.10	<0.10	<0.10
C33	<0.10	<0.10	<0.10	<0.10	<0.10
C41	0.60	0.90	0.53	1.20	0.53
C42	0.19	0.30	0.16	0.3	0.22
C43	<0.10	<0.10	<0.10	<0.10	<0.10
C51	4.69	10.00	2.50	5.00	1.15
C52	1.00	2.00	1.00	2.13	0.39
C53	0.10	0.19	0.09	0.19	0.16
C61	20.19	64.29	15.63	28.13	2.03
C62	3.33	7.50	3.00	5.00	0.65
C63	1.25	2.50	1.25	2.50	0.22
C64	5.00	16.67	10.00	10.00	2.99

Table 3 Execution times of various approaches in seconds on WRELP instances

Instance	GA	HDEM	HDPSO	ABC	HABC-A
C11	<0.10	<0.10	<0.10	<0.10	<0.10
C12	<0.10	<0.10	<0.10	<0.10	<0.10
C13	<0.10	<0.10	<0.10	<0.10	<0.10
C21	<0.10	<0.10	<0.10	<0.10	<0.10
C22	<0.10	<0.10	<0.10	<0.10	<0.10
C23	<0.10	<0.10	<0.10	<0.10	<0.10
C31	0.33	0.67	0.50	0.40	0.19
C32	<0.10	<0.10	<0.10	<0.10	<0.10
C33	<0.10	<0.10	<0.10	<0.10	<0.10
C41	0.45	0.75	0.50	0.40	0.45
C42	0.19	0.33	0.20	0.40	0.18
C43	<0.10	<0.10	<0.10	<0.10	<0.10
C51	5.00	6.25	3.33	6.25	1.58
C52	1.00	2.00	0.80	1.33	0.39
C53	0.10	0.25	0.13	0.17	0.13
C61	22.5	60.00	17.50	18.50	2.00
C62	4.29	10.00	5.00	8.33	0.55
C63	1.25	3.75	1.25	2.50	0.19
C64	3.75	12.50	3.13	4.17	2.67

Table 4 Relative contribution of two local searches and artificial bee colony framework on WRALP instances

Instance	HABC-A				FABC-A				ABC-A			
	Best	Avg	SD	AvT	Best	Avg	SD	AvT	Best	Avg	SD	AvT
C11	161	161.00	0.00	0.01	161	161.00	0.00	0.01	161	161.00	0.00	0.01
C12	116	116.00	0.00	0.01	116	116.00	0.00	0.01	116	116.00	0.00	0.01
C13	116	116.00	0.00	0.01	116	116.00	0.00	0.01	116	116.00	0.00	0.01
C21	525	525.00	0.00	0.07	525	525.00	0.00	0.07	525	525.00	0.00	0.07
C22	243	243.00	0.00	0.05	243	243.00	0.00	0.05	243	243.09	0.51	0.05
C23	141	141.00	0.00	0.02	141	141.00	0.00	0.02	141	141.00	0.00	0.02
C31	1574	1574.00	0.00	0.23	1574	1574.00	0.00	0.23	1574	1574.00	0.00	0.23
C32	941	941.00	0.00	0.09	941	941.00	0.00	0.09	941	941.00	0.00	0.09
C33	563	563.00	0.00	0.04	563	563.00	0.00	0.04	563	563.00	0.00	0.04
C41	2581	2581.00	0.00	0.53	2581	2581.00	0.00	0.52	2581	2581.00	0.00	0.52
C42	1482	1482.00	0.00	0.22	1482	1482.00	0.00	0.22	1482	1482.00	0.00	0.22
C43	612	612.00	0.00	0.07	612	612.00	0.00	0.07	612	612.00	0.00	0.07
C51	4265	4265.00	0.00	1.15	4265	4265.00	0.00	1.15	4265	4265.00	0.00	1.15
C52	2323	2323.00	0.00	0.39	2323	2323.00	0.00	0.39	2323	2323.00	0.00	0.39
C53	912	912.00	0.00	0.16	912	912.00	0.00	0.16	912	912.00	0.00	0.16
C61	5762	5762.00	0.00	2.03	5762	5762.00	0.00	2.02	5762	5762.00	0.00	2.02
C62	2696	2696.00	0.00	0.65	2696	2696.00	0.00	0.65	2696	2696.00	0.00	0.65
C63	1453	1453.00	0.00	0.22	1453	1453.00	0.00	0.22	1453	1453.00	0.00	0.22
C64	27779	27779.00	0.00	2.99	27779	27779.06	0.28	2.98	27779	27779.23	0.58	2.98

Table 5 Relative contribution of two local searches and artificial bee colony framework on WRELP instances

Instance	HABC-E				FABC-E				ABC-E			
	Best	Avg	SD	AvT	Best	Avg	SD	AvT	Best	Avg	SD	AvT
C11	185	185.00	0.00	0.01	185	185.00	0.00	0.01	185	185.00	0.00	0.01
C12	137	137.00	0.00	0.01	137	137.00	0.00	0.01	137	137.00	0.00	0.01
C13	137	137.00	0.00	0.01	137	137.00	0.00	0.01	137	137.00	0.00	0.01
C21	583	583.00	0.00	0.07	583	583.00	0.00	0.07	583	583.00	0.00	0.07
C22	352	352.00	0.00	0.03	352	352.00	0.00	0.03	352	352.00	0.00	0.03
C23	199	199.00	0.00	0.02	199	199.00	0.00	0.02	199	199.00	0.00	0.02
C31	1657	1657.00	0.00	0.19	1657	1657.00	0.00	0.19	1657	1657.00	0.00	0.19
C32	941	941.00	0.00	0.08	941	941.00	0.00	0.08	941	941.00	0.00	0.08
C33	618	618.00	0.00	0.04	618	618.00	0.00	0.04	618	618.00	0.00	0.04
C41	2745	2745.00	0.00	0.45	2745	2745.00	0.00	0.45	2745	2745.00	0.00	0.45
C42	1760	1760.00	0.00	0.18	1760	1760.00	0.00	0.18	1760	1760.00	0.00	0.18
C43	683	683.00	0.00	0.07	683	683.00	0.00	0.07	683	683.00	0.00	0.07
C51	4283	4284.11	1.16	1.58	4283	4284.55	1.24	1.58	4283	4284.59	1.30	1.58
C52	2488	2488.00	0.00	0.39	2488	2488.00	0.00	0.39	2488	2488.00	0.00	0.39
C53	1015	1015.00	0.00	0.13	1015	1015.00	0.00	0.13	1015	1015.00	0.00	0.13
C61	5953	5953.00	0.00	2.00	5953	5953.00	0.00	2.00	5953	5953.00	0.00	2.00
C62	2901	2901.00	0.00	0.55	2901	2901.00	0.00	0.55	2901	2901.00	0.00	0.55
C63	1506	1506.00	0.00	0.19	1506	1506.00	0.00	0.19	1506	1506.00	0.00	0.19
C64	29245	29245.00	0.00	2.67	29245	29245.02	0.14	2.67	29245	29245.06	0.24	2.67

of comparing execution times of various approaches. No matter how fast the best solution is obtained, it is returned only when the program finishes execution, and hence, comparison of time required to reach the best solution does not make sense. For small instances C11, C12, C13, C21, C22, C23, C32, C33 and C41, [7] did not report the average time till best precisely and mentioned that they are < 0.001 seconds, and hence, for these instances we have not reported the execution times precisely in Table 2. However, precise execution times for HABC-A are reported in Table 4. In a manner similar to Table 2, Table 3 compares the average execution time of HABC-E on WRELP instances with that of GA, HDEM, HDPSO and ABC approaches. These tables clearly show the superiority of HABC-A and HABC-E in terms of execution times over other methods on large instances of WRALP and WRELP both. Moreover, the difference in speed between our approaches and other methods widens with increase in number of demands. Please note that we have executed our approaches on a 2.83 GHz Intel Q9550 processor based system which is different from the system used to execute GA, HDEM, HDPSO and ABC approaches (2.66 GHz Intel Q9450 processor). However, Q9550 and Q9450 processors belong to the same series of processors and Q9550 is the immediate successor of Q9450. Hence, there is only a slight difference is processing speeds of the two systems and conclusions drawn here take into account this difference.

To show the relative contribution of two local searches and artificial bee colony framework, we have implemented HABC-A and HABC-E approaches without any local search and with only first local search. The versions without any local search will be referred to as ABC-A and ABC-E, whereas the versions with only first local search will be referred to as FABC-A and FABC-E respectively. Tables 4 & 5 report the results. For each instance, we report the best solution (column Best), average solution quality (column Avg) and standard deviation of solution values (column SD) over 100 runs found by HABC-A, FABC-A, ABC-A or HABC-E, FABC-E, ABC-E as the case may be along with their respective average execution times (column AvT) in seconds. These tables clearly show that local searches contribute little to the success of artificial bee colony algorithm which is capable of finding best solutions on its own in most runs.

7 Conclusions

In this paper, we have proposed hybrid artificial bee colony algorithm based approaches for two real-world $\mathscr{NP}$-hard problems belonging to the domain of optical ring networks. Computational results on the standard benchmark instances of the problems show the effectiveness of the proposed approaches. Our ABC approaches are capable of finding high quality solutions on their own even without the use of local search.

As a future work, we would like to work on a multi-objective version of ring loading problems involving multiple costs. Approaches similar to our approaches can be designed for other related assignment problems.

Acknowledgments Authors are grateful to Dr. A. M. Bernardino for providing the test instances for WRELP/WRALP. Authors would like to thank two anonymous reviewers also for their valuable comments and suggestions which helped in improving the quality of this manuscript.

References

1. Banda J, Singh A (2015) A hybrid artificial bee colony algorithm for the terminal assignment problem. In: Swarm, evolutionary, and memetic computing, lecture notes in computer science, vol 8947, Springer-Verlag, pp 134–144
2. Bernardino A, Bernardino E, Sánchez-Pérez J, Gómez-Pulidoua J, Vega-Rodríguez M (2009) Solving the ring loading problem using genetic algorithms with intelligent multiple operators. In: International symposium on distributed computing and artificial intelligence 2008 (DCAI 2008), Springer, pp 235–244
3. Bernardino A, Bernardino E, Sánchez-Pérez J, Gómez-Pulidoua J, Vega-Rodríguez M (2009) Solving the weighted ring edge-loading problem without demand splitting using a hybrid differential evolution algorithm. In: 2009 IEEE 34th Conference on local computer networks, IEEE, pp 562–568
4. Bernardino A, Bernardino E, Sánchez-Pérez J, Gómez-Pulidoua J, Vega-Rodríguez M (2010) A discrete differential evolution algorithm for solving the weighted ring arc loading problem. In: International conference on industrial, engineering and other applications of applied intelligent systems, Springer, pp 153–163
5. Bernardino A, Bernardino E, Sánchez-Pérez J, Gómez-Pulidoua J, Vega-Rodríguez M (2010) Efficient load balancing for a resilient packet ring using artificial bee colony. In: Proceedings of applications of evolutionary computation: EvoApplications 2010, lecture notes in computer science, vol 6025, Springer-Verlag, pp 61–70
6. Bernardino A, Bernardino E, Sánchez-Pérez J, Gómez-Pulidoua J, Vega-Rodríguez M (2010) A hybrid ant colony optimization algorithm for solving the ring arc-loading problem. In: Hellenic conference on artificial intelligence, Springer, pp 49–59
7. Bernardino A, Bernardino E, Sánchez-Pérez J, Gómez-Pulido J, Vega-Rodríguez M (2011) Solving ring loading problems using bio-inspired algorithms. J Netw Comput Appl 34(2):668–685
8. Bernardino AM, Bernardino EM, Sánchez-Pérez JM, Pulido JAG, Vega-Rodríguez MA (2009c) Solving the non-split weighted ring arc-loading problem in a resilient packet ring using particle swarm optimization. In: Proceedings of the international conference in evolutionary computations, pp 230–236
9. Chaurasia S, Singh A (2015) A hybrid swarm intelligence approach to the registration area planning problem. Inf Sci 302:50–69
10. Cho K, Joo U, Lee H, Kim B, Lee W (2005) Efficient load balancing algorithms for a resilient packet. ETRI J 27(1):110–113
11. Cosares S, Saniee I (1994) An optimization problem related to balancing loads on sonet rings. Telecommun Syst 3(2):165–181
12. Davik F, Yilmaz M, Gjessing S, Uzun N (2004) Ieee 802.17 resilient packet ring tutorial. IEEE Commun Mag 42(3):112–118

13. Dell'Amico M, Labbé M, Maffioli F (1999) Exact solution of the {SONET} ring loading problem. Oper Res Lett 25(3):119–129
14. Frank A, Nishiseki T, Saito N, Suzuki H, Tardos E (1992) Algorithms for routing around a rectangle. Discret Appl Math 40:363–378
15. Goldberg DE, Deb K (1991) A comparative analysis of selection schemes used in genetic algorithms. In: Proceedings of the 1991 conference on foundations of genetic algorithms, Morgan Kaufmann, pp 69–93
16. Goralski W (2002) SONET. McGraw-Hill Professional
17. Karaboga D (2005) An idea based on honey bee swarm for numerical optimization. In: Technical Report-TR06, Erciyes University, Engineering Faculty, Computer Engineering Department, Turkey
18. Karaboga D, Akay B (2007) A powerful and efficient algorithm for numerical function optimization: artificial bee colony (ABC) algorithm. J Glob Optim 39(3):459–471
19. Karaboga D, Akay B (2008) On the performance of artificial bee colony (ABC) algorithm. Appl Soft Comput 8(1):687–697
20. Karaboga D, Akay B (2009) A comparative study of artificial bee colony algorithm. Appl Math Comput 214(1):108–132
21. Karaboga D, Gorkemli B, Ozturk C, Karaboga N (2014) A comprehensive survey: artificial bee colony (ABC) algorithm and applications. Artif Intell Rev 42(1):21–57
22. Karunanithi N, Carpenter T (1994) A ring loading application of genetic algorithms. In: Proceedings of the 1994 ACM symposium on applied computing, ACM, New York, NY, USA, SAC '94, pp 227–231
23. Khanna S (1997) A polynomial time approximation scheme for the sonet ring loading problem. Bell Labs Tech J 2(2):36–41
24. Kim SS, Kim IH, Mani V, Kim H (2008) Ant colony optimization for sonet ring loading problem. Int J Innov Comput Inf Control 4(7):1617–1626
25. Kubat P, Smith J (2005) Balancing traffic flows in resilient packet rings. Springer, US, pp 125–140
26. Myung YS, Kim HG (2004) On the ring loading problem with demand splitting. Oper Res Lett 32(2):167–173
27. Myung YS, Kim HG, Tcha DW (1997) Optimal load balancing on sonet bidirectional rings. Oper Res 45(1):148–152
28. Pan Q, Tasgetiren M, Suganthan P, Chua T (2011) A discrete artificial bee colony algorithm for the lot-streaming flow shop scheduling problem. Inf Sci 181(12):2455–2468
29. Pandiri V, Singh A (2015) Two metaheuristic approaches for the multiple traveling salesperson problem. Appl Soft Comput 26:74–89
30. RPR Alliance (2004) A summary and overview of the IEEE 802.17 resilient packet ring standrad
31. Schrijver A, Seymour P, Winkler P (1998) The ring loading problem. SIAM J Discret Math 11(1):1–14
32. Sharma TK, Pant M (2013) Enhancing the food locations in an artificial bee colony algorithm. Soft Comput 17(10):1939–1965
33. Singh A (2009) An artificial bee colony algorithm for the leaf-constrained minimum spanning tree problem. Appl Soft Comput 9(2):625–631
34. Singh A, Sundar S (2011) An artificial bee colony algorithm for the minimum routing cost spanning tree problem. Soft Comput 15(12):2489–2499
35. Wang B (2005) Linear time algorithms for the ring loading problem with demand splitting. J Algorithms 54(1):45–57
36. Yuan P, Gambiroza V, Knightly E (2004) The ieee 802.17 media access protocol for high-speed metropolitan-area resilient packet rings. IEEE Netw 18(3):8–15

Alok Singh received the B.Sc. (Hons.) and M.Sc. degrees in Computer Science from the Banaras Hindu University, Varanasi, India in 1996 and 1998 respectively and the D.Phil. degree in Science from the University of Allahabad, Allahabad, India in 2006. He is currently an Associate Professor in the School of Computer and Information Sciences at the University of Hyderabad, Hyderabad, India. His primary research interests lie in the area of combinatorial optimization using heuristic and metaheuristic techniques. He has published more than 80 papers including 45 journal papers. He is a senior member of IEEE, USA, an elected life member of the National Academy of Sciences, India, an associate editor for the journal Swarm and Evolutionary Computation, and, a member of the editorial board for the journal Applied Soft Computing.

Jayalakshmi Banda received B.E. degree in Computer Science and Engineering from Osmania University, Hyderabad, India in 2005 and M.Tech. degree in Computer Science from University of Hyderabad, Hyderabad, India in 2010. She is currently pursuing the Ph.D. degree in Computer Science in the School of Computer and Information Sciences at the University of Hyderabad, Hyderabad, India. Her research interests include study and development of heuristics and metaheuristics for solving combinatorial optimization problems.

Imperial Journal of Interdisciplinary Research (IJIR)
Vol-3, Issue-10, 2017
ISSN: 2454-1362, http://www.onlinejournal.in

STATCOM using A Control Scheme for Power Quality Improvement

Jarapala Ramesh Babu[1] & Jatoth Ramesh[2]
[1,2]Methodist College of Engineering & Technology Hyderabad, Telangana-India

Abstract:- *The influence of the wind turbine in the grid system concerning the power quality measurements are-the P in watt, Q in var, variation of voltage, flicker, harmonics, and electrical behavior of switching operation and these are measured according to national/international guidelines. The main functional requirements of the FACTS-devices are to provide shunt compensation, operating in capacitive mode only, in terms of the following; Voltage stability control in a power system, as to compensate the loss voltage along transmission the paper study demonstrates the power quality problem due to installation of wind turbine with the grid. In this proposed scheme STATCOM is connected at a point of common coupling. The STATCOM control scheme for the grid connected wind energy generation system for power quality improvement is simulated using MATLAB/SIMULINK in power system block set.*

Key words:- *STATCOM, BESS, Power quality, Wind energy System (WES).*

I. INTRODUCTION

Flexible AC Transmission Systems, called FACTS, got in the recent years a well-known term for higher controllability in power systems by means of power electronic devices. Several FACTS-devices have been introduced for various applications worldwide. A number of new types of devices are in the stage of being introduced in practice. In most of the applications the controllability is used to avoid cost intensive or landscape requiring extensions of power systems, for instance like upgrades or additions of substations and power lines. FACTS-devices provide a better adaptation to varying operational conditions and improve the usage of existing installations [1]. The basic applications of FACTS-devices are Power flow control, Increase of transmission capability, Voltage control, Reactive power compensation, Stability improvement, Power quality improvement, Power conditioning, Flicker mitigation, Interconnection of renewable and distributed generation and storages. The influence of FACTS-devices is achieved through switched or controlled shunt compensation, series compensation or phase shift control. The devices work electrically as fast current, voltage or impedance controllers. The power electronic allows very short reaction times down to far below one second.

The right column of FACTS-devices contains more advanced technology of voltage source converters based today mainly on Insulated Gate Bipolar Transistors (IGBT) or Insulated Gate Commutated Thyristors (IGCT). Voltage Source Converters provide a free controllable voltage in magnitude and phase due to a pulse width modulation of the IGBTs or IGCTs. High modulation frequencies allow to get low harmonics in the output signal and even to compensate disturbances coming from the network. The disadvantage is that with an increasing switching frequency, the losses are increasing as well. Therefore special designs of the converters are required to compensate this[2].

II. STATIC SYNCHRONOUS COMPENSATOR (STATCOM)

The STATCOM is a solid-state-based power converter version of the SVC. Operating as a shunt-connected SVC, its capacitive or inductive output currents can be controlled independently from its terminal AC bus voltage. Because of the fast-switching characteristic of power converters, STATCOM provides much faster response as compared to the SVC. In addition, in the event of a rapid change in system voltage, the capacitor voltage does not change instantaneously[2]-[5]; therefore, STATCOM effectively reacts for the desired responses. For example, if the system voltage drops for any reason, there is a tendency for STATCOM to inject capacitive power to support the dipped voltages. STATCOM is capable of high dynamic performance and its compensation does not depend on the common coupling voltage. Therefore, STATCOM is very effective during the power system disturbances.

2.1 CONTROL OF STATCOM

The controller of a STATCOM operates the converter in a particular way that the phase angle between the converter voltage and the transmission line voltage is dynamically adjusted and synchronized so that the STATCOM generates or absorbs desired VAR at the point of coupling

connection. Figure 3.4 shows a simplified diagram of the STATCOM with a converter voltage source __1*E* and a tie reactance, connected to a system with a voltage source, and a Thevenin reactance, X*TIEX_THV*TH.

2.2 Two Modes of Operation

There are two modes of operation for a STATCOM, inductive mode and the capacitive mode. The STATCOM regards an inductive reactance connected at its terminal when the converter voltage is higher than the transmission line voltage. Hence, from the system's point of view, it regards the STATCOM as a capacitive reactance and the STATCOM is considered to be operating in a capacitive mode. Similarly, when the system voltage is higher than the converter voltage, the system regards an inductive reactance connected at its terminal. Hence, the STATCOM regards the system as a capacitive reactance and the STATCOM is considered to be operating in an inductive mode. In other words, looking at the phasor diagrams on the right of Figure 3.4, when1*I*, the reactive current component of the STATCOM, leads (*THVE*−1) by 90º, it is in inductive mode and when it lags by 90º, it is in capacitive mode. This dual mode capability enables the STATCOM to provide inductive compensation as well as capacitive compensation to a system. Inductive compensation of the STATCOM makes it unique. This inductive compensation is to provide inductive reactance when overcompensation due to capacitors banks occurs. This happens during the night, when a typical inductive load is about 20% of the full load, and the capacitor banks along the transmission line provide with excessive capacitive reactance due to the lower load. Basically the control system for a STATCOM consists of a current control and a voltage control.

III. BASIC OPERATING PRINCIPLES OF STATCOM

The STATCOM is connected to the power system at a PCC (point of common coupling), through a step-up coupling transformer, where the voltage-quality problem is a concern. The PCC is also known as the terminal for which the terminal voltage is UT. All required voltages and currents are measured and are fed into the controller to be compared with the commands. The controller then performs feedback control and outputs a set of switching signals (firing angle) to drive the main semiconductor switches of the power converter accordingly to either increase the voltage or to decrease it accordingly. A STATCOM[6]-[9] is a controlled reactive-power source. It provides voltage support by generating or absorbing reactive power at the point of common coupling without the need of large external reactors or capacitor banks. Using the controller, the VSC and the coupling transformer, the STATCOM operation is illustrated in Figure below.

The charged capacitor Cdcprovides a DC voltage, Udcto the converter, which produces a set of controllable three-phase output voltages, U in synchronism with the AC system. The synchronism of the three-phase output voltage with the transmission line voltage has to be performed by an external controller. The amount of desired voltage across STATCOM, which is the voltage reference, Uref, is set manually to the controller. The voltage control is thereby to match UT with Uref which has been elaborated. This matching of voltages is done by varying the amplitude of the output voltage U, which is done by the firing angle set by the controller. The controller thus sets UT equivalent to the Uref. The reactive power exchange between the converter and the AC system can also be controlled. This reactive power exchange is the reactive current injected by the STATCOM, which is the current from the capacitor produced by absorbing real power from the AC system.

IV. TOPOLOGY FOR POWER QUALITY IMPROVEMENT

The STATCOM based current control voltage source inverter injects the current into the grid in such a way that the source current are harmonic free and their phase-angle with respect to source voltage has a desired value. The injected current will cancel out the reactive part and harmonic part of the load and induction generator current, thus it improves the power factor and the power quality. To accomplish these goals, the grid voltages are sensed and are synchronized in generating the current command for the inverter. The proposed grid connected system is implemented for power quality improvement at point of common coupling (PCC), as shown in Fig. 1. The grid connected system in Fig. 1, consists of wind energy generation system and battery energy storage system with STATCOM.

4.1. Wind Energy Generating System

In this configuration, wind generations are based on constant speed topologies with pitch control turbine. The induction generator is used in the proposed scheme because of its simplicity, it does not require a separate field circuit, it can accept constant and variable loads, and has natural protection against short circuit. The available power of wind energy system is presented as under in (6).

Where *p* (kg/m) is the air density and A (m2) is the area swept out by turbine blade, Vwind is the wind speed in mtr/s. It is not possible to extract all kinetic energy of wind, thus it extract a

fraction of power in wind, called power coefficient *Cp*of the wind turbine, and is given in (7).
Where *Cp*is the power coefficient, depends on type and operating condition of wind turbine. This coefficient can be express as a function of tip speed ratio and pitch angle. The mechanical power produce by wind turbine is given in (8)

$$P_{\text{mech}} = \frac{1}{2}\rho\Pi R^2 V_{\text{wind}}^3 C_p$$

Where R is the radius of the blade (m).

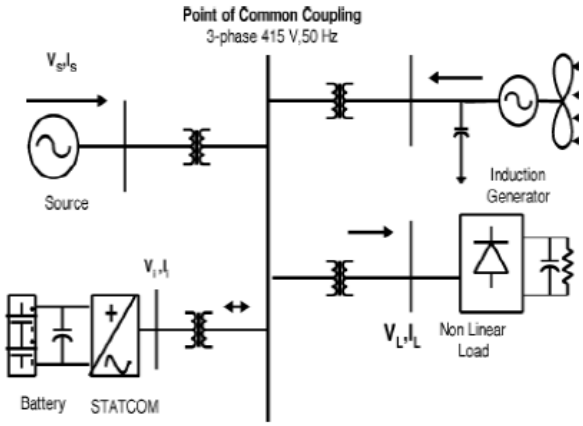

Fig. 1. Grid connected system for power quality improvement.

4.2 BESS-STATCOM

The battery energy storage system (BESS) is used as an energy storage element for the purpose of voltage regulation. The BESS will naturally maintain dc capacitor voltage constant and is best suited in STATCOM since it rapidly injects or absorbed reactive power to stabilize the grid ystem. It also controls the distribution and transmission system in a very fast rate. When power fluctuation occurs in the system, the BESS can be used to level the power fluctuation by charging and discharging operation. The battery is connected in parallel to the dc capacitor of STATCOM [4]–[9]. The STATCOM is a three-phase voltage source inverter having the capacitance on its DC link and connected at the point of common coupling. The STATCOM injects a compensating current of variable magnitude and frequency component at the bus of common coupling.

4.3. System Operation

The shunt connected STATCOM with battery energy storage is connected with the interface of the induction generator and non-linear load at the PCC in the grid system. The STATCOM compensator output is varied according to the controlled strategy, so as to maintain the power quality norms in the grid system. The current control strategy is included in the control scheme that defines the functional operation of the STATCOM compensator in the power system. A single STATCOM using insulated gate bipolar transistor is proposed to have a reactive power support, to the induction generator and to the nonlinear load in the grid system. The main block diagram of the system operational scheme is shown in Fig. 2.

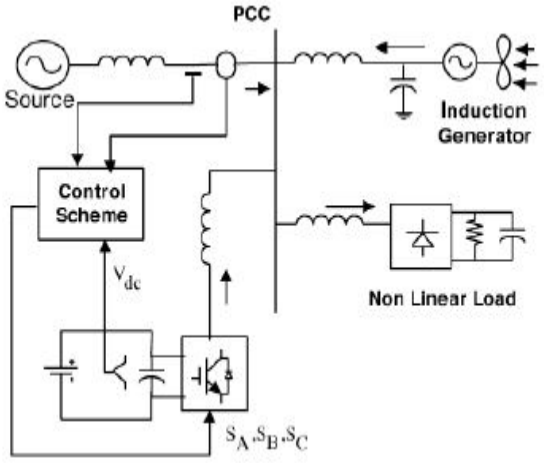

Fig. 2. System operational scheme in grid system.

V. CONTROL SCHEME

The control scheme approach is based on injecting the currents into the grid using ―bang-bang controller.‖ The controller uses a hysteresis current controlled technique. Using such technique, the controller keeps the control system variable between boundaries of hysteresis area and gives correct switching signals for STATCOM operation. The control system scheme for generating the switching signals to the STATCOM is shown in Fig. 3.

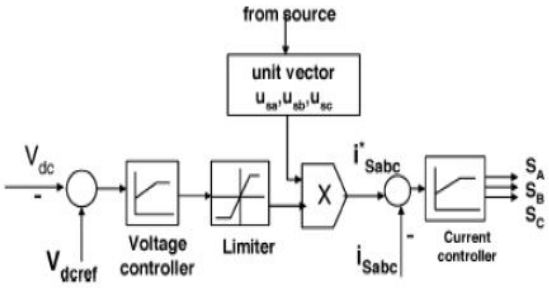

Fig. 3. Control system scheme.

The control algorithm needs the measurements of several variables such as three-phase source current isabc, DC voltage Vdc , inverter current isabc with the help of sensor. The current control block, receives an input of reference current isabc* and actual current isabc are subtracted so as to activate

the operation of STATCOM in current control mode [6]–[8].

5.1. Grid Synchronization

In three-phase balance system, the RMS voltage source amplitude is calculated at the sampling frequency from the source phase voltage (VsaVsbVsc) and is expressed, as sample template *Vsm*, sampled peak voltage, as in (9).

$$V_{sm} = \left\{ \frac{2}{3} \left(V_{sa}^2 + V_{sb}^2 + V_{sc}^2 \right) \right\}^{1/2}. \qquad (9)$$

The in-phase unit vectors are obtained from AC source—phase voltage and the RMS value of unit vector as shown in (10).

$$u_{sa} = \frac{V_{Sa}}{V_{sm}}, \quad u_{sb} = \frac{V_{Sb}}{V_{sm}}, \quad u_{sc} = \frac{V_{Sc}}{V_{sm}}. \qquad (10)$$

The in-phase generated reference currents are derived using in-phase unit voltage template as, in (11)

$$i_{Sa}^* = I.u_{Sa}, \quad i_{Sb}^* = I.u_{Sb}, \quad i_{Sc}^* = I.u_{Sc} \qquad (11)$$

Where I is proportional to magnitude of filtered source voltage for respective phases. This ensures that the source current is controlled to be sinusoidal[4]-[9]. The unit vectors implement the important function in the grid connection for the synchronization for STATCOM. This method is simple, robust and favorable as compared with other methods [8]. The proposed control scheme is simulated using SIMULINK in power system block set. The system parameter for given system is given Table I. The system performance of proposed system under dynamic condition is also presented.

5.2. Voltage Source Current Control—Inverter Operation

The three phase injected current into the grid from STATCOM will cancel out the distortion caused by the nonlinear load and wind generator. The IGBT based three-phase inverter is connected to grid through the transformer. The generation of switching signals from reference current is simulated within hysteresis band of 0.08. The choice of narrow hysteresis band switching in the system improves the current quality. The control signal of switching frequency within its operating band, as shown in Fig. 4. The choice of the current band depends on the operating voltage and the interfacing transformer impedance. The compensated current for the nonlinear load and demanded reactive power is provided by the inverter. The real power transfer from the batteries is also supported by the controller of this inverter. The three phase inverter injected current are shown in Fig. 5

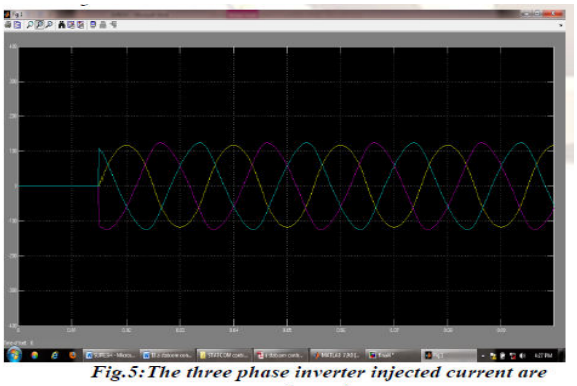

Fig.5:The three phase inverter injected current are shown in

5.3. STATCOM—Performance Under Load Variations

The wind energy generating system is connected with grid having the nonlinear load. The performance of the system is measured by switching the STATCOM at time t=0.7s in the system and how the STATCOM responds to the step change command for increase in additional load at 1.0 s is shown in the simulation. When STATCOM controller is made ON, without change in any other load condition parameters, it starts to mitigate for reactive demand as well as harmonic current. The dynamic performance is also carried out by step change in a load, when applied at 1.0 s. This additional demand is fulfill by STATCOM compensator. Thus, STATCOM can regulate the available real power from source. The result of source current, load current are shown in fig.6

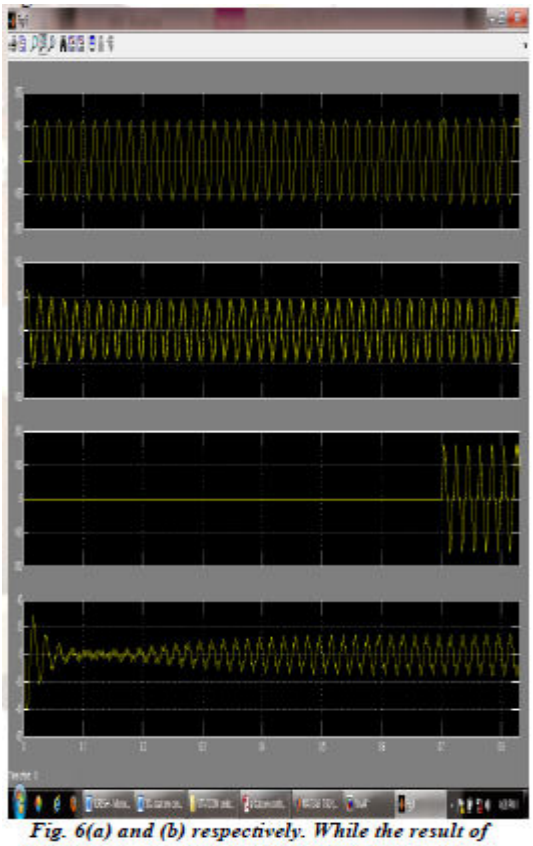

Fig. 6(a) and (b) respectively. While the result of injected current from STATCOM is shown in Fig. 6(c) and the generated current from wind generator at PCC are depicted in Fig. 6(d)

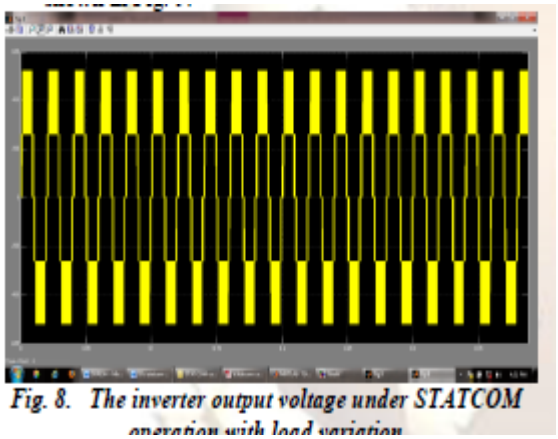

Fig. 8. The inverter output voltage under STATCOM operation with load variation

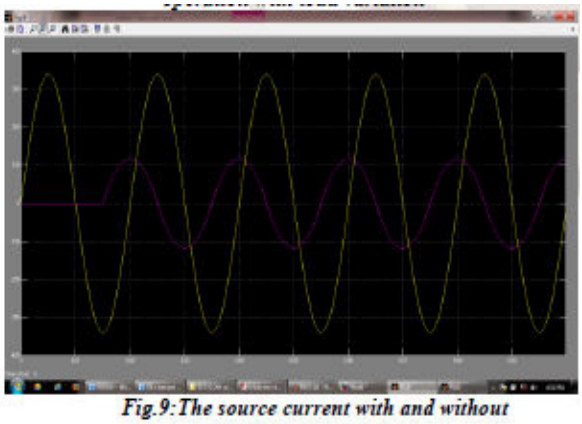

Fig.9:The source current with and without STATCOM operation

5.4. Power Quality Improvement

It is observed that the source current on the grid is affected due to the effects of nonlinear load and wind generator, thus purity of waveform may be lost on both sides in the system. The inverter output voltage under STATCOM operation with load variation is shown in Fig. 8[9]. The dynamic load does affect the inverter output voltage. The source current with and without STATCOM operation is shown in Fig. 9.

This shows that the unity power factor is maintained for the source power when the STATCOM is in operation. The current waveform before and after the STATCOM operation is analyzed. The Fourier analysis of this waveform is expressed and the THD of this source current at PCC without STATCOM is 4.71%, The power quality improvement is observed at point of common coupling, when the controller is in ON condition. The STATCOM is placed in the operation at 0.7 s and source current waveform with its FFT. It is shown that the THD has been improved considerably and within the norms of the standard. The above tests with proposed scheme has not only power quality improvement feature but it also has sustain capability to support the load with the energy storage through the batteries.

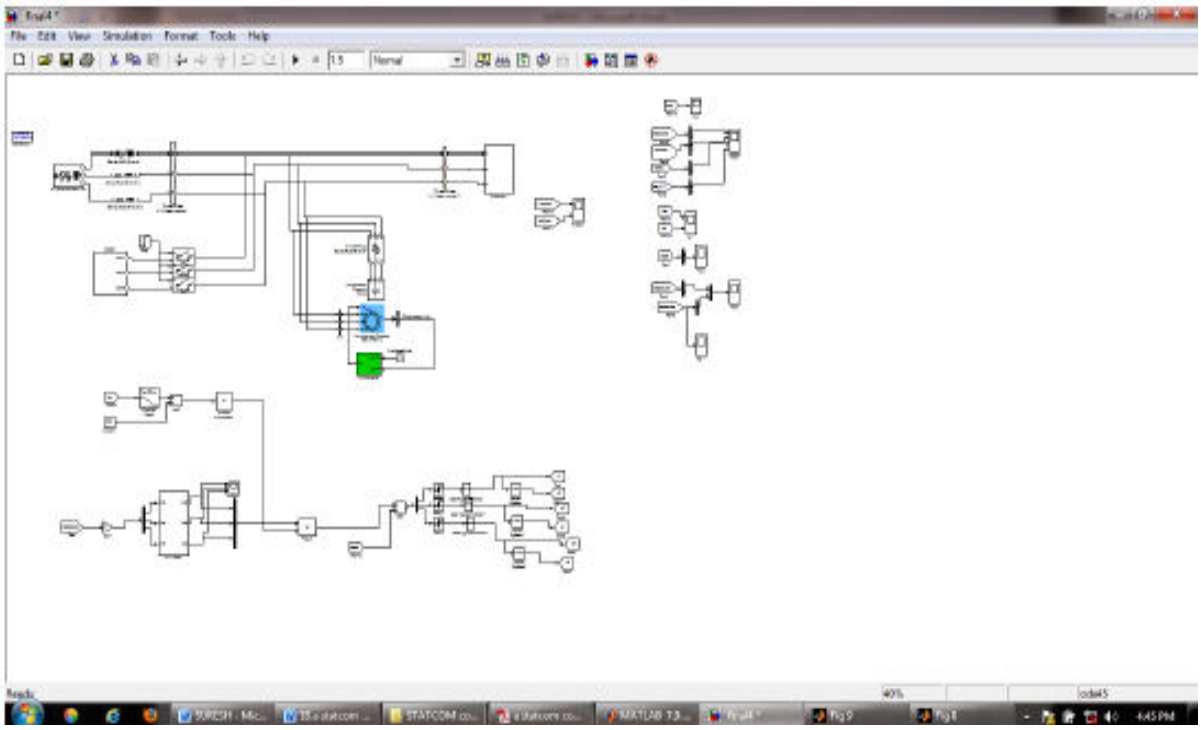

Fig.10: Mat lab model of proposed circuit.

VI. CONCLUSION

The FACTS-based control scheme for power quality improvement in grid connected wind generating system and with nonlinear load. The power quality issues and its consequences on the consumer and electric utility are presented. The operation of the control system developed for the STATCOM-BESS in MATLAB/ SIMULINK for maintaining the power quality is simulated. It has a capability to cancel out the harmonic parts of the load current. It maintains the source voltage and current in-phase and support the reactive power demand for the wind generator and load at PCC in the grid system, thus it gives an opportunity to enhance the utilization factor of transmission line. The integrated wind generation and STATCOM with BESS have shown the outstanding performance.

REFERENCES

[1] Sannino, ―Global power systems for sustainable development,‖ in *IEEE General Meeting, Denver, CO, Jun. 2004.*

[2] K. S. Hook, Y. Liu, and S. Atcitty, ―Mitigation of the wind generation integration related power quality issues by energy storage,*" EPQU J., vol. XII, no. 2, 2006*.

[3] R. Billinton and Y. Gao, ―Energy conversion system models for adequacy assessment of generating systems incorporating wind energy,‖ IEEE Trans. on E. Conv., vol. 23, no. 1, pp. 163–169, 2008, Multistate.

[4] Wind Turbine Generating System—*Part 21*, International standard-*IEC 61400-21, 2001.*

[5] Manel, ―Power electronic system for grid integration of renewable energy source: A survey,‖ *IEEE Trans. Ind. Electron., vol. 53, no. 4, pp. 1002–1014, 2006, Carrasco*.

[6] M. Tsili and S. Papathanassiou, ―A review of grid code technology requirements for wind turbine*," Proc. IET Renew.power gen., vol. 3,pp. 308–332, 2009.*

[7] S. Heier, Grid Integration of Wind Energy Conversions. Hoboken, *NJ: Wiley, 2007, pp. 256–259*.

[8] J. J. Gutierrez, J. Ruiz, L. Leturiondo, and A. Lazkano, ―Flicker measurement system for wind turbine certification*," IEEE Trans. Instrum. Meas., vol. 58, no. 2, pp. 375–382, Feb. 2009.*

[9] A STATCOM-Control Scheme for Grid Connected Wind Energy System for Power Quality Improvement ,Sharad W. Mohod, *Member, IEEE*, and Mohan V. Aware, *IEEE SYSTEMS JOURNAL, VOL. 4, NO. 3, SEPTEMBER 2010*

About the Authors:

*R*amesh babu Jarapala received his B.Tech degree in Electrical and Electronics Engineering and M.E in Power system Engineering from University College of Engineering, Osmania University , Hyderabad, Telangana, India, In 2007 To 2009 respectively. 2009 to 2012, he is

Assistant Professor in KSIT Engineering college, 2012 to 2014 he is Assistant Professor in PBIT engineering college,2014 to 2017 Assistant Professor in AHTC engineering college and since 2014 he is Assistant Professor Methodist College Of Engineering &Tech Hyderabad, Telangana-India.

Ramesh Jatoth received his B.Tech degree in Electrical and Electronics Engineering and M.Tech in Power System from NIT calicut, Kerala, India, in 2008 to 2010 respectively. since 2014 he is Assistant Professor Methodist College Of Engineering &Tech Hyderabad, Telangana-India.

Journal of Theoretical and Applied Information Technology
30th November 2017. Vol.95. No 22

ISSN: 1992-8645 www.jatit.org E-ISSN: 1817-3195

DR-QPO: DISCRETE RANK BASED QUERY PATTERN OPTIMIZATION TOWARDS PARALLEL QUERY PLANNING AND EXECUTION FOR DISTRIBUTE TRIPLE STORES

K.SHAILAJA[1], DR. P.V. KUMAR[2], DR S.DURGA BHAVANI[3]
[1]Department of CSE, Methodist College of Engineering and Technology, Hyderabad, Telangana State, India
[2]UCE, OU, HYDERABAD, Telangana State
[3]School of IT, JNTUH Hyderabad, Telangana State, India
Email: [1] shailajamtech2006@yahoo.co.in, [2] pvkumar58@gmail.com, [3] sdurga.bhavani@gmail.com

ABSTRACT

This manuscript proposed and explored a novel strategy for query pattern optimization towards parallel query planning and execution in Distributed RDF environments. The critical objective of the proposal is to optimize the query patterns from the query chains initiated to execute parallel in distributed RDF environment, which is unique regard to the earlier contributions related to parallel query planning and execution strategies found in contemporary literature. All of these existing models aimed to notify the query patterns from the given query chain, which are less significant to optimize the parallel process of the query patterns that discovered from multiple query chains submitted in parallel in distributed environment (such as cloud computing) to query the distributed triple stores. In order to this, the Discrete Rank based Query Pattern Optimization (DR-QPO) strategy is proposed. The DR-QPO optimizes the query patterns from multiple query chains initiated in parallel. A novel scale called Discrete Rank Consistence Score (DRDCS) defined, which uses the order of other metrics query pattern occurrence count, search space utilization, and access cost as input. The experiments conducted on the proposed model and other benchmark models found in contemporary literature. The results obtained from the experimental study evincing that the proposed model is significant and robust to optimize the query patterns in order to execute distribute query chains in parallel. The comparative analysis of the results obtained from DR-QPO and other contemporary models performed using ANOVA standards like t-test, Wilcoxon signed rank test.

Keywords: *RDF, Query Optimising, Parallel Planning, SPARQL, DRDCS, Access Cost Search Space Utilization Distributed Query Science.*

1 INTRODUCTION

Semantic web solutions are gaining prominence, and RDF (Resource Description Framework) is one of the flexible data models that are developed for semantic web [1]. RDF is profoundly used in varied range of applications like Semantic Web [2] [3], scientific applications and web 2.0 solutions [4] and databases [5]. Numerous researches were carried out and contemporary solutions were developed with distributed solutions for storage and querying in RDF data.

Some of the contemporary RDF data storage solutions are Babel Peers [6], 3rdf [7], RDF Peers [8], Atlas [9] and Gride Vine [10] which uses P2P overlay networks for storing and querying RDF data using distributed process. To obtain quality search results, RDF triples with same concept, predicament is stored three times in the network for every triple component in an individual manner, in the RDF data stores.

Usually the triples are clustered with same identifier over the same peer, and such action address the issue of constraint search for a specific subject, predicate or an object from a local database. Though SPARQL3, RDF query language has varied salient features like aggregation and optional clause, still the popular dialect adapted is the conjunctive queries like BGP (Basic Graph Pattern) queries that typically feature in many equality joins.

ISSN: 1992-8645 www.jatit.org E-ISSN: 1817-3195

Despite the fact that no single partitioning can assure that all the queries are PWOC, still majority of the queries need processing across varied nodes and hence, data redistribution across nodes are essential. Based on the complexity of the processed query, the impact of evaluating distributed part of the query plan might vary. In deciding the pattern of decomposing and evaluating a RDF query over a parallel context, logical query optimization plays a vital role. In the distributed data management [11], for effective assessment of queries, there is need for maximizing parallelism and taking advantage of distributed processing capacity, which essentially reduces the response time.

In the context of a parallel RDF query evaluation, intra-operator parallelism depends on combined operators which process the chunks of data in parallel. Developing massively –parallel plans can support in improving the inter-operator parallelism, as few combined operators are feasible to any root-to-leaf path in the plan. Such development could be attributed to processing carried out by the joints directly and it doubles up in the response time. Some of the earlier works like binary joints organized in bushy plans [12] with joints (n>2) in the first level of plans and the binary joins in next level [13] [14] [15] or the joins at all the levels [16], but with organized in left deep plans. The aforesaid methods result in high plans and high responses times.

However, Hadoop RDF [17] is an effective model designed for developing bushy plans of joins, but the constraints pertaining to assurance of flat plans is not guaranteed. The other major constraint observed in the aforesaidmodels are about overlay load balancing. As a result of non-uniform distribution of the frequency relate to subject, predicate and object oriented occurrences in triples, it is feasible that the triples may not be stored over the peers of underlying the networks in a uniform manner.

It is imperative from the constraints discussed above, that query optimization is certainly a NP-hard problem and many of the near-optimal query plans proposed are of NP-hard [18]. Runtime increment issues are envisaged for the algorithms upon the rising number of joins and contemporary application scenarios [19]. Also the complexity of systems over which the query is processed also increases because of load factor. To address such issues, contemporary models have put forth new models and contemporary processing operators for introducing varied new parameters for tuning the query processing [20] [21]. Such significant developments can support query optimization much harder than the size of search space increment. Further, many of the developments also influence new cost metrics for considering query plans apart from the execution time. In the other dimension, the challenge is that when multiple plan cost metrics are considered, it could lead to harder-set of query optimization too [22] [23] [24]. In a comprehensive scenario, it can be stated that majority of the emerging solutions for query optimization are resulting in NP hard and also increase the need for parallel query optimization algorithms.

In regard to this, the contribution of the manuscript tends to achieve the following:

- Optimizing the parallel queries targeted to search on distributed RDF store.
- A distributed ranking model should depict to optimize the query processing time and resource utilization
- Optimization process should evince the linear complexity

2 RELATED WORK

Parallel query optimization can be termed as the serial optimization algorithms generating plans, which are executed in parallel [25] for query processing. Though contextually there are varied considerations in realizing the term, in the current scenario a parallel algorithm for generating query plans are discussed.

In [8] the authors have focused on issue of load-balancing by curtailing the storage of very popular URIs and literals, depending on storage capacity of local peers. Though the process might provide the desired outcome, still the challenge is about probable loss of complete result. In [6] the study has targeted to address the problem by developing an overlay tree over DHT position of an overly popular triple component. Such type of load balancing shall be very fragile in the instance of node failure in overlay tree, and could even result in loss of the complete branch of tree.

In [26], the study has worked on huge variation among the peer's data load upon triples

ISSN: 1992-8645 www.jatit.org E-ISSN: 1817-3195

being indexed 3 times by fixed hash depth of 1. For improving the data distribution, the proposed model has focused on idea of indexing triples using random hash depth, wherein for every depth there shall be equal number of potential location keys for triple components. It showed that with higher value of hash depth, the better is the triples distribution among peers. But it comes with cost of network communication in the instance of query evaluation, as many peers are queried for evaluation of triple pattern.

In [27], for addressing the hotspots of unfair load balancing, a solution in terms of indexing a triple for every possible combination of its two components like subject + object, predicate + object, subject + predicate and such combination are proposed. The impact of such process was extra storage of triples in the network, despite of achieving fair triple load distribution.

In [9], for improving the query load distribution, study has focused on additionally indexed triples by combination of varied triple components, resulting in 7 replications for every triple in total. It is used in extra storage overhead for distribution of query processing load amidst the peers. But the key element missing was about studying the utilization of overhead for improving the response time for query processing.

In [28], the notion of quad is used for representing the RDF data and a solution with optimized index structure for supporting evaluation of RDF queries in centralized RDF data stores are considered.

The study reflects that only 6 indexes are essential for covering the entire range of 16 access patterns, but every access pattern is considered a quad when there is combination of subject, predicate, object or the context is either defined or a variable. Considering such scope for reducing the number of essential indexes, in section IV-B only 3 indexes are required for new index scheme to ensure coverage of all the 8 possible triple patterns.

The proposed work connects to the earlier works that parallelize classical dynamic program designed with query optimization algorithm [29], [30], [31], [32], [33], [34], and [35]. Many of the prior algorithms were devised for shared-memory structures, which lack scalability over a certain level of parallelism [36]. In the other way, prior algorithms evaluated to consider certain volume, but the algorithm devised in [35] evinced scalability with shared-nothing architecture comprising over 250 workers. Some of the key factors that differentiate prior algorithms to proposed algorithm is the limitation and scalability.

In the earlier algorithms, the query patterns that are independent, cyclic or recursive only planned to execute in parallel as independent threads and there is presumption that all the threads might share common data structures and thus it is easier to access intermediary results generated in the other threads. This practiceleads to huge communication overhead over shared-nothing architectures and moreover, these algorithms least significant towards optimizing query patterns found multiple query chains submitted in distributed environment. In addition, the earlier algorithms have relied on central coordinator for assigning rather fine-tuned optimization of tasks to the work threads. Two of the key disadvantages of such process are: i) it needs considerable communication among the master and workers ii) increased levels of time complexity in managing at central system, which leads to delay in implementing parallelism.

In regard to this, the proposed algorithm does optimize the query patterns that are independent, recursive or cyclic in multiple query chains that effectively workin shared nothing distributed environment with multiple clients and multiple distributed triple stores.

3 DISCRETE RANK BASED QUERY PATTERN OPTIMIZATION

This section explores the methods and materials used discrete rank based query pattern optimization for distributed query planning for RDF stores. The initial step of the proposed model finds the query patterns of size 1 to n and ranks them in ascending order of their occurrence count, such that highest rank is most optimal. Further rank these patterns in descending of respective search space utilization, such that the query pattern with highest rank is most optimal. Afterwards, allocate ranks to the same patterns in descending order of their access cost that similar to the ranking strategy followed for search space utilization, such that the pattern with highest rank is most optimal towards access cost. At this stage, each pattern discovered enlisted with three discrete ranks corresponding to their occurrence count, search space utilization and access cost. Further the process of estimating theDiscrete Rank distribution consistency score (DRDCS) of the query patterns is performed, which

ISSN: 1992-8645 www.jatit.org E-ISSN: 1817-3195

considers further toallocate global rank of each of the pattern. The global rank assigned to all of these patterns in descending order of their DRDCS. The detailed exploration of these phases depicted in following sections.

RDF structure based semantic web search usually carried out using SPARQL queries by indicating them in the form of tree structure. Query chosen for the process categorizes in to three distinct formats like left deep, right deep and bidirectional deep tree, which is termed as bushy tree. In the instance of any of the trees retaining subjects, predicates, or the objects as leads and join them as nodes, then the depth first tree is formed first, and the connection amidst the nodes will form a bushy structure, whereas the join connected to subject predicate or object connects to the other join which could conclude left deep tree. The emphasis of proposed model is to optimize the parallel query planning process and reduce the cost of execution. Hence, the query structure chosen for exploring the proposed solution is bidirectional or bushy tree.

The depicted model is explored by considering the query structures defined in renowned query language called SPARQL However this model can adapt to any of the formal query languages available.

3.1 Query Patterns discovery

This section explores the Tabu Search based query patterns and their occurrence count discovery. Initial task of the proposed model is to identify the query patterns of size 1andtabu transactions (no need to search) respective to each discovered pattern of size 1. Further, the search will be conducted recursively for two-size query patterns to max possible size of query patterns. During the search, the insignificant patterns and insignificant transactions respective to significant patterns place in respective tabu lists, which ignores from search space in further iterations.The proposed model is using tabu search in order to limit the process time.The detailed pattern discovery process explored following:

All query elements $E = \{e_1, e_2, - - - - e_m\}$ of size m are a finite set those appear in the set Q of distributed query-chains given. The query-chain set Q of size n represents the all distributed query chains $\{q_1, q_2, q_3, ..., q_n\}$ such that each query-chain formed by the subset of query elements in set E, such that each query-chain $\{q_r \exists q_r \in Q \wedge 1 \le r \le n\}$ is the superset of one or more query elements QE. Each query-chain is notified by a unique query-chain id $\{r \exists 1 \le r \le n\}$, which referred further as qid. Each query element e_j in a given query-chain represents query element e with id $1 \le j \le m$.

Further, the query elements E considers as 1-size patterns set and determines their occurrence count and tabu list of transactions respective to each 1-size pattern as follows.

$qp_1 \leftarrow E$ // clone the set of all query elements as 1-size query patterns set qp_1

$qps \leftarrow qp_1$ // The set qps retains all possible query patterns discovered that initialized by moving all 1-size patterns

step 1. $\overset{m}{\underset{i=1}{\forall}} \{p_i \exists p_i \in qp_1\}$ Begin

step 2. $o(p_i) = 0$ // denotes the occurrence count of pattern p_i that initialized to 0;

step 3. $o(p_i) = \sum_{j=1}^{n} \{1 \exists p_i \subseteq q_j \wedge q_j \in Q\}$

step 4. $tlq(p_i)$ // is an empty list contains the query chains those not having query pattern p_i

step 5. $\overset{n}{\underset{j=1}{\forall}} \{tlq(p_i) \leftarrow q_j \exists p_i \not\subset q_j \wedge q_j \in Q\}$ // moving all query chains those not having query pattern p_i

step 6. End //of step 1

The notations used in the algorithm are as follows:

step 1. $s=2$ // represents the size of the query-patterns to be discovered in sequence, which is initialized by 2. Since the algorithm uses the query-patterns of size 1 as input.

step 2. tlp // Tabu list of query-patterns:

step 3. Tabu list of query-chains $tlqc$:

step 4. Prepare tabu list of Query-chains tlt : query-chains that are having one or zero items from 1-size patterns list

step 5. Main Loop: While (True) Begin

ISSN: 1992-8645 www.jatit.org E-ISSN: 1817-3195

step 6. Pick $s-1$ size patterns

step 7. $\forall_{j=1}^{|qp_{(s-1)}|}\{p_j \exists p_j \in qp_{(s-1)} \wedge p_j \notin tlp\}$ Begin //for each query pattern p_j in $qp_{(s-1)}$

step 8. $\forall_{k=1}^{|qp_{(s-1)}|}\{p_k \exists p_k \in qp_{(s-1)} \wedge j \neq k \wedge p_k \notin tlp\}$ Begin //for each query pattern p_k in $qp_{(s-1)}$, such that $j \neq k$

step 9. $p_{jk} = p_j \bigcup p_k$ // results new query pattern p_{jk} that contains all unique query elements in p_j and p_k

step 10. $o(p_{jk}) = \sum_{j=1}^{n}\{1 \exists p_{jk} \subseteq q_j \wedge q_j \in Q\}$ // find the occurrence of pattern p_{jk}

step 11. $if\,(o(p_{jk}) > 0)$ Begin

step 12. $qp_s \leftarrow p_{jk}$ //move pattern p_{jk} to the query pattern set qp_s

step 13. $\forall_{j=1}^{n}\{tlq(p_{jk}) \leftarrow q_j \exists p_{jk} \not\subset q_j \wedge q_j \in Q\}$ find all tabu query chains related to pattern p_{jk}

step 14. End // of step 11

step 15. Else $tlp \leftarrow p_{jk}$ // move pattern p_{jk} to tabu pattern list tlp, since the pattern does not exists in an query chain

step 16. End // of step 8

step 17. End // of step 7

step 18. $if\,(|\,qp_s\,| > 0)$ begin //If qp_s is not empty

step 19. Update tabu list of Query-chains: query-chains that are having one or zero patterns from qp_s list

step 20. $qps \leftarrow qp_s$ // moving all patterns from qp_s to qps

step 21. $s = s+1$

step 22. End //of step 19

step 23. Else break the main loop in step 5

step 24. End // of step 5

The process explored in step 1 to step 24, discovers all possible patterns as set qps and their respective occurrence count. Further, this set qps used as input to allocate discrete ranks to all patterns about occurrence count, max search space required and access cost required respectively. The discrete rank allocation for each pattern explored in following sections.

3.2 Search Space Utilization

To track the optimality of a query formed in to a bushy tree, two metrics "minimal access cost" and "search of minimal combinations" were defined in the earlier contribution [37]. As both the metrics are fundamental for estimating the optimality of a query pattern, the search space is used is proportionate to the varied combinations traversed because of tow query elements connected under a join node pattern. Hence, the metric search of minimal combinations supports to assess the search space utilization. About this observation, the metric "search of minimal combinations" [37] adapted and the result obtained for this metric from each query pattern considered as search space utilization of the respective query pattern. The process of the estimating this metric of a given query pattern is as follows:

Search of minimal combinations could be defined as the cumulative outcome of combinations amidst the subjects and count of objects in a chosen predicate. Estimation of max possible combination are carried out as:

$$mpc(p_k) = \sum_{i=1}^{|S|}\sum_{j=1}^{|O|}\{1 \exists p(s_i \rightarrow o_j) \equiv P\}$$

// in the equation above, the counting of the possible combinations for a subject s_i and object o_j with anticipated predicate P, $p(s_i \rightarrow o_j)$ is concrete predicate of the subject s_i and object o_j. " $mpc(J_k)$ " denotes the max possible combinations for a query pattern p_k //.

3.3 Query Pattern Access cost

Other significant factor is the access time which is unique for all query elements in a query pattern which targets the single RDF store. However, if the triple stores that are targeted are differing from the every query element in a chosen query pattern constituted, accordingly the access time might vary for varied query elements. In order to address the constraint, the other significant metric "minimal cost" is considered in the earlier solution [37], which is also adapted in the second model. The metric is very much reliant on the metric "search by

ISSN: 1992-8645 www.jatit.org E-ISSN: 1817-3195

minimal combinations". The process of evaluating the metric explored are:

Minimal access cost is the cumulative of costs for accessing the Distributed RDFs over varied subjects to attain the objects within expected predicate that is assessed using the following equation.

$$ac(p_k) = \sum_{i=1}^{|S|} \sum_{j=1}^{|DRDF|} \{ac(s_i \Rightarrow rdf_j) \otimes vc\}$$

// in the equation above, |S| is the cumulative number of subjects over a given query pattern,

$|DRDF|$ Is the number of RDFs measured under distributed architecture, $ac(s_i \Rightarrow rdf_j)$ shall be access cost to rdf_j under the selected subject s_i and vc is indicating the number of visits. The notation $ac(p_k)$ indicates the minimal access cost of the query pattern p_k.

3.4 Ranking by their occurrence count

Clone qps as set $oqps$ and refine it as if any pattern p_i is subset of other pattern p_j with same occurrence count, then discard p_i from $oqps$. The model adapted to prune the patterns as follow:

step 1: $\forall_{i=1}^{|oqps|} \{p_i \exists p_i \in oqps\}$ Begin // for each pattern p_i that exists in $opqs$

step 2: $\forall_{j=i+1}^{|oqps|} \{p_j \exists p_j \in oqps \wedge p_i \neq p_j\}$ Begin // for each pattern p_j of set $opqs$, which is not equal to pattern p_i

step 3: *if* $\left(p_i \subset p_j \wedge o(p_i) \equiv o(p_i)\right)$ Begin // if pattern p_i is subset of p_j and the occurrence count of both patterns is identical

step 4: $opqs \setminus p_i$ //prune the pattern p_i from set $opqs$

step 5: $i = i - 1$ // decrementing the index of the loop in step 1

step 6: Go to step 1;

step 7: End // of step 3

step 8: End // of step 2

step 9: End // of step 1

Rank the query patterns in $oqps$ in ascending order of their respective occurrence count, such that patterns having same occurrence count will have same rank and pattern with highest occurrence count entitles highest rank. The process of rank allocation as follows:

step 10: $\forall_{i=1}^{|oqps|} \{p_i \exists p_i \in oqps\}$ Begin // for each pattern p_i that exists in $opqs$

step 11: $\forall_{j=i+1}^{|oqps|} \{p_j \exists p_j \in oqps \wedge p_i \neq p_j\}$ Begin // for each pattern p_j of set $opqs$, which is not equal to pattern p_i

step 12: $t = j$

step 13: $\forall_{k=j+1}^{|oqps|} \{p_k \exists p_k \in oqps \wedge p_k \neq p_j\}$ Begin // for each pattern p_k of set $opqs$, which is not equal to pattern p_j

step 14: *if* $\left(o(p_k) < o(p_j)\right)$ $t = k$

step 15: End // of step 4

step 16: End //of step 2

step 17: *if* $\left(o(p_i) > o(p_k)\right)$ p_i □ p_k // if occurrence count of pattern p_i is greater than occurrence count of pattern p_k swap their positions in $oqps$

step 18: $idx = 0$ // ranking index initialized by 0

step 19: $\forall_{i=1}^{|oqps|} \{p_i \exists p_i \in oqps\}$ Begin //

step 20: *if* $\left(i \neq 1 \&\& o(p_{i-1}) \equiv o(p_i)\right)$ $r_o(p_i) = idx$

step 21: Else Begin

step 22: $idx+ = 1$

step 23: $r_o(p_i) = idx$

step 24: End //of step 12

3.5 Ranking by search space utilization

Clone qps as set $sqps$, and refine the set $sqps$, such that if any pattern p_i is subset of other pattern p_j and search space usage of p_i is equal to search space usage of p_j then discard p_i from $sqps$. Further, Rank the query patterns in $sqps$ in descending order of their respective occurrence count, such that patterns having same search space usage will have same rank and pattern with

ISSN: 1992-8645 www.jatit.org E-ISSN: 1817-3195

lowestsearch space usage entitles highest rank. The sorting and ranking procedure depicted as follows:

$$\overset{|sqps|}{\underset{i=1}{\forall}}\left\{\overset{|sqps|}{\underset{j=1}{\forall}}\left\{(sqps \setminus p_i)\exists\begin{Bmatrix} p_i \subseteq p_j \wedge \\ mpc(p_i) \equiv mpc(p_j) \wedge \\ [p_i, p_j] \in sqps \end{Bmatrix}\right\}\right\}$$

// The equation is pruning the query patterns if any of the pattern p_i is subset of the pattern p_j and the search space utilization of the both patterns $mpc(p_i)$ *and* $mpc(p_j)$ are identical.

Then sort the leftover patterns of *sqps* in descending order of their search space utilization (the similar process that explored in steps 10 to 17 in section 3.4 should apply on *sqps* instead of *oqps* and comparison should do about search space utilization instead of occurrence count. Further, rank them according to their order of presence in the set *sqps*, such that the distinct query patterns having same search space utilization enlists with same rank. The process explored in steps 18 to 24 is compatible to tank the query patterns in set *sqps*, which should do by comparing their search space utilization instead of occurrence count. The ranks allotted to each query pattern p_i in set *sqps* denoted by $r_s(p_i)$.

3.6 Ranking by access cost

Clone *qps* as set *aqps*, and refine if any pattern p_i is subset of other pattern p_j and access cost of p_i is more or equal access cost of p_j then discard p_i. Further, rank the query patterns in *aqps* in descending order of their respective occurrence count, such that patterns having same access cost will have same rank and pattern with lowest access cost entitles highest rank. The process that adapted to prune the query patterns in section 3.3 can merely follow to prune records from set *aqps*. The condition to prune record should compare their access cost instead occurrence count (see step 1 to 9 in section 3.4). Further, the sorting and ranking is similar to steps 10 to 24 in sec 3.3 and the query patterns should sort in descending order of their access cost instead occurrence count.

The ranks assigned to the query patterns in set *aqps* refersas the notation $r_a(p_i)$, which denotes the rank assigned to query pattern p_i based on its access cost.

3.7 Discrete Rank Distribution Consistency Score (DRDCS)

This section adapts the mean square distance [38] between the distinct ranks assigned to each query pattern to estimate the rank distribution consistency. In order to define the DRDC for each pattern, initially identifies all unique patterns from set *oqps*, set *sqps* and set *aqps*, which denotes further as set *uqps*. The foremost step to discover DRDCS of the patterns in *uqps* is, if any of the query pattern p_i from set *uqps* not exists in any of the sets *oqps*, *sqps and aqps*, then identify the super set of that query pattern p_j with highest rank from the respective set and assign the rank of superset query pattern p_j to the corresponding query pattern p_i. Further assess the DRDCS of the each pattern from the respective ranks of occurrence count, search space utilization and access cost those assigned to each query pattern as follows:

step 1: $\overset{|uqps|}{\underset{i=1}{\forall}}\{p_i \exists p_i \in uqps\}$ Begin / for each query pattern p_i in set *uqps*

step 2: $m_r(p_i) = \dfrac{r_o(p_i) + r_s(p_i) + r_a(p_i)}{3}$ // Finding the mean of the all distinct ranks assigned to pattern p_i

step 3: $d_r(p_i) = \dfrac{\begin{pmatrix} \sqrt{(m_r(p_i) - r_o(p_i))^2} + \\ \sqrt{(m_r(p_i) - r_o(p_i))^2} + \\ \sqrt{(m_r(p_i) - r_o(p_i))^2} \end{pmatrix}}{3}$ /Finding the mean square distance of the distinct ranks assigned to pattern p_i

step 4: $cs(p_i) = \left(\dfrac{d_r(p_i)}{r_o(p_i)}\right)^{-1}$ // the discrete rank distribution consistence score is estimated as inverse ratio of the mean square distance

ISSN: 1992-8645 www.jatit.org E-ISSN: 1817-3195

against the rank assigned for occurrence count.

step 5: End// of step 1

The discrete rank distribution consistence score estimated as the ratio of mean square distance against the rank assigned to occurrence count of the respective query pattern. This is due to the ambiguity of the root mean square distance obtained for the distinct lowest ranks that approximately equal and the distinct highest ranks that also approximately equal. As an example, the rank set (3, 2, 1) of query pattern p_i and the rank set (33, 32, 31) of query pattern p_j gets the equal value 2 a mean square distance, but ratio of these mean square distances against to the rank assigned under occurrence count of the respective query patterns p_i *and* p_j are 0.666666667 and 0.060606061 which are distinct. These ratio values are lowest for highest distinct ranks and highest for lowest distinct ranks. Hence, the inverse ratio s obtained as consistency score. The consistence score observed for respective example given are 1.5 for query pattern p_i with distinct rank set (3, 2, 1)and 16.5 for query pattern p_j with distinct rank set (33, 32, 31) . Here the rank assigned for occurrence count is considered to assess the discrete rank consistence score, which is since the most occurrences indicates the associability of the respective pattern towards the multiple query chains given as input to query processing. If a query pattern is having highest rank in regard to occurrence count, the execution of respective query pattern accomplish the partial results extraction for the multiple number of query chains that represented by the occurrence count of the respective query pattern.

These query patterns scheduled further in the order of their discrete rank distribution consistence score. The scheduling of these patterns is parallel, which in the context of first come first serve scheduling strategy.

4 EXPERIMENTAL SETUP AND PERFORMANCE ANALYSIS

The proposed model DR-QPO and other contemporary models [31] [32] [33] [35] adapted to compare are implemented using java and executed on Intel 5th generation platform. The distributed environment of multiple triple stores and multiple clients is simulated using java RMI, such that clients can submit SPARQL queries in parallel. The performance statistics of the results obtained from DR-QPO and other contemporary models assessed using expression language R [39].

4.1 The Input Query Formation

Each client of the distributed environment creates synthesizes set of SPARQL query chains such that each query chain contains varied number of query patterns that extracts the results from triple stores and submits to query processing module in parallel. The set of noteworthy RDF stores such as FACTBOOK, FOAF, and LUBM [40-42] adapted as distributed triple stores for experiments. The number of query elements in each query chain is in the range of 5 to 25 and total number of query chains submitted in parallel is in between 10 to 60.

4.2 Performance Analysis

The metric "average query processing time" considered for assessing the performance of the DR-QPO and other contemporary models adapted. The "residual memory ratio", which is the percentage of the memory not in use against to total memory allocated for query processing. Along the side of these two metrics, access cost dissemination ratio, which is the ratio of access cost diffused by executing a cyclic or recursive query pattern only once. The existing contemporary models are considering these cyclic recursive patterns exist in a given single query chain, contrast to this, the DR-QPO is considering the recursive query patterns from the multiple query chains submitted in parallel.

Table 1: The Results Obtained For T-Test and Wilcoxon Test Performed On Average Query Processing Time Observed From Dr-Qpo and Other Contemporary Models

Average Query Processing Time				
	T-test		Wilcoxon Test	
	t-score	p-value	z-score	p-value
Trummer et al., [35]	-6.27786	< .00001	-3.0594	0.00111
chen et al.,[33]	-6.475	< .0000	-3.059	0.00111

ISSN: 1992-8645 www.jatit.org E-ISSN: 1817-3195

	81	1	4	
w. zuo et al., [32]	-6.50351	<.00001	-3.0594	0.00111
F.M waas et al., [31]	-8.59106	<.00001	-3.0594	0.00111

Table 2: The results obtained for t-test and Wilcoxon test performed on residual memory observed from DR-QPO and other contemporary models

Residual Memory				
	T-test		Wilcoxon Test	
	t-score	p-value	z-score	p-value
Trummer et al., [35]	-6.40203	<.00001	-3.0594	0.00111
chen et al.,[33]	-9.28173	<.00001	-3.0594	0.00111
w. zuo et al., [32]	-9.35815	<.00001	-3.0594	0.00111
F.M waas et al., [31]	-13.12842	<.00001	-3.0594	0.00111

Table 3: The results obtained for t-test and Wilcoxon test performed on access cost dissemination observed from DR-QPO and other contemporary models

Access Cost Dissemination				
	T-test		Wilcoxon Test	
	t-score	p-value	z-score	p-value
Trummer et al., [35]	4.01221	0.000293	-3.0594	0.00111
chen et al.,[33]	3.77302	0.000524	-3.0594	0.00111
w. zuo et al., [32]	3.74915	0.000555	-3.0594	0.00111
F.M waas et al., [31]	3.80887	0.00048	-3.0594	0.00111

The consistency of the proposed model evinced through t–test and Wilcoxon signed rank test [43] applied on the values obtained for respective metrics of DR-QPO and other contemporary models adapted. The tables 1, 2 and 3 exploredthe t-score, z-score and respective degree of probability observed between the divergent metric values obtained from DR-QPO and other models. The degree of probability observed for t-test and Wilcoxon signed rank test between DR-QPO and other models is almost nullified (almost zero), hence it is obvious to conclude that the proposed model DR-QPO significantly outperformed all other contemporary models considered for comparison.

5 CONCLUSION

Discrete Rank based Query Pattern Optimization (DR-QPO) towards Parallel Query Planning and Execution for RDF Stores proposed here in this manuscript. Unlike the existing parallel query planning and execution models [31-33, 35] found in contemporary literature, the proposed model is optimizing the query patterns planning and execution in parallel for distributed query chains. The contemporary models limited to optimize the cyclic and recursive patterns found in individual query chain. Contrast to this, the DR-QPO optimizing the query patterns those are recursive in multiple query chains submitted in distributed environment. The metrics such as query pattern occurrence count (pattern exists in multiple query chains), search space utilization and access cost are consider to assign distinct ranks to each query pattern. Further, estimates the discrete rank distribution consistence score (DRDCS) of each query pattern, which is critical contribution of the manuscript. Further, query patterns planned to execute according to their DRDC observed. The results obtained from experimental study evincing that the proposed model consistently outperformed the other contemporary models. The performance analysis of the model proposed and other contemporary models done, which is by comparing the results obtained suing ANOVA standards like t-test and Wilcoxon signed rank test. The scope of this manuscript is optimizing the query patterns discovered from distributed query chains given as input to parallel query processing against diversified triple stores. Hence, in this regard the exploration limited to the model devised to optimize the order of query patterns in regard to discrete ranks assigned under divergent factors such

ISSN: 1992-8645 www.jatit.org E-ISSN: 1817-3195

as the pattern associability to query chains (occurrence count), search by minimal combinations (search space utilization) and minimal access cost. The future research can contribute an optimal scheduling strategy to schedule the query patterns to execute in parallel.

REFERENCES

[1] P. Hayes, "RDF Semantics," W3C Recommendation, February 2004, http://www.w3.org/TR/rdf-mt/.

[2] S. Auer, C. Bizer, G. Kobilarov, J. Lehmann, R. Cyganiak, and Z. G. Ives, "DBpedia: A Nucleus for a Web of Open Data," in ISWC, 2007.

[3] F. M. Suchanek, G. Kasneci, and G. Weikum, "Yago: A Core of Semantic Knowledge," in WWW, 2007.

[4] D. Huynh, S. Mazzocchi, and D. R. Karger, "Piggy Bank: Experience the Semantic Web inside your web browser," J. Web Sem., vol. 5, no. 1, 2007.

[5] E. I. Chong, S. Das, G. Eadon, and J. Srinivasan, "An Efficient SQL based RDF Querying Scheme," in VLDB, 2005.

[6] D. Battr´e, F. Heine, A. H¨oing, and O. Kao, "On Triple Dissemination, Forward-Chaining, and Load Balancing in DHT based RDF Stores," in Proceedings of the 2005/2006 international conference on Databases, information systems, and peer-to-peer computing, 2007, pp. 343–354.

[7] L. Ali, T. Janson, and G. Lausen, "3rdf: Storing and Querying RDF Data on Top of the 3nuts Overlay Network," in 10th International Workshop on Web Semantics, Toulouse, France, August 2011, pp. 257–261.

[8] M. Cai and M. Frank, "RDFPeers: a scalable distributed RDF repository based on a structured peer-to-peer network," in Proceedings of the 13th international conference on World Wide Web, 2004, pp. 650–657.

[9] E. Liarou, S. Idreos, and M. Koubarakis, "Evaluating Conjunctive Triple Pattern Queries over Large Structured Overlay Networks," in International Semantic Web Conference, 2006, pp. 399–413.

[10] K. Aberer, P. Cudre-Mauroux, M. Hauswirth, and T. V. Pelt, "GridVine: Building Internet-Scale Semantic Overlay Networks," in the Semantic Web – ISWC 2004, vol. 3298. Springer-Verlag, 2004, pp. 107–121.

[11] M. T. O¨ zsu and P. Valduriez, Distributed and Parallel Database Systems (3rd. ed.). Springer, 2011.

[12] L. Galarraga, K. Hose, and R. Schenkel, "Partout: A Distributed Engine for Efficient RDF Processing," Technical Report: CoRR abs/1212.5636, 2012.

[13] J. Huang, D. J. Abadi, and K. Ren, "Scalable SPARQL Querying of Large RDF Graphs," PVLDB, vol. 4, no. 11, 2011.

[14] K. Lee and L. Liu, "Scaling Queries over Big RDF Graphs with Semantic Hash Partitioning," PVLDB, vol. 6, no. 14, Sep. 2013.

[15] K. Hose and R. Schenkel, "WARP: Workload-Aware Replication and Partitioning for RDF," in DESWEB, 2013.

[16] N. Papailiou, I. Konstantinou, D. Tsoumakos, P. Karras, and N. Koziris, "H2RDF+: High-performance Distributed Joins over Large-scale RDF Graphs," in IEEE BigData, 2013.

[17] M. Husain, J. McGlothlin, M. M. Masud, L. Khan, and B. M. Thuraisingham, "Heuristics-Based Query Processing for Large RDF Graphs Using Cloud Computing," IEEE TKDE, vol. 23, no. 9, Sep. 2011.

[18] S. Chatterji and S. Evani. On the complexity of approximate query optimization. In PODS, pages 282–292, 2002.

[19] O. Cure and G. Blin.RDF Database Systems: Triples Storage and SPARQL Query Processing. 2014.

[20] H. Kllapi, E. Sitaridi, M. M. Tsangaris, and Y. E. Ioannidis. Schedule Optimization for Data Processing Flows on the Cloud. In SIGMOD, 2011.

[21] S. Agarwal, A. Iyer, and A. Panda. Blink and it's done: interactive queries on very large data. In VLDB, volume 5, pages 1902–1905, 2012.

[22] I. Trummer and C. Koch. Approximation schemes for many-objective query optimization. In SIGMOD, pages 1299–1310, 2014.

[23] I. Trummer and C. Koch. An incremental anytime algorithm for multi-objective queries optimization. In SIGMOD, pages 1941–1953, 2015.

ISSN: 1992-8645 www.jatit.org E-ISSN: 1817-3195

[24] I. Trummer and C. Koch.Multi-objective parametric query optimization. VLDB, 8(3):221–232, 2015.

[25] C. Chekuri, W. Hasan, and R. Motwani. Scheduling Problems in Parallel Query Optimization. In PODS, pages 255–265, 1995.

[26] R. Mietz, S. Groppe, O. Kleine, D. Bimschas, S. Fischer, K. Roomer, and D. Pfisterer, "A p2p semantic query framework for the internet of things," Praxis der Informationsverarbeitung und Kommunikation, vol. 36, no. 2, pp. 73–79, 2013.

[27] L. Ali, T. Janson, G. Lausen, and C. Schindelhauer, "Effects of Network Structure Improvement on Distributed RDF Querying," in 6th International Conference on Data Management in Cloud, Grid and P2P Systems (Globe 2013), Prague, Czech Republic, September 2013.

[28] A. Harth and S. Decker, "Optimized index structures for querying rdf from the web," Web Congress, Latin American, vol. 0, pp. 71–80, 2005.

[29] W.-S.Han, W. Kwak, J. Lee, G. M. Lohman, and V. Markl. Parallelizing query optimization. VLDB, 1(1):188–200, Aug. 2008.

[30] W.-S.Han and J. Lee. Dependency-aware reordering for parallelizing query optimization in multi-core CPUs. In SIGMOD, pages 45–58, 2009.

[31] F. M. Waas and J. M. Hellerstein. Parallelizing extensible query optimizers. In SIGMOD, page 871, New York, New York, USA, 2009.ACM Press.

[32] W. Zuo, Y. Chen, F.He, and K. Chen. Optimization Strategy of Top-Down Join Enumeration on Modern Multi-Core CPUs. Journal of Computers, 6(10):2004–2012, Oct. 2011.

[33] Y. Chen and C. Yin. Graceful Degradation for Top-Down Join Enumeration via similar sub-queries measure on Chip Multi-Processor. Applied Mathematics and Information Sciences, 941(3):935–941, 2012.

[34] M. a. Soliman, M. Petropoulos, F. Waas, S. Narayanan, K. Krikellas, R. Baldwin, L. Antova, V. Raghavan, A. El-Helw, Z. Gu, E. Shen, G. C. Caragea, C. Garcia-Alvarado, and F. Rahman. Orca: A modular query optimizer architecture for big data. In SIGMOD, pages 337–348, 2014.

[35] Trummer, Immanuel, and Christoph Koch."Parallelizing query optimization on shared-nothing architectures." Proceedings of the VLDB Endowment 9.9 (2016): 660-671.

[36] M. Stonebraker. The Case for Shared Nothing. IEEE Database Engineering Bulletin, 9(1):4–9, 1986.

[37] Shailaja, K., P. V. Kumar, and S. Durga Bhavani. "Progressive Genetic Evolutions-Based Join Cost Optimization (PGE-JCO) for Distributed RDF Chain Queries." Proceedings of the First International Conference on Computational Intelligence and Informatics. Springer Singapore, 2017.

[38] Carmines, Edward G., and Richard A. Zeller. Reliability and validity assessment. Vol. 17. Sage publications, 1979.

[39] Ihaka, Ross, and Robert Gentleman. "R: a language for data analysis and graphics." Journal of computational and graphical statistics 5.3 (1996): 299-314.

[40] The Friend of a Friend (FOAF) project. Retrieved from foaf-project.org: http://www.foaf-project.org/ (2000).

[41] Agency, C. I. The CIA World Factbook 2015.New Yark: Skyhorse Publishing Inc (2014).

[42] Guo, Yuanbo, Zhengxiang Pan, and Jeff Heflin. "LUBM: A benchmark for OWL knowledge base systems." Web Semantics: Science, Services and Agents on the World Wide Web 3.2 (2005): 158-182.

[43] Cleophas, Ton J., and Aeilko H. Zwinderman. "Paired Continuous Data (Paired T-Test, Wilcoxon Signed Rank Test)." Clinical Data Analysis on a Pocket Calculator. Springer International Publishing,2016.31-36.

Imperial Journal of Interdisciplinary Research (IJIR)
Vol-3, Issue-10, 2017
ISSN: 2454-1362, http://www.onlinejournal.in

Micro Genetic Algorithm based Overload minimization approach for Transmission Expansion Planning

Jarapala Ramesh Babu
Methodist College of Engineering & Tech Hyderabad, Telangana-India

Abstract—*Broadly two solution approaches are used in solving the Transmission Expansion Planning (TEP) problem namely, Load curtailment minimization approach and Overload minimization approach. Overload minimization approach involves lesser computational efforts but has problem of non convergence of load flow in presence of isolated nodes. In literature, isolated nodes are dealt with modeling system Z-bus with fictitious lines of high impedance from reference to new nodes. This paper incorporates this technique in Micro Genetic Algorithms (MGA) and Genetic Algorithms (GA)to solve TEP problem. The fitness function is defined as inversely proportional to sum of weighted investment cost and overloads on the lines. The plans with high fitness and zero overloads are chosen, which are then tested for their utility by a Utilization Index (UI). The congestion costs for all chosen plans are also estimated. Multiple plans are analyzed across different attributes by trade off approach to help the decision maker. The complete algorithm implementation is described. The results for a practical Brazilian 87-bus test case are obtained and compared with results in literature.*

Index Terms*—Power Deregulation, Gauss Seidel, Micro Genetic algorithm, Transmission expansion planning and System overload.*

I INTRODUCTION

The basic principle of TEP is to minimize the network construction and operational costs while satisfying the requirement of delivering electric power safely and reliably to load centers along the planning horizon [1]. The expansion of a transmission network may include the construction of new overhead lines or underground cable in new corridors, and the upgrading of existing lines or cables in corridors already in use by increasing the number or the capacity of lines or cables, increasing the rated voltage, the improvement on the capacity and control equipment (FACTS, Capacitor banks etc.). In a more broad sense, one may also consider the introduction of generators in appropriate places to allow a better balance between generation and loads, and better use of the network, increasing the transmission capacity of the network

From the stake-holders point of view, transmission expansion should attend the following targets [2].

- Encourage and facilitate competition among market participants;
- Provide non-discriminatory access to cheap generation for all consumers;
- Alleviate transmission congestion;
- Minimize the investment, the risk of investments and operation costs;
- Increase the reliability of the network;
- Increase the flexibility of system operation while reducing the network charges;
- Minimize the environmental impacts;
- Allow better voltage level regulation.

Even though the principles are quite simple, the complexity of the problem and the impact on society due to the heavy investments that have to be made, together with the costs incurred due to failures, make TEP on as a challenging issue. The following are some of the factors that distinguish TEP as a challenging field in power system analysis [2].

- Complexity of the problem; TEP is a complex problem because it has a mixed integer nonlinear programming nature. It is also a complex mathematical problem as it involves, typically, a large number of variables.
- Usually, heavy investments must be made. This kind of investments goes a long way to strain the economy of the country or region undergoing such expansion plans.

Transmission expansion planning addresses the problem of strengthening an existing transmission network to optimally serve a growing electricity market while satisfying a set of economic and technical constraints. Various techniques, including simulated annealing, tabu search, evolution strategies, greedy randomized adaptive search procedure (GRASP), probabilistic reliability criteria (PRC), and probabilistic load flow (PLF), have been used to study the problem [3] – [7]. It is difficult to obtain the optimal solution of a composite power considering the generators and transmission lines simultaneously in an actual system, and therefore, transmission expansion

planning is usually performed after generation expansion planning.

This paper presents a method for determining the optimal number of transmission circuits required in each network corridor using genetic algorithm (GA). Gauss – siedel power flow algorithm was used to determine the line flows and voltage magnitudes in each network corridor and network bus respectively. The static transmission expansion planning (STEP) problem was formulated using a DC power flow model [8], [9].

II. MICRO GENETIC ALGORITHM(MGA)

Genetic algorithms are simple, robust, flexible, and able to find the global optimal solution. They are especially useful in finding solution to problems for which other optimization techniques encounter difficulties [8]. A basic genetic algorithm is constituted by a random creation of an initial population and a cycle of three stages, namely: • evaluation of each chromosome; • chromosomes selection for reproduction; • genetic manipulation to create a new population, which includes crossover and mutation. Each time, this cycle is completed, it is said that a generation has occurred. A.Standard Micro genetic algorithm The disadvantage of GAs is the high processing time associated. That is due to their evolutionary concept, based on random processes that make the algorithm quite slow. However, different methods for reducing processing time have already been proposed, such as more appropriate choice of solution coding and reduction of search space using the specialist knowledge. One alternative method known as micro genetic algorithms, whose processing time is considerably smaller, is shown in [11] .

Most GAs produce poor results when populations are small, because insufficient information is processed about the problem and, as a consequence, premature convergence to a local optimum occurs. Population size generally varies from 30 to 300 individuals. In contrast, MGAs explore the possibility to work with small populations (from five to 20 individuals usually) in order to reduce the processing time. From a genetic point of view, it is known that frequent reproductions inside a small population may disseminate hereditary diseases rarely found in large populations. On the other hand, small populations can act as natural laboratories where desirable genetic characteristics quickly can emerge. In MGAs, mutations are unnecessary because after a certain number of generations, the best chromosome is maintained and the rest are substituted by randomly generated ones. On the other hand, it requires adoption of some preventive strategy against loss of diversity in population. The MGA implemented in the present work is reported in the following algorithm:

1) Select a population of n randomly generated individuals. Alternatively, n-1 individuals may be generated randomly together with one good individual obtained from previous search

2) Evaluate fitness and determine the best individual which is always transferred to the next generation. This “elitist” strategy guarantees against the loss of good information embedded in the best individual produced thus far

3) Select individuals for reproduction with the tournament selection strategy (for example with k=2)

4) Apply crossover with probability equal to 1 to favor exchange of genetic information among the population

5) Check for convergence by measuring the amount of diversity left in the population (by counting the total number of bits which are unlike those possessed by the best individual). If population diversity has fallen under a preselected threshold, go to Step 1; otherwise, go to Step 2.

III.GENETIC ALGORITHM (GA)

The use of Genetic Algorithm for problem solving is not new. The pioneering work of J.H. Holland in the 1970’s proved to be a significant contribution for scientific and engineering applications. GA is inspired by the mechanism of natural selection, a biological process in which the stronger individuals are likely to be the winners in the competing environment. Here, GA uses the direct analogy of such natural evolution. It presumes that the potential solution of a problem is an individual and can be represented by a set of parameters. Standard genetic algorithm is a random search method that can be used to solve non-linear system of equations and optimize complex problems. The base of this algorithm is the selection of individuals. It doesn’t need a good initial estimation for sake of problem solution, In other words, the solution of a complex problem can be started with weak initial estimations and then be corrected in evolutionary process of fitness [10]. GA also combines various operators namely; selection, crossover, and mutation operators with the goal of finding the best solution to a problem. GA searches for this optimal solution until a specified termination criterion is met. A proto-typical GA consists of the following steps.

- Generate initial generation
- Measure fitness
- Select a mating pool
- Mutate randomly selected member of the mating pool
- Pair the members of the mating pool.
- Perform crossover to obtain the new generation
- Iteration continues until some stopping condition is satisfied.

The Mutation operator selects one of existed integer numbers from the mating pool and then

changes its value randomly. Reproduction operator, similar to standard form, reproduces each individual proportional to the value of its objective function. Therefore, the individuals which have better objective functions will be selected more probable than other chromosomes for the next population [15].

The selection operator selects the individual in the population for reproduction. The more fit the individual, the higher its probability of being selected for reproduction. The crossover operator involves theswapping of genetic material (bit-values) between the two parent strings. Based on predefined probability, known as crossover probability, an even number of individuals are chosen randomly. Each individuals (children) resulting from each crossover operation will now be subjected to the mutation operator in the final step to forming the new generation. The mutation operator enhances the ability of the GA to find a near optimal solution to a given problem by maintaining a sufficient level of genetic variety in the population, which is needed to make sure that the entire solution space is used in the search for the best solution.

In the context of TEP, the alternative expansion plans are referred to as the individuals. These individuals are what make up the mating pool as stated above. The power flows in the network together with other line flow constraints are all modeled mathematically and constitute part of the Algorithm [10], [11].

IV. MATHEMATICAL MODELLING

In this section, the mathematical models as proposed in [8], [12] and [13] are outlined. It consists of a Power flow model and a static transmission expansion planning (STEP) model.

A.Power flow model:

This provides a model of the nonlinear relationships among bus power injections, power demands, bus voltages and angles with the network constants providing the circuit parameters.

The power flow model provides information on the electrical performance of the lines with actual power flows in such lines. They also provide information about the line and transformer loads as well as losses throughout the system and voltages at different points in the system [12].

In developing power flow equations, a 3 – phase balanced system operation is assumed; hence per – phase analysis is utlized to obtain the necessary equations.

$$S_i \triangleq S_{Gi} - S_{Di} \quad (1)$$

$$I_i = I_{Gi} - I_{Di} \quad (2)$$

$$I_i = \sum_{k=1}^{n} Y_{ik} V_k \quad (3)$$

$$S_i = V_i I_i^* = V_i \sum_{k=1}^{n} Y_{ik}^* V_k^* \quad (4)$$

$$V_i \triangleq |V_i| e^{\angle V_i} = |V_i| e^{j\theta_{ik}} \quad (5)$$

$$\theta_{ik} = \theta_i - \theta_k \quad (6)$$

$$Y_{ik} \triangleq G_{ik} + jB_{ik} \quad (7)$$

$$S_i = \sum_{k=1}^{n} |V_i||V_k|(G_{ik}\cos\theta_{ik} + B_{ik}\sin\theta_{ik}) \quad (8)$$

Resolving real and imaginary ports we otain

$$P_i = \sum_{k=1}^{n} |V_i||V_k|(G_{ik}\cos\theta_{ik} + B_{ik}\sin\theta_{ik}) \quad (9)$$

$$Q_i = \sum_{k=1}^{n} |V_i||V_k|(G_{ik}\sin\theta_{ik} - B_{ik}\sin\theta_{ik}) \quad (10)$$

Gauss – Siedel power flow modification was also adopted as highlighted in this section. Recall from equation 4 that:

$$P_i - jQ_i = V_i^* I_i = V_i^* \sum_{k=1}^{n} Y_{ik} V_k$$

$$= |V_i|(\cos\delta_i - j\sin\delta_i)\sum_{k=1}^{n}|Y_{ik}V_k|(\cos\theta_{ik} + j\sin\theta_{ik})(\cos\delta_k + j\sin\delta_k) \quad .....11$$

$$= \sum_{k=1}^{n}|Y_{ik}V_iV_k|(\cos\delta_i - j\sin\delta_i)(\cos\theta_{ik} + j\sin\theta_{ik})(\cos\delta_k + j\sin\delta_k) \quad .....12$$

Where Pi and Qi are the net real and reactive powers expressed in per-unit. Thus, for buses where real and reactive power are injected into the bus, such as generator buses, and have positive values. For Load buses where real and reactive powers are flowing away from the bus, Pi and Qi have negative values.

$$P_i = \sum_{k=1}^{n}|Y_{ik}V_iV_k|\cos(\theta_{ik} + \delta_k - \delta_i) \quad .....13$$

$$Q_i = -\sum_{k=1}^{n}|Y_{ik}V_iV_k|\sin(\theta_{ik} + \delta_k - \delta_i) \quad .....14$$

For the voltage controlled buses, the bus voltage must be equal to the specified voltage. Also, the maximum and minimum reactive powers at these buses are also specified and the value of Qi(for i=1,2,3,….n)must lie between these limits. [23], [24].

1. $|V_i| = |V_i|_{spec}\ for\ i = 2,3,\ldots\ldots n$
2. $Q_{i\,min} < Q_i < Q_{i\,max}\ for\ i = 2,3,\ldots\ldots n$

If during any of the iterations, we find out that Qi is outside the limits specified, Qi is fixed at the minimum or the maximum value as the case may be and then the bus is treated as a PQ bus (load bus).

B. Static transmission expansion planning model

Generally, transmission expansion planning could be classified as static or dynamic. Static expansion determines where and how many new transmission lines should be added to the network up to the planning horizon [8]. Implicitly, we could infer the major goal of Static TEP is finding an appropriate number of new circuits that should be added to the transmission network.

The Static transmission expansion planning problem was formulated as follows using a DC power flow model [8], [9].

$$TC = \sum_{i,j \in \Omega}^{n} C_{IJ} Xn_{IJ} \quad \text{.....15}$$

TC: Construction cost of lines along the planning horizon C_{IJ} : Construction cost of each line in corridor.

Equation 17 represents the construction cost of new lines which should be added to the network for delivering safe and reliable electric power to load centers over the planning horizon. Several constraints are also modeled in a mathematical representation to ensure that the mathematical solutions are in line with planning requirements. These constraints are stated in the following sections [8].

$$P_i = \sum_{J}^{NB} P_{ij} + d_i \text{ (I=1,2,....NB) } (i, j \in \Omega) \text{.....16}$$

Where, NB = total number of buses in the network

P_i & d_i : Generation and demand on bus i

P_{ij} : Power flow of each branch i-j

Equation is known as the Dc power flow node balance constraint. Also,

$$P_{ij} = \gamma_{ij} X (n^{0}_{ij} + n_{ij}) X (\theta_i - \theta_j) \text{ .....17}$$

Where

γ_{ij} : Total Susceptance of circuits in corridor

$(\theta_i - \theta_j)$: Voltage phase angles of buses respectively

IV. IMPLEMENTATION

The Gauss – Siedel power flow model was implemented using MATLAB. The flowchart used in implementing the Gauss – Siedel Power flow model is shown in Figure 1 and that of the Genetic algorithm is shown in Figure *2*.The output of the Gauss –Siedel load flow algorithm constitutes the input of the Micro Genetic Algorithm and Genetic algorithm flowchart. The various blocks in the Micro Genetic Algorithm and Genetic Algorithm flowchart are described in section.

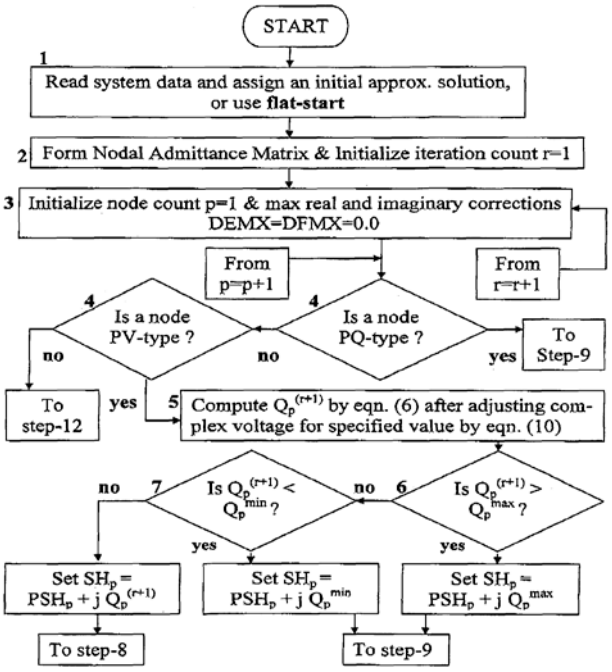

Fig:1 **Prior Art: Flow-chart of Gauss-Seidel Loadflow (GSL) Method**

Fig 1 Gauss – Siedel (GS) Power Flowchart

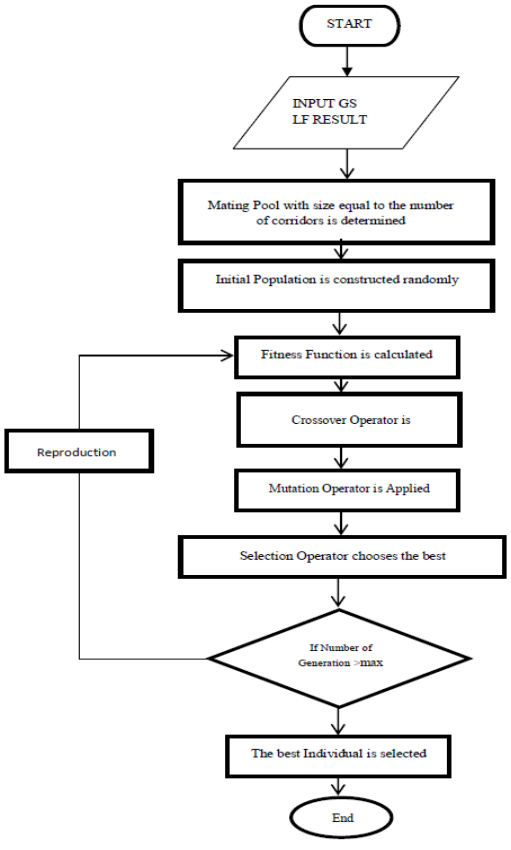

Fig. 2 Genetic Algorithm Flowchart

V. RESULTS AND DISCUSSION

IEEE 14 – bus network was used as a test system to demonstrate the effectiveness of the chosen method. The network data for the IEEE 14 – bus test network was gotten from [14].The voltage magnitude, voltage angle and line flow of the IEEE 14 – bus network as calculated are shown in tables I and II. Also, the optimal number of extra lines required in each network corridor as calculated is tabulated in Table III.

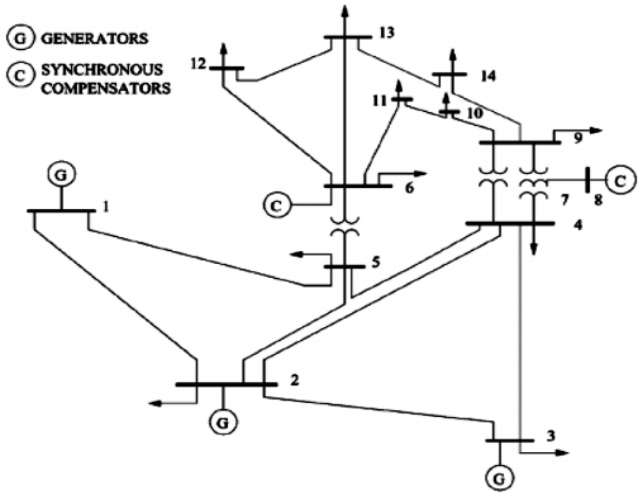

Fig:3 IEEE 14 – bus test network

Table I: Voltage Magnitude And Voltage Angle

Bus Number	Voltage Magnitude(p.u.)	Voltage Angle
1.	1.0600	0
2.	1.0186	-4.6495
3.	1.0047	-13.0577
4.	0.9940	-10.2633
5.	0.9998	-8.7037
6.	0.9721	-15.0821
7.	0.9828	-13.8216
8.	1.0131	-13.8216
9.	0.9596	-15.7607
10.	0.9537	-15.9883
11.	0.9590	-15.6947
12.	0.9559	-16.1048
13.	0.9509	-16.1923
14.	0.9359	-17.1686

Table II: Line Flows

From Bus	To Bus	Line Flow (p.u.)
1	2	2.0220
1	5	2.8506
2	3	0
2	4	0
2	5	0.3277
3	4	0
4	5	0
4	7	0
4	9	0
5	6	0
6	11	0
6	12	0
6	13	0
7	8	0
7	9	0.6353
9	10	0.2140
9	14	0.1568
10	11	0.0373
12	13	0.0274
13	14	0

Table III: Number of New Circuits and Network Adequacy

S/NO	BRANCH	NEW CIRCUITS	NETWORK ADEQUACY (YEARS)
1.	1 – 2	4	6
2.	1 – 5	5	1
3.	2 – 5	0	5
4.	9 – 10	0	5

Table I and Table II show us the status of the network during the expansion year. A load growth coefficient of 1.07 was used to ascertain how the network would fare with yearly increase in demand. The transmission network adequacy is a measure of the length of time within which the transmission expansion plan would still be viable. The following can be inferred from the results so obtained:

- Line flow in branch 1 – 2 already exceeds the transmission capacity of the Line, thus the TEP proposes that 4 extra lines of the same capacity be constructed to relieve the already existing line in the branch. It also stipulates that the extra lines would become inadequate 6 years after expansion.
- Line flow of the line in corridor 1 – 5 also exceeds the transmission capacity of the line, much more than that of the line in corridor 1 – 2. Thus the TEP proposes that extra 5 lines of same capacity be constructed to relieve the already the congested line. However, the network adequacy of this plan is just 1 year. Improving the network adequacy would require an increase in the generation capacity, possibly in bus 2.
- Lines in corridors 2 – 5 and 9 – 10 both do not require extra lines; however the network adequacy of both lines is set at 5 years.

VI. CONCLUSION

This work addresses transmission system expansion planning using genetic algorithm. The number of transmission lines to decongest the branches and the corresponding network adequacy were both determined using this method. This work also provides a practical approach that could serve as a

useful guide for the decision maker in selecting a reasonable expansion plan in the face of the prevalent circumstances.The model was also tested on IEEE 14 – bus network in order to ascertain the viability of the chosen methodology on diverse network models. They also suggest that transmission congestion occurs when actual or scheduled flows of electricity on a transmission lines are restricted below the level that grid users desire or when actual or scheduled flows exceeds the transmission capacity of the line.

REFERENCES

[1] Jalilizadeh, Saieed, et al, "Technical and Economic Evaluation of Voltage level in Transmission network expansion planning using GA," *Energy Conversion and Management*, 2007.

[2] Buygi, M. Oloomi; Shanechi, H.M; Balzer, G; Shahidehpour, M.; " Network Planning in unbundled power systems," *IEEE Trans. Power Syst.*,vol. 21, no. 3, pp. 1379 – 1387, Aug. 2006.

[3] A.S Braga, J.T Saraiva, "Transmission Expansion Planning and Long term marginal prices calculation using simulated annealing," *in proc. IEEE Power Tech. Conf.*, Bologna: Italy, June. 2003.

[4] Hiroyuki Mori and Yoshinori Iimura, "Transmission network expansion planning with hybrid meta-heuristic method of parallel tabu-search and ordinal optimization," *in proc. International Conf. on ISAP*, Kaohsiung, Taiwan, Nov. 2007 .

[5] Armando M. Leite da Silva, Warlley S. Sales, Leonidas C. Resende et al, "Evolution strategies to transmission expansion planning considering unreliability costs," *in proc. 9th International Conf. on Probabilistic methods applied to power systems*, Stockholm: Sweden; June, 2006.

[6] Silvio Binato, GersonCouto de Oliveira, and Joao Lizardo de Araijo, "A greedy randomized adaptive search procedure for transmission expansion planning," *IEEE Trans. Power Systs.*,vol. 16, no. 2, pp. 247 – 253, May, 2007. [7] J. Choi, Trungtinh Tran, A. El-Keib, Robert Thomas, et al, "A method for transmission system expansion planning considering probabilistic reliability criteria," *IEEE Trans. Power Syst.*, vol. 20, no. 3, pp. 885 – 895, Aug. 2005.

[8] MeisamMahdavi, Hassan Monsef, "Review of static transmission expansion planning," *Journal of Electrical and Control Engineering*, vol. 1, No. 1, pp. 11 – 18, 2011.

[9] D.J. Silva, M.J. Rider, R. Romero and C.A. Murari, "Transmission expansion network planning considering uncertainties in demand," *in Proc. IEEE Power Eng. Society General Meeting*, vol. 2, pp. 1424 – 1429 , 2005. [10] M. OloomiBuygi, H.M Shanechi, G. Balzer, M. Shahidepour, " Transmission planning approaches in restructured power systems," *in proc. IEEE Power Tech. Conf.*, Bologna, Italy, June 2003.

[11] Barros, Joao Ricardo P.; Melo, Albert C.G. and Silva, Armando M. Leite, "An approach to the explicit consideration of unreliability costs in transmission expansion planning," *Euro. Trans. Elect.Power*, vol. 17, pp. 401- 412, 2007. [12] B.R. Gupta, "Power system analysis and design," S. Chand and Company, Ram Nagar, New Delhi, India, 2005.

[13] Arthur R. Bergen, Vijay Vittal, "Power System Analysis," Prentice Hall, Upper Saddle River, New Jersey, 2000.

[14] Power Systems Test Case Archive, [Online]. www.ee.washington.edu/research/pstca/pf14/pg_tca14bus.htm (Accessed 8th October 2013).

[15] H. Shayeghi, M. Mahdavi, H. Haddadian, "DCGA based transmission network expansion planning considering network adequacy," *World Academy of Science, Engineering and Technology*, vol. 24, pp. 807 – 812, 2008.

About the Authors:

*R*amesh babu Jarapala received his B.Tech degree in Electrical and Electronics Engineering and M.E in Power system Engineering from University College of Engineering, Osmania University , Hyderabad, Telangana, India, In 2007 To 2009 respectively. 2009 to 2012, he is Assistant Professor in KSIT Engineering college, 2012 to 2014 he is Assistant Professor in PBIT engineering college,2014 to 2017 Assistant Professor in AHTC engineering college and since 2014 he is Assistant Professor Methodist College Of Engineering &Tech Hyderabad, Telangana-India.

International Journal of Innovations & Advancement in Computer Science
IJIACS
ISSN 2347 – 8616
Volume 6, Issue 9
September 2017

Social Media: To Deal Crisis Circumstances

Thirupathi Lingala,
Asst. Prof., CSE Department, Methodist College of Engineering & Technology-Hyderabad, Telangana –INDIA
Sandeep Ravikanti,
Asst. Prof., CSE Department, Methodist College of Engineering & Technology-Hyderabad, Telangana –INDIA

Abstract:

Social media and online services with user-generated content (e.g., Twitter, Facebook, Instagram and YouTube) have made a mystifying amount of information obtainable. Administration officials seek to resistor these resources to progress services and communication with citizens. Important potential exists to classify issues in real time, so crisis managers can monitor and respond to issues about public safety. Yet, the complete capacity of social data brooks creates extensive noise that must be filtered in order to discover expressive patterns and trends. Vital events can then are recognized as points in activity, while event meaning and penalties can be deciphered by tracking variations in content and community sentiment. This Paper presents results from an investigative study with the comprehensive objective of understanding social media use by administration officials as well as community administrations, industries, and the community at huge. A key objective was also to understand social media use specifically for dealing crisis circumstances.

Keywords: Social media, Crisis information, Information visualization, Word cloud, Focus group study.

1. Introduction

People are increasingly relying on social media for communication with their family, friends, colleagues, businesses, and the administration. The capabilities to enable group interaction provide new and exclusive chances for public leaders, elected officials, and administration service providers to inform, and be informed by, the citizenry [1]. Twitter, Facebook, Instagram, YouTube, and other services with user-generated content have made a staggering amount of information available online. In 2017, during the period of our study, worldwide, there are over 1.94 billion monthly active Facebook users for March 2017 (Facebook MAUs) which is an 18 percent increase year over year. There are 1.15 billion mobile daily active users (Mobile DAU) for December 2016, an increase of 23 percent year-over-year. 1.28 billion People log onto Facebook daily active users (Facebook DAU) for first Quarter of 2017, which represents an 18% increase year over year (Source: Facebook as 05/03/17). There are 1.74 billion mobile active users (Mobile Facebook MAU) for December 2016 which is an increase of 21% year-over-year (Source: Facebook as of 02/01/17). At 1.94 billion, Facebook has more monthly active users than WhatsApp (1 billion), Twitter (328 million) and Instagram (700 million)—combined (Source: CNBC). Facebook continues to reign in popularity over other social media channels, but the competition is mounting [2][3].

All this information and deep reach are readily accessible for administration officials to tap into and influence for enhanced services. However, the treasure trove of information comes with extensive noise that must be cleaned to make this information beneficial and reliable.

Administration officials seek to leverage these resources to progress services and communication with people; especially segments of the population that previously were problematic to scope. Yet, the complete volume of social data streams generates extensive noise that must be cleaned to be useful. The desire and potential exist for classifying and responding to issues in real time for more operational emergency management as well as enhanced public safety and general quality of life. For example, critical events of interest (e.g., earthquake, flash mob gatherings, protests etc.) can be recognized as points in the social media volume. Problems of concern for public safety or general quality of life can be discovered, monitored, and mitigated by analyzing social media streams to detect meaningful patterns and trends (Fig.1).

Similarly, monitoring these patterns and themes over time could provide officials with visions into the observations and mood of the community that cannot be collected through outdated approaches (e.g., phone or mail surveys) due to a diversity of reasons, including the excessive cost as well as the limited window of opportunity for influencing or mitigating events as they evolve. Perhaps most significantly for emergency management, no outdated technique can provide insight in real time. Investigations require significant time and effort prior to data collection, during the collection process, and for analyses of the results, which often take months to finish. Secondly, practical costs are associated with survey activities, making them especially difficult in light of reduced and shrinking budgets of

Academic Science

International Journal of Innovations & Advancement in Computer Science
IJIACS
ISSN 2347 – 8616
Volume 6, Issue 9
September 2017

administrations at all levels. Finally, once completed a survey captures observations at a single point in time. Although it is possible to use surveys at intervals to screen the progress, it is not a mutual practice, considerably raises costs, and frequently does not reach important sections of the public.

Fig1. Social media streams to improve services and communication with people.

Data mining of different real-time feeds of social streams related to real-world events are needed to enable officials to make sense of the massive amount of information generated. In so doing, administration should be able to act more efficiently on matters both in on-going issues of public concern and major weather or traffic disruption, public safety. Specifically, we have begun to:

1) Leverage and further refine tools for gathering and connecting large amounts of public social media data appropriate to Arlington County.

2) Store the collected social media data over a period of time into a digital library, and

3) Classify research and implement applications of multimedia analytics and text mining for administration services and communication.

To address these goals, we conducted investigative focus group interviews with key stakeholders in administration and community organizations, and developed tools to analyze and extract data more significant and practical for local organizations, administrations and citizens.

Our target information sources included official Arlington County Facebook pages [4], Twitter feeds [5], blogs [6], news, community forums, and appropriate postings by the community on social media sites. Applications of such examines could include observing public belief before and after large public events, checking scheduled or unexpected activities, recognizing and classifying imperative public matters over time and location, enhancing civic recovery in response to emergencies or misfortunes, and tracing the expansion of long-running themes in domestic lifespan.

Contemporary case studies, such as published by Queensland Police Service [7] outlined the experiences and best practices for engaging and informing citizens during a historic flood. To the best of our knowledge, this study is the first to survey across a wide range of administration agencies and public organizations, maintained by data analysis of present online communications.

2. Social Media and Administration

Social media are internet-based applications designed to facilitate social interaction and for using, developing and spreading information through the world. Social media build on several of the same concepts and technologies of Web 2.0, most basically, the creation and exchange of user generated content [8]. Broadly, Web 2.0 and social media are considered social software, i.e., software that enables people to connect or collaborate through computer-mediated communication [9] [10].This type of software has happened for years in the form of online bulletin board systems, forums, and newsgroups. In recent times, however, blogs and micro blogs (e.g. twitter), RSS feeds, tagging systems and collaborative filters have made social software easy to use and extremely scalable leading to superior acceptance and usage.

a. Social Media Use by People

Social media have changed the way people get information about what's going on in their societies, and national and global existing proceedings. They deliver innovative methods for residents to share information and to interact with each other with chosen bureaucrats and administration agencies. A national study conducted by Pew Internet & American Life in 2010 finds that almost a third (31%) of all online adults in the USA used social tools such as blogs, social networking sites, and online video as well as email and text alerts to keep informed about administration activities[11].

A survey conducted in the US by the American Red Cross [12], 75% of respondents reported they would use social media in predicament and civic-related situations (e.g., traffic jam, car crash, potential crime, or downed power lines). Nearly half of accused reported that they would use social media to let others know they were safe in an emergency; 86% report they would use Facebook; 28% would use Twitter, and 11% would use a blog.

According to Palen, Hughes, and colleagues [13][14]. These studies specifically focus on the use of Twitter during tragedies and conditions of social meeting, such as mass political protests, rallies. They stated that twitter use under pressure and the users may broadcast more up to date and timely information than administration organizations.

b. Social Media Use by Administration

Twitter and other social sources have been

effective in early event spotting [15] [16], the reaction time of which can be even sooner than authorized sources (e.g., earthquake reporting). In the case of nonstop monitoring, social media can help quantity the effectiveness of control processes and propaganda.

We have been reading social media usage and influence as part of an on-going longitudinal research of Internet use and impact in Blacksburg, Virginia and environs [17]. The communications specialists in town administration monitors twitter for related posts that would help from a reply or should be brought to the attention of town council as a citizen suggestion.

From our preliminary study of social media use in Blacksburg, we found that most often the person posting tweets or managing an organization's Facebook page was not from the organization's leadership. Instead, a college student or other young adult was often working in tandem on behalf of the organization to post announcements, updates, or other information.

3. Learning Approaches

We gathered and examined area-specific social media sources, and conducted focus group interviews with county officials (specifically, personnel from emergency management services, the police department, and volunteer leadership office), including a questionnaire about their social media use and community association. We were able to recruit 50 participants and organized them into three separate focus group sessions held in April and May 2017 in Arlington. At the inception of each of the interview sessions, we asked participants to complete an online questionnaire.

The focus group sessions continued in two key phases. They began with participants involved in electronic brainstorming to create a number of thoughts rapidly, followed by a process whereby they recognized categories that grouped the thoughts by relationship.

We used different Twitter analytical tool, such as the Archivist [18] to collect tweets from local organizations, including Arlington administration that were public in nature.

We did semantic analyses on the Twitter data to detect common topics and to distinguish followers by their profile data; we conducted simple frequency counts to calculate number of ‘followers’ and ‘followers of followers’ of a given organization.

We used the visualization software wordle [19] to represent the results of the Twitter analyses as tag clouds in order to be able to cleanse and make greater sense of huge volumes of data faster and simply. For the YouTube video collections, we searched all YouTube videos for the tags or video with the title ‘Arlington County’ and signified the search results in a tag cloud demonstrating the most frequent tags in the image collection.

4. Outcomes

Our findings from the experimental study are based on the focus group interviews and participant questionnaires (N=50), and the development of tools to analyze social media data we collected.

The results fall into three main zones:

1) Local administration uses social media without knowing its costs and benefits, or who their actual audience is, who in their society should monitor communications, how and when they should be answering, and what effect their social media communications have on the public;

2) New tools are needed to help administration and nations make sense of the massive volume of data that is being produced, to exemplary the flow of information, and to detect patterns over time; and

3) Digital libraries are needed to archive and curate produced content, especially for crisis and social meeting circumstances.

Framing questions for focus group interviews are as shown in below topics:
1. Missions and objectives of the organization. 2. Achievement using the social media. 3. Concerns and difficulties about using the social media. 4. Social media that would be helpful to the society.

a. Focus Groups: Questionnaire

Each of the 50 focus group participants completed an online questionnaire at the beginning of their focus group interview session. Of this sample, 30 (60%) were female and 20 (40%) were male. The majority (84%) was white, 64% were married and 92% were employed on a full-time basis.

Most respondents stated that they have ideas for refining things in their community at least once a month (76%) and that they regularly get together with others who are well informed about local issues. 36% are reported that they worked to bring about change in their community on a daily basis. Almost half of the participants (48%) reported that they either posted comments, pictures or video online, or blogged about a political or social issue in the past year. Over half (56%) of respondents used social networking sites on a daily basis, and 76% used these sites at least once a week.

All respondents felt that the region administration should contact citizens by way of phone call or text message during a crisis. 84% felt that social networking sites also should be used for this purpose, and 72% felt that blogs or micro blogs

International Journal of Innovations & Advancement in Computer Science
IJIACS
ISSN 2347 – 8616
Volume 6, Issue 9
September 2017

should be as well. Over half (56%) of respondents stated that they were at least somewhat likely to use one or more types of social media to contact family members during a crisis. However, only 24% were likely to report a crisis to local administration agencies via social media. The majority of respondents stated that talking to others in person or by telephone was the most important source of local information.

b. Focus Groups: Organization Factors

The organization factors that focus group participants recognized include policies, legal issues, costs and training. The organization requires that polices be adopted to provide the environment needed for employees to attain their work objectives. To utilize social media effectively, employee activities and roles are established through HR to clarify job descriptions and ensure connected types of communication are managed. Some evolving applications allow people to contribute geo-tagged photos and video to a community database.

Preliminary evidence from a national study [20] indicates that the use of social media for public purposes is not as powerfully connected with education. This may be because powerful individuals exist at all social levels, and they may deliver information to members of their social circles not only face to face, but also by mobiles.

c. Analysis of Facebook Comments

Arlington County administration had roughly 12166 fans at the end of 19th June 2017. We analyzed a two-month period (April 1–May 31, 2017) of posts by the county and comments from the public by conducting a simple content analysis by topic. There were a total of 88 posts; the top most frequent topics are shown in Fig.2

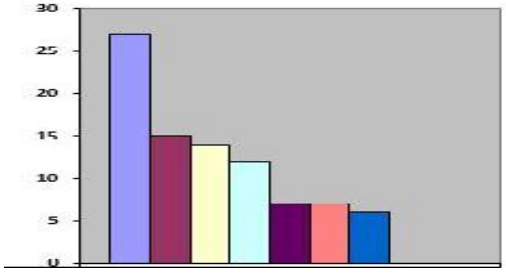

Fig. 2. Facebook topics Arlington County.

Traffic	27
PSA	15
News	14
Weather	12
Misc Event	7
Food Event	7
Exercise Event	6

The most common posts by the County on the Facebook page were about traffic, followed by public service announcements (PSA), news and weather related posts were followed by various events (biking paths, walking, music or film) in terms of frequency of posts during this two-month period.

There were a total of 174 public comments to the county posts during this two-month period. Half of the comments related to about a fifth (19%) of the county posts. Fig. 3 shows the distribution of the bulk of the comments on the same top County posts seen in Fig.2.

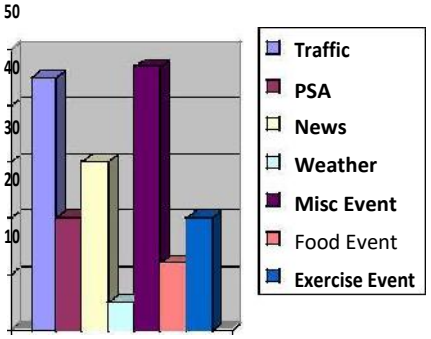

Fig.3: Public comments by Arlington Facebook topic.

The comments are mostly related to traffic and miscellaneous events (such as food, music, and film). Exercise events (biking, walking) and news announcements generated the next most frequent number of comments from the public. Almost all the comments were highly consistent with the social media policy of the County (e.g., no vulgarity or off topic comments) and were very positive in tone, including many “Likes”.

Lastly, we collected videos in YouTube relating to Arlington, Virginia and conducted a tag analysis of the video collection .We performed a search and the phrase ‘Arlington County;’ this produced about 3480 videos from YouTube (Upload date by this month). We generated two types of tag clouds using video titles and tags (see Fig.4).

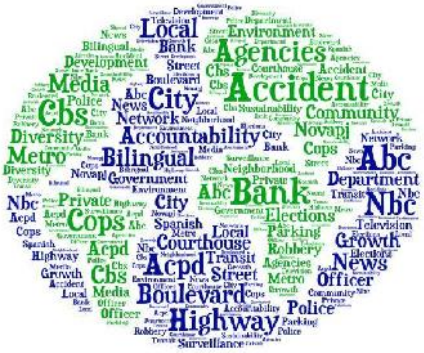

Fig.4: Tag cloud of Arlington YouTube videos.

As noted earlier, a tag cloud as visualization fast and simply represents the frequency with which dissimilar terms appear in a search thereby providing a snapshot of what is in a large isolated collection. The more frequently a term appears in an image collection, the larger it appears in a tag cloud. The cloud visualization also provides a sign of the importance of various public problems to members of the community. The recurrent civic themes revealed in the video analysis can be further illustrated in to categories shown in Table 1.

Law enforcement	Police, cops, officer, courthouse, robbery, accident, ACPD, surveillance
Social issues	Environment, diversity, community, city, neighborhood, accountability
Transportation	Metro, street, boulevard, highway accident, parking, transit
Economic development	Growth, sustainability, development, bank, private, local
Political	Government, electronics, agencies, department
Communication	Media, ABC, NBC, CBS, television, news, network, bilingual, Spanish

Table 1: Tag cloud categories for Arlington videos.

A further clustering of video tags and video titles as shown in Table 1 allows administrations and other users to make sense more easily of the interests and needs of the community as expressed in the YouTube collection at any given point.

5. Debate and inferences

The experimental study was intended to advance technologies and systems for social media analysis relating to both routine day-today civil life and critical incidents. The results begin to recognize and address a combination of technical and social science challenges. On the technical side, these include:

1. Recognizing related information precisely and in a timely manner, particularly from short content micro-blogging sites; the limited information in a tweet (i.e., less than 140 characters) makes it difficult to classify its meaning and context which may lead to incorrect classification and misleading analysis of data;

2. Alerting administration officials to the analyzed information from multiple social media sources; due to the enormous size of the social media data stream, it is a contest to rapidly analyze the composed information from dissimilar sources and to make a conclusion based on the analysis; and

3. Visualizing the present and former status of incoming information and the analysis of it; simple yet informative visualization design is essential in making-sense of the data presented. We support the sense-making process by integrating interaction methods with visualization to deal with huge quantities of data.

On the social science side, our experimental study results build on social network analysis and the use of social media. We focus on Arlington as our test case in order to analyze information, its use and impact related to local, state, national, and international events — since it has close connections to the US capital.

Our social media data analyses are intended to help administrations and nations of Arlington county to know how and where to get useful information and acute communication in the event of a crisis or social meeting condition. Our tools should help administrations and citizens to monitor and make sense of the multiplicity of voices and information that improve the quality of life in their communities.

By mining content and services covering multiple media types (i.e., text, audio, image, and video) we can develop tools to recognize events and alert administrations/governments, citizens, and community groups to see quickly the ‘big picture’ through visualizations of social media activity, content and changes in both over time. The intent is to enable preemptive responses, as routine problems or crises start to emerge, as events reveal, as individuals and groups react, and as plans are made for improved services and communication. Such capabilities are relevant to a broad range of administration throughout the US and globally. Given the efficiency of communication provided by social media, coupled with the potential to reach many constituents quickly, administration should seek to understand and to influence these increasingly popular communication channels.

Administrations, local organizations and citizens will continue to use a combination of outdated communication approaches (e.g., newspapers, radio, televisions, magazines, telephone) and evolving tools, smartphones and social media. Government knows they have miscellaneous audiences with diverse needs and preferences. Social media are just additional set of communication channels to get word out and help the interests of people.

There will remain to be legal issues regarding the interaction between outdated communication approaches and social media. These include managing diverse methods that the community can report a problem to the specialists.

Future research will help people and administrations to direct the evolution from outdated approaches to evolving developments. The rising number of cities and towns that have additional involvement with new media will guide others in diminishing the costs and drawbacks.

The aids, especially to the residents, in terms of larger access to information (e.g., searchable online video of meetings of interest) and larger distribution of worries and thoughts will lead to augmented consciousness, shared efficiency and community contribution. The aids to administration include preemptive problem solving and positive public relations that lead to greater political efficiency and civic hope.

6. References

1. Golbeck, J., Grimes, J. M., & Rogers, A. (2010). Twitter use by the U.S. Congress. Journal of the Association for Information Science and Technology, 61(8), 1612–1621, http://dx.doi.org/10.1002/asi.21344
2. The Top 20 Valuable Facebook Statistics – Updated May 2017; from https://zephoria.com/top- 15-valuable-facebook-statistics/
3. Statista,2016. Leading Social Networks Worldwide as of April 2016, Ranked by Number of Active Users (in Millions). Retrieved from http://www.statista.com/statistics/272014/global-social-networks-ranked-by-number-of-users/
4. Arlington County Facebook Profile. Retrieved from http://www.facebook.com/ArlingtonVA
5. Arlington County News on Twitter. Retrieved from http://twitter.com/Arlingtoncounty.
6. Arlington County Blog Central, Retrieved from http://www.arlingtonva.us/departments/Communicati ons/page70455.aspx
7. Queensland Police Service, QPS Social Media Case Study : From https://www.police.qld.gov.au/corporatedocs/reports Publications/other/Documents/QPSSocialMediaCase Study.pdf
8. O'Reilly, T. (2007). What is Web 2.0: Design patterns and business models for the next generation of software. Communications & Strategies, 65, 17– 37(1st Quarter).
9. Boyd, D., & Ellison, N. (2007). Social network sites: Definition, history and scholarship. Journal of Computer-Mediated Communication.
10. Lampe, C., Ellison, N., & Steinfield, C. (2006). A face (book) in the crowd: Social searching vs. social browsing.
11. Smith, A. (2010). Government online: Pew internet & American life project.
12. American Red Cross: Social Media in Disasters and Emergencies, Retrieved from http://www.redcross.org/www-files/Documents/pdf/other/SocialMediaSlideDeck.pdf.
13. Hughes, A. L., & Palen, L. (2009). Twitter adoption and use in mass convergence and emergency events. Gothenburg, Sweden.
14. Hughes, A. L., Palen, L., Sutton, J., Liu, S. B., Vieweg, S.(2008). "Site-seeing" in disaster: An examination of online social convergence.
15. Opsahl, A., 2010 County Experiments with Monitoring Social Media in Emergencies.
16. Sakaki, T., Okazaki, M., & Matsuo, Y. (2010). Earthquake shakes Twitter users: Real-time event detection by social sensors. Proceedings of the 19th international conference on World wide web (pp. 851–860). Raleigh, NC, USA: ACM.
17. Social Media Sells. Ogilvy & Mather, from http://www.ogilvy.com/News/Press-Releases/November-2010-Social-Media-Sells.aspx
18. Twitter analytical tool http://www.tweetarchivist.com/
19. Visualization software 'wordle' http://www.wordle.net
20. Smith, A., Verba, S., Brady, H., & Schlozman, K. (2009). The internet and civic engagement: Pew internet & American life project.

Control of a Bidirectional Converter to Interface Electrochemical double layer capacitors with Renewable Energy Sources

Namburi Nireekshana

Assistant Professor
Electrical Electronics Engineering Department
Methodist College of Engineering and Technology

Abstract- This paper highlights the controller of a bidirectional converter to interface an ultra-capacitor as storage device to renewable energy systems. Ultra-capacitors are typically used in renewable energy systems to improve the system's reliability and energy conversion efficiency. The controller of the converter system has been designed and simulated based on the integration of both Current Mode Control and Linear Quadratic Regulator methods. The controller performance is tested under different modes of operating conditions in bidirectional converter using MATLAB/Simulink simulation package. The simulation results show that a good DC bus voltage regulation is achieved in the tested conditions. In addition to that, the controller ensures smooth transition between the buck and boost modes of the bidirectional converter operation.

Keywords—bidirectional converter; ultra-capacitor; peak current mode control; linear quadratic regulator.

I.INTRODUCTION

The continual rise in electricity demand, combined with serious environmental problems created by traditional energy systems have been driving societies towards the use of renewable energy sources. Besides being environmentally friendly, renewable energy sources are continually renewed by the cycle of nature and are considered to be practically inexhaustible [1-4]. As a result, the future of these sources as a typical alternative for the traditional sources looks very bright

However, the natural variability of some renewable sources due to their strong dependence on the weather conditions result to a high fluctuated output power, which impacts on the local loads that are sensitive to pulsating power [5-6]. Moreover, the renewable sources generated power does not always match the demanded load power. Hence, there is a need to support these sources by use of energy storage device, where it either injects its stored energy or absorbs the excess energy during the transients in the renewable source; resulting in a smooth output power to the load [7-9].

Amongst storage devices, ultra-capacitor is preferred due to its long life-time, good electrical behavior and to its relatively low initial cost in comparison with modern batteries [10]. In addition, it is positively characterized by its high power density, low losses while charging and discharging, and it’s very low equivalent series resistor (ESR) which allows it to deliver and absorb very high currents and to be charged very quickly [11-12]. Furthermore, ultra-capacitor can provide large transient power instantly [13]. Consequently, the use of ultra-capacitor as a storage element increases the effectiveness of the renewable energy source utilization and

also improves the capability of dealing with steady-state and transient dynamics.

Connecting the renewable source and the ultra-capacitor requires a power converter and a DC link. The converter must have the capability to allow both directions of power flow between the ultra-capacitor and the DC link, and also the ability to increase or decrease the voltage level in each power flow direction; since the voltage level of the ultra-capacitor and the DC link are different. Therefore, a bidirectional DC-DC converter is used. In bidirectional DC-DC converters, there are two modes of operation. The first mode is the boost mode, where the ultra-capacitor is discharged to a higher voltage level at the DC link; in the second mode, namely the buck mode; here the excess power from the renewable source charges ultra-capacitor.

Various control methods have been proposed in the literature to interface renewable energy sources with a storage device using a bidirectional converter. The authors in reference [13] applied the dynamic evolution control method to interface a fuel cell and the ultra-capacitor. In literature [5], the PI controller was designed for the integration of wind energy conversion system and ultra-capacitor. The current programmed mode (CPM) duty ratio control and linear PI compensator was reported in [14] for controlling a bidirectional converter interfacing wind energy conversion and battery storage system. A combination of both fuzzy and sliding-mode control strategies to interface the wind energy conversion system and the storage device has been proposed in [15]. Different from that available in the literature, the proposed controller in this paper introduces feedback paths that are calculated optimally to minimize an associated cost function, which is expected to improve the dynamic performance of the system.

Due to its simplicity, high bandwidth, and low implementation cost, current mode control (CMC) approach is popular in controlling the power electronic converters [16]. Among the different types available for CMC, Peak current mode control (PCMC) is the most common one in which the peak value of the inductor current is sensed and compared with the current reference for the generation of the PWM signal [17]. Another control method that is most cited for controlling the PWM converters is linear quadratic regulator (LQR) control [18]. Since the controller feedback gain-vector is determined optimally in LQR, the designers can guarantee that the converter has good closed-loop behavior, and is relatively insensitive to system parameter variations or external disturbances. In addition, LQR controllers can be applied with independence of the order of the system, and their design can be straightforwardly calculated from the matrices of the system's small-signal model [19]. Combining the two methods (CMC and LQR) has been done in many studies [3, 19]. The combination indicates that a good response and disturbance rejection were achieved in the tested conditions.

II.ULTRACAPACITOR

Electric double-layer capacitors, also known as supercapacitors, electrochemical double layer capacitors (EDLCs) or ultra-capacitors are electrochemical capacitors that have an unusually high energy density when compared to common capacitors, typically several orders of magnitude greater than a high-capacity electrolytic capacitor.

The electric double-layer capacitor effect was first noticed in 1957 by General Electric engineers experimenting with devices using porous carbon electrode. It was believed that the energy was stored in the carbon pores and it exhibited "exceptionally high capacitance",

although the mechanism was unknown at that time.

General Electric did not immediately follow up on this work, and the modern version of the devices was eventually developed by researchers at Standard Oil of Ohio in 1966, after they accidentally re-discovered the effect while working on experimental fuel cell designs. Their cell design used two layers of activated charcoal separated by a thin porous insulator, and this basic mechanical design remains the basis of most electric double-layer capacitors to this day. With advances made on both materials and manufacturing process, today Tecate Group PowerBurst® product show a superior advantage amongst all other ultracapacitors in the market.

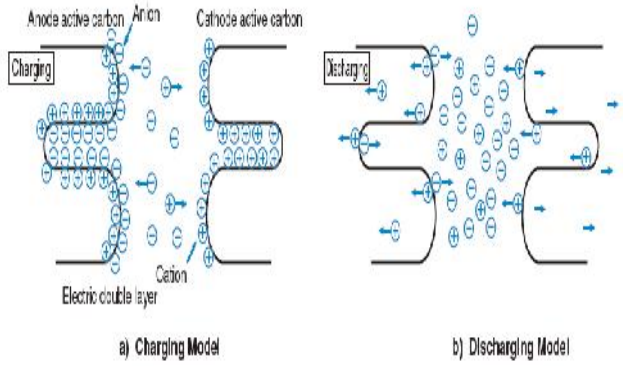

Figure 2: Ultracapacitor Charge Separation

Each application needs to be evaluated based on its requirements. Below are some of the advantages and disadvantages when considering the use of EDLCs:

2.1 Advantages:

• High energy storage. Compared to conventional capacitor technologies, EDLCs possesses orders of magnitude higher energy density. This is a result of using a porous activated carbon electrode to achieve a high surface area.

• Low Equivalent Series Resistance (ESR). Compared to batteries, EDLCs have a low internal resistance, hence providing high power density capability.

• Low Temperature performance. Tecate Group PowerBurst® products, with their use of patented technology, are capable of delivering energy down to -40°C with minimal effect on efficiency.

• Fast charge/discharge. Since EDLCs achieve charging and discharging through the absorption and release of ions and coupled with its low ESR, high current charging and discharging is achievable without any damage to the parts.

The specifics of ultracapacitor construction are dependent on the manufacturer, and the intended application. The materials may also differ slightly between manufacturers or due to specific application requirements. The commonality among all ultracapacitors is that they consist of a positive electrode, a negative electrode, a separator between these two electrodes, and an electrolyte filling the porosities of the two electrodes and separators.

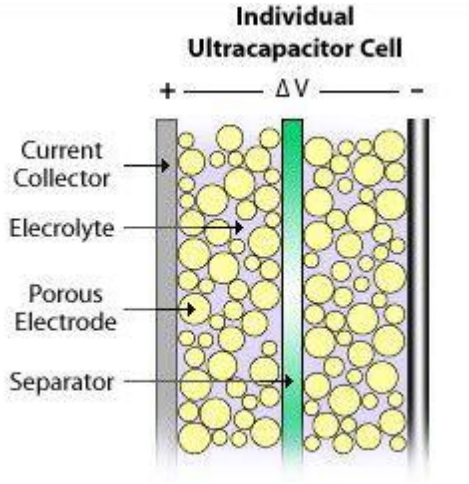

Figure: Internal Cell Construction

III.MODELING OF THE ULTRA CAPACITOR AND BIDIRECTIONAL DC-DC CONVERTER

The equivalent circuit of ultra-capacitor model is applied to simulate the ultra-capacitor. As represented in Fig.3, the model consists of a capacitance Cus ,an equivalent parallel resistance Rp , and an equivalent series resistance Rs .

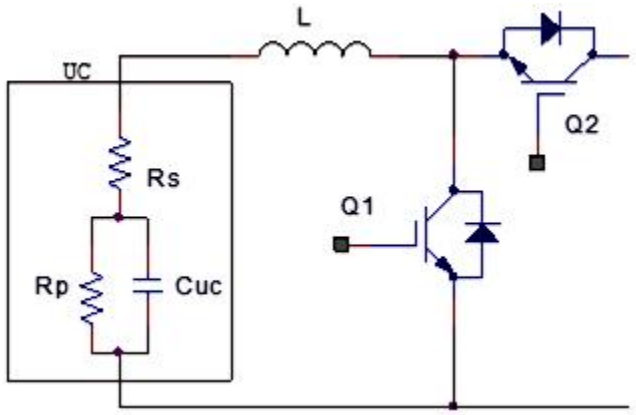

Fig. 3 The electrical circuit of ultra-capacitor-bidirectional DC-DC converter

Topology

To realize the reversible direction of power flow in bidirectional DC-DC converters, the switch should ideally carry the current in both directions. Therefore, it is usually implemented with a unidirectional semiconductor power switch connected in parallel to a diode [22]. In the first direction, the converter transfers the energy from the ultra-capacitor to the DC bus when starting up the renewable generation system, and during the transient load conditions. When there is an excess energy at the DC bus, the converter charges the ultra-capacitor in its low-side. The buck charging and boost discharging current modes share the same power plant transfer function, therefore, sharing a unified controller is tolerable. The unified controller concept means one controller can be used for both switches, whereby they are controlled in a complementary fashion [13, 24]. In this work, the boost modeof operation is selected for the purpose of designing the controller. Hence, the small-signal model of the boost converter is derived. The renewable energy source is modelled as a current source connected to the DC bus.

To derive the current-mode controlled model of the boost converter, the new continuous time (NCT) model of the PCMC in [27-28] is used. It is generally accepted due to its simplicity and accuracy [27, 29]. The block diagram of NCT model is represented in Fig. 3.2, where Vin, Vo,Il and dare the perturbations of the input voltage, output voltage, inductor current, and the duly-cycle of the power stage, respectively. The variable v c is the perturbation of the reference voltage of the current loop. In this study, vc is the LQR controller output. Ri is the effective linear gain from the sensed current to the comparator input. kf and kr are the feedforward and feedback gains, and they are different for the different for each different type of converters. Hi is the sampling gain which is used to model the sampling action in the current loop, and for controller design purpose it is taken as a unity.

The modulator gain F_m is the ac gain from the error current signal to the duty-cycle. F_m , k_f and k_r can be expressed as:

$$F_m = \frac{1}{(M_1 + M_c)T_s}$$

$$k_f = \frac{-T_s R_i}{2L}$$

$$k_r = \frac{-D'^2 T_s R_i}{2L}$$

where 1 M is the rising slope of the inductor current, Mc is the slope of the artificial ramp signal that is used for slopecompensation.

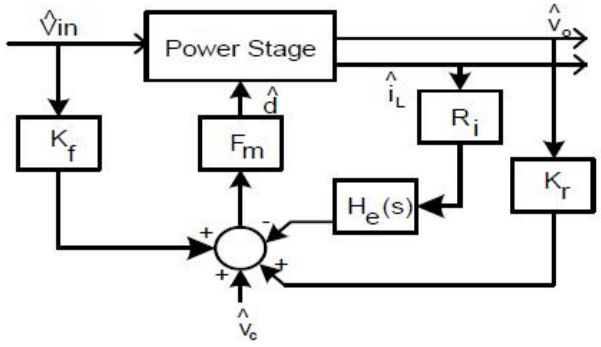

Fig.3. 2. The small-signal model of PCMC converter.

3.1The Linear Quadratic Regulator– CurrentMode Controlled Model

As aforementioned, the objective of the controller in this paper is to ensure a good voltage regulation at the DC bus. Thus, the small signal model of the CMC boost converter is augmented to include the new feedbacks from the state variables of the converter. In addition, a new state variable, the error between the reference and the output voltage, is added, as shown in Fig. 3.3

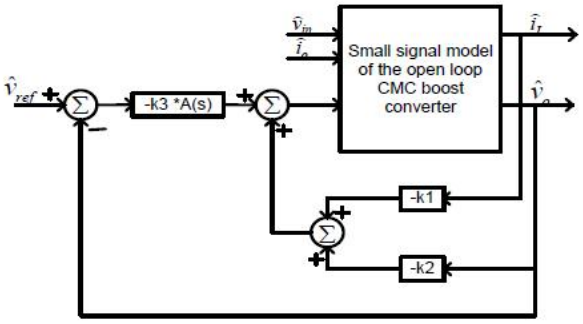

Fig. 3.3 The small signal model of closed-loop CMC PWM boost converter with linear feedback control.

IV.SIMULATION RESULTS

The MATLAB/Simulink simulation results for different operation modes of the bidirectional converter that interfaces the ultra-capacitor to the DC bus are depicted and discussed. The simulated system diagram is shown in Fig.4,

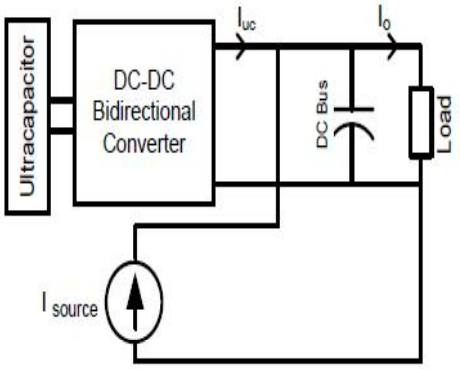

Fig.4. The block diagram of the proposed interfacing system.

The simulation results for the first case system test are shown in Fig. 4.2, where the renewable source current was maintained fixed at 10 A while the load current was changed in steps from 5 A to 15 A and then to 5 A. As illustrated in the Fig. 4.2(a), in the first interval (between t=0 and t=0.02 s) the renewable source covered the load demand and injected its excess current to the ultra-capacitor. In this interval, the bidirectional converter operated in a buck mode. However, when an additional 10 A was required by the load (between =0.02 and t=0.05 s), the renewable source was not able to provide the full load demand. Thus, in this interval, the bidirectional converter switched to a boost mode to discharge the ultra-capacitor and supply the extra load demand (5 A).

When the load current returned to its initial value (between t=0.05 and t=0.08 s), the bidirectional converter softly changed its

mode of operation into the buck mode. Fig. 4.2(b) depicts the DC bus voltage. As can be seen, it was regulated at the desired value (100 V) regardless of the changes that happened in the load current. The figure clearly shows that the two modes of the converter operation altered softly.

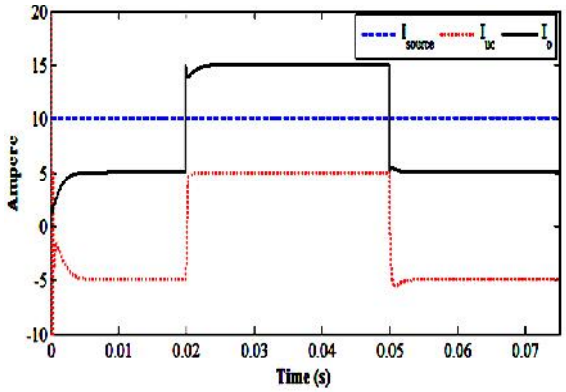

(a)

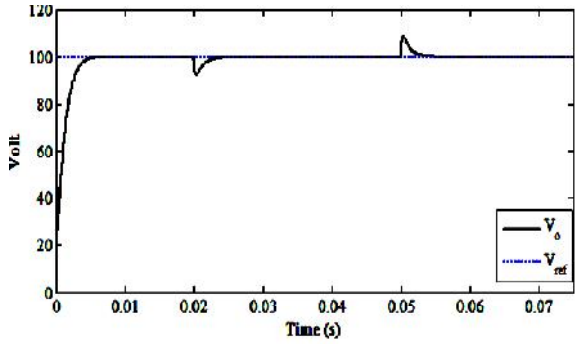

(b)

Fig. 4.2. The responses of a step variation in the load current from 5 A to 15 A and then to 5 A of: (a) Load and ultra-capacitor currents (Io, Iuc), (b) Output and reference voltages (Vo, Vref).

V.CONCLUSION

This paper has include the discussion of a new control method based on LQR and CMC control for a bidirectional DC-DC converter that interfaces ultra-capacitor energy storage to a renewable energy system. The LQR-CMC method has been successfully applied to control the bidirectional converter in the case of boost and buck modes. The objectives of the controller were to regulate the output voltage and to achieve a smooth transition between the two operation modes of the bidirectional converter, namely buck and boost modes. In addition, the proposed controller ensures continuous power supply the load, regardless of the load and renewable energy power changes. In short, the proposed controller is capable of increasing the reliability and energy conversion efficiency of renewable energy systems.

REFERENCES

[1] M. A. Abdullah, et al., "A study of maximum power point tracking algorithms for wind energy system," in 2011 IEEE First Conferenceon Clean Energy and Technology (CET), Kuala Lumpur Malaysia, 2011, pp. 321-326.

[2] M. A. Abdullah, et al., "A review of maximum power point tracking algorithms for wind energy systems," Renewable and Sustainable Energy Reviews, vol. 16, pp. 3220-3227, 2012.

[3] M. A. Abdullah, et al., "Input Current Control of Boost Converters using Current-Mode Controller Integrated with Linear Quadratic Regulator," International Journal of Renewable Energy Research(IJRER), vol. 2, pp. 262-268, 2012

[4] C. N. Bhende, et al., "Permanent Magnet Synchronous Generator- Based Standalone Wind Energy Supply System," IEEE Transactions on Sustainable Energy, vol. 2, pp. 361-373, 2011.

[5] M. Bottu, et al., "Design of a Conditioner for smoothing wind turbine output power," in North American Power Symposium (NAPS), 2010, 2010, pp. 1-6.

[6] M. A. G. de Brito, et al., "Evaluation of the Main MPPTTechniques for Photovoltaic

Applications," IEEE Transactions on Industrial Electronics, vol. 60, pp. 1156-1167, 2013.

[7] A. A. Hussein, et al., "Distributed Battery Micro-Storage Systems Design and Operation in a Deregulated Electricity Market," IEEETransactions on Sustainable Energy,, vol. 3, pp. 545-556, 2012.

[8] M. H. Nehrir, et al., "A Review of Hybrid Renewable/Alternative Energy Systems for Electric Power Generation: Configurations, Control, and Applications," IEEE Transactions on SustainableEnergy, vol. 2, pp. 392-403, 2011.

[9] M. L. Rahman, et al., "Hybrid Power Generation System Using Offshore-Wind Turbine and Tidal Turbine for Power Fluctuation Compensation (HOT-PC)," IEEE Transactions on SustainableEnergy, vol. 1, pp. 92-98, 2010.

[10] J. Leuchter, "Bi-Directional DC - DC Converters for BatteryBuffers with Supercapacitor " in Energy Storage in the Emerging Era of Smart Grids, R. Carbone, Ed., ed: InTech, 2011
.

[11] Y. Zhao, et al., "Design on Triple Bi-directional DC/DC Converter Used for Power Flow Control of Energy Storage in Wind Power System Communication Systems and Information Technology." vol. 100, M. Ma, Ed., ed: Springer Berlin Heidelberg, 2011, pp. 7- 14.

[12] J. Lopes, et al., "Optimal sizing of batteries and ultracapacitors for fuel cell electric vehicles," in IECON 2011 - 37th AnnualConference on IEEE Industrial Electronics Society, 2011, pp. 4603- 4608.

[13] A. S. Samosir and A. H. M. Yatim, "Implementation of Dynamic Evolution Control of Bidirectional DC-DC Converter for Interfacing Ultracapacitor Energy Storage to Fuel-Cell System," IEEE Transactions on Industrial Electronics, vol. 57, pp. 3468-3473, 2010.

[14] M. S. Khan, "Supervisory Hybrid Control of a Wind Energy Conversion and Battery Storage System," Ph.D. dissertation, Electrical and Computer Engineering, University of Toronto, 2008.

[15] A. Hajizadeh, "Control of hybrid wind/energy storage power generation systems during voltage disturbance," in 2011 2nd PowerElectronics, Drive Systems and Technologies Conference(PEDSTC),, 2011, pp. 20-26.

Imperial Journal of Interdisciplinary Research (IJIR)
Vol-3, Issue-10, 2017
ISSN: 2454-1362, http://www.onlinejournal.in

Reactive Power Compensation in High Power Applications by Bidirectionalcasceded H-Bridge Based Statcom

Namburi Nireekshana
Assistant Professor, Electrical and Electronics Engineering Department
Methodist College of Engineering and Technology

Abstract*: In this paper, a simple static var compensating scheme using a cascaded two-level inverter-based multilevel inverter is proposed. The topology consists of two standard two-level inverters connected in cascade through open-end windings of a three-phase transformer. The dc-link voltages of the inverters are regulated at different levels to obtain four-level operation. The simulation study is carried out in MATLAB/SIMULINK to predict the performance of the proposed scheme under balanced and unbalanced supply-voltage conditions.*
Index Terms—DC-link voltage balance, multilevel inverter, power quality (PQ), static compensator (STATCOM).

I.INTRODUCTION

THE application of flexible ac transmission systems (FACTS) controllers, such as static compensator (STATCOM) and static synchronous series compensator (SSSC), is increasing in power systems. This is due to their ability to stabilize the transmission systems and to improve power quality (PQ) in distribution systems. STATCOM is popularly accepted as a reliable reactive power controller replacing conventional var compensators, such as the thyristor-switched capacitor (TSC) and thyristor-controlled reactor (TCR). This device provides reactive power compensation, active power oscillation damping, flicker attenuation, voltage regulation, etc.
[1].

Generally, in high-power applications, var compensation is achieved using multilevel inverters [2]. These inverters consist of a large number of dc sources which are usually realized by capacitors. Hence, the converters draw a small amount of active power to maintain dc voltage of capacitors and to compensate the losses in the converter. However, due to mismatch in conduction and switching losses of the switching devices, the capacitors voltages are unbalanced. Balancing these voltages is a major research challenge in multilevel inverters. Various control schemes using different topologies are reported in [3]–[7]. Among the three conventional multilevel inverter topologies, cascade H-bridge is the most popular for static var compensation
[5], [6]. However, the aforementioned topology requires a large number of dc capacitors. The control of individual dc-link voltage of the capacitors is difficult.

Static var compensation by cascading conventional multilevel/ two level inverters is an attractive solution for high-power applications. The topology consists of standard multilevel/two-level inverters connected in cascade through open-end windings of a three-phase transformer. Such topologies are popular in high-power drives [8]. One of the advantages of this topology is that by maintaining asymmetric voltages at the dc links of the inverters, the number of levels in the output voltage waveform can be increased. This improves PQ [8]. Therefore, overall control is simple compared to conventional multilevel inverters

In this paper, a static var compensation scheme is proposed for a cascaded two-level inverter-based multilevel inverter. The topology uses standard two-level inverters to achieve multilevel operation. The dc-link voltages of the inverters are regulated at asymmetrical levels to obtain four-level operation. To verify the efficiency of the proposed control strategy, the simulation study is carried out for balanced and unbalanced supply-voltage conditions.

II. PRAPOSED CONCEPT

Modern power systems are of complex networks, where hundreds of generating stations and thousands of load centers are interconnected through long power transmission and distribution networks. Even though the power generation is fairly reliable, the quality of power is not always so reliable. Power distribution system should provide with an uninterrupted flow of energy at smooth sinusoidal voltage at the contracted magnitude level and frequency to their customers. PS especially distribution systems, have numerous nonlinear loads, which significantly affect the quality of power.

Apart from nonlinear loads, events like capacitor switching, motor starting and unusual faults could also inflict power quality (PQ) problems. PQ problem is defined as any manifested problem in voltage or current or leading to frequency deviations that result in failure or mal operation of customer equipment. Voltage sags and swells are among the many PQ problems the industrial processes have to face. Voltage sags are more severe. During the past few decades, power industries have proved that the adverse impacts on the PQ can be mitigated or avoided by conventional means, and that techniques using fast controlled force commutated power electronics (PE) are even more effective. PQ compensators can be categorized into two main types. One is shunt connected compensation device that effectively eliminates harmonics.

The STATCOM used in distribution systems is called DSTACOM (Distribution-STACOM) and its configuration is the same, but with small modifications. It can exchange both active and reactive power with the distribution system by varying the amplitude and phase angle of the converter voltage with respect to the line terminal voltage. A multilevel inverter can reduce the device voltage and the output harmonics by increasing the number of output voltage levels. There are several types of multilevel inverters: cascaded R-bridge (CRB), neutral point clamped, flying capacitor. In particular, among these topologies, CRB inverters are being widely used because of their modularity and simplicity. Various modulation methods can be applied to CRB inverters. CRB inverters can also increase the number of output voltage levels easily by increasing the number of R-bridges.

Alternating current transmission systems incorporating power electronics based and other static controllers to enhance controllability and power transfer capability.

The basic applications of facts-devices are:

- Power Flow Control.
- Increase of Transmission Capability.
- Voltage Control.
- Reactive Power Compensation.
- Stability Improvement.
- Power Quality Improvement.
- Power Conditioning.
- Flicker Mitigation.
- Interconnection of Renewable and Distributed Generation and Storages.

Fig. 1 shows the circuit topology of the cascaded two-level inverter-based multilevel STATCOM using standard two-level inverters. The inverters are connected on the low-voltage (LV) side of the transformer and the high-voltage (HV) side is connected to the grid. The dc-link voltages of the inverters are maintained constant and modulation indices are controlled to achieve the required objective.

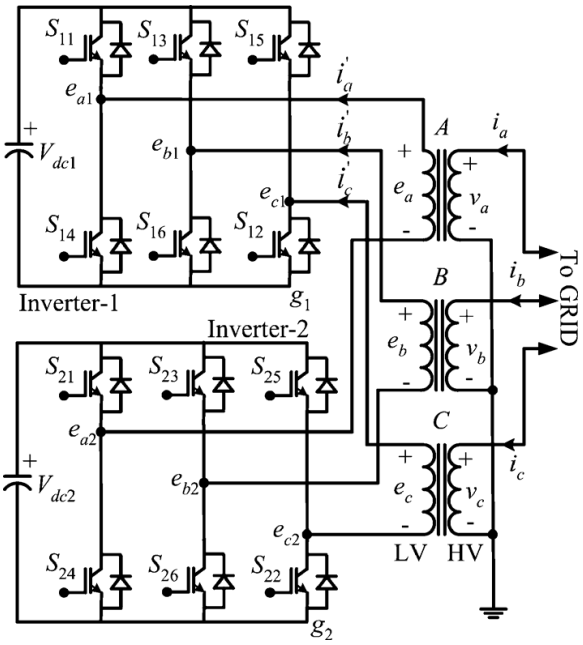

Fig. 1. Cascaded two-level inverter-based multilevel STATCOM.

III. DISTRIBUTION STATIC COMPENSATOR (DSTATCOM)

A D-STATCOM (Distribution Static Compensator), which is schematically depicted in Figure, consists of a two-level Voltage Source Converter (VSC), a dc energy storage device, a coupling transformer connected in shunt to the distribution network through a coupling transformer. The VSC converts the dc voltage across the storage device into a set of three-phase ac output voltages. These voltages are in phase and coupled with the ac system through the reactance of the coupling transformer. Suitable adjustment of the phase and magnitude of the D-STATCOM output voltages allows effective control of active and reactive power exchanges between the D-STATCOM and the ac system. Such configuration allows the device to absorb or generate controllable active and reactive power.

The VSC connected in shunt with the ac system provides a multifunctional topology which can be used for up to three quite distinct purposes:

1. Voltage regulation and compensation of reactive power;
2. Correction of power factor; and
3. Elimination of current harmonics.

Here, such device is employed to provide continuous voltage regulation using an indirectly controlled converter.

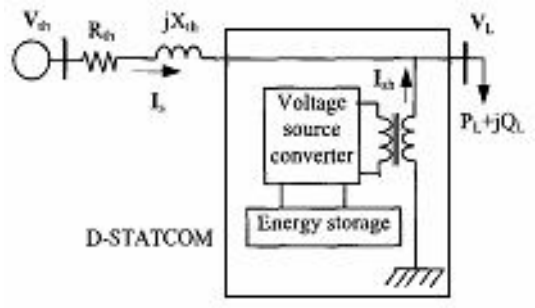

Figure 3.1 Block diagram of D-STATCOM

the shunt injected current I_{sh} corrects the voltage sag by adjusting the voltage drop across the system impedance Z_{th}. The value of I_{sh} can be controlled by adjusting the output voltage of the converter.

The shunt injected current I_{sh} can be written as,

$$I_{sh} = I_L - I_s = I_L - \frac{V_{Th} - V_L}{Z_{Th}}$$

$$I_{sh}\angle\eta = I_L\angle -\theta - \frac{V_{th}}{Z_{th}}\angle(\delta-\beta) + \frac{V_L}{Z_{th}}\angle -\beta$$

The complex power injection of the D-STATCOM can be expressed as,

$$S_{sh} = V_L I_{sh}^{*}$$

It may be mentioned that the effectiveness of the D-STATCOM in correcting voltage sag depends on the value of Z_{th} or fault level of the load bus. When the shunt injected current I_{sh} is kept in quadrature with V_L, the desired voltage correction can be achieved without injecting any active power into the system. On the other hand, when the value of I_{sh} is minimized, the same voltage correction can be achieved with minimum apparent power injection into the system.

IV.TEST SYSTEM

Figure shows the test system used to carry out the various D-STATCOM simulations.

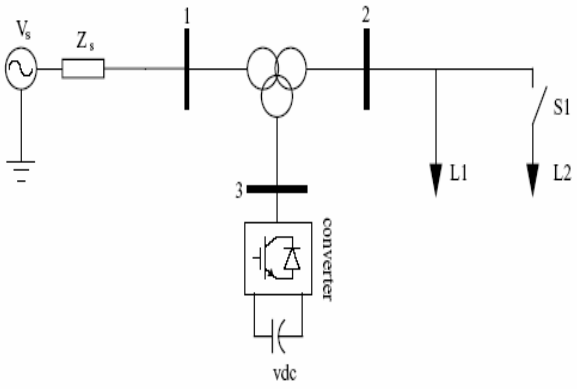

Fig.4 Single line diagram of the test system for D-STATCOM

V. MODELING AND SIMULATION RESULTS

MATLAB is a high-performance language for technical computing. It integrates computation, visualization, and programming in an easy-to-use environment where problems and solutions are expressed in familiar mathematical notation. Typical uses include-

- Math and computation
- Algorithm development
- Data acquisition
- Modeling, simulation, and prototyping
- Data analysis, exploration, and visualization
- Scientific and engineering graphics

MATLAB is an interactive system whose basic data element is an array that does not require dimensioning. This allows solving many technical computing problems, especially those with matrix and vector formulations, in a fraction of the time it would take to write a program in a scalar non-interactive language such as C or FORTRAN.

5.1MATLAB/SIMULATION RESULTS

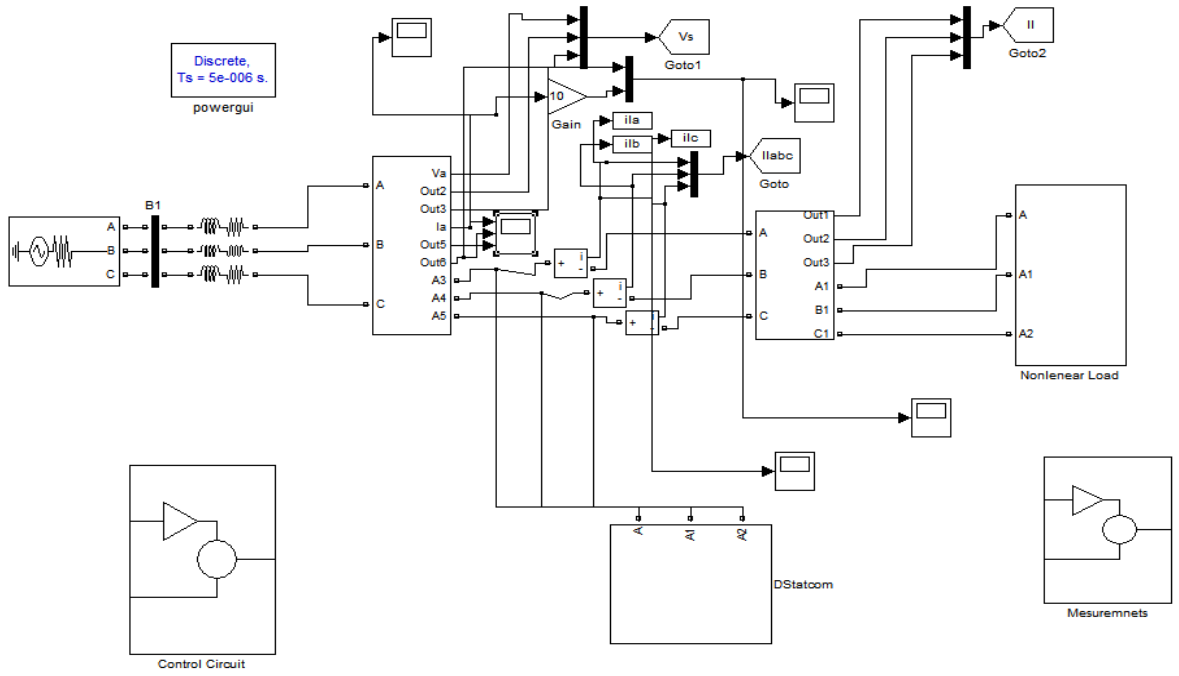

Fig.5.1 Multilevel statcom

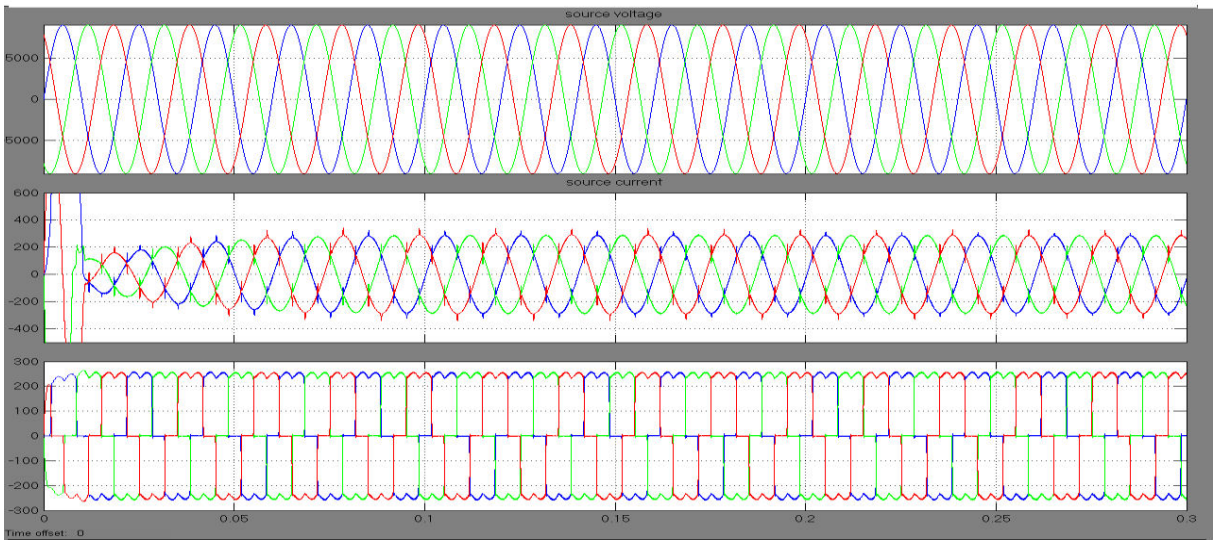

Fig.5.2 Sourse voltage,current and load current with statcom

Scale: a) on y-axis voltage in kv
On x-axis time secs
b) on y- axis current in amperes
on x-axis time in secs
c) on y- axis current in amperes
time in secs

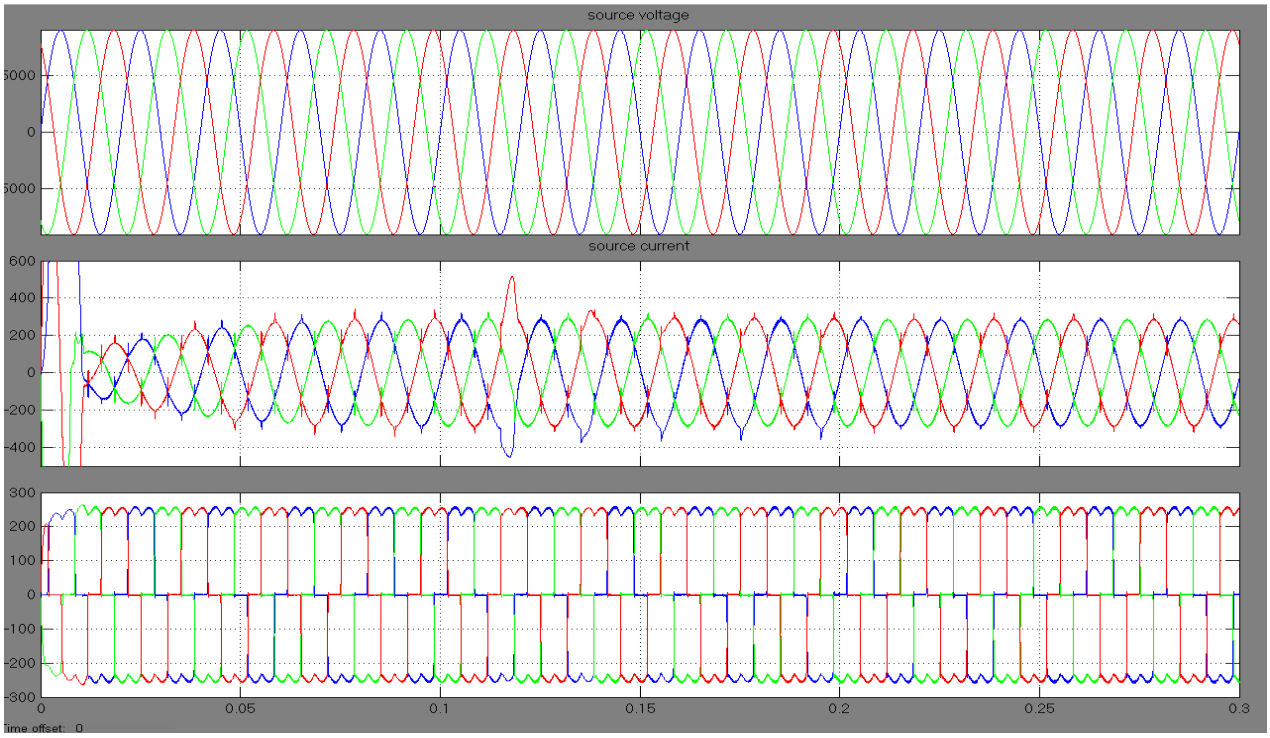

Fig.5.3 Wave form of fault mitigation method

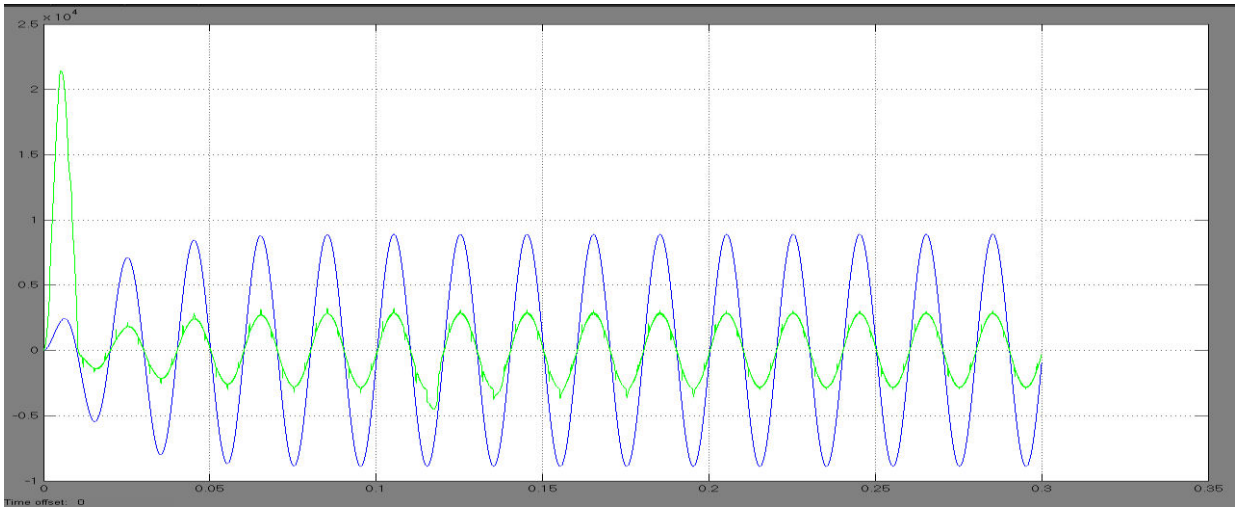

Fig. 5.4 both voltage and current are in phase (unity power factor)

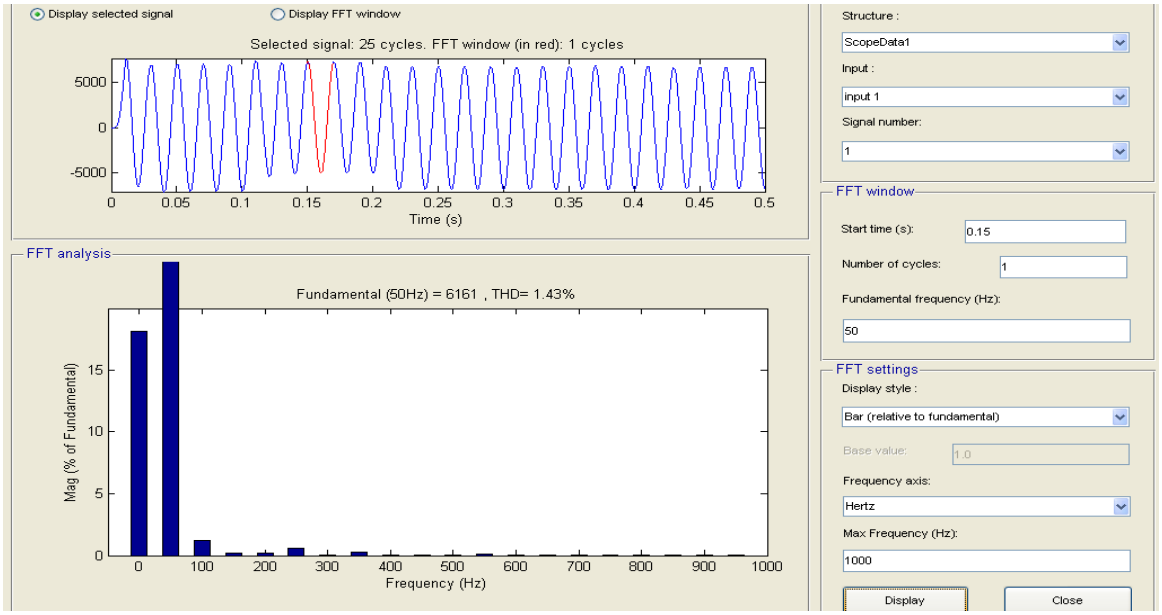

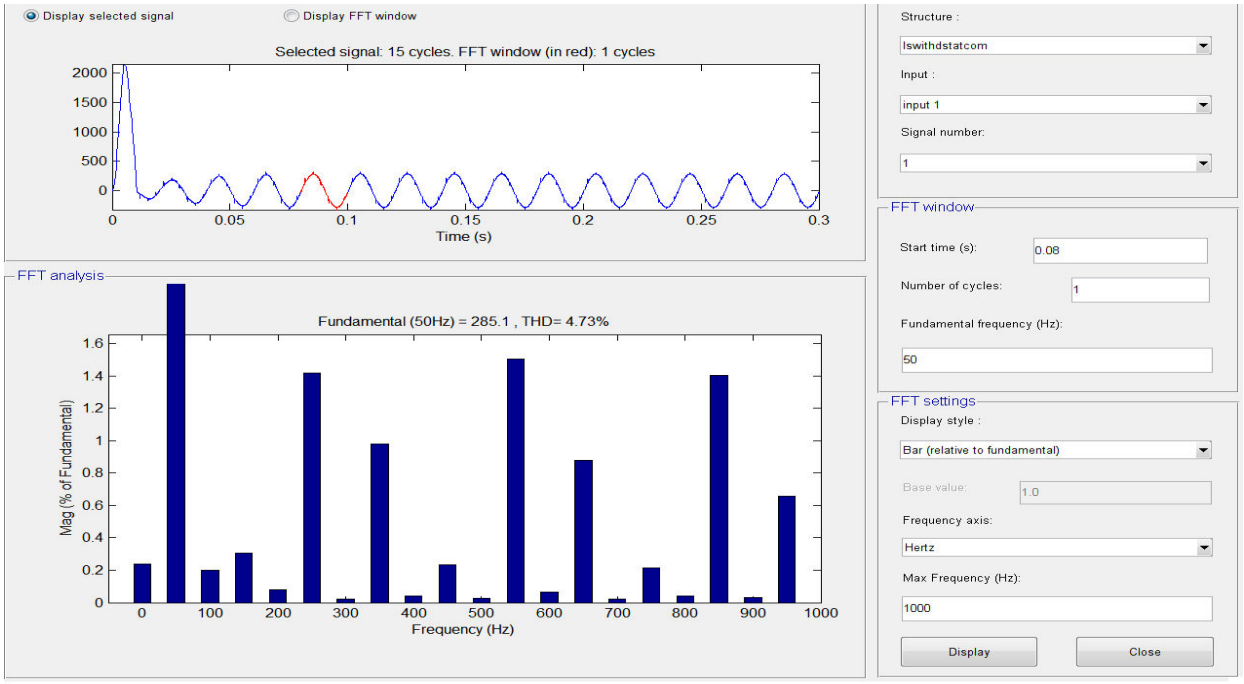

Fig.5.5,5.6 Harmonic spectrum of phase-A source current with DSTATCOM

VI.CONCLUSION

Improving of power quality and power factor by using DSTATCOM. Without Dstatcom harmonic contents are more and THD level is more than 5%. With Dstatcom is redused to less than 5% i.e. 4.014%. Corresponding wave forms are as shown in above figures. In fault mitigation system if any fault occures the output is not effected. If we are not giving the triggering pulse to any one switch in Converter Bridge still the output is constant and THD level is same as previous value. The wave forms are as shown in the above figures.

DC-link voltage balance is one of the major issues in cascaded Inverter-based STATCOMs. In this paper, a simple var compensating scheme is proposed for a cascaded two-level inverter- based multilevel inverter. The scheme ensures regulation of dc-link voltages of inverters at asymmetrical levels and reactive power compensation. The performance of the scheme is validated by simulation and experimentations under balanced and unbalanced voltage conditions. Further, the cause for instability when there is a change in reference current is investigated. The dynamic

model is developed and transfer functions are derived. System behavior is analyzed for various operating conditions. From the analysis, it is inferred that the system is a nonminimum phase type, that is, poles of the transfer function always lie on the left half of the -plane. However, zeros shift to the right half of the -plane for certain operating conditions. For such a system, oscillatory instability for high controller gains exists.

REFERENCES

[1] N. G. Hingorani and L. Gyugyi, *Understanding FACTS*. Delhi, India: IEEE, 2001, Standard publishers distributors.
[2] B. Singh, R. Saha, A. Chandra, and K. Al-Haddad, "Static synchronous compensators (STATCOM): A review," *IET Power Electron.*, vol. 2, no. 4, pp. 297–324, 2009.
[3] H. Akagi, H. Fujita, S. Yonetani, and Y. Kondo, "A 6.6-kV transformerless STATCOM based on a five-level diode-clamped PWMconverter: System design and experimentation of a 200-V 10-kVA laboratory model," *IEEE Trans. Ind. Appl.*, vol. 44, no. 2, pp. 672–680, Mar./Apr. 2008.
[4] A. Shukla, A. Ghosh, and A. Joshi, "Hysteresis current control operation of flying capacitor multilevel inverter and its application in shunt compensation of distribution systems," *IEEE Trans. Power Del.*, vol. 22, no. 1, pp. 396–405, Jan. 2007.
[5] H. Akagi, S. Inoue, and T. Yoshii, "Control and performance of a transformerless cascaded PWM STATCOM with star configuration," *IEEE Trans. Ind. Appl.*, vol. 43, no. 4, pp. 1041–1049, Jul./Aug. 2007.
[6] Y. Liu, A. Q. Huang, W. Song, S. Bhattacharya, and G. Tan, "Smallsignal model-based control strategy for balancing individual dc capacitor voltages in cascade multilevel inverter-based STATCOM," *IEEE Trans. Ind. Electron.*, vol. 56, no. 6, pp. 2259–2269, Jun. 2009.
[7] H. P.Mohammadi andM.T. Bina, "Atransformerlessmedium-voltage STATCOM topology based on extended modular multilevel converters," *IEEE Trans. Power Electron.*, vol. 26, no. 5, pp. 1534–1545, May 2011.
[8] X. Kou, K. A. Corzine, and M. W. Wielebski, "Overdistention operation of cascaded multilevel inverters," *IEEE Trans. Ind. Appl.*, vol. 42, no. 3, pp. 817–824, May/Jun. 2006.
[9] K. K. Mohaptra, K. Gopakumar, and V. T. Somasekhar, "A harmonic elimination and suppression scheme for an open-end winding induction motor drive," *IEEE Trans. Ind. Electron.*, vol. 50, no. 6, pp. 1187–1198, Dec. 2003.
[10] Y. Kawabata, N. Yahata,M. Horii, E. Egiogu, and T. Kawabata, "SVG using open winding transformer and two inverters," in *Proc., 35th Annual IEEE Power Electron. Specialists Conf.*, 2004, pp. 3039–3044.
[11] S. Ponnaluri, J. K. Steinke, P. Steimer, S. Reichert, and B. Buchmann, "Design comparison and control of medum voltage STATCOM with novel twin converter topology," in *Proc., 35th Annu. IEEE Power Electron. Specialists Conf.*, 2004, pp. 2546–2550.
[12] N. N. V. Surendra Babu, D. Apparao, and B. G. Fernandes, "Asymmetrical dc link voltage balance of a cascaded two level inverter based STATCOM," in *Proc., IEEE TENCON*, 2010, pp. 483–488.
[13] *IEEE Criteria for Class IE Electric Systems*, IEEE Standard 141-1993.
[14] C. Schauder and H. Mehta, "Vector analysis and control of advanced static VAr compensators," in *Proc. Inst. Elect. Eng. C.*, Jul. 1993, vol. 140, no. 4, pp. 299–305.
[15] D. G. Holmes and T. A. Lipo, "IEEE series on power engineering," in *Pulse Width Modulation for Power Converters: Principles and Practice*. Piscataway, NJ, USA: IEEE, 2003. input," *IEEE Trans. Ind. Appl.*, vol. 47, no. 3, pp. 825–835, May/Jun.
2011.
:

IOSR Journal of Electrical and Electronics Engineering (IOSR-JEEE)
e-ISSN: 2278-1676,p-ISSN: 2320-3331, Volume 12, Issue 4 Ver. I (Jul. – Aug. 2017), PP 47-53
www.iosrjournals.org

Electric Vehicle Mathematical Modelling and Simulation Using MATLAB-Simulink

*Y Mastanamma [1], Dr M Aruna Bharathi[2]
[2]*Associate Professor in EEE Department , Methodist College of Engineering and Technology , Hyderabad*
[2]*Professor in EEE Department, Bhoj Reddy Engineering College for Women, Hyderabad*
*Corresponding Author: *Y Mastanamma*

Abstract: *As Electric Vehicle is becoming a promising alternative for sustainable and cleaner energy emission in transportation, modelling and simulation of Electric Vehicle has attracts increasing attentions to the researchers. This paper presents a simulation model of Full Electric Vehicle in Matlab-Simulink platform to examine power flow during motoring and regeneration. Every components of the key system drive train consist of motor, battery, motor controller and battery controller were acknowledged and modelled from their mathematical equations. All simulation results were plotted and discussed. The torque and speed conditions during motoring and regeneration were used to determine the energy flow, performance and efficiency of the drive.*

Key words: *Electric Vehicle, Dc motor battery, controller*

Date of Submission: 04-07-2017 Date of acceptance: 20-07-2017

I. Introduction

The first electric vehicle (EV) was built between 1832 and 1839, was not until 189[3], after A.L. Ryker built an electric tricycle and William Morrison built a six-passenger wagon, In 1902 Wood created the Electric Phaeton, which was more than an electrified horseless carriage and surrey. "The Phaeton had a range of 18 miles, a top speed of 14 mph and cost $2,000 [1]. In the 1960s and 1970s electric vehicles reemerged because internal combustion vehicles were creating an unhealthy environment for the people at that time.

II. Description of an Electric Vehicle

The electric vehicle (EV) is propelled by an electric motor, powered by rechargeable battery packs, rather than a gasoline engine. From the outside, the vehicle does not appear to be electric. In most cases, electric cars are created by converting a gasoline-powered car. Often, the only thing that clues the vehicle is electric is the fact that it is nearly silent [3].

Under the hood, the electric car has: 1) An electric motor 2) A controller 3) A rechargeable battery. The electric motor gets its power from a controller and the controller gets its power from a rechargeable battery. The electric vehicle operates on an electric/current principle. It uses a battery pack (batteries) to provide power for the electric motor. The motor then uses the power (voltage) received from the batteries to rotate a transmission and the transmission turns the wheels [2]. Four main parts make up the electric vehicle: the potentiometer, batteries, direct current (DC) controller, and motor.

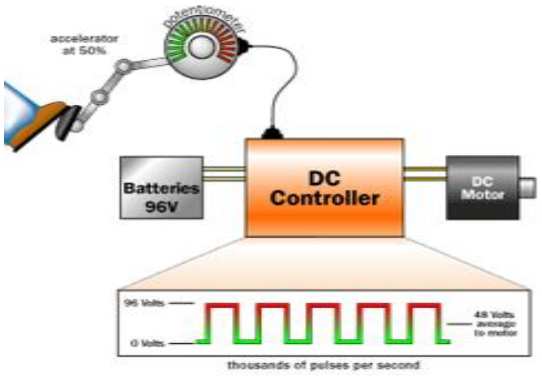

Figure 1: Parts of an electric vehicle

III. Parts and their Functions

Potentiometer: It is circular in shape and it is hooked to the accelerator pedal. The potentiometer, also called the variable resistor, provides the signal that tells the controller how much power is it supposed to deliver.

Batteries: The batteries provide power for the controller. Three types of batteries: leadacid, lithium ion, and nickel-metal hydride batteries.

DC Controller: The controller takes power from the batteries and delivers it to the motor. The controller can deliver zero power (when the car is stopped), full power (when the driver floors the accelerator pedal), or any power level in between. If the battery pack contains twelve 12-volt batteries, wired in series to create 144 volts, the controller takes in 144 volts direct current, and delivers it to the motor in a controlled way [2].

The controller reads the setting of the accelerator pedal from the two potentiometers and regulates the power accordingly. If the accelerator pedal is 2 percent of the way down, the controller pulses the power so it is on 2 percent of the time and off 7percent of the time. If the signals of both potentiometers are not equal, the controller will not operate [2].

Motor. The motor receives power from the controller and turns a transmission. The transmission then turns the wheels, causing the vehicle to run.

IV. Theory of Operation of EV

When the driver steps on the pedal, the potentiometer activates and provides the signal that tells the controller how much power it is supposed to deliver. There are two potentiometers for safety. The controller reads the setting of the accelerator pedal from the potentiometers, regulates the power accordingly, takes the power from the batteries and delivers it to the motor. The motor receives the power (voltage) from the controller and uses this power to rotate the transmission. The transmission then turns the wheels and causes the car to move forward or backward.

If the driver floors the accelerator pedal, the controller delivers the full battery voltage to the motor. If the driver takes his/her foot off the accelerator, the controller delivers zero volts to the motor. For any setting in between, the controller chops the battery voltage, thousands of times per second to create an average voltage somewhere between 0 and full battery pack voltage. The drive shown in Fig 1 shows consumes energy from the battery during motoring. The drive train can also add charge to the battery if the motor is operated as a generator during regeneration. This can occur during braking

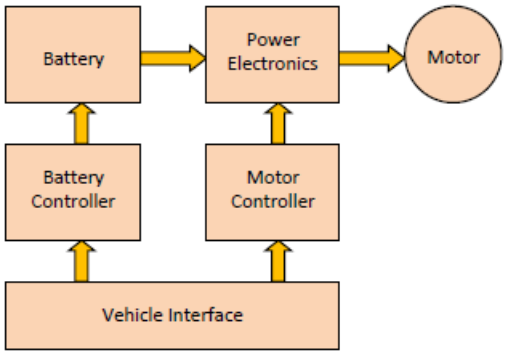

Figure 2: Electric Vehicle Drive Train.

or if the vehicle is being powered by an Internal Combustion Engine (ICE). In the diagram, the battery is frequently constructed of Lithium Ion cells, and supplies 300+ volts and high current to the power electronics. A battery controller monitors key battery parameters and controls the battery pack.

The power electronics unit inverts the DC battery voltage into three-phase AC voltage at the proper frequency and voltage for the motor to meet the requested speed and torque. The AC motor is typically a high efficiency AC Induction Motor (IM) or Permanent Magnet Synchronous Motor (PMSM). These motors can supply either acceleration torque or braking torque for both directions of rotation. When the vehicle's brakes are applied, the motor operates in regeneration mode thus reversing both the current direction and torque direction. The reversed torque direction provides vehicle braking torque while helping to recharge the battery.

The Vehicle Interface communicates with the Battery Controller and Motor Controller, and provides an interface with the vehicle-level controls and sensors. Communication between the separate units involves the use of a Controller Area Network (CAN) communications system.

V. Speed and Torque Values

The simulation that is presented assumes known speed and torque values. If speed values are assumed, then the torque values can be calculated if the wheel dimensions are available and the road load values encountered by the vehicle values are known. The total road load is the sum of the rolling resistance, air resistance, and gradient resistances are known or can be calculated.

VI. Key Equations

Determining the key equations and their corresponding variables and parameters is a necessary first step in model development. Each block in this simplified model represents one or more major equations as listed below.

DC Motor:

As noted earlier, Battery Electric Vehicles (BEV) and Hybrid Electric Vehicles (HEV) frequently use special, high efficiency Permanent Magnet Synchronous Motors (PMSM). This type of motor may be referred to as a brushless DC motor because it runs from DC voltage but does not have brushes. PMSM motors use AC voltage that is supplied by the Motor Controller. The motor controller inverts the DC voltage to produce an AC voltage at the proper voltage and frequency. The voltage and frequency are adjusted to provide the proper motor speed and magnetic field values.

A DC permanent magnet motor was used in the simulation model presented below. This type of motor is not appropriate for BEV or HEV applications due to weight and efficiency considerations.

The motor model includes some terms and parameters for power loss and time lag while other terms were omitted from the model. The model accounts for power loss in the winding resistance and time lag due to the energy storage in the magnetic field of the winding inductance. There is no field power loss because it is a permanent magnet field.

The model does not include power loss due to friction and other rotational losses of hysteresis, eddy current, and windage. The model also does not include the time lag due to energy storage in the rotor inertia. The motor model is based on the following equations.

Developed Torque is proportional to armature current:

Developed motor torque:

$T_d(Nm) = K_m * I_A(Amp)$ --- Eq(1)

Developed motor voltage:

$V_D(Volt) = W_D\ (rad/sec)/K_m$ --- Eq(2)

Motor armature input or terminal voltage is equal to the sum of developed voltage plus resistance and inductance voltage drops. In addition, the motor High Side voltage and current are directly connected to, and therefore identical to, the motor controller High Side voltage and current.

$V_H(Volt) = I_H(Amp) * R_A(Ohm) + L_H(Henry) * di(t)/dt(A/s) + V_D(V)$ --- Eq(3)

Shaft output torque is equal to developed torque minus friction loss (Bw) and inertial loss (J*dw(t)/dt). Friction and inertial were not specified in the model and are assumed equal to zero. Therefore, developed torque and output torque are equal in this model. However, the model could be easily modified to include these parameters in the future.

The motor physical constant, Km, is a physical parameter that depends upon the construction of the motor. In the SI system Km has units of (Amp/Nm) or (Volt/(rad/sec)).At the electrical– mechanical interface inside the motor the developed electrical power ($P = I_A * V_D * K_m$) is equal to the developed mechanical power ($P = K_m * T_d * W_D$).

In the motor model the mechanical friction and inertia as well as the magnetic power losses have been set to zero. Therefore, the power loss will only occur in the armature resistance, and the time lag will only occur in the armature inductance.

Motor Controller:

The motor controller is assumed to be an ideal controller with no power loss and no time lag. The controller simply raises the battery voltage to meet the higher voltage needs of the motor. The dimensionless constant gain or K ratio of the input and output voltages is determined in order to meet the motor's needs. The same K ratio is used to adjust the current so that input and output power values are equal.

High side voltage is equal to K times the low side voltage:

$V_H = K * VL$ --- Eq (4)

Controller High Side Current:

High side current is equal to 1/K times the low side voltage:

$I_H = (1/K) * V_L$ --- Eq(5)

Battery:
The battery is modelled as a voltage source with an internal resistance. The model accounts for internal power loss in the resistance of the battery. There is no time lag component in the model. The battery is assumed to have a constant internal voltage, EB . The battery terminal voltage V_B, is equal to the sum of the internal voltage and resistance voltage drop. The battery voltage and battery current are equal to the controller low side voltage and current.

$V_B(Volt) = I_A(Amp) * R_A(Ohm) + E_B(Volt)$
--- Eq(6) Battery model calculation:

$V_L (Volt) = I_L(Amp) * R_A(Ohm) + E_B(Volt)$
--- Eq(7)

Assuming: $V_B = V_L$ and $I_A = I_L$

The battery model uses the current and voltage information from the Motor Controller to calculate the required battery's internal voltage. This voltage is compared with the actual EB value to create a battery voltage error, BEER, and that error is used by the PI controller model to adjust the loop gain.

BERR = EB (actual) - EB (calculated)--- Eq(8)

Proportional Integral (PI) Controller:
The PI controller accepts the BERR signal from the Battery Model and uses proportional (Kp) and integral (Ki) to calculate the gain K value that is used by the Motor Controller.

$K = (Kp + s*K_I)*BERR$ ---- Eq(9)

VII. Simulink Model and Results

The electrical vehicle simulated model is shown in Figure 3.

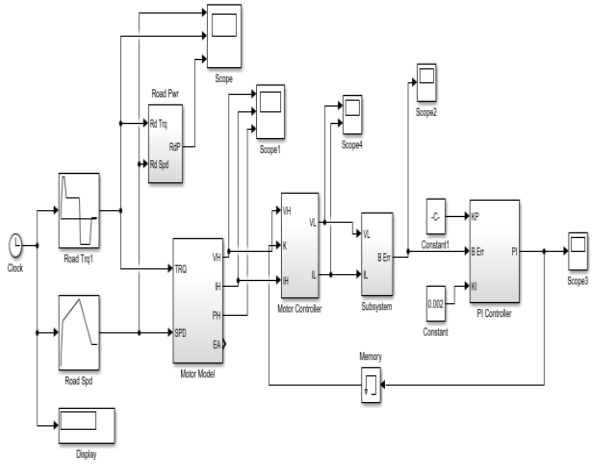

Figure 3: Simulink model of Electric Vehicle

Road speed values can be assumed depending on road characteristics.If speed values are assumed then the torque values can be calculated if the wheel dimensions are available. The road load values encountered by the vehicle values are known. The total road load is the sum ofthe rolling resistance, air resistance, and gradient resistances which are known or can be calculated.

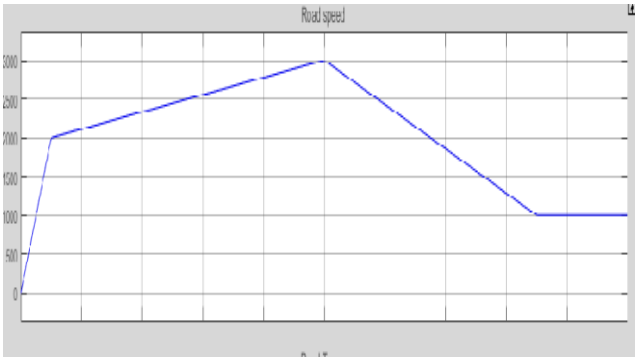

Figure 4: Road Speed characteristics

Speed values=[0 2000 3000 1000 1000]
Speed time= [0 5 50 85 100]
Torque values = [0 330 330 160 160 -220 -220 0 0]
Torque time = [0 5 10 15 50 55 80 85 100]

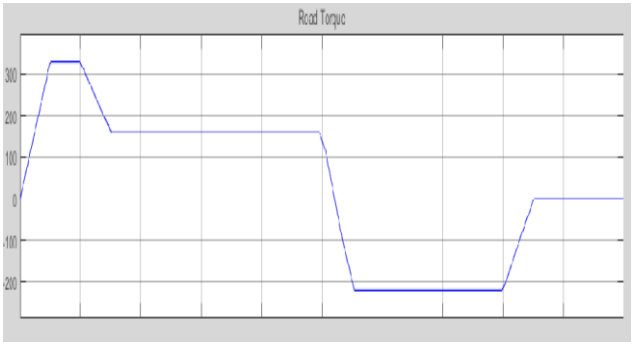

Figure 5: Road Torque characteristics

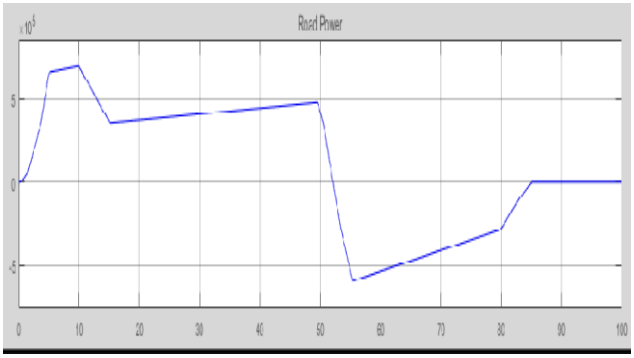

Figure 6: Road Power Characteristics

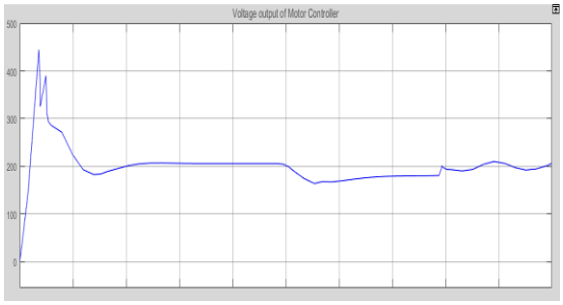

Figure 7: Voltage output of motor controller

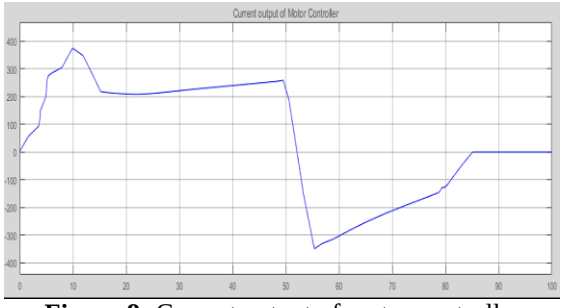

Figure 8: Current output of motor controller

When both torque and speed are positive values the DC Motor is providing torque in the direction of rotation. This is normal motoring operation. However, when the motor torque is in the opposite direction to the speed, then the motor is being pushed and acting as a generator.

A conventional Speed-Torque 4-Quadrant map shows +/-Speed on the x-axis and +/-Torque on the y-axis. When the speed and torque have the same polarity then power is being transferred from the motor to the load,

and the motor is in the motoring mode or 1st Quadrant operation. However, when the speed is positive and the torque is negative, then the motor is being pushed by the external mechanical source. This results in energy being transferred back to the battery. In this case the motor is operating in the 4th Quadrant of the Speed-Torque map.

When both current and voltage are positive values then the DC Motor is providing torque in the direction of rotation and power is being transferred to the load. This is normal motoring operation. However, when the motor current is in the opposite polarity of the voltage at T=50 ms then the motor is being pushed and acting as a generator with current flow back into the battery.

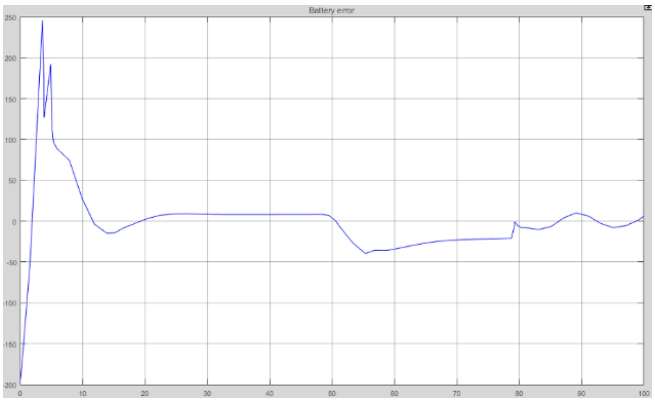

Figure 9: Battery Voltage Error

The simulation model adjusts the controller gain (K) to meet drive torque and regeneration requirements. The simulation compared the nominal battery internal voltage, VB =200 volts or VBatt(actual), with a calculated battery voltage based on the motor voltage and current values to get VBatt(calculated). The difference, VBerr, was used as an error signal input to the Proportional Integral (PI) Controller. This VBerr signal was plotted over the range of the simulation operation. This plot is shown below in Figure 9: Battery Voltage Error (BErr).

The maximum error of -200 occurs at the very beginning of the simulation. This large error is a natural response to starting the simulation. The simulation quickly recovers and holds an error of about +76 during the initial starting of the motor. It is normal to have a higher error here because the motor developed voltage, VD(Volt) = WD (rad/sec)/Km, is low during startup, especially when the current is increasing.

The negative error occurs during regeneration. By reviewing the motor voltage drop equation, VL (Volt) = IL(Amp) *RA(Ohm) + EB(Volt), the change in current polarity will cause the reverse polarity of the IL(Amp) *RA(Ohm) term. This voltage change will impact the magnitude of the input and output of the PI controller because of the reduced difference between the calculated and actual voltage in the error equation, BERR = EB (actual) - EB (calculated).

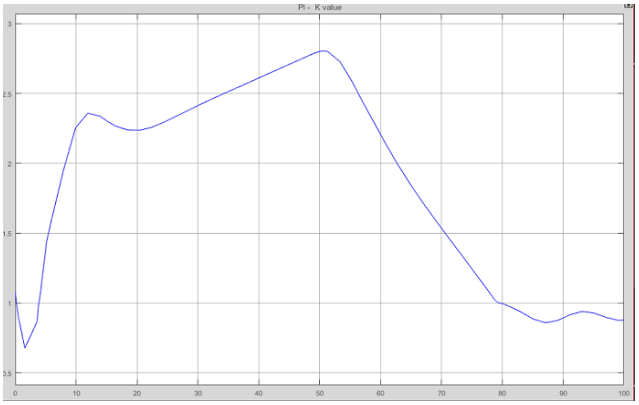

Figure 10: PI controller -K value

The minimum value of Gain K is 0.4 and maximum value of gain K is 2.8.

The battery in electric vehicle is producing sufficient electric power required to overcome the road speed and torque in the simulated results.

VIII. Future of the EV

Future electric cars will most likely carry lithium-ion phosphate($LiMn_2PO_4$) batteries that are now becoming popular in other countries. The $LiFe_2\ PO_4$ batteries are rechargeable and powerful and are being used in electric bikes and scooters. Electric cars will most likely adopt this technology in the future.

Another technology that is likely for future electric cars is the increased use of supercapacitors and ultracapacitors for storing and delivering electrical charge. Many of these batteries are currently being used in conjunction with hybrid car prototypes, so these are expected in the electric car future markets as well.

If the developers of future electric cars can create vehicles with a range of 300 miles per charge, a charging time of five to ten minutes, and safety in operating the vehicles, the market is wide open for them. Researchers are working on improved battery technologies to increase driving range and decrease recharging time, weight, and cost. These factors will ultimately determine the future of EVs [8].

IX. Conclusion

In this paper road speed and torque values are taken and simulated using MATLAB/Simulink. The battery voltage required is calculated and the torque and speed conditions during motoring and regeneration were simulated to determine the energy flow and performance of the drive. This simulation results can be used for electric vehicle applications.

References

[1]. Larminie, J. and Lowry, J. (2003) Electric Vehicle Technology Explained. John Wiley and Sons Ltd., Chichester.
[2]. Bellis,M.HistoryofElectric Vehicles. Retrieved January 31, 2010 fromhttp://inventors.about.com/library/weekly/aacarselectrica.htm.
[3]. Brain, M. (2002). How Electric Cars Work. Retrieved January 29, 2010 from http://auto.howstuffworks.com/electric-car2.htm.
[4]. Electric Vehicles (EVs).(2009) Retrieved January 31, 2010 fromhttp://www.fueleconomy.gov/feg/evtech.shtml[4] Dunn, P. (2006) Hybrid Cars – Pros and Cons. Retrieved February 20, 2010 from http://www.physorg.com/news10031.html.
[5]. Future Electric Cars (2007) Retrieved January 29, 2010 from http://www.future-car.ghnet/future-electric-cars.html.

IOSR Journal of Electrical and Electronics Engineering (IOSR-JEEE) is UGC approved Journal with Sl. No. 4198, Journal no. 45125.

Y Mastanamma . "Electric Vehicle Mathematical Modelling and Simulation Using MATLAB-Simulink." IOSR Journal of Electrical and Electronics Engineering (IOSR-JEEE) 12.4 (2017): 47-53.

LSBSM: A Novel Method for Identification of Near Duplicates in Web Documents

Lavanya Pamulaparty
Research Scholar, Department of CSE
JNTUH, Hyderabad, India
lavanya.post@gmail.com

Dr. C.V. Guru Rao
Department of CSE, S R Engineering College
JNT University, Warangal, India.

Dr. M. Sreenivasa Rao
Department of CSE, School of IT
JNT University, Hyderabad, India

***Abstract*—Documents that are 100% similar are termed to be duplicate documents and near duplicate documents (NDD) are not bitwise identical but strikingly similar. If the NDD papers are clustered then they almost share the same cluster. The existence of near duplicate web pages are due to exact replica of the original site, mirrored sites, versioned sites, and multiple representations of the same physical object and plagiarized documents. The proposed algorithm comprises of three phases – Transliterate phase, filtering and Location Sensitive Bitwise Similarity method (LSBSM). It is to identify the query page is how similar to all the records in the repository. We have analyzed the system using the parameters like precision, recall, f-measure and efficiency, the results showed improvement in the values when compared with systems using existing weighting schemes which clarifies the efficiency of the proposed system. Mainly the elapsed time for the identification of near duplicate web pages has reduced and accuracy has increased.**

Keywords- Location Sensitive Bitwise Similarity, Near-duplicate detection, Web Crawlers.

I. INTRODUCTION

The WWW has witnessed exponential growth of web documents. The huge amount of data is downloaded by web crawler and finding the useful data during runtime is a challenge for search engine retrieve the data and Detecting duplicate documents and near duplicate documents will help search engines to improve their performance. The Dennis survey which uncovers that approximately 30% of web contents are near duplicates [1]. Near duplicate web pages are not bit-wise indistinguishable to one another but rather they bear a striking similarity [2]. Duplicate documents can be easily detected. However, detecting near duplicates is much harder (Sood & Loguinov, 2011; Jiang & Sun, 2011) [3]. The detection of the near duplicate pages help the accompanying the topical crawling, enhances the nature of indexed lists and recognition on spam [3], [4], [5]. Elimination of near duplicates saves network bandwidth, reduces storage costs and improves the quality of search indexes. It also reduces the load and remote host that is serving such Webpages [8]. Mathematically, NDD can be said that : Given a set of existing n documents D={d1,d2,d3…..dn}, a similarity function like Jaccard coefficient or cosine between document feature vectors, hamming distance between document signatures, Euclidean distance or a Dice function for w€ {0,1} and a new document dnew. Finding all documents d € D such that w(d, dnew) >= t, where t is the similarity threshold for NDD on similarity function w.

The remainder of the paper is structured as follows. Section 2 reviews literature on the prior works of near duplicate detection. Section 3 provides details of preliminaries pertaining to the proposed solution for near duplicate detection. Section 4 presents the proposed solution that implements our NDD algorithm. Section 5 presents experimental results while section 6 concludes the paper besides providing directions for future work.

II. RELATED WORK

This section review literature on detecting near duplicate documents. Yang and Callan [11] applied near duplicate detection method to near duplicate comments that are in electronic format. Text clustering and retrieving algorithms are used to detect duplicates. Deng and Rafiei [13] used stable bloom filters to detect duplicates in streaming data. The stable bloom filter has proved to be accurate and time efficient when compared with its predecessors. Bern Stein and Zobel [16] applied duplicate detection mechanism for identifying co-derivative documents. They employed hash – based algorithm for identifying duplicate chunks in the given dataset. Yang and Kallan [21] used instance – level constrained clustering for near duplicate detection. They used content structure and document attributes in the process of clustering. Their method showed that the algorithm is as accurate as human experts. Foo and Sinha [1] proposed a method for near duplicate detection of redundant bit vectors as part of image detection mechanism. They achieved 91% precision and 98% recall. Chang and Wang [8] employed near duplicate detection t digital libraries. They used sentence level approach for duplicate detection. Their method showed high accuracy and efficiency.

Theobald et al. [5] proposed an algorithm named “SpotSigs” that make use of extracting signatures from documents for near duplicate detection. Mehtha et al. [18] proposed near duplicate detection method for detecting image spam. Their method also uses visual features besides duplicate detection. Their solution showed 98% accuracy in detecting image spam. Huang et al. [24] explored in achieving high precision and high recall in near duplicate detection. They used Longest Common Sequence (LCS) method to achieve this. Chu

https://sites.google.com/site/ijcsis/
ISSN 1947-5500

and Lin [6] applied near duplicate detection technique for consumer photo management application. Their work is based on filtering approaches such as probabilistic latent semantic, region based and point based.

Fisichella et al. [9] proposed a method known as locality sensitive hashing which is meant for near duplicate detection incrementally. They applied the technique for finding near duplicate detection of images. Hartrumpe et al. [20] proposed a method based on shallow and parser for near duplicate detection. In-depth analysis of near duplicate texts is explored that are useful for question answering systems and search engines. Bueno et al. [4] explored Bayesian approach for near duplicate detection of images. The specialty of this approach is that it uses local descriptors which are supported by decision theory for flexibility. Stoica [10] proposed Delaunay Diagram Representations for duplicate detection of images. All existing methods for near duplicate detection focus on detection of near duplicates. Our Proposed work not only concentrates on the text but also on images.

III. PROPOSED WORK

In this Paper, our proposed work has been carried out as for an input record r1, the near duplicate verification is done on set of n records stored in the repository {r1, r2, r3…..rn} and the ratio of similarity is also returned. The similarity verification is mainly based on the bit by bit comparisons. The duplicate and near duplicate detection is done by our novel method Location Sensitive Bitwise Similarity method (LSBS) is used to compute the difference. Our main objective is to find how to identify the query page is how similar to all the records in the dataset. A three stage approach is proposed.

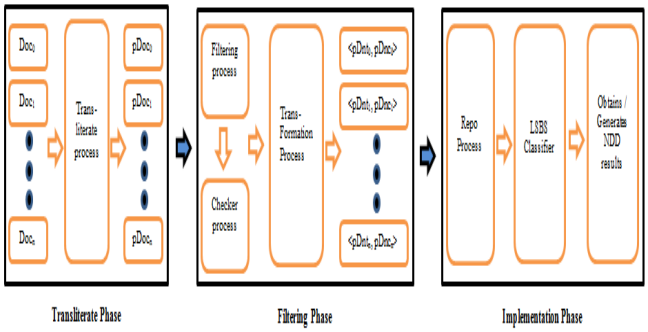

Figure 1. Three phase LSBS approach

The Document size Ds has also shown an important role in near duplicate detection. Our approach is considering the size of the new record set r1 with the whole record set Os= {d1, d2, d3, d4…dn}.The greater the difference of size the lesser chances of near duplicates.

One more advantage of the proposed approach is it provides a unique feature of searching near duplicates only within the relevant categories based on the document type like .pdf, .html, .doc, .txt etc. This method can be used as a tool for identification NDD in different categories.

In the first phase, called as Transliterate phase for the input query r the standard preprocessing methods like removal of whitespaces are applied and {x1,x2,x3…..xm} are retrieved where x is a sentence in a record set and m is the total number of sentences.

In the second phase, called as filtering phase the input file a text file is visualized in terms of the numbers by the ASCII equivalent and is converted to binary format to get the binary stream. For example 'R' uses 8 bits which is stored as 01010010. The document sizes are compared with the sizes of the individual files in the dataset and the decision is taken whether it has to be compared or not. Our approach concentrates not only on the text but also on images and special symbols. In the input page the text followed by images and special symbols are collected and converted to binary.

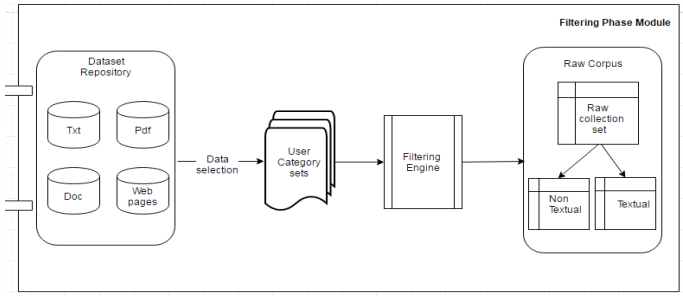

Figure 2. Filtering Phase

A. *Algorithm for Document Filtering Phase*

Input: The input page type can be any of the following Webpage, PDF Document, Word Document, Text Document, Records in the Repository (Record Set)

Output: Obtaining the filtered data from the documents in textual (Dnt) and non-textual (Dnc) content sets.

Steps:

1. Consider the given dataset Dn as

$$Dn = \sum_{t=1}^{n} Dnt$$

Dn <- *Total n number of docs considered in Dataset*

Dnt <- *Each doc considered in a given Dn*

2. In each Dn, extract

$$T_{LWS} <- \sum_{i=1}^{m} trim\left(\sum_{t=1}^{n} D(X)\right)_i$$

$\sum_{t=1}^{n} D(X)$ <- Identifying the lines in x document within the given D.

3. $Dnc <- \sum_{t=1}^{n} D(Sx)$

4. $Dnt <- \sum_{t=1}^{n} D(Tlws - Sx)$

$Tlws$ <- *trimmed line*

Sx* <- *Special Character line

https://sites.google.com/site/ijcsis/
ISSN 1947-5500

In Filtering algorithm, Massive datasets of various categories were collected and maintained in the repository will be considered as databases. It will take only one type of categorical data as input at each run. Given dataset will be processed, trimmed and filtering the data within the considered dataset. Extract each and every document from the given dataset and trims the lines and additional spaces to obtain the raw corpus which stores in temporary dataset vectors. In the next step the raw corpus from temporary dataset will be categorized into the two vectors, One vector will parse the raw data and collects all the text oriented sets such as alphabets, numerical and so on where as the other vector collects non-textual data such as images.

In the third phase, The LSBS (Location Sensitive Bitwise Similarity) method name is abbreviated for our convenience. The LSBS is used to identify the near duplicate documents. The input record 'r' binary Data is converted into chunks of sizes 8 bits or 10 bits. The chunk size can be increased also per our requirement. We have considered a chunk size of 8 bits.

The current chunk size = Total characters/ (chunk size of 8 bits)

Current chunk1 = Txt0 (1:8)

Current chunk2= Txt1 (9:16)

….

Chunk n = Txtn (m-8: m)

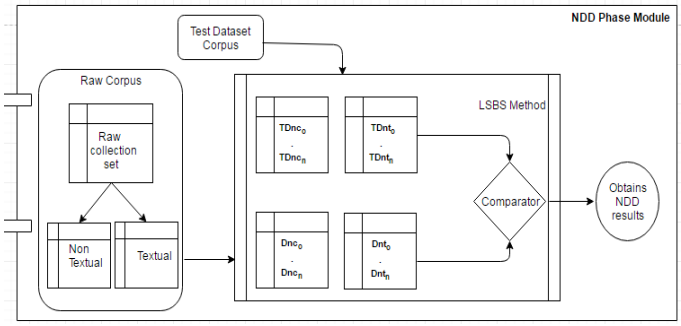

Figure 3. NDD Phase

B. Algorithm for Near Duplicate Detection

Input: The filtered input which any of the following Webpage, PDF Document, Word Document, Text Document, Records in the Repository (Record Set) and similarity threshold (t)

Output: Obtaining the LSBS featured sets for the given filtered content sets thereby results the NDD of documents.

Steps:

1. For a given filtered input, finding the chunks based on LSBS method as feature intervals and label the each featured chunks as cnk0,cnk1 … cnkn
2. Obtaining the chunks separately for Dnc and Dnt content sets
    a. Numbers of Chunks = (Dnt/Sz) V (Dnc/Sz)
    b. Sz <- chunk size (multiples of 8 bits, as we considered Sz as 8 bits only)
    c. e.g. cnk0 = txt0(0:7), cnk1 =txt1(8:15) … cnkn=txtn(n:m)
3. Identifying the similarity for all LSBS chunks obtained for Dnc and Dnt sets
   Featured Chunk (FC) <- LSBS_Method (Dtxti, cnki)
   The input document chunks are compared with every document chunks of the database.
4. LSBS method will give vote for each chunk if they are similar to the compared chunk in the repository. The numbers of votes are calculated.
5. Based on the threshold 't' given and similarity labels ratios, the NDD will be identified.
6. If the input document is an NDD then it is discarded otherwise added into the repository.
7. Steps 3 to 6 repeated for all documents in the database.

In NDD algorithm, it accepts two vectors as inputs to process further. Given vectors will be parsed and bit conversion will be made in the form of chunks up to the length of given vectors. Every feature conversion will be appropriately labeled and user considerable size chunks will be generated mostly in the multiple of eight. Here we considered the chunk size of eight bits. Every chunk in the vector will be compared with the given another dataset vectors as the bit-by-bit difference between the each chunk and the other chunks are found out and total number of bit difference is computed. The bit-by bit difference value is compared with the predefined threshold TB. If the bit difference value is less or equal to than the threshold, the input page is considered as a near duplicate page. If the difference value exceeds the threshold then it is not considered as NDD and it is added to the existing database.

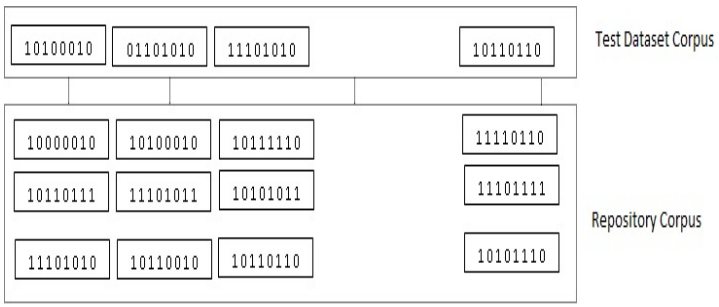

Figure 4. Dataset Repository

IV. EXPERIMENTAL SETUP

After In this section, results of several experiments are presented. Comparisons are also done with other methods to demonstrate the effectiveness of our proposed approach. To conduct required experiments we used various datasets like Enron, RCV1, Reuters, and C50. The Enron document set (Enron email dataset, 2012) includes the mailbox e-mails of 150 users. Most of the users are executives of Enron. The Enron set contains 128,173 e-mails and takes 310 MB in size, as shown in Table 3. The RCV1 document set was edited and collected by Reuters. It includes 223,496 full English text news

https://sites.google.com/site/ijcsis/
ISSN 1947-5500

from 20 August 1996 to 30 November 1996, as also shown in Table 1. Each news in RCV1 contains 109 words and 13 sentences on average.

TABLE I. TYPES OF DOCUMENTS USED IN EXPERIMENTS

Datasets	No.of Doc	Size(MB)
Enron	128,173	310
C50	5000	228
RCV1	223,496	652

We collected Webpages using an online tool wget to download the pages in voluminous amount. Whenever any input query which can be of any type like .pdf, .html, .doc, .txt file is given and its corresponding datasets are considered. The threshold is considered as user input and the LSBSM algorithm is run. The similarity is greater than the threshold percentage then is considered to be NDD and is discarded otherwise is stored in the database. All the programs that follow were implemented as a compact Java prototype using matlab and run on an Intel Core i5 quad-core CPU 2.80 GHz with 8.00 GB RAM.

A. *Experiment - I*

The The Enron document set [6] contains many spam e-mails which are just slight modifications of the original e-mails. So the set contains many e-mails which are similar to each other. The Enron document set (Enron email dataset, 2012) includes the mailbox e-mails of 150 users. Most of the users are executives of Enron. Then we compute similarity degree sim(X, Y). If sim(X, Y)> T, X and Y are labeled to be near-duplicates. Otherwise, X and Y are labeled as non near-duplicates. T is the threshold percentage entered by the expert like sim(X, Y)> 0.7.

B. *Experiment - II*

Headings, The C50 dataset is considered for the text documents evaluation. The experimental evaluation was done for a small sample of 10 pages to 1000 pages with different sizes and the time elapsed was collected. The following table represents the same.

TABLE II. DOCUMENT ELAPSED TIME

Data Set	Type	#No.of Documents	Size	Time(Sec)	Accuracy
C50	.txt	10	50KB	3.38	95
C50	txt	50	300KB	14.78	95
Enron	.pdf	10	300KB	196.20	96
Enron	.pdf	50	36.5MB	846.02	95
Reuters	.pdf	10	5.56MB	30.19	97

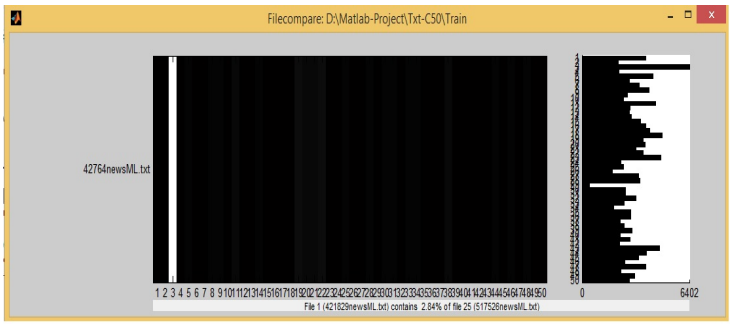

Figure.5. Training set computation

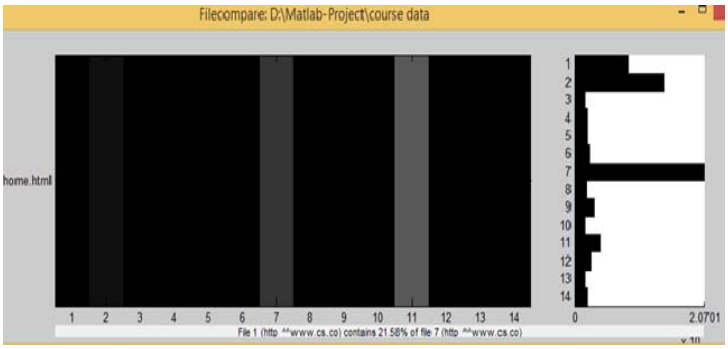

Figure 6. Computing the Near Dup document

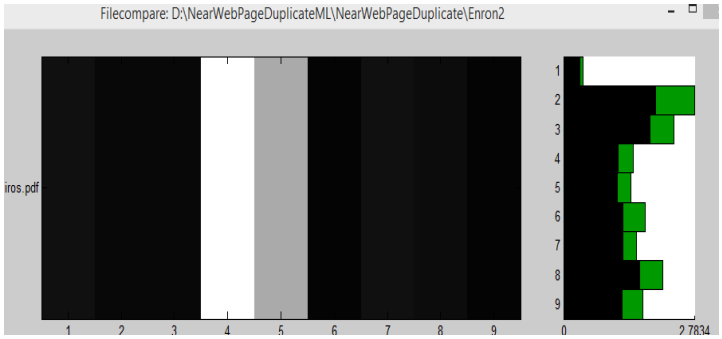

Figure 7. Identifying the Dup document

V. EVALUATION MEASURES

We the evaluations of the proposed approach are done using information retrieval effectiveness measures like precision and recall. Precision can be defined as the fraction of retrieved items that are relevant to all retrieved items or the probability given that an item is retrieved it will be relevant and recall as the fraction of relevant items that are retrieved to relevant items in the database or the probability given that an item is relevant it will retrieved [40]. The lower the values indicates bad performance of the system and the higher the values the more the user is encouraged to use the system due to the anticipation of getting more of the relevant search items. These evaluation measures are inter-dependent measures in that as the number of retrieved items increases the precision usually decreases while recall increases. In Table.3, the "Retrieved" documents are those that have been detected as duplicate by a duplicate detection algorithm, and the

https://sites.google.com/site/ijcsis/
ISSN 1947-5500

"Duplicate" documents are really duplicates manually labeled by annotators.

Precision = P = A/A+B - (1)

Recall = R = A/A+C - (2)

TABLE III. FALSE ALARM – MISS RATE STRUCTURE

	Duplicate	Not Duplicate
Retrieved	A	B
Not Retrieved	C	D

We combined precision and recall values with F-measure [RIJ1979].It is the weighted harmonic mean of precision and recall.

The F-measure used in the study is given as follows:

$$F = 2 * P * R / P + R \quad - (3)$$

Accuracy: The accuracy is the perhaps the most intuitive performance measure. It is simply the ratio of correctly predicted observations i.e. Proportion of the true positives and true negatives. The input datasets of type txt, pdf, html, and doc are given to the LSBM approach to evaluate its accuracy. The computed values are plotted as a graph give in Figure 6. From the analysis of the above graphs we can infer that accuracy is good for the symmetric datasets like pdf, txt and doc where the class distribution is 50/50 and the cost of false positives and false negatives are roughly the same.

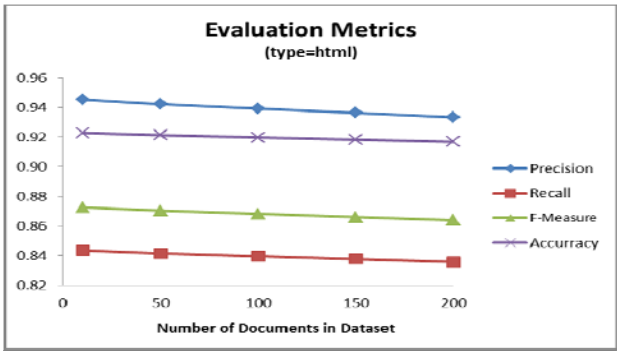

Figure 8.1 Metrics computations with html datasets

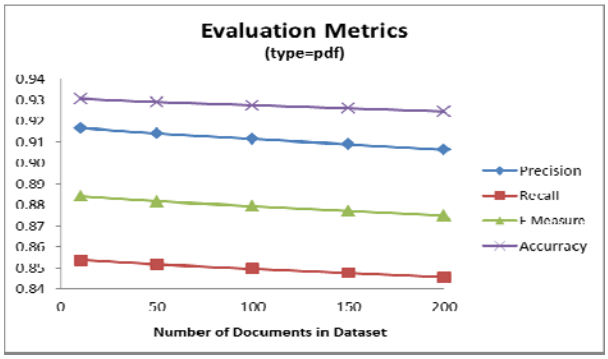

Figure 8.2 Metrics computations with pdf datasets

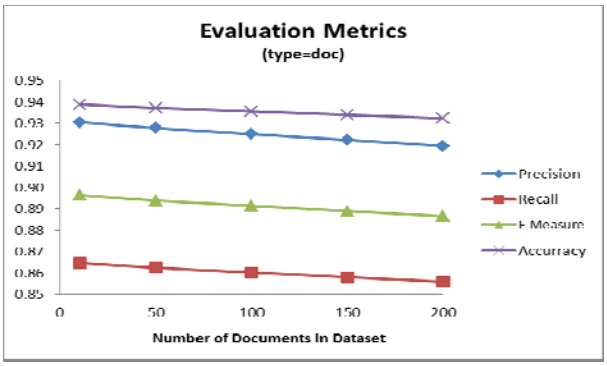

Figure 8.3 Metrics computations with doc datasets

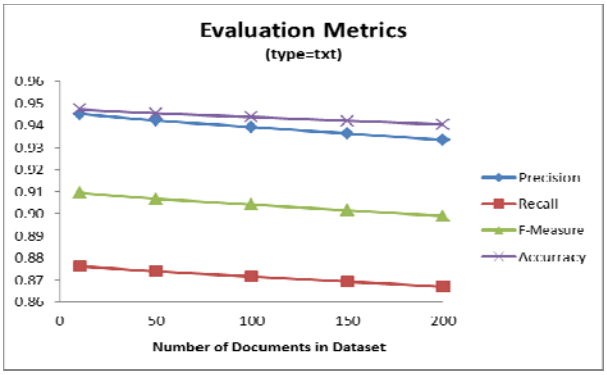

Figure 8.4 Metrics computations with txt datasets

Computation Time: For our proposed approach the computation time is considered as the time taken to compute the consolidated similarity score between the query and the reference web pages or documents in the database. . So, time incurred usually vary with the number of webpages or documents in the database. More number of documents in the database means that the new webpage have to be compared with more number of web documents. The time response for each is plotted in the Figure7 and the Table 4 gives the sample details. In the proposed approach the time taken to identify near duplicates is very less compared with the existing methods like Manku.

TABLE IV. COMPUTATION HISTORY LOG FOR DATASETS W. RT. THRESHOLD

Dn	Similarity Threshold	System Elapsed time(sec)			
		Txt	doc	Pdf	html/webpages
10	50	2.73	6.99	412.27	2.74
	60	2.73	7.68	443.93	3.79
	70	2.71	7.99	578.01	5.36
	80	2.66	8.35	614.64	6.47
	90	2.63	9.46	767.76	7.71
50	50	14.79	13.53	824.46	10.43
	60	14.72	14.90	886.48	11.79
	70	14.69	15.90	912.88	13.92
	80	14.68	16.80	932.90	14.43
	90	14.55	18.11	946.79	14.88

https://sites.google.com/site/ijcsis/
ISSN 1947-5500

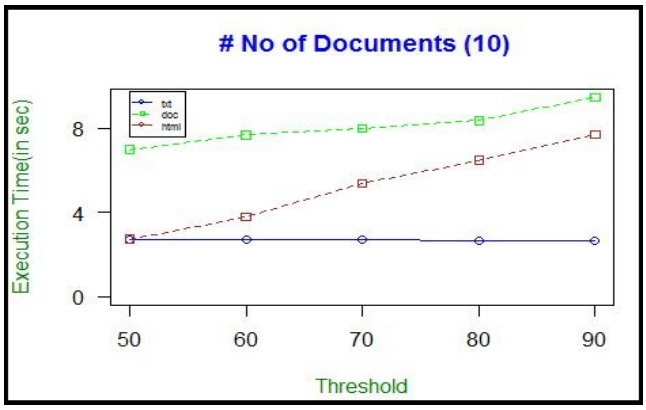

Figure 9.1 Elapsed time for the considered 10docs in datasets

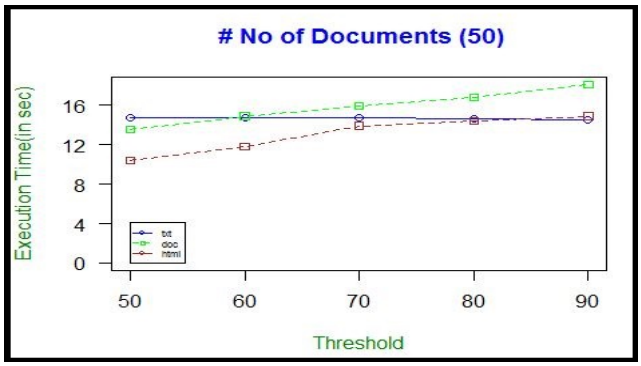

Figure 9.2 Elapsed time for the considered 50docs in datasets

VI. Effectiveness Measures

We tested the effectiveness of the algorithm using a corpus of various categorical documents. In order to perform this experiment, we extracted this many items from Enron, RCV1 and Reuters datasets from a respective open source sites and forums. We inspected each document from the respective category and with various in size as well.

With the same infrastructure testbed, we performed the experiments varying the corpus sizes and number of documents within the relative size. We found at performance of our algorithm comparatively as the best value at various threshold levels. The performances of LSBS decreases with higher values of corpus since more corpus require more memory.

We compared the effectiveness of our solution with other existing methods, i.e. SpotSig [11], Simhash [42] and Imatch [41].We executed these algorithms using the Java implementation provided by the authors of SpotSig [11], setting the default parameters. Figure 8 reports the performance values for several assigned threshold values.

We performed separated runs for each corpus, starting each run with an empty set. The more the hourly documents corpus grow, the more comparisons the algorithm performs, and the more the computation time increases, achieving the value of 0.8 seconds with 1000 number of documents within the corpus.

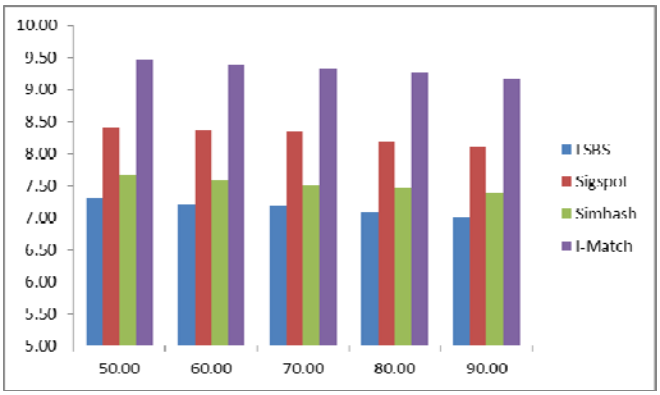

Figure 10. Elapsed time comparison with considered methods

CONCLUSION

The human community is dependent on internet for communication and information. It is consisting of voluminous amount of digital documents which are copied and pasted or modified continuously. During web crawling these are affecting space to store indexes, time, bandwidth and redundancy is frustration to the user. However identification is not at all an easy task. In this paper we have proposed a three phase efficient approach for detecting duplicate and near duplicate pages using Location Sensitive Bitwise Similarity method(LSBS).The main advantage of the proposed approach is it not only considers text but also images and hyperlinks. Our method can be applied to .doc, .docx, .pdf, .html documents. The experimental results have proved improved precision, Recall and F-measure. The execution time and accuracy for various types of documents are recorded. In future we would like to develop it as a tool for identification of duplicate and near duplicate documents which can be used in the study of data analytics.

References

[1] Dennis Fetterly, Mark Manasse, and Marc Najork. “On the Evolution of clusters of Near Duplicate Web Pages”. In proceedings of the first Latin American Web Congress, LA-WEB 2003, IEEE, ISBN)-7695-2058-8/03. 25, 32

[2] [2] Xiao, C, Wang, W. Lin, X. Xu Yu, J., "Efficient Similarity Joins for Near Duplicate Detection", Proceeding of the 17th international conference on World Wide Web, pp: 131-140., 2008.

[3] Conrad, J. G., Guo, X. S, and Schriber, C. P, “Online Duplicate Document Detection: Signature Reliability in a Dynamic Retrieval Environment”, Proceedings of the Twelfth International Conference on Information and knowledge Management, New Orleans, LA, USA, pp. 443- 452, 2003.

[4] Fetterly. D, Manasse, M, and Najork, M, “On the Evolution of Clusters of Near-Duplicate Web Pages”, Proceedings of the First Conference on Latin American Web Congress, pp.37.2003.

[5] Monika Henzinger, "Finding Near-Duplicate Web Pages: a Large-Scale Evaluation of Algorithms", In Proceedings of the 29th annual international ACM SIGIR conference on Research and Development in Information retrieval, pp: 284-291, 2007.

[6] Enron email dataset. (2012). <http://www.cs.cmu.edu/enron/>.

[7] Jun Jie Foo and Ranjan Sinha. (2007). Using Redundant Bit Vectors for Near-Duplicate Image Detection. LNCS. 0 (0), p472-484.

[8] Marco Baroni Æ Silvia Bernardini Æ Adriano Ferraresi Æ Eros Zanchetta. (2009). The WaCky wide web: a collection of very large

https://sites.google.com/site/ijcsis/
ISSN 1947-5500

linguistically processed web-crawled corpora. Lang Resources & Evaluation. 0 (0), p210-226.

[9] Tanvi Gupta1 and Latha Banda. (2012). A HYBRID MODEL FOR DETECTION AND ELIMINATION OF NEAR- DUPLICATES BASED ON WEB PROVENANCE FOR EFFECTIVE WEB SEARCH. ISSN. 4 (1), p192-205.

[10] Lucas Moutinho Bueno, Eduardo Valle, Ricardo Torres. (2011). BAYESIAN APPROACH FOR NEAR-DUPLICATE IMAGE DETECTION.FAPESP. 0 (0), p1-4.

[11] Martin Theobald Jonathan Siddharth Andreas Paepcke. (2008). SpotSigs: Robust and Efficient Near Duplicate Detection in Large Web Collections. SIGIR. 0 (0), p1-8.

[12] Wei-Ta Chu and Chia-Hung Lin. (2010). Consumer Photo Management and Browsing Facilitated by Near-Duplicate Detection with Feature Filtering. -. 0 (0), p1-28.

[13] Matt Thomas, Bo Pang, and Lillian Lee. (2005). Get out the vote: Determining support or opposition from Congressional floor-debate transcripts. EMNLP. 0 (0), p1-10.

[14] Hung-Chi Chang1 and Jenq-Haur Wang2. (2007). Organizing News Archives by Near-Duplicate Copy Detection in Digital Libraries. ICADL. 0 (0), p410-419.

[15] Marco Fisichella, Fan Deng, and Wolfgang Nejdl. (2010). Efficient Incremental Near Duplicate Detection Based on Locality Sensitive Hashing. LNCS. 0 (1), p152-166.

[16] Adina Raluca Stoica,Annandale-on-Hudson. (2011). Delaunay Diagram Representations for Use in Image Near-Duplicate Detection. -. 0 (0), p1-85.

[17] Hui Yang, Jamie Callan. (2005). Near-Duplicate Detection for eRulemaking.-0 (0), p1-9.

[18] Henry S. Baird. (2014). Difficult and Urgent Open Problems in Document Image Analysis for Libraries. IEEE. 0 (0), p1-8.

[19] Fan Deng,Davood Rafiei. (2006). Approximately Detecting Duplicates for Streaming Data using Stable Bloom Filters. SIGMOD. 0 (0), p1-15.

[20] Bassma S. Alsulami, Maysoon F. Abulkhair, Fathy E. Eassa. (nd). Near Duplicate Document Detection Survey. ISSN. 2(2) (0), p147-151

[21] Y. Syed Mudhasir, J. Deepika, S. Sendhilkumar, G. S. Mahalakshmi. (2011). Near Duplicates Detection and Elimination Based on Web Provenance for Effective Web Search. Ijidcs. 1 (1), p22-31

[22] Yaniv Bernstein, Justin Zobel. (2006). Accurate discovery of co-derivative documents via duplicate text detection$. Elsevier. 0 (0), P595-609.

[23] Leonardo S. de Oliveira, Zenilton K. G. do Patrocínio Jr, Silvio Jamil F. Guimarães. (2013). Searching for Near-duplicate Video Sequences from a Scalable Sequence Aligner. -. 0 (0), P1-5.

[24] Bhaskar Mehta, Saurabh Nangia, Manish Gupta. (2008). Detecting Image Spam using Visual Features and Near Duplicate Detection. -. 0 (0), P497-506.

[25] Midhun Mathew, Shine N Das, T R Lakshmi, Pramod K. (2011). A Novel Approach for Near-Duplicate Detection of Web Pages using TDW Matrix. International Journal of Computer Applications. 9 (7), P16-21.

[26] Sven HARTRUMPF, Tim VOR DER BRÜCK, Christian EICHHORN. (2010). Detecting Duplicates with Shallow and Parser-based Methods. IEEE. 0 (0), p1-8.

[27] Hui Yang, Jamie Callan. (2006). Near-Duplicate Detection by Instance-level Constrained Clustering. -. 0 (0), P1-9.

[28] Fan Deng, Davood Rafiei. (ND). Estimating the Number of near Duplicate Document Pairs for Massive Data Sets using Small Space. -. 0 (0), P1-10.

[29] Ismet Zeki Yalniz, Ethem F. Can, R. Manmatha. (2011). Partial Duplicate Detection for Large Book Collections. -. 0 (0), P1-6.

[30] "Doe, John" "Mary K. Smith. (March 2, 2004). EnronDataset. Available: https://www.cs.cmu.edu/~./enron/. Last accessed 10th march 2015

[31] David D. Lewis. (2005). RCV1 (Reuters Corpus Volume 1). Available: http://www.daviddlewis.com/resources/testcollections/rcv1/. Last accessed 10th march 2015.

[32] Yuen-Hsien Tseng. (Nov. 8, 2002). Tools for Reuters-21578 Text Categorization Dataset. Available: http://lins.fju.edu.tw/~tseng/Collections/Reuters-21578.html. Last accessed 10th march 2015

[33] Wu, Y. et al (26, 3 2012). Efficient near-duplicate detection for Q&A forum. Retrieved from http://aclweb.org/anthology-new/I/I11/I11-1112.pdf

[34] Maosheng Zhong, Yi Hu, Lei Liu and Ruzhan Lu, A Practical Approach for Relevance Measure of Inter-Sentence, Fifth International Conference on Fuzzy Systems and Knowledge Discovery, pp: 140-144, 2008

[35] Theobald, M., Siddharth, J., and Paepcke, A. 2008. Spotsigs: robust and efficient near duplicate detection in large web collections. In SIGIR. 563–570

[36] A. Broder, S. Glassman, M. Manasse and G. Zweig. Syntactic clustering of the web. In Proc. of the 6th International World Wide Web Conference, Apr. 1997

[37] Krishnamurthy Koduvayur Viswanathan and Tim Finin, Text Based Similarity Metrics and Delta for Semantic Web Graphs, pp: 17-20, 2010

[38] Salha Alzahrani and Naomie Salim, Fuzzy Semantic-Based String Similarity for Extrinsic Plagiarism Detection, 2010

[39] Lavanya Pamulaparty, Dr. C.V Guru Rao, Dr. M. Sreenivasa Rao. (2015). XNDDF: Towards a Framework for Flexible Near-Duplicate Document Detection Using Supervised and Unsupervised Learning.Procedia Computer Science. 48 (5), p228 – 235.

[40] C. D. Manning, et al., Introduction to Information Retrieval: Cambridge University Press, 2008.

[41] A. Kolcz et al. Improved robustness of signature-based near replica detection vialexicon randomization. In KDD 2004.

[42] P. Indyk et al. Approximate nearest neighbors: towards removing the curse ofdimensionality. In STOC 1998.

AUTHORS PROFILE

Lavanya Pamulaparty, Research Scholoar, Department of CSE, JNTUH, Hyderabad, obtained her Bachelor's degree in computer science from Nagpur University of KITS, Nagpur, India, and Masters Degree in Software Engineering from School of Informatics from JNT University Hyderabad, India, and Pursuing the PhD degree in computer science and engineering from JNT University. Her research interests include information storage and retrieval, Web Mining, Clustering technology and computing, performance evaluation and information security. She is a senior member of the ACM, IEEE and Computer Society of India

Dr. Guru Rao C. V received his Bachelor's Degree in Electronics &Communications Engineering from VR Siddhartha Engineering College, Vijayawada, India. He is a double post graduate, with specializations in Electronic Instrumentation and Information Science & Engineering. He is a Doctorate holder in Computer Science & Engineering from Indian Institute of Technology, Kharagpur, India. With 24 years of teaching experience, currently he is the Professor & Principal, SR Engineering College Warangal, India. He has more than 25 publications to his credit. He is a life member of Indian Society for Technical Education,Instrumentation Society of India and member of Institution of Engineers, Institution of Electronics & Telecommunications Engineers and Institution of Electrical & Electronics Engineers (USA).

Dr. M Sreenivasa Rao, Professor, School of Information Technology, JNT University, Hyderabad, obtained his Graduation and Post-graduation in Engineering from JNTU, Hyderabad and Ph D from University of Hyderabad. Over 28 Years of IT Experience in the Academia& industry. As a Dean of the MS IT Program, in association with Carnegie Melon University, USA. De-signed and conducted post graduations level MSIT program. Guided more than 10 research students in JNTU, and continuing the research in IT.

https://sites.google.com/site/ijcsis/
ISSN 1947-5500

Critical review of various near-duplicate detection methods in web crawl and their prospective application in drug discovery

Article *in* International Journal of Biomedical Engineering and Technology · October 2017

DOI: 10.1504/IJBET.2017.087723

CITATIONS
0

READS
29

3 authors, including:

Lavanya Pamulaparty
Methodist College of Engineering and Technology
8 PUBLICATIONS **7** CITATIONS

SEE PROFILE

Chakunta Venkata Guru Rao
SR Engineering College, Warangal, India
175 PUBLICATIONS **431** CITATIONS

SEE PROFILE

Critical review of various near-duplicate detection methods in web crawl and their prospective application in drug discovery

Lavanya Pamulaparty*

Department of Computer Science and Engineering,
Jawaharlal Nehru Technological University Hyderabad,
Hyderabad, India
Email: lavanyaphdjntu@gmail.com
*Corresponding author

C.V. Guru Rao

Department of Computer Science and Engineering,
SR Engineering College,
Warangal, India
Email: guru_cv_rao@hotmail.com

M. Sreenivasa Rao

School of Informatics,
Jawaharlal Nehru Technological University Hyderabad,
Hyderabad, India
Email: srmeda@jntuh.ac.in

Abstract: For near-duplicate detection, various methods available in the literature are compared in terms of their application, utility, and context. In most of the cases the performances are highlighted so that anyone interested in choosing an algorithm can find this useful. Moreover, certain futuristic algorithms like oblique and streaming random forest are reported which will help the researcher to develop new algorithms especially suitable for Big Data and cloud environment. The coverage is not exhaustive but, nevertheless, considers all important algorithms used in practice so that any practitioner can find it handy to take implementation decision. As application case study application of random forest approach to near-duplicate detection is used in Chinese herbal drug discovery application is proposed.

Keywords: near-duplicate detection; big data; cloud environment; web crawling; random forest.

Reference to this paper should be made as follows: Pamulaparty, L., Rao, C.V.G. and Rao, M.S. (2017) 'Critical review of various near-duplicate detection methods in web crawl and their prospective application in drug discovery', *Int. J. Biomedical Engineering and Technology*, Vol. 25, Nos. 2/3/4, pp.212–226.

Biographical notes: Lavanya Pamulaparty, Research Scholar, pursuing PhD in Computer Science and Engineering from JNTUH, obtained her Bachelor's degree in Computer Science and Engineering from Nagpur University of KITS, Nagpur, India, and Master's degree in Software Engineering from School of Informatics from JNT University Hyderabad, India, and pursuing the PhD degree in Computer Science and Engineering from JNT University. Her research interests include information storage and retrieval, web mining, clustering technology and computing, performance evaluation and information security. She is a senior member of the ACM, IEEE and Computer Society of India.

C.V. Guru Rao received his Bachelor's degree in Electronics & Communications Engineering from VR Siddhartha Engineering College, Vijayawada, India. He is a double postgraduate, with specialisations in Electronic Instrumentation and Information Science & Engineering. He received his MTech in Electronic Instrumentation from Regional Engineering College, Warangal, India, and ME in Information Science & Engineering from Motilal Nehru Regional Engineering College, Allahabad, India. He is a Doctorate holder in Computer Science and Engineering from Indian Institute of Technology, Kharagpur, India. With 24 years of teaching experience, currently he is the Professor in SR Engineering College, Warangal, Andhra Pradesh, India. He has more than 25 publications to his credit. He is a life member of Indian Society for Technical Education, Instrumentation Society of India and member of Institution of Engineers, Institution of Electronics & Telecommunications Engineers and Institution of Electrical & Electronics Engineers (USA).

M. Sreenivasa Rao, Professor in CSE and Director-Academic Audit Cell, JNT University, Hyderabad, obtained his graduation and postgraduation in Engineering from JNT University Hyderabad and PhD from University of Hyderabad. He has over 28 years of IT experience in the Academia & industry, as a Dean of the MSIT program, in association with Carnegie Melon University, USA, and designed and conducted postgraduations level MSIT program. He guided more than ten research students in JNTUH, and continuing the research in IT.

1 Introduction

A web crawler is a meta-web index, which combines three or more search engines to access large data. A web crawler is otherwise also called a web spider or web robot, and is a programming code which surfs the internet in the methodical and computerised way. The searching process, specifically web crawlers, uses the spidering procedure to give the synopsis of websites. The site incorporates both the URL link and their content. The web crawlers are utilised to create a list of URLs matching with the requested query which diminishes the measure of expending the time and resource.

The challenge faced in web crawl is in handling huge data download and identifying useful data on the fly without affecting the crawl behaviour. Crawl administrator would like to identify similar pages that cluster them in real time such that it can reduce priority for the links from spam page, provide lower priority to forums and blogs such that it can direct towards specific topics. This is achieved by identifying similar documents and

clustering them efficiently and accurately. In the web nearly 29.2% pages are similar and 22.2% are identical virtually. Thus, many methods and algorithms are evolved for identifying them.

The online drug databases are getting more popular and utilised by many large-scale companies in drug preparation, treatments, and many another purpose, since there is not a proper way to identify the forged sites. Numbers of forged sites are in the Alive mode, which are involved in fraudulent activities to deceit the users. Since drugs are sensitive products, identifying the duplicates sites will be partially helpful for users for safe analysing of herbal items for preparation of drug products. It's not easy to identify the forged sites from the millions of sites without any proper approach.

The random forest approach efficiently handles large data and provides more accuracy on finding the duplication comparing with other algorithms. This approach runs for thousands of input data without removing any single URL of them. In existing techniques, the random forest approach in a web is used to find out the hidden sites only. In this paper, we discuss the various algorithms available to make aware the algorithms available for the near-duplicate identification problem. The purpose is to know which one is suitable for a particular application scenario and thus will pave way for identifying further methods based on the limitations of existing ones as well. The methods discussed are not in any order and also is not exhaustive but covers the majority of them in use.

2 Related work

Probabilistic Simhash Matching (Sood, 2011) achieves query performance using less memory. It achieves a reduction in space by a factor of 5 while improving the query time by a factor of 4 with a recall of 0.95 for finding all near duplicate when the data set is in memory. A query time improvement by a factor of 4.5 is also achieved by finding first the near duplicate for an in-memory data set. Data set is stored in disk for an improvement in performance by seven times for finding all near duplicates and by 14 times when finding the first near duplicate. For details of the method and results refer to Sood (2011). Keyword Extraction Method (Subramanya Sharma et al., 2016) discusses a novel and efficient approach lies on the premise of keywords obtained from a particular page on the website; the proposed method effectively deletes the duplicated pages productively, with reduced memory and improved search engine quality. In this method pre-processing adapted to process images, colour text, Hyperlinks, Blinking words and high priority text/words.

The main part of Sentence Level features and Supervised Learning Method (Lin et al., 2013) is feature selection, discriminant derivation, and similarity measure. During pre-processing each sentence is fetched and weighted as a term and a heavily term has selected a feature of the sentence. Thus, document is converted into feature and similarity measure with the help of the combination of both vector machine and discriminant learning of trained pattern. This is processed by identifying near duplicate based on similarity degree. This method avoids trial-and-error methods adopted by conventional methods. Accuracies ranging from 95% to 98% achieved for various similarity measures. Besides single, two- and three-dimensional similarity vectors with Jaccard similarity measure carried out and a best result of 99.55% for one-dimensional,

99.45% for two-dimensional and 99.5% for three-dimensional similarity vectors are achieved. Efficient detecting and shunning duplicate documents (Prasanna Kumar and Govindarajulu, 2009) method uses keywords and similarity measures to achieve the goal. The similarity score and its threshold level help in eliminating and shunning near-duplicate pages. The main advantage of this process is to minimise the memory space of the repository and better search engine quality.

Clustering and Load Balancing Optimisation (Zhu et al., 2012; Pamulaparty et al., 2014), Parallel clustering and multidimensional mapping to optimise load are the keys to this method. Several approximation techniques are used while handling the distributed duplicate clusters having direct relationships. Experiments carried to evaluate the incremental process, by acquiring the advantages of multidimensional plotting and bring out ability to reduce online cost and search quality. The Relative Error Precision (REP) ranges from 0.8% for 10 million to 1.3% for 100 million data sets. Therefore, the entire saving ranges to 25.6% to 8.2%. This method minimises the communication usage and maximises the throughput of online server. This method uses both offline and online schemes to remove redundant content. Comparative analysis of near-duplicate detection (Panwar, 2016) is classified as conventional and modern. In conventional following methods are considered they are keyword-based approach, URL-based approach, cluster-based approach, shingling approach, and fingerprint approach. In modern methods considered is Locality sensitive hashing, it was proved modern approach. In this work conventional and modern approach were compared, modern approaches perform better in terms of time taken to crawl and redundancy removal. The modern approach also performs better in finding the number of duplicate URLs.

In parallel correlation clustering on big graphs (Pan et al., 2015), correlation clustering classifies similar and dissimilar items apart. KwikCluster is one of the correlation clustering algorithms. Parallel correlation clustering algorithms like C4 and ClusterWild are considered in this paper. Experiments demonstrate their clustering accuracy and running time. These algorithms can cluster billions-edge graphs in under 5 seconds on 32 cores and achieve a 15X speed-up. Focused Crawler (Patani et al., 2014) required and relevant topics from the internet can be picked by using focused crawler that is explained in detail in this paper. Thus, it can act as an information aggregator. Cloud-Based Computing (Yadav and Gulati, 2012) is an emerging concept with benefits like improved adaptability and provisioning capability, and also it has advantage of reduced storage cost and framework, less maintenance, improvement in (effective resource usage, utilisation) advancement in resource utilisation, advancement in associated capability, providing variable computing cost based on usage, ability to adopt the varied framework and processing power, eco-friendly for the minimised surroundings, maximised real-time hazards recovery, Replicate Data Detection Algorithm (RDDA), proposed and its efficiency under cloud environment is substantiated.

Web Scale Parallel Text (Smith et al., 2013) can be used in multilanguage documents and one of the cheapest methods available in practice. Spatial and Semantic Cues (Zhang et al., 2011), Retrieval Precision and efficiency are the key merits for this method. This approach is used in image retrieval. Simhash and Shingles (Williams and Giles, 2013), the two algorithms, are compared in this work. The method provides high precision and recalls Stable Bloom Filters (SBF) (Deng and Rafiei, 2006). This method is suitable for

streaming data where many of the other method are not. SBF is more improved in terms of correctness and duration. Suggested future work is used in sliding window to tackle streaming data. The System of Associative Relations (SOAR) (Hebbar, 2011) method is suitable for hardware implementation. A better precision and lower false positive rates are merits of the SOAR. It has reduced computational complexity and makes hardware implementation straight forward. Found to be robust suitable for images and streaming videos, Meta-Search Engine (Bravo-Marquez and L'Huillier, 2011) is only method available to use meta-search by the limited amount of accuracy and rapid minimisation of processing interval. It achieves 86% reduction in execution time. Automatic Approach (Muthumann and Petrova, 2014) makes use of supervised classifier providing improved processing. This approach is found to be very fast.

Latest problem in the near-duplicate detection (Potthast and Stein, 2007), Shingling, Super shingling and Fuzzy fingerprinting performs better when issues like reclaiming recall and precision, and index size of the chunk detail are considered. Efficient Semantic-Aware Detection (Ioannou and Papapetrou, 2010) approach utilises the framework of resource description (RDF) which is a standard web framework representations of resources and also employs index using Locally Sensitive Hashing in terms of effective identification of duplicates. Probabilistic analysis is provided to construct the algorithm based on the particular requirements quality. When the volume is more in huge repository TDW Matrix method is useful (Mathew et al., 2011). Rendering, filtering, and verification are the three phases of TDW Matrix method. Rendering fixes the threshold, Filtering reduces the size of records, and optimisation happens in the verification phase. This one is concluded with the two benchmark values, recall, and precision, reduced computing size.

Set-Similarity Joins (Vernica, 2011) adopts three-stage approach to joining by fuzzy methodology, and MapReduce Framework, next improving queries and finally in terms of data-intensive computing. This technique found effective in speed-up and scale-up. Fingerprinting with Simhash (Manku et al., 2007) is an online algorithm. Simhash method utilises 64-bit fingerprint proved to store 8B web content. Streaming Quotient Filer (SQF) (Dutta et al., 2013) is a data structure used for near-duplicate detection. It is ideal for real-time memory-efficient applications. It is superior to other methods in terms of memory and accuracy. Parallel and Dynamic SQF is also discussed in this work. Efficient Similarity Joins (ESJ) (Xiao et al., 2008) exploits ordering information that is integrated into existing methods thus reducing candidate size and improving efficiency. It can achieve from 2.6X to 5X improvement in speed.

As application case study of near-duplicates detection healthcare problem of virtual screening of herbs for drug discovery is considered for Indian herbs (Naderi et al., 2014; Shen et al., 2003; Qiao et al., 2002; Yan et al., 1999; Ehrman et al., 2007). Drug discovery needs to identify similar molecules in the database for which Random forest and its variations are successfully applied and in this work virtual screening for Indian herbs is attempted through near-duplicate detection problem in very large databases; the methods for this are already attempted in references mentioned above for Chinese herbs.

3 Problem definition

Web crawling is the important part of the search engine framework. Increased size of comments from society produces near-duplicate documents that increase processing and storage costs. With rising feature of data and the need to access data from different sources leads to finding near-duplicate information efficiently. There are many methods and algorithms devised in the past but when the information is large with big data characteristics of volume, velocity, variability and veracity one need to find efficient algorithms and tools that will help in providing an efficient solution.

4 Proposed approach

In this research, we have identified various random forest algorithms like the random forest, Streaming Random Forest (SRF) and Oblique Random Forest (ORF) which are applied to near-duplicate detection problem in the fairly large information base. Various performance measures are identified to compare the methods and recommend the suitable ones for different varieties of data sets. The basic purpose of this research is to develop the efficient and innovative way of detecting near duplicates in web documents by applying random forest method so that it becomes suitable for handling big data scenarios efficiently. The comparative chart and associated analysis will clearly bring out the various applications and also pave way for hybrid methods for the near-duplicate detection problem thus providing an opportunity to evolve robust, novel and efficient ways of solving the near-duplicate detection problem at large.

ORF (Menze et al., 2011) is one of the sources for the futuristic algorithms that can be explored for near-duplicate detection especially when we are dealing with Big Data. This method is amenable to massive parallelisation. SRF (Abdulsalam and Skillicorn, 2007) is another candidate of futuristic algorithms when streaming data sets are involved with databases of Big Data category. This method can be implemented in Big Data and cloud environment with associated analytics.

Figure 1 The diagrammatic representation of the overall process

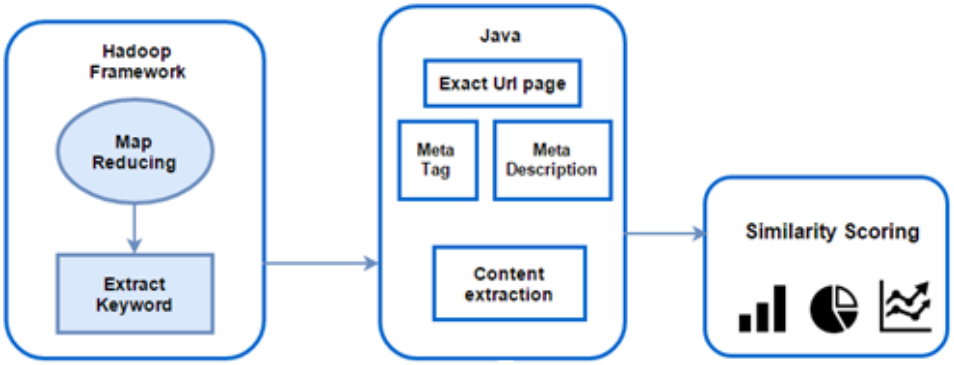

The initial phase is the keyword extraction done by using the map reducing by utilising the Hadoop framework tool. The second phase is the URL indexing where the meta-tag and meta-description are extracted and utilised during the duplication checking. The each and every URL can be fetched via meta-tag and the meta-description. The last phase is obtaining the similarity percentage and representing it in various charts (line, bar and pie charts).

5 Similarity score calculation

A quantitative way of finding the near duplicates between two sites can be calculated from similarity score. It measures the degree of the resemblance. The keyword obtained from the page is started to compare with another page for calculating the duplication. There is a little possibility to extract new keywords by combining and calculating the similarity between the pages. The resemblance of the two sites is taken as:

Consider U_1, U_2 as URL table which provides the obtained keywords and their respective number of counts.

U_1	KW_1	KW_2	KW_4	KW_5	…	KW_n
	C_1	C_2	C_4	C_5	…	C_n

U_2	KW_1	KW_3	KW_2	KW_4	…	KW_n
	C_1	C_3	C_2	C_4	…	C_n

The keywords in the tables are considered individually for the similarity score calculation. If a keyword is present in both the tables, the formula used to calculate the similarity score of the keyword is as follows.

$$x = \Delta\left[KW_i\right]_{u_1}$$

$$y = \Delta\left[KW_i\right]_{u_2}$$

Here, X and Y mention the keyword index for two URLs:

$$Sim\left(x, y\right) = \frac{\left|x \cap y\right|}{\left|x\right| + \left|y\right| - \left|x \cap y\right|} = \frac{\left|x \cap y\right|}{\left|x \cup y\right|}$$

The above equation is used to find the internal similarity between the pair of the keywords from the URL table.

Shared keywords:

$$S = \left\{\left(x_i, y_j\right) \middle| x_i \in x \Lambda y_j \in y : sim\left(x_i, y_j\right) \geq 0\right\}$$

Unique keywords:

$$U = \left\{x_i \middle| x_i \in x \Lambda y_j \in y : \left(x_i, y_j\right)\right\}$$

6 Near-duplicate detection algorithm

1 Consider a series of individual one from the preparation group as *N*. During this stage, the test of these *N* cases is taken indiscriminately but with substitution. This specimen is preparation group for developing the single one.

2 Assume *M* as the input content, where $m < M$ is indicated with the end goal that at every hub, *m* variables are chosen indiscriminately from the *M*. The perfect part from the '*m*' is used to part the hub. Each tree is developed to the biggest degree conceivable and there is no pruning.

3 Predict new information by accumulating the forecasts of the '*n*' trees (i.e. greater part votes in favour of order, normal for relapse).

Input: *M* = List of URLs, *m* = sample URL, *N* = training sets URL
Output: Near-duplicate detection
1. Search from query
2. /*Start Crawling*/
3. For each URL, *m* performs pre-processing
4. Finding the near duplication for each URL
5. Read the initial URL
6. Extract keyword from the page
7. If keyword extracted from initial URL as *N*
8. choose the next URL to obtain similarity
9. Randomly choose *K* page from the URL
10. Find matching for each of the *K* pages from the keyword
11. If matching occur
12. Start scoring the similarity as $N \cap m_i$
13. If (match is greater than 80%)
14. Make it as near-duplicate content
15. else
16. mark it as non-duplicate content
17. else no matching
18. fetch the next URL m_i
19. Repeat Step 8
20. Discard the marked in near-duplicate URL from the list.
21. Replace it with the new URL.
22. end if
23. end Procedure

7 Flow chart

Figure 2 Represent the flow of the near-duplicate detection algorithm

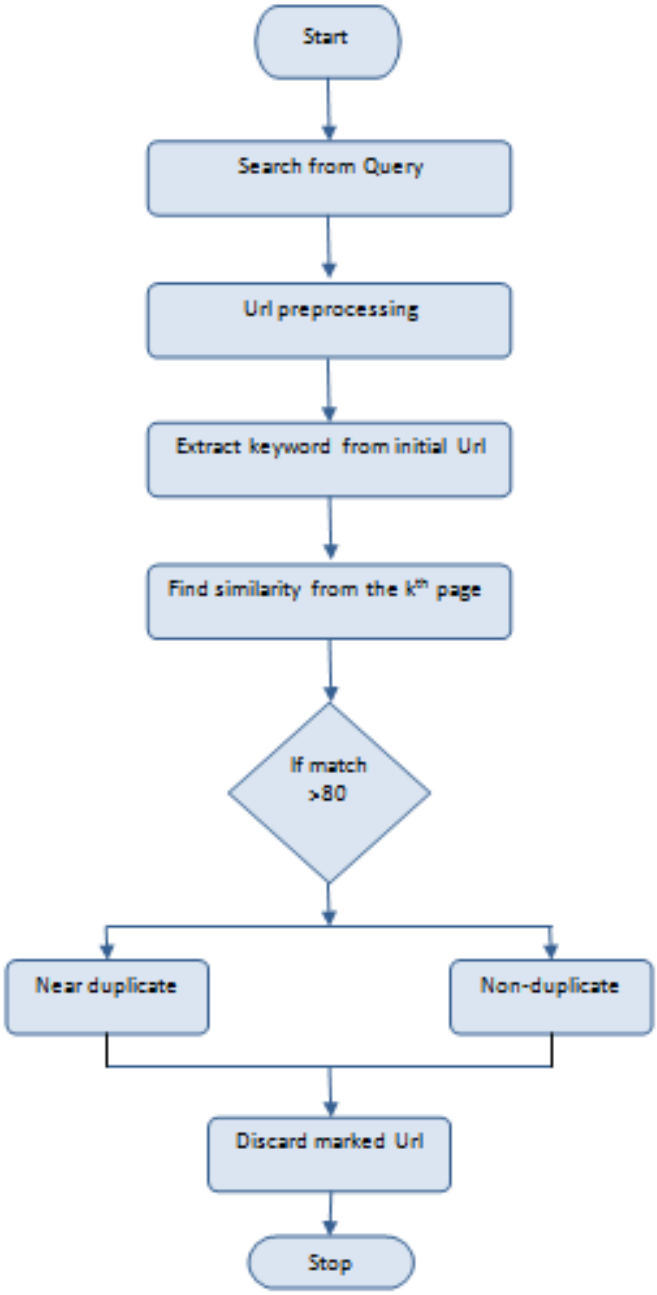

8 Comparative analysis

As a result of a comparative analysis, the values and benefits of important methods are tabulated in Table 1 that can be used along with features and functions to do further innovations and commercial implementation of the method. It will be useful to brand the method for commercialisation purpose as well.

Table 1 Values and benefits of representative methods

Method	*Values*	*Benefits*
Probabilistic Simhash Matching	Faster initial duplicate identification	Applications where identifying first duplicate quickly is important
Keyword Extraction Method	Keyword approach with pre-processing	Pre-processing helps to normalise the text
Clustering and Load Balancing Optimisation	Optimisation of load	Can be used when load is high
Cloud-based Computing	Suitable for cloud environment	Used in cloud applications
Web Scale Parallel Text	Handles multilingual text	Used when multilingual texts are encountered
Stable Boom Filter	Handles streaming data	Used in streaming applications
Set similarity Joins on Large filter	Handles Big Data	Used in Big Data applications
Streaming Quotzient filter	Real-time and memory efficient	Used in real-time memory efficient applications
Oblique and Streaming Random forest	Big Data, cloud and streaming environment	Used when cloud, Big Data and Streaming applications are needed

Table 2 Some of the websites are listed from the data sets for informatics-related TCM

Website	*Description*
Tcmassistant.com	Contains herbs name, their formulas, their usage in curing disease and patent description.
Alternativehealing.org	Have herbal names with their formula, the amount of toxicity and their side effects.
dnp.chemnetbase.com	Contains the herbal products chemical equation, and also it has biological, toxical data too.
Neotrident.com	Provide detailed description about Chinese products for more than 40,000 products.
cambridgesoft.com	Contains information regarding >10,000 compounds structures of more than 4500 species.
ars-grin.gov	Provide information regarding herbal plants among 10,000 plants.
ukcrop.net	Have Chemical formula for 1278 herbal products.
sw16.im.med.umich.edu	Contains herbal products information which mainly cures cancer.
tcm.cz3.nus.edu.sg	Nearly 1098 herbal products and 9852 constituents.

Table 2 Some of the websites are listed from the data sets for informatics-related TCM (continued)

Website	*Description*
xin.cz3.nus.edu.sg	Contains information for 1894 formulas, 5028 drugs
dddc.ac.cn	Provide information for 830 unresolved diseases.
cintcm.com	Contains the bibliographic and herbal details.
tcm.lifescience.ntu.edu	Contains information about herbal details covering protein–protein interactions and biological pathways.

9 Experimental results

In the test set-up, using the Hadoop framework we are extracting the content from the URL www.tcmassistant.com and the map reducing procedure (6180 ms of CPU time) carried out for each of the URL uploaded in the terminal. Almost 16,542 URLs are crawled from the web which was used as the data sets. Then the tcmassistant.com is considered as the training set and we are obtaining the meta-keywords and content. The similarity for the dnp.chemnetbase.com shows the 16% duplicates, 32% near duplicates, and 52% non-duplicates.

Again this testing process is carried out two times from a new crawling process for two different URLs by using the same training set where the duplication results are tabulated as below.

Based on our study, there are various techniques that have been developed to identify the duplicates and near duplicates, everything was in comprehensive approach where results are not shown in an experimental way and also duplication identification has been concluded with different goals (such as identifying similarity between documents, site content).

Table 3 The percentage result duplicates and non-duplicates for two URLs

Websites	*Duplicates*	*Near duplicates*	*Non-duplicates*
www.cintcm.com	9%	4%	87%
www.dddc.ac.cn	12%	7%	81%

Figure 3 Extracting the content from the initial URL (tcmassistant.com)

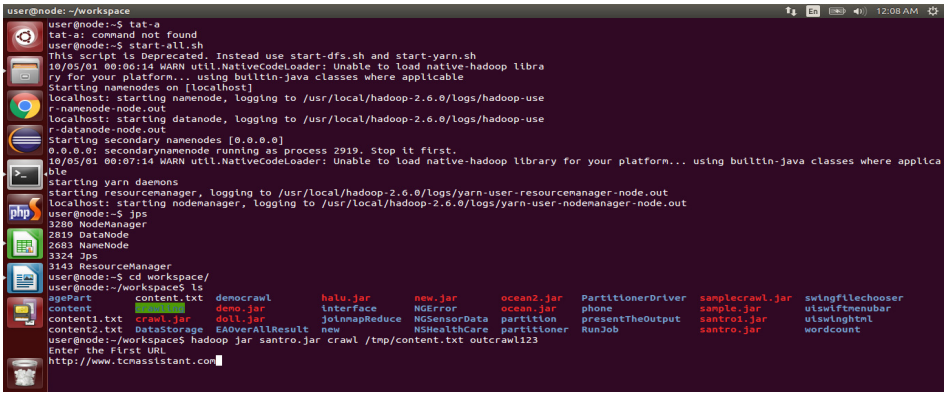

Figure 4 Content extracted from the initial URL (tcmassistant.com)

Figure 5 Uploading the second URL (dnp.chemnetbase.com)

Figure 6 Map reducing the URL

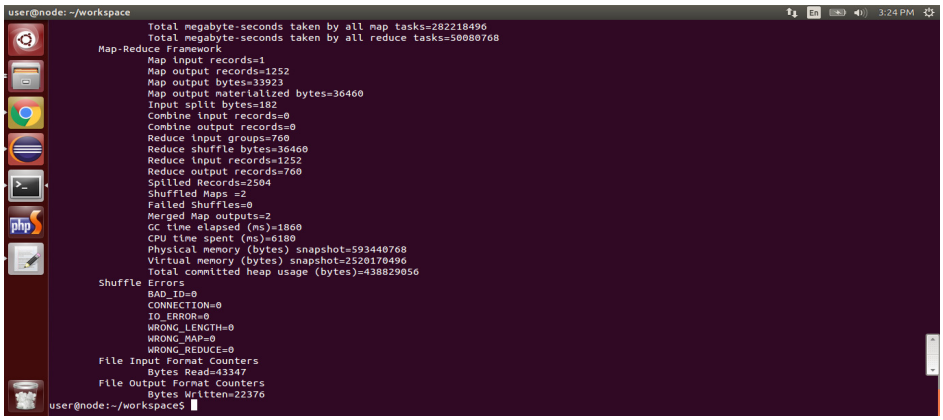

Figure 7 Similarity score mentioned in duplicates, near duplicates with non-duplicates

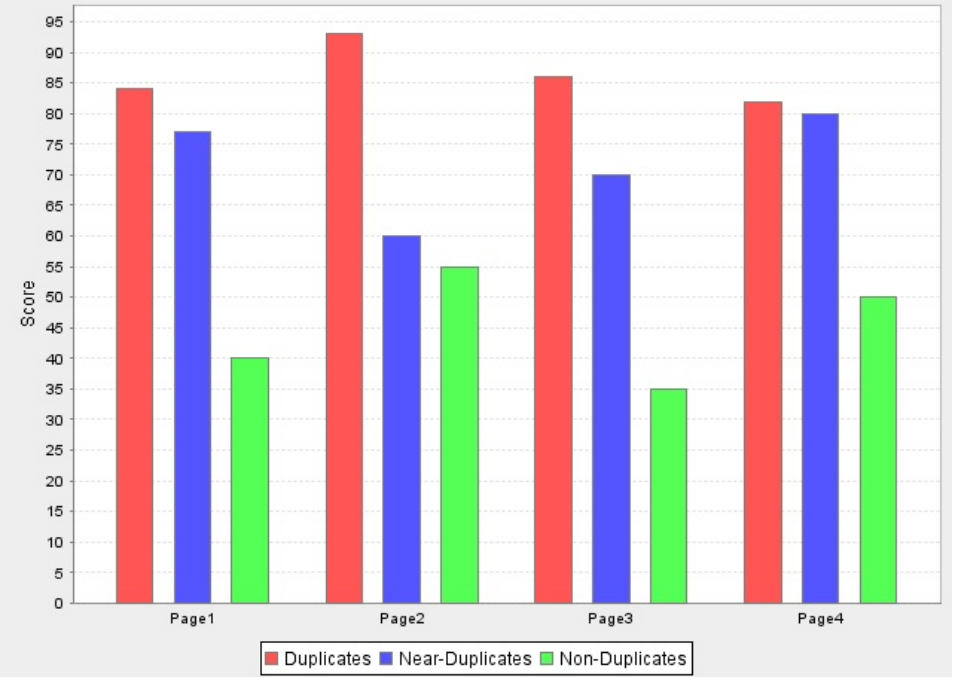

10 Conclusion

Various algorithms and methods used in the near duplicate search in the context of the large database, Big Data are compared and their relative merits are brought out. Most of the algorithms relative performances are mentioned to enable one to choose an algorithm for their implementation. Random forest algorithm as futuristic algorithms is suggested to cater to the need of crawling the web by utilising the big data methodologies. For further improvement, the near duplicates are determined in the herbal products by crawling the URLs. The random forest algorithm categorises the herbal products.

References

Abdulsalam, H. and Skillicorn, D.B. (2007) 'Streaming random forests', *Database Engineering and Applications Symposium*, Banff, Alberta, Canada.

Bravo-Marquez, F. and L'Huillier, G. (2011) 'A text similarity meta-search engine based on document fingerprints and search results records', *International Conference on Web Intelligence and Intelligent Agent Technology*, IEEE, Washington, DC, pp.146–153.

Deng, F. and Rafiei, D. (2006) 'Approximately detecting duplicates for streaming data using stable bloom filters', *Proceeding of the SIGMOD '06 International Conference on Management of Data*, ACM, Chicago, IL, pp.25–36.

Dutta, S., Narang, A. and Bera, S.K. (2013) 'Streaming quotient filter: a near optimal approximate duplicate detection approach for data streams', *The 39th International Conference on Very Large Data Bases*, Vol. 6, No. 8, pp.589–600.

Ehrman, T.M., Barlow, D.J. and Hylands, P.J. (2007) 'Phytochemical databases of Chinese herbal constituents and bioactive plant compounds with known target specificities', *Journal of Chemical Information and Modeling*, Vol. 47, pp.254–263.

Hebbar, N. (2011) *Near-Duplicate Detection Using System of Associative Relations*, MS Thesis, San Diego State University.

Ioannou, E. and Papapetrou, O. (2010) 'Efficient semantic-aware detection of near-duplicate resources', *The Semantic Web: Research and Applications on the 7th Extended Semantic Web Conference*, Springer, Berlin.

Lin, Y-S., Liao, T-Y. and Lee, S-J. (2013) 'Detecting near-duplicate documents using sentence-level features and supervised learning', *Expert Systems with Applications*, Vol. 40, No. 5, pp.1467–1476.

Manku, G.S., Jain, A. and Sarma, A.D. (2007) 'Detecting near-duplicates for web crawling', *International World Wide Web Conference Committee*, ACM, Banff, Alberta, Canada, pp.141–150.

Mathew, M., Das, S.N. and Lakshmi, T.R. (2011) 'A novel approach for near-duplicate detection of web pages using TDW matrix', *International Journal of Computer Applications*, Vol. 19, No. 7, pp.16–21.

Menze, B.H., Kelm, B.M., Splitthoff, D.N., Koethe, U. and Hamprecht, F.A. (2011) 'On oblique random forests', *Machine Learning and Knowledge Discovery in Databases*, Vol. 6912, pp.453–469.

Muthumann, K. and Petrova, A. (2014) 'An automatic approach for identifying topical near-duplicate relations between questions from social media Q/A sites', *WSCBD '14*, ACM, New York.

Naderi, H., Salehpour, N. and Farokhi, M.N. (2014) 'The search for new issues in the detection of near-duplicated documents', *International Journal of Current Research and Academic Review*, Vol. 2, No. 2.

Pamulaparty, L., Guru Rao, C.V. and Sreenivasa Rao, M. (2014) 'A near-duplicate detection algorithm to facilitate document clustering', *International Journal of Data Mining & Knowledge Management Process*, Vol. 4, No. 6, pp.39–47.

Pan, X., Papailiopoulos, D., Oymak, S., Recht, B., Ramchandran, K. and Jordan, M.I. (2015) *Parallel Correlation Clustering on Big Graphs*, Cornell University Library, arxiv:1507.05086.

Panwar, S. (2016) *Comparative Analysis of Approaches for Detecting Near-Duplicate URLs for Search Engine*, ME Thesis, Thapar University.

Patani, V., Shah, R. and Shah, V. (2014) 'Social media aggregator using a focused crawler and a web & android UI', *International Journal on Recent and Innovation Trends in Computing and Communication*, Vol. 2, No. 10, pp.3222–3225.

Potthast, M. and Stein, B. (2007) 'New issues in near-duplicate detection', *Proceedings of the 31st Annual Conference of the German Classification Society*, Springer, Berlin.

Prasanna Kumar, J. and Govindarajulu, P. (2009) 'Efficient web crawling by detecting and shunning near-duplicate documents', *Georgian Electronic Scientific Journal: Computer Science and Telecommunications*, Vol. 5, No. 22, pp.109–114.

Qiao, X., Hou, T.J., Zhang, W., Guo, S.L. and Xu, X.J. (2002) 'A 3D structure database of components from Chinese traditional medicinal herbs', *Journal of Chemical Information and Computer Sciences*, Vol. 42, pp.481–489.

Shen, J.H., Xu, X.Y., Cheng, F., Liu, H., Luo, X.M., Shen. J.K., et al. (2003) 'Virtual screening on natural products for discovering active compounds and target information', *Current Medicinal Chemistry*, Vol. 10, pp.2327–2342.

Smith, J.R., Saint-Amand, H., Plamada, M. and Lopez, A. (2013) 'Dirt cheap web-scale parallel text from the common crawl', *Proceedings of the 51st Annual Meeting of the Association for Computational Linguistics (ACL 2013)*, Association for Computational Linguistics, Sofia, Bulgaria, pp.1374–1383.

Sood, S. (2011) *Probabilistic Simhash Matching*, MS Thesis, Texas A&M University.

Subramanya Sharma, K., Srujan Raju, K. and Yadagiri, P. (2016) 'An efficient approach for near-duplicate page detection in web crawling', *Imperial Journal of Interdisciplinary Research*, Vol. 2, No. 1, pp.258–264.

Vernica, R. (2011) *Efficient Processing of Set-Similarity Joins on Large Clusters*, PhD Thesis, University of California.

Williams, K. and Giles, L. (2013) 'Near duplicate detection in an academic digital library', *DocEng '13 Proceedings of the 2013 ACM Symposium*, ACM, Florence, Italy, pp.91–94.

Xiao, C., Wang, W. and Lin, X. (2008) 'Efficient similarity joins for near duplicate detection', *International World Wide Web Conference Committee*, ACM, Beijing, China, pp.131–140.

Yadav, P. and Gulati, A. (2012) 'A novel approach for cloud-based computing using replicate data detection', *Global Research in Computer Science*, Vol. 3, No. 8, pp.12–16.

Yan, X., Zhou, J. and Xie, G. (1999) *Traditional Chinese Medicines: Molecular structures, Natural Sources, and Applications*, Milne GWA, Ashgate.

Zhang, S., Tian, Q. and Hua, G. (2011) 'Modeling spatial and semantic cues for large-scale near-duplicated image retrieval', *Computer Vision and Image Understanding*, Vol. 115, pp.403–414.

Zhu, S., Potapova, A., Alabduljalil, M., Liu, X. and Yang, T. (2012) 'Clustering and load balancing optimization for redundant content removal', *WWW '12 Companion Proceedings of the 21st International Conference on World Wide Web Conference Committee (IW3C2)*, ACM, 16–20 April, Lyon, France.

International Journal for Research in Applied Science & Engineering Technology (IJRASET)
ISSN: 2321-9653; IC Value: 45.98; SJ Impact Factor:6.887
Volume 5 Issue XI November 2017- Available at www.ijraset.com

Experimental Investigation on CI Engine for Performance, Emission and Combustion Characteristics of Dual Biodiesel Blended in Diesel

Md. Fakhruddin H.N[a,*], Dr. Mohammed Yousuf Ali[b], Dr. M.Manzoor Hussain[c]
[a]*Methodist College of Engg. & Tech., Osmania University – Hyderabad, Telangana – 500001, India*
[b]*Avanthi Institute of Engineering & Technology, Hyderabad, Ranga Reddy, India*
[c]*JNT University H, College of Engineering Kukatpally, Hyderabad, Telagana, 500085, India*

Abstract— ***Need for alternate fuel in CI engine for which a lot of experimental research is being done worldwide. Intense research is already done with biodiesel blended in diesel. And Dual biodiesel blended in diesel research is underway, which gain importance because feasibility to materialize locally available feed stock. In this contest the experimental research is being carried out to examine the performance and combustion of Waste Cooking Oil biodiesel (WCOBD) and Palm Stearin biodiesel (PSBD) blended in diesel. Result shows that B20 mixture stand close to pure diesel without much engine modification. Brake thermal efficiency and brake specific fuel consumption differ by 12.99percent and 23.5percent. CO differs by 16.5% and HC differ by 3.09% that of pure diesel mode. Whereas NOx increased by 8.9% for optimal load and blend ratio. Peak in-cylinder pressure and net heat release rate differ by 2.05% and 3.1% respectively. Properties for pure diesel and dual biodiesel blends of diesel are also enclosed.***
Keywords: Dual Biodiesel, WCOBD, Palm Stearin Bio-diesel, Combustion

I. INTRODUCTION

Biodiesel is known to be biodegradable, so it is considered to be much less damaging to the environment if divulge. The advantage about biodiesel is that it is made from plants and animals resources which are not depleted when used. The non renewable of world petroleum and increased environmental impact has reviving interest in another possible sources for petroleum based fuels. Biodiesel extracted from vegetable oil or animal fats by transesterification (with alcohol like methanol and ethanol) is advised for use in place of petroleum-based diesel, because biodiesel has more oxygen , not depleted when used, biodegradable and environmental amiable. The used cooking oil is considered as waste, while it has potential as a liquid fuel by physical and chemical conversion remains same.

Waste Cooking Oil as biodiesel

Biodiesel fuel produced successfully from waste cooking oils by an alkali-catalyzed transesterification process and can be considered as alternative fuel in diesel engines and various utilities. Need only to convert waste cooking oil from kitchen waste into biodiesel and transesterification is the most appropriate process for this conversion [1].

Palm Stearin as biodiesel

Palm stearin is the solid fraction of palm oil that is produced by partial crystallization at controlled temperature [2]. After fractionation the liquid portion is known as palm olefin, which is commonly bottled and sold as cooking oils. The solid fat portion is known as palm stearin and is normally used to formulate trans-free fats such as margarine, shortening and vegetable ghee [3] and soap industry. Palm oil is mainly used for edible purposes while palm kernel oil is used for non-edible purposes such as making soaps, cosmetics and detergents as it contain cholesterol.

II. MATERIALS AND METHODS

Engine Specification

Performance test is carried out in a research engine test rig having the specification as mention here, kirlosker make single cylinder four stroke diesel engine. This has stroke length and bore diameter of 110mm, and 87.5mm respectively. Power 3.5kw speed 1500rpm compression ratio 17.5 injection opening pressure 225bar and eddy current loading unit.

Experimental Procedure

Experimental work is carried out first with pure diesel at four different loading and performance parameters are evaluated. Next pure diesel is blended with dual biodiesel of WCO and PS at three different proportions. i.e. 5WCOBD5PSBD90D, 10WCOBD10PSBD80D & 15WCOBD15PSBD70D and experimented for different loadings.

III. TABLES

Table1.1 Fuel Properties for Pure Diesel, Biodiesels and Diesel Blends

Property	Diesel	WCOBD	PSBD	B10(5WCOBD+5PSBD+90D)
Density (kg/m^3)	832	878	898	837.6
Viscosity at 40˚C (mm^2/s)	2.6	3.35	4.12	2.71
Calorific value (MJ/Kg)	46.049	45.080	39.507	45.673

Fuel Properties for Pure Diesel, Biodiesels and Diesel Blends Contd…

Property	**B20 (10WCOBD+10PSBD+80D)***		B30 (15WCOBD+15PSBD+70D)
Density (kg/m^3)	841.6	**842.12***	841.6
scosity at 40˚C (mm^2/s)	2.827	**2.84***	2.827
alorific value (MJ/Kg)	45.297	**45.505***	45.297

*Properties are test verified at Vimta Labs Ltd.

IV. RESULTS AND DISCUSSION

Brake Thermal Efficiency

Brake thermal efficiency is the measure of performance of the engine calculated as the ratio of brake power generated to the heat input. It is the indication of the ability of engine to transform energy input to useful work.

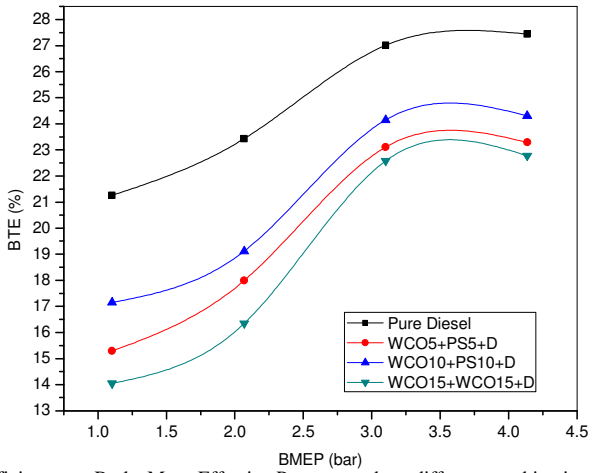

Fig.1. Brake Thermal Efficiency vs. Brake Mean Effective Pressure at three different combinations compared with pure diesel

BTE for conventional diesel is greater than its blends. The variations in the thermal efficiency of the biodiesel blends are due to the lower calorific value of WCOBD & PSBD when compared to diesel. Further, higher viscosity and slow vaporization of biodiesel present in these blends leads to inferior combustion of biodiesel which causes reduction in brake thermal efficiency [4, 5, 6].

It is noticed that as the biodiesel is blended with diesel for all proportions, brake thermal efficiency decreases.
Under full load condition for WCOBD5+PSBD5+D(B10), WCOBD10+PSBD10+D(B20) and WCOBD15+PSBD15+D(B30) percentage of substitution, brake thermal efficiency is found to be 16.6%, 12.99% and 18.4% lower than that of pure diesel mode respectively.
It is further to note that for all the fuels used BTE increases with increasing load steeply except at full load.
BTE is lower for B10 and increase with the blending ratio of B20 thereafter falls with further increase to B30, B20 being optimum blending ratio. This trend is also experienced by previous researchers [8].
The lowest value of brake thermal efficiency was noted may be due to the large amount of bio diesel supplied to the engine when compared to diesel in order to maintain the equal energy input to the engine[9,10]. The high viscosity of the blended fuels inhibits the proper atomization, fuel vaporization, and combustion. This tendency is due to the combined effect of lower calorific value, higher density, and viscosity of the blended fuel. These results are in accordance with experimental work done by the previous researchers[11,12].

Brake Specific Fuel Consumption

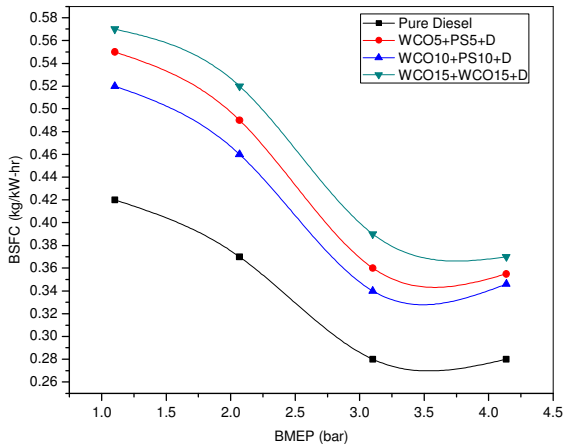

Fig.2. Brake Specific Fuel Consumption vs. Brake Mean Effective Pressure at three different combinations compared with pure diesel

The reason for the higher BSFC of biodiesel can be due to the effects of the relative fuel density, viscosity and heating value of blends.Biodiesel fuel is delivered into the engine on a volumetric basis per stroke, thus, larger quantity of biodiesel is supplied into the engine. Therefore, to produce the equal power, more biodiesel fuel is needed.
It is observed that BSFC decreases as the load increases for all the test fuels and is lowest for diesel fuel mode, since brake thermal efficiency was more than that of any percentage of biodiesel substitution; hence brake specific fuel consumption has minimum value for pure diesel operation at all loading conditions compared to different biodiesel substitution. Minimum BSFC is observed for pure diesel at full load is 0.28kg/kW-hr and for blended diesel at full load for WCOBD10+PSBD10+D(B20) is 0.346kg/kW-hr.
BSFC is the ratio between mass flow of the tested fuel and effective power[13]. The BSFC of diesel engine depends on the relationship among volumetric fuel injection system, fuel density, viscosity and lower heating value[14].

Carbon Monoxide Emission

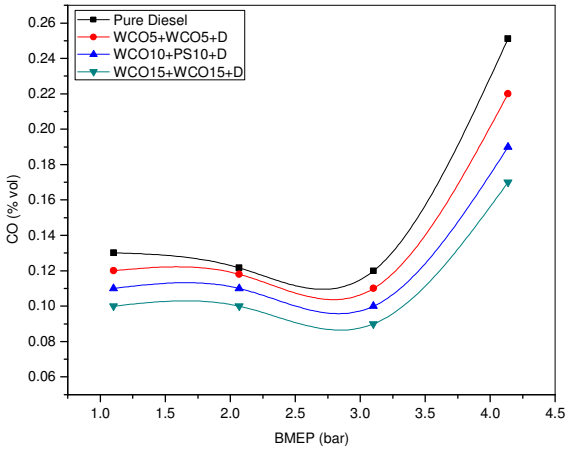

Fig.3. Variation of Carbon Monoxide Emission with Brake Mean Effective Pressure at three different combinations compared with pure diesel

It is observed that as the load increase up to 75%, the formation of CO decrease at any proportion of biodiesel blend in a dual fuel mode. In a pure diesel mode operation, due to the presence of more excess air, the carbon oxidation reaction is almost completed the considerable amount of CO is not produced until the smoke limit is reached. But as the load was increased from 75% to full load, CO formation increases rapidly, because CO is a product of incomplete combustion due to insufficient amount of air in Air Fuel mixture or insufficient time in the cycle for completion of combustion, at full load. The optimum CO content is observed for B20 at 75% load is 0.1% by volume and for diesel 0.1199% by volume.

Hydrocarbons Emission

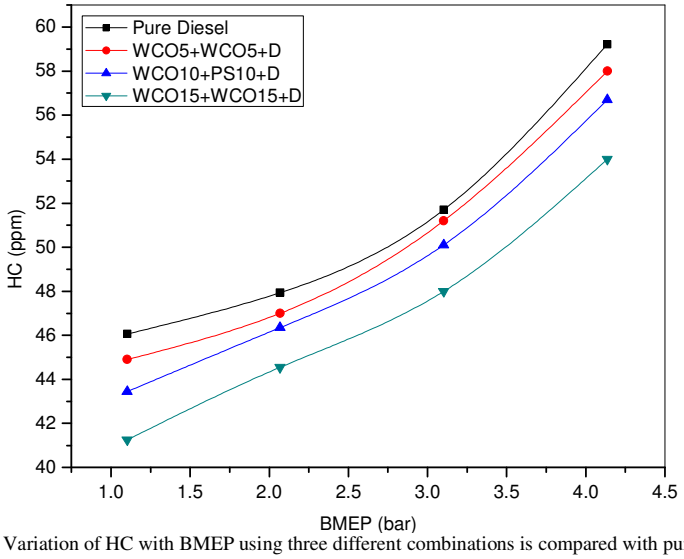

Fig.4. Variation of HC with BMEP using three different combinations is compared with pure diesel

As depicted in figure that there is a continuous increment in HC content as the load increases. HC content will be low for B30 at full load i.e. 54.01ppm, formation of HC contents will be low because of proper mixing of fuel droplets with air. But since maximum brake thermal efficiency is for B20 i.e. for 20% bio diesel substitution, an optimum blending ratio its HC content at optimal loading is found to be 50.1ppm, and for pure diesel it is 51.7ppm. Hydrocarbon emission dropped further due To the increased wall temperature[15].

NOx Emission

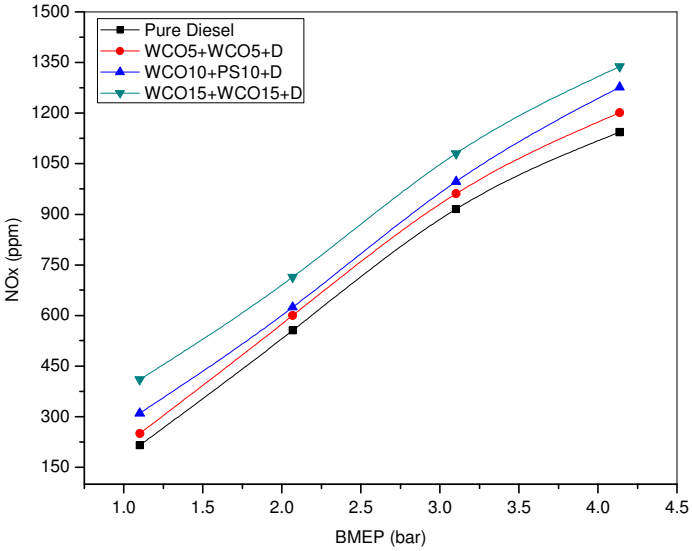

Fig.5. Variation of NOx with BMEP using three different combinations is compared with pure diesel

NOx concentration varies linearly with the load of the engine. As the load increases, the overall fuel-air ratio increases, resulting in an increase in the average gas temperature in the combustion chamber and this increases the NOx. The in-cylinder temperature was very high which leads to the formation of NOx due to the presence of excess of oxygen. High biodiesel blends substantially increased the NOx emissions. Maximum amount of NOx were found B30 i.e. 1338ppm, which is 17.06% more than that of pure diesel mode. And for optimum blend it is 1276.6ppm at full load. And for optimal load it is 996.6ppm for B20 and 915ppm for pure diesel.
The oxides of nitrogen in the exhaust emission are the combination of nitric oxide (NO) and nitrogen dioxide (NO2). The formation of NOx is highly dependent on in-cylinder temperature, oxygen concentration in the cylinder[16].

Cylinder Pressure

Peak in-cylinder pressure is higher for diesel fuel at all tests. This result can be related to the differences in the heat release pattern. The peak in- cylinder pressure mainly depends on the combustion rate in initial stages, which is influenced by the fuel taking part in uncontrolled heat release phase. High viscosity and low volatility of the biodiesel lead to poor atomization and mixture preparation with air during the ignition delay period. The peak in- cylinder pressure of biodiesel blends are lower due to the deterioration during the preparation process of air–fuel mixture as a result of high fuel viscosity. Peak in- cylinder pressure slightly decreases with the addition of biodiesel content in the blend. With the addition of biodiesel content in the blend, the peak cylinder gas pressure slightly goes away from top dead center (TDC) due to poor atomization, mixture preparation and combustion process [7]. For optimal blend and loading peak pressures ate 57.84bar and 56.65bar for pure diesel and B20 respectively.

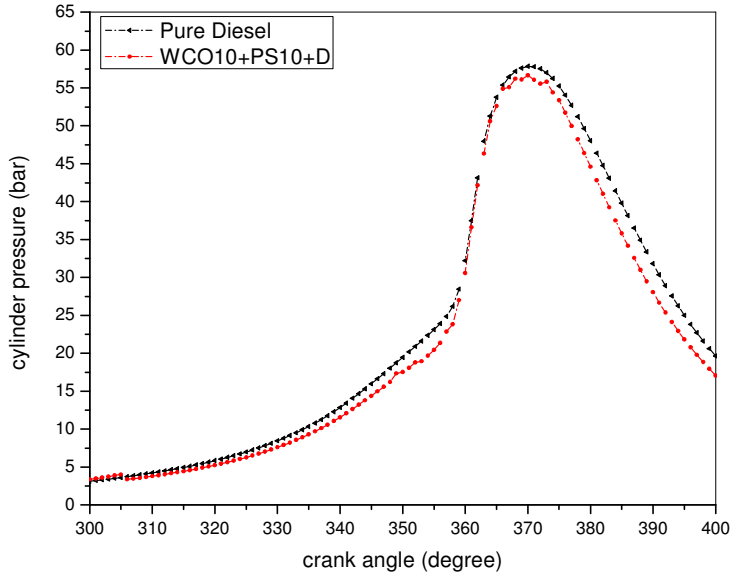

Fig.5. Cylinder pressure with crank angle compared for pure diesel and optimum blend of diesel

The peak Cylinder gas pressure of biodiesel and its blends were lower due to the deterioration during the preparation process of air–fuel mixture as a result of high fuel viscosity[17].

Net Heat Release Rate

It is one of the most important parameter to characterize the combustion process in CI engine. Using the net heat release rate it is possible to determine ignition delay, start of combustion and peak set heat release rate, because of the vaporization of the fuel accumulated during ignition delay, at the beginning a negative HR is observed and after combustion, this behavior becomes positive. After the ignition delay, premixed fuel air mixture burns rapidly, followed by diffusion combustion, where the burn rate is controlled by fuel–air mixture.

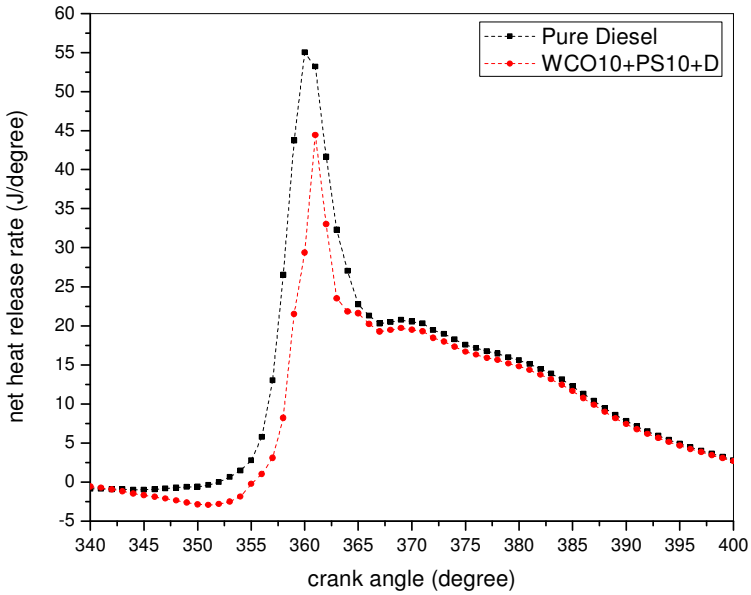

Fig.6. Net heat release rate with crank angle compared for pure diesel and optimum blends of diesel

Combustion starts earlier for biodiesel blends under all engine operating conditions (not shown in figure) and it becomes more prominent with higher biodiesel addition in the blends. The premixed combustion heat release is higher for diesel owing to higher volatility and better mixing of diesel with air [7]. Another reason may possibly be the longer ignition delay of diesel, which leads to a larger amount of fuel accumulation in the combustion chamber at the time of the premixed combustion stage, leading to a higher Net Heat Release Rate. Heat release rate for pure diesel is 53.32J/deg and for B20 is 55.00J/deg.
longer ignition delay of diesel, which leads to a larger amount of fuel accumulation in the combustion chamber at the time of the premixed combustion stage, leading to a higher rate of heat release[18].

V. CONCLUSION

- Brake thermal efficiencies for diesel, B10, B20 and B30 are 26.01%, 21.32%, 22.13% and 20.68574% respectively.
- Brake specific fuel consumption is 0.28kg/kW-hr for diesel, 0.36 kg/kW-hr for B10, 0.34 kg/kW- hr for B20 and 0.39 kg/kW-hr for B30
- It is noticed that WCOBD10+PSBD10+D(B20) blend is having higher brake thermal efficiency when compared to the other two blends and the same blend is having minimum brake specific fuel consumption, therefore it is selected as an optimum blending ratio of biodiesel in pure diesel.
- CO content for B20 at full load i.e. 0.19% by volume and HC content at full load was found to be 56.7ppm, which is 11.8% less than that of pure diesel mode.
- Maximum B30 NOx was found to be 1338ppm, which is 17.06% more than that of pure diesel mode. And for optimum blend shows 1276.6ppm.
- The peak in-cylinder pressure conditions when engine is operating under pure diesel and B20 are found to be 57.8468, 56.6573bars respectively.
- Maximum heat release for diesel which is 55.00J/deg and for biodiesel 53.3J/deg.
- Net heat release rate slightly goes away from top dead center (TDC). For diesel 360degree and for biodiesel it is 361 degree.

REFRENCES

[1] Tomasevic AV, Siler-Marinkovic SS. Methanolysis of used frying oil. Fuel Process Technol 2006;81:1–6 .www.sciencedirect.com/science/journal /03783820/81/1
[2] Narayana Reddy, J. and Ramesh A., 2006, “Parametric studies for improving the performance of a Jatropha oil-fuelled compression ignition engine”, Renewable Energy, Vol.31, No.12, pp.1994-2016.
[3] Tsolakis A, Megaritis A, Wyszynski ML, Theinnoi K. Engine performance and emissions of a diesel engine operating on diesel-RME (rapeseed methyl ester) blends with EGR (exhaust gas recirculation). Energy 2007; 32:2072-80.

[4] R. Anand, G.R.kannanb, P.karthikeyan, A study of the performance emission and combustion characteristics of a DI diesel engine using waste cooking oil methyl ester-ethanol blends, proceedings of the ASME 2012 international mechanical engineering congress & exposition imece2012 november 9-15, 2012, houston, texas, USA.
[5] Narayana Reddy, J. and Ramesh A., 2006, "Parametric studies for improving the performance of a Jatropha oil-fuelled compression ignition engine", Renewable Energy, Vol.31, No.12, pp.1994-2016.
[6] Huseyin Aydin, Cumali IlKilic, 2010, "Effect of ethanol blending with biodiesel on engine performance and exhaust emissions in a CI engine", Applied Thermal Engineering, Vol.30, pp.1199-1204.
[7] Gumus *Automotive Division, Department of Mechanical Education, Marmara University, Ziverbey 34722, Istanbul, Turkey]
[8] Jegadheesan.C, Somasundaram.P, Meenakshipriya.B,Vignesh.U.P. "Effect of DEE Injection in Pongamia Pinnata Biodiesel Fulled CI Engine using Hydrogen as Secondary Fuel" Advanced Materials Research Vol. 768 (2013) pp 188-194 Online: 2013-09-04 © (2013) Trans Tech Publications, Switzerland
[9] Senthilkumar M, Remesh A, Nagalingam B. Complete vegetable oil fueled dual fuel compression ignition engine. SAE technical paper 2001-28-0067.
[10] Nazar J, Ramesh A, Sharma RP, Performance and emission Studies of use SVO and bio diesel from different Indian feed stock, SAE technical paper 2004-28-071.
[11] Sukumar Puhan N, Vedaraman G, Sankaranarayanan Boppana V, Bharat Ram. Performance and emission study of Mahua oil (Madhuca Indica oil) Ethyl ester in a 4-stroke natural aspirated direct injection diesel engine. Renew Energy 2005; 30:1269-78.
[12] Suresh Kumar K, Velraj R, Ganesan R. Performance and exhaust emission characteristics of a C.I engine fueled with Pungamia Pinnata Methyl Ester (PPME) and its blends with diesel, International Journal of Renew Energy 2008; 33: 2294.
[13] M. Mofijur, H.H. Masjuki, M.A. Kalam, A.E. Atabani, Department of Mechanical Engineering, University of Malaya, 50603 Kuala Lumpur, Malaysia. Energy 55 (2013) 879e887
[14] Qi DH, Chen H, Geng LM, Bian YZ. Experimental studies on the combustion characteristics and performance of a direct injection engine fueled with biodiesel/diesel blends. Energy Convers Manag 2010;51:2985e92.
[15] http://www.palmoilworld.org/about_palmoil.html
[16] American Journal of Engineering Research (AJER) e-ISSN : 2320-0847 p-ISSN : 2320-0936 Volume-03, Issue-02, pp-184-190 www.ajer.org
[17] Kumar MS, Ramesh A, Nagalingam B. An experimental comparison of methods to use methanol and Jatropha oil in a compression ignition engine. Biomass Bioenergy 2003;25:309–18.
[18] M. Gumus, Automotive Division, Department of Mechanical Education, Marmara University, Ziverbey 34722, Istanbul, Turkey, Fuel 89 (2010) 2802–2814

International Journal of Automotive and Mechanical Engineering
ISSN: 2229-8649 (Print); ISSN: 2180-1606 (Online);
Volume 14, Issue 4 pp. 4634-4648 December 2017

DOI: https://doi.org/10.15282/ijame.14.4.2017.4.0365

Analysis of hydrogen enriched treble biofuel blended with diesel for performance, emission and combustion characteristics on CI engine

H.N. Md. Fakhruddin[1], Mohammed Yousuf Ali[2] and M. Manzoor Hussain[3]

[1]Mechanical Engineering Department,
Methodist College of Engineering and Technology - Hyderabad – 500001, India
Email: mfhnn@yahoo.com; Phone No. +919963584450
[2]Avanthi Institute of Engineering & Technology
Gunthapally Village, Hayathnagar (M), RR Dist. Hyderabad-India
Email: yousufonline@yahoo.com;
Phone No. +919866301410
[3]JNTUH College of Engineering Kukatpally, Hyderabad (Autonomous)
Email: manzoorjntu@gmail.com;
Phone No. +919848211005

ABSTRACT

The need of the hour is to look forward to alternative fuels to swipe out the dependence on fossil fuels, as biofuels from various feedstocks are being experimented worldwide. However, it is difficult to implement biodiesel from a single feedstock to replace the existing fossil fuels. It is reliable to obtain biodiesel from local feedstock and to make multiple biodiesel mixtures blended with diesel. The present work relies more on biofuels and acts as a step towards fossil fuel-free engine or at least to snatch the lion's share of the fossil fuels. In this contest, the experiment was carried out by using treble biofuels i.e., WCOBD + PSBD + Bio-hydrogen at different injection pressures (i.e., 200bar, 225bar and 250bar) and compared them with a similar engine that utilised fossil fuel as the stand-alone fuel. The mixture ratios were B10, B20 and B30 and the enrichment of hydrogen was done at 4lpm, 6lpm and 8lpm. The results showed that the brake thermal efficiency of dual biofuel blended diesel decreased as compared to that of the base fuel and increased with hydrogen enriched biodiesel. Hence, the brake specific energy consumption decreased for the hydrogen enriched fuel and the exhaust emissions of CO and CO_2 were reduced, however, NOx showed an increasing trend as usual.

Keywords: Bio-hydrogen, waste cooking oil biodiesel, palm biodiesel, treble blend and injection pressure.

INTRODUCTION

Nowadays, alternative fuels for diesel engines is an emerging topic among researchers due to decreasing petroleum reserve and hazardous health and environmental effects of engine exhaust gases. Edible-based biodiesel sources pertaining to food chain are not considered feasible due to price fluctuation, and land limitation, also, they are contrary to the current social movement and energy policies, therefore, their industrial expansion has been limited [1]. Biomass sources, particularly vegetables oils, have attracted much attention as alternative energy sources due to easy availability, renewable and cleaner burning than fossil fuels [2, 3]. In addition, biodiesel has lower sulphur and aromatic

contents and net carbon dioxide (CO_2) emission. Biodiesel can be used immediately in diesel power generators without many modifications as it can be mixed at any proportion with diesel [3]. Besides that, biodiesel cost is a major concern for its commercialisation. Biodiesel produced from vegetable oil or animal fat is 10-15% more expensive than petroleum-based diesel fuel. The feedstock cost comprises approximately 70-95% of total operating costs of a biodiesel plant [2]. Locally available biofuel should be an alternative source for petroleum and able to be made in any local area [4]. Waste cooking oil (WCO) is one of biodiesel sources, unlike the high speed diesel (fossil fuel) that may cause harm in future. WCO is a renewable fuel extracted from the residual waste of used cooking oil. It is very cheap, non-volatile, safe to store, releases comparatively less carbon dioxide and has a cleaner exhaust. Depending on its source and availability, WCO costs less than neat vegetable oils. Hotels and other public eateries are the major contributors to WCO production. Over cooked WCO can cause adverse health issues like cataracts, liver damage and jaundice and can damage the immune system in children. Recycling is the best way to use WCO properly without compromising its adverse effects. Animal feed production is a major part of recycled WCO and a small portion is used to manufacture soaps and biodegradable lubricants. Consumption of food of animal origin like milk, meat, poultry and other products may cause undesirable contaminants to enter the human body and pose serious long term health hazards. Therefore, a major portion of the recycled WCO is available to be used as an alternative fuel in compression ignition (CI) engines after suitable modifications in the fuel properties [5, 6]. Palm oil is semi-solid at room temperature (20^{o}C). The liquid part may be physically separated from the solid part of palm oil via fractionation method. After fractionation, it is known as palm olein, which is commonly sold as cooking oil, while the solid fat portion is known as palm stearin, which is normally used to formulate trans-free fats such as margarine, soap, shortening and vegetable ghee.

Many refined virgin vegetable oils, such as palm, canola, soybean and corn, have been used to produce biodiesel to substitute petroleum diesel. Due to the high cost of cooking oils, palm stearin (PS) may become a promising alternative feedstock for biodiesel production. PS is the solid fraction obtained by fractionation of palm oil after crystallisation at a controlled temperature. It is not used directly for edible purposes due to its high melting point that ranges from 44 to 56 ^{o}C [7] . The physical characteristics of PS differ significantly from those of palm olein. The high degree of saturation of PS poses problems in edible fats manufacturing as it confers low plasticity to the end product, thus, limiting the commercial exploitation of the material [7]. Renewable fuels are those produced from renewable resources in nature. Examples include biofuels e.g., ethanol and methanol from clean energy, vegetable oil used as fuel, carbon dioxide or biomass, biodiesel and hydrogen fuel (when produced with renewable processes). An important future application of hydrogen could be as an alternative for fossil fuels, only once the oil deposits are depleted. However, this application relies on the storing techniques development to enable a proper storage, effective distribution and good hydrogen combustion. If the cost of hydrogen production and distribution decreases, then end-user technologies could pick up and hydrogen fuel could be entering the market in 2020 [8].

Fossil energy source cannot be regenerated and will be exhausted with increasing fossil fuel consumptions. Hydrogen energy is a new energy source with abundant reserves and does not depend on fossil fuel. Moreover, hydrogen energy conforms to the requirement of the worldwide environmental protection, thus, receives more attention all over the world. Hydrogen may be produced in biosystem, which includes two ways of light-drive process and anaerobic fermentation, the former is theoretically a perfect

process that transforms solar energy into hydrogen by photosynthetic bacteria. However, due to low utilisation efficiency of light and difficulties in designing light reactor, this method is hard to be applied in practice. The latter carries out anaerobic fermentation by hydrogen, which has many advantages, such as rapid, simple, easy operation and hydrogen production by renewable resources and organic waste [9]. Compared to the light-drive reactor, anaerobic fermentative hydrogen-production is easier to conduct and suitable for the demands of sustainable development strategy. At present, the yield and rate of hydrogen production are still low. With the rapid development of molecular biological technology, the directional heredity reconstruction for microbe becomes the new research hotspot, which can radically change microbial biological properties and metabolic modes to cultivate superior microbial strains more beneficial to bio-hydrogen production, economise costs and increase production efficiency and yield, and provide more efficient pathways for the exploitation and popularisation of hydrogen energy sources [10]. The objective of the paper is to experimentally analyse the performance, emission and combustion characteristics of diesel engine that runs on treble biofuels blended with diesel. Among them is hydrogen, that will boost the combustion due to its high calorific value and flame velocity.

MATERIALS AND METHODS

Engine Specifications

A performance test was carried out in a research engine test rig as shown in Figure 1 and the specification is tabulated in Table 2. The uncertainties in the measured parameters in the present study are given in Table 1.

Table 1. Uncertainties in measured experimental variables.

Make	Kirloskar
Number of cylinder	1
Number of stroke	4
Fuel	Diesel
Cooling Type	Water
Model	TV1
Stroke length	110 mm
Bore diameter	87.5 mm
Volume	661 cc
Power	3.5 kw
Speed	1500 rpm
Compression ratio	17
Injection pressure	Variable injection pressure
Range	200bar to 250bar
Loading unit	Eddy current
Dynamometer type	Eddy current & Water cooled

Variation of Injection Pressure

The experiment was conducted at various injection opening pressures (IOPs) to find the optimum injection pressure at which a good engine performance can be obtained. Three different injection pressures i.e., 200bars, 225bars and 250bars were set by rotating the compression spring load screw until the associated pressure sensor displayed the desired value on the monitor.

Table 2. Engine specification.

Particulars	Specifications	Uncertainty
Dynamometer	Eddy current dynamometer of Model AG10, Make Saj Test Plant Pvt. Ltd.	Speed ±1% and torque ±0.4%
Load sensor	Make Sensortronics, Model 60001.	±0.2%
Air flow transmitter	Make Wika, Model SL1 Range 0- 25mbar	± 0.5%
Fuel flow transmitter	Differential pressure type-Make Yokogawa – Model EJA110E-S1-JMS5J-912NN Made in Japan.	±0.065%
Piezo Sensors	Make PCB Piezotronics, Model SM111A22 Diaphragm stainless steel type & hermetic Sealed Range 0-350 bar	±0.1%
Crank angle sensor	Make Kubler-Germany, Model 8.3700.1321.0360.	± 0.2%
Temperature sensor	Make Radix, Type RTD, PT100 measures engine water inlet temperature, engine water outlet temperature, calorimeter water inlet temperature and calorimeter water outlet temperature Range 0-250 ^{o}C	±1%
	Make Radix, Thermocouple type K (Chromel /Alumel) measures Exhaust gas temperature at calorimeter inlet and outlet Range 0-400^{o}C	±0.8%
Rotameter	Eureka model PG-1 to 21 For Calorimeter, range from 25-250 LPH, For Engine, range from 40-400 LPH	±2%

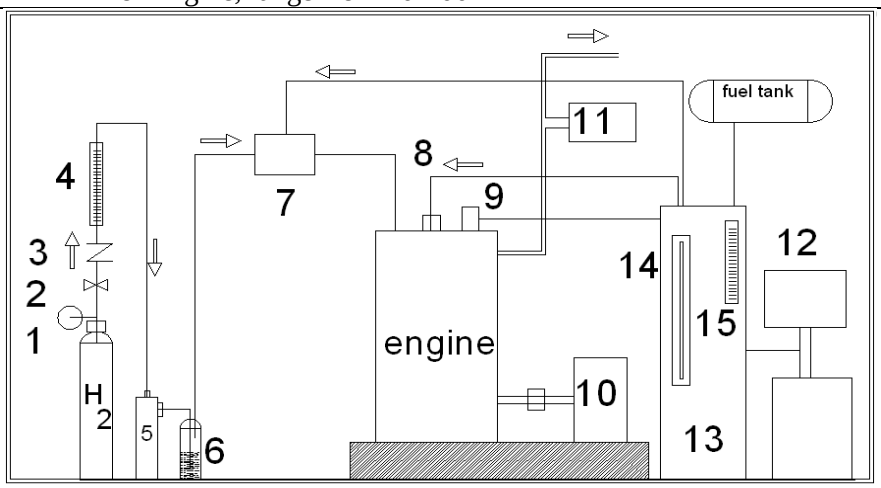

1. Hydrogen cylinder with pressure gauge
2. Pressure regulating valve
3. Non return valve
4. Hydrogen flow meter
5. Flash back arrester
6. Flame trapper
7. Mixing box
8. Fuel injector
9. Cylinder pressure sensor
10. Eddy current dynamometer
11. Exhaust gas analyser
12. Computer interface
13. Control panel
14. Manometer
15. Burette

Figure 1. Schematic diagram of the experimental setup.

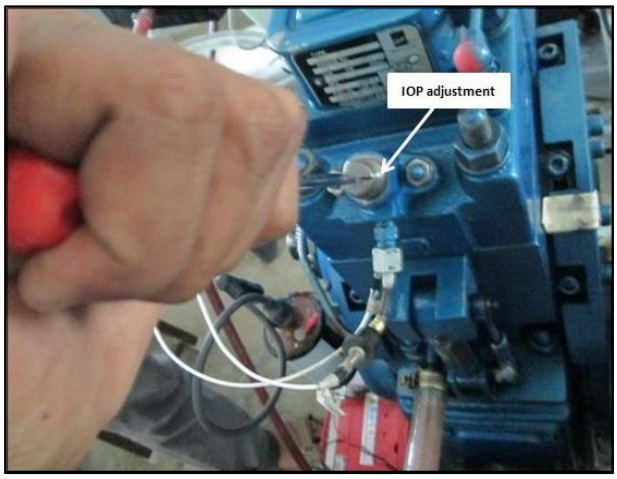

Figure 2. Physical experimental setup for variation in Injection Opening Pressure (IOP).

Mixing of Hydrogen with Air

Figure 3 shows the modified engine for direct induction of hydrogen through the inlet manifold and the hydrogen pressure was controlled directly by the pressure regulator provided at the hydrogen cylinder opening. The constant speed operation diesel was controlled by the governor mechanism provided in the engine.

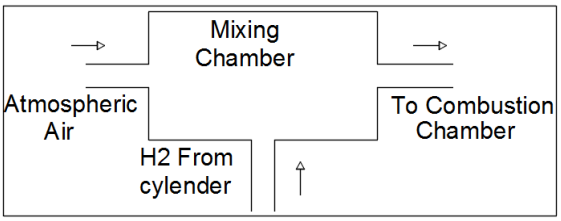

Figure 3. Mixing chamber of hydrogen and air.

Experimentation

The mass flow rate of the blended fuel was calculated via volumetric basis by using a burette and a stop watch. The exhaust gas temperature was measured by using a thermocouple attached with a digital temperature indicator, while the pressure was recorded by using a piezo pressure sensor fitted in the head of the engine cylinder.

Experimental Procedure

In the first step of experiment, the engine was operated with pure diesel and its performance and emission characteristics were calculated for three different injection opening pressures. In the second step of experiment, the engine was operated to run with emulsions made with 5WCOBD5PSBD90D, 10WCOBD10PSBD80D and 15WCOBD15PSBD70D for three different injection opening pressure ratios. The 10WCOBD10PSBD70D blend was optimal among those tested in terms of BTE and BSFC. In the third step of experiment, the engine was operated to run with optimal emulsion of the above said biodiesels blended with diesel and compressed hydrogen gas (to further enhance combustion) introduced by induction through the intake manifold at three different flow rates of 4lpm, 6lpm and 8lpm as shown in Table 3. The performance results and emission parameters were compared.

Table 3. Composition of fuel mixtures and test matrix.

Spell of Experiment	Feedstock: % by volume			Cycle of Experiment for different Injection Opening Pressures (IOPs)			H_2 lpm
	Pure diesel	Waste cooking oil biodiesel	Palm Stearin Biodiesel	A	B	C	
1	100	-	-	200bar	225bar	250bar	-
	90	5	5	200bar	225bar	250bar	
2	80	10	10	200bar	225bar	250bar	-
	70	15	15	200bar	225bar	250bar	
				200bar	225bar	250bar	4
3	80	10	10	200bar	225bar	250bar	6
				200bar	225bar	250bar	8

Table 4. Fuel properties for pure diesel, biodiesels and diesel blend of dual biodiesel

Property	Diesel	WCOBD	PSBD	B30 (15WCOBD+15PSBD+70D)
Density (kg/m^3)	832	878	898	848.8
Viscosity at 40˚C (mm^2/s)	2.6	3.35	4.12	2.94
Calorific value (MJ/Kg)	46.049	45.080	39.507	44.922

Table 5. Energy equivalent and energy share.

Strategy of Experiment	Load % age	Energy Equivalent of diesel KW	Energy Equivalent of WCOBD KW	Energy Equivalent of PSBD KW	Energy Equivalent of H_2 KW	Diesel Energy Share (%)	WCOBD Energy Share (%)	PSBD Energy Share (%)	H_2 Energy Share (%)
225 bar									
10WCOBD +10PSBD +80D+ $H_2$4lpm	50	8.406	1.763	1.545	0.655	67.9	14.2	12.4	5.2
	75	9.611	2.016	1.766	0.655	68.4	14.3	12.5	4.6
	100	11.2	2.351	2.060	0.655	68.8	14.4	12.6	4.0
10WCOBD +10PSBD +80D+ $H_2$6lpm	50	7.081	1.485	1.301	0.983	65.2	13.6	11.9	9.0
	75	8.406	1.763	1.545	0.983	66.2	13.8	12.1	7.7
	100	9.611	2.016	1.766	0.983	66.8	14.0	12.2	6.8
10WCOBD +10PSBD +80D+ $H_2$8lpm	50	6.728	1.411	1.236	1.31	62.9	13.2	11.5	12.2
	75	8.406	1.763	1.545	1.31	64.5	13.5	11.8	10.0
	100	10.350	2.171	1.902	1.31	65.7	13.7	12.0	8.3

The calorific value of diesel is higher than its diesel blends due to high oxygen content than fossil diesel [11]. Two main factors that are responsible for higher viscosity and density of biodiesel are large molecular weight and complex chemical structure [12-15]. Table 4 reveals that PS biodiesel has less calorific value and lower viscosity and density than WCO biodiesel. For different hydrogen flow rates i.e., 4lpm, 6lpm and 8lpm, the mass flow rate of hydrogen at all loads in terms of kg/sec was calculated. Then, the energy share of hydrogen (kW) = mass flow rate of hydrogen (kg/sec) × lower calorific value of hydrogen (kJ/kg). Similarly, the energy share for diesel and biodiesel fuels were calculated by using the formula; energy share (kW) = mass flow rate of main fuel (kg/sec) × lower calorific value (kJ/kg) as shown in Table 5 for 225 bar injection opening pressure.

RESULTS AND DISCUSSION

Brake Thermal Efficiency

Brake thermal efficiency is the indication of the engine ability to transform energy input to useful work. Figure 4 and 5 show the brake thermal efficiency of all test fuels at different injection opening pressures (IOPs). BTE for pure diesel was more than the blends. The slight variations in the thermal efficiency of the biodiesel blends were mainly due to the lower calorific value of WCOBD and PSBD when compared with diesel [16, 17]. Furthermore, the higher viscosity and slow vaporisation of biodiesel present in these blends led to inferior combustion of biodiesel which caused the brake thermal efficiency to be low [18-20] . BTE was lower for B10 and increased with the blending ratio of B20, thereafter, it fell with further increase to B30. The optimum blending ratio was B20. For all IOPs, BTE increased with the increase of load until 75%, thereafter, decreased at full load. Hence, the optimum loading was 75%. In Figure 5, the biodiesel blends in diesel were plotted against different IOPs. From the figure, 225bar was the optimum IOP with maximum BTE for baseline fuel and B20 at 27.44% and 24.31%, respectively, which were lower than the baseline fuel i.e., diesel by 12.06%. The optimised values i.e., B20 at 225bar IOP and 75% loading were further tested with hydrogen induction at different rates of admission.

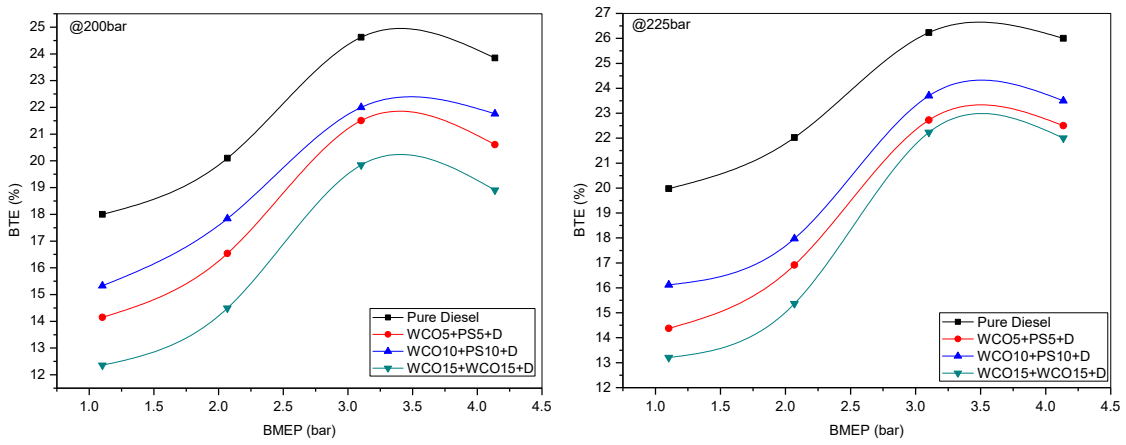

Figure 4. Variation brake thermal efficiency versus brake mean effective pressure at 200 bar and 225 bar injection opening pressures for dual biodiesel blended in diesel.

Figure 6 shows that the peak performance was at 75% load i.e., 31.3% with 6lpm H_2. The engine conditions became unstable at 100% loading conditions with reduction in BTE to 29.8%. Therefore, the optimal loading was 75%, this trend was also experienced by previous researchers [21]. The reduced power production faced by the biodiesel combustion was resolved by hydrogen that assisted dual biodiesel blends of diesel fuel combustion, examined as a promising solution to enhance biodiesel combustion processes [22]. With the induction of hydrogen in dual biodiesel blended with diesel, the brake thermal efficiencies were 29.31%, 31.3%, 30.5% for 4, 6, and 8lpm, respectively, which were 20.56%, 28.75% and 25.46% more compared to biodiesel. Large amount of heat energy was released when the injection pressures were increased in the CI engine, thereby, the ignition delay was reduced and the fuel became completely burnt [23]. Figure 7 shows the increase of brake thermal efficiency from IOP of 200bar to 225 bar. With further increase of injection IOP i.e., to 250 bar, the ignition delay period decreased, which in

turn decreased the homogeneous mixing that led to incomplete combustion and less brake thermal efficiency.

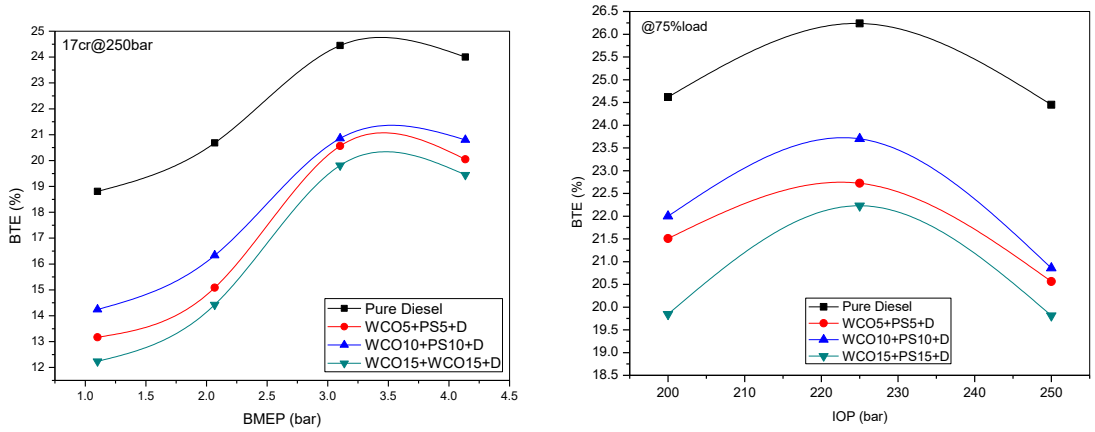

Figure 5. Variation brake thermal efficiency versus brake mean effective pressure at 250 bar and all injection opening pressures for dual biodiesel blended in diesel.

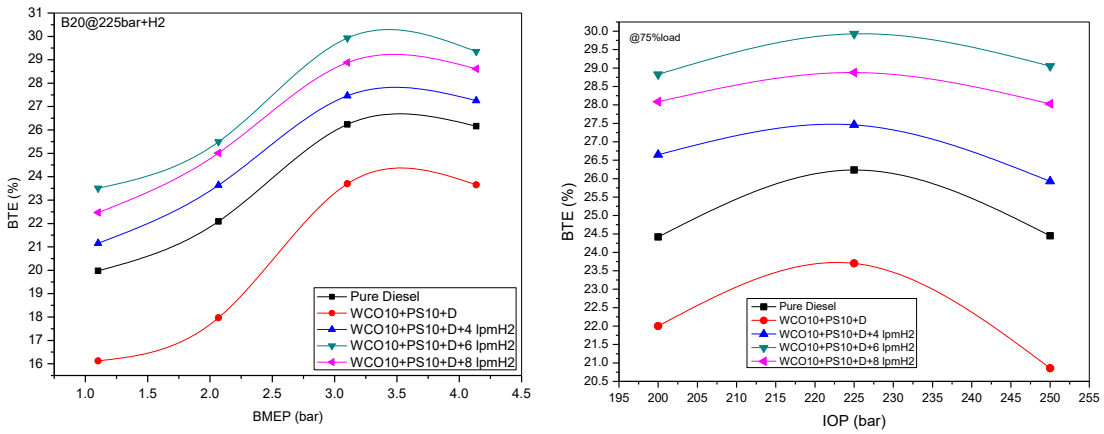

Figure 6 Variation brake thermal efficiency versus brake mean effective pressure at 225bar and injection opening pressure at 75% load for dual biodiesel blended in diesel along with hydrogen induction.

Brake Specific Energy Consumption

Brake specific fuel consumption is the ratio between mass flow rate of the tested fuel and effective power [11]. The brake specific fuel consumption of CI engine depends on the relationship among volumetric fuel injection system, density of fuel, lower heating value and viscosity [24]. Brake specific energy consumption is a more authentic parameter for comparing fuels with different calorific values and densities. This energy consumption can be obtained as the product of brake specific fuel consumption and calorific value of the fuel. The energy equivalents and energy shares are shown in Table 5 for B20 along with 4, 6 and 8 lpm rate of hydrogen induction.

The variation of brake specific energy consumption (BSEC) with brake mean effective pressure (BMEP) for different fuels is presented in Figure 7. The reason for the higher BSEC of biodiesels in Figure 7 can be attributed to the combined effects of the three variables i.e., relative fuel density, viscosity and heating value of the blends [25]. Biodiesel fuel was administered in the engine on a volumetric basis per stroke, thus, larger quantities of biodiesel were nourished into the engine. Hence, to produce the same power,

excess biodiesel fuel was needed due to its less calorific value compared to diesel fuel [26, 27]. BSEC reduced with the increase in injection pressure for all fuels tested. This was due to the better atomisation at higher injection pressure which exhibited more surface area of fuel droplets to the high temperature air salient to complete fuel combustion [28]. Further increase in IOP, i.e., 250 bar, decreased the ignition delay, which in turn decreased homogeneous mixing possibility and led to incomplete combustion, hence, more BSEC. A similar trend was observed by previous researchers [11]. The hydrogen-assisted combustion dual biodiesel blends showed a decrease in BSEC with increasing flow of hydrogen, which can be attributed to the uniform mixing of hydrogen with air and diffusivity and led to the near complete combustion of the fuel. For this reason, the fuel consumption was decreased.

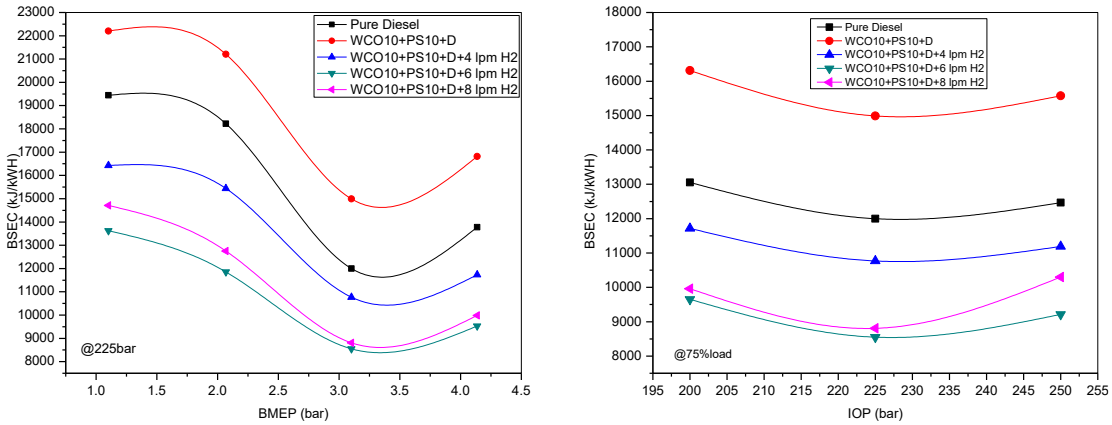

Figure 7 Variation brake specific energy consumption versus brake mean effective pressure at 225bar and for injection prresure at 75%load for dual biodiesel blended in diesel along with hydrogen induction at three different rates.

Emission Analysis

The emission constituents considered were carbon monoxide (CO), oxides of nitrogen (NO_x) and unburned hydrocarbon (HC). The effect of IOP on the emission constituents for Diesel+WCOBD+PSBD blends and diesel for different test pressures are shown in Figure 8 and 9. Features like higher cetane number than diesel and less sulphur and more oxygen, are environmentally friendly and can reduce HC and CO in the exhaust gas. For these reasons, different studies have been conducted on biodiesel blended with diesel and the results show that emission concentration varies and depends on biodiesel source and engine condition [14, 20, 29]. Hydrogen possesses many superior combustion and emission characteristics than other liquid or gas fuels. For instance, due to the omission of the carbon atom, hydrogen combustion does not produce any harmful emissions such as HC, CO, sulphur oxides, or organic acids [30].

Carbon Monoxide Emission

Figure 8 shows the effect of IOP on CO for biodiesel and biodiesel blends of diesel. The CO emission reduced with increased IOP. This may be due to the fuel being atomised into very fine droplets and more surface areas were accessible for combustion, which resulted in the formation of a good quality fuel mixture that caused a complete combustion [28]. Whereas for pressure of 250bar, the performance drop led to an incomplete combustion which resulted in the increase of CO emission at all loads. Consistent and

tangible reduction in CO emission were found at 75% load with 225 bar pressure for dual biodiesel blended with diesel 0.08% and the reduction percentages in the CO emission were 7.5%, 26.257% and 12.5% with 4 lpm, 6 lpm and 8 lpm of H_2 induction to emulsified fuel. The primary reason for the reduced CO emission was due to the decrease in the amount of total carbon in the inducted fuel.

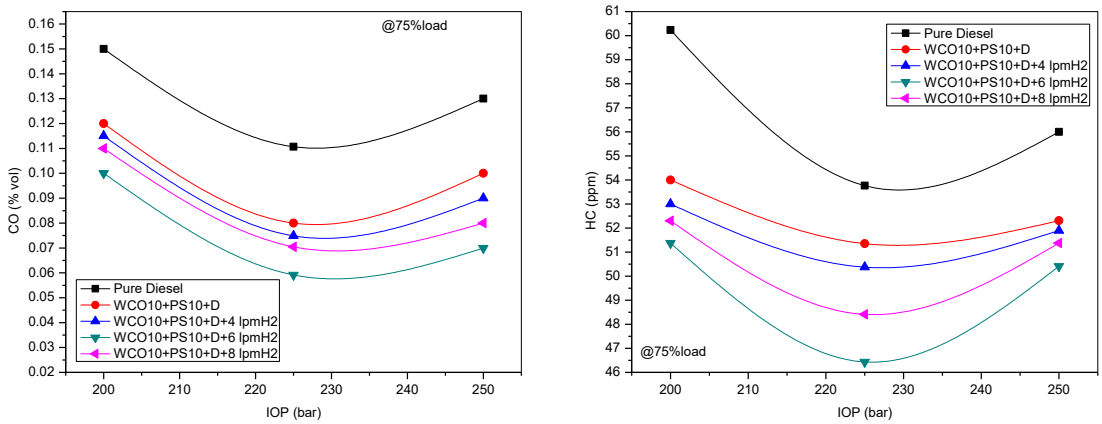

Figure 8. Variation of carbon monoxide and unburned hydrocarbon versus injection opening pressure at 75% load for dual biodiesel blended in diesel along with hydrogen induction at three different rates.

Unburned Hydrocarbon

The unburned hydrocarbon of tested engine with different injection pressures for the pilot fuel, base line fuel and fuel with hydrogen induction is shown in Figure 8. HC emission reduced with increased IOP of engine for base line fuel, biodiesel blended diesel mixture and biodiesel blended diesel mixture with hydrogen. HC emission increased for all test fuels with load, and there was a reduction in HC emission for biodiesel compared to diesel due to the presence of oxygen in its molecular structure that led to an efficient combustion [29, 31]. The decreasing trend of UHC was observed with increasing %age of H_2 substitution when compared with pure diesel because of its high flammability limit and calorific value [32]. At 225 bar, proper atomisation and mixing with maximum %age of burnt carbon content were achieved and UHC formation was greatly minimised.

Oxides of Nitrogen (NO_x) **Emission**

Comparison of NO_x emission for different injection pressures of the test fuels is illustrated in Figure 9. The NO_x emission level increased with increasing injection pressure because of a faster combustion and greater cylinder gas temperature due to peak pressure which occurred at the earlier crank angle [19, 33]. At pressure of 225bar, the NO_x emissions were 802.1 ppm, 890 ppm, 952.16 ppm, 1020.12 ppm and 1103.52 ppm for base line fuel, dual biodiesel blends of diesel, emulsified fuel with 4lpm, 6lpm, and 8lpm of H_2 induction, respectively. But this could be potentially established by the use of EGR technique and emulsified biodiesel as presented by Korakianitis et al. [34]. Nevertheless, a contrary trend was also observed by other researchers who claimed that the NO_x emissions were smaller for dual fuel combustion, particularly at medium and high engine loads, and they attributed it to the combined effects of hydrogen incantation and late pilot fuel injection, that contributed to low temperature combustion [35, 36]. Experimental and simulated analysis of inline cylinder pressure for B20+6lpm H_2. Pressure and temperature contours for bio-diesel 10WCOBD+10PSBD+80D+6lpm H_2. From Figure 10, it can be

seen that the experimented and simulated peak pressures for 10WCOBD+10PSBD+80D+6lpm H_2 were 68.95bar and 70.87bar, respectively, with a variation of approximately 2.78%.

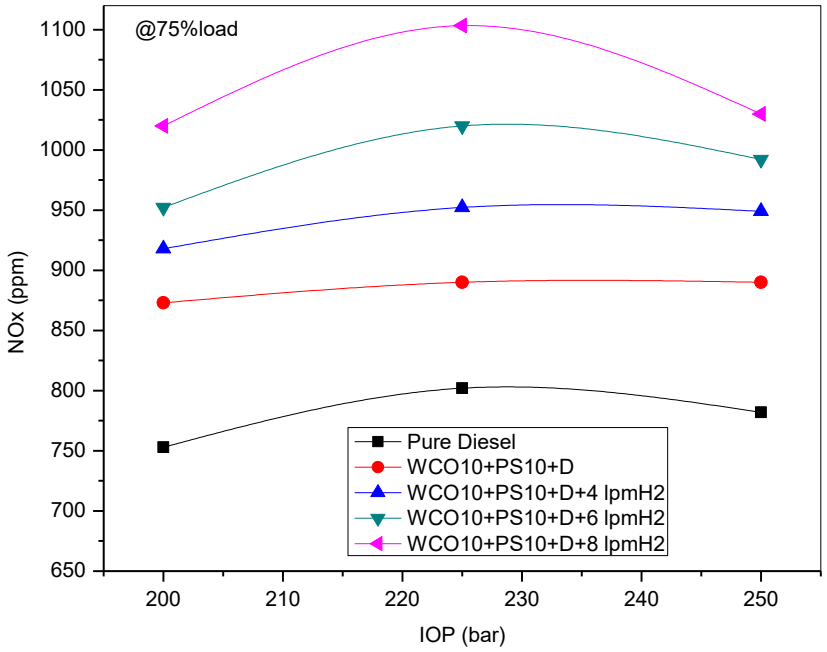

Figure 9. Variation of oxides of nitrogen versus injection opening pressure at 75% load for dual biodiesel blended in diesel along with hydrogen induction at three different rates.

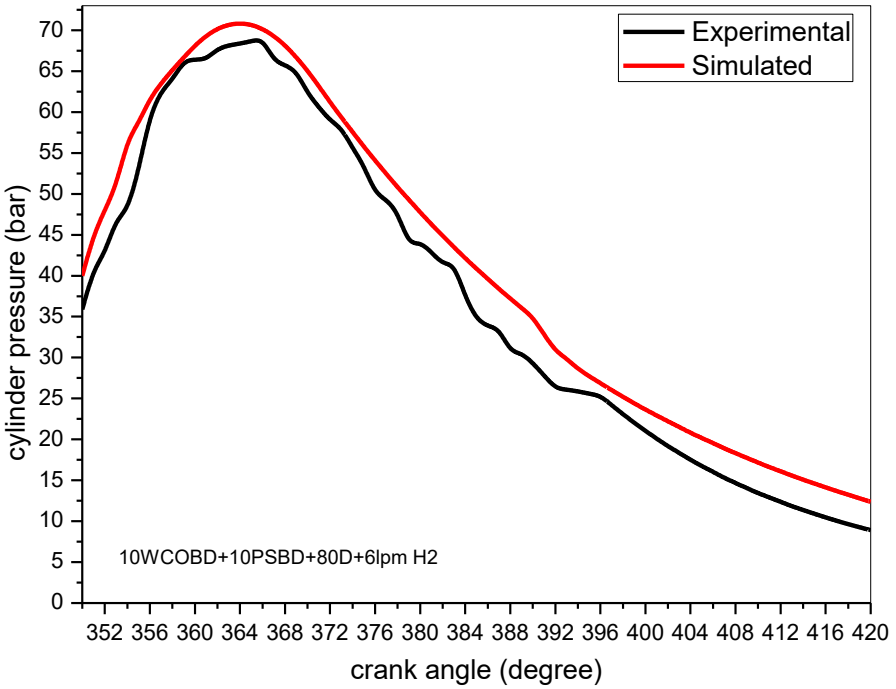

Figure 10. Comparison of simulated and experimental values of peak in-cylinder pressures against crank angles for 10WCOBD+10PSBD+80D+6lpm H_2.

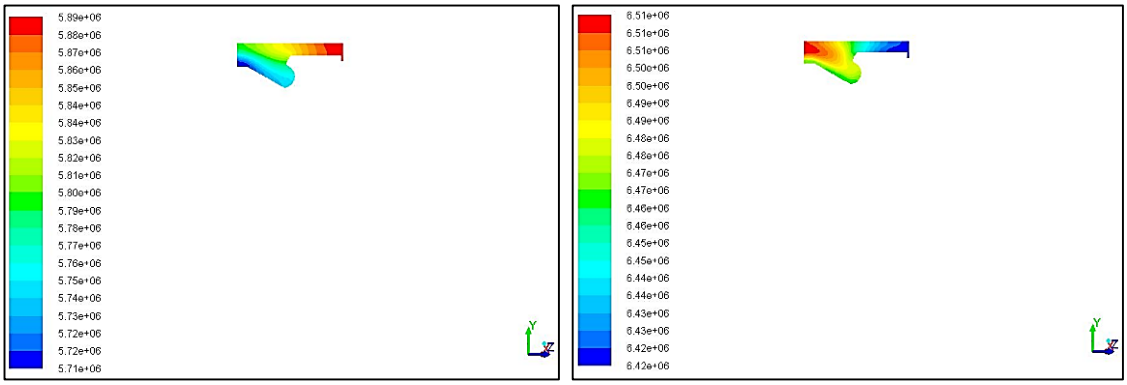

(a) (b)

Figure 11. Pressure contour at crank angle (a) 352 degree and (b) 364 degree for 10WCOBD+10PSBD+80D+6lpm H_2.

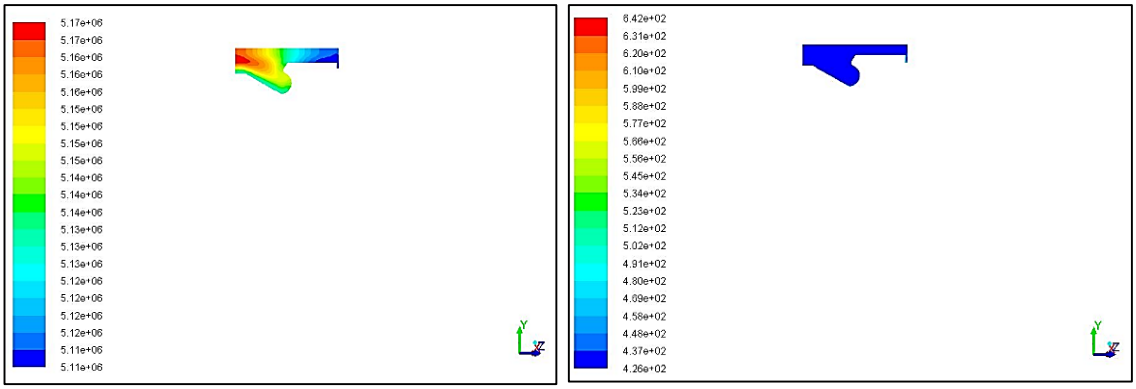

(a) (b)

Figure 12. Pressure and temperature contours at crank angle (a) 372 degree and (b) 364 degree, respectively for 10WCOBD+10PSBD+80D+6lpm H_2.

CONCLUSIONS

Based on the experimental investigation to study the performance, emission and combustion characteristics of a single cylinder diesel engine using treble biodiesel blended with conventional diesel, which included hydrogen as the third biofuel to assist the combustion, the following conclusions were drawn:

- Emulsifying WCOBD and PSBD in conventional diesel to 10WCOBD10PSBD80D proportion; thermal efficiency decreased by 12.06%.
- BSEC was increased by 24.94% i.e., 11997.22kj/kwh for diesel and 14990.49kj/kwh for emulsified fuel
- BSEC for optimal blend i.e., B20+6lpm H_2 was 8550.89kJ/kwh, which was less than diesel.
- CO emission decreased by 27.27% i.e., for diesel CO was 0.11% and emulsified fuel was 0.08%. HC emission for diesel was 53.768ppm and biodiesel blend was 51.354% (decreased by 4.48%). No_x showed an increasing trend, 802.14ppm for diesel and 890ppm for biodiesel blend, which was 10.95 % more.
- As emulsified fuel was assisted by hydrogen induced combustion, the performance was increased with respect to the base line test fuel i.e., diesel, BTE being 26.2354% and 29.9314%, respectively, for an increase of 14.08%. BSEC decreased by 28.72%.

- CO emission decreased i.e., 0.05915% and 011071% for hydrogen assisted and pure diesel, respectively. HC emission decreased by 13.63%. No_x increased by 37.53% i.e., 1103.52ppm and 802.144 ppm, respectively.
- Best injection opening pressure was 225bar, where all parameters were optimised.
- Data acquisition was done after normalising the engine and 75% loading condition for all test fuel was optimum.
- Hydrogen induction was done at three different rates and 4lpm was the ideal rate, where the operating condition was optimum.
- Induction of hydrogen inline of biodiesel had outlaid the performance of diesel as a stand-alone fuel. Difficulty in storage and transportation only.

Maximum utilisation of WCO is recommended to convert it to biodiesel, with a neat disposal to ovoid spill that can damage the environment. Hydrogen induction enhances engine performance.

ACKNOWLEDGEMENTS

Author acknowledge contribution of Methodist College of Engineering & Technology for sparing time and money behind the research finding and Dr. S. Azam Pasha Quadri at Lords Institute of Engineering & Technology for providing logistical support.

REFERANCES

[1] Adam IK, A. Aziz AR, Yusup S. Determination of diesel engine performance fueled biodiesel (rubber seed/palm oil mixture) diesel blend. International Journal of Automotive and Mechanical Engineering. 2015;11:2675-85.

[2] Pai PS, Rao BS. Artificial neural network based prediction of performance and emission characteristics of a variable compression ratio CI engine using WCO as a biodiesel at different injection timings. Applied Energy. 2011;88:2344-54.

[3] Belyamin B, Noor AM, Hussein MH, Said M. Characterization of Diesel Engine Generator Operating at Different Compression Ratio Fuelled with Palm Oil Biodiesel. Applied Mechanics and Materials: Trans Tech Publ; 2013. p. 241-5.

[4] Hoque N, Mourshed M, Das BK. Performance and emission comparison of Karanja (pongamia pinnata), Pithraj (aphanamixis polystachya), Neem (azadira chtaindica) and Mahua (madhuca longofolia) seed oil as a potential feedstock for biodiesel production in Bangladesh. International Journal of Automotive and Mechanical Engineering. 2015;12:2967-82.

[5] Zheng S, Kates M, Dubé M, McLean D. Acid-catalyzed production of biodiesel from waste frying oil. Biomass and bioenergy. 2006;30:267-72.

[6] Tomasevic A, Siler-Marinkovic S. Methanolysis of used frying oil. Fuel Processing Technology. 2003;81:1-6.

[7] Tao Y, Chen Y, Wu Y, He Y, Zhou Z. High hydrogen yield from a two-step process of dark-and photo-fermentation of sucrose. International Journal of Hydrogen Energy. 2007;32:200-6.

[8] Simbollotti G. IEA Energy Technology Essentials-Hydrogen Production and Distribution. International Energy. 2017;544.

[9] Laia O, Ghazalia H, Cho F, Chong C. Physical and textural properties of an experimental table margarine prepared from lipase-catalysed transesterified palm stearin: palm kernel olein mixture during storage. Food Chemistry. 2000;71:173-9.

[10] Xing X, Zhang C. Research progress in dark microbial fermentation for bio-hydrogen production. Chinese Journal of Bioprocess Engineering. 2005;3:1-8.

[11] Mofijur M, Masjuki H, Kalam M, Atabani A. Evaluation of biodiesel blending, engine performance and emissions characteristics of Jatropha curcas methyl ester: Malaysian perspective. Energy. 2013;55:879-87.
[12] Agarwal AK. Biofuels (alcohols and biodiesel) applications as fuels for internal combustion engines. Progress in Energy and Combustion Science. 2007;33:233-71.
[13] Nalgundwar A, Paul B, Sharma SK. Comparison of performance and emissions characteristics of DI CI engine fueled with dual biodiesel blends of palm and jatropha. Fuel. 2016;173:172-9.
[14] Khalid A, Tajuddin ASA, Jaat N, Manshoor B, Zaman I, Hadi SAA, et al. Performance and emissions of diesel engine fuelled with preheated biodiesel fuel derived from crude palm, jatropha, and waste cooking oils. International Journal of Automotive and Mechanical Engineering. 2017;14:4273-84.
[15] Shukri MR, Rahman MM, Ramasamy D, Kadirgama K. Artificial neural network optimization modeling on engine performance of diesel engine using biodiesel fuel. International Journal of Automotive and Mechanical Engineering. 2015;11:2332-47.
[16] Nayak SK, Mishra PC. Emission from a dual fuel operated diesel engine fuelled with Calophyllum Inophyllum biodiesel and producer gas. International Journal of Automotive and Mechanical Engineering. 2017;14:3954-69.
[17] Dubey P, Gupta R. Study of the performance and emission characteristics for a dual fuel powered single cylinder diesel engine. International Journal of Automotive and Mechanical Engineering. 2016;13:3373-88.
[18] Anand R, Kannan G, Karthikeyan P. A Study of the Performance Emission and Combustion Characteristics of a DI Diesel Engine Using Waste Cooking Oil Methyl Ester-Ethanol Blends. ASME 2012 International Mechanical Engineering Congress and Exposition: American Society of Mechanical Engineers; 2012. p. 935-42.
[19] Reddy JN, Ramesh A. Parametric studies for improving the performance of a Jatropha oil-fuelled compression ignition engine. Renewable Energy. 2006;31:1994-2016.
[20] Jaat N, Khalid A, Andsaler AR, Sapit A, Razali A, Basharie M. Effects of ambient temperature and injection pressure on biodiesel ignition delay. Journal of Mechanical Engineering and Sciences. 2017;11:2723-33.
[21] Jegadheesan C, Somasundaram P, Meenakshipriya B, Vignesh U. Effect of DEE Injection in Pongamia Pinnata Biodiesel Fulled CI Engine Using Hydrogen as Secondary Fuel. Advanced Materials Research: Trans Tech Publ; 2013. p. 188-94.
[22] An H, Yang W, Maghbouli A, Li J, Chou S, Chua KJ, et al. Numerical investigation on the combustion and emission characteristics of a hydrogen assisted biodiesel combustion in a diesel engine. Fuel. 2014;120:186-94.
[23] Mahalingam S, Suresh M, Pranesh R. Experimental study of performance and emission characteristics of a bio dual fuel blends in diesel engine for variation of injection pressures. Proceedings of the World Congress on Engineering: Citeseer; 2013.
[24] Qi D, Chen H, Geng L, Bian YZ. Experimental studies on the combustion characteristics and performance of a direct injection engine fueled with biodiesel/diesel blends. Energy Conversion and Management. 2010;51:2985-92.
[25] Chauhan BS, Kumar N, Cho HM. A study on the performance and emission of a diesel engine fueled with Jatropha biodiesel oil and its blends. Energy. 2012;37:616-22.
[26] Lin B-F, Huang J-H, Huang D-Y. Experimental study of the effects of vegetable oil methyl ester on DI diesel engine performance characteristics and pollutant emissions. Fuel. 2009;88:1779-85.
[27] Tsolakis A, Megaritis A, Wyszynski M, Theinnoi K. Engine performance and emissions of a diesel engine operating on diesel-RME (rapeseed methyl ester) blends with EGR (exhaust gas recirculation). Energy. 2007;32:2072-80.

[28] Channapattana S, Pawar AA, Kamble PG. Effect of injection pressure on the performance and emission characteristics of VCR engine using honne biodiesel as a fuel. Materials Today: Proceedings. 2015;2:1316-25.

[29] Sasongko MN, Wijayanti W. Effect of ethanol addition on the performance and exhaust emissions of a spark ignition engine. Journal of Mechanical Engineering and Sciences. 2017;11:2734-42.

[30] SinghYadav V, Soni S, Sharma D. Performance and emission studies of direct injection CI engine in duel fuel mode (hydrogen-diesel) with EGR. International Journal of Hydrogen Energy. 2012;37:3807-17.

[31] Bhaskar K, Sendilvelan S, Muthu V, Aravindraj S. Performance and emission characteristics of compression ignition engine using methyl ester blends of jatropha and fish oil. J Mech Eng Sci. 2016;10:1994-2007.

[32] Quadri SAP, Masood M, Kumar PR. Effect of pilot fuel injection operating pressure in hydrogen blended compression ignition engine: An experimental analysis. Fuel. 2015;157:279-84.

[33] Bari S, Yu C, Lim T. Effect of fuel injection timing with waste cooking oil as a fuel in a direct injection diesel engine. Proceedings of the Institution of Mechanical Engineers, Part D: Journal of Automobile Engineering. 2004;218:93-104.

[34] Korakianitis T, Namasivayam A, Crookes R. Diesel and rapeseed methyl ester (RME) pilot fuels for hydrogen and natural gas dual-fuel combustion in compression–ignition engines. Fuel. 2011;90:2384-95.

[35] Miyamoto T, Hasegawa H, Mikami M, Kojima N, Kabashima H, Urata Y. Effect of hydrogen addition to intake gas on combustion and exhaust emission characteristics of a diesel engine. International Journal of Hydrogen Energy. 2011;36:13138-49.

[36] Yoon SH, Lee CS. Experimental investigation on the combustion and exhaust emission characteristics of biogas–biodiesel dual-fuel combustion in a CI engine. Fuel Processing Technology. 2011;92:992-1000.

NOMENCLATURES

WCOBD	Waste cooking oil biodiesel
PSBD	Palm stearin biodiesel
B10(5WCOBD5PSBD90D)	5%WCOBD+5%PSBD+90%Diesel
B20(10WCOBD10PSBD80D)	10%WCOBD+10%PSBD+80%Diesel
B30(15WCOBD15PSBD70D)	15%WCOBD+15%PSBD+70%Diesel
lpm	Liters per minute
CO	Carbon monoxide
HC	Hydro carbon
CO_2	Carbon dioxide
NOx	Oxides of nitrogen
BTE	Brake thermal efficiency
BSFC	Brake specific fuel consumption
BSEC	Brake specific energy consumption
IOP	Injection opening pressure
CR	Compression ratio
WCO	Waste cooking oil
PS	Palm stearin

Available online at www.sciencedirect.com

ScienceDirect

Materials Today: Proceedings 4 (2017) 835–841

materialstoday: PROCEEDINGS

www.materialstoday.com/proceedings

5th International Conference of Materials Processing and Characterization (ICMPC 2016)

Evaluation of Strain and Strain rates at different stages of Superplastic Cone Forming

P Shailesh[a,]*, K Vijaya Kumar[b], J Babu[c], K Srinivasa Raghavan[a]

[a]*Mechanical Engineering Department, MCET/Osmania University, Hyderabad,500001, India*
[b]*MED, Research Scholar, NIT, Warangal, 506004, India*
[c]*MED, St. Joseph's College of Engineering& Technology, Choondacherry, Kerala , 686579, India*

Abstract

Superplastic forming (SPF) is a powerful tool to manufacture complex parts for industries like automobile and aerospace where strength to weight ratio of the part is the main criterion. Superplastic forming (SPF) of a sheet metal has been used to produce very complex shapes and integrated structures at much lighter and stronger than the assemblies they replace. Superplastic formed shapes like conical, hemispherical poses a problem of large thickness variation, minimum thickness results at the portion where die contact is made last. Proper understanding of strain and strain rates during forming and using the pressures accordingly can minimize this problem. The present investigation focused on the study of strain and strain rates during the forming, Experiments were carried on a model material Sn-Pb, which can be applicable for any other Superplastic materials. Results revealed that strain rates in the present study are within the range of superplastic regime and no failure of the formed part because of the thinning. Results also revealed that forming time can be reduced by increasing the pressure which in turn increase the strain rate.

Selection and peer-review under responsibility of Conference Committee Members of 5th International Conference of Materials Processing and Characterization (ICMPC 2016).

*Keywords:*Superplastic forming, Conical shape, Strain, Strain rate

1. Introduction

Superplastic materials are polycrystalline solids which are having the ability to undergo very large and uniform tensile elongations before the failure occurs. Generally elongations higher than 200% indicate the superplasticity.

* Corresponding author. Tel.: +91-8790595450;
*E-mail address:*vijay.nitw2@gmail.com

Selection and peer-review under responsibility of Conference Committee Members of 5th International Conference of Materials Processing and Characterization (ICMPC 2016).

Due to this property superplastic forming (SPF) is increasingly used industries like aerospace and automobile to produce complex parts at much lesser efforts and costs when compared with conventional machining [1-3]. Wide varieties of materialsaluminum, magnesium and titanium alloys exhibit the phenomena of superplasticity, when subjected to certain conditions of pressure, temperature and strain-rates [4, 5].The conditions that are necessary for any material to be superplastic material are grain size $\leq 10\mu m$, strain - rates $\leq 10^{-3}$ s^{-1} and temperatures ≥ 0.5 T_m where T_m is the melting point of the material under investigation [6].Most often ultra-fine grained materials are obtained by using severe plastic deformation methods like: high pressure torsion (HPT) [7, 8] equal-channel angular pressing (ECAP) [8,9], multiple forging [3], and multi-axis restrain deformation *(Max Strain)* [10] or cyclic extrusion-compression (CEC) [9].Blow forming of single sheet is essentially based on the application of a gas pressure differential on the super plastic diaphragm, resulting in the deformation of the material into a given die configuration. Pressure, typically in the range 10–30 bars, is applied through the injection, via a series of inlet tubes, of either air or a protective gas (typically argon), depending on the affinity to oxygen of the material to be formed. Die and sheet are maintained at the same temperature within a heating press. The gas pressure is imposed over the sheet causing the sheet to form into the lower part of the die. While it is being formed, the sheet simply vents the gas to atmosphere which was initially located within the lower die chamber. The lower die chamber may be held either under vacuum or under some back pressure to control or even to prevent cavitation in the formed material (e.g. aluminum alloys) [11]. The mechanical characteristics of the finished product are very good, because the hardening of material is practically absent and spring-back is zero, with benefit of obtained dimensional accuracy. The surface finish is excellent, so there is no need to make finish operations [12-15].

Nomenclature

A_f	Surface area of the frustum
ao	Original radius of the circular blank
A_s	Surface area of the dome shape at the required instance ($2\pi\rho h_s$)
a	Radius at the smaller end and the cone
ρ	Radius of curvature
l	Slant length of circular blank at the die opening
h_f	Vertical height of the truncated cone
h_s	vertical height of the dome shape in the total deformed components at any instant
h	Total formed height of the component (measured with depth micrometer) ($h=h_f+h_s$)
ε	Strain
$\acute{\varepsilon}$	Strain rate
σ	Stress

2. Methods and materials

Lead –Tin (Pb-40% -Sn-60%) alloy which is used as solders is available in the form of bars was used in the present study. This alloy was cast to slab of dimensions 68mm wide x 720mm long x 30 mm thickness and cold rolled at room temperature to a thickness of 2.45 mm as shown in Fig.1 in a rolling mill at Non-Ferrous Materials Technology Development Centre (NFTDC), Hyderabad, Telangana, India. The lamellar grains broke down to fine globular grains of average size 8 μm as shown in Fig.2. Cone forming tests were carried out in Low cost experimental setup as shown in Fig 3. Sn-Pb blanks of 80mmΦ x 2.45mm thickness were blown by Argon gas in a conical die of 80mm Φ x apex angle 60^0 as shown in Fig 4. under constant gas pressures 3 bar,6 bar and 8 bar. The progress of deformation of the cone with time was monitored at different stages of forming.

- Free Blowing (deformation without touching die wall)
- Free Blowing (max. limit of deformation without touching die wall)
- Cone wall making tangent to the membrane
- Cone wall formation + free blowing of dome

These four stages go on repeating further till the cone shape is formed.

Fig.1.Experimental Set Up.

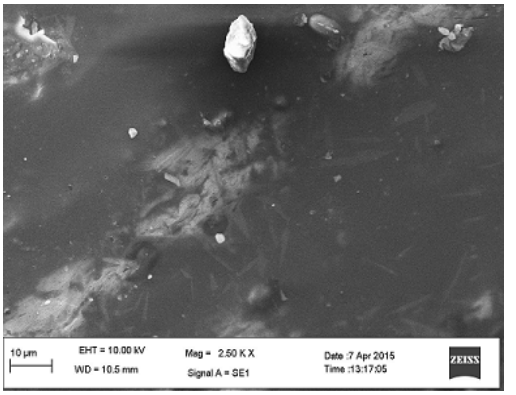

Fig.2. SEM images of Lead –Tin (Pb-40% -Sn-60%) alloy after rolling.

Fig.3. Lead –Tin (Pb-40% -Sn-60%) Alloy sheet thickness of 2.14 mm.

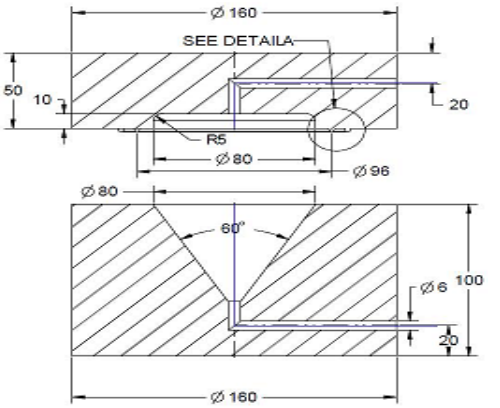

Fig.4. Various stages of superplastic forming in conical die.

As soon as the membrane touches the conical die wall, the thickness freezes and further thinning occurs on the free dome portion.As a result of these dome thickness is less than the cone wall thickness. And finally, in the formed cone the thickness reduces progressively from the base of the cone to the apex.Stress and strains were calculated at different stages of forming for the forming pressures 3 bar, 6 bar and 8 bar.

3. Determination of Stress and Strains at different stages of forming

Stress and strain values of at different stages of forming are calculated. Sample calculations for a forming pressure of 3 bar are shown below

Stage 1. Free Blowing

Original area of the circular blank

$$\text{Ao} = \pi(\text{ao})2 = \pi(40)2 = 5026.5\ \text{mm}2$$

Depth of the formed dome shape = h

$$h = \rho - \frac{(\rho 2 - \text{ao}2)1}{2} = 1.1547\ \text{ao} - \frac{\left((1.1547)2 - \text{ao}2\right)1}{2} = 0.578 * \text{ao} = 23.12\ \text{mm}$$

$$\rho = \text{ao}2\frac{h2}{2h}(or)\rho = \text{ao}/\sin 60 = 1.1547\text{ao}$$

Stage 2. Free Blowing (max. limit of deformation without touching die wall)

Surface area of truncated cone $= \pi\ (r + R)\ l$

$= \pi\ (a+ao)\ l$

Vertical height of the truncated cone (h_f)

$= l \cos(\theta/2)$ $(\theta=60^0)$

$= l \cos 30^0$

Stage 3. Cone wall making tangent to the membrane

Surface area of the frustum $A_f = \pi (ao+a)\, l$

Vertical height of the frustum = h_f

h = Total formed height of the component (measured with depth micrometer)

$h=h_f+h_s$ $h_f = l \cos 30^0$

$h_s = h - h_f$

Stage 4. Cone wall formation + free blowing of dome

Surface area of the dome shape at the required instance.

$$A_s = 2\pi\rho h_s$$

Where

ρ =radius of curvature of the dome shape.

$$\rho = a^2+h_s^2/2h_s$$

hs = vertical height of the dome shape at that instance.

Total formed area of the deformed components

$$A = A_f + A_s$$

Strain

$$\varepsilon = \ln (A/A_0)$$

Strain rate:

$$\acute{\varepsilon} = \varepsilon/\text{time}$$

$$\text{Stress},\sigma = \left(\frac{\rho}{2t}\right)\mathbf{*P}$$

$$\sigma = \left(\left(\frac{A}{2\pi h}\right)/\left(\frac{Aoto}{A}\right)\right)\mathbf{*P}$$

$$\sigma 3\text{bar} = ((6599.18)\mathbf{2/}(4\pi \times 23.4 \times 5026.5 \times 2.45)) \times 0.03 = 0.360\ \text{N/mm2}$$

For dome:

Radius of curvature

$\rho = (a2+ h2)/ 2h = (402+22.382)/ (2\times22.38)= 46.93$ mm

Area of dome

$A = 2\pi\rho h= 2\pi\times46.93\times22.38= 6599.18$ mm2

Strain

$\varepsilon = A/A0= 6599.18/5026.5= 0.272$

Strain rate

$\acute{\varepsilon} = 0.272/ (50\times60)= 9.06\times10\text{-}5/\text{sec}$

For Truncated Cone

$h_s = h-h_f = 46.38-32.04= 14.34$ mm

Radius of dome

$a = hs/0.578= 24.8$ mm

$\rho = a/\sin60^0= 28.64$mm

Area of dome

$A_s = 2\pi\rho h_s= 2\pi\times28.64\times28.64= 2580.48$ mm2

Area of frustum

$A_f = \pi l\ (ao +a)= \pi \times 37(40+24.8)= 7532.28$ mm2

$A = (As +Af) =10112.76$ mm2

Strain

$\varepsilon = A/Ao= 10112.76/5026.5= 0.699$

Strain rate

$\acute{\varepsilon} = 0.699/ (80\times60) = 1.45\times10\text{-}4$ /sec

4. Results and Discussion

Fig.5 Formation of conical dome at 3 bar pressure at different time intervals in minutes (a) 5 (b) 20 (c) 80 (d) 110

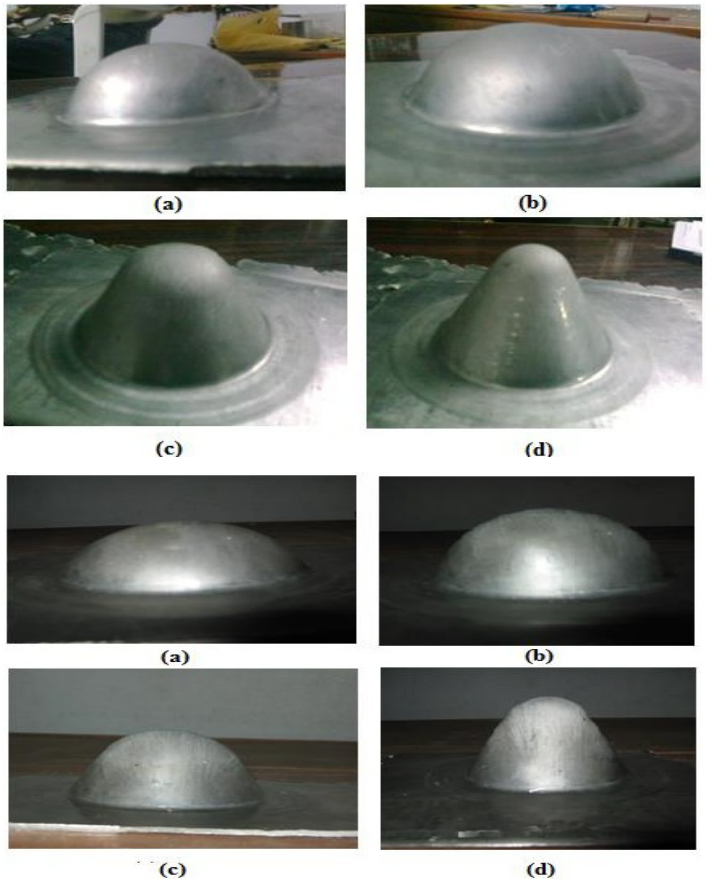

Fig.6 Formation of conical dome at 6 bar pressure at different time intervals in minutes (a) 5 (b) 30 (c) 40 (d) 45

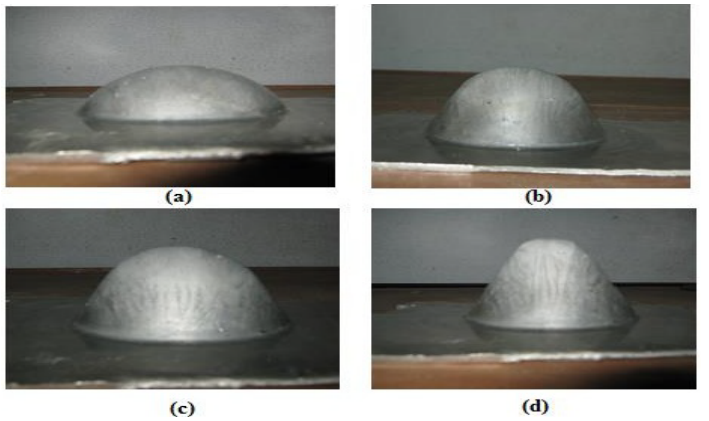

Fig.7 Formation of conical dome at 8 bar pressure at different time intervals in minutes (a) 5 (b) 10 (c) 15 (d) 20

Stress and strain values of at different stages of forming for the forming pressure 3 bar, 6 bar and 8 bar are calculated as per the calculations mentioned in the section.3, and are shown in Tables 1,2 and 3. Conical domes formed at forming pressure 3 bar, 6 bar and 8 bar with different stages are shown Figures 5, 6 and 7.

From the Table 1, one can observe that strain on the material in increasing, but strain rate is decreased in the time interval 5-20 min shows the initial strain hardening of the material, further in the 20-50 min time interval strain rate

is increased as the material is free forming without touching the walls of the conical die. After the touching the wall of the die for 80-140 min time interval the strain rate gradually decreasing and remains a constant value.

Table.1. Strain and Strain rates at different stages of forming at a forming pressure of 3 bar

Time (minutes)	Slant height (mm)	Depth (mm)	Radius of Curvature (mm)	Area (mm^2)	Strain	Strain rate /sec
5	0	5.13	158.51	5109.2	0.016	5.43×10^{-5}
20	0	7.00	117.78	5180.2	0.030	2.50×10^{-5}
50	0	22.38	46.93	6599.18	0.272	9.06×10^{-5}
80	37	46.38	28.64	10112.76	0.699	1.45×10^{-4}
110	51.5	54.38	19.53	10404.52	0.727	1.10×10^{-4}
140	58.3	62.50	24.01	12947.30	0.946	1.10×10^{-4}

Table.2. Strain and Strain rates at different stages of forming at a forming pressure of 6 bar

Time (minutes)	Slant height (mm)	Depth (mm)	Radius of Curvature (mm)	Area (mm^2)	Strain	Strain rate /sec
5	0	18.30	52.86	6078.63	0.190	6.33×10^{-4}
10	0	23.40	42.88	6746.75	0.294	4.90×10^{-4}
15	7.07	27.98	43.67	7722.60	0.429	4.76×10^{-4}
20	16.05	32.00	36.13	7702.60	0.426	3.55×10^{-4}
30	22.54	39.27	39.45	10147.88	0.702	3.90×10^{-4}
40	39.25	48.34	28.66	10579.25	0.744	3.10×10^{-4}
45	47.62	54.50	26.49	11623.02	0.838	3.10×10^{-4}

Table.3. Strain and Strain rates at different stages of forming at a forming pressure of 8 bar

Time (minutes)	Slant height (mm)	Depth (mm)	Radius of Curvature (mm)	Area (mm^2)	Strain	Strain rate /sec
5	0	22.45	46.85	6606.56	0.273	9.10×10^{-4}
10	13.20	31.15	39.39	7950.51	0.458	7.63×10^{-4}
15	22.64	38.10	36.95	9412.27	0.627	6.98×10^{-4}
20	43.05	50.41	33.34	12008.32	0.737	6.14×10^{-4}

At higher forming pressures 6 bar and 8 bar (Table 2 and Table 3) strain rate is gradually decreasing and remains a constant value. However, the initial values strain rates are higher when compared to the forming pressure of 3 bar.It is known facts that blow forming of a cone with apex angle nearer to 60^0, under constant strain rate can be achieved by applying a constant gas pressure [13]. In other wards constant gas pressure induces a constant stress in the membrane which in turn produces constant strain rate. In the present investigation similar behavior is observed.

From the Table 2 and Table 3, it can be observed that at higher forming pressures the forming time can be reduced considerably. This is because of higher strains and strain rates. However higher strain rates lead to the local thinning of the formed part. This can be explained as for superplastic deformation, elastic strains are negligible; therefore, constancy of volume can be assumed. From this consideration, the sum of the plastic strains is zero, and tensile strain in one direction must be balanced by compressive (negative) strain in another. The strains are:

$$\varepsilon_1 + \varepsilon_2 + \varepsilon_3 = 0$$

Where ε is the strain and the subscripts indicate the principal directions. For the present sheet forming operation under plane strain conditions, $\varepsilon_2 = 0$ and $\varepsilon_3 = -\varepsilon_1$, the thinning strain ($\varepsilon_3$) is equal and opposite to the longitudinal tensile strain ($\varepsilon_{1)}$ and the thinning will therefore match the tensile deformation. For large tensile strains, the thinning will be corresponding large. Present investigations do not show any failure of the part during forming because of thinning. This shows pressures considered in the study are suitable forming the conical domes. Calculated strain rate values for the different forming pressures at different stages of forming are within the range of superplastic forming regime, which resulted the forming of conical parts without fracture.

5. Conclusions

Conical forming of lead –tin samples at different pressure were carried out in the present study to know the feasibility of forming without failure of the part. The following conclusions are drawn for this study.

- Rolling of the cast slab of lead and tin alloy can reduce the grain size approximately 8 μm, which is suitable for superplastic forming.

- Calculated strain rate values at different stages of forming at forming pressure are almost a constant which is good agreement with published results.
- Strain rates are higher at higher forming pressures which resulted in lesser the forming time.
- Calculated strain rate values for the different forming pressures are within the range of superplastic forming regime, which resulted the forming of conical parts without fracture.

References

[1] Barnes J, Superplastic Forming 40 Years and Still Growing, J. Mater. Eng. Perform. 2007; 16: 440-447.
[2] Serra D, 6th EUROSPF Conference EuroSPF08, 3-5 September 2008, Carcassonne, France p 1-10.
[3] Davis.B and Hryn. J. Report, Argonne National Laboratory, U.S. Department of Energy laboratory, 31 January 2008, Assessed online at http://www.osti.gov/bridge/product.biblio.jsp?osti_id=924692, p 9.
[4] Hamilton CH, Paton N, Proceedings of the International conference on the Minerals, Metals and Materials Society, USA, 1988; p706.
[5] ARGARD-LS-154, Advisory Group for Aerospace Research and Development, NATO,1987; p 204.
[6] Hiroyuki Wadena H, Toshiji Makati, Kenji Higashi. Scripta Mater 1999;40(4):477-484.
[7] Sergueeva AV, Stolyarov VV, Valiev RZ, Mukherjee AK, Materials Science Engineering A 2002; 323: 318-325.
[8] Valiev RZ, Islamgaliev RK, Alexandrov IV, Progress in Materials Science 2000; 45 :103-189.
[9] Richert M, Materials Engineering 1997; 2: 59-69.
[10]Chen WC., Ferguson DE., Ferguson HS, Mishra R.S, Jin Z, Materials Science Forum 2001; 357-359: 425-430.
[11] Super plastic forming of Advanced Metallic Materials: Methods and Applications, edited by Gillo Giuliano. 50-51.
[12] Cappetti N, Garofalo L, Naddeo A, Nastasia M, Pellegrino A, Journal of Achievements in Materials and Manufacturing Engineering 2010; 38(2): 187-194.
[13] R.J. Ledrich, S.M.L. Sastry, M. Hayase and T.L. Mackay, Journal of Metals,Aug 1982 pp15-20.
[14] Nitin Kotkunde, Nitin Krishnamurthy, A. K. Gupta, S. K. Singh, Advanced Materials Manufacturing and Characterization 2013; Vol3, Issue 1.
[15] Haoxiang Gao, Nan Li, Hongliang Ho, Yanling Zhang, Ning Zhang, Liliang Wang, Jianguo Lin, Materials Today: Proceedings 2S (2015) S408 – S413.

INTERNATIONAL JOURNAL OF RESEARCH
In Advanced Engineering Technologies

Volume 6, Issue 2 JULY 2017

DESIGN AND ANALYSIS OF GAS TURBINE BLADE

[1] Kottha Srinivas, [2] Mr. M.Prasad

[1] PG Scholar, Department of MECH, **Methodist COLLEGE of Engineering & Technology.**

Abids, Hyderabad – 500 001.

[2] Assistant Professor, Department of MECH, **Methodist COLLEGE of Engineering & Technology.**

Abids, Hyderabad – 500 001.

Abstract

A gas turbine used in power generation by converting kinematic energy into mechanical energy by rotors. The rotors has to withstand high temperatures, pressure, stresses and strains during compression and expansion in turbine and it has to increase thermal efficiency. The life of the blade is also important by avoiding fatigue. Solidworks software is used to model it. Meshing, analysis is performed by Ansys 14.5 software. Rotors cooling methods are also analyzed to improve convection and decrease temperatures on blades. Deformations are analyzed by static structural analysis. Thermal stresses and strains results by software are compared for different materials. This analysis is done to introduce new innovated materials into real-time application on existing or new products to increase efficiency and life.Structural load like Pressure analysis is done at required areas to choose a best material. Vibrational frequency in turbine are also estimated by modal analysis.

Fig: Gas turbine blade with rotor

1. Introduction:

Gas turbines are used for power generation. Today, gas turbines are one of the most widely-used power generating technologies. Gas turbines are a type of internal combustion (IC) engine in which burning of an air-fuel mixture produces hot gases that spin a turbine to produce power. It is the production of hot gas during fuel combustion, not the fuel itself that the gives gas turbines the name. Gas turbines can utilize a variety of fuels, including natural gas, fuel oils, and synthetic fuels. Combustion occurs continuously in gas turbines, as opposed to reciprocating IC engines, in which combustion occurs intermittently.

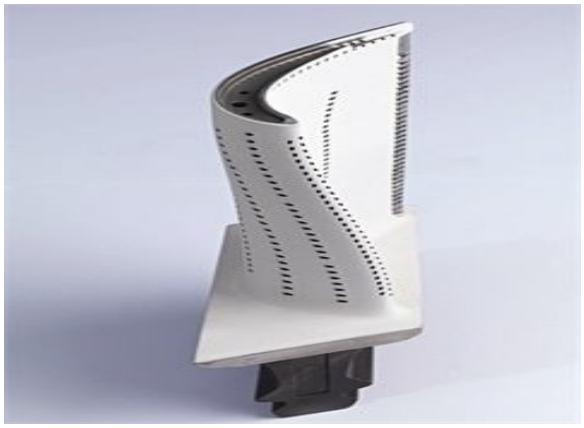

Fig: Gas turbine rotor blade

2. How does a gas turbine works:

Gas turbines are comprised of three primary sections mounted on the same shaft: the compressor, the combustion chamber (or combustor) and the turbine. The compressor can be either axial flow or

centrifugal flow. Axial flow compressors are more common in power generation because they have higher flow rates and efficiencies. Axial flow compressors are comprised of multiple stages of rotating and stationary blades (or stators) through which air is drawn in parallel to the axis of rotation and incrementally compressed as it passes through each stage. The acceleration of the air through the rotating blades and diffusion by the stators increases the pressure and reduces the volume of the air. Although no heat is added, the compression of the air also causes the temperature to increase.

The compressed air is mixed with fuel injected through nozzles. The fuel and compressed air can be pre-mixed or the compressed air can be introduced directly into the combustor. The fuel-air mixture ignites under constant pressure conditions and the hot combustion products (gases) are directed through the turbine where it expands rapidly and imparts rotation to the shaft. The turbine is also comprised of stages, each with a row of stationary blades (or nozzles) to direct the expanding gases followed by a row of moving blades. The rotation of the shaft drives the compressor to draw in and compress more air to sustain continuous combustion. The remaining shaft power is used to drive a generator which produces electricity. Approximately 55 to 65 percent of the power produced by the turbine is used to drive the compressor. To optimize the transfer of kinetic energy from the combustion gases to shaft rotation, gas turbines can have multiple compressor and turbine stages.

Because the compressor must reach a certain speed before the combustion process is continuous or self-sustaining – initial momentum is imparted to the turbine rotor from an external motor, static frequency converter, or the generator itself. The compressor must be smoothly accelerated and reach firing speed before fuel can be introduced and ignition can occur. Turbine speeds vary widely by manufacturer and design, ranging from 2,000 revolutions per minute (rpm) to 10,000 rpm. Initial ignition occurs from one or more spark plugs (depending on combustor design). Once the turbine reaches self-sustaining speed – above 50% of full speed – the power output is enough to drive the compressor, combustion is continuous, and the starter system can be disengaged.

3. Gas Turbine Working Principle

Gas turbine engines derive their power from burning fuel in a combustion chamber and using the fast flowing combustion gases to drive a turbine in much the same way as the high pressure steam drives a steam turbine.

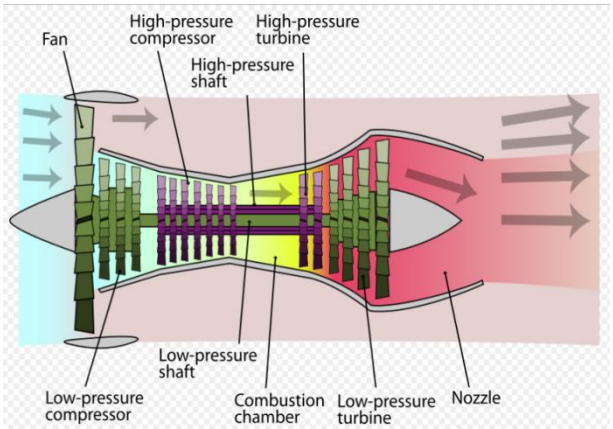

Fig: gas turbine combustion

One major difference however is that the gas turbine has a second turbine acting as an air compressor mounted on the same shaft. The air turbine (compressor) draws in air, compresses it and feeds it at high pressure into the combustion chamber increasing the intensity of the burning flame.

It is a positive feedback mechanism. As the gas turbine speeds up, it also causes the compressor to speed up forcing more air through the combustion

chamber which in turn increases the burn rate of the fuel sending more high pressure hot gases into the gas turbine increasing its speed even more. Uncontrolled runaway is prevented by controls on the fuel supply line which limit the amount of fuel fed to the turbine thus limiting its speed.

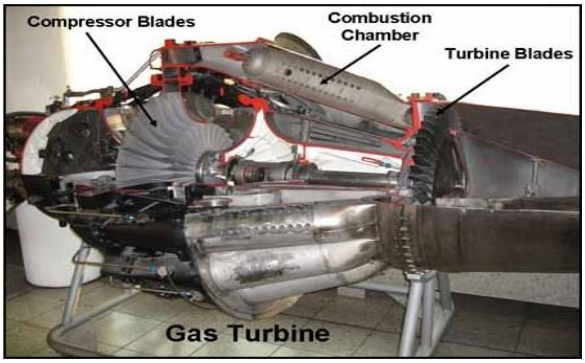

Fig: Gas turbine

The thermodynamic process used by the gas turbine is known as the Brayton cycle. Analogous to the Carnot cycle in which the efficiency is maximized by increasing the temperature difference of the working fluid between the input and output of the machine, the Brayton cycle efficiency is maximized by increasing the pressure difference across the machine. The gas turbine is comprised of three main components: a compressor, a combustor, and a turbine. The working fluid, air, is compressed in the compressor (adiabatic compression - no heat gain or loss), then mixed with fuel and burned by the combustor under constant pressure conditions in the combustion chamber (constant pressure heat addition). The resulting hot gas expands through the turbine to perform work (adiabatic expansion). Much of the power produced in the turbine is used to run the compressor and the rest is available to run auxiliary equipment and do useful work. The system is an open system because the air is not reused so that the fourth step in the cycle, cooling the working fluid, is omitted.

Gas turbines have a very high power to weight ratio and are lighter and smaller than internal combustion engines of the same power. Though they are mechanically simpler than reciprocating engines, their characteristics of high speed and high temperature operation require high precision components and exotic materials making them more expensive to manufacture.

4. Solidworks

Solid Works is mechanical design automation software that takes advantage of the familiar Microsoft Windows graphical user interface.

It is an easy-to-learn tool which makes it possible for mechanical designers to quickly sketch ideas, experiment with features and dimensions, and produce models and detailed drawings.

Introduction to Solidworks:

Solidworks mechanical design automation software is a feature-based, parametric solid modeling design tool which advantage of the easy to learn windows ™ graphical user interface. We can create fully associate 3-D solid models with or without while utilizing automatic or user defined relations to capture design intent.

Parameters refer to constraints whose values determine the shape or geometry of the model or assembly. Parameters can be either numeric parameters, such as line lengths or circle diameters, or geometric parameters, such as tangent, parallel, concentric, horizontal or vertical, etc. Numeric parameters can be associated with each other through the use of relations, which allow them to capture design intent.

5. Design procedure of Gas Turbine Blade

For designing the gas turbine blade the following procedure has to be follow

Go to features and select curves and coordinates as follows

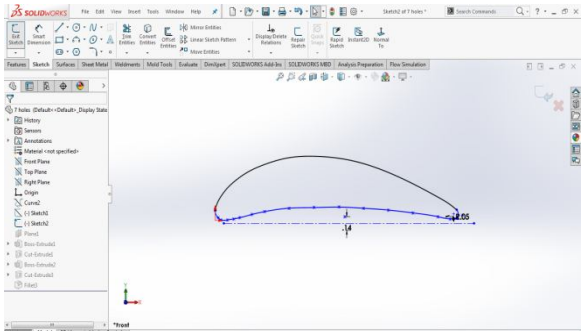

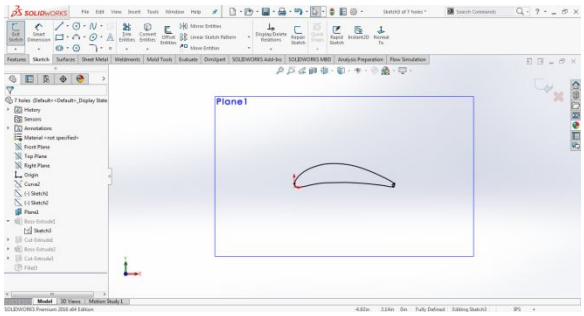

Now go to features and extrude it as follows

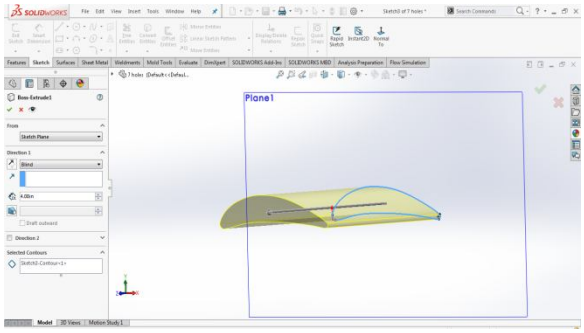

Draw the sketch as follows

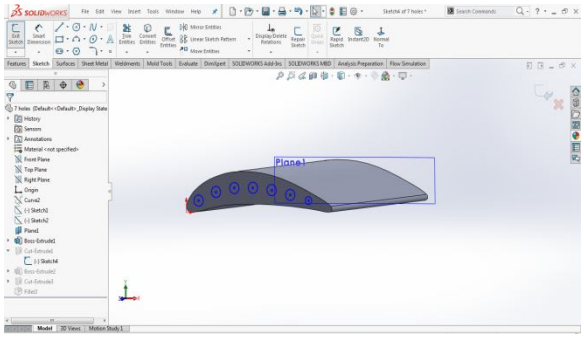

Draw the sketch as follows to make extrude

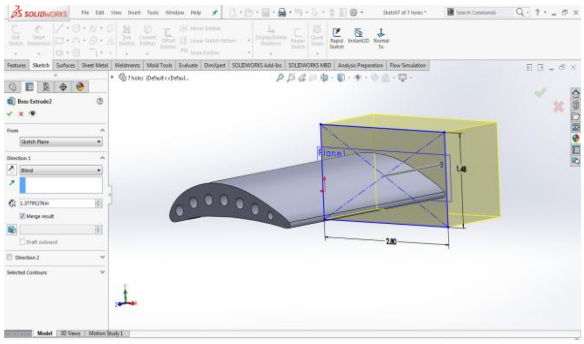

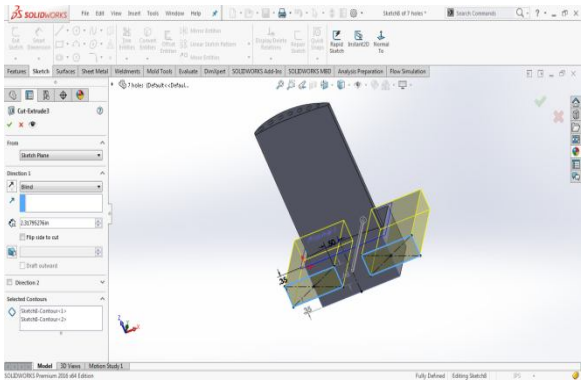

Gas turbine rotor blade

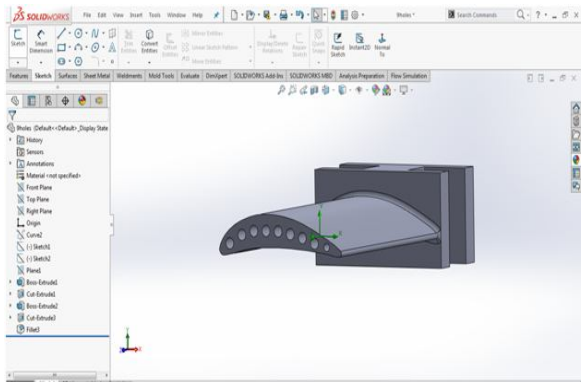

Four views of gas turbine rotor blade

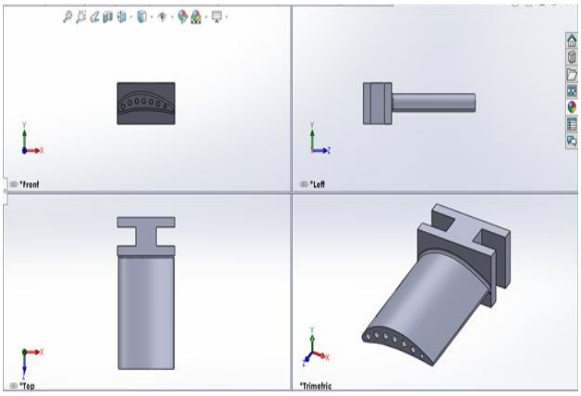

6. Finite Element Analysis:

Introduction:

Finite Element Analysis (FEA) is a computer-based numerical technique for calculating the strength and behaviour of engineering structures. It can be used to calculate deflection, stress, vibration, buckling behaviour and many other phenomena. It also can be used to analyze either small or largescale deflection under loading or applied displacement. It uses a numerical technique called the finite element method (FEM).

Basic Concepts of Analysis:

Meshing:

The software uses the Finite Element Method (FEM). FEM is a numerical technique for analyzing engineering designs. FEM is accepted as the standard analysis method due to its generality and suitability for computer implementation. FEM divides the model into many small pieces of simple shapes called elements effectively replacing a complex problem by many simple problems that need to be solved simultaneously.

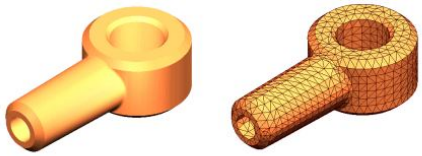

CAD model of a part

Model subdivided into small pieces (elements)

Material data:

Material	Density (kg/m³)	Young's modulus (pa)	Poison's ratio	Bulk modulus (pa)	Shear modulus (pa)	Thermal conductivity (W/m°C)
Stainless steel	7750	1.93E+11	0.31	1.693E+11	7.3664E+10	15.1
Titanium alloy	4620	9.6E+10	0.36	1.1429E+11	3.529E+10	21.9
Inconel	8440	2.05E+10	0.28	1.553E+18	8.0078E+17	9.7

7. Structural analysis on Gas Turbine

Fixed support

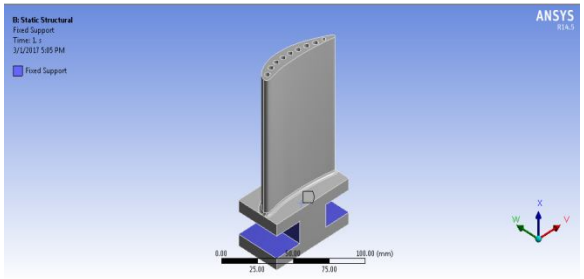

Pressure (1 MPA)

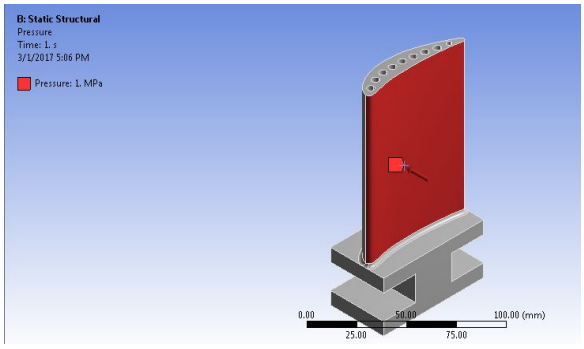

Meshing

Size: fine

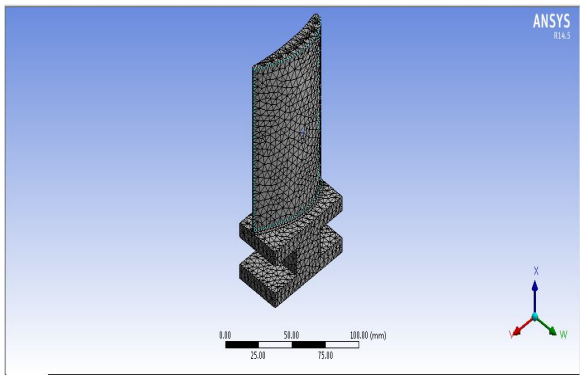

Material: Stainless Steel

Maximum stress

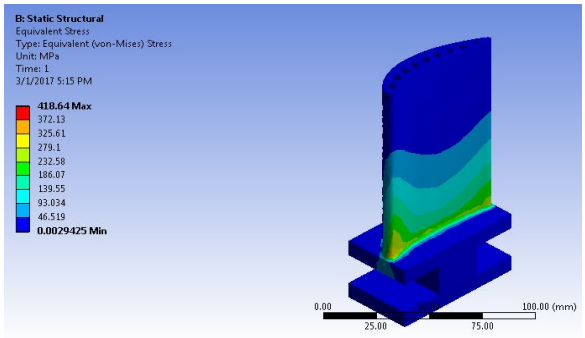

Total deformation

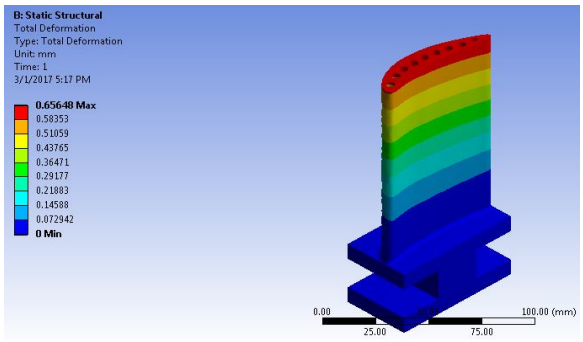

Maximum strain

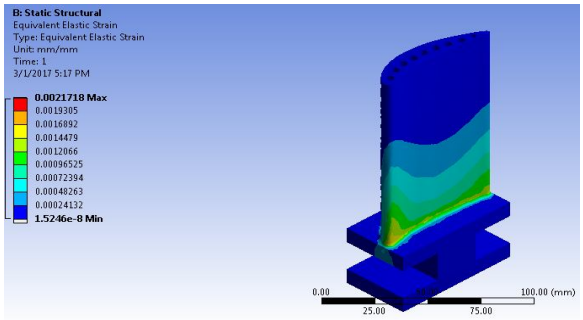

Material: Titanium alloy

Maximum stress

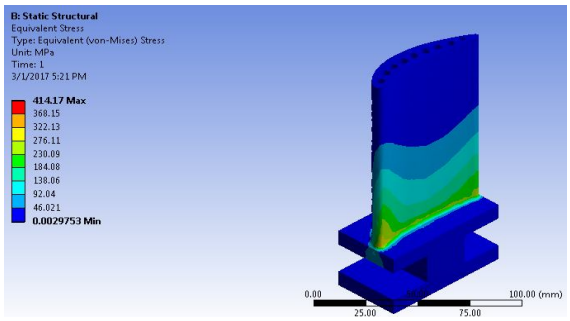

Total deformation

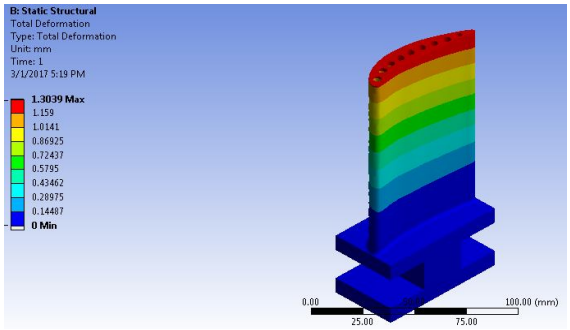

Maximum strain

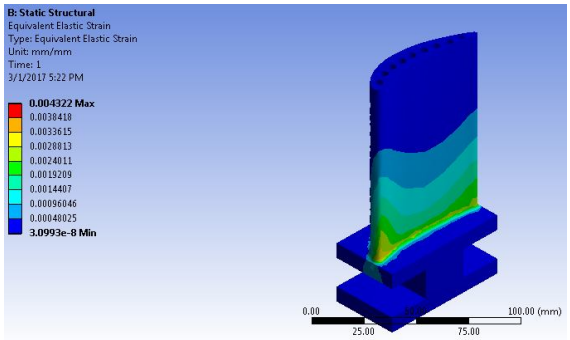

Material: Inconel (Nickel 625 Alloys)

Maximum stress

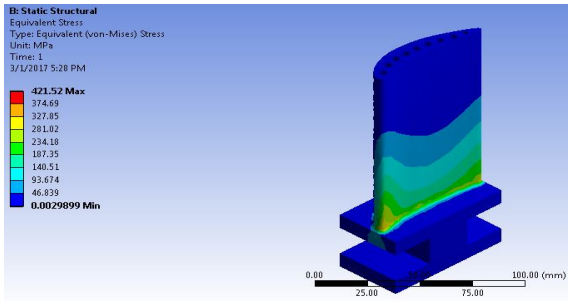

Total deformation

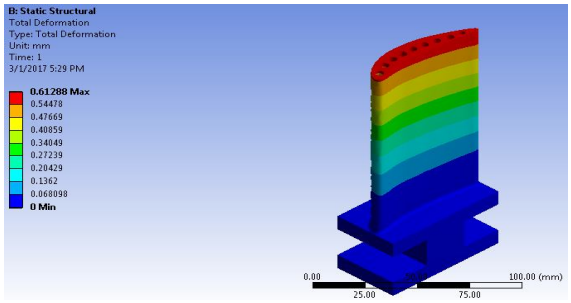

Maximum strain

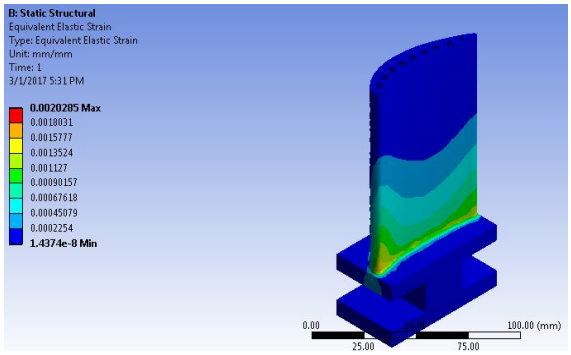

8. Steady State Thermal Analysis on Gas Turbine Rotor Blade

Temperature (900 c)

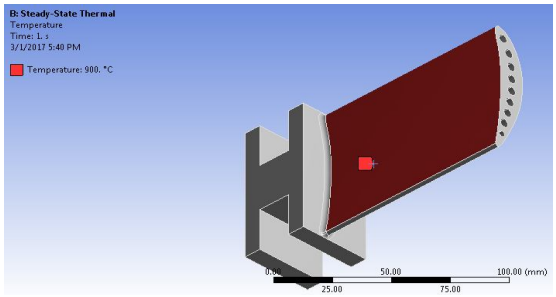

Convection (27 c)

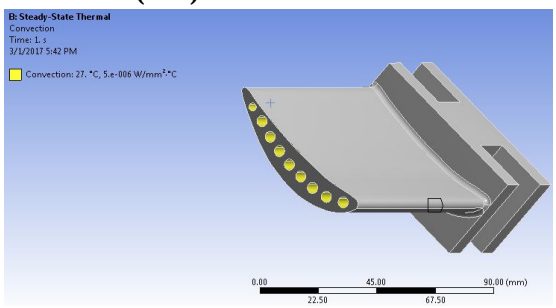

Material: Stainless Steel

Temperature Distribution

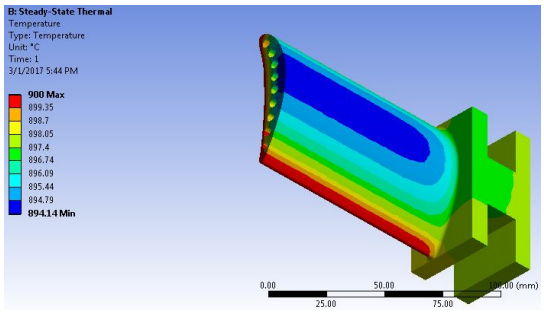

Total Heat Flux

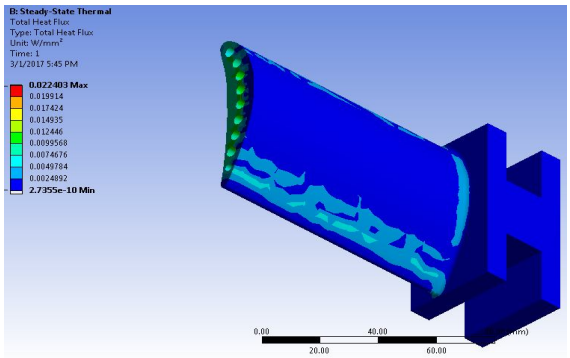

Material: Titanium Alloy

Temperature Distribution

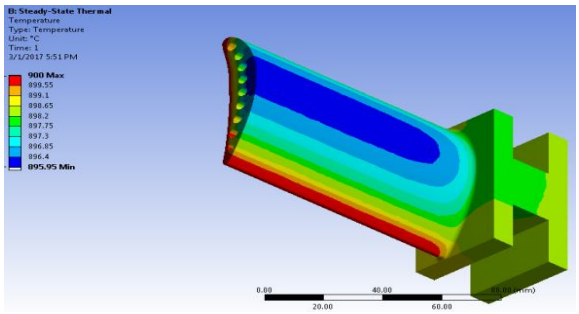

Total Heat Flux

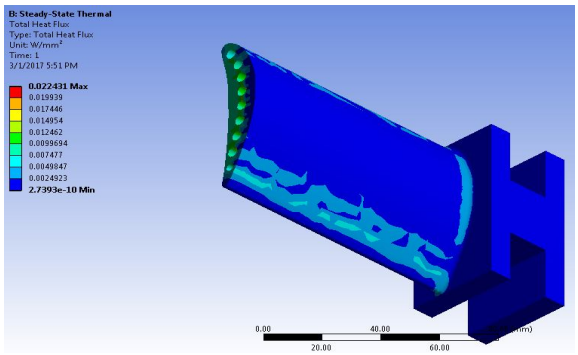

Material: Inconel (Nickel 625 Alloys)

Temperature Distribution

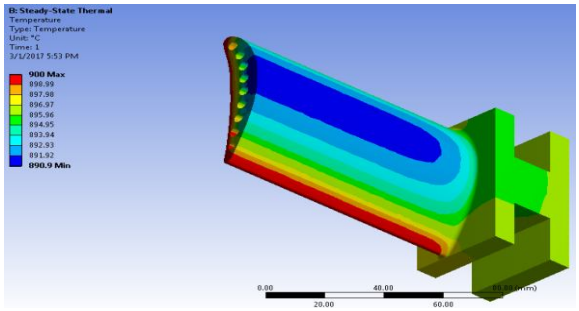

Total Heat Flux

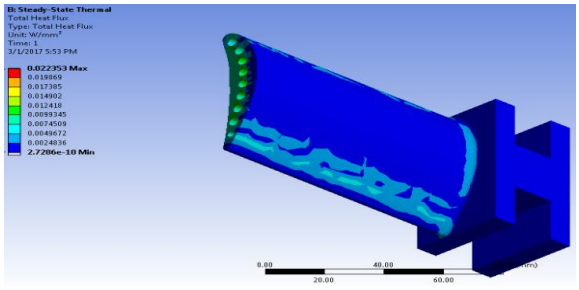

10. Dynamic (Modal) Analysis

Material: Stainless Steel

Mode-1

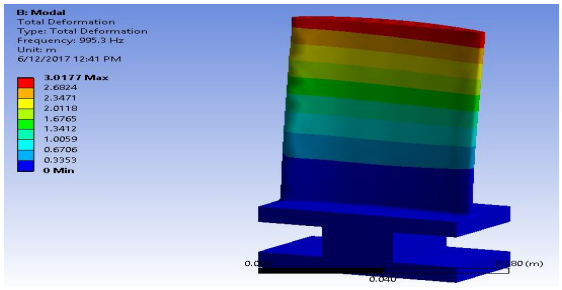

Mode-2

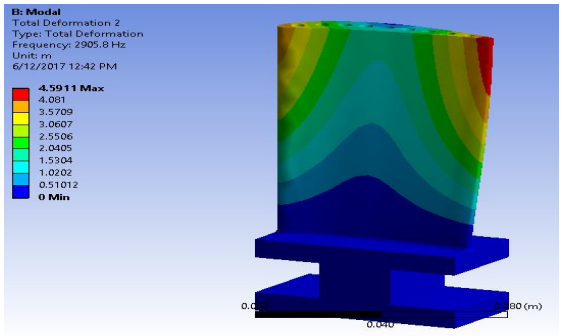

Mode-3

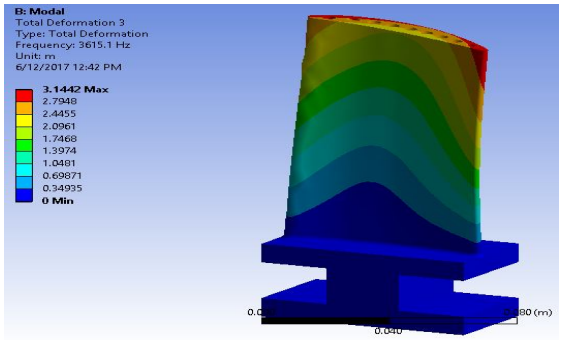

Mode-4

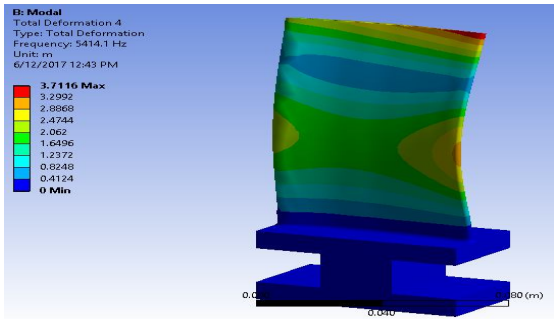

11. Results

Experimental Results

Material	Stress (max)	Strain (max)	Total deformation (max)	Temperature distribution		Total heat flux
				max	min	
Stainless steel	418.64	0.0021	0.6564	900	894.14	0.0224
Titanium alloy	414.17	0.0043	1.3039	900	895.95	0.0224
Inconel	421.52	0.0020	0.6128	900	890.90	0.0223

MODAL Analysis Results

Model (B4) > Modal (B5) > Solution (B6) > Results

Object Name	Total Deformation	Total Deformation 2	Total Deformation 3	Total Deformation 4	Total Deformation 5
State	Solved				
Scope					
Scoping Method	Geometry Selection				
Geometry	All Bodies				
Definition					
Type	Total Deformation				
Mode	1.	2.	3.	4.	5.
Identifier					
Suppressed	No				
Results					
Minimum	0. m				
Maximum	3.0177 m	4.5911 m	3.1442 m	3.7116 m	5.9683 m
Information					
Frequency	995.3 Hz	2905.8 Hz	3615.1 Hz	5414.1 Hz	8952. Hz

12. Conclusion

- Modeling and analysis on gas turbine rotor blade is done.
- Static structural analysis and thermal analysis are done.
- In static structural analysis 1 mpa pressure is applied by assigning four various materials such as stainless steel, titanium alloy, and inconel
- Maximum stress, strain & deformations are obtained titanium is showing least stress values compared to stainless steel and inconel
- Inconel (Nickel 625 Alloy) showing least strain value as well as least deformation value compare to titanium & stainless steel.
- In steady state thermal analysis maximum temperature is given as 900^0C and convection through holes is 27^0C
- Temperature distribution and total heat flux values are studied and tabulated. Max heat dissipation that is cooling is done by inconel materials followed by stainless steel.
- Decreased failure rates by stress analysis and thermal analysis.

References:

[1] Gowreesh, S., Sreenivasalu Reddy, N. and Yogananda Murthy, NV. 2009. Convective Heat Transfer Analysis of a Aero Gas Turbine Blade Using Ansys, International Journal of Mechanics

and Solids. 4: 39-46.

[2] Facchini, B. and Stecco. S.S. 1999. Cooled expansion in gas turbines: a comparison of analysis methods, Energy Conversion and Management. 40: 1207-1224.

[3] Mohammad, H., Albeirutty., Abdullah, S., Alghamdi., Yousef, S. Najjar. 2004. Heat transfer analysis for a multistage gas turbine using different blade-cooling schemes, Applied Thermal Engineering. 24: 563-577.

[4] Mahfoud, K. and George, B. 1997. Computational study of turbine blade cooling by slot-injection of a gas, Applied Thermal Engineering. 17: 1141-1149.

[5] Moyroud, F., Fransson, T. and Jacquet-Richardet, G. 2002. A comparison of two finite element

reduction techniques for mistuned bladed-disks, Journal of Engineering for Gas Turbines and Power. 124: 942-953.

[6] Giovanni, C., Ambra, G., Lorenzo, B. and Roberto, F. 2007 Advances in effusive cooling techniques of gas turbines, Applied Thermal Engineering. 27: 692-698.

[7] Cun-liang, L., Hui-ren, Z., Jiang-tao, B. and Du-chun, X. 2010. Film cooling performance of converging slot-hole rows on a gas turbine blade, International Journal of Heat and Mass Transfer. 53: 5232-5241.

[8] Zhang, JJ.,Esat, II. and Shi, YH. 1999. Load Analysis with Varying Mesh Stiffness, Computers and Structures. 70: 273-280.

[9] Hildebrabd, FB. 1997. Introduction to Numerical Analysis, McGraw-Hill, New York.

[10] MoussaviTorshizi, SE.,YadavarNikravesh, SM. and Jahangiri, A. 2009. Failure analysis of gas turbine generator cooling fan blades, Engineering Failure Analysis. 16: 1686-1695.

[11] Cleeton, JPE., Kavanagh, RM. and Parks, GT. 2009. Blade cooling optimisation in humid-air and steam-injected gas turbines, Applied Thermal Engineering. 29: 3274-3283.

[12] Krishnamoorthy, C. 1994. Finite Element Analysis Theory and Programming,Tata McGraw-Hill, New Delhi.

[13] Martin, HC. and Carey, GF. 2006. Introduction to the Finite Element Analysis,McGraw Hill Publishing Co Ltd, New Delhi.

FLOW ANALYSIS OF POSITIVE DISPLACEMENT PUMP LOBE ROTOR USING ANSYS WORKBENCH

[1] MOHD SALMAN AHMED SIDDIQUI, [2] Mr. M.PRASAD

[1] PG Scholar, Department of MECH, **Methodist College of Engineering & Technology.**
Abids, Hyderabad – 500 001.

[2] Assistant Professor, Department of MECH, **Methodist College Of Engineering & Technology.**
Abids, Hyderabad – 500 001.

Abstract

The rotary device comprises counter-rotating lobes used in Circulating Fluidized Bed Combustion based Power Plant concerns reduction in volumetric efficiency and generation of excessive noise due to leakage of flow/unequal velocity distribution. To troubleshoot or overcome these problems, measurements at plant site or prototype test results through scale down experiments at laboratory are not only complex task in terms of money and time but also will not yield expected flow characteristics that will aid to improve performance of component. Alternatively, the flow inside the rotary blower/pump also known as roots blower can be obtained through computational fluid dynamics techniques. Accordingly, the assembly of this blower has been studied and a solid model was created. Flow passage of suction, discharge, casing comprises lobes are extracted. Due to presence of small clearances of the order ~2-3 mm between lobe to wall and lobe to lobe, domain discretization with hexahedral elements are made to capture flow in the clearance regions. The volume mesh has imported to flow solvers to simulate compressible flow in steady state to study the leakage flow and pressure fluctuations. With the flow/thermal conditions such inlet stagnation pressure, exit static pressure, lobe rotations, and etc.Leakage mass flow rate and pressure fluctuation. was obtained through three dimensional flow simulations.

1: Introduction and problem definition

1.1 Application of lobe pump

The combustion of fuel in a CFBC boiler, whose schematic is shown in Figure-1.1, takes in a vertical chamber. The gas is generated by fuel combustion, while introducing about 40-50% of total air as primary air through distributor and remaining as secondary air into lower sections of the furnace for complete combustion. Flue gas is produced from the solids out of the combustor to refractory lined cyclone.

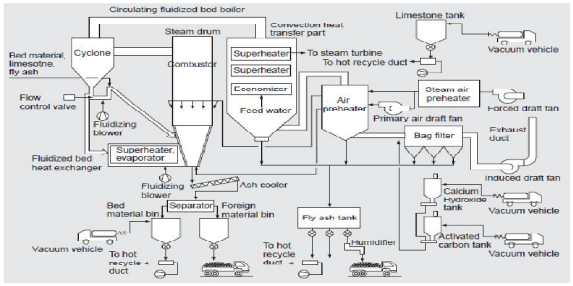

Fig 1.1 Schematic diagram of CFBC boiler

The cyclone collects more than 99% of the incoming solids and uncollected coarse particles from the cyclone bottom are sucked by the rotary blower/pump. The rotary blower creates positive pressure in the furnace and the negative pressure in cyclone collector. This pressure prevents the flow of material back up the cyclone from the bottom of the furnace. The solid particles from the rotary blower are subjected through control valves towards

Fluidized Bed Heat Exchanger where its temperatures are reduced. The cooled ash particles are then returned to combustor for generation of gas. Rotary blowers located below the cyclone and Fluidized Bed Heat Exchanger are also called positive displacement pump comprises casing, rotors and suction and discharge ducts. The number of rotating lobes in the blower can vary from two to four lobes based on pressure ratios and flow quantity. Depending upon operating speed and pressure ratio, the efficiency of rotary blower can be obtained through the nomograms.

The efficiency point will rise with the increasing boost and will move towards right over increase in blower speed. It can be seen that, at moderate speed and low boost, the efficiency of the blower will be over 90%.In this zone, the rotary blowers are normally to be operated. Boost is given in terms of pressure ratio, which is the ratio of absolute air pressure before the blower to the absolute air pressure after compression by the blower.

If no boost is present, the pressure ratio will be 1.0 means outlet pressure is equals to inlet pressure. For the reference boost, that is slightly above a pressure ratio of 2.0 compared to atmospheric pressure the efficiency of rotary blowers are in the range of 50% - 58%. Replacing a smaller blower with a larger one moves the point to the left means that it falls in higher efficiency areas. These rotary blowers are so rugged machines which makes very noisy and inefficient in nature. In general, the noise levels are more than 110 dB (at 10m), and the efficiency is less than 65% level.

Moreover, the characteristic curves run very steep; i.e., nearly constant volume flow is produced over a wide range of pressure ratio. Thus, to control the flow rates at the same pressure ratio is difficult and requires design changes in lobes/rotors profiles.

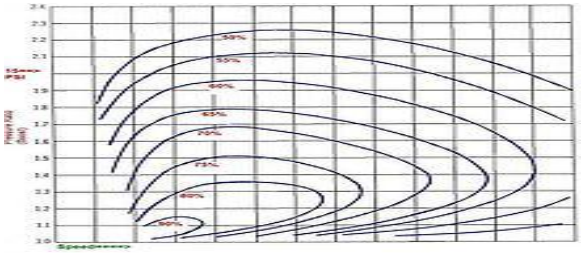

Figure 1.2 nomogram of efficiency of rotary blower

In order to meet customers concern related to its performance due to prevailing flow distribution inside the rotary blower, a detailed analytical study for two lobe configuration are reported. The study described is related to multi-recompression heater embodied as a modified roots compressor, wherein leakage effect was investigated. With the help of this research study, comprehensive numerical model dealing with flow simulation in the rotary blower comprises three lobes for an application to compressor was investigated. In this work numerical techniques were employed to determine flow characteristics for different orientation of rotors placed in the blower casing. The unsteady simulation of roots blower as a function of different angles indicates fluctuations of air velocities in the casing around lobes will have significant effect on estimation of exhaust rate. However, with rapid computer development in numerical simulation using Computational Fluid Dynamic (CFD) techniques, several industrial components [7-10] were analyzed, whose results have provided valuable insights for design improvement.

1.2 Working Principle

Twin Lobe Rotary Air Blowers belong to the category of Positive Displacement Blowers. They consist of a pair of lobes, rotating inside a properly shaped casing, closed at ends by side plates. The

drive to be is connected to the driven lobe, through a pair of gears and they always rotate in opposite directions. As the rotors rotate, air is drawn into inlet side of the cylinder and forced out the outlet side against the system pressure. With each revolution, four such volumes are displaced. The air which is forced out is not allowed to come back due to the small internal clearance within the internals of the machine except a very small amount called 'SLIP'. There is no change in the volume of the air within the machine but it merely displaces the air from the suction end to the discharge end, against the discharge system resistance .Lobe pumps are similar to external gear pumps in operation in that fluid flows around the interior of the casing. Unlike external gear pumps, however, the lobes do not make contact.

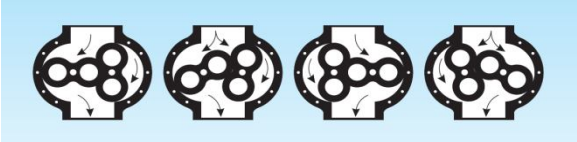

Figure 1.3 Working of lobe rotor

Lobe contact is prevented by external timing gears located in the gearbox. Pump shaft support bearings are located in the gearbox, and since the bearings are out of the pumped liquid, pressure is limited by bearing location and shaft deflection. As the lobes come out of mesh, they create expanding volume on the inlet side of the pump. Liquid flows into the cavity and is trapped by the lobes as they rotate.

Liquid travels around the interior of the casing in the pockets between the lobes and the casing -- it does not pass between the lobes. Finally, the meshing of the lobes forces liquid through the outlet port under pressure.

1.3 Problem Statement

The rotary blowers are so rugged machines which are noisy and inefficient in nature. In general, the noise levels are more than 110 dB , and the efficiency is less than 65% level. Moreover, the characteristic curves run very steep (Figure 1.2) i.e., nearly constant volume flow is produced over a wide range of pressure ratio. Thus, to control the flow rates at the same pressure ratio is difficult and requires design changes in lobes/rotors profiles. To troubleshoot or overcome these problems, measurements at plant site or prototype test results through scale down experiments at laboratory are not only complex task in terms of money and time but also will not yield expected flow characteristics that will aid to improve performance of component. Alternatively, the flow inside the rotary blower/pump also known as roots blower can be obtained through computational fluid dynamics techniques.

1.4 Methodology

Due to unavailability of factory dimensions existing model of lobe rotor was imported in altair hypermesh software from public domain. This model as IGES file comprises surfaces, splines, points imported to preprocessor Hypermesh for fluid portion extraction.

On its import the model surfaces are grouped into different type collectors. After importing the pump assembly extraction of fluid portion (rotors along with casing and inlet/outlet pipes).

Due to presence of small clearances of the order ~2-3 mm between lobe to wall and lobe to lobe, domain discretization with hexahedral elements are made to capture flow in the clearance regions.

2. Impeller Geometry

The Roots compressor has a two-lobe design for the impellers. The two-lobe design has a high volumetric displacement. Figure 2.1 shows the actual shape of the impeller in the Roots compressor, called the “design shape” (solid line). Another shape called the “base shape” is defined which has a circle-involutes-circle profile (dashed line). Mathematical equations

are first derived for the "base shape" and are then modified to arrive at the equations of the "design shape."

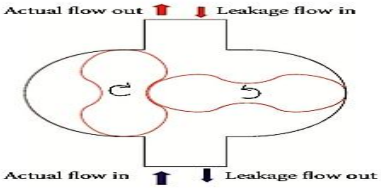

Figure 2.1 Schematic of a two-lobe Roots-type multi-recompression

For θ = [0, β1],

$x1 = R1 \cos(\pi - \frac{5\theta}{4}) + x0$,

$y1 = R1 \sin(\pi - \frac{5\theta}{4})$ 1

For θ = [β1, β2],

2.1 Base shape

If we consider the first quadrant the involute profile shown in Figure 2.2 is a combination of three arcs: the mouth (or waist) and upper portion of the lobe are circular (R1 and R2) and the convex arc connecting them is an involute, which is formed by tracing the end of the string unrolling from the base circle (Rb) The current profile is created with the following parametric equations for the waist, involute and upper lobe shapes.

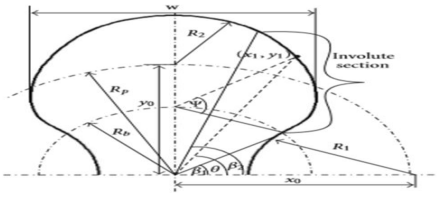

Figure 2.2 Base shape of rotor blade

$x1(\theta) = R21(\psi)\cos(-\beta1) + R22(\psi)\sin(-\beta1)$

$y1(\theta) = R22(\psi)\cos(-\beta1) - R21(\psi)\sin(-\beta1)$, 2

$R21(\psi) = Rb\{\cos\psi + \psi \cdot \sin\psi\}$,

$R22(\psi) = Rb\{\sin\psi - \psi \cdot \cos\psi\}$. 3

The angle "ψ" goes from 0◦ to 86.4708◦ when θ goes from 40◦ to 70◦. The relation between ψ and θ is as follows:

$\theta = \tan^{-1}(\frac{\sin\psi - \psi \cdot \cos\psi}{\cos\psi + \psi \cdot \sin\psi})$. 4

For θ = [β2, π/2],

$x1(\theta) = R3 \cos(52.6\pi(\theta - \beta2)/180(\pi/2 - \beta2) + 37.4\pi/180)$,

$y1(\theta) = R3 \cdot \sin(52.6\pi(\theta - \beta2)/180(\pi/2 - \beta2) + 37.4\pi/180 + y0$ 5

The values shown in Figure 1.33 are as follows (inches for linear dimensions and radians for angles): R1 = 1.44, Rb =0.8 ∗Rp = 1.787, R3 = 1.37, x0 = 2.255, y0 = Rp = 2.239, β1 = 4π/18, and β2 = 7π/18. By substituting the above values in (1)–(5), it is found that the lobe is 3.119 inches wide.The design shape is a modification of the base shape. To adjoin the "add-ons" to the involute curve, the normal to the involute curve has to be found. To find the normal to the involute at any point, the gradient (slope) of the normal is first found out by taking negative reciprocal of dy/dx,

$\frac{-1}{dy/dx} = m = \frac{\sin\psi \cdot \sin\beta1 - \cos\psi \cdot \cos\beta1}{\sin\psi \cdot \cos\beta1 + \cos\psi \cdot \sin\beta1}$ 6

The thickness of add-ons is "a" = 0.04115 in. Hence, the extra material added will be

$Xadd = a \cdot \cos(\tan^{-1}m)$

$Yadd = a \cdot \sin(\tan^{-1}m)$ 7

We add this to the x and y coordinates of the "base shape."Hence,

Xdesign=x1(θ)+Xadd,

Ydesign=y1(θ)+Yadd. 8

x1(i),y1(i)

x2(j), y2(j) 9

For the "tip strip" a value of 0.055 is added for θ = 89.444◦ to 90◦. This is the angle where the tip strip starts and is obtained from the machine drawing of the "design shape."

3. Experimental Methodologies

3.1 Computation Fluid Dynamics

Computational fluid dynamics (CFD) is a branch of fluid mechanics that uses numerical analysis and data

structures to solve and analyze problems that involve fluid flows. The design of turbo machinery components such as fans, blowers and pumps are based on empirical formulae

3.2 Description of lobe pump

Figure 3.1 shows typical rotary positive displacement with its end covers removed. The drive shaft is connected to drive shaft through a pair of helical gearings at the rear end. The drive shaft front end is connected to an electric motor drive using a belt drive arrangement. The lobed shafts rotate with equal rotational speed in opposite directions. The bearings and gears are splash lubricated by oil filled in the end cover chambers.

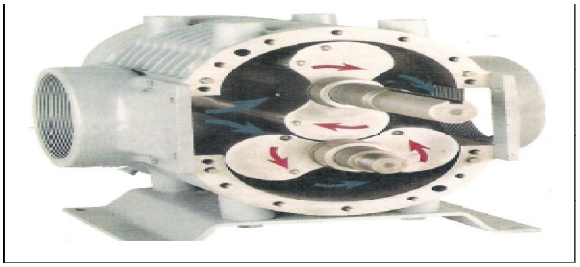

Figure 3.1 rotary positive displacement pumps without end cover

For requirements of pressure rise at blower discharge, the drive shaft rotates in an anti-clock wise direction (viewed from drive end). The direction of blower shaft is reversed for suction pressure requirements. The gas handled by such blower is oil free as the gas path is not coming into contact with lubricating oil circuit. The axes of the drive and driven lobes are set at right angles and working clearances between lobes, casing and the side plates. In one working period, the rotors rotate in a reverse direction; the fluid is compressed and transported from the inlet to the outlet via the chamber.

As soon as the impeller passes the breakaway point, the gas in the well mixes with the gas in the blower casing. After multiple rotations, pressure starts building up in the outlet region and a blower casing is developed. This causes leakage gas to flow back into the low-pressure region through the clearances. The leaked gas, being at a high-temperature, heats the incoming gas. The volume of the incoming gas increases, decreasing the volumetric efficiency and hence reducing the mass flow rate significantly.

3.3 CAD Modal Lobe Pump

Three dimensional solid model was generated using the dimensions in front/top and side views of several part and assembly drawings using industry standard CAD modeler commercial software package. This model as IGES file comprises surfaces, splines points are exported to another preprocessor Hypermesh for fluid portion extraction. On its import the model surfaces are grouped into five groups as shown in Figure-3.2. Since the lobes rotating counter clockwise direction and it is essential to consider orientation at 15 degrees. This involves lot of simulation and pre-processing work and the present report is considered only two orientations wherein rotors are at 180- 90 Figures 3.3.

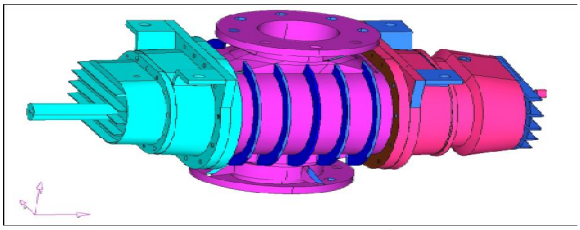

Figure 3.2 Imported model of lobe rotor

In order to account fluid passage due to change of lobes rotation at 45^0, the lobes are rotated about its pivot point in center in x direction.

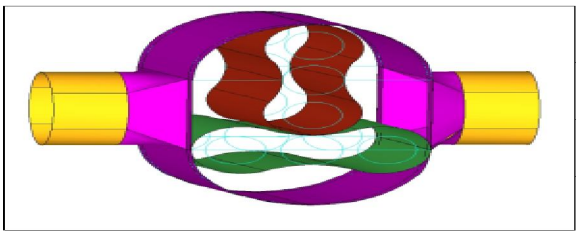

Figure 3.3 Lobe rotors at 180-90 orientation

The model for roots blower with the rotating lobes connecting suction and discharge duct is shown in

Figure-3.4. In order to to carryout compute pressure and velocities of entrained air when the lobes are subjected rotations, flow passage has to be discredited with computational mesh comprises different types of elements. Using above surface model, with the closure of inlet and exit duct end faces, volume can be generated filled with tetrahedral elements. In order to account fluid passage due to change of lobes rotation at 45^0, the lobes are rotated about its pivot point in center in x direction.

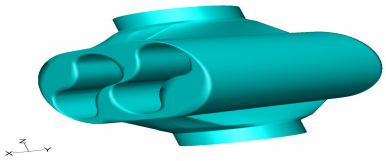

Figure 3.4 Roots blower connecting suction and discharge duct.

3.4 Computational Grid Generation

At the core of CFD, computational grid is central element, which often considered as most important and time consuming part in simulation projects. The quality of the grid plays a direct role on the quantification of flow results, regardless of the flow solver used for simulation..

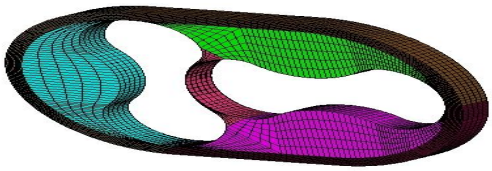

Figure 3.6 hexahedral mesh for one end of the lobe pump

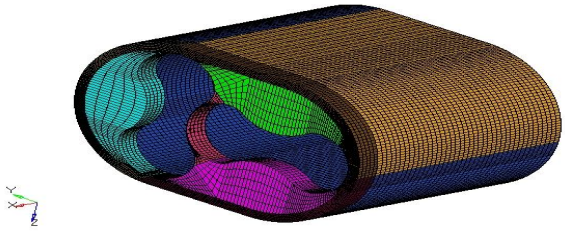

Figure 3.7 Mesh element of casing region

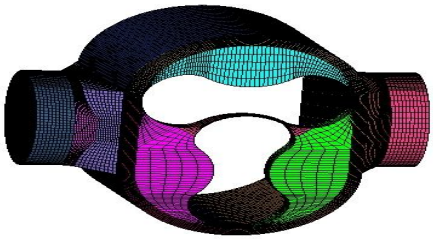

Figure 3.8 mesh continuity with inlet and exit pipes

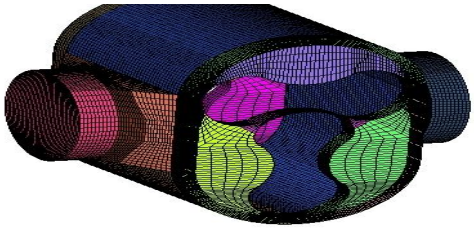

Figure 3.9 solid mesh of lobe pump block

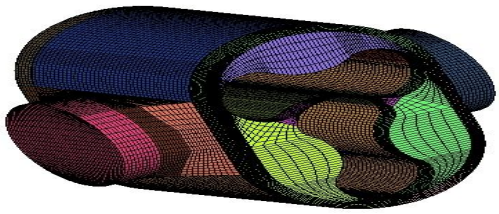

Figure 3.10 mesh generation of complete element

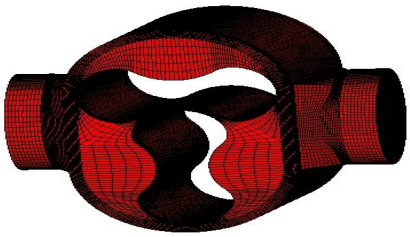

Figure 3.11 grid generation of lobe rotor

With the help of above grid, boundary conditions like inlet, exit, rotating wall1 and rotating wall2 are created. The main grid collectors with these boundary conditions regions shown in Figure 3.12 with appropriate solver deck can be exported for flow simulation.

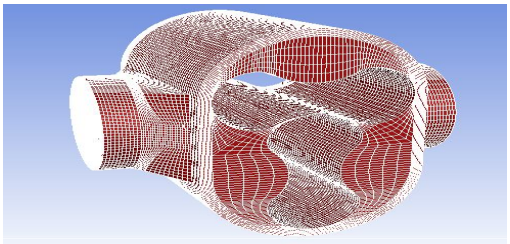

Figure 3.12 grid collectors with boundary condition

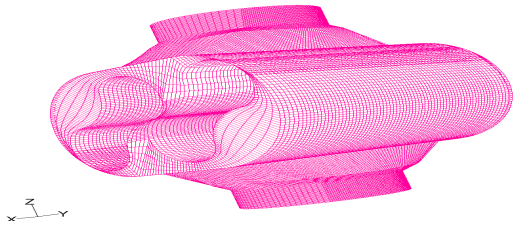

Figure 3.13 Orientation of lobes in 45 degrees position

After exporting the mesh into the flow solver, the working fluid will be ideal gas, compressible, steady, three dimensions. The several plane slices in x direction of computational domain provides valuable flow results. `

3.5 Selection of Flow Solver

ANSYS Fluent is a state-of-the-art computer program for modeling fluid flow, heat transfer, and chemical reactions in complex geometries.

However the input to the solver must be grid file saved as .cas file. The software can be activated by double clicking the .case file in the relevant directory. It reads geometrical information and checks the grid quality for negative volume displays the mesh along with boundary conditions regions as shown in Figure 3.19

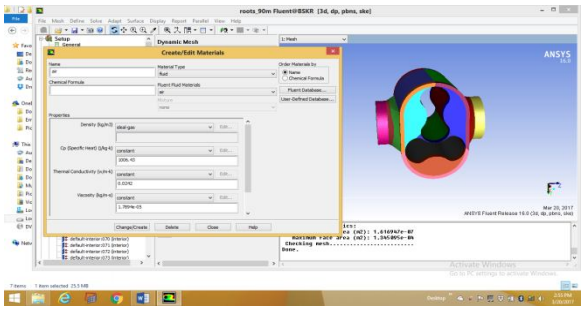

Figure 3.19 mesh generation with geometrical condition

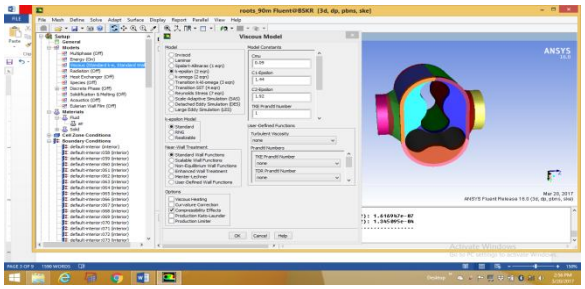

Figure 3.20 selection of available model on viscosity

In order to see the results are computed in right direction, using report mass flow flux values of at inlet and outlets are computed and shown below.

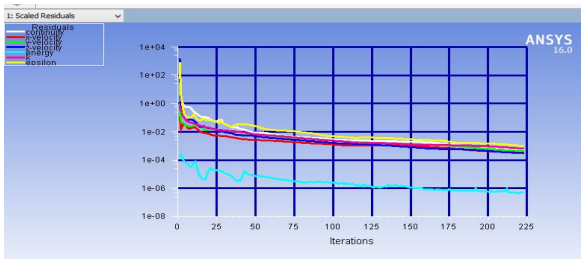

Figure 3.21 Scale residuals graph with rotors perpendicular

In order to see the results are computed in right direction, using report mass flow flux values of at inlet and outlets are computed and shown below

Mass Flow Rate	(kg/s)
inlet	0.18000001
exit	-0.18018808

In order to carryout flow analysis in the lobe pump, wherein the rotors are reoriented to 45 degrees are modeled geometrically and generated the computational mesh. The mesh along with inlet, exit, rotating walls are format output of equation residuals exported to fluent solver as shown in the exported format output of equation residuals exported to fluent solver .

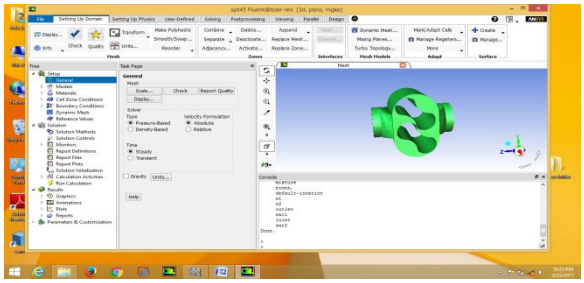

Figure 3.22 mesh element exported to fluent solver

After checking the mesh quality, scaling, materials like compressible air ideal gas has been considered whose working pressure is 1 atm. To capture viscous losses, Reynolds Average Navier Stokes two equation turbulence model with standard wall function are considered

For the rotating walls, in the boundary condition wall motion is selected as moving with rotational speed 272.2 Rad/sec whose screen shot is shown in the Figure 3.23. .

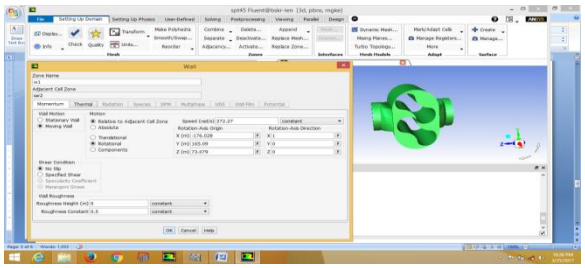

Figure 3.23 Boundary conditions for rotating walls

At the inlet of lobe pump total gauze pressure 40 Pascal's are prescribed and exit 40000 Pascal normal to boundary are assigned. For the rotating walls, in the boundary condition wall motion is selected as moving with rotational speed 272.2 Rad/sec whose screen shot is shown in the Figure 3.23. The second rotor is rotating in anti-clockwise direction whose rotational speed is assigned as -272.2 Rad/sec. Under these conditions, after initialization the governing equations, three momentum, two turbulence, continuity and energy equations are iterated to meet convergence criteria The graphical output of equation residual error over iterations are shown in Figure 3.24

The Flux of mass flow across inlet and exit locations are computed and shown below ensures the conservation of mass principle.

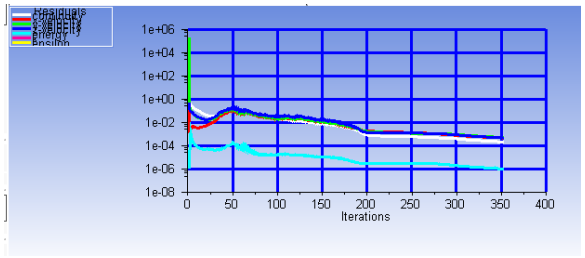

Figure .3.24 graphical output of residual error over iteration

It is observed in the case of rotational wall, the convergence of governing equations is slower than non-rotating case.

Mass Flow Rate	(kg/s)
Inlet	1.4629610
Outlet	1.4621507

Using the surface integrals, with the mass flow average, absolute pressure across the inlet and exit locations are calculated as - Mass-Weighted Average

Absolute Pressure	(Pascal)
Inlet	100167.22
Outlet	138265.83

4. Results and discussions

4.1 Vector plots

The Velocity vectors in the middle plane of lobe pump obtained in the case of rotors oriented 180 and 90 degrees positions are shown in the Figure 4.1

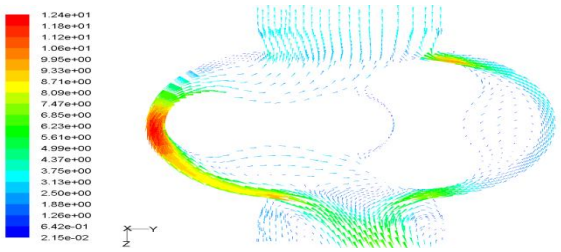

Figure 4.1 Velocity vector in middle plane at 180-90 position

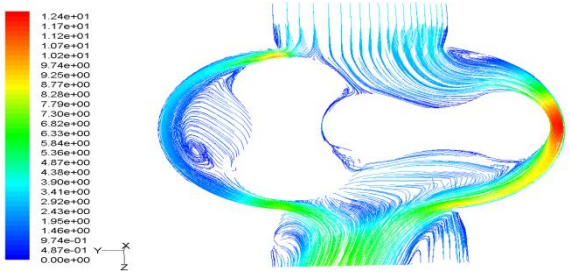

Figure 4.2 Flow circulations at the inlet with strong turbulent vortices

4.2 Flow contour

4.2 Flow contour

This is a case of assumption that the rotors are under stationary conditions, mass flow at inlet is 0.18 kg/s and exit pressure is 40530 Pascal. The velocity

vector from inlet in the lobe pump chamber is uniform and exhibits high magnitudes at the end of rotor positioned at 180 degree. The flow at the inlet also indicates quite strong turbulent vortices whose effect in the form of flow recirculation can be visualized in Figure 4.2.Being the flow is compressible the velocity Mach contours and pressure are detailed in the Figures 4.3 and 4.4

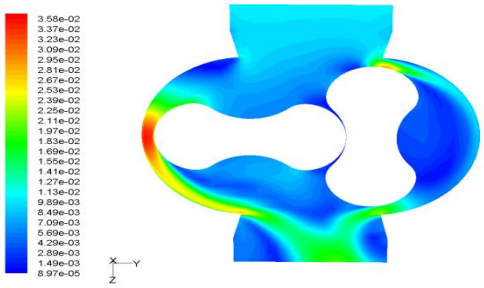

Figure 4.3 Velocity Mach contour

The Mach number variation the lobe pump plane indicates high at the location of rotor positioned at 0 degrees. As a result the Mach number exhibits high at most part of inlet location.

The pressure plot in the form of contours are generated in the lobe pump middle plane and its variation from inlet accelerates and becomes low pressure at the rotor positioned at 0 degrees and then increases at its upper surface.

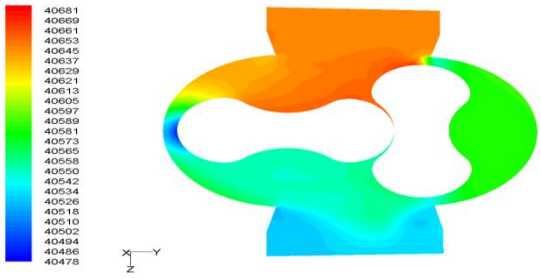

The pressure plot in the form of contours are generated in the lobe pump middle plane and its variation from inlet accelerates and becomes low pressure at the rotor positioned at 0 degrees and then increases at its upper surface. This implies that pump is attaining high pressure at the exit location. The numerical results obtained for several flow parameters are visualized in the computational domain using solver post-processor. The velocity vector in the mid-plane of the blower is shown in the Figure -4.5.

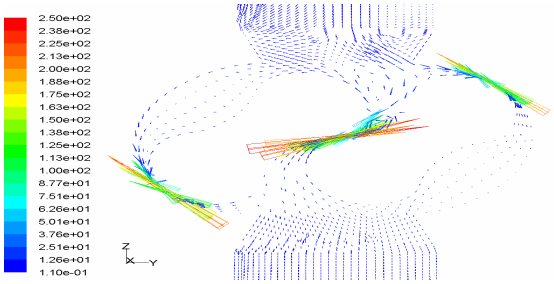

Figure 4.5 velocity vectors at mid plane of blower

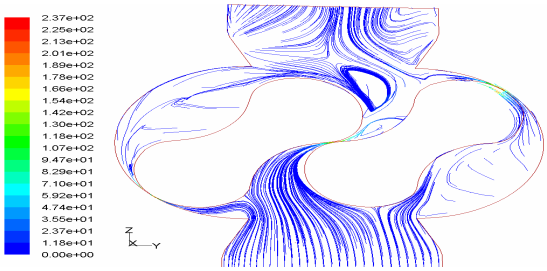

Figure 4.6 Stream line pattern of leakage flow in mid plane

The leakage flow starts from the discharge side of the blower and flows towards blower inlet. The mass averaged flow rate at inlet region is 0.14 kg/sec. Maximum velocity 13 m/sec occurs in the clearance region between drive lobe and casing. Figure-4.6 shows the stream line pattern of leakage flow in the mid plane. The flow recirculation can be seen at inlet and outlet

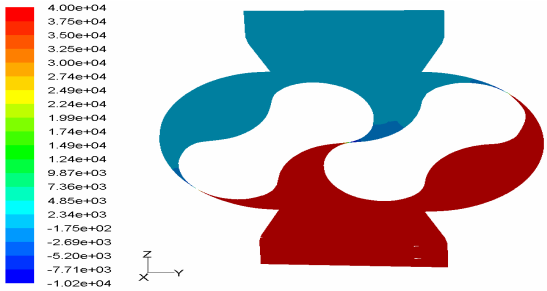

Figure 4.7 pressure variation in middle plane of root blower

Passage near the rotors and clearance area between drive lobe to casing, and also at exit location. Figure 4.7 shows the pressure variation in the middle plane of the blower the contours of maximum pressure are observed at the outlet region whereas the inlet region has lower pressure. The minimum pressure occurs in the clearance between drive lobe and casing.

4.3 Summary of Results

The summary of results obtained from the present cfd analysis is as follows

No	Mass average quantities	Inlet	Outlet
1	Flow Rate Kg/sec	0.13450293	0.134446
2	Static Pressure Pa(gauge)	19.988194	111.90541
3	Velocity m/sec	4.8759556	3.6270936
4	Total pressure Pa (gauge)	35.071281	119.97011
5	Temperature Degree K	309.69043	309.99295
6	Density Kg/m**3	.1400392	.11399997

5. Conclusion and future scope of work

5.1 Conclusion

The rotary device comprises counter-rotating lobes used in Circulating Fluidized Bed Combustion based Power Plant concerns reduction in volumetric efficiency and generation of excessive noise due to leakage of flow/unequal velocity distribution. It has also several applications in process and petro-chemical industries. To troubleshoot or overcome these problems, measurements at plant site or prototype test results through scale down experiments at laboratory are not only complex task in terms of money and time but also will not yield expected flow characteristics that will aid to improve performance of component. Alternatively, the flow inside the rotary blower/pump also known as roots blower can be obtained through computational fluid dynamics techniques.

Accordingly, the assembly of this blower has been studied and a solid model was created. Flow passage of suction, discharge, casing comprises lobes are extracted. Due to presence of small clearances of the order ~2-3 mm between lobe to wall and lobe to lobe, domain discretization with hexahedral elements are made to capture flow in the clearance regions. The volume mesh has imported to flow solvers to simulate compressible flow in steady state to study the leakage flow and pressure fluctuations. With the flow/thermal conditions such inlet stagnation pressure, exit static pressure, lobe rotations, etc., leakage mass flow rate and pressure fluctuations was obtained through three dimensional flow simulation.

Two cases have been analyzed keeping in view of difficulties for numerical simulation - first one is the rotors are positioned 0 and 90 degrees which are treated stationary state. For the inlet and exit pressure conditions, the velocity vectors exhibits high at the rotor positioned at 0 degree and its variation at inlet generates severe turbulent vortices. The absolute pressure at the middle plane of the lobe pump generates high at exit locations indicating that it acts like a pressure rise application. In case of rotating walls rotating in counter clock wise direction, the pressure drop across the blower inlet and exit locations are found to be 92 Pascal The simulation predicts the maximum velocity of 6 m/sec in the clearance between lobe and casing. The leakage flow rate calculated from the mass averaged values of velocities and density of flow medium is found to be 0,135 kg/sec. Compressible ideal flow simulation has been carried out for evaluation of leakage flow rates and volumetric efficiencies.

5.2 FUTURE SCOPE OF WORK

The Roots type supercharger shown below is used to boost the intake pressure of an internal combustion engine by approximately 12-15 PSI, drastically improving the performance of the engine. The device consists of two rotor assemblies turning

in opposite directions. The air is pushed around the outside of the rotors and out the bottom. The outer surface of each rotor lobe contains a Teflon seal strip to prevent leakage. In order to reduce pulsing of the pressure, the lobes are often twisted along the rotational axis, or helically, as shown Figure 5.1

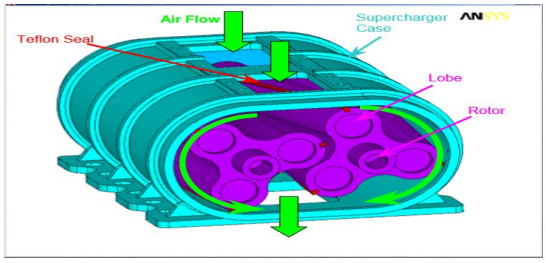

Figure 5.1 Lobe rotors with three lobes and supercharger case

One of the future scopes of for this class of problem is to determine the clearance or interference of the rotor lobe seals and the case. Minimizing this clearance under start-up and operating temperatures is crucial to supercharger performance

R E F E R E N C E S

1.Rajaram S, Natarajan R, Design features and operating experience of BHELs First CFBC boiler installed at Sinarmas, BHEL Jrnl, Vol 21 pp 58-66, 2000.

2.Iwao OHTANI and Tetsuo IWAMOTO, Reduction of Noise in Roots Blower, Bul. JSME, Vol. 24, No.189, 1991

3.G.Mimmi and P.Pennachi, Analytical model of a particular type of positive displacement blower Procgs. of Institution of Mechanical Engineers, Vol 215 Part-C pp 517-526, 1999

4.David I. Blekhman, Joseph C. Mollendorf, James D. Felske, and John A. Lordi,Multi-Control-Volume Analysis of the Compression Process in a High-Temperature Root's Type (four lobes) Compressor, International journal of Rotating Machinery, 10: 45–53, 2004

5.Z.F.Huang and Z X Liu, Numerical Study of a Positive displacement Blower (three lobes), Procgs of Institution of Mechanical Engineers, Vol. 233,Part-C, pp 2309-2316, 2009

6.Ashish M. Joshi et.al Clearance Analysis and Leakage Flow CFD Model of a Two-Lobe Multi-Recompression Heater , Intl. Jrnl of Rotating Machinery Article ID 79084, Pages 1–10, 2006

7.Bhasker C, Numerical simulation of turbulent flow in complex geometries used in power plants, International Journal- Advances in Engineering Software, UK Vol.33, pp 71-83, 2002.

8.Bhasker C., Flow Simulation in Industrial Cyclone Separator, International Journal – Advances in Engineering Software, UK, Vol 43, pp 220-228, 2010

9.Bhasker, C., Troubleshooting Steam Turbine Bypass Valves – Role of CFD as a key Analytical tool, Technical Torque, PVS Industrial Magazine, India, pp 20-24, May-June, 2010.

10.Bhasker, C., Hydraulic Control Valve Flow Simulation, Prediction of flow Pattern in Globe type Control Valve using CFD, Technical Torque, PVS Industrial Magazine, pp 14-21, July, Aug, 2010

11.Thomson, J.F et.al Numerical Grid Generation – Foundations and Applications, North Holland, Amsterdam, 1985

12.ShekarMajumdar Pressure based finite volume algorithm for viscous flow computation, Lecture Notes, CFD Advances and Applications, NAL, Bangalore, India, 1994.

TWO PHASE FLOW SIMULATION IN "Y" JOINT DUCT USED IN PIPELINE APPLICATIONS

[1] JALA HARIKA [2] Mr. M.PRASAD

[1] PG Scholar, Department of MECH, **Methodist College of Engineering & Technology.**
Abids, Hyderabad – 500 001.

[2] Assistant Professor, Department of MECH, **Methodist College of Engineering & Technology.**
Abids, Hyderabad – 500 001.

Abstract

Flow diversion through Y branch and T junction ducts are extensively used in pipeline applications for uniform distribution of fluids. In order to understand flow uniformity, typical geometrical situations of different configurations are developed for CAD models using Altair Hyper mesh. The of curvatures in the duct geometry flow takes sharp turns leading to severe turbulent fluctuations whose consequent effects give rises to unequal flow at its exit location. In many physical situations, these ducts are subjected to more than one fluid is called two phase air-dust particles or water and sand particles. In order to understand flow mechanism, geometrical models generated are further subjected computational mesh on which conservation equations are iterated to obtain successful solution with inlet velocity and exit pressure conditions. After successful flow simulation discrete phase module is activated to track particle trajectories along with impact parameters. From the solution, several parameters through graphical forms are visualized and interpreted. In order to improve velocity and flow path in computational domain, several simulations are repeated with refinements in the mesh elements in terms of type and density. It is expected that two phase flow analysis dealing with fluid-particles will provide several insights for design of pipeline layout for proper flow distribution.

1. Introduction

Pipe networks are very common in industries, where fluid or gases to be transported from one location to the other. The pressure loss may vary depending on the type of components coming across in the network, material of the pipe, the fluid that is being transported through the network and pipe fitting. The analysis of pipe network is very important in engineering point of view. A lot of engineering problem dealt with it. Due to rigorous engineering application and implications the analysis is important. Fittings are used in pipe and plumbing systems to connect straight pipe or tubing sections, to adapt to different sizes or shapes, and for other purposes, such as regulating or measuring fluid flow. A wye branch (as the name implies, this fitting device is "Y" shaped) allows splitting a branch line equally in two directions. It is a fitting with three openings and is used to create branch lines. A standard wye allows one pipe to be joined to another at a 45 degree angle. Wyes are similar to this except that the branch line is angled to reduce friction that could hamper the flow and that the connection is typically at a 45-degree angle rather than a 90-degree angle . Economy wyes are often spot welded together; industrial wyes have a continuous weld at each seam. In the present work, fluid dynamic analysis for different Y- shape connections will be done, for laminar. The effect of bend angle, pipe diameter, pipe length, Reynolds number on the resistance coefficient is studied and. It

was observed that resistance coefficient vary with the change in flow.

Multiphase flow in reciprocating internal combustion engines is widely used for prediction of thermodynamic parameters of gases in the branched ducts of inlet and outlet systems. These ducts are connected to the branch of "Y" and "T" type, where the gas is transferred from supplier pipes to the outflow pipes in varying of changing in the time gas properties. In the engine ducts the gas parameters are a function of temperature and chemical composition. Taking into account the dynamics of the gases with incident and reflected pressure waves the filling and emptying of the cylinder depends on the flow in the branches particularly in multi-cylinder engines. The concept of calculations, based on the balance of mass, energy, and the values of the pressure loss between the pipes oriented relative to each other, has to determine the thermodynamic parameters of gas and the mass fraction of each component in the branch node. Although the model refers to the three branched ducts, and test results are considered to "T" type of branched pipes, one can apply it to the layout consisting of more pipes. This allows a definition of incoming or outgoing pressure waveforms in the ducts from the valves or the ports of individual cylinders in internal combustion engines. Unsteady gas flow in the engine ducts influences on the mass filling ratio of the gas in each cylinder. In the simulation of any engine, where its performance is related to the mass trapped in the cylinder and pressure wave motion through the branched pipes was considered .

Flexible duct junction boxes are commonly used to split airflows in residential heating, ventilation, and air conditioning (HVAC) systems of insulated flexible ducts. Junction boxes typically are made of fiberglass duct board or insulated sheet metal. Junction boxes are popular and, properly designed, can result in an HVAC system that performs well. However, junction boxes that are poorly designed can have high pressure losses relative to other duct fittings. That is, each junction box creates a higher resistance (e.g., duct friction) that may impede the ability of the air handler unit (AHU) to move the air through the ducts, which in turn may result in occupant comfort complaints. With any duct runout, balancing dampers are needed to adjust the pressure of airflow through the outlets because self-balancing systems are not realistic. Junction boxes are not necessarily the most energy-efficient option for an HVAC system. It is important to weigh their benefits as a low first-cost and easily installed option versus the benefits of using a trunk and branch system that will provide more certainty to Effective Length values information provided other calculation tools and information provided by manufacturers' performance data. This measure guideline assumes that designers have an understanding of load calculations for system and room airflow requirements and duct run attributes such as airflow rate, velocity, and friction rate.

1.2. Problem definition

The transport of fluids in branched duct generated pressure losses and turbulence due to different turns around sharp corners.The curvatures in the duct geometry flow takes sharp turns leading to severe turbulent fluctuations whose consequent effects give rises to unequal flow at its exit location. Performance degradations of ducts will be more significant if the working fluid is of particulate laden nature.

Besides thermal gradients on wall surfaces, structurally ducts are subjected to large deformations altering principal stresses.

In order to understand multiphase flow mechanism in the branched duct, detailed numerical studies are essential under three dimensional environments.

3. EXPERIMENTAL METHODOLOGY

3.1 Overview of Altair-Hyperworks

HyperWorks Desktop is an integrated user environment for modeling and visualization. It can be used to pre-and post-process finite element and multi-body dynamics simulations as well as to manage and visualize simulation and test data.

3.1.2 Construction of Geometrical Model

When Altair-Hypermesh is activated on the desktop/laptop, graphical user display opens as shown in Figure 3.1 for development of geometrical model using bottom up approach.

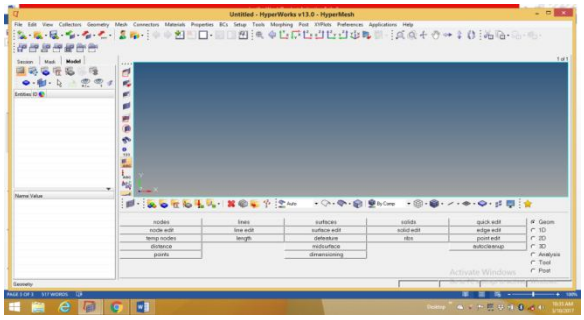

Figure: 3.1 Development of Geometrical Model Using Bottom up Approach

With the options available in 2dimensional options, the line drag command is used to generate the cylindrical tube Surface in xy direction. In the line drag options, one must ensure that drag geometrical option – line to be selected and type should be toggled to surface.

With these options, the geometry of cylindrical tube in xy plane will be generated. Using tools, the lines drawn can be deleted. The topologically, the cylindrical tube is not closed and hence shows its ends are in red colour as shown in Figure 3.2

Using windowing options undesired surfaces will be deleted. The resulting error free closed surface of y branch is shown in figure.3.3

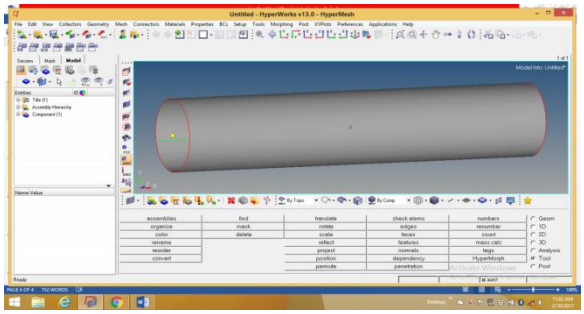

Figure: 3.2 Geometry of Cylindrical Tube

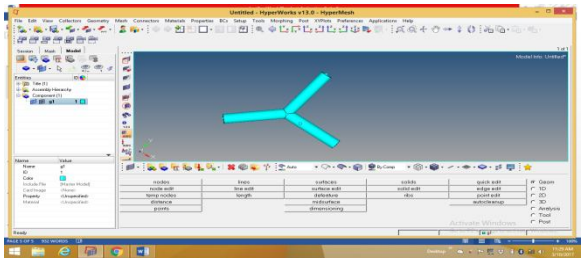

Figure3.3: selecting all surfaces and executing trim option

The last step left for completion of geometry is generation of volume using the surfaces of geometrical model. The software provides generation of solid part option once activated it expects error free closed surfaces. The moment all surfaces are selected and execute the create operation it generates solid part of the model as shown in Figure 3.4

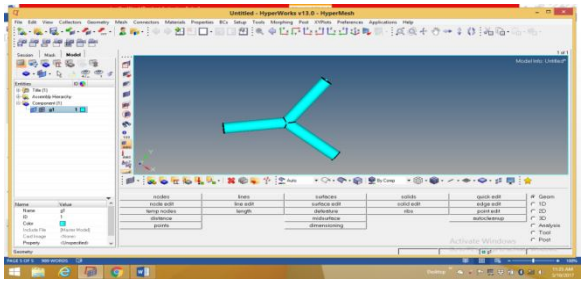

Figure: 3.4 Generation of volume using the surface of geometric model

In order to extend the geometry for structural analysis, thickness of 2 units above inside cylinders are added and associated surfaces at junction are trimmed as shown in the Figure 3.5

After checking the surfaces through topology the volumes of cylindrical y duct with thickness has been created as shown in the Figure 3:6

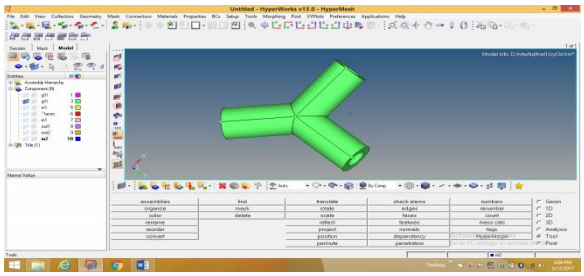

FIGURE 3.5 Geometry for structural Analysis

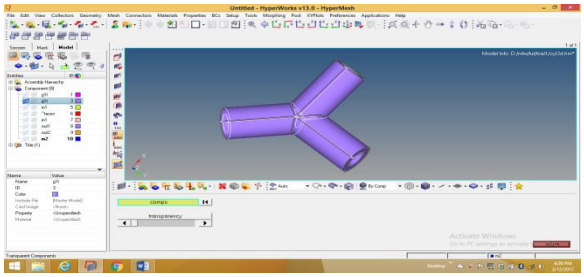

FIGURE 3.6 Volume of cylindrical Y duct with thickness

3.2 Computational Grid Generation:

At the core of CFD, computational grid is central element, which often considered as most important and time consuming part in simulation projects. The quality of the grid plays a direct role on the quantification of flow results, regardless of the flow solver used for simulation. The mesh generation concepts were comprehensively discussed and reviewed has resulted to several commercial software's which are being extensively used for several industrial components was shown in

Figure 3-7.

The geometrical model generated with volume generated in previous chapter is discretized with volume tetrahedral elements using 3d panel tool as shown in Figure 3.8.

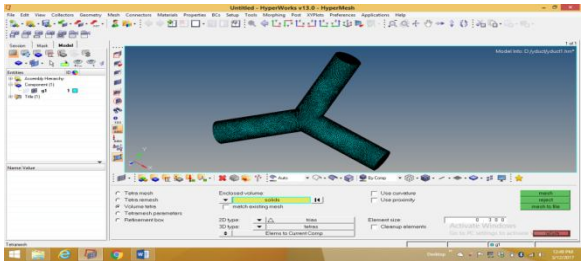

FIGURE 3.7 volume tetrahedral elements using 3d panel tool

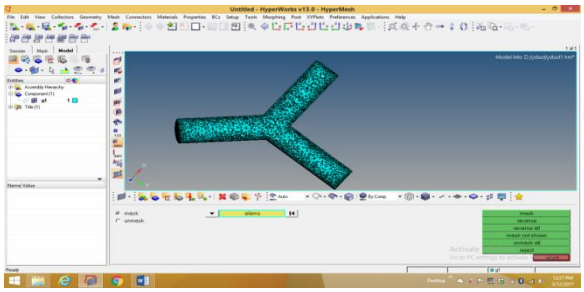

FIGURE 3.8 selection elements under tools panel and mask option

The element size by default will be 4 with which the grid density is very coarse and the same has been gradually decreased to the value 0.3 so that the mesh size 36805 nodes.

Using Tools panel face option by selection of elements, surface grid is generated and shown in figure 3.9

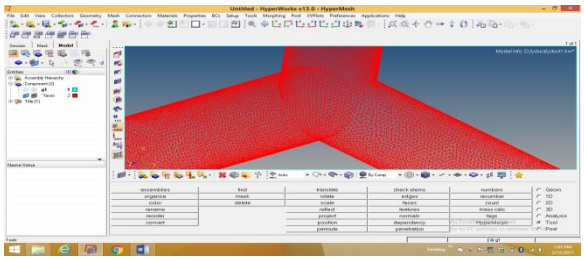

FIGURE 3.9Face option by selection of elements

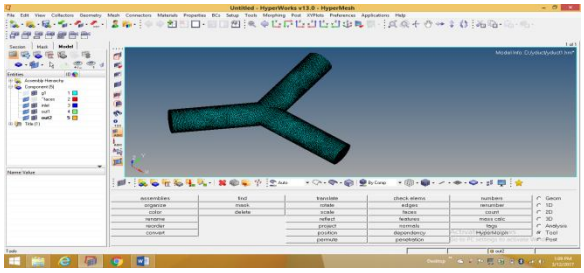

FIGURE 3.10 Creating boundary conditions

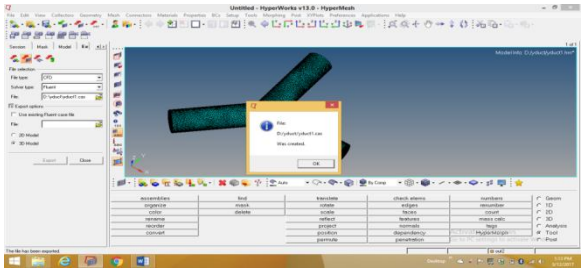

FIGURE 3.11 Selecting solver desks CFD

After generating the volume for thickness of y duct cylinders, the tetrahedral mesh has been generated by

providing the suitable element size as shown in Figure: 3.12.

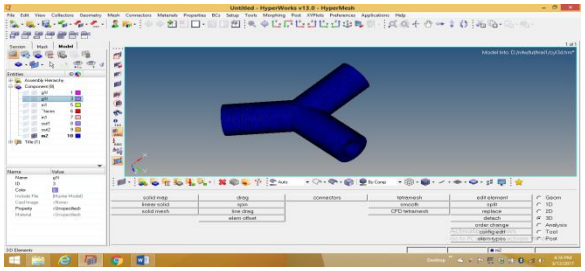

FIGURE 3.12 Tetrahedral meshes

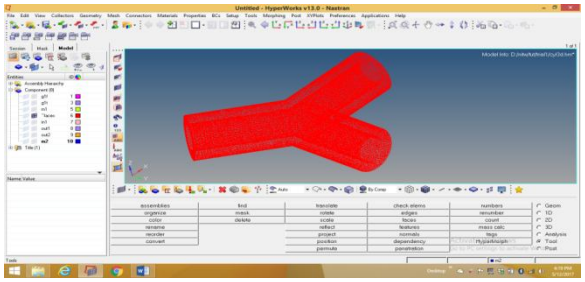

FIGURE 3.13 Distortion of elements specially at junction location

After examining the mesh visually, the grid is imported by selecting the NASTRAN Solver Deck by using long format as.bdf file which can be read in static structural analysis solver via finite element modeler of Ansys Products.

3.3 Finite element Analysis of Solids

Finite element analysis is a computer based numerical technique for calculating the strength and behavior of engineering structures. It can be used to calculate deflection, stress, vibration, buckling behavior and many other phenomena. It can analyze elastic deformation or "permanently bent out of shape" deformation.

3.4 Selection of Flow Solver – Ansys Fluent:

ANSYS Fluent is a state-of-the-art computer program for modeling fluid flow, heat transfer, and chemical reactions in complex geometries

However the input to the solver must be grid file saved as .cas file. The software can be activated by double clicking the .case file in the relevant directory. It reads geometrical information and checks the grid quality for negative volume displays the mesh along with boundary conditions region Figure 3.21

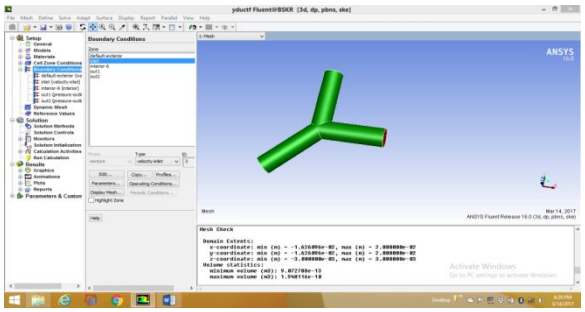

FIGURE 3.21 Checks the grid quality for negative volume displays the mesh along with boundary conditions region

However, in most flow simulation cases, two equation RANS model can be used to account the turbulent losses in the computational domain.

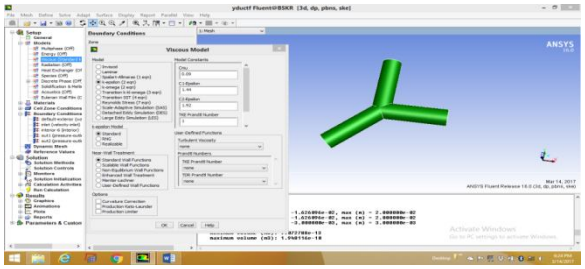

FIGURE 3.22 Viscous models

The material of working fluid by default can be air, depending upon requirements; the user can add different fluid from its data base like water or other gases. Next physics set up is the boundary condition whose values are highly influences the equation residuals. When the grid from third party software is imported, the boundary conditions like inlet, exit, shows as wall type and needs to be changed to respective option like inlet/pressure outlet. The values of velocity in m/sec for most case works fine with default values of turbulent length scale and viscosity. Some this gives trouble; user may change velocity option to mass flow. Generally operating pressures are one bar i.e., 101325 Pascal's and its

value in the pressure out boundary condition should be mentioned as zero. .

The calculate command solves transport equations using iteratively to reduce the errors and its convergence history for the case one of y-duct geometry is shown in Figure: 3.23

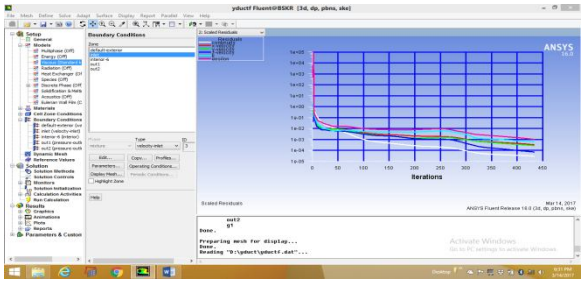

FIGURE 3.23 Command solves transport equation using iterations

In order to see the results are computed in right direction, using report mass flow flux values of at inlet and outlets are computed and shown below.

In order to see the results are computed in right direction, using report mass flow flux values of at inlet and outlets are computed and shown below.

MassFlowRate	(kg/s)
inlet	0.00017288377
out1	0.00014094961
out2	3.1955055e-05

The balance of mass flow across inlet and exit locations ensures the mass conservation principle which implies that quantity of mass entered in the volume of the component should leave with the same amount.

3.5 Simulation of Discrete Phase Model using Ansys Fluent:

The flowing fluid in the y-duct is subjected to micron level dust/carbon particles, component performance via particle motion can be simulated using discrete phase model available in Fluent Solver. However the computational grid used for flow simulation along with the turbulence model selected is remain same. When discrete phase model is made on, a pop-up menu shown in Figure 3.24 displays on the flow solver.

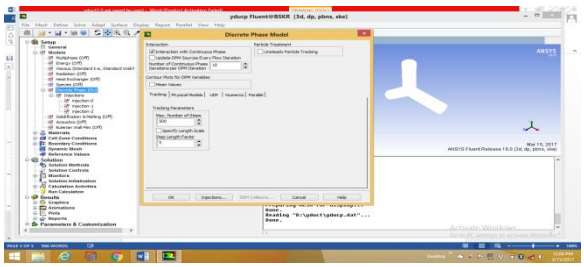

FIGURE 3.24 Discrete phase model

Under Discrete phase model, the solver expects to choose injection of particles which a pop-up-menu shown in Figure: 3.25

In the analysis three injection locations are chosen with the particle sizes 1 micron, 10 microns and 100 microns. The particles are considered to spherical whose drag law available in the solver is utilized.

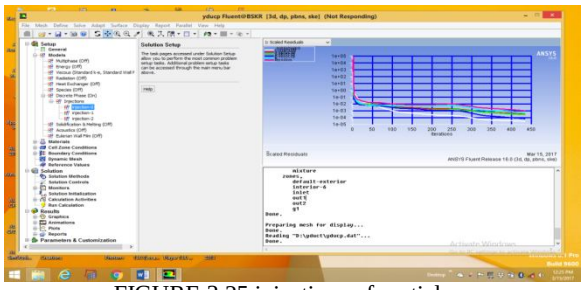

FIGURE 3.25 injections of particles

The flows with particles are simulated whose convergence history of equation residuals is shown in Figure 3.26.

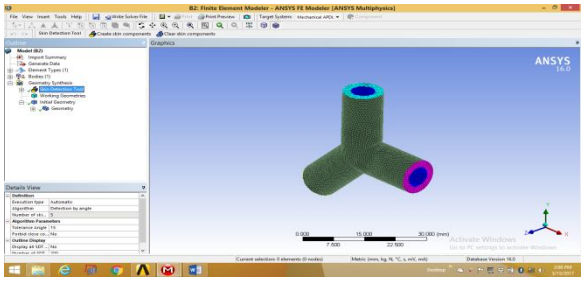

FIGURE 3.26 convergence history of equation residual

3.6 Structural Analysis of Y duct using Ansys Work Bench:

The geometry of Y-duct with thickness created and mesh generated in Altair Hypermesh has been saved with the user preferences as NASTRAN. The mesh

file has been saved as long format of NASTRAN Solver deck as .bdf File. When structural analysis for Y-duct envisaged, one of the essential condition is pressure load which comes from CFD solution

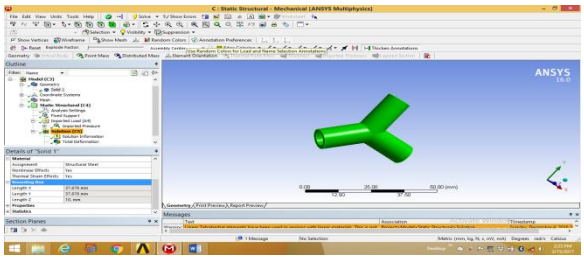

Figure 3.27 Structural analysis graphic user displays

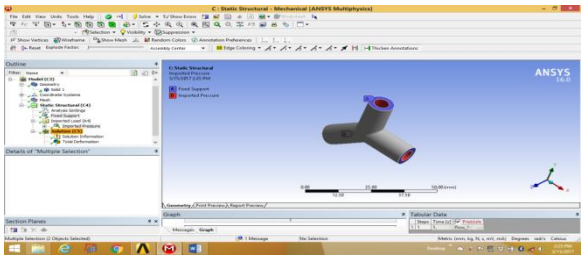

Figure 3.28 Structural Analysis

Under analysis settings, solver expects user inputs as constraints as fixed support has been used and imported pressure load inner surface of y-duct has been assigned. With these boundary conditions, the solver executed to simulate the structural analysis for total deformation and equivalent stresses.

4. Discussion of Results

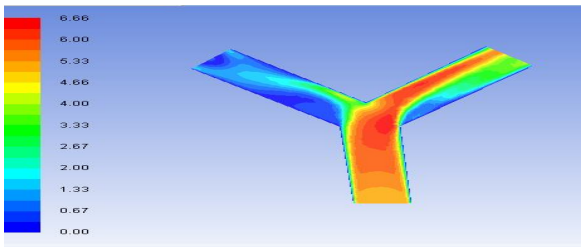

FIGURE 4.1 velocity magnitudes in the plane of computational along z direction

It is observed that velocity of fluid up to junction of y-duct is uniform and at the location of turning, the flow left side taking place on upper portion creating turbulence at bottom portion of right side cylinder. However there exists small quantity of flow left side cylinder upper portion and at rest of the place flow is creating strong turbulence.

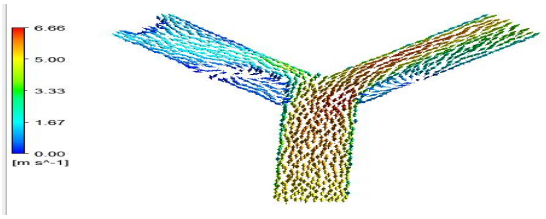

FIGURE 4.2 Backflow occurring in y-duct vector plot

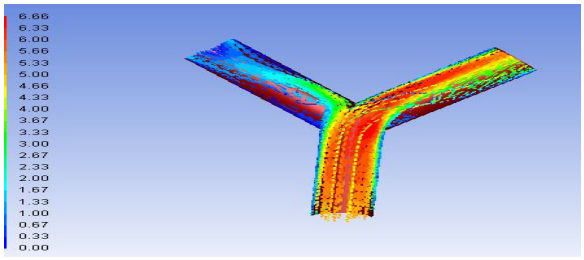

FIGURE 4.3 Flow Recirculation

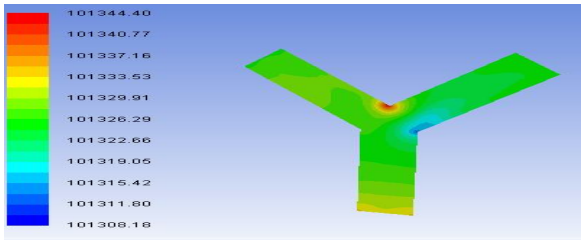

FIGURE 4.4 Absolute pressure variations in the plane

The pressure on Pascal's indicates lowest at junction location of Y-duct and maximum exhibits at the location where three pipes in x y z direction meeting. For considered inlet velocities, the pressure drop across inlet and exit can be estimated using reports/surface integrals/mass averaged quantity inlet to outlet1 is as follows.

Absolute Pressure	(Pascal)
Inlet	101333.07
out1	101325.00

Similarly the pressure drop across inlet to out2 of y-duct pipe estimated with the help of reports/surface integrals/mass weight average/absolute pressure as

Absolute Pressure	(Pascal)
Inlet	101333.07
out2	101325.00

The pressure drop across inlet and exit location for the considered flow velocity and pressure comes to be 8pascals.The absolute pressure on wall surface in terms of Pascal's are shown in Figure 4.5

Where in at inlet pressure is high and decelerates up to junction point forming right side cylinder low pressure and generating high pressure on left side cylinder upper portion. The pressure distribution is non-uniform requires geometrical or flow conditions correction

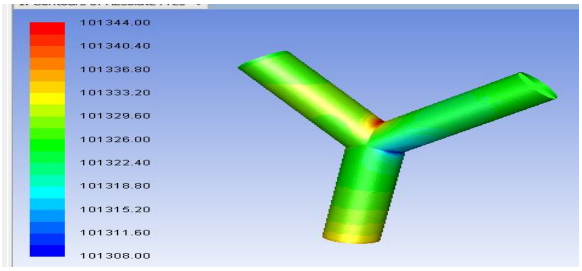

FIGURE 4.5 Absolute pressures on wall surface in terms of Pascal's

When the particles are added to flowing with the same velocity, the trajectories of particles in case of 1 micron follows the flow motion. However 10 micron size particles injected from the inlet location is shown in Figure 4.6

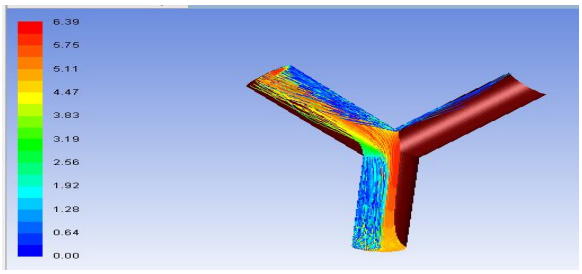

FIGURE 4.6 Inlet locations

The trajectory of particles from inlet with higher velocity travels up to junction location leaves through left side cylinder of y-duct. Due to exchange of mass/momentum the particles have lost inertia and exhibits lower velocities and diverts on the both side of the cylindrical tube. Concentration of higher velocity may lead to erosion problem of Y-duct pipe. The trajectories of 100 micron size particles on particle velocity released from inlet location of the y-duct is shown in the Figure 4.7

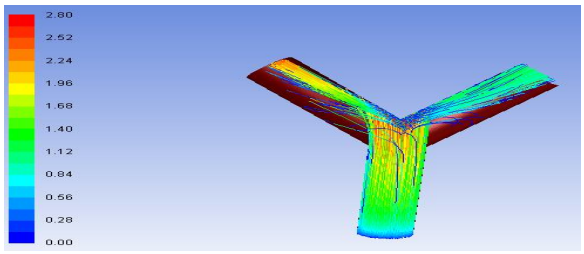

FIGURE 4.7 velocity released from inlet location of the y-duct

Higher size particle follows with fluid velocity at inlet location and increases its velocity upto junction point and then diverts towards both the cylindrical tubes in x and y directions. However, the particle concentration is higher on left side cylindrical tube than right side cylindrical tube. In this plot, the particle higher velocity concentrates at junction location of y-duct tube.

The effect of particles in flowing fluids through its trajectories determines the possible location of erosion damage which can be obtained through tracks in Figure 4.8

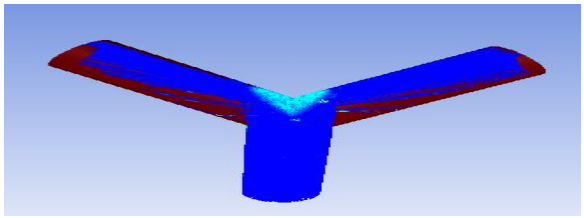

FIGURE 4.8 Erosion damage which can obtain through tracks

For the fixed support of y duct ends, pressure load mapping from CFD result file analysis has been carried out to predict the structural deformations and equivalent stresses on the component in the Figures 4.9& 4.10.

The deformation is though small and variation in terms of maximum taking place wall surfaces of the y-duct and minimum is occurring at end locations of cylindrical tubes.

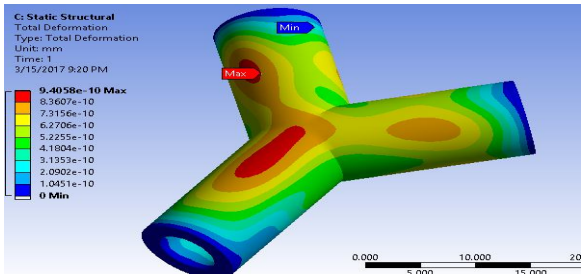

FIGURE 4.9 structural deformations and stresses

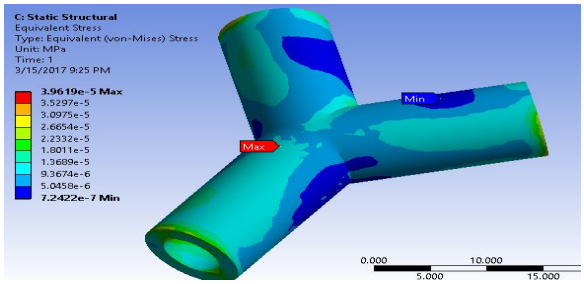

FIGURE 4.10 structural deformations and stresses

Equivalent stress shown on mega Pascal's shows on the deformed body taking place at junction location and minimum occurs on left cylinder top portion and right side cylindrical surfaces whereas the same has been taken place bottom side of flow direction cylinder. Equivalent stress variation on component surface indicates that stresses are below yield and safe.

5. Conclusions:

The problem of y branch duct for transport of fluids in pipeline applications are geometrically constructed using bottom-up approach. In order to understand the pressure drop and flow fluid especially when it is diverting both the sides of cylinders, modern computational tool CFD is employed. The pre-requisites for geometrical input, computational grid required are generated using commercial software's Altair Hypermesh in three dimensional environments. For the considered flow velocities at inlet, working pressure the computational grid has been simulated for turbulent flow and several results in terms of velocity magnitude, vectors, flow path and absolute press in the plane of computational domain has been obtained and explained graphically. The variations and highlights of each variable are discussed at length in the results and discussions.

It is of interest when the flowing fluid suspended particles especially the problem is viewed from the point of two phase flow applications; discrete phase model available in fluent software is employed. After successful simulation, different types of particle trajectories released from the inlet of computational domain tracked and explained graphically. The particle trajectories on velocity scale provides higher velocity regions which may also erosive nature is also computed and shown graphically.

The pressure fluctuations, unequal velocity distributions, particle trajectories, the component may become weaken from structural aspects. To examine the component deformation is small and equivalent stresses are below yield, static structural analysis has been carried out and interpreted the output variables physically through graphical illustrations.

5.2 Future scope of work

The problem of y branch duct for flow distribution, particle trajectories and structural aspects provide valuable basis for refining the work. One of the problem noticed when the flow is along flow direction when diverting through other cylinders it is taking only one side. This needs improvement if the y duct is to be properly designed one. This aspect can be refined through flow simulation with different mesh type elements and size of computational grid.

The study also reports the particle trajectories and impact parameters indicate the erosion location at junction location which needs to be improved. In order to improve problem requires number of simulations for different mass flow and velocity and pressures to predict realistic pressure drop with realistic measurement data. It is also essential reduce

presence of flow recirculation so that low pressure zones and high velocity regions in the duct chamber can be minimized.

The problem also finds air-conditioning and ventilation ducts which are subjected to thermal gradient. With the suitable flow conditions future scope of work for numerical simulations to estimate wall heat transfer, temperature profiles are essential using the CFD solver. To complete the analysis, thermal stress with the mapping of fluid pressure load acting on the y duct wall surface provide design solutions to understand the deformations and equivalent stresses prevailing on the y duct external surfaces. Considerations of more complex configurations of y duct with down ward components like a valve in piping network also forms the future scope of work. Analysis procedure for different physical aspects along with model construction and computational mesh generation will form valid reference for future research.

6. REFERENCES

1. Romero-Gomez, et al .*Mixing at Cross Junctions in Water Distribution Systems - Part I. A Numerical Study*, ASCE Journal of Water Resources Planning and Management, pp. 284-294. 2008

2. Austin, R. G., et.al *Mixing at Cross Junctions in Water Distribution Systems – Part II. An Experimental Study*, ASCE Journal of Water Resources Planning and Management pp. 295-302, 2008

3. Aslam A. Hirani et al. *CFD Simulation and Analysis of Fluid Flow Parameters within a Y-Shaped Branched Pipe* Journal of Mechanical and Civil Engineering Volume 10, Issue 1 PP 31-34, 2013

4. Chen C et. al *A comparison between alternative methods for gas flow and performance prediction of internal combustion engines* SAE 921734 Warren dale, 1992

5.Mitianiec,W, *Determination of thermodynamic gas parameters in branched pipes in internal combustion engines*, Journal of Physics: Conference Series 530, 2014

6. Shirish L. K et.al *Literature Review –on CFD Study of Producer Gas Carburetor IJSRD* - International Journal for Scientific Research & Development Vol. 2, Issue 05, 2014

7. T. R. Anil, et. al .*CFD Analysis of Mixture Flow in a Producer Gas Carburetor* International Conference on Computational Fluid Dynamics, Acoustics, Heat Transfer and Electromagnetic CFEMATCON- 06, 2006.

8. Beach R et.al *Measure Guideline: Optimizing the Configuration of Flexible Duct Junction Boxes* NREL Technical Monitor: Michael Gatwick, internal report 2014

9. Rutkowski, H. Manual D—Residential Duct Systems, 3rd edition, Version 1.00. Arlington, VA: Air Conditioning Contractors of America. 2009

10. Hein, A G, *Electro-static Precipitation Dust Movement and Gas Flow optimization*, 8th International Conference on ESP, Ala-bema, USA, 2001.

11. Gallimberti, *Recent Advancements in the Physical modeling of Electro-static Precipitators*, Journal of Electrostatics, Vol 43, pp 219-247, 1998

12. Beach, R et.Al*CFD Analysis of Flexible Duct Junction Box Design*. National Renewable Energy Laboratory. DOE/GO-102013, 2013.